Top Quark Spin and Polarization Properties in Searches for New Phenomena with the CMS Detector at the LHC

Dissertation

zur Erlangung des Doktorgrades

an der Fakultät für Mathematik, Informatik und Naturwissenschaften

Fachbereich Physik

der Universität Hamburg

vorgelegt von

Afiq Aizuddin Anuar

aus Teluk Intan, Malaysia

Hamburg

2019

Gutachter der Dissertation:	Prof. Dr. Christian Schwanenberger
	Prof. Dr. Peter Schleper
	Dr. Mark Owen
Gutachter der Disputation:	Prof. Dr. Christian Schwanenberger
	Prof. Dr. Peter Schleper
	Dr. Alexander Grohsjean
	Prof. Dr. Georg Weiglein
	Prof. Dr. Günter Sigl
Datum der Disputation:	13. Dezember 2019
Vorsitzender des Prüfungskommission:	Prof. Dr. Günter Sigl
Vorsitzender des Fach-Promotionsauschusses Physik:	Prof. Dr. Günter Sigl
Leiter des Fachbereichs Physik:	Prof. Dr. Wolfgang Hansen
Dekan der Fakultät MIN:	Prof. Dr. Heinrich Graener

Eidesstattliche Versicherung / Declaration on oath

Hiermit erkläre ich an Eides statt, dass ich die vorliegende Dissertationsschrift selbst verfasst und keine anderen als die angegebenen Quellen und Hilfsmittel benutzt habe.

I hereby declare, on oath, that I have written the present dissertation by my own and have not used other than the acknowledged resources and aids.

Hamburg, den 25. September 2019 Afiq Anuar

Was yea erra chs ieeya, en sol anw yeal.

– Haruka Shimotsuki, `EXEC_VIENA/.`

ACKNOWLEDGMENT

The author has received the support of many people towards the completion of this work. This part of the thesis is dedicated to them. Only those whose actions have impacted the author most directly are named; it does him pain to have to omit the rest for want of space.

The author wishes, foremostly, to thank his DESY supervisors Alexander Grohsjean and Christian Schwanenberger. The breadth and depth of their skill and knowledge continue to amaze, and serve as a sobering reminder of how much there remains to learn. Just as great are their kindness and patience in imparting them, even when the other end of the communication is not necessarily the brightest student out there. Their passion for the field also shows in every single discussion; they have always been frank and direct to the point.

Second in line is Gerrit Van Onsem, with whom the author has worked on the A/H analysis. The experience has been, on the whole, smooth and a great pleasure, no doubt due to him having been a fantastic colleague. Also to thank is Kelly Beernaert, with whom the author has not managed to enjoy as much direct interaction due to her having worked in a separate parallel analysis, but nonetheless has taught the author a great deal. He wishes only the best for the two in their current and future endeavors.

The author is also thankful to the remaining members of the A/H, $\mathrm{t\bar{t}}$ spin correlation and EGM HLT teams, with whom the achievements documented in this work are shared. In particular, the author thanks Andrey Popov, Jacob Linacre and Sam Harper for their support.

In addition, the author is indebted to Stephanie Beauceron, Andreas Meyer and the others that have been involved in offering him a PhD candidacy. It was a chance unlike any other, which had given the author a great many wonderful experiences.

Finally, the author expresses his gratitude to Nur Zulaiha Jomhari, together with whom he has spent the larger part of life throughout the PhD. It would have been different without her, perhaps inconceivably so. She has been very significant in making the work what it is.

ABSTRACT

In this work, a search for heavy pseudoscalar and scalar (A/H) Higgs bosons decaying to top-anti-top quark pairs ($t\bar{t}$) and a measurement of top quark polarization and $t\bar{t}$ spin correlation are presented, performed using 35.9 /fb of data recorded by the CMS experiment in 2016. The dileptonic $t\bar{t}$ final state is investigated in both analyses.

The A/H Higgs boson search exploits the 2-dimensional spectrum of $t\bar{t}$ invariant mass and an angular observable sensitive to both the spin and parity of the $t\bar{t}$ system. The search probes mass and relative decay width ranges of 400 - 750 GeV and 0.5% - 50%, respectively. An excess consistent with the A(400 GeV, 5%) signal hypothesis is observed with a local significance of 4σ in the dileptonic channel and 3.7σ in the combination of dileptonic and semileptonic channels. The global significance of such an excess is found to be 2σ. Exclusion regions on the coupling modifier of the A/H to top quarks are derived. These results are converted into exclusion regions in the context of a supersymmetric model, the hMSSM, and are given in the parameter space m_A-$\tan\beta$.

In the spin correlation measurement, the distributions of all independent observables that are directly sensitive to the elements of top quark polarization vector and $t\bar{t}$ spin density matrix are measured, unfolded to the level of generated partons, and extrapolated to the full phase space. In addition, the distributions of two angles between the charged leptons in the laboratory frame, which are, however, only indirectly sensitive to the $t\bar{t}$ spin correlations but can be extracted with excellent experimental resolution, are measured. An overall good agreement with the standard model is observed. However, there is some tension between the data and predictions in the distribution of the azimuthal gap between the charged leptons in the laboratory frame. The measurements are used to constrain anomalous contributions within an Effective Field Theory framework.

ZUSAMMENFASSUNG

In dieser Arbeit wird eine Suche nach pseudoskalaren und skalaren (A/H) Higgs-Bosonen präsentiert, die in Top-Antitop-Quark-Paare ($t\bar{t}$) zerfallen. Außerdem wird eine Messung der Top-Quark-Polarisation und der $t\bar{t}$ Spinkorrelation vorgestellt. Hierbei wird ein Datensatz von 35.9 /fb verwendet, der 2016 vom CMS-Experiment aufgenommen worden ist. In beiden Analysen wird der dileptonische $t\bar{t}$-Endzustand untersucht.

In der Suche nach A/H-Higgs-Bosonen wird das zweidimensionale Spektrum der invarianten $t\bar{t}$-Masse und einer Winkelobservablen, die sensitiv auf den Spin und die Parität des $t\bar{t}$-Systems ist, analysiert. Es werden Massenbereiche von 400 - 750 GeV beziehungsweise relative Zerfallsbreiten von 0.5% - 50% untersucht. Ein Überschuss, der mit einer Signalhypothese eines A(400 GeV, 5%)-Teilchens konsistent ist, wird mit einer lokalen Signifikanz von 4σ im dileptonischen Kanal beziehungsweise einer lokalen Signifikanz von 3.7σ bei der Kombination von dileptonischem und semileptonischem Kanal beobachtet. Die globale Signifikanz des Überschusses beträgt 2σ. Es werden Ausschlussregionen auf die Stärke der Kopplungen zwischen dem A/H und dem Top-Quarks bestimmt. Diese Resultate werden in Ausschlussregionen in einem supersymmetrischen Modell, dem hMSSM, als Funktion von m_A und $\tan\beta$ übersetzt.

Bei der Messung der Spinkorrelation werden Verteilungen aller voneinander unabhängingen Observablen, die direkt sensitiv auf die Elemente der Top-Quark-Polarisations-Vektoren und der $t\bar{t}$-Spin-Dichte-Matrix sind, gemessen, auf das Niveau generierter Partonen entfaltet und auf den vollen Phasenraum extrapoliert. Zusätzlich werden die Verteilungen zweier Winkel zwischen den geladenen Leptonen im Laborsystem gemessen, die zwar nur indirekt sensitiv auf $t\bar{t}$-Spinkorrelationen sind, aber mit einer exzellenten experimentellen Auflösung extrahiert werden können. Eine insgesamt gute Übereinstimmung mit dem Standardmodell wird beobachtet. Allerdings gibt es leichte Unterschiede zwischen den Daten und der Vorhersage bei der Messung des Azimuthalwinkels zwischen den beiden geladenen Leptonen im Laborsystem. Die Messungen werden dazu benutzt, Einschränkungen an anomale Beiträge im Rahmen einer effektiven Feldtheorie zu erhalten.

CONTENTS

CHAPTER

1

INTRODUCTION

Curiosity has been the driving force of much of the activities of mankind. We seek to understand and explain things, and that includes the natural world we find ourselves in. One direction for such a pursuit is to understand the building blocks of the world at the most fundamental level, in which significant progress has been made. Our latest and most thorough understanding of matter and interactions between them is summarized in a theory that is referred to as the standard model (SM). It is rather amusing how dull a name this is, especially considering the vast array of phenomena that it describes. Furthermore, it has made predictions that are later experimentally verified and withstood all attempts to supersede it so far.

This work presents two additional attempts at finding a crack in this extremely tough theory. Both are focused on the properties of the top quark as a way forward. The first attempt is a search for new neutral particles that are not part of the SM. They are assumed to interact preferentially with particles of high mass, making the top quark - the heaviest member of the SM - an ideal way to probe for their existence. As these particles have definite masses, the search strategy involves scrutinizing the spectrum of invariant mass of top quark pairs. Whether or not the new particles exist is then a question of finding local modifications in this spectrum with respect to the shape predicted by the SM. In order to enhance this modification, a second observable that expresses the degree to which the spins of a pair of top quarks are aligned to each other is used, exploiting the fact that this alignment is different for the new particles and the SM.

The degree to which the spins of top quarks are aligned is known as spin correlation. In addition to the aforementioned observable, the alignment of top quark spins along arbitrarily chosen directions is also studied. Appropriately chosen, it can reveal much insight about the underlying processes that produce the top quark pairs. For example, defining the reference axes to be the directions of motion of the top quarks, an observable that expresses the relative contribution of like- and unlike-helicity top quark pairs can be defined. This observable is invaluable in testing the SM prediction that at low invariant mass, top quark pairs are

produced dominantly with like helicities. In the same framework, one can also study the polarization of top quarks, which also offers important insights into their production dynamics.

Thus we see that the measurement of top quark polarization and top pair spin correlation is at once a stringent test of the SM and a very powerful probe for the physics beyond. This is the subject of our second attempt. Here we relax the assumption that the new physics is manifested as new particles that can be directly produced. It may be new particles that are too heavy and therefore are out of our reach, or it might be that top quarks interact in more ways than those dictated by the SM. This requires that we work in a framework that can flexibly extend the SM. We do so here - the framework of choice is one that allows for all possible contributions as long as the symmetries of the SM is respected. In a sense, this approach is the opposite of the one we adopt in the first case, where the new particles and interactions are completely specified right from the beginning.

This work is structured as follows. Chapter 2 presents a brief overview of the theoretical aspects that form the foundation for both the search and the measurement. Chapter 3 and Chapter 4 are dedicated to the experimental aspects that make our analyses possible - the collider, the detectors, how the data is recorded and the reconstruction steps to combine the detector information into sets of analyzable objects. Chapter 5 focuses on electron reconstruction at the trigger level and the necessity of defining a proper selection criteria in order to be able to record all events of interest. Chapter 6 on the other hand discusses aspects that are common to both the analyses, which includes the dataset used, the event selection criteria and the treatment of systematic uncertainties. Chapter 7 then discusses the first analysis - a search for heavy scalar bosons decaying to top quark pairs. Chapter 8 is where the measurement of top quark polarization and top pair spin correlation is discussed. Finally, this work is summarized in Chapter 9.

CHAPTER

2

THEORETICAL OVERVIEW

Contents

The majority of works within the field of experimental sciences are guided by a theoretical foundation and this work is no exception. This chapter is dedicated to the discussion of this foundation. First, an overview of the SM of particle physics is given. The discussion then narrows down to facets of SM that are directly relevant to this work; the physics of top quark production. We then enter into the more speculative realm of physics beyond the SM, where several attempts to extend the SM and their impact to the SM top quark production are discussed. The chapter is closed with a discussion on the formalism of spin correlation in top pair production, which is of central importance in this work.

2.1 The Standard Model of Particle Physics

The SM is the highly successful description of matter particles and interactions between them at energy scales of interest in this work. As a quantum field theory, its fundamental objects are the fermion and boson fields representing matter and interaction respectively. Three types of interaction are described by the SM; the electromagnetic, weak and strong interactions, with the former two having been combined into one single electroweak (EWK) interaction [1, 2]. The particle content of the SM is summarized in Figure 2.1.

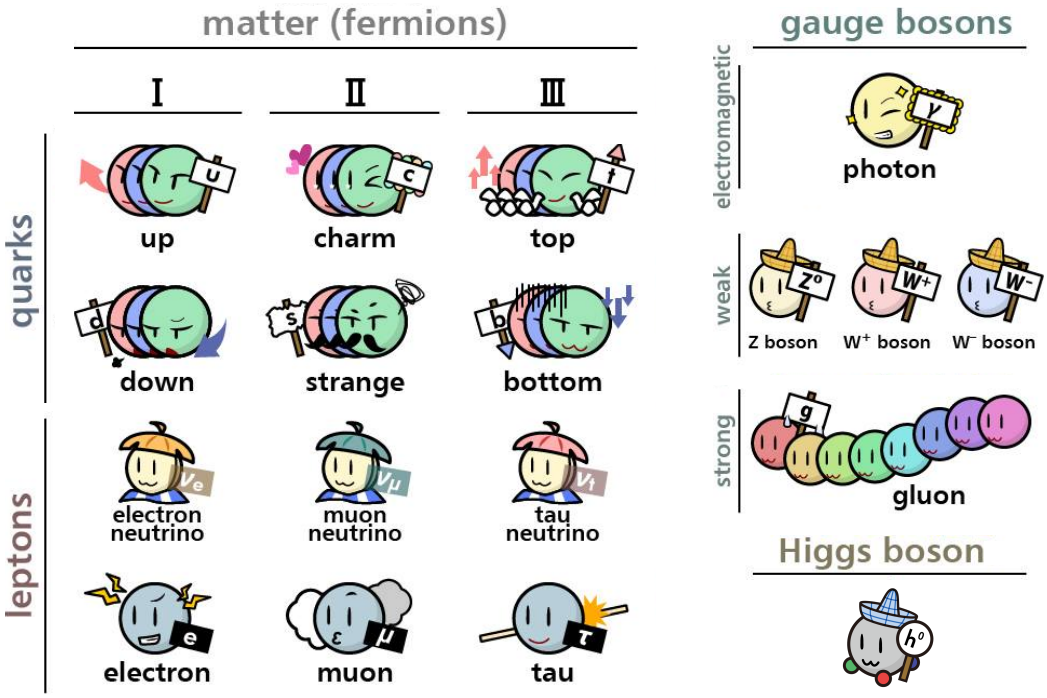

Figure 2.1: The particle content of the SM. Figure is taken from Reference [3].

The matter particles, i.e. spin 1/2 fermions, are divided into quarks and leptons; the distinction is that quarks interact through the strong interaction while leptons do not. The left-chiral quarks and leptons are assigned to pairs referred to as up- and down-type respectively, only members of a given pair can couple to the W boson. There are six such pairs corresponding to three generations of quarks and leptons; two fermions that differ only in their generation share all of their properties except mass. A fermion of a particular generation and position in the pair is said to be of a particular flavor - for example, the top quark is the up-type quark of the third generation i.e. the heaviest up-type quark. In the SM, all fermions are of the Dirac type, meaning they are associated with antiparticles that have the same properties except for their charges that flip in sign. In this work, the word particles will include the antiparticles unless mentioned otherwise. The values of the parameters of the SM such as the fermion masses can be found in Reference [4].

2.1.1 Electroweak interaction

The EWK interaction is mediated by four vector bosons $W^{\pm}$, Z and γ. All SM fermions couple to the W and Z bosons, while neutrinos, being electrically neutral, do not couple to the photon. The theory belongs to the gauge group SU(2) $\times$ U(1), whose fundamental fields are $W^1_\mu, W^2_\mu, W^3_\mu$ and B_μ; the physical states $W^{\pm}$, Z and γ are orthogonal combinations of these fundamental fields.

It is worth noting that the W boson couples to the flavor eigenstates of the fermions, which in general are not the same as their mass eigenstates. The two eigenstates are related through a mixing matrix, which for quarks (defining the up-type flavor and mass eigenstates to be the same) is called the CKM matrix, denoted as V [5]. As this matrix is largely diagonal, the couplings of an up-type quark from one generation and down-type quark from another to the W boson is suppressed. In the original version of the SM, the neutrinos are assumed to be massless, therefore there is no corresponding mixing in the leptonic sector. As neutrinos are now known to be massive [6], one of the approaches to accommodate this fact is to add also for them the right-chiral singlets, which amounts to having neutrinos acquire their masses in the same way as other SM fermions. A mixing matrix in the leptonic sector is then obtained, it is called the PMNS matrix [7].

2.1.2 Strong interaction

The strong interaction is mediated by gluons. As the name implies, at low energy scales it is much stronger than the other interactions described by the SM. The theory describing this interaction is called the quantum chromodynamics (QCD); it belongs to the SU(3) gauge group. There are three different 'colors' in QCD; they play a similar role as the electric charge in electromagnetism.

Unlike photons, gluons carry the charge of the interaction that they themselves mediate, allowing them to also interact between themselves. This makes QCD considerably more complicated to analyze, but it also brings about interesting consequences, one of them being quark confinement. This refers to the fact that at low temperature quarks can never be observed as isolated particles. Instead, only color-neutral bound states called hadrons are observable. Going to a higher energy scale, the asymptotic freedom is observed; where the strong interaction becomes gradually weaker and quarks behave as free particles. The QCD coupling α_s is said to 'run', i.e. α_s is not a constant but is instead a function of momentum transfer. For perturbative QCD calculations to be performed, α_s has to be small, which is the case only at high momentum transfer, so we rely on the factorization theorem to split the low- and high-scale aspects of the problem [8].

2.1.3 Higgs mechanism

The renormalizability of the EWK theory requires that all its gauge bosons are massless [9], which is in blatant contradiction to the experimental observations [10–13]. This is

resolved by adding a complex scalar SU(2) doublet to the theory [14–16]:

$$\phi = \begin{pmatrix} \phi^+ \\ \phi^0 \end{pmatrix} = \frac{1}{\sqrt{2}} \begin{pmatrix} \phi^1 + i\phi^2 \\ \phi^3 + i\phi^4 \end{pmatrix} \tag{2.1}$$

with real ϕ^a corresponding to the degrees of freedom of the doublet. The potential of this field $V(\phi)$ is given as:

$$V(\phi) = \mu^2 \left|\phi^\dagger \phi\right| + \lambda \left|\phi^\dagger \phi\right|^2 \tag{2.2}$$

with $\lambda > 0$ to ensure that the potential has at least one minimum. When $\mu^2 < 0$, the minimum of this potential occurs at nonzero values $v = \pm\mu^2/\lambda$. The minimum is also called the vacuum expectation value (VEV). As the direction of the VEV in SU(2) space is unspecified, it can be chosen such that:

$$\langle\phi\rangle = \frac{1}{\sqrt{2}} \begin{pmatrix} 0 \\ v \end{pmatrix} \tag{2.3}$$

where v refers to the VEV. This choice, through the kinetic terms of the ϕ fields, gives mass only to the W and Z bosons - leaving the photon massless - in accordance with experimental constraints. Since the W mass can also be obtained from the Fermi constant G_F as $\mathrm{m}_\mathrm{W}^2 = \sqrt{2}g^2/8G_\mathrm{F} = v^2g^2/4$, with g being the SU(2) coupling, the VEV is estimated to be about 246 GeV.

The Higgs doublet can also be used to generate fermion masses. This is achieved through a Yukawa interaction between the Higgs and fermion fields [17], which provides the latter with masses proportional to the VEV and the Yukawa coupling Y_f between the Higgs and the fermion; $\mathrm{m}_f = vY_f/\sqrt{2}$. For this reason, the Higgs boson interacts more strongly with heavier fermions, a fact that we will be relying on later in this work.

The experimental discovery of a boson compatible with the Higgs by the ATLAS and CMS collaborations was an important vindication of the Higgs mechanism [18, 19]. Subsequent measurements of its properties through multiple decay channels indicate that it is indeed, or is very similar to, the Higgs boson as predicted by the SM [20, 21]. As of 2019, the world average of the measured mass of this boson is 125.10 ± 0.14 GeV [4].

2.1.4 Going beyond

While the SM is a highly successful theory that has withstood all experimental tests so far, it is not seen as the final description of the physical world. For one, it does not describe gravity, which is the dominant interaction at both the smallest and largest distance scales. It is also completely silent regarding the nature of dark matter and dark energy, which are known to exist from astronomical measurements [22, 23]. For these reasons there are many attempts to extend the SM to a larger framework. Reference [24] contains a general discussion on such beyond the SM (BSM) frameworks that are available to date.

2.2 Proton-Proton Collisions

The proton p is a hadron consisting of three valence quarks uud embedded in a sea of gluons that are consistently interacting and splitting into quark-antiquark pairs. Collectively, constituents of the proton are referred to as partons. The number of partons that can be found within the proton is not a constant as it depends on the scale of momentum exchanged between the proton and a probe during the scattering process.

Proton-proton collisions are studied in this work. Although they can be classified into many different categories, we will be focusing on a special class of inelastic scattering where the momentum transfer is large. Such collisions are referred to as hard scattering events. Within this regime, the collinear factorization theorem is valid [8], meaning the methods of perturbative QCD are applicable. The scale that separates the hard and soft part of the description of a reaction pp $\rightarrow X$ is called the factorization scale μ_{F}. The total inclusive cross section of this reaction is given by:

$$\sigma^{\mathrm{pp}\rightarrow X} = \sum_{i,j} \int \mathrm{d}x_i \mathrm{d}x_j \, f(x_i,\, \mu_{\mathrm{F}})\, f(x_j,\, \mu_{\mathrm{F}}) \times \sigma^{ij\rightarrow X}(\hat{\mathrm{s}},\, \mu_{\mathrm{F}},\, \mu_{\mathrm{R}}) \tag{2.4}$$

where x_i is the ratio of the momentum of parton i with respect to the proton momentum, and $f(x_i, \mu_{\mathrm{F}})$ is its associated parton distribution function (PDF) that expresses the probability of finding the parton with momentum fraction x_i at some scale μ_{F}. In practice, PDFs are derived from fits to experimental measurements [25, 26]. $\sigma^{ij\rightarrow X}$ is the partonic cross section for the final state X that depends on the partonic center of mass-energy $\hat{\mathrm{s}} = x_i x_j \mathrm{s}$, with s being the pp center of mass-energy, and the scale choices μ_{F} and μ_{R}, with the latter being the renormalization scale that needs to be introduced when dealing with the infinities that appear in higher order calculations. The choice of μ_{R} and μ_{F} are both arbitrary. The sum runs over all initial state partons i and j.

The partonic cross section $\sigma^{ij\rightarrow X}$ is calculated within perturbative QCD from the matrix elements (MEs) of all contributing diagrams evaluated at a given order. In this work, the word order, when discussing the accuracy of a ME calculation, is used as follows. The leading order (LO) accuracy refers to the set of diagrams with the lowest power of the relevant couplings that gives a nonzero contribution to the cross section. The next-to-LO (NLO) and next-to-NLO (NNLO) are then simply the set of diagrams that involve successively higher powers of the couplings. Due to the complexity of the phase space integrals involved, MEs are often evaluated using Monte Carlo methods. Dedicated tools are available for this purpose, including but not limited to POWHEG [27] and MG5_aMC@NLO [28].

For a realistic simulation of pp collision events, the ME generator has to be interfaced with a parton shower (PS) program. The PS perform the initial- and final-state radiation (ISR and FSR) on the ME partons and perform the backward and forward evolution from them to the initial protons and the final state hadrons [29]. As the partonic evolution series contains terms that are of similar magnitude at each order, it is necessary that the entire series is considered without any truncation to a given finite order. A technique known as resummation is used for this purpose up to some finite logarithmic accuracy [30]; the lowest

logarithmic accuracy is known as the leading logarithm (LL), followed by next-to-LL (NLL) and so on. One common PS tool that is used in this work is PYTHIA8 [31], which also handles the treatment of the interactions of spectator partons in the proton, known as the underlying event (UE). Since the MEs can also be evaluated for processes where additional partons are produced, a scheme has to be defined to correctly assign the contributions as belonging to the ME or to the PS. This is achieved by defining a boundary in the interface between the two, where the PS handles only the emission of additional partons below a certain momentum scale. This procedure is known as merging. Due to the different subtleties involved when virtual higher-order corrections are included, different merging schemes are used at LO [32] and NLO [33].

2.3 The Top Quark in the Standard Model

The top quark couples to all the gauge bosons in the SM, providing multiple means of its production in pp collisions. As a strongly interacting particle, it is produced predominantly in pairs through processes involving gluons. Its decay proceeds through the EWK interaction, which is also how single top quarks are produced. In this section, the production and decay of top quarks are discussed.

2.3.1 Top pair production

As noted earlier, in pp collisions most of the top quarks are produced in pairs through the strong interaction. At LO, there are two production mechanisms; quark-antiquark annihilation and gluon fusion, which are shown in Figure 2.2. The latter mode is the dominant one, both due to the proliferation of the gluon PDF at low momentum fraction and the suppression of the quark annihiliation diagrams, as they involve antiquarks in the initial state which exist in the proton only as sea quarks. The $t\bar{t}$ inclusive cross section is known up to NNLO + NNLL accuracy to be 832 pb [34]. The total relative uncertainty of this calculation is about 6%, which is dominated by the PDF choice and the value of α_s. The latest measurements of 826 ± 20 pb by the ATLAS collaboration [35] and 803 ± 32 pb by the CMS collaboration [36] are consistent with this prediction.

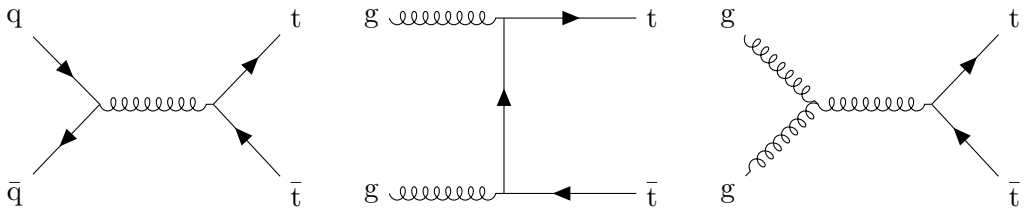

Figure 2.2: Examples of Feyman diagrams of top pair production at LO. The quark annihiliation diagram on the left has two corresponding diagrams where the gluon mediator is replaced by Z/γ. The middle and right diagrams are the gluon fusion diagrams.

2.3.2 Other top production modes

Another production mode is that of single top quark, which proceeds through the interaction of a down-type quark and a W boson. At LO QCD, there are three distinct processes through which this can occur; *s*-channel, *t*-channel and tW-channel, each leading to a different final state. The diagrams of these processes are shown in Figure 2.3.

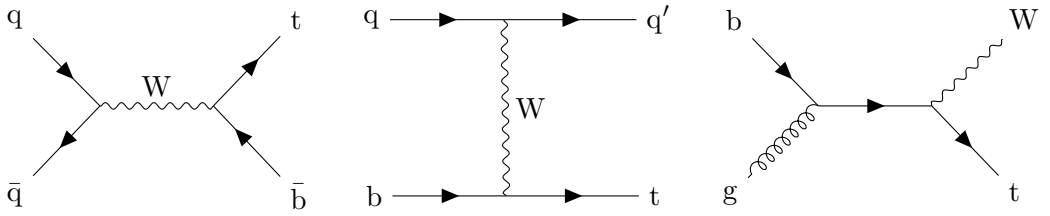

Figure 2.3: Feyman diagrams of single top production modes at LO. From the left they are the *s*-channel, *t*-channel and tW-channel diagrams.

While single top cross sections are significantly smaller than that of $t\bar{t}$ production, they provide a direct sensitivity to the CKM matrix element $|V_{tb}|$, since in this case its measurement can be performed without making any assumptions on the number of quark generations and/or the unitarity of CKM matrix. At the LHC, the *t*-channel process is the most precisely measured one [37], thanks to both its relatively high cross section and its distinctive final state topology [38]. Due to the presence of a W boson in the diagram, single top processes also offer unique possibilities of probing specific scenarios of anomalous couplings that are not possible with $t\bar{t}$ events [39].

Other top production modes are also available at the LHC where more than two top quarks are produced in one event. For example, four top quarks can be produced with diagrams similar to Figure 2.2 together with the emission of a gluon or a Higgs boson which subsequently splits into another top pair. However, these production modes are much rarer due to the higher energy that is needed to produce multiple top quarks and the small value of the products of the couplings involved in the diagrams.

2.3.3 Top quark decay

Due to its large mass of 172.9 ± 0.4 GeV [4] and the fact that $|V_{tb}| \gg |V_{ts}|, |V_{td}|$, the top quark decaying to a W boson and a bottom quark is by far the dominant channel. Its width Γ_t of 1.4 ± 0.2 GeV [4] is far larger than the scale at which non-perturbative effects become important, meaning that it decays before spin decorrelation or hadronization. One consequence of this is that its properties such as spin are transferred to its decay products, providing a unique situation where the properties of a 'bare' quark can be measured.

The $t \to Wb$ decay is of the vector minus axial current (V−A) structure, as with any other reaction involving the W boson. The branching ratio (BR) of the decay to a zero helicity[1] i.e.

[1]Helicity of a particle is the projection of its spin onto the direction of its momentum. Particles with positive helicity is said to be right-handed.

transversely polarized W boson is the leading one at 0.7, followed by the decay to a negative helicity W boson with a BR of 0.3. This is because the couplings of fermions to zero-helicity W boson are equal to Y_f, which for the top quark is higher than its weak coupling. As the BR of $t \to Wb$ channel is almost 100%, the final state topology of $t\bar{t}$ events can be classified by the subsequent W boson decays. The case of both W boson decaying hadronically is called the fully hadronic mode, which occurs about 4/9 of the time since at LO the W BRs are 1/3 and 2/3 into the leptonic and hadronic modes respectively. The semileptonic channel is when one of the W boson decays leptonically and the other hadronically, which occurs also about 4/9 of the time. Finally, the dileptonic channel is when both W bosons decay leptonically with a BR of 1/9.

One remarkable consequence of the top decay structure is that the flight direction of the down-type daughter of the W boson from the top decay is aligned to the direction of top quark spin. This follows from the factorizability of the double differential energy and angular distribution (defined in the top rest frame) into their respective 1D components, which is only true for this daughter [40, 41]. In order to quantify this concept, the spin analyzing power κ is introduced, which takes on the maximum value of 1 if the momentum direction of the daughter is always aligned to the spin of its parent top quark and -1 if it always points opposite to it. As shown in Reference [42], higher-order QCD corrections do not alter the values of κ significantly, making the down-type daughter of the W boson a perfect spin analyzer of the top quark. As in this work we are concerned primarily with the spin properties of top quarks, the dileptonic channel is a natural choice since the charged lepton is both precisely measurable and is the perfect top spin analyzer. The dileptonic channel is also the one with the smallest background contamination due to the presence of two leptons in the event, with the largest background source being the Drell-Yan (DY) process [43]. We will be restricting ourselves to only electrons and muons however, since the short lifetime of the tau lepton means that it is both more challenging to reconstruct and its decay results in a dilution of the spin analyzing power of its daughters.

In anticipation of the following section, one may wonder if the charged lepton remains an ideal spin analyzer in the presence of BSM physics. In general, the answer is no; for example the $t \to H^+b$ decay does not proceed through $V - A$ interaction and so results in a different spin analyzing power of all top daughters. However, the contributions of these effects are heavily constrained [44, 45], and within the range of their allowed values, only a small rescaling of the spin analyzing power is possible. As such, their impact on the observables that depend on κ is only minimal [46, 47].

2.4 Top Quark Beyond the Standard Model

Many BSM theories predict additional top quark production modes at the LHC, one example being that of a heavy Z' boson decaying into $t\bar{t}$ [48], which would manifest itself as a bump in the spectrum of the invariant $t\bar{t}$ mass $m_{t\bar{t}}$. In other models, the interaction between the existing particles are somewhat different compared to what is predicted by the SM. These different interactions can be incorporated as modifications to the existing SM vertices that can be expressed as small contributions of additional operators within an effective field theory

(EFT) that incorporates the SM as a subset. It is worth noting that these different approaches to extending the SM are not mutually exclusive, for e.g. if the Z′ boson is too heavy to be directly produced at the LHC, the $m_{t\bar{t}}$ distribution is not measurable up to the region where the bump appears; instead its presence is manifested as small deviations with respect to SM predictions that can be expressed as nonzero contributions of some EFT operators. In this section we will be focusing on two BSM scenarios that are investigated in this work; the production of heavy Higgs bosons and the aforementioned EFT approach.

2.4.1 Heavy Higgs bosons decaying to top pairs

A possible extension of the SM Higgs sector consists in adding another scalar doublet [49]. Such two-Higgs-doublet models (2HDMs) result in a rich phenomenology due to its prediction of four scalar states in addition to the one required by the SM [50]. The five states are the electrically neutral pseudoscalar A, the electrically neutral scalars h and H (where H is the heavier one by definition) and two charged scalars $H^{\pm}$. If CP conservation is assumed in the extended Higgs sector, then the neutral states of definite parities also correspond to the physical states with definite masses. In this case, two important parameters are α and $\tan\beta$, where α is a rotation angle that diagonalizes the pure scalar mass matrix and $\tan\beta$ is the ratio of the VEVs of the two doublets. There are multiple versions of 2HDMs; one example being the Type-II 2HDM where up-type quarks couple solely to one doublet, and down-type fermions to the other. Denoting the neutral scalar states as Φ, the coupling modifiers of the SM particles to the neutral scalar states relative to their couplings to the SM Higgs boson are given in Table 2.1. Note that in Type-II 2HDM the coupling modifiers of charged leptons are the same as down quark couplings, while neutrinos are assumed to be SM-like and hence do not couple to any of the neutral scalars.

Table 2.1: Coupling modifiers of the neutral scalar states Φ to the SM particles in the Type-II 2HDM relative to their couplings to the SM Higgs boson.

Φ	$g_{\Phi u\bar{u}}$	$g_{\Phi d\bar{d}}$	$g_{\Phi VV}$
A	$\cot\beta$	$\tan\beta$	0
h	$\cos\alpha\,/\,\sin\beta$	$-\sin\alpha\,/\,\cos\beta$	$\sin(\beta-\alpha)$
H	$\sin\alpha\,/\,\sin\beta$	$\cos\alpha\,/\,\cos\beta$	$\cos(\beta-\alpha)$

In this work, we will denote the observed 125 GeV state as h. Since the couplings of this state are compatible with that of SM Higgs boson [20], we will consider only the region of the parameter space where the properties of h approach that of SM Higgs boson. If $\tan\beta$ is small enough and the A/H bosons are sufficiently heavy, their decay into $t\bar{t}$ is the dominant channel due to the large Yukawa coupling of the top quark. Furthermore, their production rates, which are dominated by the gluon fusion diagram, are also enhanced from the enhancement of the top quark loop. On the other hand, at large values of $\tan\beta$ both the top loop contribution and the decay rate into $t\bar{t}$ are reduced, decreasing the relevance of top quarks in exploring the extended Higgs sector. This justifies the choice made in the search for A/H

that is discussed in Chapter 7 to consider only the gluon fusion mode in the signal simulation. The Feynman diagram for this production mode is shown in Figure 2.4. As in this work we are not concerned with channels that do not involve top quarks, we will denote the coupling modifiers of A/H to top quarks as simply $g_{A/H}$.

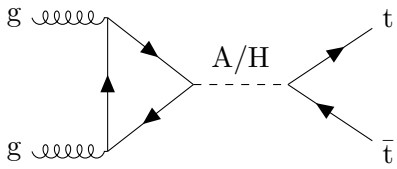

Figure 2.4: Feyman diagram of A/H production through the gluon fusion mode involving a top quark loop at LO and its subsequent decay to $t\bar{t}$.

As the $A/H \to t\bar{t}$ production involves the same initial and final states as gluon fusion SM $t\bar{t}$ production, there is an interference between the two [51, 52]. One of the most striking consequence of this interference is that A/H manifest themselves not as a bump in the $m_{t\bar{t}}$ distribution, but instead as a peak-dip structure near $m_{A/H}$. As illustrated in Figure 2.5, both the position and relative contribution of the peak and the dip depend on $m_{A/H}$, with the peak being more prominent in the low $m_{A/H}$ region. In the $m_{A/H} \in [500, 600]$ GeV range, the peak and dip contribution are roughly of the same size, leaving the total $t\bar{t}$ production rate the same as the SM-only case.

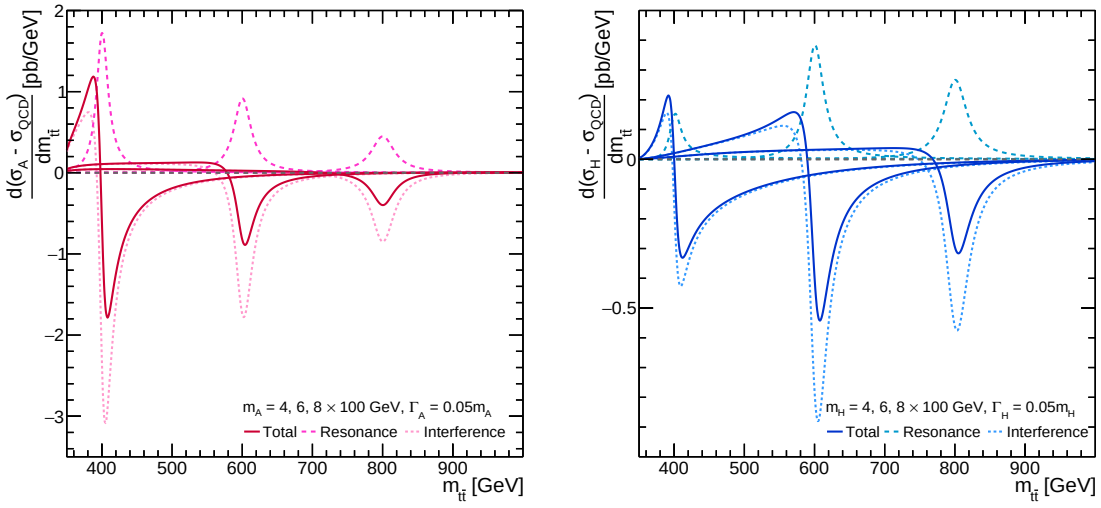

(a) $gg \to A \to t\bar{t}$ (b) $gg \to H \to t\bar{t}$

Figure 2.5: Differential A/H contribution as functions of $m_{t\bar{t}}$ for three different masses, computed using the expressions in Reference [52]. $g_{A/H}$ is assumed to be 1 and the relative total A/H width is fixed to 0.05. The solid line shows the total A/H contribution, while the dashed and dotted lines show the resonance and interference contributions respectively.

One interesting example of the 2HDM is the minimally supersymmetric standard model (MSSM) scenario [53]. In particular, we will be considering the hMSSM, a subset of MSSM that incorporates the existence of the SM Higgs boson at 125 GeV. As is shown in Reference [54], the supersymmetry scale must be high compared to the scales typically probed at the LHC for both the 125 GeV state and low values of $\tan\beta$ to be possible. This implies that radiative supersymmetric corrections have only a small impact, which in turn means that the hMSSM sector can be fully described with only two additional parameters, m_A and $\tan\beta$. The search of $A/H \to t\bar{t}$ is highly relevant also in this subset as discussed in Reference [55].

Due to its relatively unexplored nature, the Higgs sector is considered by some to be related to the dark matter (DM) sector. A popular baseline for DM searches at the LHC is the simplified model [56], where one of the SM-DM mediators may be a pseudoscalar or scalar with couplings to the SM fermions that are Yukawa in structure. In this case, the top quark with its large mass assumes a special role also in exploring the DM sector, and the $A/H \to t\bar{t}$ search performed in this work may be complementary to the DM searches at the LHC that focus on events with a larger invisible component than that which can be attributed to neutrinos.

2.4.2 The effective field theory approach

The search for heavy Higgs bosons discussed earlier is an example of direct searches for BSM physics. The main advantage of this approach is that it is direct - specific kinematical effects, such as the presence of a new particle or particular deviations to some observable distributions, are searched for and if they are discovered, serve as a verification of the underlying theory. However, this requires that such direct searches are possible to begin with, which may not always be the case if for example the new particles are out of our reach or the form of the BSM theory is not yet established. It is helpful to still have a way to probe BSM physics even when direct searches are not possible, preferably in a way such that the results of our investigations can be used to infer the form of the underlying theory. This is the aim of the EFT approach; to quantify the deviations from SM predictions of the interactions of known particles without making further assumptions on the underlying BSM theory beyond the fact that it reproduces the SM in the energy regime it is known to be valid.

The idea of the EFT approach is as follows. Similar to other physical theories that is superseded by the SM, the latter is assumed to be a low-energy effective description of the physical world that is valid up to some energy scale Λ [57]. Physical degrees of freedom above this scale will show up only as virtual corrections to the low energy description that can be integrated out. The effective Lagrangian is then given as a series in powers of Λ:

$$\mathcal{L}_{\text{SM+EFT}} = \mathcal{L}_{\text{SM}} + \sum_{i=5}^{\infty} \frac{C_i}{\Lambda^{i-4}} \mathcal{O}_i \tag{2.5}$$

where $\mathcal{O}_i$ are all the possible operators of mass dimension i that are allowed by the symmetries and particle content of the SM, and C_i their associated Wilson coefficients that express the strength of their contributions. Operators of dimensions higher than 4 are supressed by higher powers of Λ, reducing their impact. This means that for the purposes of expressing the

deviations from SM predictions, it is sufficient to truncate the series to the first few i, similar to what is done in perturbative SM calculations. Only operators with $i = 6$ are considered in this work since the only operator with $i = 5$ is responsible for the mass generation of Majorana neutrinos [58], and the number of operators increases exponentially as i increases. The remaining operators serve as degrees of freedom to be constrained in global fits using as input the results of many different measurements. One example of such a global fit is reported in Reference [59].

2.5 Spin Correlation in Top Pair Production

The spins of top quarks in $\mathrm{t\bar{t}}$ events are in general correlated, the exact degree of which is determined by the production dynamics. For example, when a H is produced with zero orbital angular momentum that subsequently decays into a $\mathrm{t\bar{t}}$ pair, the top and antitop quarks have like helicities in the zero-momentum frame (ZMF) of the H boson from the conservation of angular momentum. This effect is experimentally observable since the top quark spin is transferred to its decay products. In this section, the theoretical formalism behind $\mathrm{t\bar{t}}$ spin correlation is described and the spin correlation observables i.e. the observables with which this effect is measured are introduced.

2.5.1 Theoretical introduction

The ME of $\mathrm{t\bar{t}}$ production is proportional to the spin density matrix R that is given as [60]:

$$R \propto \mathrm{A}\, \mathbb{1} \otimes \mathbb{1} + \mathrm{B}_i^1\, \sigma^i \otimes \mathbb{1} + \mathrm{B}_i^2\, \mathbb{1} \otimes \sigma^i + \mathrm{C}_{ij}\, \sigma^i \otimes \sigma^j \tag{2.6}$$

where $\mathbb{1}$ is the 2×2 identity matrix and σ^i the Pauli matrices. The $\mathrm{B}_i^1\, \sigma^i \otimes \mathbb{1}$ tensor product refers to the spin space of the top quark while $\mathrm{B}_i^2\, \mathbb{1} \otimes \sigma^i$ refers to the spin space of the antitop quark. A determines the total $\mathrm{t\bar{t}}$ production cross section and other spin-independent kinematical distributions e.g. $\mathrm{m_{t\bar{t}}}$. $\vec{\mathrm{B}}^a$ are three-dimensional vectors that are directly related to the relevant top polarization vectors, with indices 1 and 2 used to refer to the top and antitop quarks respectively. C on the other hand is a 3×3 matrix that encodes the spin correlation between the top and antitop quarks. All of A, $\vec{\mathrm{B}}^a$ and C are functions of $\hat{\mathrm{s}}$. $\vec{\mathrm{B}}^a$ and C also depend on the top quark scattering angle θ_{t}^*, which is defined as the angle between the top quark and one of the incoming partons. The scattering plane is defined as the plane containing the top and antitop quarks and the two incoming partons. The momenta of the incoming partons and the outgoing top and antitop quarks are evaluated in the $\mathrm{t\bar{t}}$ ZMF.

Spin quantization axes have to be defined in order to evaluate the relevant theoretical predictions. It is desirable that the axes form a basis as this makes the components of $\vec{\mathrm{B}}^a$ and C independent from each other. In this work, we adopt the basis that is suggested in Reference [46]. The direction of the top quark is taken to be one direction, and is denoted as $\hat{\mathrm{k}}$. This is a natural choice considering it is the helicity axis of the top quark. The other direction, $\hat{\mathrm{r}} = \frac{1}{\sin\theta_{\mathrm{t}}^*}\left(\hat{\mathrm{p}} - \cos\theta_{\mathrm{t}}^* \hat{\mathrm{k}}\right)$ - with $\hat{\mathrm{p}}$ being the direction of one of the incoming partons - is the direction perpendicular to $\hat{\mathrm{k}}$ within the scattering plane. The basis is completed by the direction $\hat{\mathrm{n}} = \frac{1}{\sin\theta_{\mathrm{t}}^*}\left(\hat{\mathrm{p}} \times \hat{\mathrm{k}}\right)$ which is normal to the scattering plane. Before going further, it is worth noting that the gg initial state is Bose-symmetric, which has the effect of forcing

all the coefficients in the $\hat{r}$ and $\hat{n}$ directions to be zero. In order to allow non-zero values for these coefficients, a 'forward' direction is defined for each event by transforming these axes in the following way; $\hat{r} \to \text{sign}(\cos\theta_t^*)\,\hat{r}$ and $\hat{n} \to \text{sign}(\cos\theta_t^*)\,\hat{n}$, exploiting the fact that the scattering angle is Bose-antisymmetric. In Figure 2.6, this $\{k, r, n\}$ coordinate system is visualized for two events with different values of $\cos\theta_t^*$. The scattering plane in the visualization coincides with the page. One sees that while in both cases the coordinate system is right handed, the second case is not obtained through a simple rotation by $\Delta\theta_t^*$ of the first case. In other words, the sign correction to the r and n axes is performed to ensure that the projections of the k and r axes onto a given incoming parton direction always have the same sign without altering the handedness of the coordinate system.

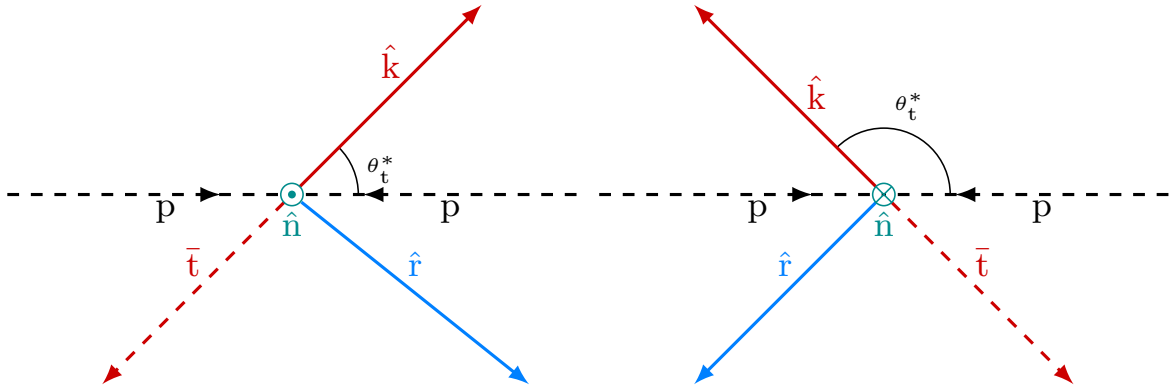

Figure 2.6: Visualization of the $\{k, r, n\}$ system at two different values of the top quark scattering angle. The k-axis points along the top quark momentum in the $t\bar{t}$ ZMF, the r-axis points in the direction perpendicular to the k-axis within the $pp \to t\bar{t}$ scattering plane and the n-axis points transverse to the scattering plane.

Two additional axes are also considered; k^* and r^*. Within each event, they are either parallel or opposite to the k and r axes based on the sign of the difference between the absolute rapidities of top and antitop quarks, $\left|y^t\right| - \left|y^{\bar{t}}\right|$, evaluated in the laboratory frame. These axes are introduced because they provide sensitivities to different combinations of P-odd four-quark operators as compared to the k and r axes, which will be explored in Chapter 8. However, as they are only event-by-event redefinitions of the existing axes, we will continue to refer to the five axes collectively as the $\{k, r, n\}$ coordinate system.

For a given sample of top and antitop quarks in $t\bar{t}$ events, their degrees of polarization with respect to reference axes i and j are given by:

$$\vec{P}^1(i) = \langle 2s_1 \cdot i \rangle, \quad \vec{P}^2(j) = \langle 2s_2 \cdot j \rangle \tag{2.7}$$

where $\vec{P}^1(i)$ is the polarization vector of the top quark with respect to axis i and s_1 is the top quark spin operator. $\vec{P}^a$ are related to $\vec{B}^a$ by:

$$B_i^1 = \kappa\,\vec{P}^1(i), \quad B_j^2 = -\kappa\,\vec{P}^2(j) \tag{2.8}$$

with κ being the spin analyzing power of a chosen spin analyzer. As discussed in Section 2.3, the charged lepton is the best spin analyzer with $\kappa \sim 1$. Equation 2.8 suggests that we ought to choose the spin quantization axes for the antitop quark to be the opposite to the ones that we use for the top quark i.e. $\{-\mathrm{k}, -\mathrm{r}, -\mathrm{n}\}$. By doing so, $\vec{\mathrm{B}}^1 = \vec{\mathrm{B}}^2$ holds when the underlying theory is CP-invariant, which is the case for QCD. Indeed, the main advantage of the $\{\mathrm{k}, \mathrm{r}, \mathrm{n}\}$ coordinate system is that the components of $\vec{\mathrm{B}}^a$ and C have definite properties with respect to discrete symmetries. For example, a positive value of $\mathrm{B}^a_{\mathrm{k}}$ means that the top quarks are produced predominantly right-handed. As such, its value can be large only when the underlying interaction violates the P transformation. Nonzero values of $\mathrm{B}^a_{\mathrm{n}}$ coefficients on the other hand are induced by an interaction that violates the T transformation, which in QCD is induced only by higher-order absorptive terms and is therefore predicted to be small. Going to C, its diagonal elements are given by the coefficients C_{ii}, which are induced by P- and CP-conserving interactions and can therefore be large. The non-diagonal elements on the other hand are given by the sums and differences of the 'cross' coefficients C_{ij}, which are useful for distinguishing between the different scenarios of discrete symmetry violation. For example, only amplitudes that violates CP while respecting P contribute to $\mathrm{C}_{\mathrm{rk}} - \mathrm{C}_{\mathrm{kr}}$, while amplitudes that violate both P and CP contribute to $\mathrm{C}_{\mathrm{nr}} - \mathrm{C}_{\mathrm{rn}}$ and $\mathrm{C}_{\mathrm{nk}} - \mathrm{C}_{\mathrm{kn}}$. Quantitative predictions for the case of $\mathrm{t\bar{t}}$ production at the LHC is available in Reference [46].

Although the $\{\mathrm{k}, \mathrm{r}, \mathrm{n}\}$ system is advantageous, that it requires the momentum of the incoming partons to be known means that it is not experimentally viable. In order to get around this problem, the basis is slightly modified by redefining $\hat{\mathrm{p}}$ to be the direction of the proton beam heading in the +z direction in the laboratory frame; $\hat{\mathrm{p}} = (0, 0, 1)$. In this way we retain the desirable properties of the original $\{\mathrm{k}, \mathrm{r}, \mathrm{n}\}$ system, but with the added advantage that all the necessary ingredients are based on final state observables[2].

2.5.2 Polarization and spin correlation observables

Individual components of $\vec{\mathrm{B}}^a$ and C can be probed by their corresponding leptonic angular distributions. Taking $\hat{\ell}^1$ and $\hat{\ell}^2$ to be the direction of the charged lepton daughter of the top and antitop quarks in their parents' rest frame respectively[3], the four-fold normalized differential cross section, in absence of any kinematic cuts, is given by:

$$\frac{1}{\sigma}\frac{\mathrm{d}^4\sigma}{\mathrm{d}\Omega_1 \mathrm{d}\Omega_2} = \frac{1}{(4\pi)^2}\Big(1 + \vec{\mathrm{B}}^1 \cdot \hat{\ell}^1 + \vec{\mathrm{B}}^2 \cdot \hat{\ell}^2 - \hat{\ell}^1 \cdot \mathrm{C} \cdot \hat{\ell}^2\Big) \tag{2.9}$$

where Ω_a is the solid angle, $\mathrm{d}\Omega_a = \mathrm{d}\cos\theta^a\,\mathrm{d}\phi^a$, with the polar angle θ^1 defined as the angle between the $\hat{\ell}^1$ and a reference axis. The sign in front of C is chosen such that C_{kk} is positive for a sample dominated by like-helicity $\mathrm{t\bar{t}}$ pairs. Integrating over the ϕ^a, a two-fold angular distribution is obtained:

$$\frac{1}{\sigma}\frac{\mathrm{d}^2\sigma}{\mathrm{d}\cos\theta_1^i \mathrm{d}\cos\theta_j^2} = \frac{1}{4}\Big(1 + \mathrm{B}_i^1 \cos\theta_1^i + \mathrm{B}_j^2 \cos\theta_j^2 - \mathrm{C}_{ij}\cos\theta_1^i \cos\theta_2^j\Big) \tag{2.10}$$

[2]The original and modified $\{\mathrm{k}, \mathrm{r}, \mathrm{n}\}$ systems coincide with each other in $2 \to 2$ scattering processes if one of the incoming partons is parallel to the +z proton.

[3]As a reminder, the evaluation is done in $\mathrm{t\bar{t}}$ ZMF, meaning both the charged leptons and top quarks are first boosted into the $\mathrm{t\bar{t}}$ ZMF before the leptons are boosted into the relevant top quark ZMF.

Figure 2.7 shows again the $\{\mathrm{k},\mathrm{r},\mathrm{n}\}$ system in Figure 2.6, but this time with one of the spin analyzers added to illustrate the observables that are to be measured in Equation 2.10. This expression can be reduced to one dimension [46]:

$$\frac{1}{\sigma}\frac{\mathrm{d}\sigma}{\mathrm{d}\cos\theta_a^i} = \frac{1}{2}\left(1 + \mathrm{B}_i^a \cos\theta_a^i\right), \quad \text{and} \tag{2.11}$$

$$\frac{1}{\sigma}\frac{\mathrm{d}\sigma}{\mathrm{d}\cos\theta_1^i\,\cos\theta_2^j} = \frac{1}{2}\left(1 - \mathrm{C}_{ij}\cos\theta_1^i\cos\theta_2^j\right)\ln\left(\frac{1}{\left|\cos\theta_1^i\cos\theta_2^j\right|}\right) \tag{2.12}$$

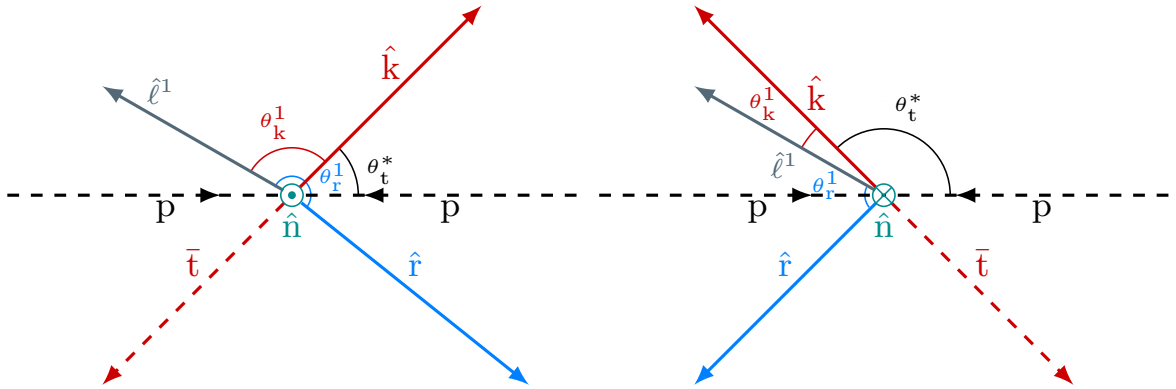

Figure 2.7: Visualization of the $\{\mathrm{k},\mathrm{r},\mathrm{n}\}$ system at two different values of the top quark scattering angle and with one of the spin analyzers illustrated.

Equations 2.11 and 2.12 express the association between the observables and the measured coefficients B_i^a or C_{ij}. In this work, we shall use this association to simplify the notation for the observables; for any measured coefficient B_i^a or C_{ij}, their corresponding observables shall be denoted with a lower case letter. Therefore we have $\mathrm{b}_i^a \equiv \cos\theta_a^i$ and $\mathrm{c}_{ij} \equiv \cos\theta_1^i\cos\theta_2^j$. In this notation, the expression for $\mathrm{c}_{ij} \pm \mathrm{c}_{ji}$ is [61]:

$$\frac{1}{\sigma}\frac{\mathrm{d}\sigma}{\mathrm{d}x} = \frac{1}{2}\left(1 - \frac{\mathrm{C}_{ij} \pm \mathrm{C}_{ji}}{2}x\right)\cos^{-1}|x|, \quad \text{where } x = \mathrm{c}_{ij} \pm \mathrm{c}_{ji} \text{ (for } i \neq j) \tag{2.13}$$

In addition to the 10 b_i^a, 3 c_{ii} and 6 $\mathrm{c}_{ij} \pm \mathrm{c}_{ji}$, in this work three other observables that are sensitive to spin correlation are considered. The first one is $\mathrm{c}_{\mathrm{hel}}$[4], which is the cosine of the full opening angle between the leptons in the $\{\mathrm{k},\mathrm{r},\mathrm{n}\}$ system; $\mathrm{c}_{\mathrm{hel}} = \hat{\ell}^1 \cdot \hat{\ell}^2$. Its expression is:

$$\frac{1}{\sigma}\frac{\mathrm{d}\sigma}{\mathrm{d}\mathrm{c}_{\mathrm{hel}}} = \frac{1}{2}(1 - \mathrm{D}\mathrm{c}_{\mathrm{hel}}) \tag{2.14}$$

where D is the measured coefficient characterizing the $\mathrm{c}_{\mathrm{hel}}$ distribution. As $\mathrm{c}_{\mathrm{hel}}$ amounts to the projection of the top quark spins onto each other, $\mathrm{D} = -\frac{1}{3}\sum_{i\in\{\mathrm{k},\mathrm{r},\mathrm{n}\}}\mathrm{C}_{ii}$. The second one is called $\mathrm{c}_{\mathrm{lab}}$, it is the counterpart of $\mathrm{c}_{\mathrm{hel}}$ in the laboratory frame; $\mathrm{c}_{\mathrm{hel}} = \hat{\ell}^1_{\mathrm{lab}} \cdot \hat{\ell}^2_{\mathrm{lab}}$. The third is $\Delta\phi_{\ell\ell} = \left|\phi^{\ell} - \phi^{\bar{\ell}}\right|$, which is the azimuthal gap between the charged leptons in the laboratory

[4]This observable is also called $\cos\varphi$ in the literature e.g. Reference [46].

frame. While both c_{lab} and $\Delta\phi_{\ell\ell}$ are sensitive to spin correlation effects, the fact that they are evaluated in the laboratory frame means that the normalized distributions are affected not just by spin correlation, but also by any boosts to the top and antitop quarks, which can come either from an inherently high $m_{t\bar{t}}$ in the event, or to the $t\bar{t}$ system as a whole due to the emission of additional partons and also from the inequal momenta of the colliding partons. For this reason their respective analytical forms do not depend only on C, and while this may appear to be a disadvantage, they are measurable with excellent experimental resolution, since their reconstruction requires no boosting to the $t\bar{t}$ ZMF unlike the other observables.

One can extract the values of the relevant coefficients by fitting the measured distributions to the functional forms of each observable (Equations 2.11, 2.12, 2.13 and 2.14) or by computing their expectation values. The coefficients can also be extracted from the distribution asymmetries with respect to their centers. For a given distribution of a bounded observable x, the adopted convention for asymmetry A^x in this work is to compute it from right to left. Let $N^x_{\leftarrow}$ be the total cross section, number or fraction events, function integral etc within the range bounded by the lower bound of the distribution to its center (i.e. half of the sum of its lower and upper bound), and $N^x_{\rightarrow}$ the same quantity within the range bounded by the center and the upper bound. A^x is then given by:

$$A^x = \frac{N^x_{\rightarrow} - N^x_{\leftarrow}}{N^x_{\rightarrow} + N^x_{\leftarrow}} \tag{2.15}$$

Due to the unknown analytical forms of c_{lab} and $\Delta\phi_{\ell\ell}$ in terms of C, they will be characterized by their asymmetries, denoted as $A^{c_{lab}}$ and $A^{\Delta\phi_{\ell\ell}}$, instead of coefficients. Asymmetries of other spin correlation observables are similarly denoted e.g. $A^{c_{hel}}$, $A^{b^1_k}$.

As an aside, it is noted in Reference [46] that it is the sums and differences of B^a_i coefficients that are more directly affected by different discrete symmetries. One may then wonder if it is better to measure the distributions of $b^1_i \pm b^2_i$ and extract these sums and differences instead of considering the individual b^a_i distributions separately. From the measurement point of view the answer to this question is a definite no; the explanation for this is deferred to Chapter 8 where the measurement is discussed in detail. The full list of spin correlation observables and their associated coefficients is given in Table 2.2.

2.6 Bibliography

[1] S. Weinberg, "A Model of Leptons", *Phys. Rev. Lett.* **19** (1967) 1264–1266, doi:10.1103/PhysRevLett.19.1264.

[2] A. Salam and J. C. Ward, "Weak and electromagnetic interactions", *Il Nuovo Cimento* **11** (February, 1959) 568–577, doi:10.1007/BF02726525.

[3] "HiggsTan". https://higgstan.com/.

[4] Particle Data Group Collaboration, "Review of Particle Physics", *Phys. Rev.* **D98** (2018), no. 3, 030001, doi:10.1103/PhysRevD.98.030001.

Table 2.2: Spin correlation observables considered in this work and the coefficients characterizing the shapes of their one-dimensional distributions.

Observable	Coefficient	Normalized distribution	Additional remark
b^1_k	B^1_k	$\frac{1}{2}(1+\mathrm{B}^a_i \mathrm{b}^a_i)$	$\mathrm{B}^a_i = 3\langle \mathrm{b}^a_i \rangle = 2\mathrm{A}^{\mathrm{b}^a_i}$
b^2_k	B^2_k		
b^1_r	B^1_r		
b^2_r	B^2_r		
b^1_n	B^1_n		
b^2_n	B^2_n		
$\mathrm{b}^1_{\mathrm{k}^*}$	$\mathrm{B}^1_{\mathrm{k}^*}$		
$\mathrm{b}^2_{\mathrm{k}^*}$	$\mathrm{B}^2_{\mathrm{k}^*}$		
$\mathrm{b}^1_{\mathrm{r}^*}$	$\mathrm{B}^1_{\mathrm{r}^*}$		
$\mathrm{b}^2_{\mathrm{r}^*}$	$\mathrm{B}^2_{\mathrm{r}^*}$		
c_kk	C_kk	$\frac{1}{2}(1-\mathrm{C}_{ii}\mathrm{c}_{ii})\ln\left(\frac{1}{\lvert \mathrm{c}_{ii}\rvert}\right)$	$\mathrm{C}_{ii} = -9\langle \mathrm{c}_{ii} \rangle = -4\mathrm{A}^{\mathrm{c}_{ii}}$
c_rr	C_rr		
c_nn	C_nn		
$\mathrm{c}_\mathrm{rk} + \mathrm{c}_\mathrm{kr}$	$\mathrm{C}_\mathrm{rk} + \mathrm{C}_\mathrm{kr}$	$\frac{1}{2}\left(1 - \frac{\mathrm{C}_{ij} \pm \mathrm{C}_{ji}}{2} x\right)\cos^{-1}\lvert x\rvert$ where $x = \mathrm{c}_{ij} \pm \mathrm{c}_{ji}$ (for $i \neq j$)	$\mathrm{C}_{ij} \pm \mathrm{C}_{ji} = -9\langle \mathrm{c}_{ij} \pm \mathrm{c}_{ji} \rangle = -\frac{16}{\pi}\mathrm{A}^{\mathrm{c}_{ij} \pm \mathrm{c}_{ji}}$
$\mathrm{c}_\mathrm{rk} - \mathrm{c}_\mathrm{kr}$	$\mathrm{C}_\mathrm{rk} - \mathrm{C}_\mathrm{kr}$		
$\mathrm{c}_\mathrm{nr} + \mathrm{c}_\mathrm{rn}$	$\mathrm{C}_\mathrm{nr} + \mathrm{C}_\mathrm{rn}$		
$\mathrm{c}_\mathrm{nr} - \mathrm{c}_\mathrm{rn}$	$\mathrm{C}_\mathrm{nr} - \mathrm{C}_\mathrm{rn}$		
$\mathrm{c}_\mathrm{nk} + \mathrm{c}_\mathrm{kn}$	$\mathrm{C}_\mathrm{nk} + \mathrm{C}_\mathrm{kn}$		
$\mathrm{c}_\mathrm{nk} - \mathrm{c}_\mathrm{kn}$	$\mathrm{C}_\mathrm{nk} - \mathrm{C}_\mathrm{kn}$		
c_hel	D	$\frac{1}{2}(1-\mathrm{Dc}_\mathrm{hel})$	$\mathrm{D} = -3\langle \mathrm{c}_\mathrm{hel} \rangle = -2\mathrm{A}^{\mathrm{c}_\mathrm{hel}} = -\frac{1}{3}\sum_{i\in\{\mathrm{k,r,n}\}} \mathrm{C}_{ii}$
c_lab	$\mathrm{A}^{\mathrm{c}_\mathrm{lab}}$	-	-
$\Delta\phi_{\ell\ell}$	$\mathrm{A}^{\Delta\phi_{\ell\ell}}$	-	-

[5] M. Kobayashi and T. Maskawa, "CP Violation in the Renormalizable Theory of Weak Interaction", *Prog. Theor. Phys.* **49** (1973) 652–657, doi:10.1143/PTP.49.652.

[6] F. Capozzi et al., "Neutrino masses and mixings: Status of known and unknown 3ν parameters", *Nucl. Phys.* **B908** (2016) 218–234, doi:10.1016/j.nuclphysb.2016.02.016, arXiv:1601.07777.

[7] Z. Maki, M. Nakagawa, and S. Sakata, "Remarks on the unified model of elementary particles", *Prog. Theor. Phys.* **28** (1962) 870–880, doi:10.1143/PTP.28.870.

[8] J. C. Collins, D. E. Soper, and G. F. Sterman, "Factorization of Hard Processes in QCD", *Adv. Ser. Direct. High Energy Phys.* **5** (1989) 1–91, doi:10.1142/9789814503266_0001, arXiv:hep-ph/0409313.

[9] G. 't Hooft, "Renormalization of Massless Yang-Mills Fields", *Nucl. Phys.* **B33** (1971) 173–199, doi:10.1016/0550-3213(71)90395-6.

[10] UA1 Collaboration, "Experimental Observation of Isolated Large Transverse Energy Electrons with Associated Missing Energy at s**(1/2) = 540-GeV", *Phys. Lett.* **B122** (1983) 103–116, doi:10.1016/0370-2693(83)91177-2.

[11] UA2 Collaboration, "Observation of Single Isolated Electrons of High Transverse Momentum in Events with Missing Transverse Energy at the CERN anti-p p Collider", *Phys. Lett.* **B122** (1983) 476–485, doi:10.1016/0370-2693(83)91605-2.

[12] UA1 Collaboration, "Experimental Observation of Lepton Pairs of Invariant Mass Around 95-GeV/c**2 at the CERN SPS Collider", *Phys. Lett.* **B126** (1983) 398–410, doi:10.1016/0370-2693(83)90188-0.

[13] UA2 Collaboration, "Evidence for Z0 —> e+ e- at the CERN anti-p p Collider", *Phys. Lett.* **B129** (1983) 130–140, doi:10.1016/0370-2693(83)90744-X.

[14] F. Englert and R. Brout, "Broken Symmetry and the Mass of Gauge Vector Mesons", *Phys. Rev. Lett.* **13** (1964) 321–323, doi:10.1103/PhysRevLett.13.321.

[15] P. W. Higgs, "Broken Symmetries and the Masses of Gauge Bosons", *Phys. Rev. Lett.* **13** (1964) 508–509, doi:10.1103/PhysRevLett.13.508.

[16] G. S. Guralnik, C. R. Hagen, and T. W. B. Kibble, "Global Conservation Laws and Massless Particles", *Phys. Rev. Lett.* **13** (1964) 585–587, doi:10.1103/PhysRevLett.13.585.

[17] H. Yukawa, "On the Interaction of Elementary Particles I", *Proc. Phys. Math. Soc. Jap.* **17** (1935) 48–57, doi:10.1143/PTPS.1.1.

[18] ATLAS Collaboration, "Observation of a new particle in the search for the Standard Model Higgs boson with the ATLAS detector at the LHC", *Phys. Lett.* **B716** (2012) 1–29, doi:10.1016/j.physletb.2012.08.020, arXiv:1207.7214.

[19] CMS Collaboration, "Observation of a new boson at a mass of 125 GeV with the CMS experiment at the LHC", *Phys. Lett.* **B716** (2012) 30–61, doi:10.1016/j.physletb.2012.08.021, arXiv:1207.7235.

[20] ATLAS, CMS Collaboration, "Measurements of the Higgs boson production and decay rates and constraints on its couplings from a combined ATLAS and CMS analysis of the LHC pp collision data at $\sqrt{s} = 7$ and 8 TeV", *JHEP* **08** (2016) 045, doi:10.1007/JHEP08(2016)045, arXiv:1606.02266.

[21] CMS Collaboration, "Observation of $t\bar{t}H$ production", *Phys. Rev. Lett.* **120** (2018), no. 23, 231801, doi:10.1103/PhysRevLett.120.231801, arXiv:1804.02610.

[22] F. Zwicky, "On the Masses of Nebulae and of Clusters of Nebulae", *Astrophys. J.* **86** (1937) 217–246, doi:10.1086/143864.

[23] R. Durrer, "What do we really know about Dark Energy?", *Phil. Trans. Roy. Soc. Lond.* **A369** (2011) 5102–5114, arXiv:1103.5331. [J. Cosmol. 15, 6065 (2011)].

[24] J. D. Lykken, "Beyond the Standard Model", in *CERN Yellow Report CERN-2010-002, 101-109*. 2010. arXiv:1005.1676.

[25] S. Forte and G. Watt, "Progress in the Determination of the Partonic Structure of the Proton", *Ann. Rev. Nucl. Part. Sci.* **63** (2013) 291–328, doi:10.1146/annurev-nucl-102212-170607, arXiv:1301.6754.

[26] J. M. Campbell, J. W. Huston, and W. J. Stirling, "Hard Interactions of Quarks and Gluons: A Primer for LHC Physics", *Rept. Prog. Phys.* **70** (2007) 89, doi:10.1088/0034-4885/70/1/R02, arXiv:hep-ph/0611148.

[27] S. Alioli, P. Nason, C. Oleari, and E. Re, "A general framework for implementing NLO calculations in shower Monte Carlo programs: the POWHEG BOX", *JHEP* **06** (2010) 043, doi:10.1007/JHEP06(2010)043, arXiv:1002.2581.

[28] J. Alwall et al., "The automated computation of tree-level and next-to-leading order differential cross sections, and their matching to parton shower simulations", *JHEP* **07** (2014) 079, doi:10.1007/JHEP07(2014)079, arXiv:1405.0301.

[29] Z. Nagy and D. E. Soper, "What is a parton shower?", *Phys. Rev.* **D98** (2018), no. 1, 014034, doi:10.1103/PhysRevD.98.014034, arXiv:1705.08093.

[30] S. Catani and L. Trentadue, "Resummation of the QCD Perturbative Series for Hard Processes", *Nucl. Phys.* **B327** (1989) 323–352, doi:10.1016/0550-3213(89)90273-3.

[31] T. Sjöstrand et al., "An Introduction to PYTHIA 8.2", *Comput. Phys. Commun.* **191** (2015) 159–177, doi:10.1016/j.cpc.2015.01.024, arXiv:1410.3012.

[32] J. Alwall et al., "Comparative study of various algorithms for the merging of parton showers and matrix elements in hadronic collisions", *Eur. Phys. J.* **C53** (2008) 473–500, doi:10.1140/epjc/s10052-007-0490-5, arXiv:0706.2569.

[33] R. Frederix and S. Frixione, "Merging meets matching in MC@NLO", *JHEP* **12** (2012) 061, doi:10.1007/JHEP12(2012)061, arXiv:1209.6215.

[34] "NNLO+NNLL top-quark-pair cross sections". https://twiki.cern.ch/twiki/bin/view/LHCPhysics/TtbarNNLO.

[35] ATLAS Collaboration Collaboration, "Measurement of the $t\bar{t}$ production cross-section and lepton differential distributions in $e\mu$ dilepton events from pp collisions at $\sqrt{s} = 13$ TeV with the ATLAS detector", Technical Report ATLAS-CONF-2019-041, CERN, Geneva, Aug, 2019.

[36] CMS Collaboration, "Measurement of the $\mathrm{t\bar{t}}$ production cross section, the top quark mass, and the strong coupling constant using dilepton events in pp collisions at $\sqrt{s} =$ 13 TeV", *Eur. Phys. J.* **C79** (2019), no. 5, 368, doi:10.1140/epjc/s10052-019-6863-8, arXiv:1812.10505.

[37] A. Giammanco, "Single top quark production at the LHC", *Rev. Phys.* **1** (2016) 1–12, doi:10.1016/j.revip.2015.12.001, arXiv:1511.06748.

[38] CMS Collaboration, "Measurement of the t-channel single-top-quark production cross section and of the $| V_{tb} |$ CKM matrix element in pp collisions at $\sqrt{s}$= 8 TeV", *JHEP* **06** (2014) 090, doi:10.1007/JHEP06(2014)090, arXiv:1403.7366.

[39] CMS Collaboration, "Search for the associated production of a Higgs boson with a single top quark in proton-proton collisions at $\sqrt{s} = 8$ TeV", *JHEP* **06** (2016) 177, doi:10.1007/JHEP06(2016)177, arXiv:1509.08159.

[40] A. Czarnecki et al., "Lepton spectra from decays of polarized top quarks", *Nuclear Physics B* **351** (1991), no. 1, 70 – 80, doi:10.1016/0550-3213(91)90082-9.

[41] M. Jezabek, "Top quark physics", *Nucl. Phys. Proc. Suppl.* **37B** (1994), no. 2, 197, doi:10.1016/0920-5632(94)90677-7, arXiv:hep-ph/9406411.

[42] A. Brandenburg, Z. G. Si, and P. Uwer, "QCD corrected spin analyzing power of jets in decays of polarized top quarks", *Phys. Lett.* **B539** (2002) 235–241, doi:10.1016/S0370-2693(02)02098-1, arXiv:hep-ph/0205023.

[43] S. D. Drell and T.-M. Yan, "Massive Lepton Pair Production in Hadron-Hadron Collisions at High-Energies", *Phys. Rev. Lett.* **25** (1970) 316–320, doi:10.1103/PhysRevLett.25.316,10.1103/PhysRevLett.25.902.2. [Erratum: Phys. Rev. Lett. 25, 902 (1970)].

[44] M. Fabbrichesi, M. Pinamonti, and A. Tonero, "Limits on anomalous top quark gauge couplings from Tevatron and LHC data", *Eur. Phys. J.* **C74** (2014), no. 12, 3193, doi:10.1140/epjc/s10052-014-3193-8, arXiv:1406.5393.

[45] Q.-H. Cao et al., "A general analysis of Wtb anomalous couplings", *Chin. Phys.* **C41** (2017), no. 6, 063101, doi:10.1088/1674-1137/41/6/063101, arXiv:1504.03785.

[46] W. Bernreuther, D. Heisler, and Z.-G. Si, "A set of top quark spin correlation and polarization observables for the LHC: Standard Model predictions and new physics contributions", *JHEP* **12** (2015) 026, doi:10.1007/JHEP12(2015)026, arXiv:1508.05271.

[47] M. Baumgart and B. Tweedie, "A new twist on top quark spin correlations", *JHEP* **03** (2013) 117, doi:10.1007/JHEP03(2013)117, arXiv:1212.4888.

[48] P. Langacker, "The Physics of Heavy Z' Gauge Bosons", *Rev. Mod. Phys.* **81** (2009) 1199–1228, doi:10.1103/RevModPhys.81.1199, arXiv:0801.1345.

[49] T. D. Lee, "A Theory of Spontaneous T Violation", *Phys. Rev.* **D8** (1973) 1226–1239, doi:10.1103/PhysRevD.8.1226.

[50] G. C. Branco et al., "Theory and phenomenology of two-Higgs-doublet models", *Phys. Rept.* **516** (2012) 1–102, doi:10.1016/j.physrep.2012.02.002, arXiv:1106.0034.

[51] K. Gaemers and F. Hoogeveen, "Higgs production and decay into heavy flavours with the gluon fusion mechanism", *Physics Letters B* **146** (1984), no. 5, 347 – 349, doi:10.1016/0370-2693(84)91711-8.

[52] D. Dicus, A. Stange, and S. Willenbrock, "Higgs decay to top quarks at hadron colliders", *Phys. Lett. B* **333** (1994) 126–131, doi:10.1016/0370-2693(94)91017-0, arXiv:hep-ph/9404359.

[53] A. Djouadi, "The Anatomy of electro-weak symmetry breaking. II. The Higgs bosons in the minimal supersymmetric model", *Phys. Rept.* **459** (2008) 1–241, doi:10.1016/j.physrep.2007.10.005, arXiv:hep-ph/0503173.

[54] A. Djouadi et al., "The post-Higgs MSSM scenario: Habemus MSSM?", *Eur. Phys. J.* **C73** (2013) 2650, doi:10.1140/epjc/s10052-013-2650-0, arXiv:1307.5205.

[55] A. Djouadi et al., "Fully covering the MSSM Higgs sector at the LHC", *JHEP* **06** (2015) 168, doi:10.1007/JHEP06(2015)168, arXiv:1502.05653.

[56] J. Abdallah et al., "Simplified Models for Dark Matter Searches at the LHC", *Phys. Dark Univ.* **9-10** (2015) 8–23, doi:10.1016/j.dark.2015.08.001, arXiv:1506.03116.

[57] W. Buchmuller and D. Wyler, "Effective Lagrangian Analysis of New Interactions and Flavor Conservation", *Nucl. Phys.* **B268** (1986) 621–653, doi:10.1016/0550-3213(86)90262-2.

[58] S. Weinberg, "Baryon and Lepton Nonconserving Processes", *Phys. Rev. Lett.* **43** (1979) 1566–1570, doi:10.1103/PhysRevLett.43.1566.

[59] A. Buckley et al., "Constraining top quark effective theory in the LHC Run II era", *JHEP* **04** (2016) 015, doi:10.1007/JHEP04(2016)015, arXiv:1512.03360.

[60] W. Bernreuther, A. Brandenburg, Z. G. Si, and P. Uwer, "Top quark pair production and decay at hadron colliders", *Nucl. Phys.* **B690** (2004) 81–137, doi:10.1016/j.nuclphysb.2004.04.019, arXiv:hep-ph/0403035.

[61] CMS Collaboration, "Measurement of the top quark polarization and $\mathrm{t\bar{t}}$ spin correlations using dilepton final states in proton-proton collisions at $\sqrt{s} = 13$ TeV", *Phys. Rev.* **D100** (2019) 072002, doi:10.1103/PhysRevD.100.072002, arXiv:1907.03729.

CHAPTER

3

EXPERIMENTAL SETUP

Contents

Observations form a very crucial part of science; they are the absolute arbiter between the hypotheses we make. Experiments are therefore indispensable in our quest for an increasingly accurate description of nature in the most extreme of conditions. In this chapter the experimental setup and data processing workflow relevant to this work are discussed.

3.1 The Large Hadron Collider

The LHC [1] is a superconducting hadron accelerator-collider 8.5 km in diameter operated by the European Organization of Nuclear Research (CERN, 'Conseil Européen pour la Recherche Nucléaire'), and is currently the final stage of a complex accelerator chain (shown in Figure 3.1) [2]. It was designed to collide protons on protons at a center of mass-energy

($\sqrt{s}$) of 14 TeV with a bunch crossing rate of 40 MHz at a peak instantenous luminosity $\mathcal{L}$ of 1×10^{34} cm^{-2}s^{-1}. This is related to the event rate of a process i with cross section σ_i by:

$$\frac{dN_i}{dt} = \mathcal{L}\sigma_i \tag{3.1}$$

As in the final analyses we are typically more interested in the total number of events of a given process rather than its rate, it is convenient to take as the measure of the amount of data the integrated luminosity $L = \int \mathcal{L}dt$. L has the dimension of inverse area and it is commonly expressed in the inverse of the unit of cross section: /pb where 1 /pb = 1 $\times10^{-36}$ cm^{-2}.

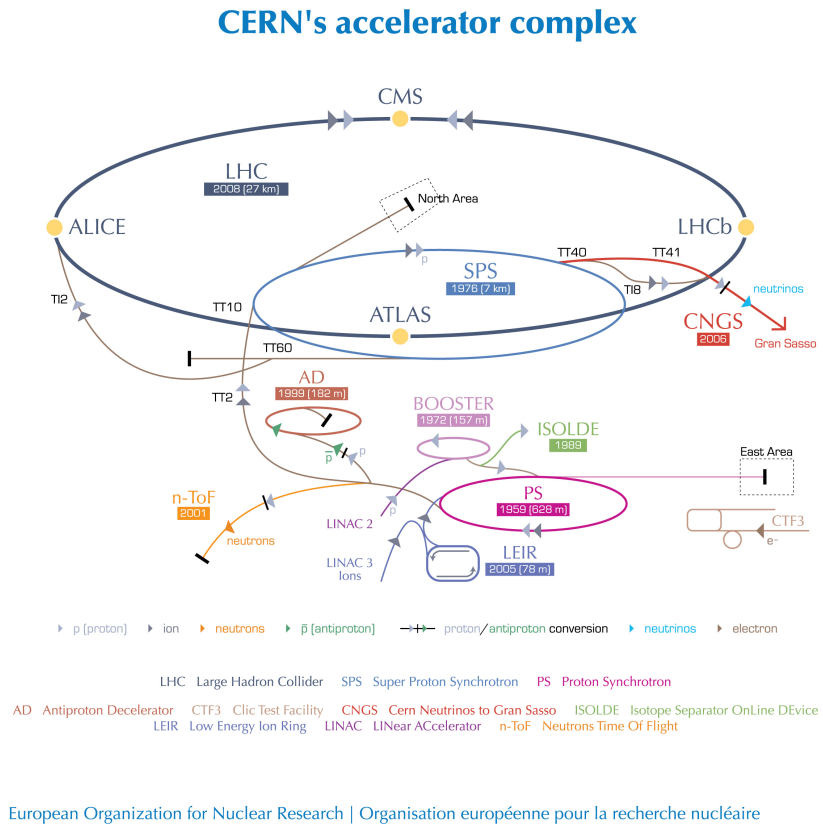

Figure 3.1: CERN accelerator complex showing the accelerator chain leading up to the LHC. Figure taken from Reference [2].

There are four points along the LHC where protons collide; they are all instrumented with detectors making up the four major LHC experiments. In alphatical order, they are:

- **ALICE** (A Large Ion Collider Experiment) focuses on heavy ion collisions and the production of quark-gluon plasma [3].
- **ATLAS** (A Toroidal LHC ApparatuS) is one of the two LHC general purpose detectors emphasizing on phenomena involving high momentum transfer [4].
- **CMS** (Compact Muon Solenoid) is the LHC general purpose detector that we are primarily concerned with in this work.

- **LHCb** (Large Hadron Collider beauty) is a single-arm detector specializing in the detection of B hadrons [5].

The LHC has operated at three different pp center of mass-energies, $\sqrt{s} = 7$, 8 and 14 TeV, and a number of different heavy ion collision scenarios involving lead or xenon nuclei, so far. The 7 and 8 TeV pp operation began in 2010 and ended in 2012, a period that is referred to as Run 1 in this work. The 13 TeV operation on the other hand began in 2015 and ended in 2018; this period is referred to as Run 2. Run 3 is scheduled to start in 2021, during which LHC is foreseen to start colliding protons at the design $\sqrt{s}$ of 14 TeV. It is worth remarking that at design luminosity 25 events are expected to be produced at each bunch crossing. While these events are mostly soft interaction events, detector signals are produced at the same time order of the bunch crossing rate, and so the soft contributions from the same and also neighboring crossings may 'pile-up' on top of hard interaction events of interest which has to be treated in some way. For this reason these additional soft events are referred to as pile-up (PU). In the 2016 data taking that we are primarily concerned with in this work, the average number of PU interactions is 23 [6].

3.2 CMS Experiment - Detector

The CMS experiment [7, 8] is a general purpose detector whose design is based on a superconducting magnet generating a uniform field of 3.8 T along the beam axis to precisely measure muon momenta. This means that tracker and calorimeter have to be accommodated inside the 12.9 m long, 5.9 m wide central solenoid - this space limitation forces a compact design on these components. A schematic diagram of the detector is shown in Figure 3.2.

3.2.1 Coordinates

In the CMS experiment, two coordinate systems are used. They will be described in momentum space as we will be primarily dealing with momenta in this work. The first system, $\{p_x, p_y, p_z\}$, is based on the right-handed Cartesian coordinate system. The z-axis coincides with one of the beam directions at the nominal beam crossing point within the detector. The x-axis points toward the center of the LHC ring and the y-axis points up toward the sky.

The second system, $\{p_T, \eta, \phi\}$, is derived from the cylindrical coordinate system $\{p_T, \theta, \phi\}$. The two are related as follows. The transverse momentum p_T is given by the magnitude of the momentum parallel to the plane transverse to the beam direction i.e. the z-axis. In other words, it is the magnitude of the momentum components pointing along the x and y axes:

$$p_T^2 = p_x^2 + p_y^2 \tag{3.2}$$

The pseudorapidity η is given by:

$$\eta = -\ln\left(\tan\frac{\theta}{2}\right) = \frac{1}{2}\ln\left(\frac{|p| + p_z}{|p| - p_z}\right) = \tanh^{-1}\frac{p_z}{|p|} \tag{3.3}$$

The choice of using η over θ is due to the transformation properties of their separation e.g. $\Delta\eta = |\eta_1 - \eta_2|$. For massless particles, their $\Delta\eta$ is invariant under Lorentz boost along the

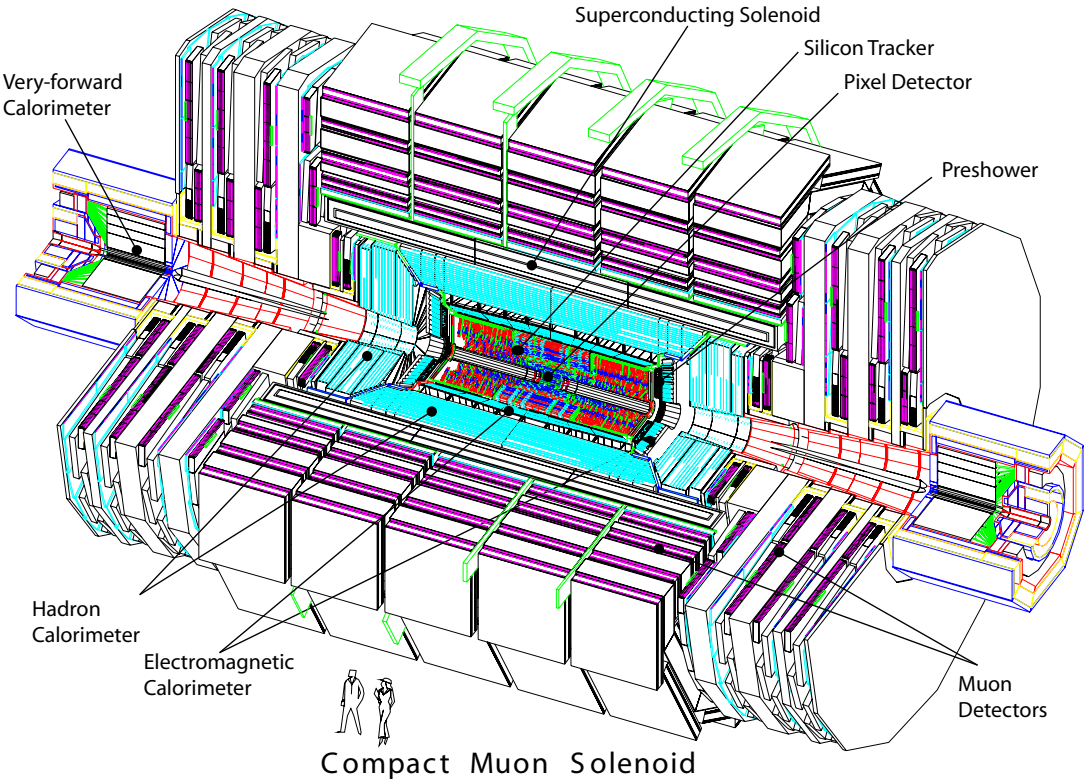

Figure 3.2: Schematic diagram of the CMS detector, with the subdetector components labelled. Figure taken from Reference [7].

z-axis, which is not the case for $\Delta\theta$. This property is crucial especially in hadron collisions, as the momenta of the interacting partonic constituents are unknown on an event-by-event basis.

From $\Delta\eta$ and $\Delta\phi$, a distance parameter $\Delta\mathrm{R} = \sqrt{\Delta\eta^2 + \Delta\phi^2}$ is defined as a measure of how separated the trajectories of two objects are. Another quantity that is commonly encountered is the rapidity y:

$$y = \frac{1}{2}\ln\left(\frac{\mathrm{E} + \mathrm{p_z}}{\mathrm{E} - \mathrm{p_z}}\right) \tag{3.4}$$

As is clear from their respective definitions, y reduces to η for the case of massless particles. y is also invariant under Lorentz boost along the z-axis, but unlike $\Delta\eta$ this invariance holds also for massive particles.

3.2.2 Magnet

Among the primary CMS design goals are the unambiguous charge determination of TeV-range muons, which requires a momentum resolution of $\Delta\mathrm{p}/\mathrm{p} \sim 0.1$ at 1 TeV. This in turn demands a large bending power from the magnet; in meeting this requirement the collaboration has chosen to opt for a superconducting one for its ability to generate higher field strengths. The superconducting coils are designed to withstand a current of 19.5 kA, generating a field of 4 T with 2.7 GJ of stored energy. In running conditions the operating field is

set to 3.8 T in order to increase the longevity of the magnet.

The solenoid is surrounded by iron yokes which serve as both the support structure for the detector and to contain and guide the field, preventing leakage to the outside environment. As the muon chambers are interspersed between these yokes, muon momentum measurements benefit from the second bending provided by the returned field.

3.2.3 Muon system

The muon system makes use of three different technologies to measure muon momenta; drift tubes (DTs), cathode strip chambers (CSCs) and resistive plate chambers (RPCs). In the barrel region ($|\eta| < 1.2$), DTs are used as both the muon rate and neutron induced background is low. They are organized into four layers (called stations and labeled MB1 - 4 starting from the innermost layer, with MB standing for Muon Barrel) staggered in such a way that a high p_T muon crosses at least three stations. This is shown in Figure 3.3. The stations measure both the position and direction of a muon, with a resolution of 100 μm and 1 mrad, respectively. In the endcap region ($|\eta| \in [1.2, 2.4]$), the particle flux is high due to the small angle with respect to the beam. CSC is the technology of choice in this region due to its faster response time. As in the MB region, there are four stations labeled ME1 - 4, overlapping in ϕ to prevent any gaps in acceptance. The resolution in this region is typically 200 μm in position and 10 mrad in direction.

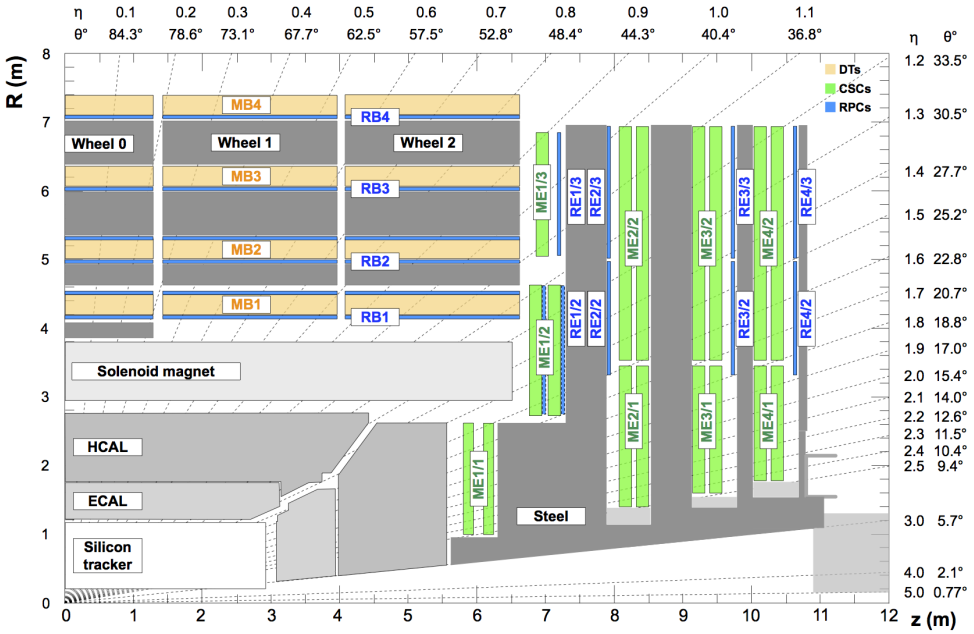

Figure 3.3: Schematic diagram of a quadrant of the muon system showing the staggered layout of its components. Figure taken from Reference [9].

Muon hit[1] positions are reconstructed in the DTs by measuring where the ionization electrons hit the wire in the tube, together with their arrival time multiplied with the known electron drift velocity in the tubes. The CSCs are based on the multi-wire proportional counters [10], but with the addition of a cathode strip readout to enable accurate hit position measurements radially and longitudinally. As with the DTs hits, timing information is recorded for each reconstructed CSC hit. Furthermore, as each chamber of these systems consists of multiple layers of detector elements, muon segments, i.e. straight line tracks, are built within each chamber from the reconstructed hits.

Each chamber in MB and ME is also coupled with RPC chambers to ensure that multiple points are crossed by each high p_T muon, yielding multiple independent and complimentary measurements from which a muon track can be built. While RPC has a coarser position resolution than either DT or CSC, it provides fast response with excellent time resolution. This gives it the ability to unambiguosly identify the correct bunch crossing, making it well suited for triggering purposes. A more detailed discussion on the muon chamber and identification performance can be found in Reference [9].

3.2.4 Tracker

The tracker is divided based on the technology it exploits; a pixel tracker for the innermost region close to the pp interaction region and a strip tracker outside of it, driven by the particle flux to be withstood by the systems. The layout of the tracker is shown in Figure 3.4. The pixel tracker consists of three barrel layers enclosed by two endcap disks at both sides. Hits in the pixel tracker are reconstructed by clustering zero-suppressed single pixel readouts and comparing the their charge distributions with that of simulation taking into account performance-affecting factors such as sensor irradiation and particle trajectory. The spatial resolution of the pixel tracker is about 10 μm in r-ϕ and up to 40 μm in z.

The strip tracker is further divided into two regions: inner and outer in the barrel region (called TIB for Tracker Inner Barrel and TOB) and TID and TEC in the endcap (for Tracker Inner Disk and Tracker EndCap respectively). These two regions are equipped with silicon sensors of differing thickness; 320 μm for the inner region and 500 μm for the outer region. The resolutions of the respective regions are up to 38 μm and 47 μm in r-ϕ and 230 μm and 530 μm in z. As with the pixel hit reconstruction, charge clustering is performed on single strips and hit positions are estimated by taking the charge-weighted average of these clusters, correcting for the effect of Lorentz drift and sensor thickness.

The tracker has a combined coverage of $|\eta| < 2.4$. The material budget of the tracker is $|\eta|$-dependent with a maximum of 2 at $|\eta| \sim 1.6$ expressed in units of radiation length[2] X_0. A more detailed discussion on the tracker and its performance can be found in Reference [11].

[1] Hit is the electrical signal produced through ionization as a charged particle passes through a detector element that is associated with a position by the use of dedicated (system-dependent) algorithms.

[2] It is defined as the mean distance traversed by a high energy electron over which it retains only 1/e of its initial energy, the rest is lost through bremsstrahlung. It is also equivalent to 7/9 times the mean free path for a high energy photon to dissociate into an electron pair.

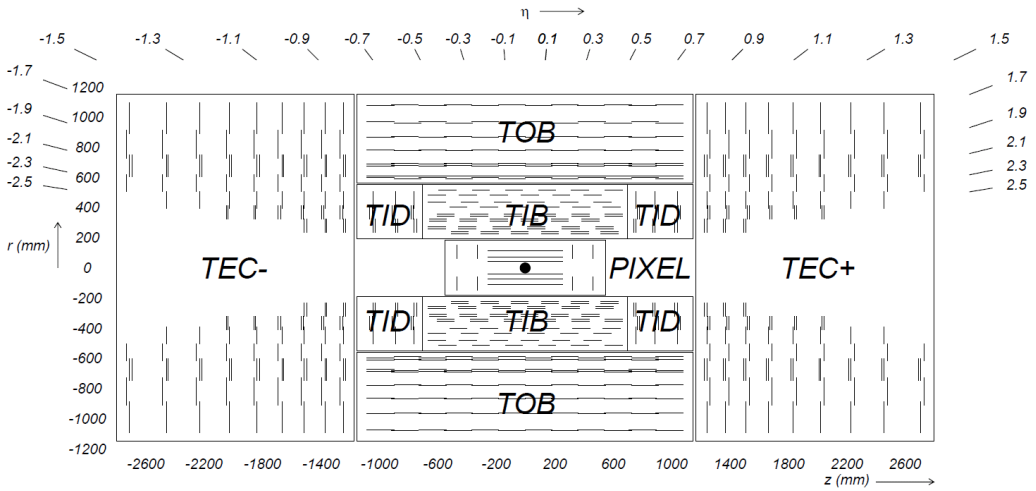

Figure 3.4: Schematic diagram of the tracker, showing the location and labeling of each components. Figure taken from Reference [8].

A new pixel tracker was installed at the end of 2016 that brought several improvements compared to the one operating up to that point [12]. It is equipped with a superior readout system, allowing operation with no data loss at a harsher environment that is anticipated in Run 3 and beyond. The new pixel tracker has an additional layer in the barrel and the endcap regions, while at the same time the power and cooling systems servicing the subdetector have been improved, leading to an overall reduction in material budget.

3.2.5 Electromagnetic calorimeter

The electromagnetic calorimeter (ECAL) is a hermetic, homogenous calorimeter whose active medium is lead tungstate ($PbWO_4$) crystals. This material is chosen due to its desirable features given the constraints imposed by CMS design and operating conditions: radiation hardness, fast light emission (of the order of LHC bunch crossing) and short radiation length ($X_0 = 0.89$ cm). The barrel section (EB for ECAL Barrel) is cylindrical in shape and provides a coverage of $|\eta| < 1.479$. The crystals, each with front face cross section of 22×22 mm^2 and length 25.8 X_0, are arranged in a way to provide a granularity of 0.0174×0.0174 in η-ϕ space. The crystals in the endcap section (EE) - of dimension 29×29 mm^2 and 24.7 X_0 - on the other hand are arranged in an x-y grid with a coverage of $|\eta| \in [1.479, 3.0]$. In the range of $|\eta| \in [1.653, 2.6]$, a preshower system (ES) is installed in front of EE to aid in the identification of neutral pions, photons and electrons. The layout of the ECAL is shown in Figure 3.5.

ECAL energy resolution can be parametrized as follows (with E measured in GeV):

$$\frac{\sigma_{\mathrm{E}}}{\mathrm{E}} = \frac{\mathrm{S}}{\sqrt{\mathrm{E}}} \oplus \frac{\mathrm{N}}{\mathrm{E}} \oplus \mathrm{C}$$

S is the stochastic term due to fluctuations in shower development[3], N is the noise term affected by the readout chain and operating environment and the constant term C describes

[3]This term is proportional to $1/\sqrt{\mathrm{E}}$ because shower development is essentially a photon counting problem.

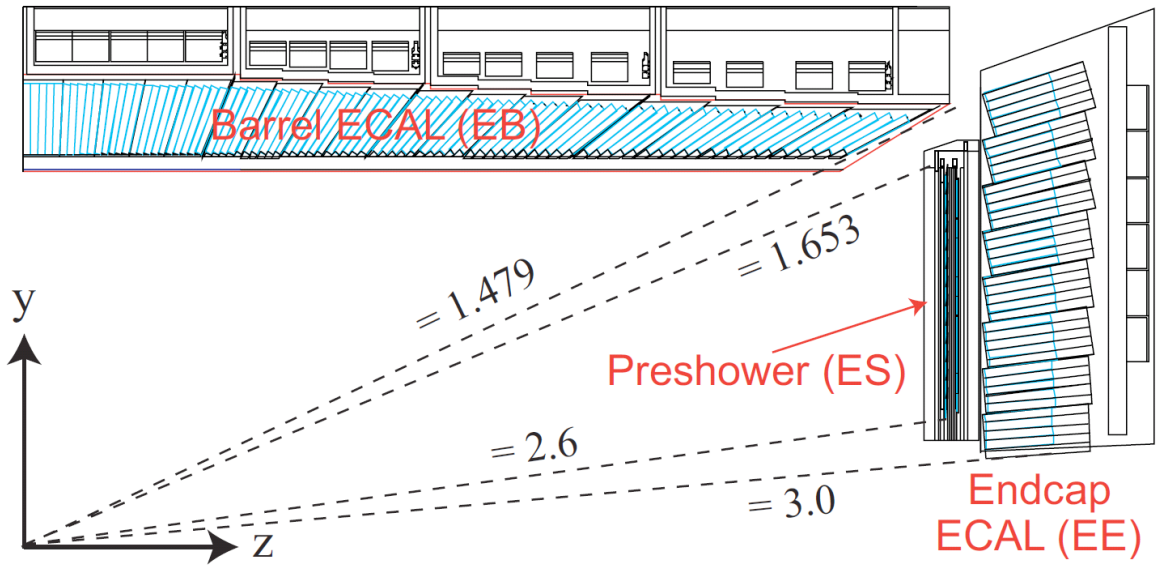

Figure 3.5: Schematic diagram of a quadrant of the ECAL with the η coverage of EB, EE and ES. Figure taken from Reference [13].

effects of calorimeter geometry, energy leakage and other energy-independent factors. Based on fits to test beam data, the values of S, N and C are 3.6%, 12% and 0.3% respectively.

Scintillation light from each crystal is read out by a photodetector glued to its rear face. To completely contain the all the photons from this light, the signal is amplified and digitized once every 25 ns over a period of 250 ns; each digitization is referred to as a time sampling. A single pulse shape is reconstructed from ten time samplings. Given the bunch crossing rate of 40 MHz, in addition to the contribution from the current bunch, each time sampling may also receive contributions from the so-called out-of-time PU (OOT PU) i.e. interactions from bunches before and after it. In order to obtain a proper measurement of the energy deposited by the current bunch (as given by the amplitude of the main pulse), these additional contributions have to be removed. This is achieved by fitting the observed pulse shape with contributions from up to ten single pulses[4], one for each crossing entering the full sampling interval. This procedure is called the Multifit algorithm.

3.2.6 Hadronic calorimeter

Given the ubiquity of hadronic showers in pp collision events, the hadronic calorimeter (HCAL) whose function is to measure their energies plays a special role in the experiment. Its design - constrained by the space limitation imposed by the magnet - emphasizes on meeting the following objectives:

- Minimizing the non-Gaussian tails in energy resolution

[4]Parametrization for single pulse shapes is obtained from beam tests; its graphical representation and discussion of amplitude reconstruction procedure used in Run 1 is available in Reference [14].

- Providing hermetic coverage for missing transverse momentum ($\not{p}_T$) measurement

These objectives are met by a sampling calorimeter design with steel and brass absorber plates interleaved with plastic scintillator tiles, the choice of which is made to maximize the material budget inside the magnet. Together the barrel and endcap regions (HB and HE) cover up to $|\eta| < 3$, which is complimented by a Cherenkov light-based forward system (HF) installed 11.2 m from the interaction point, extending the coverage to $|\eta| < 5$. Furthermore, a set of scintillators are installed just outside the magnet (and as such is called HCAL Outer HO) within the region of $|\eta| < 1.26$, increasing the effective HB material budget and improving its energy resolution.

HCAL is divided into towers; their granularity in HB is 0.087 $\times$ 0.087 in η-ϕ space, while in the HE the granularity is $|\eta|$-dependent, which can go from 0.087 $\times$ 0.087 in the finest case in the lower $|\eta|$ region to 0.35 $\times$ 0.175 at high $|\eta|$. A schematic view of HCAL towers is shown in Figure 3.6. As the pulse development in HCAL is slower than that of ECAL, it is more affected by OOT PU and also makes use of dedicated algorithms to obtain the main pulse contribution from the observed pulse. For 2016-2017 data taking, two methods were in use; Method 2 and Method 3[5]. Conceptually, Method 2 is similar to the Multifit algorithm used for ECAL pulse reconstruction in that it performs a fit on the observed pulse with contributions from the main pulse along with the two pulses before and after it. Method 3 is essentially Method 2 made simpler; by assuming fixed arrival times for the three pulses the main pulse reconstruction problem reduces to that of a 3 $\times$ 3 matrix inversion. It is therefore much faster and is used in systems where timing is a concern. As the HF signals are Cherenkov light which is an extremely fast process (the pulse development and readout take $\sim$ 10 ns), it does not suffer from OOT PU and so requires no mitigation effort.

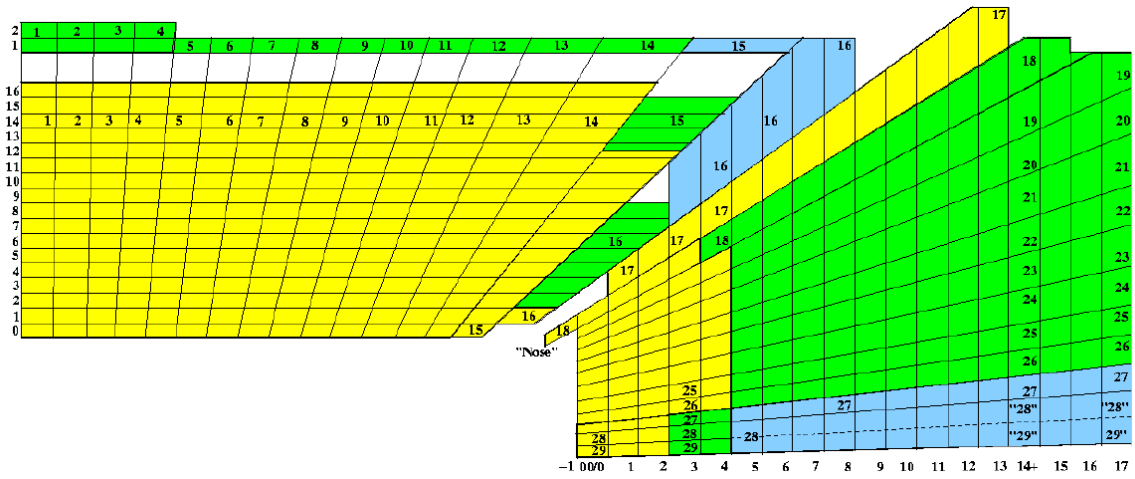

Figure 3.6: Schematic diagram of the HCAL towers in a single quadrant. Towers 1 - 16 are part of the HB while towers 17 - 29 are part of the HE. Figure taken from Reference [8].

[5]As the name suggests, there was a Method 1 being considered at some point. As it was superseded by Method 2 before the 2016 data taking period, it will not be discussed further. The algorithm used during Run 1 is called Method 0.

Considering the function of HCAL, its performance is better evaluated with the jet and $\not{p}_T$[6] resolutions of the ECAL + HCAL system rather than the single particle resolution of the HCAL alone. The jet resolution is evaluated as:

$$\frac{\sigma_{r_{E_T}^{reco.-gen.}}}{r_{E_T}^{reco.-gen.}} = \frac{S}{\sqrt{E_T^{gen.}}} \oplus \frac{N}{E_T^{gen.}} \oplus C$$

where $r_{E_T}^{reco.-gen.}$ is the ratio between reconstructed and generated jet transverse energy E_T in simulation. The values of S, N and C are 5.6, 1.25 and 0.033 respectively [8]. The $\not{p}_T$ resolution on the other hand is evaluated as:

$$\frac{\sigma_{\Sigma E_T}}{\Sigma E_T} = \frac{S}{\sqrt{\Sigma E_T}} \oplus \frac{N}{\Sigma E_T} \oplus C$$

where ΣE_T is the sum of all transverse energy deposits into the calorimeter system. The values of S, N and C are 0.97, 3.8 and 0.012 respectively [8].

3.3 CMS Experiment - Data Acquisition and Processing

At 40 MHz collision rate and 1 MB average event size, 40 PB of data has to be processed every second if every event is to be recorded. This is well beyond the capability of any existing data transfer and storage systems; the data write rate at CMS is $\mathcal{O}$(GB/s). As such, most events have to be discarded, only a tiny fraction can be kept for further analysis. CMS adopts a two-tiered system for this purpose; the Level 1 (L1) and High Level Trigger (HLT).

3.3.1 Level 1

As the vanguard against the overwhelming event rate at the LHC, the L1 system is tasked to reduce the event rate to 100 kHz to be processed by the HLT. The decision whether to accept an event has to be made within 3.2 μs, with every single step in the decision-making chain taking no longer than 25 ns. In order to fulfill these requirements L1 makes use of custom hardware installed physically near the detector [15].

The L1 decision is based on the presence of well-defined local signatures in the detector e.g. a narrow shower in the ECAL signifying the presence of a photon or electron. Following the upgrade to the system before Run 2, it became possible to also check whether the candidates are isolated, giving a powerful handle that the system can use to reject spurious events [16]. The system can also make decisions using global event information e.g. whether to accept an event based on the presence of high $\not{p}_T$.

3.3.2 High Level Trigger

The second step in event filtering, the HLT aims to reduce the event rate to 1 kHz for mass storage. This is achieved by performing the event reconstruction on a commercial processing farm with the same software as that used offline, but optimized for online use [17].

[6] Jet and $\not{p}_T$ reconstruction are discussed in Sections 4.4 and 4.5 respectively.

The full list of cuts used by the HLT is compiled in a so-called HLT menu, which consists of $\mathcal{O}(100)$ paths i.e. the smallest set of cuts to be fulfilled by an event for it to be selected. A path can impose only a very simple cut e.g. the single muon path requires only the presence of a muon above a certain p_T threshold within a certain η range that is typically isolated. There are also stronger requirements; the so-called cross paths in the menu requiring for example two electrons and two jets, which may or may not fulfill some further cuts such as the two-electron system having an invariant mass within a certain range. The HLT makes use of the full detector data in taking its decision, in principle allowing the cuts to be arbitarily complex provided they are within the timing budget of $\mathcal{O}(100$ ms).

When the rate of an HLT path[7] or L1 seed is high, one way of controlling its rate is by prescaling it. A prescale is a non-negative integer such that if a trigger has a prescale of N, then on average it records only 1/N of the events that pass its selection. This is necessary when recording events with a very high cross section e.g. minimum bias events that require only the presence of a detector signal of any kind, where the statistics is not a concern. Since a prescale of 1 means the trigger records all events that pass its selection, such triggers are also said to be unprescaled. A prescale of 0 on the other hand is reserved to the case when the trigger is not recording any events at all i.e. inactive during the data taking.

HLT paths are grouped into streams based on their expected purpose e.g. `PhysicsMuons` for physics analyses using events with muons and `EcalCalibration` whose name is self-explanatory. The streams are further divided into primary datasets (PDs) based on event topology e.g. the `SingleElectron` PD consists of events passing the single electron triggers. The PDs are not mutually exclusive i.e. events firing at least one path in each stream will be present in all of them; care has to be taken to avoid double counting if more than one PD is exploited.

3.3.3 Offline analysis

Events selected by the HLT are transferred to the Tier 0[8] computing center to be analyzed [17]. The PDs first undergo a prompt reconstruction i.e. reconstruction of higher-level objects from raw detector signals (the procedure of which will be discussed in more detail in Chapter 4) promptly after data taking, after which they are disseminated to other Tier 1 and Tier 2 centers for storage and further analysis. Re-reconstruction campaigns at later dates are common taking as input results of studies using the prompt PDs, which may include more refined calibrations and/or new reconstruction techniques.

The reconstruction and analysis are done through a single software called CMSSW (for CMS SoftWare), which is based on C++ steered by configuration files written in Python.

[7] All trigger paths in CMS that we will encounter have a `HLT_` prefix that, for the sake of brevity, will be dropped in this work. Likewise for the `L1_` prefix present in all seed names, seeds being the L1 counterpart of HLT paths.

[8] The tiering system goes from 0 to 3, with stronger demands on computing resources and connectivity placed on centers at a lower tier value [18]. There is only one Tier 0 center at CERN, a handful of Tier 1s operated by large collaborating national laboratories and $\mathcal{O}(100)$ Tier 2 and 3 centers at participating institutes all over the world. One of the Tier 2 centers is the local `T2_DE_DESY` center which has been crucial for this work.

Data is organized in the so-called Event Data Model (EDM) which aggregates the various data (which can be either digitized detector signals or reconstructed high-level physics objects) into multiple classes, all of which are accessible through a common 'Event' container [18, 19]. The event information is split into tiers corresponding to the level of abstraction of the classes; the `RAW` data tier corresponds to classes containing raw detector information including L1 and HLT decision bits, while the `AOD` tier (for Analysis Object Data), as the name implies, contains reconstructed high-level objects such as electrons, muons and jets for use in final physics analyses. In Run 2 more compact, higher level tiers were introduced; the analyses conducted in this work were primarily done using the `MINIAOD` tier.

3.4 Bibliography

[1] L. Evans and P. Bryant, "LHC Machine", *JINST* **3** (2008) S08001, doi:10.1088/1748-0221/3/08/S08001.

[2] CERN, "The particle suppliers. Les fournisseurs de particules", *CERN Bulletin* (2010) BUL–NA–2010–077.

[3] ALICE Collaboration, "The ALICE Experiment at the CERN LHC", *JINST* **3** (2008) S08002, doi:10.1088/1748-0221/3/08/S08002.

[4] ATLAS Collaboration, "The ATLAS Experiment at the CERN Large Hadron Collider", *JINST* **3** (2008) S08003, doi:10.1088/1748-0221/3/08/S08003.

[5] LHCb Collaboration, "The LHCb Detector at the CERN LHC", *JINST* **3** (2008) S08005, doi:10.1088/1748-0221/3/08/S08005.

[6] CMS Collaboration Collaboration, "Pileup mitigation at CMS in 13 TeV data", Technical Report CMS-PAS-JME-18-001, CERN, Geneva, 2019.

[7] CMS Collaboration, "The CMS Experiment at the CERN LHC", *JINST* **3** (2008) S08004, doi:10.1088/1748-0221/3/08/S08004.

[8] CMS Collaboration, G. L. Bayatian et al., "CMS Physics: Technical Design Report Volume 1: Detector Performance and Software". Technical Design Report CMS. CERN, Geneva, 2006.

[9] CMS Collaboration, "Performance of the CMS muon detector and muon reconstruction with proton-proton collisions at $\sqrt{s} = 13$ TeV", *JINST* **13** (2018), no. 06, P06015, doi:10.1088/1748-0221/13/06/P06015, arXiv:1804.04528.

[10] G. Charpak, G. Melchart, G. Petersen, and F. Sauli, "High Accuracy Localization of Minimum Ionizing Particles Using the Cathode Induced Charge Center of Gravity Readout", *Nucl. Instrum. Meth.* **167** (1979) 455, doi:10.1016/0029-554X(79)90227-1.

[11] CMS Collaboration, "Description and performance of track and primary-vertex reconstruction with the CMS tracker", *JINST* **9** (2014), no. 10, P10009, doi:10.1088/1748-0221/9/10/P10009, arXiv:1405.6569.

[12] A. Dominguez et al., "CMS Technical Design Report for the Pixel Detector Upgrade", Technical Report CERN-LHCC-2012-016. CMS-TDR-11, Sep, 2012.

[13] CMS Collaboration, "The CMS electromagnetic calorimeter project". CMS Technical Design Report. CERN, Geneva, 1997. [Addendum: CERN-LHCC-2002-027].

[14] P. Adzic et al., "Reconstruction of the signal amplitude of the CMS electromagnetic calorimeter", *Eur. Phys. J.* **C46S1** (2006) 23–35, doi:10.1140/epjcd/s2006-02-002-x.

[15] CMS Collaboration, S. Dasu et al., "CMS. The TriDAS project. Technical design report, vol. 1: The trigger systems". 2000.

[16] CMS Collaboration, "CMS Technical Design Report for the Level-1 Trigger Upgrade", Technical Report CERN-LHCC-2013-011. CMS-TDR-12, Jun, 2013.

[17] CMS Collaboration, P. Sphicas, ed., "CMS: The TriDAS project. Technical design report, Vol. 2: Data acquisition and high-level trigger". 2002.

[18] C. Grandi et al., "The CMS Computing Model", Technical Report CMS-NOTE-2004-031. CERN-LHCC-2004-035. LHCC-G-083, CERN, Geneva, 2004.

[19] G. L. Bayatyan et al., "CMS computing: Technical Design Report". Technical Design Report CMS. CERN, Geneva, 2005.

CHAPTER

4

OBJECT RECONSTRUCTION

Contents

Physics analyses begin by the reconstruction of physics objects i.e. sets of combined information from deposits in different subdetectors that can (at least to an extent) be associated with unique particle species. While the information content for each object is primarily from signals within one or two subdetectors (see Section 3.2 for a discussion on the CMS detector), correlating the measurements of many can result in improvements in the overall event description. Such an approach is called the Particle Flow (PF) reconstruction, which is at the core of the object reconstruction algorithms used in CMS [1]. This chapter is dedicated to this topic with an emphasis on the physics objects used in this work.

4.1 Particle Flow Element

The PF reconstruction starts by building basic PF elements out of deposits within each subdetector, which are then linked together to form PF objects. These elements represent

the signature caused by a single particle traversing the detector, be it a track in the tracker or muon chamber, or a cluster of calorimeter deposits.

4.1.1 Track

Track reconstruction aims at reconstructing the trajectory of a charged particle traversing the tracker, which constitutes a measurement of its momentum by analyzing its curvature due to the presence of the magnetic field. For this purpose CMS adopts a combinatorial approach based on the Kalman Filtering (KF) technique [2, 3], which is divided into three stages; track seeding, pattern recognition and final fit. In order to recover efficiency loss the track reconstruction is done in iterations, each targeting a different type of track, masking the hits used in previous iterations.

The iterations can be divided into four groups; prompt, displaced, collimated and muon. The prompt iterations, aiming at reconstructing tracks originating from the primary vertices (PVs), require pixel hits (in pairs or triplets) passing a cut on their distances to the beam axis. Displaced tracks are those whose origins are displaced with respect to the primary vertices; this is taken into account by allowing strip hits to serve as seed in the displaced iterations. The collimated iteration is dedicated to reconstructing tracks at the core of dense and high p_T jets; in this environment the hits from each track may be merged into one because of the limited strip granularity, leading to poor resolution. Finally the muon iterations are dedicated to muons, using hits in the muon chamber as well.

Having defined the track seeds, the pattern recognition step takes them as starting points to propagate particle trajectories by looking for compatible hits in succeeding layers. A final fit is performed on these tracks to smooth out their trajectories, the result of which is used to extract the track kinematics. Quality cuts are imposed on these tracks based on the goodness of fit and number of hits entering it.

4.1.2 Primary vertex

A vertex refers to a point in space where particle scattering or decay occurs; in our context the PV refers to the vertex where protons collide with each other. At the LHC usually there are multiple PVs per event due to the presence of PU; all of them are reconstructed since from the point of view of vertex reconstruction there is no difference between those from hard or soft scattering events.

The PV reconstruction takes as input high quality prompt tracks, determined on the basis of their impact parameters[1] with respect to the beam spot[2], number of hits and goodness of fit [3]. Tracks close to each other in the z-direction are clustered together by using the Deterministic Annealing algorithm [4], providing both the number and positions of the PVs. Vertex candidates with less than two associated tracks are removed and the rest are fitted using an adaptive vertex fitter [5] - which assigns a weight to each associated track expressing the likelihood of it originating from its vertex - providing estimates of their positions.

[1] The impact parameter is the closest perpendicular distance between a track and a vertex.

[2] The beam spot is the region within which most of the pp collisions take place. The procedure for its determination is discussed in Reference [3].

4.1.3 Calorimeter cluster

Single particle deposits are not necessarily contained within one calorimeter cell, especially for calorimeters with high granularity such as the ECAL. There is also the fact that particles can lose energy before reaching the calorimeter - through bremsstrahlung, Compton scattering and nuclear interactions among other means - which is desirable to be added back to the initial particles for an accurate estimate of their energy. It is therefore essential to combine deposits within neighboring cells in order to accurately measure the contribution of each particle in the event. At CMS, this procedure starts by identifying the seeds, which are cells with deposits above some energy threshold. Cells neighboring the seeds[3] are clustered together if their deposits exceed the noise level by some threshold. In case a cell is compatible with more than one seed, its energy is shared between the two clusters; the fractional assignment is determined based on the cell position relative to the respective seeds and assuming that its energy is the sum of N_{seed} deposits that are normally distributed. In this determination, the seed energies are never shared with any other cells.

4.2 Muon

Since the muon is the only visible particle that traverses the entire detector, it is the first physics object reconstructed by the PF algorithm. The reconstruction is done out of hits in the tracker and muon chamber, and can be divided into three groups [6]:

- **Standalone** muons are tracks reconstructed using hits in the muon chamber
- **Tracker** muons are reconstructed with tracker hits matched to DT or CSC segments
- **Global** muon reconstruction combine standalone and tracker muon tracks into one fit traversing the entire detector for a more precise estimation of muon momenta

Based on this procedure, several muon identification (ID) variables can be defined. Examples of such variables include the track quality, and the positional and directional matching between standalone and tracker information for global muon fits. Working points (WPs) i.e. lists of cuts on these ID variables are set aiming to define muon samples at various target efficiencies resulting into different purities. At CMS, the muon ID WPs used in physics analyses are - among others - the Tight WP meant to strongly suppress hadronic backgrounds by requiring global muon candidates passing tight quality cuts, and in addition are compatible with the PV, or the Soft ID WP focusing on low-p_T tracker muons to be used in B-physics analyses.

4.3 Electron

Electrons are reconstructed through ECAL deposits matched to a track. An electron loses energy primarily through bremsstrahlung, and because of the intervening material before the ECAL, its energy at the production point is typically split into several ECAL PF clusters instead of just one. For this reason an electron is associated to a supercluster (SC) instead,

[3]Neighboring cells are those sharing a side or a corner with the seed, such that the seed and its neighbors form a 3×3 group of cells.

made by clustering together several ECAL PF clusters mainly along ϕ direction[4]. Similarly, because of bremsstrahlung, the standard track reconstruction is suboptimal for electrons; the radiated photons introduce kinks in the electron trajectory which are not well-taken by the KF fit. To address this, electron tracks are reconstructed with a dedicated tracking algorithm called the Gaussian Sum Filter (GSF), which handles such kinks in the trajectory by using a weighted sum of multiple Gaussians to model the energy loss at each tracker layer instead of just one as used in KF [7]. At CMS there are two types of electrons corresponding to the GSF seeding strategy, ECAL- and tracker-driven [8].

ECAL-driven electrons are seeded by the SC position matched to pixel hits. First, the hit in the first pixel layer matching best to the SC is searched for by extrapolating the SC ϕ position to the beam line for both charge hypotheses accounting for the magnetic field. Once this hit is found, the z-position of the candidate is obtained by extrapolating back from the hit to the SC position. Next, using the constraints from this first hit and the SC, the best matching hits in succeeding pixel layers are searched for within some ϕ and z interval in the same way. The resulting hits serve as seed for the GSF tracking[5], the outcome of which provides the electron track. ECAL-driven seeding is the primary seeding strategy in use at CMS because it has a high reconstruction efficiency especially for prompt, isolated electrons with p_T range compatible with those coming from a Z boson decay or heavier objects.

Tracker-driven electrons on the other hand are seeded with standard tracks which either are compatible both directionally and momentum-wise with nearby ECAL PF clusters, or are of low quality indicative of significant bremsstrahlung loss. This seeding strategy is created to complement the ECAL-driven one by recovering electrons that are of low p_T and/or not isolated; they have to be correctly accounted for by the PF algorithm as they can contribute significantly to both jet and $\not{p}_T$ measurements. Both seeding strategies are used in electron reconstruction and they are not mutually exclusive; a given electron can be both ECAL- and tracker driven if both strategies succeed in its reconstruction.

4.4 Jet

As a consequence of QCD, partons are never observed as free particles, instead they manifest themselves as sprays of final state particles (most of which are hadrons) within the detector. Since it is the momenta of the partons that are typically of interest, for example in reconstructing the top quark in the $t \to b\bar{\ell}\nu$ decay chain, it is necessary to cluster this spray together into a single object called jet, which can then be traced back to its partonic origin. At CMS, jet clustering is done with the anti-k_t algorithm [9]. This algorithm clusters particle momenta sequentially i.e. the particle with the highest p_T in the event is summed up with the particle nearest to it in terms of a distance parameter based on their transverse momenta and

[4]Also in η over a smaller interval, which is relevant especially for low p_T electrons.

[5]Note that the SC position is not used to fix the end point of the track because, being an energy-weighted average position of the contributing ECAL PF clusters, it is an accurate estimate for the electron momentum before any energy loss, while the GSF track points to the PF cluster after all losses. Similarly, the positions of the contributing PF clusters are not used because it is not known a priori which cluster the track points to. Additionally, in this way two estimates of electron momentum before energy loss are obtained - one from the SC and another from the GSF algorithm - matching between the two can be used as ID variables.

ΔR between them (where ΔR in this case is different from that defined in Section 3.2 in that it uses Δy instead of $\Delta\eta$). This proceeds iteratively until the multi-particle system i.e. jet is closer to the beam than any other particles in the event. The jet is then removed from the event and the procedure starts again from the highest p_T particle among the remaining ones, until all particles in the event are assigned to a jet. In computing the distance parameter, the algorithm takes a radius parameter as a free input parameter. Jets clustered with different values of R are available in CMS, but in this work only those with R = 0.4 are used, as this is the value most compatible with the range of p_T expected of the partons produced in $t\bar{t}$ events.

In addition to the momenta of the initiating partons, we are typically interested also in their flavors. This is because some physics processes result in jet samples dominated by particular flavors. For example, top and Higgs decays result in b quarks more often than not, so the ability to distinguish jets initiated by them from gluons or other quark flavors can provide a strong background suppression for analyses involving these processes. The attempt to do so is called b-tagging, and similarly jets thought to be initiated by b quarks are referred to as b-tagged jets. b-tagging exploits observables expressing the fact that hadrons that contain b quarks tend to decay a few mm away from the PV, which is manifested as tracks within the jet having high impact parameters and/or the presence of secondary and even tertiary vertices within the jet. On average b-initiated jets also contain more tracks compared to other flavors, adding to the list of handles with which b-tagging can be performed. As there is a great amount of observables available (and them having relatively weak individual discrimination power), b-taggers are making increasingly greater use of machine learning algorithms to combine them into one strong discriminator. A detailed discussion on b-taggers in use at CMS and their performance can be found in Reference [10].

4.5 Missing Transverse Momentum

Since the colliding partons carry negligible momentum in the transverse plane, it follows from momentum conservation that the final state transverse momenta also sum up to zero. This allows us to infer on the presence of weakly interacting particles in the event such as neutrinos which are otherwise undetectable given our setup. $\not{p}_T$ is defined as the vector that is required to balance the momenta in the transverse plane of all PF objects, or equivalently the negative of the sum of the transverse components of their momenta. While there are other ways $\not{p}_T$ can be computed[6] - using only calorimeter input for instance - the $\not{p}_T$ computed using PF objects was found to be the best by the collaboration, thanks to PF's approach of combining subdetector measurements to reach a global description of the event. For this reason it is the only type of reconstructed $\not{p}_T$ that is considered in this work. A more detailed discussion on $\not{p}_T$ reconstruction and correction procedures is available in Reference [11].

4.6 Generator Object

While in most cases in this work, the physics objects used are those reconstructed from (simulated) detector signals, there are cases where it is beneficial to work with generator input

[6] Just like jet clustering algorithms, all that is needed to define a $\not{p}_T$ is the list of momenta occurring in the event, so both can be defined at multiple levels based on the input they take.

directly after showering and hadronization but before any detector simulation. Examples of such cases include evaluating the accuracy of a reconstruction algorithm or comparison between different approaches in an idealized scenario where the list of momenta in the event is not smeared by detector response, or simply unknown for some particles as is the case for the leptonically decaying top quarks due to the unmeasured neutrinos. Furthermore, inputs defined at this stage - called the generator level - are crucial as inputs to the unfolding procedure employed in the spin correlation measurement (discussed in Chapter 8) which aims to recover the underlying distributions in the data. Objects defined at the generator level are called generator objects, the definitions of which are given in this section.

4.6.1 Top quark, W and Z boson

Generator top quarks are taken directly from generator event record as those with the `isLastCopy()` flag i.e. the ones taken are the final copies after all PS corrections i.e. ISR, FSR and primordial k_t corrections [12]. The same procedure is also used to obtain generator W and Z bosons.

4.6.2 Lepton

A generator lepton is obtained by walking down the decay chain of a generator top quark (or a generator W/Z boson) and taking the first daughter that is either an electron or a muon. The lepton is not considered as a generator lepton if it is non-prompt i.e. hadrons or τs are encountered before finding it.

4.6.3 Jet

Generator jets are built by clustering the particles occuring in the event record using the anti-k_t algorithm (described in Section 4.4), considering only those with lifetimes compatible with detector dimensions ($c\tau > 1$ cm). Generator leptons and any neutrinos in the event record are not clustered.

At the generator level, b-tagging proceeds through the so-called ghost tagging procedure [13]. B hadrons occurring in the event are added to the list of particles to be clustered into jets, but with their momenta scaled down so as to be negligible in order to prevent them from influencing the resulting jet momenta. Generator b jets are then simply generator jets with these ghostly B hadrons among their constituents. For our purposes, it is convenient to further restrict the generator b jets to only those stemming from top quarks, which is obtained by requiring their B hadron constituents to be initiated by a b quark that is found within a top decay chain.

4.7 Bibliography

[1] CMS Collaboration, "Particle-flow reconstruction and global event description with the CMS detector", *JINST* **12** (2017), no. 10, P10003, doi:10.1088/1748-0221/12/10/P10003, arXiv:1706.04965.

[2] W. Adam, B. Mangano, T. Speer, and T. Todorov, "Track Reconstruction in the CMS tracker", Technical Report CMS-NOTE-2006-041, CERN, Geneva, Dec, 2006.

[3] CMS Collaboration, "Description and performance of track and primary-vertex reconstruction with the CMS tracker", *JINST* **9** (2014), no. 10, P10009, doi:10.1088/1748-0221/9/10/P10009, arXiv:1405.6569.

[4] E. Chabanat and N. Estre, "Deterministic annealing for vertex finding at CMS", in *Computing in high energy physics and nuclear physics. Proceedings, Conference, CHEP'04, Interlaken, Switzerland, September 27-October 1, 2004*, pp. 287–290. 2005.

[5] R. Fruhwirth, W. Waltenberger, and P. Vanlaer, "Adaptive vertex fitting", *J. Phys.* **G34** (2007) N343, doi:10.1088/0954-3899/34/12/N01.

[6] CMS Collaboration, "Performance of the CMS muon detector and muon reconstruction with proton-proton collisions at $\sqrt{s} = 13$ TeV", *JINST* **13** (2018), no. 06, P06015, doi:10.1088/1748-0221/13/06/P06015, arXiv:1804.04528.

[7] W. Adam, R. Fruhwirth, A. Strandlie, and T. Todorov, "Reconstruction of electrons with the Gaussian-sum filter in the CMS tracker at the LHC", *Journal of Physics G: Nuclear and Particle Physics* **31** (2005), no. 9, N9.

[8] CMS Collaboration, "Performance of Electron Reconstruction and Selection with the CMS Detector in Proton-Proton Collisions at $\sqrt{s} = 8$ TeV", *JINST* **10** (2015), no. 06, P06005, doi:10.1088/1748-0221/10/06/P06005, arXiv:1502.02701.

[9] M. Cacciari, G. P. Salam, and G. Soyez, "The anti-k_t jet clustering algorithm", *JHEP* **04** (2008) 063, doi:10.1088/1126-6708/2008/04/063, arXiv:0802.1189.

[10] CMS Collaboration, "Identification of heavy-flavour jets with the CMS detector in pp collisions at 13 TeV", *JINST* **13** (2018), no. 05, P05011, doi:10.1088/1748-0221/13/05/P05011, arXiv:1712.07158.

[11] CMS Collaboration Collaboration, "Performance of missing energy reconstruction in 13 TeV pp collision data using the CMS detector", Technical Report CMS-PAS-JME-16-004, CERN, Geneva, 2016.

[12] T. Sjöstrand et al., "An Introduction to PYTHIA 8.2", *Comput. Phys. Commun.* **191** (2015) 159–177, doi:10.1016/j.cpc.2015.01.024, arXiv:1410.3012.

[13] M. Cacciari, G. P. Salam, and G. Soyez, "The Catchment Area of Jets", *JHEP* **04** (2008) 005, doi:10.1088/1126-6708/2008/04/005, arXiv:0802.1188.

CHAPTER

5

SINGLE ELECTRON TRIGGER OPTIMIZATION

Contents

As mentioned in Section 3.3, the trigger system is charged with reducing the event rate from 40 MHz to a manageable 1 kHz by recording only the events of interest to the physics goals of the experiment. Additionally, limited buffer size means that there is a limit on the time to be taken for a decision to be made whether an event is sufficiently interesting. These constraints are not as severe in offline processing, which necessitates the use of a slightly different algorithm online i.e. at the trigger level.

Inclusive single object triggers suffer severe rate limitations since they require only the presence of one object of a given type. While one can control their rates by limiting acceptance, this is undesirable as the higher p_T thresholds can render inaccessible interesting physics processes. Consider for example the production of W bosons. At LO, the maximum p_T of the daughters is half the W mass, making it essential that the identification handles are optimized in order to ensure that the acceptance can be kept as wide as possible.

In this chapter, the optimization of the single electron trigger with the lowest p_T threshold to be unprescaled (see Section 3.3) during the 2017 data taking will be discussed. This work was performed as a service to the collaboration.

5.1 Electron Identification at the High Level Trigger

The electron reconstruction procedure described in Section 4.3 provided us with many variables that can be used to identify electrons. They can be categorized into different types which will be discussed in the following. The identification variables described here are based on the standard electron identification variables used in the collaboration, which are described in Reference [1], with some updates for use in the harsher Run 2 environment and HLT-specific optimizations.

5.1.1 Cluster shapes

Cluster shapes refer to how energy is distributed in a given ECAL PF cluster. Many such shapes can be computed, but for the purpose of discriminating electrons from jets, the most useful one is the so-called $\sigma_{i\eta i\eta}$, which is given by:

$$\sigma^2_{i\eta i\eta} = \frac{\sum_i^{5\times5} w_i(\eta_i - \bar{\eta}_{5\times5})}{\sum_i^{5\times5} w_i} \tag{5.1}$$

with 5×5 referring to the size of the crystal array centered on the seed. This size is chosen since it is the size within which single electron/photon deposits are almost fully contained. The $i\eta$ in $\sigma_{i\eta i\eta}$ refers to the fact that η is counted terms of in crystal units in Equation 5.1 above. The weight w_i is given by:

$$w_i = \max(0, C_{min} + \ln \frac{\mathrm{E}_i}{\mathrm{E}_{5\times5}}) \tag{5.2}$$

where E_i and $E_{5\times5}$ are the total energy deposits contained in a single crystal and the 5×5 crystal array respectively. C_{min} is a positive constant used to impose a cut on the minimum energy of each crystal relative to the array energy[1]. $\sigma_{i\eta i\eta}$ is therefore a measure of the spread of the shower energy in η, with multi-particle deposits naturally being more spread out and therefore tending towards higher values in the distribution.

5.1.2 Hadronic leakage

As electron energies are expected to be fully contained in ECAL, it follows that the energy in the HCAL towers directly behind the SCs ought to be small. This expectation is quantified by introducing two variables H and E. At the HLT, their definitions are:

- H: the sum of HCAL towers within a cone of $\Delta R < 0.14$ around the SC position
- E: SC energy

With the goal of expressing the smallness of H in mind, it is convenient to use the ratio, H/E, as our electron identification variable.

5.1.3 Pixel matching

At the HLT, all electrons are of the ECAL-driven type. Thus, pixel matching is required to provide the seed for the GSF tracking step. The cuts on the matching windows are intentionally kept loose in the default procedure, but for cases where a tighter matching is desired, one can cut on the combined variable s^2 instead:

$$s^2 = \left(\frac{\Delta\phi^1}{a_{\phi^1}}\right)^2 + \left(\frac{\Delta\phi^2}{a_{\phi^2}}\right)^2 + \left(\frac{\Delta z^B}{a_{z^B}}\right)^2 \tag{5.3}$$

ϕ^1, ϕ^2 and z^B refer to the search for the first hit position in ϕ, the second hit position in ϕ and the z-position of the candidate in the pixel matching procedure respectively (see Section 4.3). The Δ terms correspond to the matching windows and the a terms are measures of their spread, which are measured from simulation. The normalization is done in order to ensure that the deviation in each window is treated equally in the s^2 variable.

5.1.4 Supercluster - track matching

As electrons are SCs matched to a GSF track (from this point on simply 'track'), their degree of matching can be used as identification variable. At the HLT several identification variables are available; among them are $1/E-1/P$, missing hits, (normalized) track χ^2, $\Delta\eta^{SC}$, $\Delta\eta^{seed}$ and $\Delta\phi^{SC}$.

$1/E - 1/P$ is the difference between the inverse of SC energy (1/E) and the inverse of the magnitude of track momentum (1/P). $\Delta\eta^{SC}$, $\Delta\eta^{seed}$ and $\Delta\phi^{SC}$ are the angular differences in η and ϕ between the track and ECAL cluster. The SC superscript indicates that the difference is computed between the track and the SC while the seed superscript indicates that the position of the seed cluster is used. While the values of all these variables can be

[1] Its value is 4.7 in the official CMS reconstruction.

positive or negative, for identification purposes we are only interested in their absolute values.

In track fitting, sometimes it happens that tracks can only be formed when additional hits are introduced that are not within the list of measured hits. Such 'expected' hits are said to be missing; they are caused by among others unaccounted-for dead modules or saturated modules in a high particle-flux environment. Missing hits refer to the number of hits added to the fit in this way and track χ^2 is the quality of the said fit. While these are not measuring the SC-track matching explicitly, they are found to have some power in discriminating prompt electrons (electrons originating from the PV) from all other objects.

5.1.5 Isolation

Prompt electrons are typically isolated i.e. they occur away from other activities in the event. This statement can be quantified by summing up the p_T of all objects around the electron. At the HLT, three types of isolation are used:

- ECAL isolation: E_T sum of all ECAL PF clusters within $\Delta R < 0.3$ around the SC
- HCAL isolation: As above, but with HCAL PF clusters as input instead
- Track isolation: p_T sum of all tracks within $\Delta R < 0.2$ (0.3 in 2016) excluding contributions within $\Delta R < 0.03$ around the electron candidate

As with H, the relative form is used, meaning the quantity cut on is not the isolation itself but instead its ratio with electron E_T.

In offline reconstruction, the isolation variables used are called PF photon, neutral and charged hadron isolations. While the charged hadron isolation is very similar to track isolation at the HLT, photon and neutral hadron do not exactly correspond to ECAL and HCAL isolations although they both use the ECAL and HCAL PF clusters as input. The difference lies in the fact that in offline reconstruction, PF is completely run, so that each cluster is associated to a single PF object, while at the HLT no such cross-cleaning is done. For identification purposes, where a cut is imposed on the isolation value, in offline reconstruction the sum of all three terms is considered, which is called the combined PF isolation.

Isolation is sensitive to PU contribution in the event, which needs to be corrected in order to have a uniform efficiency for all electrons. There are several ways this can be done, but in this chapter only the 'ρ-correction' method is considered, the details of which will be discussed in Section 5.4. In offline reconstruction, this correction is performed only on the photon and neutral hadron components of PF isolation. The charged component has no PU dependence thanks to its contribution being identifiable through tracking and vertexing. However, this is not quite true for track isolation at the HLT, as shall be seen later in Section 5.4.

5.2 Trigger Performance in 2016

Before any optimization can take place, the performance of the trigger must be evaluated so that problematic areas can be identified. This is done by evaluating the trigger efficiency

ϵ[2], defined as the probability of given object to pass the trigger requirement. This may also be done in bins of variables $x_1 \ \ldots \ x_n$ to reveal the form of $\epsilon(x_1 \ \ldots \ x_n)$. This section discusses the single electron trigger performance during the 2016 data-taking, with the measurement done over 29.5 /fb of the total dataset.

5.2.1 The Tag and Probe method

It is desirable to measure the efficiency with data so that its time evolution can also be known, which is typically infeasible for simulation to keep up with. However, the inherent limitation in data is that one must work with only events that have been triggered, preventing the denominator to be obtained in an unbiased way. The Tag and Probe method circumvents this by exploiting events containing two objects of the same type compatible with well-known physics to allow for an unbiased pool of objects to be probed.

The production of Z bosons decaying to two electrons is the perfect process for our purpose of measuring the single electron trigger performance. One of the electrons is required to pass stringent identification cuts and to have triggered the event. This electron is called the *tag*. The other electron, called the *probe*, is the electron with which the efficiency is measured. The compatibility of the electron pair (ee) to that of Z boson is enforced through an invariant mass cut; $|m_{ee} - m_Z| < X$, where m_Z is the world average of the invariant mass of the Z boson (taken from Reference [2]), and X an arbitrary cutoff that depends on the desired purity. This cut will be referred to as the Z window cut from now on. The efficiency is then given as:

$$\epsilon = \frac{N_{\text{probe, pass}}}{N_{\text{probe, all}}} \tag{5.4}$$

Here $N_{\text{probe, pass}}$ stands for the amount of probes passing the cut under study, such as firing the single electron trigger, and $N_{\text{probe, all}}$ is the total amount of probes. If there is significant background contribution, $N_{\text{probe, pass}}$ and $N_{\text{probe, all}}$ can be obtained by extracting the Z-boson signal component from the m_{ee} distribution for a more accurate estimate of the efficiency. However, as will be shown later, we are dealing with a pure probe sample, so it is sufficient to simply count the $N_{\text{probe, pass}}$ and $N_{\text{probe, all}}$ as the background contribution is small.

5.2.2 Overall efficiencies of the single electron trigger in 2016

Table 5.1 summarizes the cuts applied on the tags and probes. Note that the trigger path in Table 5.1 carries a different meaning for tags and probes; for tag, it is the path to which the tag must match to while for probes, it is the path whose efficiency is being measured. The WP used in the offline cut-based ID is given in Table 5.2. The `SingleElectron` PD, recorded during the `Run2016[B-H]` and promptly reconstructed is used in this measurement. Lumi mask[3] `Cert_271036-284044_13TeV_PromptReco_Collisions16_JSON.txt`, supplied by the collaboration, is applied to select events suitable for physics analyses. A DY sample simulated at LO with no additional partons is also used. The simulation is performed using

[2]The symbol ϵ will be used to denote efficiencies in general, with the specific efficiency being discussed is usually clear from context.

[3]Lumi mask refers to the list of lumi sections that are considered good for physics analyses, which is provided by the collaboration. A lumi section is the smallest unit of data-taking interval in CMS, which is a period of time over which the instanteneous luminosity can be assumed to be constant.

MG5_aMC@NLO interfaced with PYTHIA8. For both data and simulation the `MINIAOD` tier of the samples are used.

Table 5.1: Summary of cuts applied on the tags and probes for 2016 efficiency measurement.

	Tag	Probe
E_T	> 30 GeV	
$\left\|\eta^{SC}\right\|$	< 1.444 or $\in [1.566, 2.1]$	< 2.5
Offline ID WP	2016 Tight cut-based	
Z window	< 30 GeV	
Path	`Ele27_WPTight_Gsf`	
Simulation-only	Matching (within $\Delta R < 0.1$) to truth electrons from Z decay	

Table 5.2: Offline 2016 electron ID, Tight WP. All cuts are of the 'x $\leq$ X' kind, with x denoting the variable and X the threshold. The ID variables are defined in Section 5.1 except for the conversion veto, which is explained in Reference [1].

ID variable	Tight cut-based	
	EB	EE
$\sigma_{i\eta i\eta}$	0.00998	0.0292
H/E	0.0414	0.0641
ρ-corrected combined relative PF isolation	0.0588	0.0571
$1/E - 1/P$	0.0129	0.0129
Missing hits	1	1
$\Delta\eta^{seed}$	0.00308	0.00605
$\Delta\phi^{SC}$	0.0816	0.0394
Pass conversion veto	yes	

Figure 5.1 shows the m_{ee} distributions for probes in the EB ($\left|\eta^{SC}\right| < 1.444$) and EE ($\left|\eta^{SC}\right| > 1.566$) respectively. From the ratio pad in both distributions, one can see that the simulation is describing the data poorly. This is due to the fact that the data used here is the prompt reconstruction dataset, which refers to the first reconstruction performed following data-taking where the knowledge on detector conditions and the required calibrations are not yet completely available. The simulation was therefore made assuming idealized detector

conditions that is not available during data-taking. However, this discrepancy is of little concern for our purposes; we are only interested in whether the electron sample is pure and the distributions suggest that the background contamination is small in both EB and EE. This justifies the choice for simple counting procedure in computing the efficiencies.

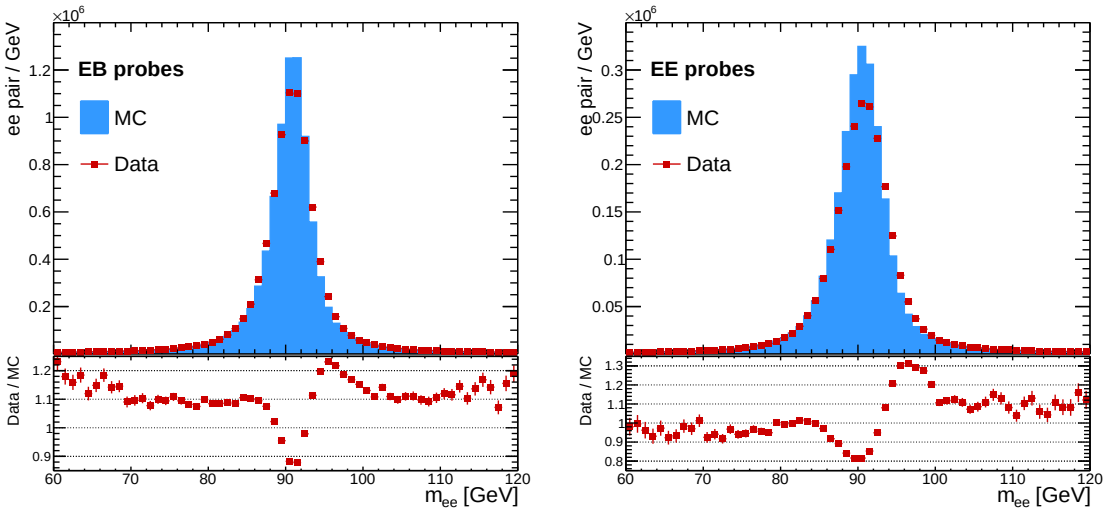

(a) m_{ee} with EB probes

(b) m_{ee} with EE probes

Figure 5.1: m_{ee} distribution split based on $\left|\eta^{SC}\right|$ of the probes for the 2016 prompt reconstruction dataset.

We can now discuss the overall performance of the single electron trigger, which is shown as functions of E_T, η^{SC} and N_{PV} in Figure 5.2. In this measurement, the data is divided into three time periods based on the differences that would impact the electron reconstruction and selection at the HLT, the information on which is collected in Table 5.3. In all these efficiencies, the contributions from L1 system have been factored out, which means that the efficiency is measured over a collection of probes that already passed the L1 cuts. This is because for our purposes only the HLT part is relevant; the L1 system and its optimization is a separate topic that is beyond the scope of this chapter.

Inspecting the distributions in Figure 5.2, we see that the efficiency in simulation is significantly higher than data, as would be expected given the ideal detector conditions assumed in the simulation. The difference caused by the unknown detector alignment is most prominent in the EE during the first part of the data taking. Looking at the $\epsilon(E_T)$ for both EB and EE probes (Figure 5.2 (a) and (b)), one notices that the efficiency is not a sharp step at 27 GeV, as would be expected given the E_T threshold of the trigger. Instead, the efficiency plateau is at a value higher than this. This is due to the difference in the E_T value reconstructed at the HLT and offline reconstruction levels, which we will be looking at in more detail later in this section. This behavior is why the $\epsilon(E_T)$ curve is sometimes known as the turn-on curve.

Moving on, it is worth noting that the efficiency is higher in the low E_T region compared

Table 5.3: Data splitting used in 2016 efficiency measurement.

Legend	Run range	Remark
MC	-	Simulation made with trigger menu matching one in the Data 1 range and ideal detector geometry
Data 1	273158 - 278240	Commissioning period where ID cuts affected by unknown detector alignment (18.01 /fb)
Data 2	278273 - 280385	Updated tune of the `EleX_WPTight_Gsf` paths to control the rates and improve purity (9.64 /fb)
Data 3	281639 - 283059	H/E computation updated to regional HCAL Method 2 instead of Method 3 (3.77 /fb)

to later data taking periods. This is because this part corresponds to runs with lower instantaneous luminosity and so lower PU, which means that several lower p_T threshold L1 seeds were available only in this period. The efficiency as a function of η^{SC} on the other hand does not look as expected, particularly the dip at low $\left|\eta^{SC}\right|$. There are no known problems with the detector around the region to explain it, so the issue is suspected to be in the electron reconstruction procedure at the HLT. Finally, the N_{PV} dependence of the efficiency reveals another interesting trend. It exhibits poor N_{PV} (and therefore PU) dependence, as indicated by the fact that in both EB and EE the efficiency becomes lower with increasing N_{PV}. This is mitigated to an extent by the changes introduced in Data 2 period, one of the goals of which is to reduce the dependence of the efficiency on PU. However, a significant slope still remains, which led the EGM[4] group to redefine the H/E variable at the HLT, this being identified as the primary source of the problems mentioned.

5.2.3 Detailed efficiencies of the single electron trigger in 2016

The dip at low η^{SC} still being present in the Data 3 period clearly shows that updating H/E is insufficient to bring the performance to a satisfactory level. It is therefore necessary to scrutinize the reconstruction procedure more deeply to identify the remaining sources of problems. One way to do this is to examine the filter-by-filter efficiency according to the order they occur in the path. However, due to the large number of filters in the single electron trigger, it is impractical to inspect every single one, each of which is to be checked as functions of multiple variables. They are instead grouped together based on the order they occur in the path: shower shapes ($\sigma_{i\eta i\eta}$ and H/E), calorimeter isolations (ECAL and HCAL isolations), GSF tracking ($1/E - 1/P$, missing hits, $\Delta\eta^{seed}$, $\Delta\phi^{SC}$) and finally track isolation.

The efficiencies of the shower shapes part is shown in Figure 5.3. Judging from time evolution of the efficiencies, it is clear that the issues previously discussed are not due to $\sigma_{i\eta i\eta}$, and to the extent that H/E is affected, is solved with the changes introduced in Data 3 period.

[4]EGM stands for Electron - Gamma (photon), as this is the group in charge of electron and photon reconstruction in the CMS collaboration.

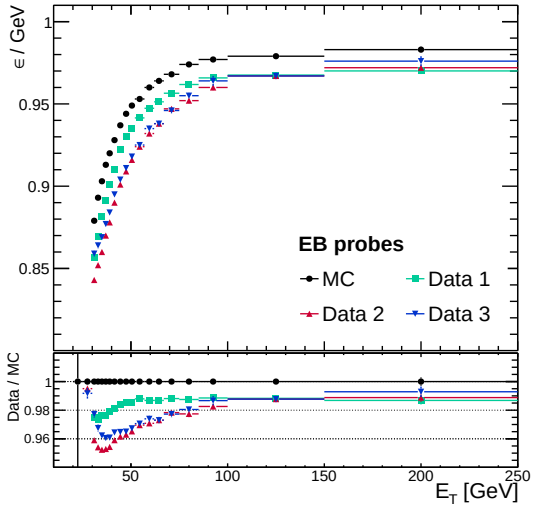

(a) $\epsilon(\mathrm{E_T})$ (EB)

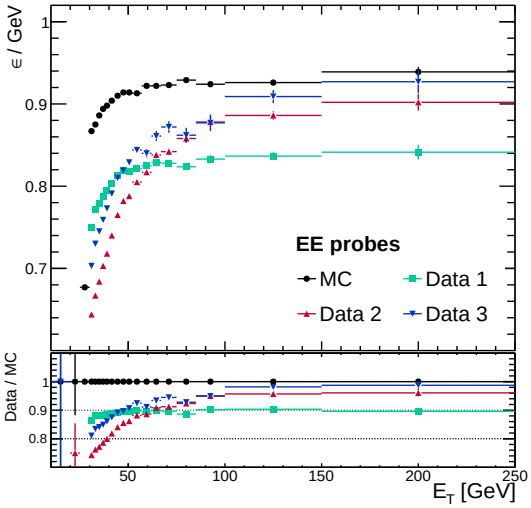

(b) $\epsilon(\mathrm{E_T})$ (EE)

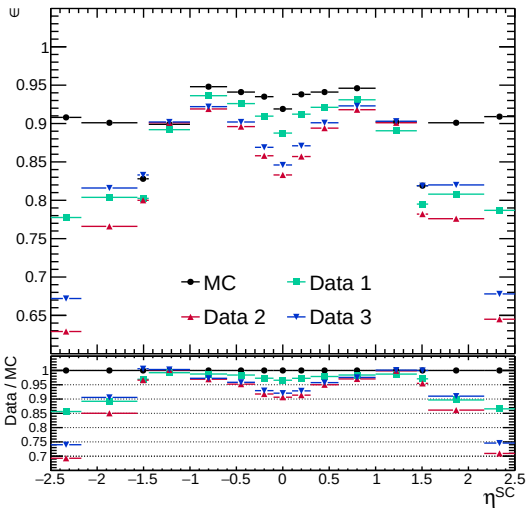

(c) $\epsilon\left(\eta^{\mathrm{SC}}\right)$

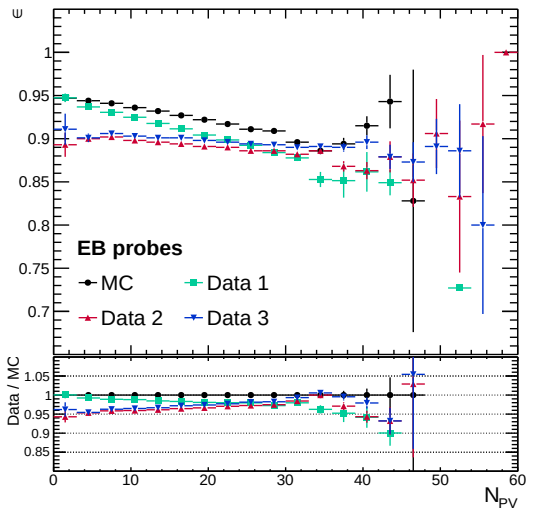

(d) $\epsilon(\mathrm{N_{PV}})$ (EB)

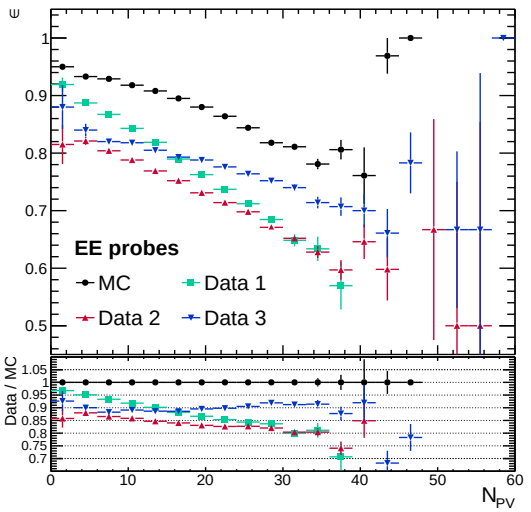

(e) $\epsilon(\mathrm{N_{PV}})$ (EE)

Figure 5.2: Overall single electron efficiency in 2016 as functions of $\mathrm{E_T}$, η^{SC} and $\mathrm{N_{PV}}$.

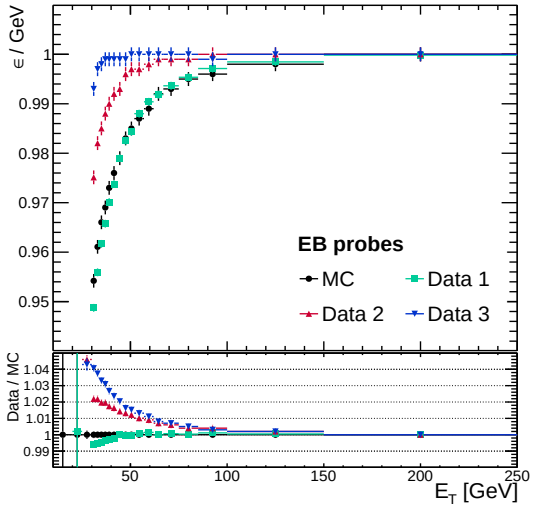

(a) $\epsilon(\mathrm{E_T})$ (EB)

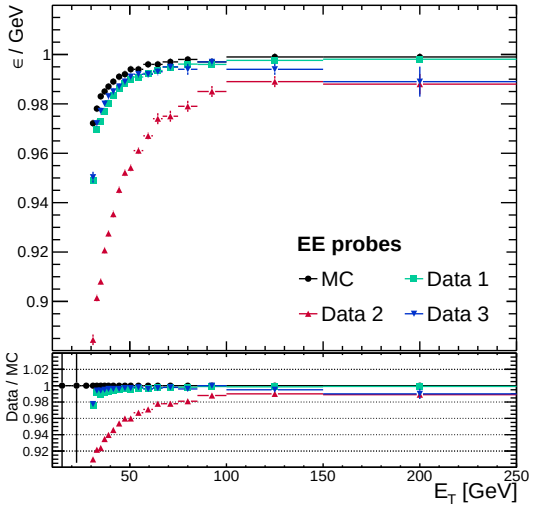

(b) $\epsilon(\mathrm{E_T})$ (EE)

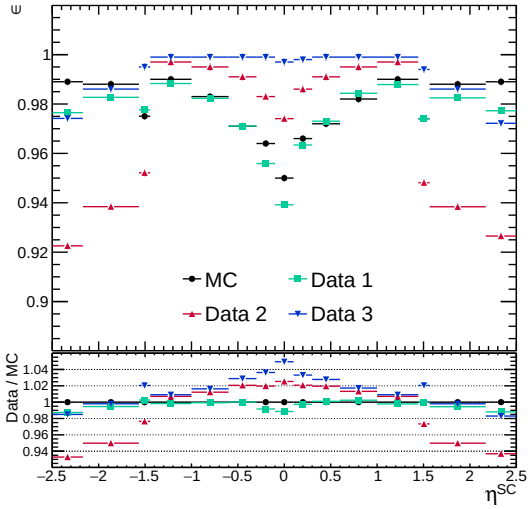

(c) $\epsilon\left(\eta^{\mathrm{SC}}\right)$

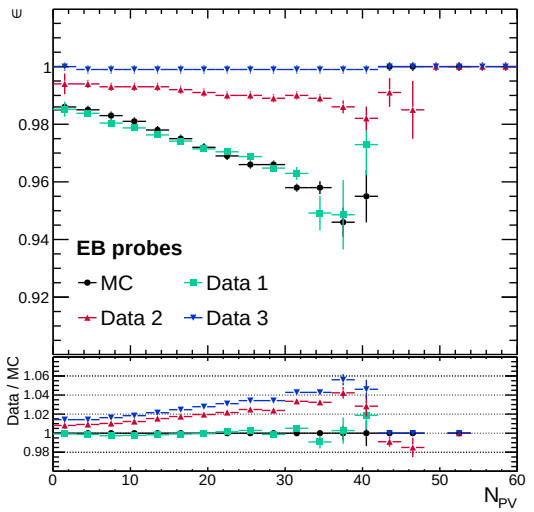

(d) $\epsilon(\mathrm{N_{PV}})$ (EB)

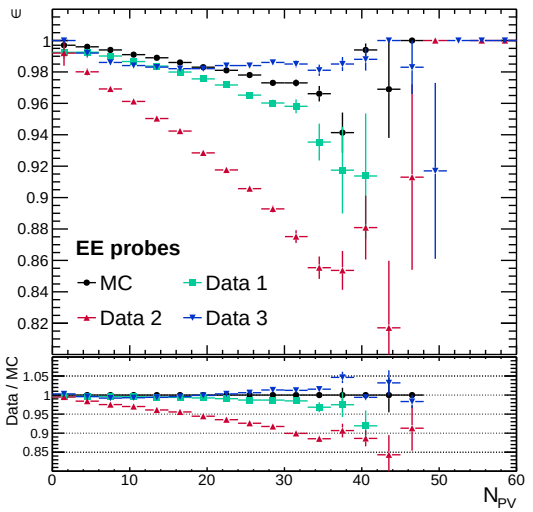

(e) $\epsilon(\mathrm{N_{PV}})$ (EE)

Figure 5.3: Efficiency of the shower shapes part of the single electron trigger in 2016 as functions of $\mathrm{E_T}$, η^{SC} and $\mathrm{N_{PV}}$.

Next, we turn to the efficiencies of the calorimeter isolations part as shown in Figure 5.4. While efficiency behavior in N_{PV} is somewhat improved, the undesirable features in E_T and η^{SC} greatly deteriorated with the introduction of new tune and its tight cuts. Considering that these features are similar to the ones shown by H/E in the Data 2 period, it is presumed that they share the same cause which will be discussed in more detail in Section 5.3.

The next part of the single electron trigger is the GSF tracking part, whose efficiencies are shown in Figure 5.5. This part explains the lower efficiencies of the Data 1 period in EE previously seen in Figure 5.2, as all the SC - track matching variables are affected by the unknown detector alignment. Furthermore, the efficiency behavior in N_{PV} is also worse in the Data 1 period; this is because the track χ^2 variable is known to have a poor PU dependence, the effect of which is reduced by loosening the cut in the new tune. The asymmtery in the efficiency as a function of η^{SC} in EB on the other hand is caused by the known asymmetry of the pixel detector, an issue that is beyond the scope of this chapter.

Lastly are the efficiencies of the track isolation filter as shown in Figure 5.6. From the plots it is concluded that this variable shows no issues except a residual PU dependence to be corrected. The efficiency drop at low E_T that is more visible in EE following the new tune is also expected; the fact that isolation generally is not proportional to electron E_T means the relative cut gets looser as E_T increases.

5.2.4 Online-offline identification variables comparison

As the probes are required to pass offline identification cuts, it is crucial that their definitions match those used online. Otherwise, the online and offline cuts introduce different distortions in the phase space and the discrepancies manifest themselves as undesirable features in the efficiency curves, such as that seen in the overall efficiency as a function of η^{SC} plot. Here we directly compare the ID variables computed at the HLT and offline reconstruction levels, using as our figure of merit a resolution parameter that is defined as:

$$\sigma_x = \frac{x_{\text{HLT}} - x_{\text{offline}}}{x_{\text{offline}}} \tag{5.5}$$

Here x denotes the variable of interest and the subscripts denote the level in which it is computed. For this comparison the latest trigger menu available in 2016 is rerun using events from the later part of data-taking, which have an average PU of above 30, as indicated in Table 5.4. On top of the basic kinematical variables, only the comparisons of H/E and calorimeter isolations will be shown, as the undesirable trends in the efficiency plots from the previous subsection are most prominent there.

Figure 5.7 shows the resolution of kinematical variables. The plots indicate that at the HLT E_T is smaller at the percent order than offline in EB and a bit more so in EE. This is attributed to the different energy regression used at the two levels. While this is an issue that ideally needs addressing, it will not be discussed further in this chapter as the typical strategy of cutting an offline object a few GeV higher than the HLT threshold sufficiently mitigates it. Turning to η^{SC} and ϕ^{SC} in the same figure, we see that the direction of the electron is accurately reconstructed at the HLT with respect to offline.

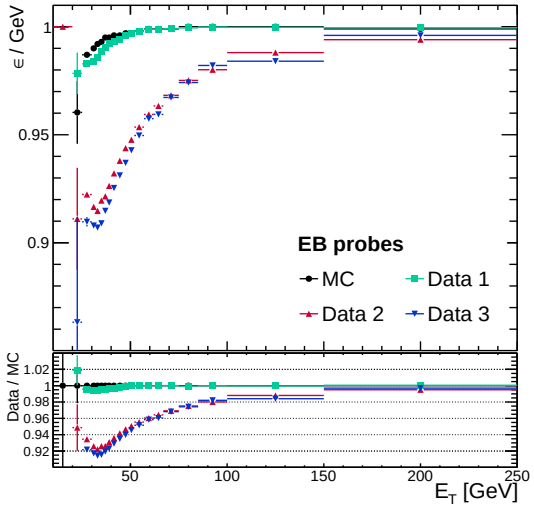

(a) $\epsilon(\mathrm{E_T})$ (EB)

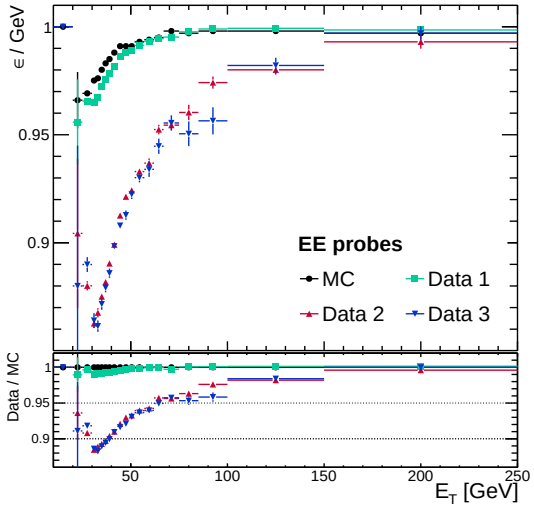

(b) $\epsilon(\mathrm{E_T})$ (EE)

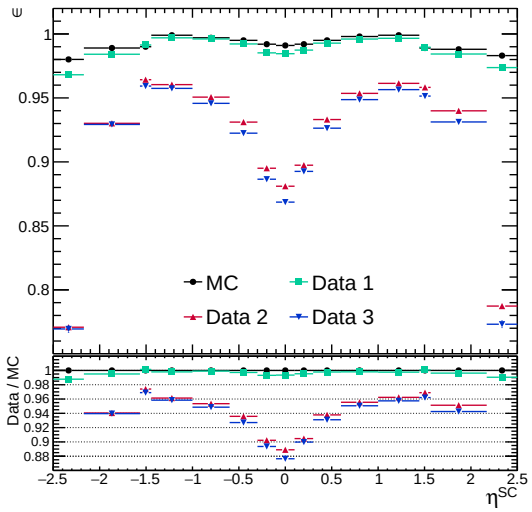

(c) $\epsilon\left(\eta^{\mathrm{SC}}\right)$

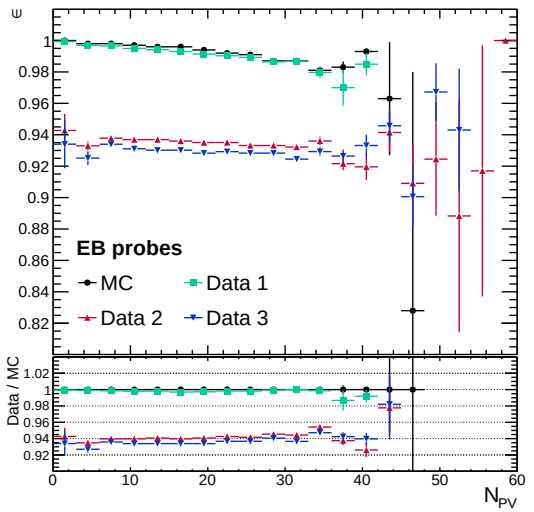

(d) $\epsilon(\mathrm{N_{PV}})$ (EB)

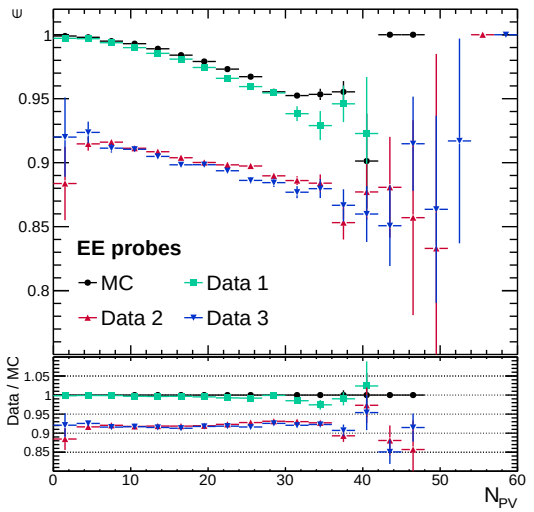

(e) $\epsilon(\mathrm{N_{PV}})$ (EE)

Figure 5.4: Efficiency of the calorimeter isolations part of the single electron trigger in 2016 as functions of $\mathrm{E_T}$, η^{SC} and $\mathrm{N_{PV}}$.

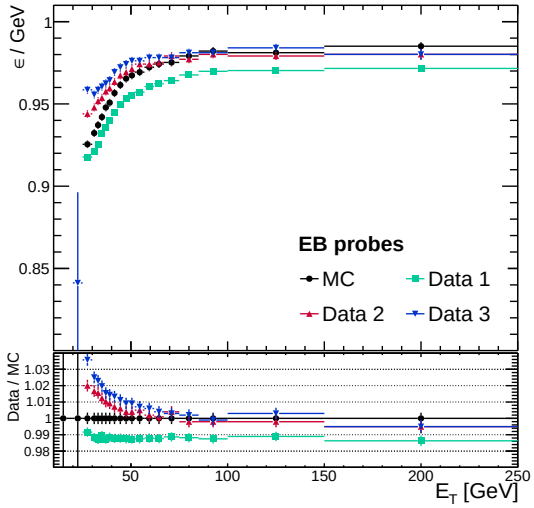

(a) $\epsilon(\mathrm{E_T})$ (EB)

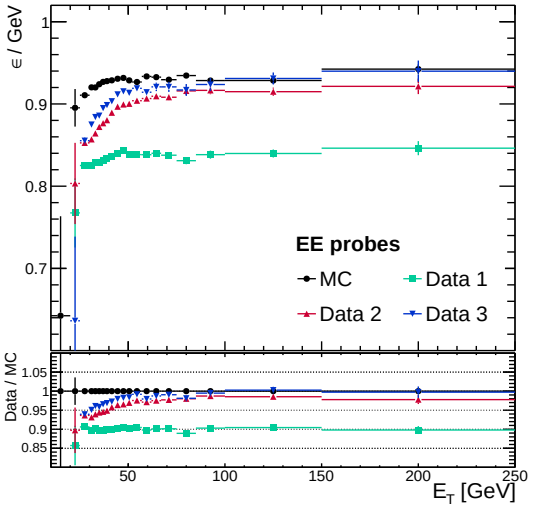

(b) $\epsilon(\mathrm{E_T})$ (EE)

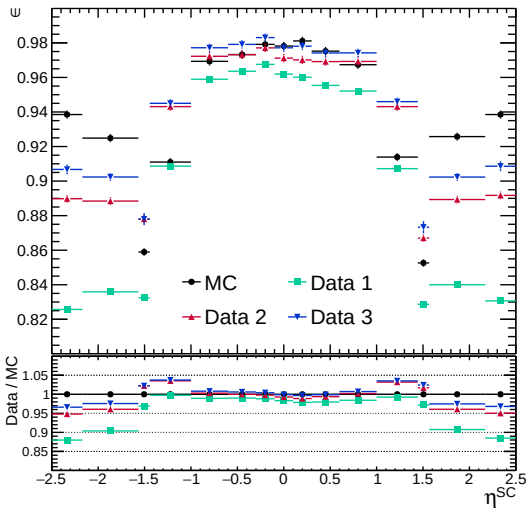

(c) $\epsilon\left(\eta^{\mathrm{SC}}\right)$

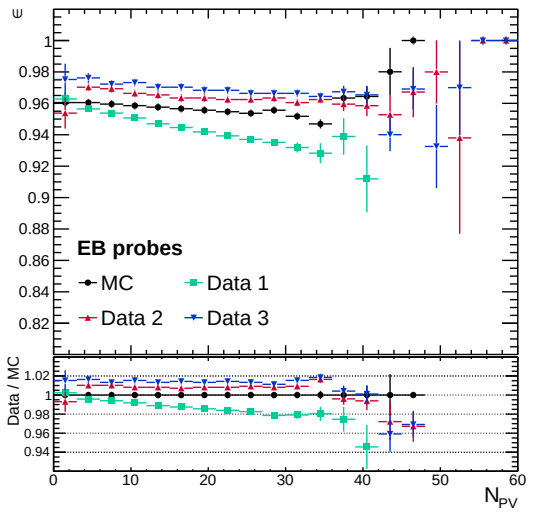

(d) $\epsilon(\mathrm{N_{PV}})$ (EB)

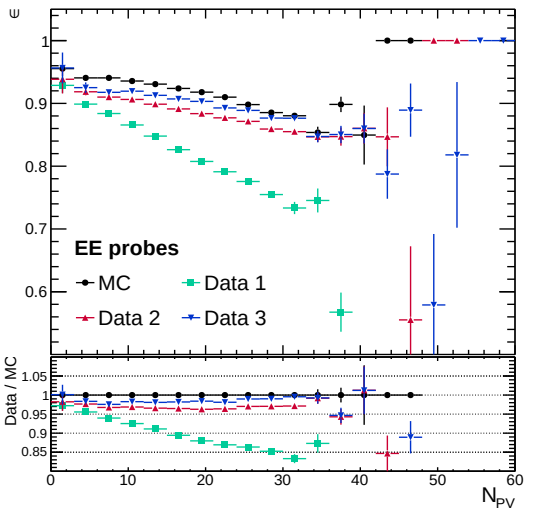

(e) $\epsilon(\mathrm{N_{PV}})$ (EE)

Figure 5.5: Efficiency of the GSF tracking part of the single electron trigger in 2016 as functions of $\mathrm{E_T}$, η^{SC} and $\mathrm{N_{PV}}$.

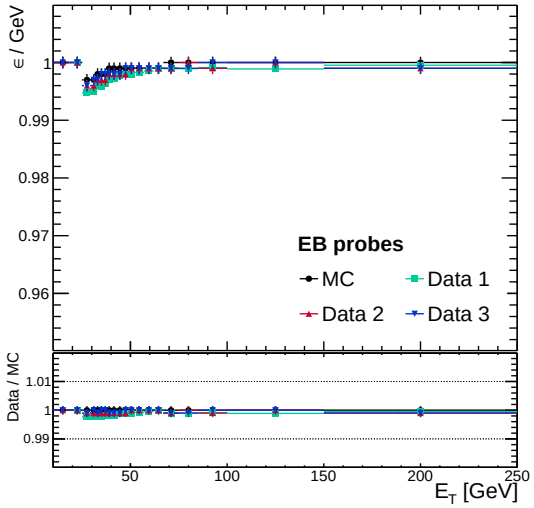

(a) $\epsilon(\mathrm{E_T})$ (EB)

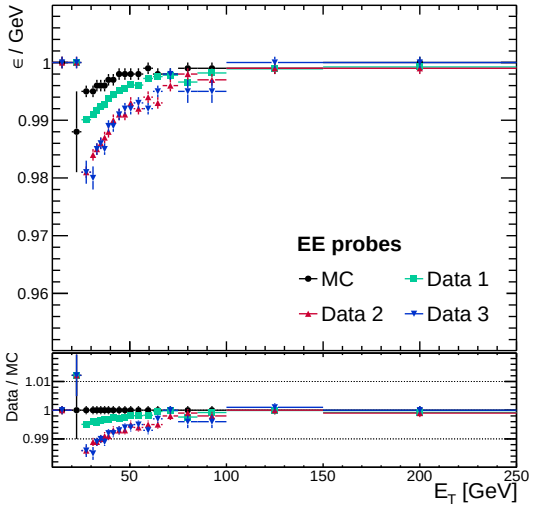

(b) $\epsilon(\mathrm{E_T})$ (EE)

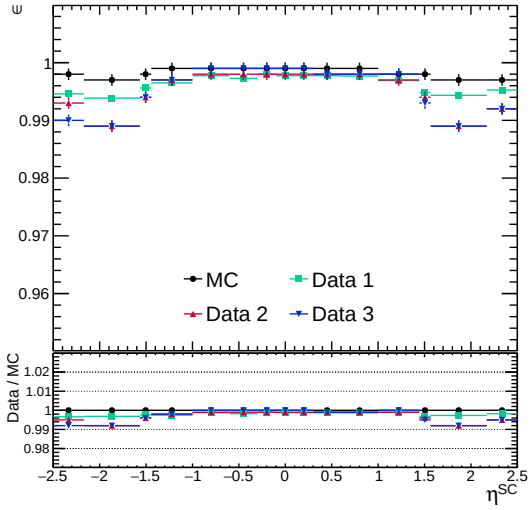

(c) $\epsilon\left(\eta^{\mathrm{SC}}\right)$

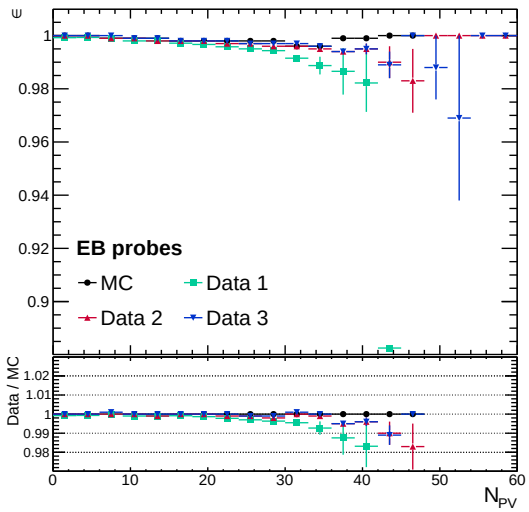

(d) $\epsilon(\mathrm{N_{PV}})$ (EB)

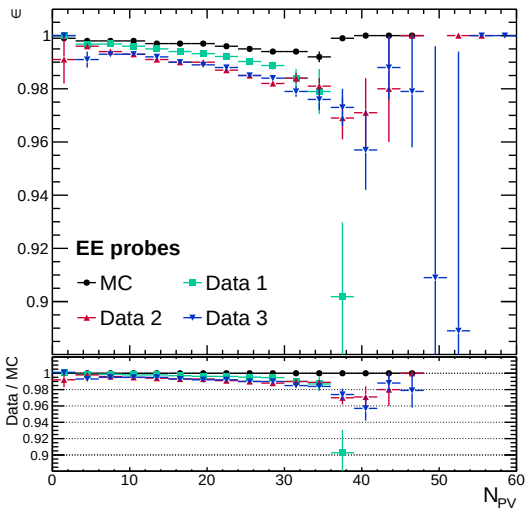

(e) $\epsilon(\mathrm{N_{PV}})$ (EE)

Figure 5.6: Efficiency of the track isolation filter of the single electron trigger in 2016 as functions of $\mathrm{E_T}$, η^{SC} and $\mathrm{N_{PV}}$.

Table 5.4: Data used for the 2016 online-offline identification variable comparison.

LHC fill	5406
Runs	283050, 283052, 283059
HLT menu	`/dev/CMSSW_8_0_0/GRun/V210`
Probe selection	As in Table 5.1 and passes L1 system cuts
Dataset	Same as Section 5.2 (`MINIAOD` and `RAW`)

Figure 5.8 shows the HLT-offline resolution of H/E and calorimeter isolations. It is clear that the resolution of H/E is significantly narrower than that of ECAL or HCAL isolations. Comparing their respective efficiency plots in Figures 5.3 and 5.4, it is supposed that H/E resolution is improved by the change introduced in the Data 3 period. As for ECAL or HCAL isolations, their large resolution means that there is little agreement between the HLT and offline, despite the fact that they are supposed to be the same quantities. This discrepancy and attempts to reduce it will be the subject of the following section.

5.3 Trigger Improvements in Preparation for 2017

Having identified the issues in the HLT electron identification variables, it is crucial that they are addressed before the start of the next round of data taking. In this section the studies conducted to address the issues identified in the previous section are discussed.

5.3.1 HCAL isolation with Method 2

Having seen that the changes in the Data 3 period have solved the H/E definition discrepancy, it is natural to expect that the same change extended to HCAL isolation will solve the issue in the latter as well, considering that prior to it they are computed using the same input. In fact, this was the plan of the EGM group when making this change, the only reason it did not cover HCAL isolation were timing concerns. This study is conducted to quantify that concern and demonstrate that it is possible to extend it to HCAL isolation while staying within the timing constraints of the HLT.

Let us begin with a more detailed discussion on how the H/E discrepancy is solved. As mentioned in Section 3.2, Method 2 is used for HCAL deposit reconstruction offline, while the faster Method 3 is used at the HLT. The two methods have poor agreement in the low energy region we are interested in. As such, electrons passing the HLT H/E cut do not necessarily pass the same cut offline; this discrepancy first manifested itself in the form of a dip in efficiency at low $|\eta|$ as seen in Figure 5.3. To solve the problem, one simply has to synchronize the reconstruction methods used at both levels. Method 2 is the obvious choice in this case, being the one used offline, but this is not feasible at the HLT due to timing restrictions. The solution reached by the EGM group was to introduce the regional Method

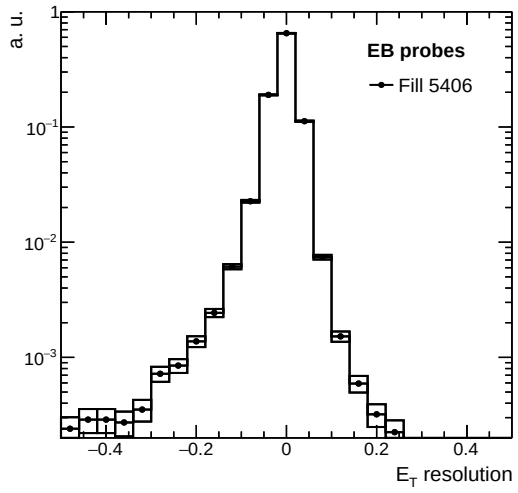

(a) E_T resolution (EB)

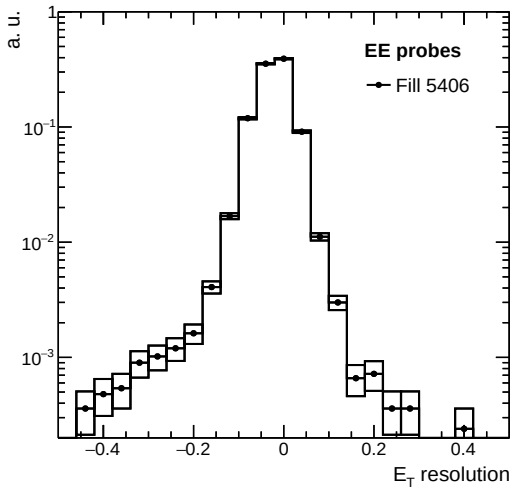

(b) E_T resolution (EE)

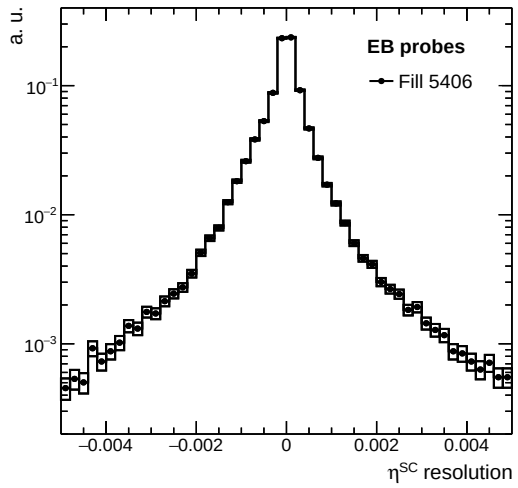

(c) η^{SC} resolution (EB)

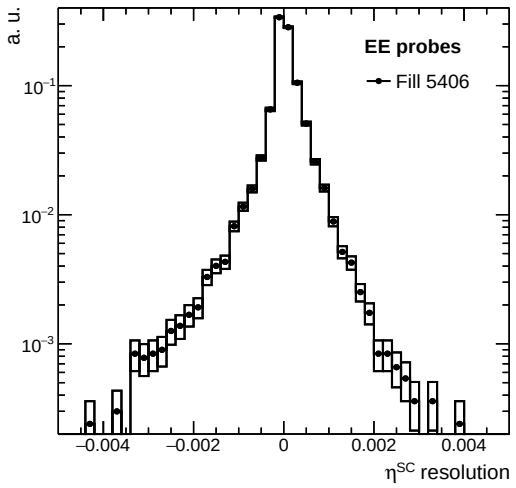

(d) η^{SC} resolution (EE)

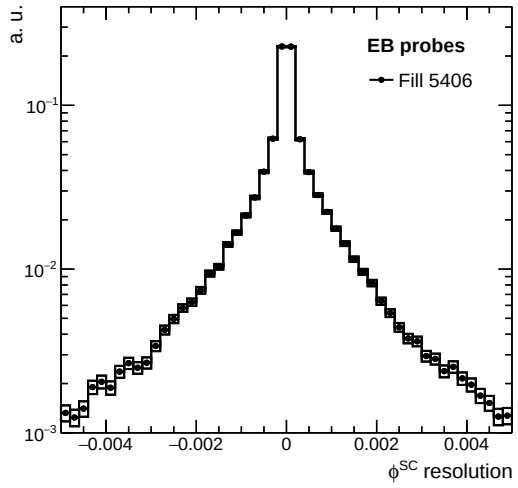

(e) ϕ^{SC} resolution (EB)

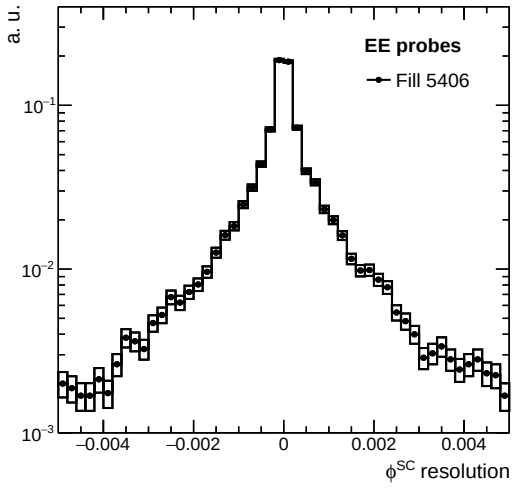

(f) ϕ^{SC} resolution (EE)

Figure 5.7: HLT-offline resolution of kinematical variables in fill 5406.

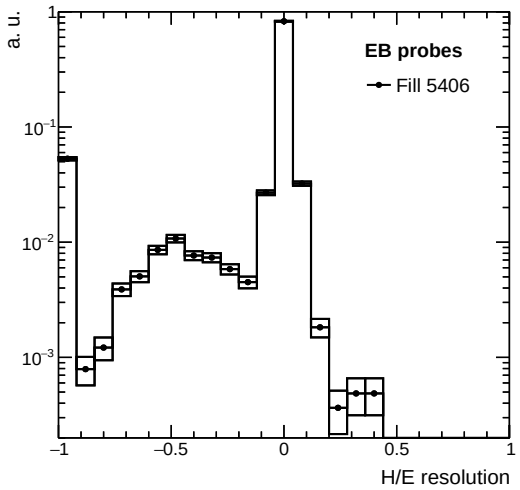

(a) H/E resolution (EB)

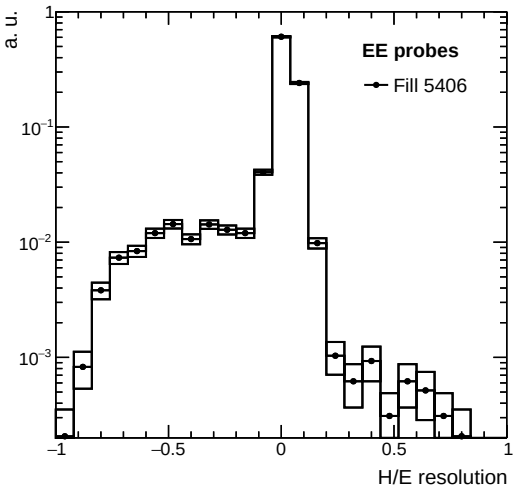

(b) H/E resolution (EE)

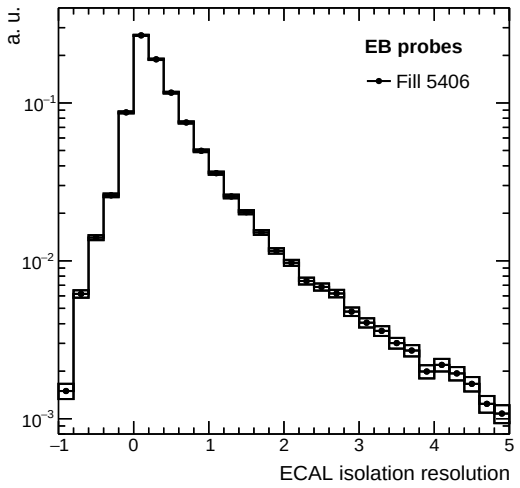

(c) ECAL isolation resolution (EB)

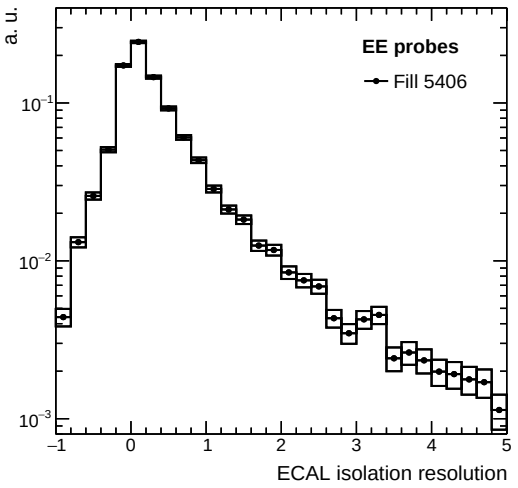

(d) ECAL isolation resolution (EE)

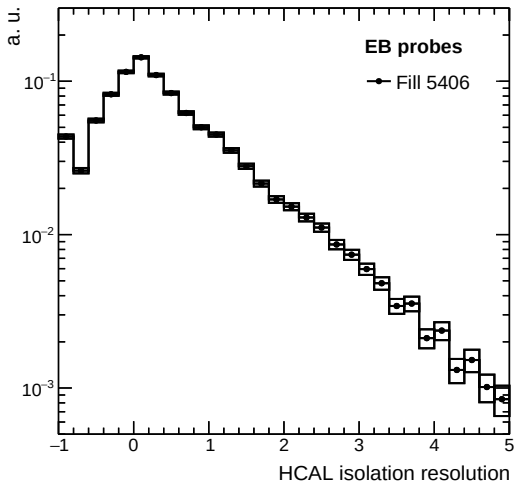

(e) HCAL isolation resolution (EB)

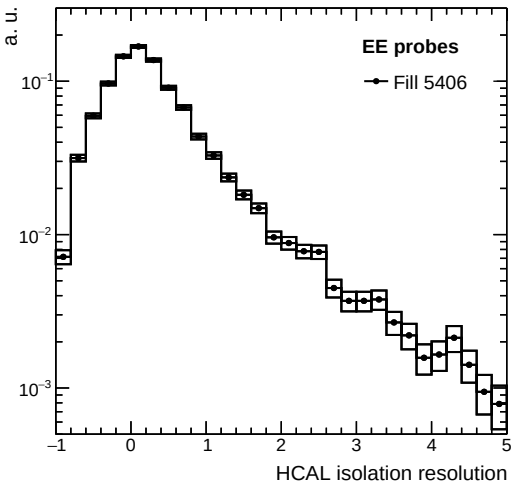

(f) HCAL isolation resolution (EE)

Figure 5.8: HLT-offline resolution of H/E and calorimeter isolations in fill 5406.

2, where Method 2 was run only if there was a SC compatible with a photon or electron in the event and only around a cone of $\Delta R < 0.25$ around this cone. This is sufficient for the purposes of synchronizing H/E at the two reconstruction levels.

The study is set up as follows. The trigger menu is modified such that the deposits used for PF clustering and subsequently HCAL isolation computation are the ones reconstructed by the regional Method 2 instead of the default Method 3. The cone size for the regional HCAL deposit reconstruction around the electron are varied and the resulting HCAL isolation resolution are compared. The data and menu used in the study are given in Table 5.5.

Table 5.5: Data used for the HCAL isolation with Method 2 study.

LHC fill	5406, 5424, 5427, 5442
Runs	283050, 283052, 283059, 283453, 283478, 283876
HLT menu	`/dev/CMSSW_8_0_0/GRun/V210`
Probe selection	As in Table 5.1 and passes L1 system cuts
Dataset	Same as in Section 5.2 (`MINIAOD` and `RAW`)

Figure 5.9 compares the HCAL isolation resolution computed with Method 3 and with the regional Method 2 of varying cone sizes. In the legend of these plots, M2 or M3 refer to the method with which the HCAL deposits are reconstructed and the numbers in parentheses, when present, refer to the cone size of the regional HCAL deposit reconstruction. The resolutions in EB and EE behave as expected; with larger cone sizes resulting in better HLT-offline agreement. It is worth noting that even with a cone size of 0.25, a region smaller than the one considered for HCAL isolation, a better agreement is obtained than taking into account the full cone size with Method 3. This is because for the low energy deposits that typically enter into HCAL isolation, the agreement between the two methods is poor as has been demonstrated internally within the collaboration. Another feature to be noted is how the resolutions keep improving as the cone size increases beyond 0.35, wider than the HCAL isolation cone size. The reason for this is that although HCAL isolation considers only HCAL PF clusters within 0.3 around the electron, deposits outside this cone can contribute to the individual clusters and performing their reconstruction over a larger cone means tighter synchronization between the HLT and offline.

What remains to be seen is whether the enlarging of regional Method 2 reconstruction is affordable timing-wise. In order to evaluate this, the timing of the full menu and the modules responsible for the regional reconstruction (separately for when the HLT electron has a corresponding L1 electron candidate and when it does not) are evaluated with each of the settings studied above, shown in Figure 5.10 and Table 5.6. As timing studies are supposed to be representative of the HLT menu as a whole, the `HLTPhysics` PD is used instead of

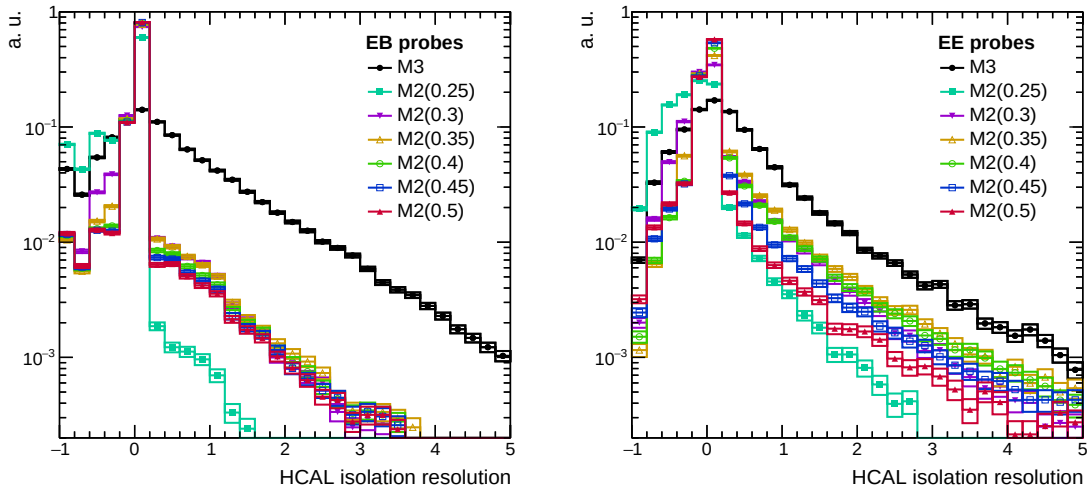

(a) EB (b) EE

Figure 5.9: HCAL isolation resolution comparing Method 3 and regional Method 2 of varying cone sizes.

the usual `SingleElectron`[5]. More detail about the timing measurement is given in Table 5.7.

These results point to several interesting features. With 0.25 being the default setting of the modules for H/E computation, updating HCAL isolation computation to use their outputs is expected to not change the timing in any way. However, this alone reduced the average event timing by 5.5 ms. This is attributed to the PF clustering step taking less time with the smaller set of inputs, although the validity of this hypothesis is not crucial to our present purposes and so is not investigated further. Taking both the resolution and timing results into account, it was decided by the collaboration that this update was feasible with a cone size of 0.4.

5.3.2 ECAL isolation with full Multifit

Following the strategy employed with HCAL isolation, the Multifit algorithm that is described in Section 3.2 is our main focus in synchronizing ECAL isolation, being the algorithm responsible for ECAL deposit reconstruction. To reduce timing, at the HLT the so-called fast Multifit is run, which first performs a prefit on the observed pulse accounting for only the current crossing. If this fit is good enough (quantified through a normalized $\chi^2 <$ X cut) then the amplitude is taken from the result of this fit. Only for low-quality fits the full Multifit algorithm is run with multiple pulse shapes. The goal of the study is therefore to understand the impact of fast Multifit on ECAL isolation at different prefit χ^2 thresholds and if it can be made to approach the full version used offline. Here, the ECAL isolation resolution is studied on simulation instead of data, considering several common processes: DY (MG5_-

[5]One is interested in the average timing of the HLT menu, and for this the `SingleElectron` PD is ill-suited to evaluate the impact of the change since it is biased towards events containing electrons. `HLTPhysics` PD on the other hand stores events that fire any L1 seed and is therefore more suitable for timing measurements.

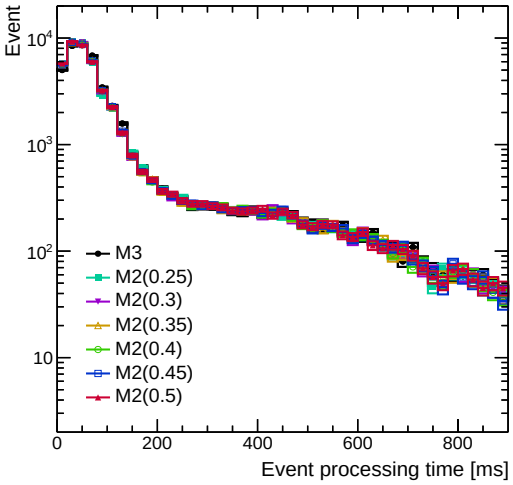

(a) Event

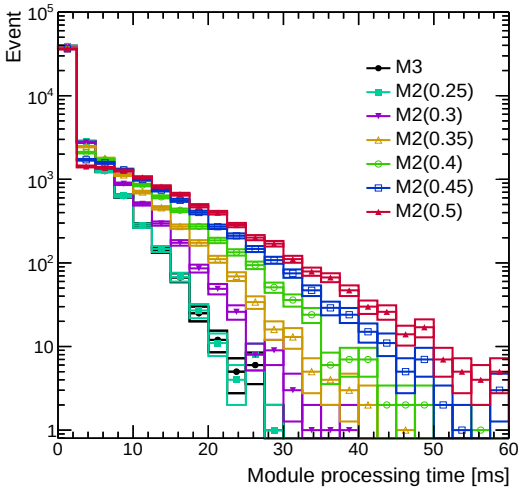

(b) L1 seeded module

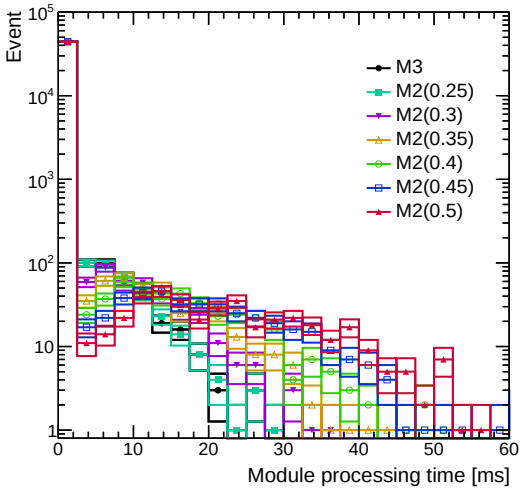

(c) Unseeded module

Figure 5.10: Event and module timing comparing Method 3 and regional Method 2 of varying cone sizes.

Table 5.6: Mean and RMS of event and module timing comparing Method 3 and regional Method 2 of varying cone sizes.

Case	Event		L1 seeded module		Unseeded module	
	Mean (ms)	RMS (ms)	Mean (ms)	RMS (ms)	Mean (ms)	RMS (ms)
M3	126.6	204.4	0.81	2.18	0.07	0.83
M2(0.25)	121.1	199.9	0.81	2.19	0.07	0.84
M2(0.3)	121.0	201.7	1.08	2.88	0.09	1.12
M2(0.35)	122.4	202.0	1.37	3.58	0.11	1.39
M2(0.4)	121.9	201.5	1.71	4.42	0.14	1.71
M2(0.45)	122.9	202.6	2.08	5.34	0.17	2.08
M2(0.5)	122.0	200.8	2.47	6.29	0.20	2.45

Table 5.7: Dataset used in HCAL isolation with Method 2 timing evaluation.

Run / statistics	283876 / 45000 events
HLT menu	`/dev/CMSSW_8_0_0/GRun/V210`
Prescale column	`1.45e34`

aMC@NLO), $t\bar{t}$ (POWHEGV2) and multijet QCD (PYTHIA8, 15 GeV $< \hat{p_T} <$ 170 GeV, where $\hat{p_T}$ refers to the minimum p_T of the outgoing parton at the ME level), in order to exploit the latest detector configuration and HLT menu at the time, which was not available for any data.

ECAL isolation resolutions at different χ^2 thresholds are compared in Figure 5.11. In these plots, the legend $\chi^2 >$ N refers to the case of fast Multifit configuration i.e. deposits for which the prefit χ^2 exceeds N are refit with the full algorithm, and 'HLT' refers to the default thresholds used in the 2016 data-taking (15 and 10 in EB and EE respectively) while 'Full' means no prefit is done. Based on the plots, the resolutions behave as expected, with the agreement improving as the HLT settings approach that of offline. As before, the timing results (performed using the same setup as in Table 5.7) are more interesting; they are shown in Figure 5.12 and Table 5.8, again separately for event and module timing.

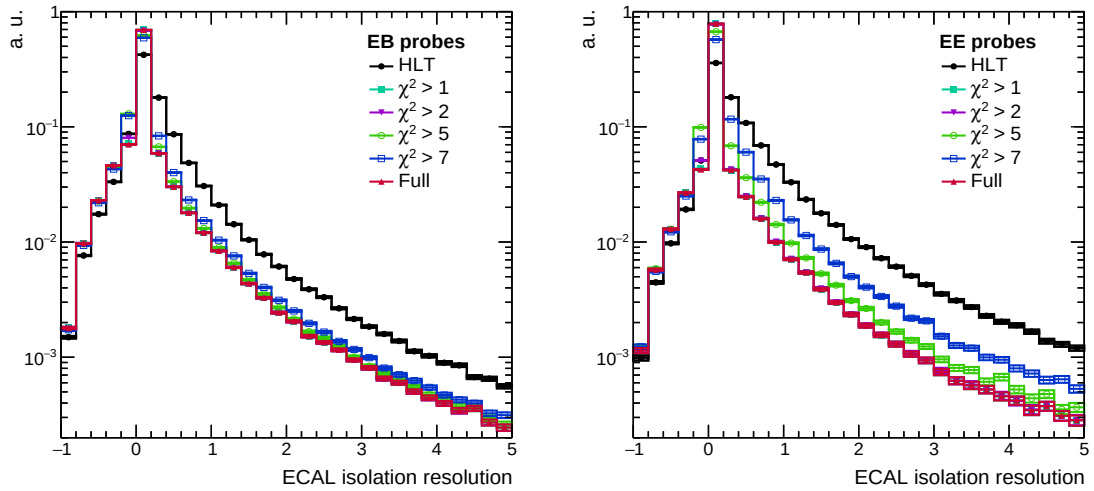

(a) EB (b) EE

Figure 5.11: ECAL isolation resolution comparing the Multifit algorithm run at different χ^2 thresholds.

While the event timing is unchanged, the module timing increases by at least 40% for all the thresholds considered in the study. More importantly, these results show that it is preferable to simply never perform the prefit instead of lowering the χ^2 thresholds. This behavior can be understood by looking at the fraction of deposits above a fixed χ^2 threshold,

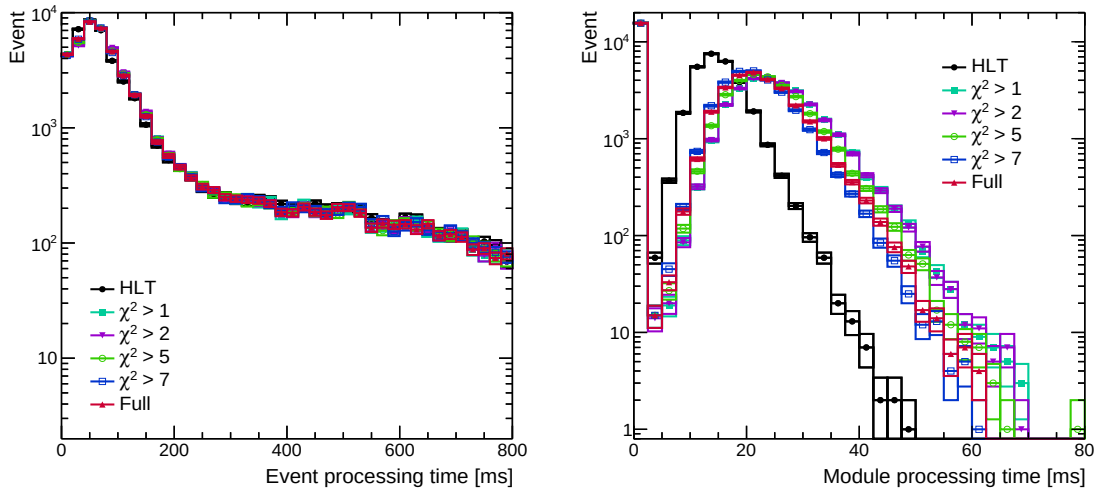

(a) Event (b) Module

Figure 5.12: Event and module timing comparing the Multifit algorithm run at different χ^2 thresholds.

Table 5.8: Mean and RMS of event and module timing comparing the Multifit algorithm run at different χ^2 thresholds.

Case	Event		Multifit module	
	Mean (ms)	RMS (ms)	Mean (ms)	RMS (ms)
HLT	141.0	230.0	9.93	8.07
$\chi^2 > 1$	138.5	218.0	16.57	13.54
$\chi^2 > 2$	139.7	218.8	16.54	13.52
$\chi^2 > 5$	140.0	221.6	15.60	12.73
$\chi^2 > 7$	140.4	224.1	14.32	11.66
Full	138.2	220.3	14.87	12.14

those for which full Multifit is run, shown for three different processes in Table 5.9. Lowering the threshold from 15 to 7 means performing the fit twice for additional deposits, which is time-intensive especially in EB with its higher deposit count and average χ^2. Taking this behavior into account, it was decided to disable the prefit to achieve the optimal HLT-offline agreement for ECAL isolation.

Table 5.9: Fraction of deposits above fixed χ^2 thresholds for DY, $t\bar{t}$ and multijet QCD. Statistical uncertainties on the fractions are negligible.

Threshold	DY		$t\bar{t}$		Multijet QCD	
	EB	EE	EB	EE	EB	EE
1	1	1	1	1	1	1
2	1	1	1	1	1	1
5	0.97	0.99	0.97	0.98	0.97	0.99
7	0.92	0.95	0.90	0.94	0.91	0.95
10	0.79	0.87	0.73	0.84	0.79	0.87
15	0.58	0.72	0.48	0.67	0.56	0.72

5.4 Single Electron Working Point Tuning for 2017

In general, a WP that is optimized for a given set reconstruction strategy, detector conditions and physics goals is only suboptimal for other sets. This is especially true for WPs that cut tightly on the phase space. As the detector conditions are changing every year, this sets the frequency with which the WP needs to be retuned.

This section discusses the tuning of the single electron trigger for the 2017 data-taking. On top of maximally exploiting the allocated rate budget, the tuning aims to fix the strong PU dependence of the 2016 WP and to explore the use of the s^2 variable (defined in Section 5.1), which has never been utilized before. The impetus for this is a stronger need to control the rate - due to the ever increasing performance of the LHC - which ideally should be achieved with as little loss of performance as possible.

The tuning is performed targeting electrons with $E_T > 35$ GeV and $|\eta| < 2.5$, with the thresholds imposed by single electron acceptance at L1.

5.4.1 Set-up

As preparation for the WP tuning, a path that, without cutting, computes all the electron ID variables that might be of interest is prepared to establish the full phase space. Any object

that passes this path is considered as an HLT electron candidate[6]. As the tuning is to be purely at the HLT, in order to disentangle ourselves from L1 effects as much as possible, the candidates are only required to be seeded by an L1 seed that imposes only minimal quality cuts. The tuning is based on simulation, considering only processes with high cross sections, as listed in Table 5.10.

Table 5.10: Simulation and cuts used in the single electron WP tuning.

Process	DY, W, $t\bar{t}$, multijet QCD (15 GeV $< \hat{p_T} <$ 600 GeV)
Seed	`SingleEG24`
E_T	> 35 GeV
$\left\|\eta^{SC}\right\|$	< 2.5

Having defined the baseline candidate collection, the efficiencies are defined as follows. For the multijet QCD process, where no true, prompt electrons are expected to be produced, it is simply given by the fraction of candidates passing a given WP. For the $t\bar{t}$ and W production, the efficiency is computed considering only the candidates that match true electrons from a W boson decay at the generator level. For the DY process where two true electrons are produced in each event, an HLT-only Tag and Probe method is employed, which is summarized in Table 5.11 (see Section 5.2 for a description of the method). The same set of candidates is also used to draw the distributions of the ID variables, where for the sake of brevity, within this section the candidates are all referred to as 'probes' even for processes where the efficiencies are not computed using the Tag and Probe method.

Table 5.11: Summary of selection cuts used in the HLT-only Tag and Probe method for single electron WP tuning.

	Tag	Probe
Acceptance	As in Table 5.10	
ID WP	2016 single electron WP	baseline
Z window	< 20 GeV	
Truth matching	$\Delta R < 0.1$ to electrons from Z decay	

5.4.2 Pile-up correction

The first step in the WP tuning is to derive the correction for PU-sensitive electron identification variables. This correction is done in order to have the WP cut electrons at the same efficiency regardless of the PU content of the event. As mentioned in Section 5.1, the

[6]Note that the requirement means that all candidates must pass all electron reconstruction steps. In other words, while the set of candidates has ~ 0 purity, the candidates must still 'look like an electron'.

correction method employed is called the 'ρ-correction' method. The method is so named because the correction is based on a fit to a parameter ρ, the median of energies calculated in a grid of η-ϕ cells, which, due to its linear dependence to the average number PU interactions, serves as an effective parametrization of PU content on an event-by-event basis [3].

The correction is derived as follows. For a given identification variable I, the I-ρ 2D distribution is drawn using a collection of DY probes. Then, a predefined quantile of I along ρ is chosen and fitted with a (in this case linear) function. The slope of the fitted line is called the effective area (EA), which expresses the dependency of I to ρ. The corrected variable I' that is used as the electron identification variable is then given by:

$$I' = I - (\mathrm{EA} \times \rho) \tag{5.6}$$

Figure 5.13 shows an illustration of the procedure. In this Figure, only DY probes with $E_T \in [35, 125]$ GeV and $\left|\eta^{SC}\right| < 1$ are considered. The 97% ECAL isolation quantile in each ρ bin is drawn as a black line, while the red line stands for a linear fit of the quantile within a subrange with sufficient statistics.

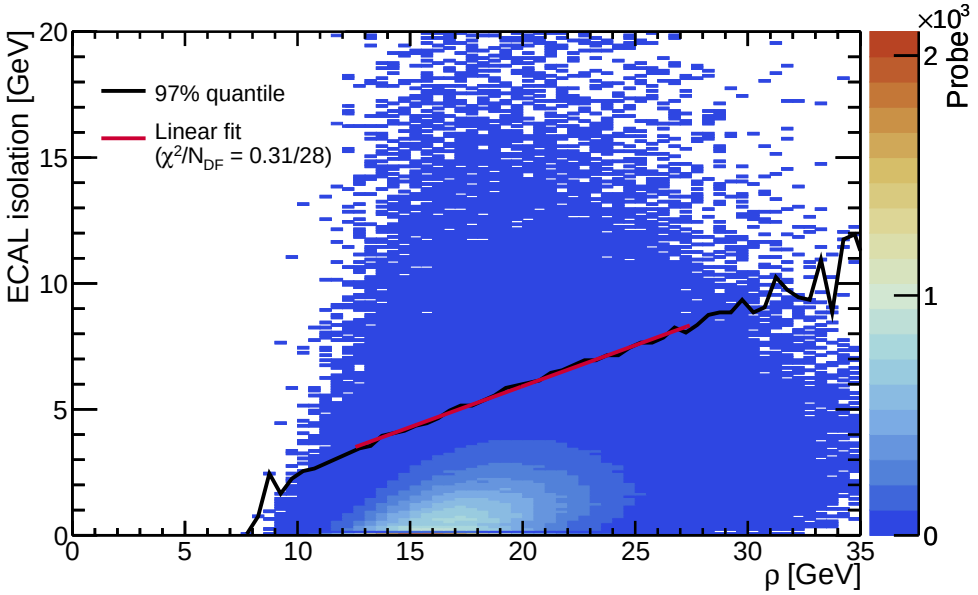

Figure 5.13: 2D distribution of ECAL isolation and ρ, illustrating the ρ-correction procedure. The black line refers to the position of the 97% ECAL isolation quantile in each ρ bin, while the red line shows a linear fit to the 97% quantile.

In early 2016, at the HLT the correction was derived for ECAL and HCAL isolations in in EB and EE. The new tune that entered from the Data 2 period (see Section 5.2) brought a number of improvements. First among them was the increased granularity of the correction from two bins in $\left|\eta^{SC}\right|$ to four bins, further splitting the EB and EE into $\left|\eta^{SC}\right|$ within [0, 1], [1, 1.479], [1.479, 2.1] and [2.1, 2.5] (although in the derivation candidates with $\left|\eta^{SC}\right|$ within [1.444, 1.566] were not considered). This was driven by the fact that the EA obtained in these

two regions were significantly different from each other, indicating that the quantiles depend on ρ differently within them. H of H/E was also corrected, having been shown to display a PU dependence (as can be seen in the shower shapes efficiencies). Due to this, the possibility that the EA depended on E_T was also explored, but the fits in two E_T bins (splitting [35, 125] GeV to [35, 70] and [70, 125] GeV) resulted only in small differences, which was averaged out in order not to increase the complexity of the WP. Finally, the correction was derived with the 95% quantile, different from the mean as was done in previous years. This was found to yield a flatter efficiency as a function of ρ. Building upon these improvements, in this round a correction is derived also for track isolation. The inclusion of the so-called noise term (NT) - the intercept of the linear fit - into the correction is also explored, updating the definition of the corrected variable I' to:

$$I' = I - (\mathrm{EA} \times \rho) - \mathrm{NT} \tag{5.7}$$

In order to check the performance of the procedure, the efficiency as a function of ρ is evaluated for corrections derived with 95% and 97% quantiles, with and without NT. In order to ensure a fair comparison, for each procedure a WP is set containing only the cuts on I' (in their respective relative forms), set such that each cut has 0.975 integrated efficiency. The result of the comparison is shown in Figure 5.14.

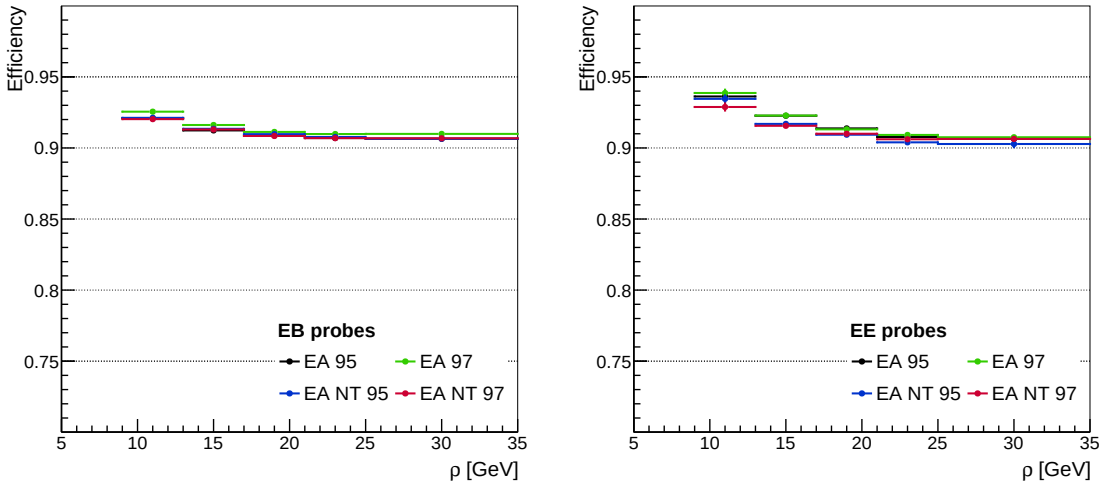

(a) EB (b) EE

Figure 5.14: WP efficiency as a function of ρ in EB and EE comparing the 95% and 97% quantiles and the usage of NT.

Based on these results, the correction using the 97% quantile with the NT taken into account is judged to be the best, as it yields the flattest efficiency as a function of ρ in both EB and EE. However, given that the differences are not very significant, especially in EB, another metric to motivate a choice is also evaluated. This is taken to be the ratio of DY and multijet QCD efficiencies of each WP, which is reported in Table 5.12.

Table 5.12: DY and multijet QCD efficiencies and their ratios for each ρ-correction WPs. The parentheses indicate the statistical uncertainties in the last digits.

Threshold	DY		Multijet QCD		Ratio	
	EB	EE	EB	EE	EB	EE
EA 95	0.9099(3)	0.9157(5)	0.167(5)	0.146(4)	5.45(16)	6.27(18)
EA 97	0.9130(3)	0.9158(5)	0.176(6)	0.147(4)	5.19(18)	6.23(17)
EA NT 95	0.9108(3)	0.9111(5)	0.171(6)	0.141(4)	5.33(19)	6.46(19)
EA NT 97	0.9100(3)	0.9114(5)	0.168(6)	0.140(4)	5.42(20)	6.51(19)

With two different ways of evaluating performance pointing to a single best WP, the 97% quantile taking NT into account method is chosen for the final ρ-correction derivation. The EAs and NTs obtained from the fits are reported in Table 5.13 and Table 5.14. For the subsequent steps in the WP tuning, all the relevant identification variables are corrected with these values according to Equation 5.7.

Table 5.13: Final EAs in each $\left|\eta^{\mathrm{SC}}\right|$ bin used in the 97% quantile ρ-corrected identification variables. The parentheses indicate the statistical uncertainties in the last digits.

Variable	Effective area (EA)			
	$\in [0, 1]$	$\in [1, 1.479]$	$\in [1.479, 2.1]$	$\in [2.1, 2.5]$
H	0.098(3)	0.159(6)	0.353(9)	0.423(12)
ECAL isolation	0.325(4)	0.296(6)	0.283(6)	0.438(6)
HCAL isolation	0.259(5)	0.328(6)	0.414(9)	0.456(9)
Track isolation	0.029(2)	0.111(5)	0.114(3)	0.032(3)

5.4.3 Tuning strategy

In the next step, the list of identification variables to be used in the WP is created. As the tuning aims to minimize the fake rate at a given signal efficiency, the variables are chosen based on their discrimination power. The distributions of each considered variables for DY and multijet QCD and their efficiency profiles are shown in Appendix A. As mentioned in Section 5.2, the track χ^2 is known to have a poor PU dependence, so in this tuning it is not included in the WP. Although applying a ρ-correction is an option, this variable has little discrimination power (see Figure A.8); there is little incentive for including it in the WP.

The tuning procedure is as follows. Discrimination profiles i.e. the curve of the multijet

Table 5.14: Final NTs in each $\left|\eta^{\mathrm{SC}}\right|$ bin used in the 97% quantile ρ-corrected identification variables. The parentheses indicate the statistical uncertainties in the last digits.

Variable	Noise term (NT)			
	$\in [0, 1]$	$\in [1, 1.479]$	$\in [1.479, 2.1]$	$\in [2.1, 2.5]$
H	0.89(5)	1.48(13)	2.67(18)	5.10(25)
ECAL isolation	-0.58(9)	-0.69(12)	-0.89(13)	-0.89(12)
HCAL isolation	0.79(11)	0.30(12)	0.40(19)	-0.06(19)
Track isolation	0.84(4)	-0.39(11)	-0.36(7)	0.71(6)

QCD rejection (which is defined as 1 - ϵ) vs DY efficiency of all variables are drawn from the efficiency profiles, which are then ranked by their discrimination power i.e. integral of the discrimination profile. Figure 5.15 shows the discrimination profiles of the three variables with the highest discrimination power in EE. A cut is set on the strongest variable with target DY efficiency of 97%. The discrimination profiles of the remaining variables are compared with the cut applied and a cut is set on the second strongest variable. This procedure is repeated iteratively until the pool of variables are exhausted and the set of cuts obtained in this way constitutes the WP.

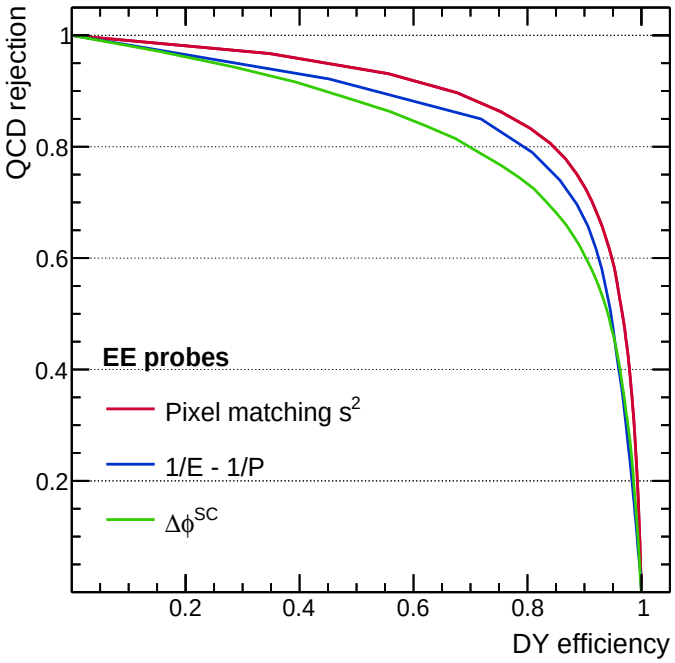

Figure 5.15: Illustration of the comparison between ID variables in determining their order in the iterative tuning procedure.

In setting the cut, the slope of the efficiency profile at cut value is taken into account; the cut is loosened slightly if it lies in the region where the slope is high so that it goes deeper into the DY efficiency plateau. This is done due to the so-called 'cut turn-on safety' concept; the shape of the efficiency profile depend on a multitude of factors collectively referred to as detector condition. For example, the $\Delta\eta^{\text{seed}}$ and $\Delta\phi^{\text{SC}}$ variables are both affected by tracker-ECAL alignment; misalignments can shift their efficiency profiles either to the right or left, the former resulting in a decrease of efficiency which can be disastrous depending on the cut value. Setting the cut within the plateau therefore gives us a degree of protection against the unexpected and ensures the WP performs stably throughout evolving detector conditions.

The results of the tuning is reported in Table 5.15. The WP is simply called 'Tight' - inheriting the same name of past years - to reflect the tight identification criteria it imposes on the electrons. This name is also easily contrasted with the 'Loose' WP that existed back in 2015 when the rate budget allowed it. In fact, a 'Loose' WP was also derived in this round, but it was not included in the HLT menu due to the rate budget.

Table 5.15: The WP derived through the tuning procedure illustrated in Figure 5.15. ρ-correction with EA and NT as in Table 5.13 and Table 5.14 is applied where relevant. All cuts are of the 'x $\leq$ X' kind, with x denoting the variable and X the threshold.

Variable	WPTight	
	EB	EE
$\sigma_{i\eta i\eta}$	0.011	0.0305
H/E	0.02	0.015
Relative ECAL isolation	0.03	0.025
Relative HCAL isolation	0.03	0.025
Pixel matching s^2	70	45
$1/\text{E} - 1/\text{P}$	0.012	0.011
Missing hits	-	1
$\Delta\eta^{\text{seed}}$	0.004	0.005
$\Delta\phi^{\text{SC}}$	0.02	0.023
Relative track isolation	0.03	0.025

5.4.4 Expected performance

Having derived a WP, we now turn to its expected performance. It is also beneficial to compare it with the performance of previous WP in order to assess whether the main objectives of the tuning have been met. However, it is necessary to keep in mind that the performance of 2016 WP in this section is evaluated with 2017 detector conditions. It is

therefore to be interpreted as the performance of the trigger if nothing is done as opposed to its performance in 2016 which we have already discussed in detail in Section 5.2. Table 5.16 reports the overall efficiency for each process considered. Up to this point the expected performance behaves as expected. An overall increase in efficiency is observed in all signal processes which is in line with the loosening of many cuts during the tuning.

Table 5.16: Overall efficiency comparing WPTight in 2016 and 2017. The parentheses indicate the statistical uncertainties in the last digits.

Process	2016 WP		2017 WP	
	EB ϵ	EE ϵ	EB ϵ	EE ϵ
DY	0.8602(4)	0.6999(8)	0.8708(4)	0.8305(7)
Multijet QCD	0.0358(28)	0.0206(15)	0.0348(28)	0.0270(17)
$t\bar{t}$	0.8394(6)	0.7222(14)	0.8423(6)	0.8205(12)
W	0.8494(23)	0.6866(38)	0.8603(22)	0.8205(31)

The fact that multijet QCD efficiency is reduced in EB although all signal efficiencies are increased hints that the tuning better exploits the available identification phase space, which is the second major objective of the tuning. In order to confirm this claim, differential DY efficiency are checked as functions of the standard variables in EB and EE. This is shown in Figure 5.16. As seen in the figure, the 2017 WP outperforms the 2016 WP, particularly in EE. Note that this check, utilizing only information available at the generator and HLT levels, is not sensitive to the feature at low $\left|\eta^{\mathrm{SC}}\right|$ seen in Section 5.2, as it is caused by discrepancies between the HLT and offline ID variables. The question of whether the feature is still present despite the improvements we have discussed so far will be discussed in Section 5.5.

As multijet QCD contribution in EE increases in 2017 WP, as indicated in Table 5.16, it is important to ensure that this is affordable rate-wise. In order to confirm this, the expected rates are compared for each process, shown in Table 5.17, assuming an instantenous luminosity of $2{\times}10^{34}$ $\mathrm{cm}^{-2}\mathrm{s}^{-1}$ and the following L1 seeds: `SingleEG40 OR SingleIsoEG36er2p1 OR SingleIsoEG38`. The rate is estimated by multiplying Equation 3.1 with efficiencies for individual processes (for multijet QCD the estimation is done separately for each $\hat{\mathrm{p}_{\mathrm{T}}}$ bin, but just like the efficiency only the total rate is reported). As expected from the efficiencies, the purity (defined as the ratio betwen the rate of signal processes and the total rate) of the WP has degraded from 59.9% in 2016 to 56.6% in 2017, due to the increased multijet QCD contribution. Despite this the 2017 WP is approved for use in data-taking: the 10% increase in rate is affordable and deemed an appropriate cost for its significantly better signal efficiency, especially in EE and at high PU.

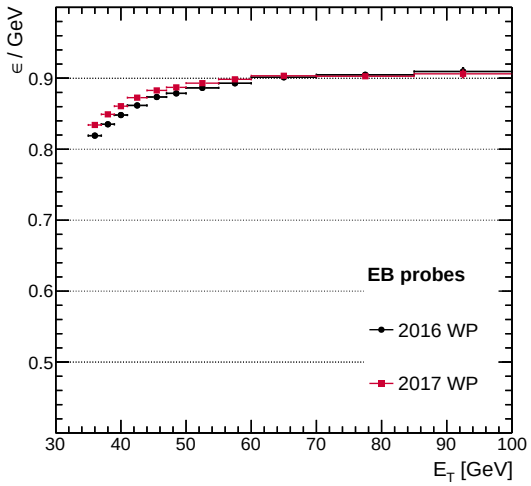

(a) $\epsilon(\mathrm{E_T})$ (EB)

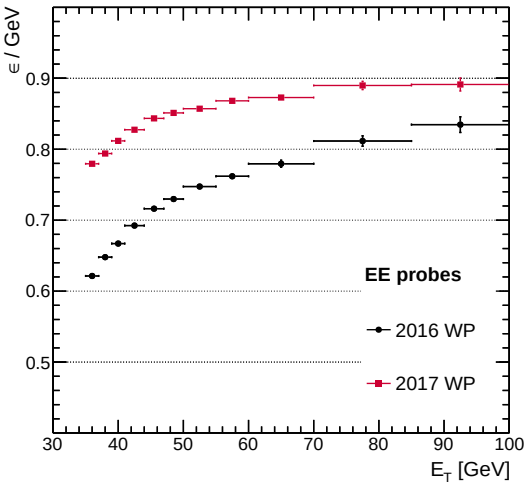

(b) $\epsilon(\mathrm{E_T})$ (EE)

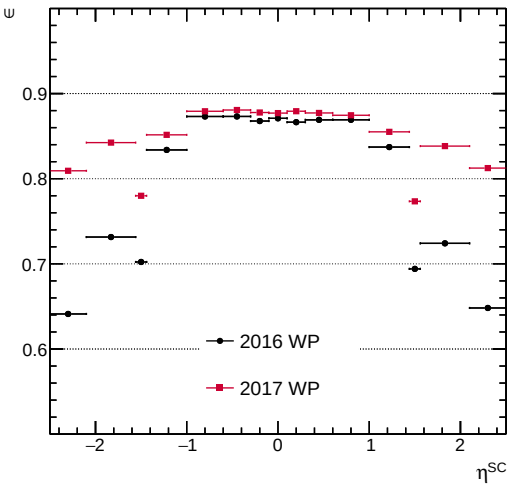

(c) $\epsilon\left(\eta^{\mathrm{SC}}\right)$

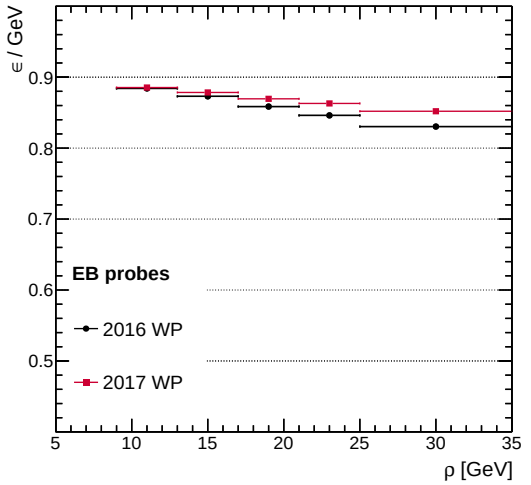

(d) $\epsilon(\rho)$ (EB)

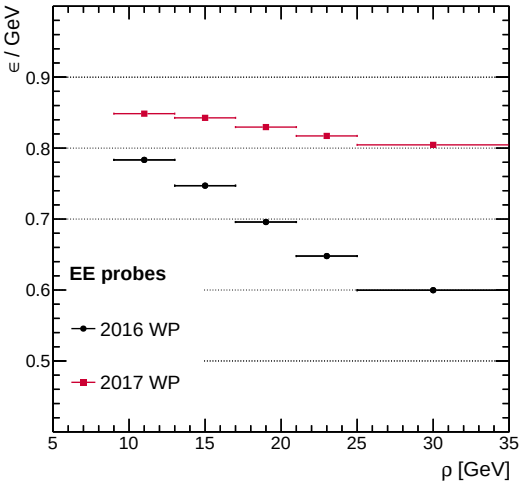

(e) $\epsilon(\rho)$ (EE)

Figure 5.16: Expected efficiencies of 2016 and 2017 WPs as functions of $\mathrm{E_T}$, η^{SC} and ρ, evaluated using the DY simulation.

Table 5.17: Expected rates of the 2016 and 2017 WP. The uncertainties are statistical.

Process	2016 WP (Hz)	2017 WP (Hz)
DY	9.00 ± 0.05	9.39 ± 0.05
Multijet QCD	29.68 ± 1.43	35.59 ± 1.64
W	35.38 ± 0.27	37.01 ± 0.28
Total	74.05 ± 1.46	81.99 ± 1.66

5.5 Trigger Performance in 2017

In deriving the WP its performance is investigated using simulation. It is crucial that this expectation is verified by measuring the performance in data taken with this WP. This is discussed in this section, where the performance of single electron trigger in 2017 is measured using data totalling 35.8 /fb.

5.5.1 Overall efficiencies of the single electron trigger in 2017

The measurement is performed in the same way as 2016 (object selection as given in Table 5.1), the only difference being a tighter cut on the electron E_T (> 35 GeV and on HLT path `Ele35_WPTight_Gsf`, which is the lowest unprescaled single electron trigger available in 2017). As before, the measurement is done using the `SingleElectron` PD (`Run2017[B-F]`) and DY simulated samples at `MINIAOD` tier. Similar to the 2016 measurement discussed Section 5.2, the data is divided based on run number; this splitting is given in Table 5.18.

Table 5.18: Data splitting used in 2017 efficiency measurement.

Legend	Run range	Remark
MC	-	Simulation made with trigger menu matching one in the Data 2 range and ideal detector geometry
Data 1	297050 - 299329	Initial commissioning period (4.73 /fb)
Data 2	299368 - 305636	Single electron trigger update to the 2017 WP (31.05 /fb)

Only the overall efficiencies will be discussed, as 2017 data has a number of other changes that are beyond the scope of this chapter making a fair detailed comparison difficult. The most prominent of these is the upgrade of the pixel detector, which introduced an additional pixel layer. This required a rewrite of the pixel matching algorithm in order to reduce the number of valid combinations involved. However, some combinations of pixel layers were missing in the initial version of this algorithm, which - coupled with dead layers being the only valid combinations in this region - caused a reduced efficiency in the positive EB region

at high ϕ. There was also a problem in early data taking where the uncertainty in the position of online beamspot was mismeasured to be significantly smaller than in later measurements. As the pixel matching algorithm relies on this measurement to define an allowed region in its first step, this caused another efficiency loss that the Tag and Probe method is not sensitive to, since both tag and probe stem from the same vertex which is inside the allowed region by construction. We will therefore concentrate only on the comparison of trigger performance before and after the introduction of the new WP and for this purpose it is sufficient to consider only the overall efficiencies. This is shown in Figure 5.17.

The data behavior in efficiency as a function of η^{SC} is a direct manifestation of the problems we discussed - the EB efficiency is not symmetric in η^{SC} only in data. That this behavior is mitigated in Data 2 is not due to the WP however - this is thanks to the update in pixel matching algorithm that happened together with the introduction of new WP. The effect of the new WP in EB is expected to be small (see Table 5.16); this is exactly the behavior seen in data at negative EB region, where the difference between Data 1 and Data 2 periods is small. The efficiency dip at low $\left|\eta^{\mathrm{SC}}\right|$ observed in Figure 5.2 has now been eliminated, confirming the hypothesis that it was caused by the discrepancies between online and offline definition of isolation inputs. Finally, the efficiency behavior in $\mathrm{N_{PV}}$ is much flatter with the new WP, showing the success of the PU correction scheme adopted in the 2017 WP.

5.5.2 Single electron rate: 2016 vs 2017

In Table 5.17 a 10% increase in total rate is anticipated in updating the WP. This estimation is made using the same simulation, but it is not completely fair in the sense that the 2016 WP was not optimized for 2017 conditions. A better figure of merit is therefore the actual rates measured in 2016 and 2017; this is shown as a function of average number of PU in Figure 5.18 for the path `Ele35_WPTight_Gsf`. The 'pre-deadtime unprescaled rate / num colliding bx' in the y-axis of Figure 5.18 refers to the correction performed on the rate taking into account the time when the detector is inactive, the L1 and HLT prescales and the number of bunch crossings, which may be different between the runs. They are necessary in order to allow a fair comparison between trigger rates of different runs, which may have been taken with different bunch schemes [4] and detector conditions. This fairer rate comparison further highlights the success of the new WP; a higher signal efficiency and a lower PU dependence have been achieved together with an overall rate reduction of 10%.

5.6 Summary and Outlook

This chapter presents the tuning of the WP that is used in the single electron trigger with the lowest $\mathrm{p_T}$ threshold to be unprescaled during the 2017 data taking. From a measurement of the trigger efficiency in different periods of the 2016 data taking, several undesirable features are observed in the efficiency distributions, the most striking among them being the lower efficiency at low values of $\left|\eta^{\mathrm{SC}}\right|$ and the decreasing efficiency as $\mathrm{N_{PV}}$ increases (see Figure 5.2). This is attributed to the different definitions of the calorimeter isolation variables that are used in electron identification at the HLT and offline reconstruction steps, a hypothesis that is confirmed by direct comparisons in Figure 5.8.

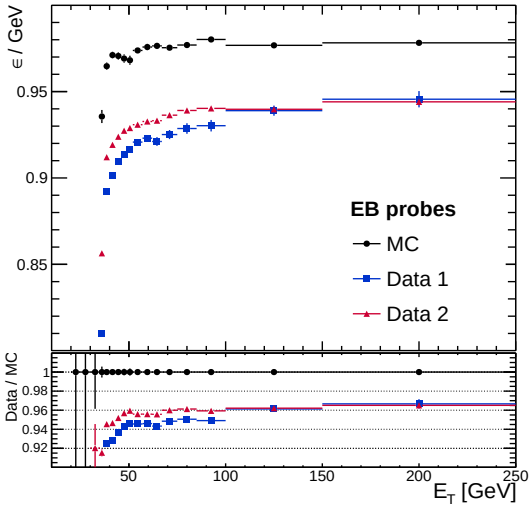

(a) $\epsilon(\mathrm{E_T})$ (EB)

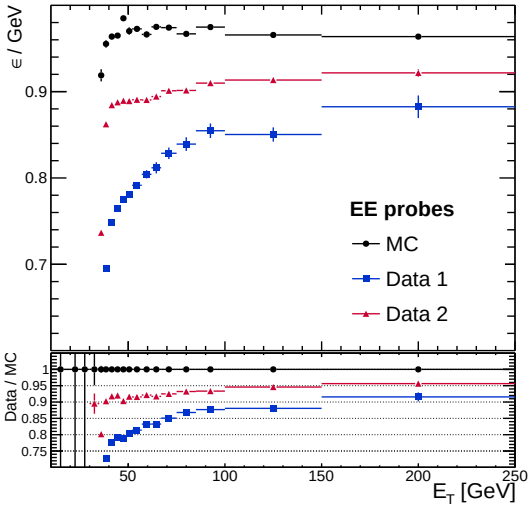

(b) $\epsilon(\mathrm{E_T})$ (EE)

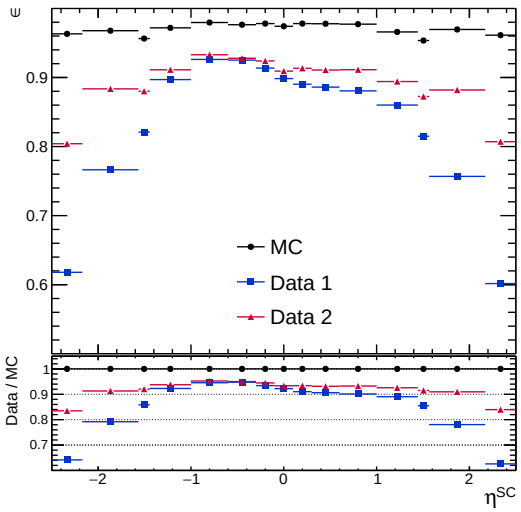

(c) $\epsilon\left(\eta^{\mathrm{SC}}\right)$

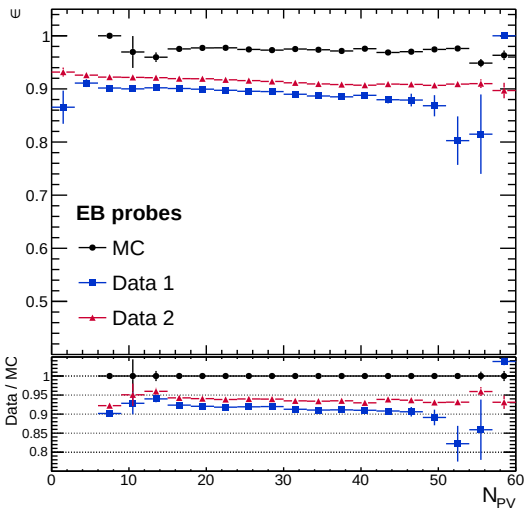

(d) $\epsilon(\mathrm{N_{PV}})$ (EB)

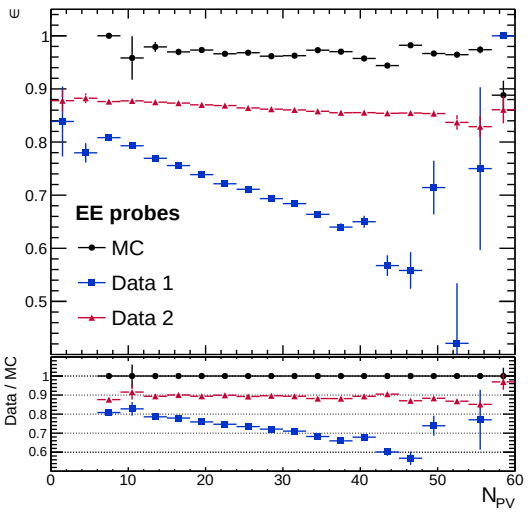

(e) $\epsilon(\mathrm{N_{PV}})$ (EE)

Figure 5.17: Overall single electron efficiency in 2017 as functions of $\mathrm{E_T}$, η^{SC} and $\mathrm{N_{PV}}$.

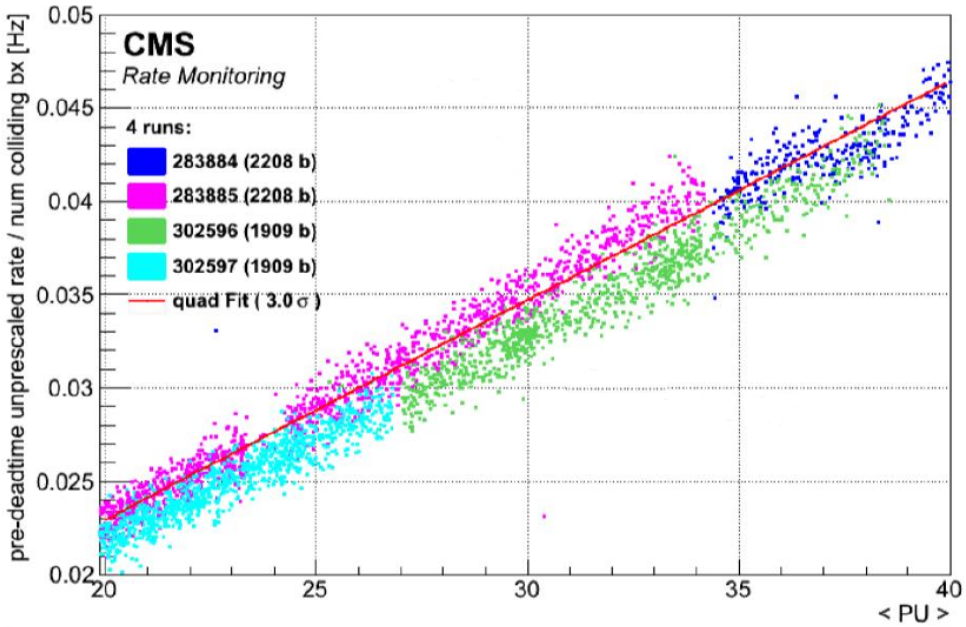

Figure 5.18: `Ele35_WPTight_Gsf` rates normalized by the number of bunch crossing in runs 283884, 283885 from 2016 and runs 302596, 302597 from 2017 as a function of PU. The red line indicates a quadratic fit to the rates in the four runs, which is used by the collaboration to estimate the rate of a trigger at PUs higher than what is observed in the data.

This difference can be removed by using the same algorithm to reconstruct the calorimeter clusters in both reconstruction steps. Since the time taken by the algorithm has been the primary motivation for using an optimized version at the HLT, the timing impact of this synchronization is studied in Section 5.3, and a setting point balancing the online-offline synchronization (and therefore the physics performance) and the HLT timing restrictions is found. A new WP is derived in Section 5.4 using the new definition of calorimeter isolations and a pixel matching variable along with other electron identification variables, including the PU correction for variables that are sensitive to PU contribution in the event. The tuning aims to maximally exploit the rate budget by increasing the efficiency of triggering on the processes of interest i.e. those with electrons from the decay of W or Z bosons, and to remove the undesirable features of the trigger WP observed in Figure 5.2. The WP has been approved for use in 2017 data taking and its performance is re-evaluated using real data and compared to the expectations of the tuning in Section 5.5. From the results, it is concluded that the goals laid down for the new WP have been met. This conclusion is independently verified by the collaboration as documented in Reference [5]. The single electron trigger is used in many different analyses in CMS covering a wide range of topics, including but not limited to those reported in References [6], [7] and [8].

Looking ahead to the LHC Run 3 data-taking period and beyond, the higher instantenous luminosity that is foreseen during these periods means that PU impact mitigation becomes increasingly more challenging. At the same time, the need to do so is increasingly more pressing to keep the rate of the trigger under control. As such, in defining future versions

of the single electron trigger, other PU mitigation approaches are well worth exploring. One such approach is called PU per particle identification approach [9], which has been used in offline reconstruction within the CMS collaboration [10]. It is interesting to explore the feasibility of this approach at the HLT - or perhaps an optimized version that uses PF clusters rather than PF objects, similar to the use of ECAL, HCAL and track isolations at the HLT instead of the photon, neutral and charged PF isolations in offline reconstruction - to provide additional handles against PU. Such a study is beyond the scope of this chapter and will be left to a future investigation.

5.7 Bibliography

[1] CMS Collaboration, "Performance of Electron Reconstruction and Selection with the CMS Detector in Proton-Proton Collisions at $\sqrt{s} = 8$ TeV", *JINST* **10** (2015), no. 06, P06005, doi:10.1088/1748-0221/10/06/P06005, arXiv:1502.02701.

[2] Particle Data Group Collaboration, "Review of Particle Physics", *Chin. Phys.* **C40** (2016), no. 10, 100001, doi:10.1088/1674-1137/40/10/100001.

[3] CMS Collaboration, "Jet energy scale and resolution in the CMS experiment in pp collisions at 8 TeV", *JINST* **12** (2017), no. 02, P02014, doi:10.1088/1748-0221/12/02/P02014, arXiv:1607.03663.

[4] L. Evans and P. Bryant, "LHC Machine", *JINST* **3** (2008) S08001, doi:10.1088/1748-0221/3/08/S08001.

[5] CMS Collaboration, "Electron trigger performance in CMS with the full 2017 data sample", CMS Detector Performance Summaries CMS-DP-2018-030, Jun, 2018.

[6] CMS Collaboration, "Measurement of differential cross sections for the production of top quark pairs and of additional jets in lepton+jets events from pp collisions at $\sqrt{s} =$ 13 TeV", *Phys. Rev.* **D97** (2018), no. 11, 112003, doi:10.1103/PhysRevD.97.112003, arXiv:1803.08856.

[7] CMS Collaboration, "Measurement of electroweak production of a W boson in association with two jets in proton-proton collisions at $\sqrt{s} = 13$ TeV", arXiv:1903.04040.

[8] CMS Collaboration, "Evidence for associated production of a Higgs boson with a top quark pair in final states with electrons, muons, and hadronically decaying τ leptons at $\sqrt{s} = 13$ TeV", *JHEP* **08** (2018) 066, doi:10.1007/JHEP08(2018)066, arXiv:1803.05485.

[9] D. Bertolini, P. Harris, M. Low, and N. Tran, "Pileup Per Particle Identification", *JHEP* **10** (2014) 059, doi:10.1007/JHEP10(2014)059, arXiv:1407.6013.

[10] CMS Collaboration Collaboration, "Pileup mitigation at CMS in 13 TeV data", Technical Report CMS-PAS-JME-18-001, CERN, Geneva, 2019.

CHAPTER

6

EVENT SELECTION AND SYSTEMATIC UNCERTAINTIES

Contents

In this chapter, the details of event selection criteria used in this work is listed. They are mostly based on recommendations by the collaboration; whenever this is the case the cuts or steps taken will be simply stated without accompanying studies. Unless mentioned otherwise, the criteria are common to both the A/H search and spin correlation measurement. As the dileptonic $t\bar{t}$ channel is exploited in this work, the selection is based on the presence of two leptons and two jets in the event, at least one of which is consistent with having been initiated by a b quark. As this chapter is dedicated to the listing of inputs to the analyses and aspects common to both of them, the reader is assumed to already be familiar with the concepts and terms discussed in the preceeding chapters, in particular Chapters 2, 3 and 4.

6.1 Trigger and Dataset

In this section, the list of events to be analyzed are defined. This is done by specifying the triggers responsible for recording them together with the PDs they are assigned to. The SM processes that are taken into account and their simulation strategies are also provided.

6.1.1 Trigger requirement

In both analyses, three orthogonal channels are defined based on flavors of the two leptons with the highest p_T: ee, eμ and $\mu\mu$. Events on each channel are required to fire channel-specific trigger paths as in Table 6.1. If a channel has more than one main dileptonic path, then an event is accepted if it fires any one of them. If none of the main dileptonic paths are fired, an event is still accepted if it fires the corresponding single lepton triggers. This recovery procedure was found to increase the event yield by around 10%.

Trigger efficiencies are determined by using the uncorrelated trigger method, where events of a given topology are required to pass a set of baseline triggers that are mostly uncorrelated with the triggers whose efficiencies are to be measured; in our case $\not{p}_T$ triggers are used as baseline to measure the trigger efficiency for events containing two leptons. Given our assumptions, the ratio between events firing the dileptonic trigger set and the baseline is the efficiency we seek to measure, as the baseline trigger efficiency cancels off. Unlike the Tag and Probe method where the efficiencies are measured at the object level, this method does so at the event level, allowing a single efficiency measurement for an arbitrary set of

triggers[1]. The efficiencies used in this work are taken from Reference [1], which also examines the assumption of no-correlation between the sets and other closure tests in more detail. The ratio between the efficiencies in data and simulation is called scale factor (SF)[2] and is used to reweight the latter.

6.1.2 Data

Data samples used are from the `DoubleEG`, `MuonEG`, `DoubleMuon`, `SingleElectron` and `SingleMuon` PDs, recorded during the `Run2016[B-H]` period. The analysis is performed with `MINIAOD` samples from the 3 February 2017 reconstruction campaign. Lumi mask `Cert_-271036-284044_13TeV_23Sep2016ReReco_Collisions16_JSON.txt`, supplied by the collaboration, is applied. In total the data sum up to 35.9 /fb.

6.1.3 Simulation

Simulated samples used in this work are produced by the collaboration in the `Summer16` campaign. The considered processes along with their nominal simulation settings and associated cross sections are given in Table 6.2. For samples generated using MG5_aMC@NLO with additional partons whose MEs are evaluated at LO accuracy, the MLM prescription is used to merge contributions from the ME and PS [2], while for samples with MEs evaluated at NLO accuracy, the FxFx prescription is used [3]. The nominal μ_R and μ_F choices for the SM $t\bar{t}$ simulation is $m_T^t = \sqrt{m_t^2 + (p_T^t)^2}$, with p_T^t evaluated in the $t\bar{t}$ ZMF.

PDF set `NNPDF30_nlo_as_0118` is used for all samples generated at NLO accuracy, while the `NNPDF30_lo_as_0130` set is used for samples generated at LO accuracy [4]. Pythia8 refers to version 8.212 for both sample generation where relevant and parton showering and hadronization for all samples [5]. Unless stated otherwise, in this step Pythia8 is configured with the `CUETP8M1` tune [6, 7].

Detector simulation is performed using Geant4 version 9.4 in all cases [8].

6.2 Object Selection

The second step of event selection is defining the type of event topology one is interested in and therefore the type of reconstructed objects such events must contain. Unlike in the previous step, where this is done only implicitly through the choice of triggers that are used to record the event, in this section the acceptance and identification cuts that are applied on each object are explicitly stated.

[1] There are two other reasons why this method is favored over Tag and Probe (see Section 5.2) for our purposes. First, Tag and Probe requires that the two leptons are triggered in sequence - one strictly before the other - which may not be the case during the data taking. Second is that since Tag and Probe makes use of the DY process, there is some concern on whether the difference in lepton kinematics means it is not optimal for $t\bar{t}$ event topology. As shown in Reference [1] however, the two methods agree well with each other.

[2] As the phrase scale factor, literally taken, implies no specific use case whatsoever, the SF abbreviation will be used in this work only when they are used as event weight in simulation to correct for some difference with respect to data, as is the case with trigger (efficiency) SFs.

Table 6.1: Trigger requirements on each analysis channel. [ElewP] and [MuWP] stand for electron and muon ID WP identifier used in the dileptonic paths which are CaloIdL_TrackIdL_IsoVL and TrkIsoVVL respectively.

Type	ee	eμ	$\mu\mu$
Dileptonic	Ele23_Ele12_[ElewP]_DZ	Mu23_[MuWP]_Ele12_[ElewP](_DZ) Mu8_[MuWP]_Ele23_[ElewP](_DZ)	Mu17_[MuWP]_(Tk)Mu8_[MuWP](_DZ)
Single lepton	Ele27_WPTight_Gsf	Ele27_WPTight_Gsf Iso(Tk)Mu24	Iso(Tk)Mu24

Table 6.2: List of simulated processes and their associated cross sections used in this work.

Process	ME generator	Cross section (pb)	Remark
$t\bar{t}$	POWHEGV2 [9]	831.76 [10]	NLO, `CUETP8M2T4` tune [6, 7]
Single t (t-channel)	POWHEG	136.02 [11]	
Single $\bar{t}$ (t-channel)		80.95 [11]	
Single t + W		71.7 [11]	Sum of both t and $\bar{t}$. Also as above
DY ($m_{\ell\ell} \in [10, 50]$ GeV)	MG5_aMC@NLO [12]	18610	LO with up to four additional partons in A/H search
DY ($m_{\ell\ell} > 50$ GeV)		5765.4	NLO with up to two additional partons in spin corr.
W		61526.7	LO with up to four additional partons
$t\bar{t}W$		0.6105	NLO with up to one additional parton
$t\bar{t}Z$		0.7826	
WW	PYTHIA8	118.7 [13]	LO
WZ		47.13	
ZZ		16.523	

6.2.1 Primary vertex

PVs are sorted by scalar sum of p_T of the tracks entering the fit, with the one with the highest sum declared to be the PV associated to the hard scattering event and is used in this work. The other PVs are attributed to PU. Quality cuts are imposed on the hard PV; it must be a real vertex with its fit having at least 4 degrees of freedom[3] and is within 24 (2) cm in the z (transverse) direction from the nominal beam spot.

As the distribution of N_{PV} in simulation is different to that of data, the former being affected by the the assumed inelastic pp cross section, the corresponding distribution at the generator level is reweighted such that it matches the data. The inelastic pp cross section is taken by the collaboration to be 69.2 mb, consistent with measurements presented in Reference [14].

6.2.2 Muon

Muons used in this work are those passing the Tight ID WP with isolation, the cuts of which are listed in Table 6.3. PU correction for muon isolation is called the $\delta\beta$ correction, which subtracts from the photon and neutral hadron components of PF isolation half the of the sum due to charged PF objects that are identified as coming from PU. Additionally, the so-called Rochester correction is applied to correct muon momentum scale and resolution against detector misalignment effects and/or magnetic field biases. Only muons with $p_T > 20$ GeV and $|\eta| < 2.4$ are considered.

The muon ID WP efficiency is computed as a function of muon p_T and η using the Tag and Probe method in both data and simulation; the ratio of the two is used to reweight the latter. The efficiency of the muon ID WP is 85% in the turn-on region and above 95% in the plateau throughout the whole η range except between the MB wheels, where it is 90%.

6.2.3 Electron

Electrons used in this work are those passing the Tight ID WP, the cuts of which are listed in Table 5.2. Electron energies are corrected with a regression and smearing procedure to match the spectrum measured in data and simulation. Furthermore, impact parameter cuts are imposed; $d_{xy} < 5$ (10) mm in EB (EE) and $d_z < 10$ (20) mm in EB (EE) respectively. Only electrons with $p_T > 20$ GeV and $\left|\eta^{SC}\right| < 1.444$ or $\in [1.566, 2.4]$ are considered.

Similar to muons, the simulation is reweighted with the ratio of electron ID WP efficiencies in data and simulation, measured with the Tag and Probe method as a function of p_T and η^{SC}. The efficiency of the electron ID WP is 60% in the turn-on region and 80% in the plateau throughout the full η^{SC} range except the EB-EE transition region where it is only 40%.

[3]The number of the degrees of freedom $N_{DF} = -3+2\sum_i^{track} w_i$, with w_i being the weight in PV subsection of Section 4.1, so this cut translates roughly to having 4 tracks entering the fit.

Table 6.3: Tight muon ID WP with isolation.

Variable	Cut
`isGlobalMuon` flag	`true`
`isPFMuon` flag	`true`
Global track fit normalized χ^2	< 10
Muon chamber hits entering global track fit count	> 0
Muon station with segments count	> 1
Tranverse impact parameter d_{xy}	< 2 mm
Longitudinal impact parameter d_{z}	< 5 mm
Pixel hit count	> 0
Tracker layer with hits count	> 5
$\delta\beta$-corr. comb. rel. PF isolation ($\Delta\mathrm{R} < 0.4$)	< 0.25, 0.15 (A/H, spin corr.)

6.2.4 Jet

Jets used in this work are those passing the Loose ID WP (of 99% efficiency), the cuts of which are listed in Table 6.4. While jet reconstruction is intended to provide a proxy to the initiating parton energy, nonlinear detector response to different particles, spurious additional contributions e.g. from PU and missing true contributions e.g. due to energy carried by neutrinos in leptonic hadron decays mean that a sufficiently accurate approximation is not reached directly from clustering the PF objects. For this reason a set of corrections (Jet Energy Corrections or JECs) are applied by multiplying the reconstructed jet momenta with SFs parametrized as functions of their properties [15]. At CMS, the corrections are applied in sequence with the input for a given step being the output of its previous step. They are:

1. The first correction is applied to remove PU contribution with SFs parametrized as a function of ρ, jet area, $\mathrm{p_T}$ and η derived from multijet QCD simulation, and to correct for detector response differences in data and simulation

2. The second correction is applied to match the momenta between reconstructed and generator jets from the previous step, with the SFs parametrized as a function of jet $\mathrm{p_T}$ and η derived from multijet QCD simulation

3. The third correction is applied only in data to correct for residual response difference with respect to simulation, with the SFs parametrized as functions of jet $\mathrm{p_T}$ and η derived using Z/γ + jet and multijet QCD simulations

Furthermore, in simulation the jet momenta are smeared to match the resolution of data. For reconstructed jets with a matching generator jet (imposed as a $\Delta\mathrm{R} < \mathrm{R_{cone}}/2$ cut such that the two jets overlap and the $\mathrm{p_T}$ difference between the reconstructed and generator jet,

Table 6.4: Loose jet ID WP.

Variable	Cut
Constituents count	> 1
Charged hadron energy fraction	> 0
Neutral hadron energy fraction	< 0.99
Photon energy fraction	< 0.99
Electron energy fraction	< 0.99

Δp_T, not exceeding three times the resolution measured in simulation), the smearing is applied by a SF multiplied with Δp_T, otherwise a stochastic smearing is applied by a SF and the p_T resolution in simulation. In either case the scaling is done such that Δp_T can only increase, leading to a worsening of resolution. Only jets with $p_T > 20$ GeV and $|\eta| < 2.4$ are considered.

Jets are b-tagged if they pass the medium (loose) WP of the `cMVAv2` (`iCSVv2`) tagger for the A/H search (spin correlation measurement). The b-tagging efficiency is measured in $t\bar{t}$ simulation for different jet flavors (light, c and b). In the A/H search, the tagging efficiency for b jets is in the 0.55 - 0.75 range, with the higher end occuring in the $|\eta| \in [0, 1]$ and $p_T \in [50, 200]$ GeV region. The c jet mistagging rate is in the 0.1 - 0.2 range, while the light jet mistagging rate is in the 0.005 - 0.025 range. In both cases the mistagging rate is higher at large $|\eta|$ and p_T values. These efficiencies are used to reweight all simulated samples with SFs as a function of jet p_T and η that are provided by the collaboration.

6.2.5 Missing transverse momentum

$\not{p}_T$ is computed using PF candidates, with a further correction accounting for modified jet momenta due to JECs. Since the $\not{p}_T$ ϕ distribution is observed to be sinusiodal in shape, while rotational symmetry in the pp collisions means it should be flat - a correction is applied to reduce the mismatch between data and simulation. Additionally, a number of filters are applied to reject events where $\not{p}_T$ are likely to be mismeasured e.g. those with high calorimeter noise or significant beam halo interactions. All the corrections above are based on the standard recipes provided by the collaboration.

6.3 Event Selection

Events are considered for further analysis if they pass the following cuts (which will be referred to as full event selection from now on):

1. The **2 lepton** cut requires the presence of exactly two opposite-sign leptons (e or μ) with $p_T > 20$ GeV and $|\eta| < 2.4$, with one of them having $p_T > 25$ GeV. The pair must have an invariant mass $m_{\ell\ell} > 20$ GeV

2. The Z **veto** cut is imposed in same-flavor (ee or $\mu\mu$) channels; events must be outside the Z window ($|m_{\ell\ell} - m_Z| > 15$ GeV) and $\not{p}_T > 40$ GeV. For historical reasons, the cut is imposed in 2 parts; the Z window part is applied right after the 2 lepton cut while the $\not{p}_T$ part is imposed after the 2 jet cut

3. The **2 jet** cut requires the presence of at least two jets with $p_T > 30$ GeV and $|\eta| < 2.4$. Additional jets in the event with $p_T > 20$ GeV and $|\eta| < 2.4$ are also accepted for further analysis. All accepted jets must be $\Delta R > 0.4$ away from the leptons

4. The **1 b-tag** cut requires at least one of the accepted jets to be b-tagged

5. The **kinematic reconstruction** cut requires the kinematic reconstruction algorithm described in Section 6.5 to return at least one solution

6.4 Background Estimation

While the cuts above result in a fairly pure dileptonic $t\bar{t}$ event sample, several other processes also contribute to it; most notably t + W production and DY. They comprise the irreducible background contribution; irreducible in the sense that the final state topology of these processes are the same as that of our process of interest. Futhermore, there is also the reducible background contribution from semileptonic $t\bar{t}$ production where one of the jets is mis-reconstructed as a lepton. In any case, their contribution to the data sample has to be estimated and subtracted out in order to measure the signal yield. For all processes considered in Table 6.2 except DY, their contributions, in both distribution shapes and rate, are estimated from simulation.

The same procedure is not used for DY because although its contribution is expected to be large, outside the Z window the modelling of the process does not accurately describe the data. Instead a data-driven approach is adopted, called the $R_{\text{out/in}}$ method [16]. The method starts by computing the ratio between DY yields outside and inside the Z window, taken from simulation and denoted as $R^{\ell\ell}_{\text{out/in}}$, separately for ee and $\mu\mu$ channels. DY contribution outside the Z window in data is then given by:

$$Z^{\text{out}}_{\ell\ell} = R^{\ell\ell}_{\text{out/in}}(N^{\text{in}}_{\ell\ell} - 0.5 N^{\text{in}}_{e\mu} k_{\ell\ell}) \tag{6.1}$$

Here $N_{\ell\ell}$ and $Z_{\ell\ell}$ ($\ell\ell = ee, e\mu, \mu\mu$) denote the data yield and the estimated DY yield of the relevant channel and the 0.5 factor is to account for the rate difference between channels, while the superscript 'out' or 'in' specifies whether the contribution is outside or inside the Z window. $k_{\ell\ell}$ is a factor that accounts for differences in electron and muon reconstruction efficiencies, which is taken to be $k^2_{ee} = N^{\text{in}}_{ee}/N^{\text{in}}_{\mu\mu}$ and $k_{\mu\mu} = 1/k_{ee}$. Per-channel SFs are defined in ee and $\mu\mu$ channels as the ratio between the DY yield thus estimated and the one from simulation, which are used to reweight the latter. DY simulation in $e\mu$ channel is also reweighted, using the geometric mean of the SFs in the same flavor channels.

All the numbers for the $R_{\text{out/in}}$ method are computed with events passing only the 2 lepton and 2 jet cuts instead of the full event selection. The values of the SFs are 1.22(1) in

the ee channel, 1.203(5) in eμ and 1.186(6) in $\mu\mu$. As is clear, the method assumes that the DY contribution is negligible in $N^{in}_{e\mu}$ compared to $N^{in4}_{\ell\ell}$.

6.5 Top Pair Kinematic Reconstruction

The $\{k, r, n\}$ coordinate system discussed in Section 2.5 is reached by boosting into top and antitop helicity frames, evaluated in the $t\bar{t}$ ZMF. This requires the momenta of the top and antitop to be known, the reconstruction of which is not straightforward since not all of its decay products are measured. In order to get around this problem a kinematic reconstruction algorithm is used, which is the subject of discussion of this section.

6.5.1 Algebraic reconstruction

The kinematic reconstruction algorithm used in this work is based on the algebraic method presented in Reference [17]. The unknown neutrino momenta in the event implies eight degrees of freedom, two of which are eliminated considering their vanishingly small masses [18]. The remaining six can be constrained by considering the measured decay products together with some assumptions on the $t\bar{t}$ event topology. Two constraints are provided by the assumption that the measured $\not{p}_T$ is entirely due to the two prompt neutrinos:

$$\not{p}_x = p^{\nu}_x + p^{\bar{\nu}}_x$$

$$\not{p}_y = p^{\nu}_y + p^{\bar{\nu}}_y$$

The remaining constraints are from fixing the masses of the W boson and the top quark. The former is fixed to a random value sampled from the W mass distribution at the generator level (shown in Figure 6.2) and the latter to the value assumed in simulation, 172.5 GeV. Note that this means that W masses are not fixed to the same value both between events and between W^+ and W^- in a given event, while the lepton and b jet masses are set to 0 and 4.8 GeV respectively (the latter being the mass of b quark used in simulation). After some algebra, these constraints lead to a polynomial of order 4 in one of the six degrees of freedom (chosen to be $p^{\bar{\nu}}_x$). It is solvable analytically, presenting up to four candidates for $t\bar{t}$ system kinematics in the event. Following the findings presented in Reference [19], this ambiguity is broken by choosing the solution with the smallest $m_{t\bar{t}}$ in the event.

Given its analytical nature, the method is sensitive to fluctuations in its input, leading to loss of solutions also for simulated $t\bar{t}$ events. In order to increase the efficiency of the algorithm[5], the method is augmented with a smearing routine as follows. For each event, a solution is attempted 100 times with the input momenta smeared at each iteration. The lepton and jet momenta are smeared in both energy and direction, with the $\not{p}_T$ corrected for this smearing. The energy smearing is implemented as a scaling of the reconstructed energy

[4] DY process contributes to the eμ channel only through the $Z \to \tau\tau \to e\mu + 4\nu$ channel. Based on BR alone, its contribution is around 3% of the total DY rate. While this is not by itself negligible, the neutrinos take away a portion of the available energy, pushing $m_{e\mu}$ to the left side of the Z window.

[5] The efficiency of the algorithm is defined as the probability for the algorithm to return a solution for a given event, computed as N_{solved}/N_{input}, with N_{input} taken to be the count of events passing the full selection described in Section 6.3 except for the kinematic reconstruction cut.

with a factor randomly sampled from the distribution of ratio between the reconstructed energy of the relevant object and the corresponding quantity at the generator level, while the directional smearing is implemented as a rotation of the reconstructed object about its own direction by a random angle sampled from the distribution of angle between it and its corresponding generator direction. The input distributions for the energy and angular smearing are made using simulated events passing up to the 1 b-tag cut, with a futher requirement that the reconstructed and generator objects match. They are shown in Figure 6.1.

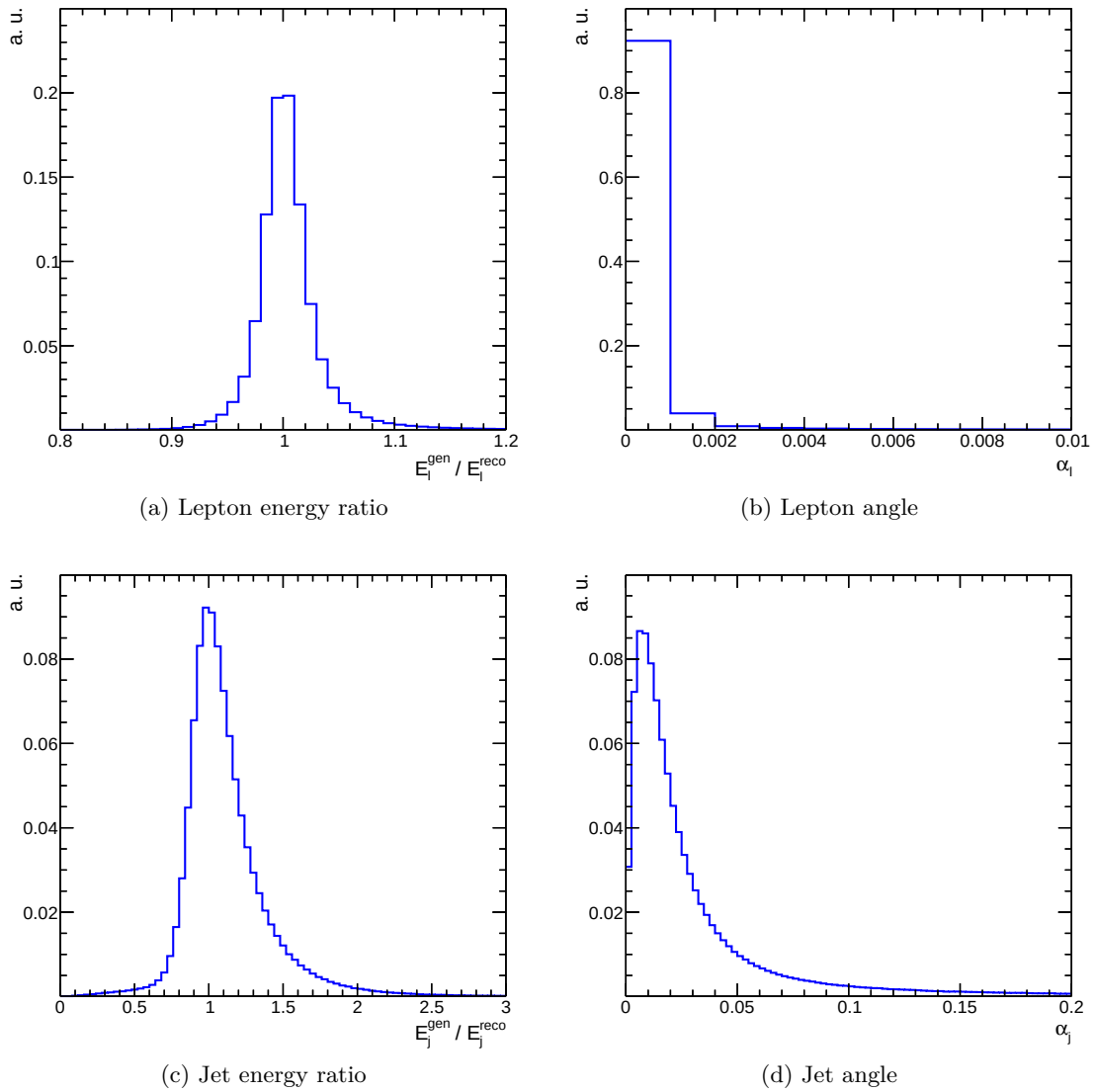

(a) Lepton energy ratio

(b) Lepton angle

(c) Jet energy ratio

(d) Jet angle

Figure 6.1: Distributions of energy ratio and angle between reconstructed and generator leptons and jets used as input for kinematic reconstruction algorithm.

While this smearing procedure is successful at increasing the efficiency of the algorithm, each smearing iteration can contribute a solution, introducing another layer of ambiguity in the solution to be chosen to represent the event. Considering the stochastic smearing it

is unclear a priori that any sorting criteria would yield a more accurate solution; they are averaged instead. Solution from a given iteration i is given a weight $w_i = P(\mathrm{m}_{\bar{\ell}\mathrm{b}}) \cdot P(\mathrm{m}_{\ell\bar{\mathrm{b}}})$, where $P(\mathrm{m}_{\bar{\ell}\mathrm{b}})$ is the probability of the observed $\mathrm{m}_{\bar{\ell}\mathrm{b}}$ based on its corresponding distribution at the generator level. This distribution is shown in Figure 6.2. The representative top momentum is then formed by the weighted average from all solutions:

$$\langle \vec{\mathrm{p}}_{\mathrm{t}} \rangle = \frac{1}{\sum w_i} \sum w_i \cdot \vec{\mathrm{p}}_{\mathrm{t},i}$$

The four momentum is completed by setting the top mass at its simulated value. Antitop, neutrino and antineutrino momenta are similarly averaged. The momenta of all measured daughters on the other hand are kept at their measured values.

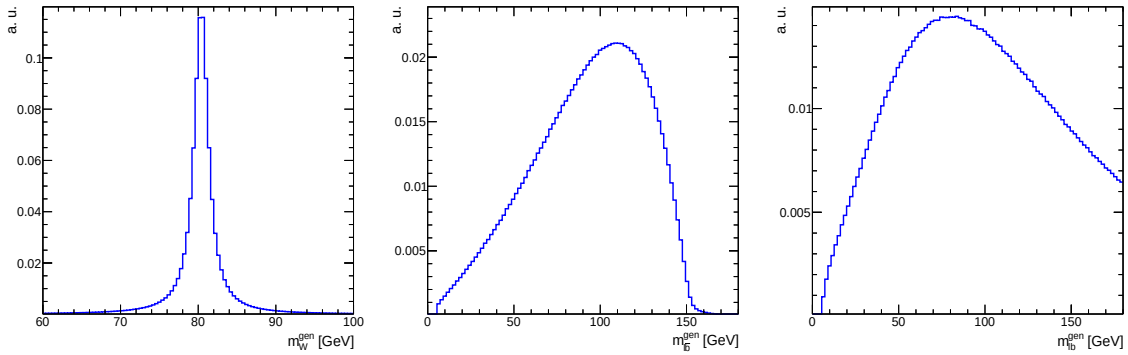

(a) Generator $\mathrm{m_W}$ (b) Generator $\mathrm{m}_{\ell\bar{\mathrm{b}}}$ (correct) (c) Generator $\mathrm{m}_{\ell\mathrm{b}}$ (wrong)

Figure 6.2: $\mathrm{m_W}$ and $\mathrm{m}_{\ell\bar{\mathrm{b}}}$ distributions used as input for the kinematic reconstruction algorithm, along with the $\mathrm{m}_{\ell\mathrm{b}}$ distribution to demonstrate the difference between correct and wrong combination, with correct meaning both particles stem from the same top quark.

One final issue remains. While leptons and antileptons can be told apart with excellent efficiency and accuracy, the same can not be said for b and $\bar{\mathrm{b}}$ jets. This problem is further exacerbated when more than two jets are present in the event, which may or may not be tagged. As a workaround, we try to obtain a solution for all possible lepton-jet configurations, with preference given to those containing higher number of tagged jets. Among permutations with the same tagged jet count, the one with the highest $\sum w_i$ is chosen.

6.5.2 Performance of the algorithm

Performance of the kinematic reconstruction algorithm will be evaluated in two different point of views; reconstruction- and generator-oriented. In the reconstruction-oriented evaluation the efficiency of the algorithm is measured in both data and simulation as functions of input variables, the result of which is shown in Figure 6.3 only for eμ channel, as the result in ee and $\mu\mu$ channels are very similar. As can be seen, the efficiencies are very similar in data and simulation. To correct for residual efficiency differences in each channel, per-channel SFs (with values very close to 1) is used to reweight the simulation events where the algorithm

returns a solution.

In the generator-oriented evaluation, the focus is on the stability of the algorithm over the generator-level $t\bar{t}$ kinematic space. The measurement is performed only in eμ channel using the SM $t\bar{t}$ simulation. The denominator definition is the same as that used in reconstruction-oriented evaluation; full event selection except the kinematic reconstuction cut. The numerator on the other hand is split into several different categories:

- Sol: events with at least one solution i.e. same as reconstruction-oriented efficiency
- Gen: events are within generator-level acceptance (simply 'acceptance' from this point onwards within this section) emulating the reconstruction level cuts:
  - Generator leptons within acceptance: $p_T^{\ell} > 20$ GeV and $\left|\eta^{\ell}\right| < 2.4$
  - Generator b jets within acceptance: $p_T^{b} > 30$ GeV and $\left|\eta^{b}\right| < 2.4$
  - Generator leptons and b jets above are separated by $\Delta R > 0.4$
  - Generator b and $\bar{b}$ jets above are separated by $\Delta R > 0.1$. This is to remove events where the ghost tagging (see Section 4.6) assigns both b and $\bar{b}$ quarks to hadrons clustered in the same jet, which happens 1% of the time
  - Generator ℓ and $\bar{\ell}$ considered above are separated by $\Delta R > 0.1$
- Sol $\cup$ Gen: events where both Sol and Gen are true
- Sol $\cup$!Gen: events where Sol is true but Gen is false
- !Sol $\cup$ Gen: events where Sol is false but Gen is true
- Match: a subset of Sol $\cup$ Gen where the jet assigned by the algorithm as the b jet matches the generator b jet within $\Delta R < 0.3$ and the $\bar{b}$ jet matches the generator $\bar{b}$ jet
- Swap: same as Match but with b jet matching generator $\bar{b}$ jet and vice versa
- Off: a subset of Sol $\cup$ Gen not belonging to either Match or Swap subsets

Figure 6.4 shows the efficiencies measured as functions of $m_{t\bar{t}}$, $p_T^{t\bar{t}}$, $y^{t\bar{t}}$, $\Delta y^{t\bar{t}}$ and $\Delta\phi^{t\bar{t}}$. The efficiency is around 97% above the $t\bar{t}$ production threshold and slowly falls off as $m_{t\bar{t}}$ increases. However, it is to be noted that only 75% of events passing the selection are also within acceptance. The efficiency for these events is above 95% which is flat across a wide $m_{t\bar{t}}$ range. Among the events within acceptance and for which a solution is obtained, the probability for the algorithm to also correctly assign the b jets is about 85% above 600 GeV. Below this value, the matching probability is significantly lower; at 400 GeV it is 55%. The trend for the algorithm to assign jets opposite to the generator-level assignment is the opposite; at 400 GeV it is 30% and approaches zero at higher $m_{t\bar{t}}$. In 15% of the events within acceptance and for which a solution is obtained, at least one of the jets picked by the algorithm are not matched to the generator b jets, the probability of which is observed to be flat in $m_{t\bar{t}}$. For 3% of the events within acceptance, the algorithm obtains no solution, with seemingly no dependence on $m_{t\bar{t}}$. Finally, among the events for which a solution was obtained, 25% of

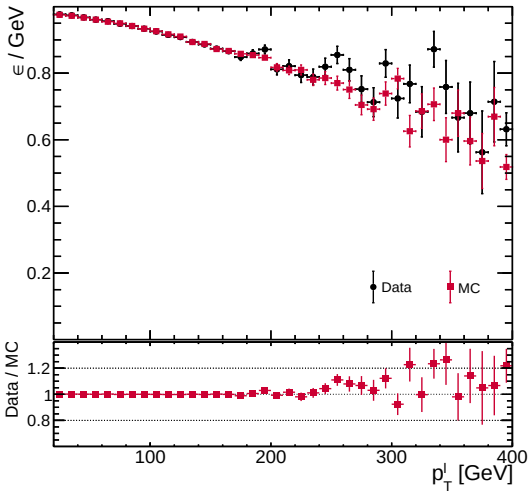

(a) $\epsilon\left(p_T^{\ell}\right)$

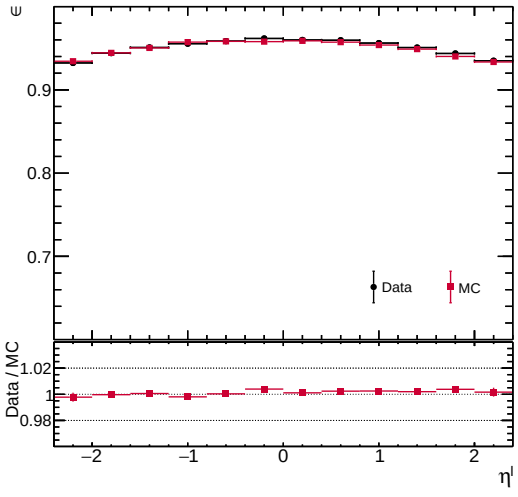

(b) $\epsilon\left(\eta^{\ell}\right)$

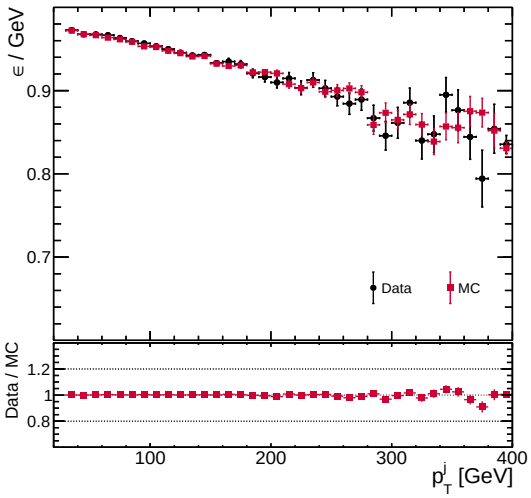

(c) $\epsilon\left(p_T^{j}\right)$

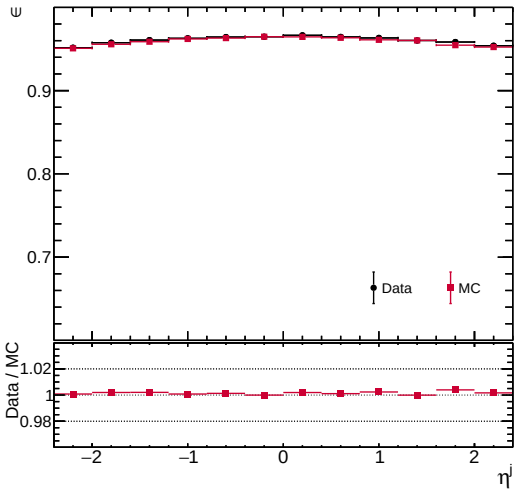

(d) $\epsilon\left(\eta^{j}\right)$

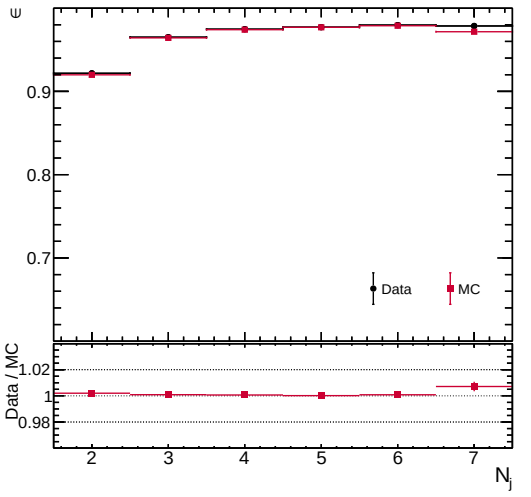

(e) $\epsilon(N_j)$

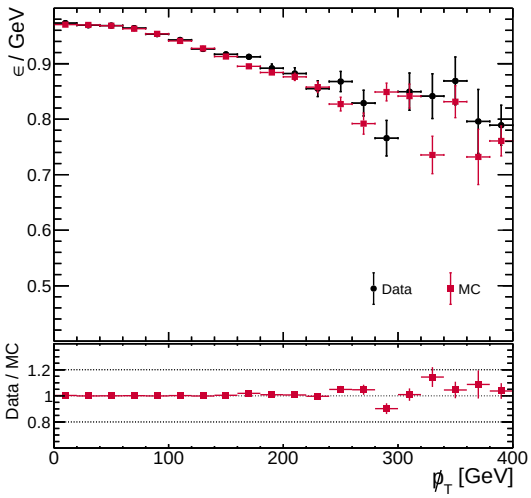

(f) $\epsilon\left(\not{p}_T\right)$

Figure 6.3: Efficiency of the kinematic reconstruction algorithm in the reconstruction-oriented evaluation. The uncertainties are statistical.

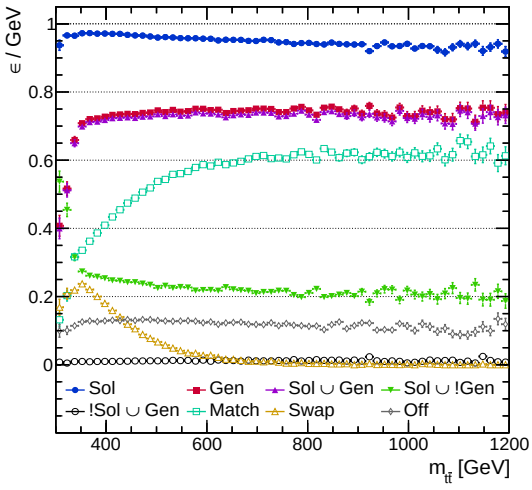

(a) $\epsilon(\mathrm{m}_{\mathrm{t\bar{t}}})$

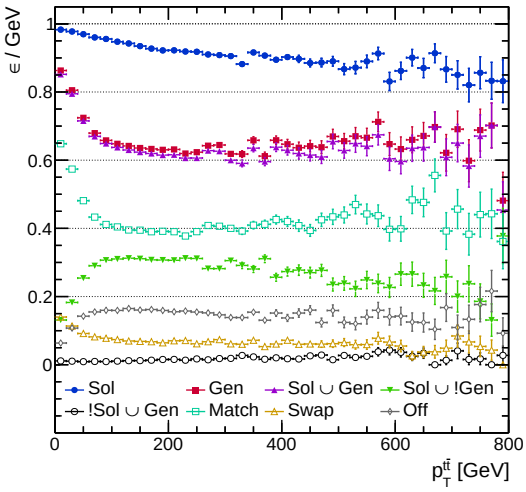

(b) $\epsilon\left(\mathrm{p}_{\mathrm{T}}^{\mathrm{t\bar{t}}}\right)$

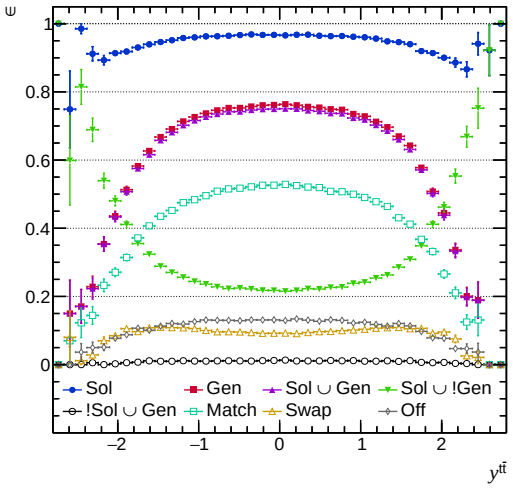

(c) $\epsilon\left(y^{\mathrm{t\bar{t}}}\right)$

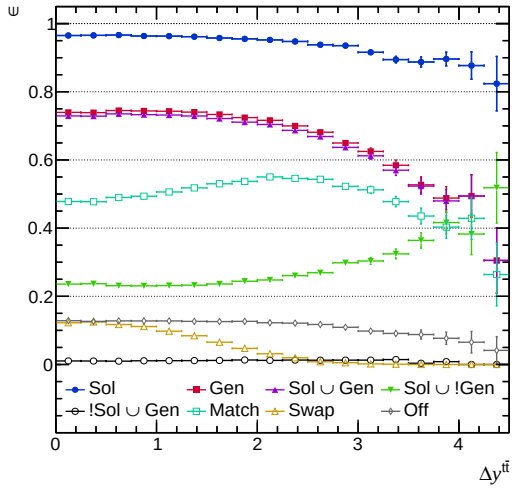

(d) $\epsilon\left(\Delta y^{\mathrm{t\bar{t}}}\right)$

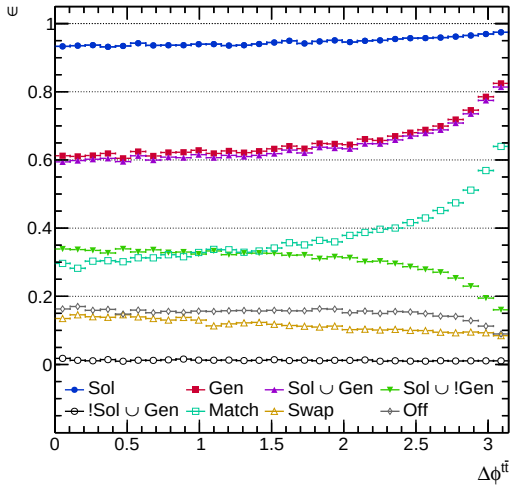

(e) $\epsilon\left(\Delta\phi^{\mathrm{t\bar{t}}}\right)$

Figure 6.4: Efficiency of the kinematic reconstruction algorithm in the generator-oriented evaluation. The uncertainties are statistical.

them lie outside acceptance.

In order to better understand these trends, we turn to the efficiencies as functions of $p_T^{t\bar{t}}$. It is immediately clear that the algorithm performs better at low $p_T^{t\bar{t}}$. This is directly a consequence of the event topology; events with low $p_T^{t\bar{t}}$ lie within acceptance 85% of the time, while only 65% of those with $p_T^{t\bar{t}}$ above 100 GeV are within acceptance. Such a trend is to be expected, as the event selection cuts require that each object is well isolated from the others, a requirement that is less often fulfilled when the $t\bar{t}$ system is boosted. For those events within acceptance, the efficiency to obtain a solution is again 95%, flat across a wide $p_T^{t\bar{t}}$ range. The efficiency for proper and swapped matching behave in a similar way, although the latter is less affected by increasing $p_T^{t\bar{t}}$.

The efficiencies in terms of $y^{t\bar{t}}$ offer us additional insights. While solutions are obtained at 90% or higher efficiency in a wide range of $\left|y^{t\bar{t}}\right| < 2$, only 75% of the events are also within acceptance, flat only over a subset of $\left|y^{t\bar{t}}\right| < 1.2$; the probability for events to be within acceptance rapidly falls outside of it. The efficiency to obtain a solution for these events is above 95% and as in the previous two variables, the trend simply follows the probability for the event to be within acceptance. Probability for a proper jet matching is 70% for these events within the approximately flat rapidity range and increases outside of it, as can be deduced from its gentler drop compared to the probability of the event to be within acceptance. The trend for the case of having a solution outside acceptance is opposite; it is 25% in the flat range and sharply increases outside; compensating for the low fraction of events within acceptance and giving rise to the flat dependence of rapidity to simply obtain a solution for events passing the selection.

Finally, we turn to the efficiencies as functions of the rapidity and azimuthal gap between the top quarks. The overall efficiencies in terms of $\Delta y^{t\bar{t}}$ behave similarly as the $y^{t\bar{t}}$ in that they are approximately flat within a range and slowly fall at higher values. Looking at the efficiencies in terms of $\Delta\phi^{t\bar{t}}$, while the efficiency to obtain a solution is flat, it is clear that events where the top quarks are back-to-back are more likely to be within acceptance. This affects the matching efficiency accordingly; events with back-to-back top quarks are more likely to be properly matched.

6.6 Systematic Uncertainties

In addition to the statistical uncertainties inherent in a finite data sample, the precision of any statements made from it is further limited by the systematic uncertainties due to imperfect knowledge on various aspects on both the experimental and theoretical sides. In this section, sources of such uncertainties and their treatment are discussed. Most sources are varied in two directions called 'up' and 'down', the magnitude of which is typically one standard deviation in respective directions with respect to their nominal values. The analyses are repeated for each such variation and the envelope formed by the two variations is taken to be the uncertainty due to a given source. Unless mentioned otherwise, the systematic sources affect all processes that are considered in each analyses. Three types of uncertainties are considered based on how they can affect the result: rate uncertainty that change only

the overall normalization of a given process, shape uncertainty that change only the relative contribution between bins of a given distribution but not its overall normalization, and shape + rate uncertainty that is a combination of the former two. Demonstration of their impact to each analysis will be deferred to their respective chapters i.e. Chapter 7 for the A/H search and Chapter 8 for the spin correlation measurement.

6.6.1 Trigger efficiencies

Systematic source due to trigger efficiencies is taken into account by varying the SFs (which are provided as a function of $|\eta|$ of the two leptons) within their uncertainties, which account for both the statistical uncertainties in the measurement and the residual correlations between the $\not{p}_{\mathrm{T}}$ and dileptonic trigger set [1]. This source is treated as a shape + rate uncertainty.

6.6.2 Lepton identification and isolation efficiencies

Systematic sources due to lepton identification and isolation efficiencies are taken into account by varying the SFs within their uncertainties and treated as shape + rate uncertainties. In A/H search they are treated as two sources (one for electron and muon respectively) while in spin correlation measurement they are treated as one source.

6.6.3 Jet energy

The JECs discussed Section 6.2 come with their associated uncertainties, which are propagated to the analyses. Each individual source of JEC uncertainties - excluding those affecting only jets outside of acceptance - is separately considered as one source. Discussion on these sources can be found in Reference [15]; each source will be referred to in the same way as in its Table 1. The source due to jet energy resolution (JER) is accounted for by SF variation. As these sources change the jet momenta, they can also change the list of jets in each event. For this reason, they are treated as shape + rate uncertainties.

6.6.4 b-tagging efficiencies

Similar to systematic sources due to other efficiencies, those caused by b-tagging are taken into account by varying the SFs. They are treated as shape + rate uncertainties. Two sources are considered; one for heavy flavor (b and c) and another for light flavor (u, d and g) jet SFs. In the A/H search, these two sources are treated independently while in the spin correlation measurement an envelope is constructed by summing them in quadrature.

6.6.5 Kinematic reconstruction efficiency

The systematic source due to kinematic reconstruction SFs (see Section 6.5) is taken into account only in the spin correlation analysis. This systematic is treated as a rate uncertainty.

6.6.6 Unclustered missing transverse momentum

One component affecting the value of $\not{p}_{\mathrm{T}}$ is due to PF objects that are not clustered into jets. The systematic source due to this is accounted for by varying the momenta of these

objects within their resolutions and recomputing $\not{p}_T$ with the updated momenta. This source is treated as a shape + rate uncertainty.

6.6.7 Pile-up

The systematic source due to PU is taken into account by varying the assumed inelastic pp cross section value used to predict the number of PU interactions by 4.6%, updating the event-by-event weights in simulation. It is treated as a shape + rate uncertainty.

6.6.8 Luminosity

The luminosity used to normalize the simulation, 35.9 /fb, is varied by 2.5% [20]. It is treated as a rate uncertainty.

6.6.9 Assigned cross sections

$t\bar{t}$ cross section is varied by $^{+5.8\%}_{-6.1\%}$ following the recommendation in Reference [10], accounting for the effect of the ME scale choice, PDF and top mass uncertainties on the NNLO $t\bar{t}$ cross section. An additional source related to the BR of dileptonic $t\bar{t}$ channels [21] is considered by varying the BR by 1.5%, only in the spin correlation measurement.

The systematic source due to single top normalization is taken into account by varying the cross sections by 15% (30%) in A/H search (spin correlation measurement). The source due to DY normalization on the other hand is taken to be 30%, from the variation between the SFs derived using events passing up to the 2 jet cut and events passing the full selection (see Section 6.4). One source is assigned for each of the other processes by varying their respective cross sections by 30% [22]. All sources related to cross sections are treated as rate uncertanties.

6.6.10 Top mass

Top-related processes are simulated assuming a m_t of 172.5 GeV. To account for the imperfect knowledge on this parameter, dedicated SM $t\bar{t}$ samples simulated assuming m_t 3 GeV away from the nominal value are used. Since the mass difference between the samples are significantly larger than the uncertainties of past m_t measurements [23], the envelope formed by these samples are linearly scaled down by a factor of 6 (3) in A/H search (spin correlation measurement). Although a different value of m_t induces a different $t\bar{t}$ cross section, the dedicated samples are normalized to the nominal cross section so as to not double count the cross section uncertainty. This source is treated as a shape + rate uncertainty.

6.6.11 Matrix element scale choice

In the A/H search, systematic sources due to the choice of μ_R and μ_F are taken into account by separately varying them by factors of 2 and 0.5 respectively. These variations are split into six uncorrelated systematic sources; two for SM $t\bar{t}$ production due to the choice of μ_R and μ_F respectively and four for the same in the resonance and interference parts of A/H signal. The SM sources are treated as shape + rate uncertainties, where - just as in the top mass case - the rate difference is only due to the difference in acceptance induced by the SM

$t\bar{t}$ scale variations. For the A/H scale variations, since there are no sources dedicated to the uncertainty in A/H cross sections, they are allowed to change the rate as well.

In the spin correlation measurement, the ME scale variations are considered only on the SM $t\bar{t}$ process. In addition to the individual μ_R and μ_F variations described above, simultaneous variations of both μ_R and μ_F by the same factor are also considered[6]. These and all sources related to PS scale variations to be described later are used to construct an envelope for a single ME + PS systematic source.

6.6.12 Parton distribution function

Up to three systematic sources are assigned due to PDF, all of which are treated as shape + rate uncertainty. The first is due to the value of α_s used in the PDF - 0.118 in NNPDF3.0 [4] - which is accounted for by reweighting the SM $t\bar{t}$ simulation with PDFs that assume α_s values 0.001 away from the nominal value. The second and third sources are obtained by reweighting the SM $t\bar{t}$ simulation with the 100 NNPDF3.0 replicas.

In the A/H search, a principal component analysis (PCA) is performed to extract the basis variations, linear combinations of which can describe the deviations due to any given replica. Two sources are assigned corresponding to the two bases with the largest impact. Taking only the most dominant two bases is sufficient because, as shown in Reference [24], their impact is two order of magnitudes larger than the basis with the third largest impact. The PCA takes into account also the results of the corresponding search in the semileptonic channel, in order to allow the two to be coherently combined into a single analysis.

In the spin correlation measurement, the source is treated based on the 'alternative MC approach' recommended in Reference [25]. The PDF replicas are ranked by their deviations with respect to nominal distributions which are then used to extract a 68% confidence level (CL) by taking the envelope formed by the 16th and 84th replica. In this approach the ranking is done for each bin, so the final envelope is not necessarily built up by the same replicas across all bins.

6.6.13 Matching of matrix element and parton shower

The value of the h_{damp} parameter in POWHEGV2 simulated samples is $1.58^{+0.66}_{-0.59}$ m_t, based on the results of Reference [26]. Dedicated $t\bar{t}$ samples with the value of this parameter varied are analyzed and assigned as one source, treated as a shape + rate uncertainty.

6.6.14 Parton shower scale

Two sources corresponding to the value of α_s in PS simulation are considered, one each for ISR and FSR, accounted for by analyzing dedicated $t\bar{t}$ samples with α_s for ISR (FSR) varied by factors of 2 and 0.5 ($\sqrt{2}$ and $1/\sqrt{2}$) [26]. As mentioned above, in the spin correlation measurement, these sources together with the sources due to ME scale choice are used to

[6]The reason for not taking the simultaneous variations into account in the A/H search is that they are treated as uncorrelated sources there and, as shown in Reference [24], the simultaneous variations can be described as a linear combination of the μ_R- and μ_F-varied systematic templates.

construct an envelope combining them into a single source. In both analyses they are treated as shape + rate uncertainties.

6.6.15 Other parton shower systematics

A number of systematic sources are considered only in the spin correlation measurement accounting for the uncertainties in various aspects of PS modelling. They are treated as shape + rate uncertainties. The UE tune source is accounted for by varying Pythia8 parameters related to UE within their uncertainties, as determined in Reference [26]. The color reconnection source on the other hand considers alternative choices of the color reconnection scheme instead of the MPI-based scheme with no early resonance decays (ERD) used in the default Pythia8 simulation. On top switching ERD on in Pythia8, the so-called gluon move and QCD-inspired schemes are considered, an envelope is constructed from the analyses of these dedicated samples [27, 28].

Sources due to b quark fragmentation i.e. the momentum transfer from b quarks to B hadrons is considered by forming an envelope from the variations of the Bowler-Lund parameter (discussed in Reference [29], its value in simulation is $0.855^{+0.224}_{-0.157}$) within their uncertainties and also considering the parametrization provided in Reference [30]. Another source is considered accounting for the assumed B hadron leptonic BRs used in simulation, which are taken from Reference [21], affecting the b jet response in the calorimeter.

6.6.16 Top transverse momentum reweighting

In Run 1, it was discovered that the top $\mathrm{p_T}$ ($\mathrm{p_T^t}$) distribution in data is not well described by simulation [31], a result that was confirmed by later measurements in Run 2 [22]. In order to improve the agreement with data, SM $\mathrm{t\bar{t}}$ events are reweighted with a SF that is given by:

$$\mathrm{SF} = e^{p_0 + p_1 \cdot \mathrm{p_T^t}}$$

where $\mathrm{p_T^t}$ refers to the $\mathrm{p_T}$ of the top or antitop quark at the generator level (see Section 4.6). The values of p_0 and p_1 are 0.0615 and -0.0005 respectively, obtained by fitting the measurements done using 2015 data [32, 33]. In this procedure, each SM $\mathrm{t\bar{t}}$ event receives a weight that is the geometrical mean of the SFs due to generator top and antitop quarks. In the A/H search, this procedure is applied in the nominal analysis and two sources are considered due to the uncertainties in p_0 and p_1.

In the spin correlation measurement, the top $\mathrm{p_T}$ reweighting is not applied in the nominal analysis. Instead, one source is assigned to account for the symmetrized difference between distributions with and without the reweighting. In either case the sources due to $\mathrm{p_T^t}$ are treated as shape uncertainties.

6.7 Control Distributions

In this section, control distributions are inspected. Since we rely on simulation at many steps in the analysis chain, including the choice of the analysis strategy itself, a good description of the data by the simulation is crucial in order to ensure that our conclusions also

apply to the data. As the analyses in this work are performed in a blind way, meaning that the choice of analysis strategy is made without regard to the presence of the signal in the data, care needs to be taken that the control distributions have little to no sensitivity to the presence of signal. This is particularly challenging for the A/H search, as it can manifest anywhere in the $m_{t\bar{t}}$ spectrum (see Figure 2.5), and so no true control region that contains only the SM $t\bar{t}$ background can be defined. In this work, the distributions of final state reconstructed object counts and kinematic properties are chosen. While they still retain some sensitivity to the presence of the A/H bosons, it is significantly diluted in comparison to observables like $m_{t\bar{t}}$, and so serve as a compromise between the need to ensure a good description of the data by the simulation and the need to be blind to the presence of the signal in the data.

The control distributions are shown for events passing the 1 b-tag cut, where the event selection is performed within the context of the A/H search. Given the flat SFs of the kinematic reconstruction step, requiring a solution to be present will not change the data-simulation agreement. As a reminder, background contributions are estimated according to the procedure discussed in Section 6.4. All the corrections discussed in Section 6.2 and Section 6.6 are applied. All the control distributions to be shown share a common legend, and for the sake of brevity it is shown only once in Figure 6.5. The impact of statistical and systematic uncertainties are shown together, however in all cases the latter dominate. Underflow and overflow entries are added to the first and last bins respectively. The control distributions for the ee channel is shown in Figure 6.6, while the distributions for the eμ channel is shown in Figure 6.7 and finally the $\mu\mu$ channel in Figure 6.8.

We see that all non-top contributions are strongly suppressed, leading to a reasonable agreement between simulation and data. We also notice that there is a residual discrepancy remaining in the object p_T distributions that is due to the interplay between not-quite-perfect description of $t\bar{t}$ in simulation - that is mitigated to an extent by the p_T^t reweighting - and the choice of event tune in the showering step. Finally we remark the persistent discrepancy in the N_{PV} distribution throughout all selection steps that is due to the imperfect description of PU in this analysis. As the same discrepancy is observed in all other CMS analyses that utilize the 2016 data and the impact of PU systematic source on the the A/H search (see e.g. Figures 7.8 and 7.9) and spin correlation measurement (see Tables 8.3 and 8.4) is only minimal, no attempt was made in this work to improve the situation.

The control distributions at other steps of the event selection are shown in Appendix B.

6.8 Bibliography

[1] T. Arndt et al., "Measurement of the 2016 Trigger Efficiencies for a dilepton selection for a ttbar analysis", CMS Analysis Note CMS AN-2016/392, 2016.

[2] J. Alwall et al., "Comparative study of various algorithms for the merging of parton showers and matrix elements in hadronic collisions", *Eur. Phys. J.* **C53** (2008) 473–500, doi:10.1140/epjc/s10052-007-0490-5, arXiv:0706.2569.

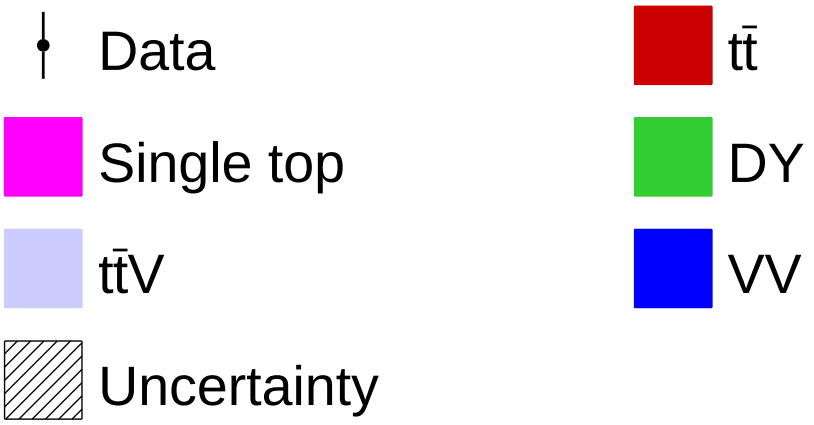

Figure 6.5: Legend for all control distributions in Figures 6.6, 6.7 and 6.8. The legend also represents the stack order i.e. $t\bar{t}$ is always at the top of the stack, followed by single top, DY and so on. Uncertainty is the combination of statistical and systematic uncertainties.

[3] R. Frederix and S. Frixione, "Merging meets matching in MC@NLO", *JHEP* **12** (2012) 061, doi:10.1007/JHEP12(2012)061, arXiv:1209.6215.

[4] NNPDF Collaboration, "Parton distributions for the LHC Run II", *JHEP* **04** (2015) 040, doi:10.1007/JHEP04(2015)040, arXiv:1410.8849.

[5] T. Sjöstrand et al., "An Introduction to PYTHIA 8.2", *Comput. Phys. Commun.* **191** (2015) 159–177, doi:10.1016/j.cpc.2015.01.024, arXiv:1410.3012.

[6] CMS Collaboration, "Event generator tunes obtained from underlying event and multiparton scattering measurements", *Eur. Phys. J.* **C76** (2016), no. 3, 155, doi:10.1140/epjc/s10052-016-3988-x, arXiv:1512.00815.

[7] P. Skands, S. Carrazza, and J. Rojo, "Tuning PYTHIA 8.1: the Monash 2013 Tune",

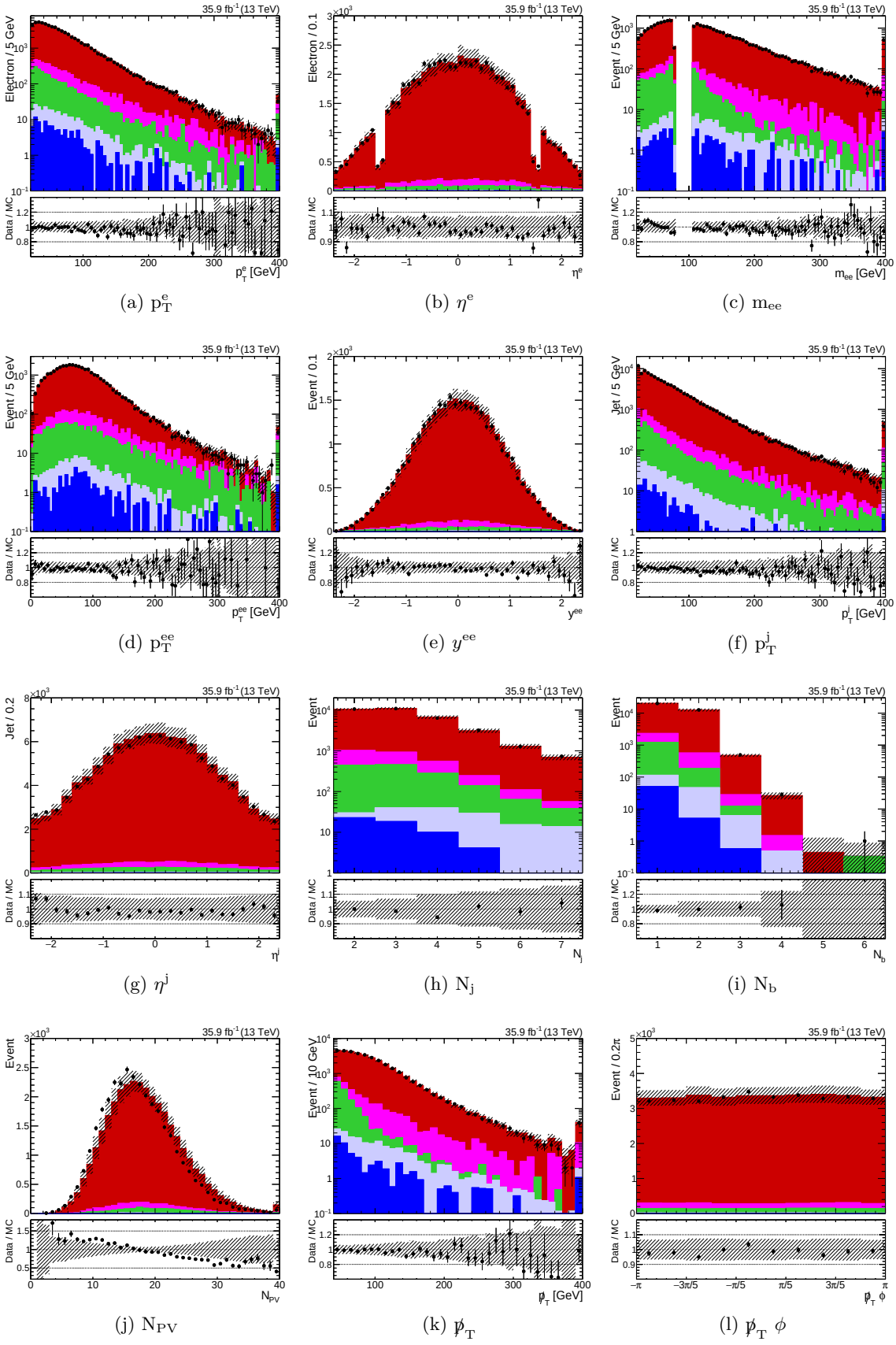

Figure 6.6: Control distributions with up to the 1 b-tag cut applied in the ee channel.

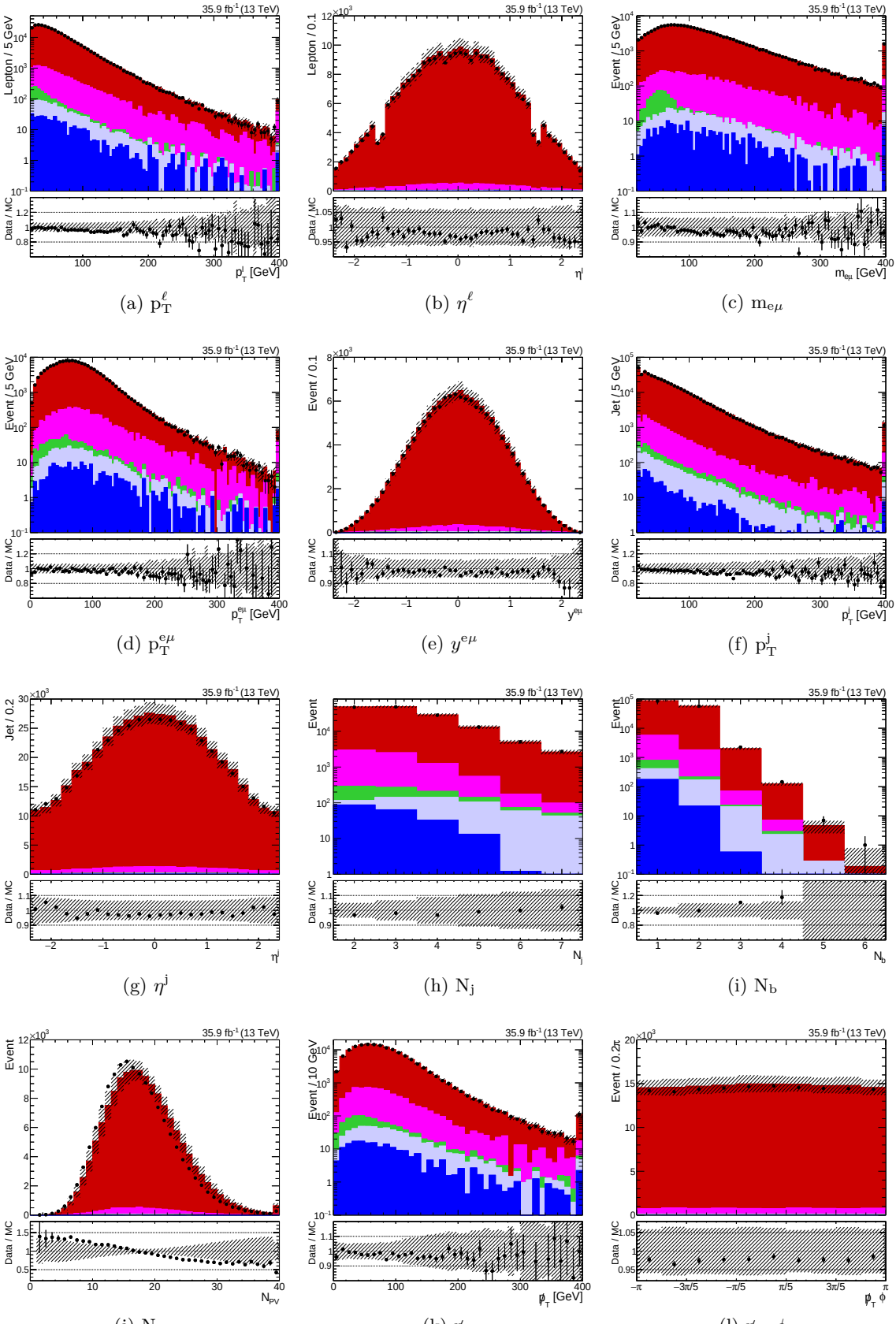

Figure 6.7: Control distributions with up to the 1 b-tag cut applied in the eμ channel.

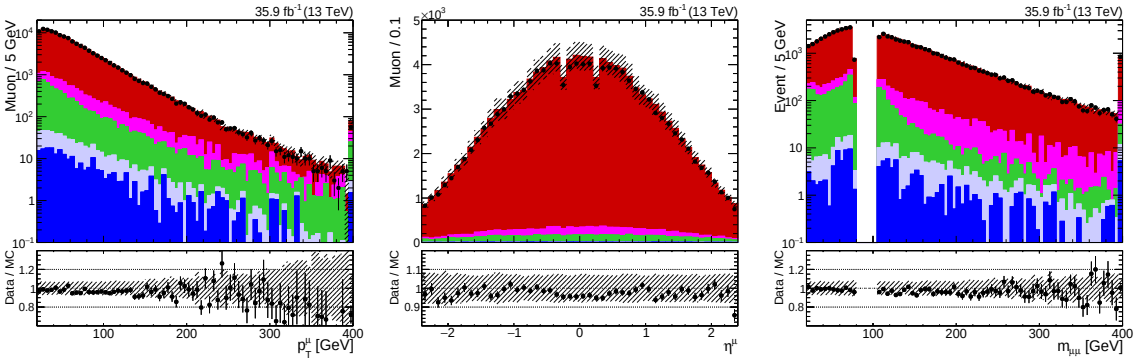

(a) $\mathrm{p_T^{\mu}}$

(b) η^{μ}

(c) $\mathrm{m_{\mu\mu}}$

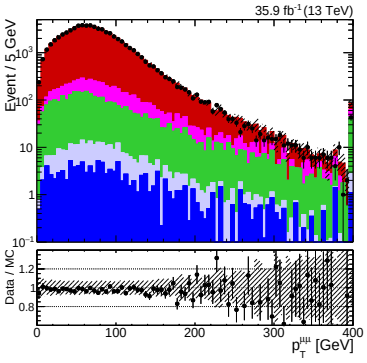

(d) $\mathrm{p_T^{\mu\mu}}$

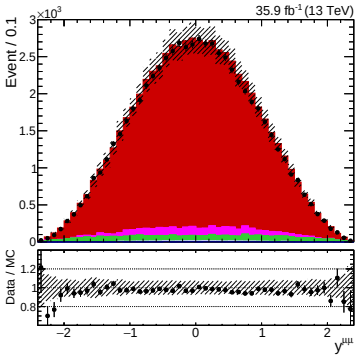

(e) $y^{\mu\mu}$

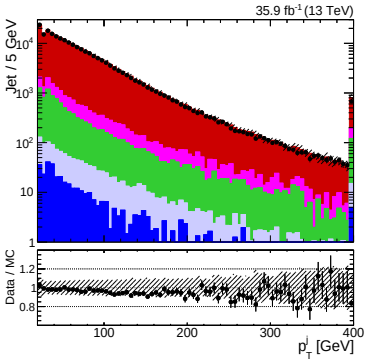

(f) $\mathrm{p_T^j}$

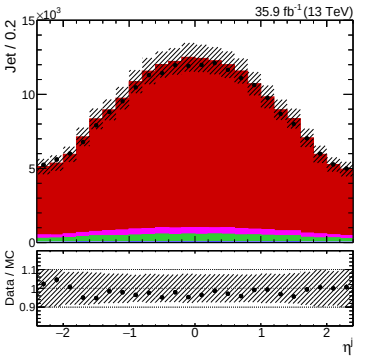

(g) η^{j}

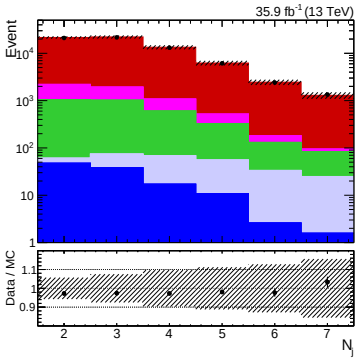

(h) $\mathrm{N_j}$

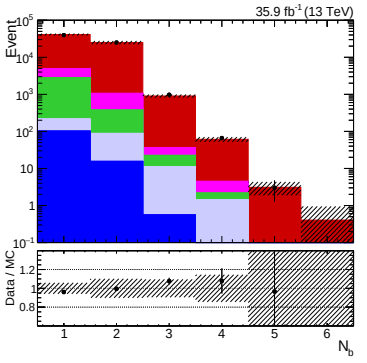

(i) $\mathrm{N_b}$

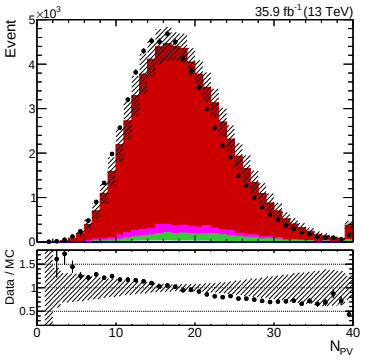

(j) $\mathrm{N_{PV}}$

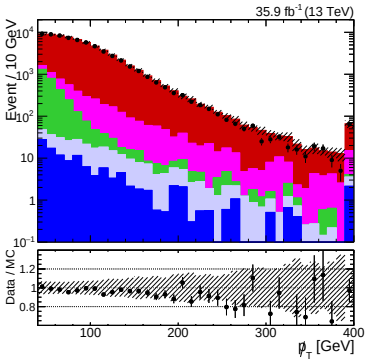

(k) $\not{p}_{\mathrm{T}}$

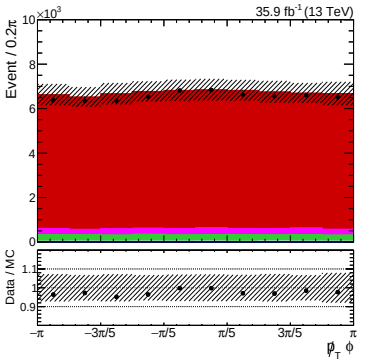

(l) $\not{p}_{\mathrm{T}}$ ϕ

Figure 6.8: Control distributions with up to the 1 b-tag cut applied in the $\mu\mu$ channel.

Eur. Phys. J. **C74** (2014), no. 8, 3024, doi:10.1140/epjc/s10052-014-3024-y, arXiv:1404.5630.

[8] GEANT4 Collaboration, "GEANT4: A Simulation toolkit", *Nucl. Instrum. Meth.* **A506** (2003) 250–303, doi:10.1016/S0168-9002(03)01368-8.

[9] S. Alioli, P. Nason, C. Oleari, and E. Re, "A general framework for implementing NLO calculations in shower Monte Carlo programs: the POWHEG BOX", *JHEP* **06** (2010) 043, doi:10.1007/JHEP06(2010)043, arXiv:1002.2581.

[10] "NNLO+NNLL top-quark-pair cross sections". https://twiki.cern.ch/twiki/bin/view/LHCPhysics/TtbarNNLO.

[11] "NLO single-top channel cross sections". https://twiki.cern.ch/twiki/bin/view/LHCPhysics/SingleTopRefXsec.

[12] J. Alwall et al., "The automated computation of tree-level and next-to-leading order differential cross sections, and their matching to parton shower simulations", *JHEP* **07** (2014) 079, doi:10.1007/JHEP07(2014)079, arXiv:1405.0301.

[13] T. Gehrmann et al., "W^+W^- Production at Hadron Colliders in Next to Next to Leading Order QCD", *Phys. Rev. Lett.* **113** (2014), no. 21, 212001, doi:10.1103/PhysRevLett.113.212001, arXiv:1408.5243.

[14] CMS Collaboration, "Measurement of the inelastic proton-proton cross section at $\sqrt{s} = 13$ TeV", *JHEP* **07** (2018) 161, doi:10.1007/JHEP07(2018)161, arXiv:1802.02613.

[15] CMS Collaboration, "Jet energy scale and resolution in the CMS experiment in pp collisions at 8 TeV", *JINST* **12** (2017), no. 02, P02014, doi:10.1088/1748-0221/12/02/P02014, arXiv:1607.03663.

[16] CMS Collaboration, "Measurement of the $t\bar{t}$ production cross section and the top quark mass in the dilepton channel in pp collisions at $\sqrt{s} = 7$ TeV", *JHEP* **07** (2011) 049, doi:10.1007/JHEP07(2011)049, arXiv:1105.5661.

[17] L. Sonnenschein, "Analytical solution of ttbar dilepton equations", *Phys. Rev.* **D73** (2006) 054015, doi:10.1103/PhysRevD.73.054015, arXiv:hep-ph/0603011. [Erratum: Phys. Rev.D78, 079902 (2008)].

[18] F. Capozzi et al., "Neutrino masses and mixings: Status of known and unknown 3ν parameters", *Nucl. Phys.* **B908** (2016) 218–234, doi:10.1016/j.nuclphysb.2016.02.016, arXiv:1601.07777.

[19] I. Korol, "Measurement of Double Differential $\mathrm{t\bar{t}}$ Production Cross Sections with the CMS Detector". PhD thesis, U. Hamburg, Dept. Phys., Hamburg, 2016. doi:10.3204/DESY-THESIS-2016-011.

[20] CMS Collaboration Collaboration, "CMS Luminosity Measurements for the 2016 Data Taking Period", Technical Report CMS-PAS-LUM-17-001, CERN, Geneva, 2017.

[21] Particle Data Group Collaboration, "Review of Particle Physics", *Chin. Phys.* **C40** (2016), no. 10, 100001, doi:10.1088/1674-1137/40/10/100001.

[22] CMS Collaboration, "Measurements of $t\bar{t}$ differential cross sections in proton-proton collisions at $\sqrt{s} = 13$ TeV using events containing two leptons", *JHEP* **02** (2019) 149, doi:10.1007/JHEP02(2019)149, arXiv:1811.06625.

[23] CMS Collaboration, "Measurement of the top quark mass with lepton+jets final states using p p collisions at $\sqrt{s} = 13\,\text{TeV}$", *Eur. Phys. J.* **C78** (2018), no. 11, 891, doi:10.1140/epjc/s10052-018-6332-9, arXiv:1805.01428.

[24] M. Gul et al., "Search for a scalar particle decaying to top quarks in the semileptonic final state with 2016 pp dataset", CMS Analysis Note AN-2016-272, 2017.

[25] J. Butterworth et al., "PDF4LHC recommendations for LHC Run II", *J. Phys.* **G43** (2016) 023001, doi:10.1088/0954-3899/43/2/023001, arXiv:1510.03865.

[26] CMS Collaboration Collaboration, "Investigations of the impact of the parton shower tuning in Pythia 8 in the modelling of $t\bar{t}$ at $\sqrt{s} = 8$ and 13 TeV", Technical Report CMS-PAS-TOP-16-021, CERN, Geneva, 2016.

[27] S. Argyropoulos and T. Sjöstrand, "Effects of color reconnection on $t\bar{t}$ final states at the LHC", *JHEP* **11** (2014) 043, doi:10.1007/JHEP11(2014)043, arXiv:1407.6653.

[28] J. R. Christiansen and P. Z. Skands, "String Formation Beyond Leading Colour", *JHEP* **08** (2015) 003, doi:10.1007/JHEP08(2015)003, arXiv:1505.01681.

[29] M. G. Bowler, "e+ e- Production of Heavy Quarks in the String Model", *Z. Phys.* **C11** (1981) 169, doi:10.1007/BF01574001.

[30] C. Peterson, D. Schlatter, I. Schmitt, and P. M. Zerwas, "Scaling Violations in Inclusive e+ e- Annihilation Spectra", *Phys. Rev.* **D27** (1983) 105, doi:10.1103/PhysRevD.27.105.

[31] CMS Collaboration, "Measurement of the differential cross section for top quark pair production in pp collisions at $\sqrt{s} = 8\,\text{TeV}$", *Eur. Phys. J.* **C75** (2015), no. 11, 542, doi:10.1140/epjc/s10052-015-3709-x, arXiv:1505.04480.

[32] CMS Collaboration Collaboration, "Measurement of the inclusive and differential tt production cross sections in lepton + jets final states at 13 TeV", Technical Report CMS-PAS-TOP-16-008, CERN, Geneva, 2016.

[33] CMS Collaboration Collaboration, "Measurement of the differential cross section for $t\bar{t}$ production in the dilepton final state at $\sqrt{s} = 13$ TeV", Technical Report CMS-PAS-TOP-16-011, CERN, Geneva, 2016.

CHAPTER

7

SEARCH FOR HEAVY HIGGS BOSONS DECAYING TO TOP QUARK PAIRS

Contents

As noted in Section 2.4, the presence of BSM physics implies the existence of new top quark production modes at the LHC. Since the $t\bar{t}$ final state is studied in this work, searches for electrically neutral resonances are of particular interest e.g. a Z' boson [1] or Higgs bosons [2]. Such resonances would induce local modifications to the $m_{t\bar{t}}$ distribution, as well as altering the $t\bar{t}$ spin correlation (discussed in Section 2.5), in characteristic ways that reveal the form of the underlying BSM theory.

In this chapter, the search for such resonances is discussed. In particular, we focus on the heavy Higgs bosons decaying to top quark pairs that subsequently decay in the dileptonic channel. We will be considering the cases when the Higgs boson is either a pure pseudoscalar or a pure scalar, which are denoted as A and H respectively. After the details of signal simulation and normalization are presented, different aspects of the search are discussed, beginning from the search strategy, the treatment of systematic uncertainties and finally the statistical analysis procedures with which the results of the search are obtained. Results are reported in two different ways; exclusion regions on $g_{A/H}$ that consider the A/H signal points separately, one at a time, and an interpretation within the hMSSM context where there is a strict relationship between the A and H bosons. In addition to the results in the dileptonic channel, which is the primary focus of this chapter, a combined result considering also the corresponding search in the semileptonic channel is also presented.

The work presented here is submitted for publication by the collaboration as Reference [3].

7.1 Signal Simulation

A/H signal samples have been privately produced using MG5_aMC@NLO version 2.5.1 with settings matching the centrally produced background samples (see Section 6.1), at the LO accuracy using the `NNPDF30_lo_as_0130` PDF set and the `CUETP8M2T4` tune. Only A/H production through the gluon fusion process is considered in the simulation. The nominal μ_R and μ_F choices in the A/H simulation is $m_{t\bar{t}}/2$, following Reference [4]. As mentioned in Section 2.4, the A/H signal consists of the resonance and interference parts. They are separately produced, the interference part by keeping only the contribution to the ME that change in sign when calculating it at the same positive and negative coupling values of $g_{A/H}$. More details regarding this procedure and its validation are available in Reference [5]. In order to scan the parameter space, 20 points in A/H mass ($m_{A/H}$) and width (as a fraction of mass, $\Gamma_{A/H}$) space are considered, forming a grid based on these arrays: (400, 500, 600, 750) GeV $\times$ (2.5, 5, 10, 25, 50) % $m_{A/H}$. As in this search the A/H bosons are not required to decay exclusively to top quarks, the aforementioned width refers to the A/H total width. Specific signal points will be denoted as $A(500, 10\%)$, where the first number within the brackets stands for mass in GeV and the second number stands for width as a fraction of the mass. The simulation is done at LO using MG5_aMC@NLO and showered with Pythia8. Both dileptonic and semileptonic channels are taken into account, although the $W \to \tau\nu$ contribution is included only in the dileptonic channel.

The cross sections as provided by the generator are assigned to the A/H signal samples. However, since for resonance production the cross section is known at NNLO (+ NNLL) ac-

curacy [6], each signal point is scaled by the so-called k-factors - the ratio between the NNLO and LO cross sections - which are taken from Reference [7]. The generator cross sections for each point and their resonance k-factors are given in Table 7.1 for A and Table 7.2 for H. For the interference part no k-factors are available, so their k-factors are taken to be the geometrical mean of the resonance and SM parts: $k_I = \sqrt{k_R k_{SM}}$ following the suggestion in Reference [4]. k_{SM} is obtained by computing the cross sections at NNLO and LO accuracies using the `TOP++` program [8]; its value is 1.57.

7.2 Analysis Strategy

Any search for a new physical effect begins by defining a search strategy, which is the subject of this section. First, we identify the so-called parameter of interest (POI), which is a figure that quantifies the presence or lack of the sought-after effect. Next the search observables i.e. those most sensitive to the changes in POI are discussed.

7.2.1 A/H coupling modifier as the parameter of interest

Although many other searches adopt the signal strength parameter μ - the ratio of the observed signal rate to that predicted by the theory - as the POI, this does not suit our purposes since the total signal rate can be zero in some instances of the signal parameters $\vec{p}_{A/H} = \left(m_{A/H}, \Gamma_{A/H}, g_{A/H}\right)$. In finding a more suitable POI, we turn to the expression for the predicted event yield in the presence of signal $\lambda\left(\vec{p}_{A/H}, \vec{\nu}\right)$:

$$\lambda\left(\vec{p}_{A/H}, \vec{\nu}\right) = \sum_{A,\,H}\left(g^4_{A/H}\lambda^s_R\left(\vec{p}_{A/H}, \vec{\nu}\right) + g^2_{A/H}\lambda^s_I\left(\vec{p}_{A/H}, \vec{\nu}\right)\right) + \lambda^b(\vec{\nu}) \tag{7.1}$$

Here λ^s_R and λ^s_I are the contributions of the resonance and interference parts to the event yield respectively. Of the two, only λ^s_R is required to be non-negative. $\vec{\nu}$ is a set of nuisance parameters that we will encounter when discussing the statistical analysis in Section 7.4, but for the moment it suffices to mention that they represent the impact of systematic uncertainties to the search. Lastly, λ^b represents the non-negative background contribution. As can be seen in Equation 7.1, $\lambda\left(\vec{p}_{A/H}, \vec{\nu}\right)$ depends non-linearly on $g_{A/H}$, and in different ways for the resonance and interference parts. This suggests that $g_{A/H}$ is a suitable POI since it can take nonzero values even when the total rate in the presence of signal is zero.

In anticipation of the statistical analysis to be discussed in Section 7.4, we also mention an alternative version of $\lambda\left(\vec{p}_{A/H}, \vec{\nu}\right)$, $\lambda\left(\mu, \vec{p}_{A/H}, \vec{\nu}\right)$ that is obtained by attaching a signal strength modifier μ as follows:

$$\lambda\left(\mu, \vec{p}_{A/H}, \vec{\nu}\right) = \left(\mu \times \sum_{A,\,H}\left(g^4_{A/H}\lambda^s_R\left(\vec{p}_{A/H}, \vec{\nu}\right) + g^2_{A/H}\lambda^s_I\left(\vec{p}_{A/H}, \vec{\nu}\right)\right)\right) + \lambda^b(\vec{\nu}) \tag{7.2}$$

Equation 7.2 reduces to Equation 7.1 when $\mu = 1$. The background-only scenario is recovered when $g_{A/H} = 0$ in both cases.

Table 7.1: A signal points, their associated cross sections in dileptonic channel and the k-factors for the resonance part k_R. The quoted uncertainties are from ME scale variations, where the first uncertainties are due to μ_R and the second are due to μ_F. The upper uncertainties are when μ_R or μ_F are varied by a factor of 2, while the lower uncertainties are when they are varied by a factor of 0.5. Cross sections for semileptonic channel can be obtained by scaling with 2.67 which is the ratio between the two channels' BRs.

Parity	m_A (GeV)	Γ_A (% m_A)	LO cross section (pb)		k_R
			Resonance	Interference	
A	400	2.5	$1.538^{-0.260\ -0.092}_{+0.347\ +0.096}$	$-0.927^{+0.156\ +0.057}_{-0.209\ -0.060}$	2.109
		5	$0.725^{-0.122\ -0.044}_{+0.164\ +0.046}$	$-0.922^{+0.155\ +0.057}_{-0.207\ -0.060}$	2.105
		10	$0.325^{-0.055\ -0.020}_{+0.073\ +0.021}$	$-0.870^{+0.146\ +0.055}_{-0.195\ -0.058}$	2.102
		25	$0.099^{-0.017\ -0.006}_{+0.022\ +0.007}$	$-0.707^{+0.118\ +0.047}_{-0.157\ -0.050}$	2.101
		50	$0.037^{-0.006\ -0.002}_{+0.008\ +0.003}$	$-0.514^{+0.085\ +0.035}_{-0.114\ -0.038}$	2.100
	500	2.5	$0.710^{-0.117\ -0.052}_{+0.155\ +0.057}$	$-0.180^{+0.030\ +0.013}_{-0.040\ -0.014}$	2.001
		5	$0.346^{-0.057\ -0.025}_{+0.076\ +0.028}$	$-0.195^{+0.032\ +0.014}_{-0.043\ -0.015}$	1.998
		10	$0.164^{-0.027\ -0.012}_{+0.036\ +0.013}$	$-0.224^{+0.037\ +0.016}_{-0.049\ -0.017}$	1.996
		25	$0.055^{-0.009\ -0.004}_{+0.012\ +0.004}$	$-0.260^{+0.043\ +0.019}_{-0.057\ -0.020}$	1.995
		50	$0.021^{-0.003\ -0.002}_{+0.005\ +0.002}$	$-0.249^{+0.041\ +0.018}_{-0.054\ -0.020}$	1.995
	600	2.5	$0.301^{-0.049\ -0.025}_{+0.064\ +0.029}$	$0.009^{-0.002\ -0.001}_{+0.002\ +0.001}$	1.946
		5	$0.149^{-0.024\ -0.012}_{+0.032\ +0.014}$	$-0.006^{+0.001\ +0.001}_{-0.001\ -0.001}$	1.945
		10	$0.073^{-0.012\ -0.006}_{+0.016\ +0.007}$	$-0.033^{+0.005\ +0.002}_{-0.007\ -0.003}$	1.944
		25	$0.027^{-0.004\ -0.002}_{+0.006\ +0.002}$	$-0.082^{+0.013\ +0.006}_{-0.018\ -0.007}$	1.943
		50	$0.011^{-0.002\ -0.001}_{+0.002\ +0.001}$	$-0.115^{+0.019\ +0.009}_{-0.025\ -0.010}$	1.943
	750	2.5	$0.093^{-0.015\ -0.009}_{+0.019\ +0.010}$	$0.058^{-0.009\ -0.005}_{+0.012\ +0.005}$	1.899
		5	$0.047^{-0.007\ -0.004}_{+0.010\ +0.005}$	$0.049^{-0.008\ -0.004}_{+0.011\ +0.004}$	1.898
		10	$0.024^{-0.004\ -0.002}_{+0.005\ +0.003}$	$0.034^{-0.006\ -0.003}_{+0.007\ +0.003}$	1.898
		25	$0.009^{-0.002\ -0.001}_{+0.002\ +0.001}$	$-0.003^{+0.001\ +0.001}_{-0.001\ -0.001}$	1.898
		50	$0.004^{-0.001\ -0.001}_{+0.001\ +0.001}$	$-0.038^{+0.006\ +0.003}_{-0.008\ -0.003}$	1.898

Table 7.2: H signal points, their associated cross sections in dileptonic channel and the k-factors for the resonance part k_R. The quoted uncertainties are from ME scale variations, where the first uncertainties are due to μ_R and the second are due to μ_F. The upper uncertainties are when μ_R or μ_F are varied by a factor of 2, while the lower uncertainties are when they are varied by a factor of 0.5. Cross sections for semileptonic channel can be obtained by scaling with 2.67 which is the ratio between the two channels' BRs.

Parity	m_H (GeV)	Γ_H (% m_H)	LO cross section (pb)		k_R
			Resonance	Interference	
H	400	2.5	$0.139^{-0.023\ -0.009}_{+0.031\ +0.009}$	$-0.268^{+0.045\ +0.017}_{-0.060\ -0.018}$	2.123
		5	$0.069^{-0.012\ -0.004}_{+0.015\ +0.005}$	$-0.256^{+0.043\ +0.017}_{-0.057\ -0.018}$	2.125
		10	$0.034^{-0.006\ -0.002}_{+0.008\ +0.002}$	$-0.235^{+0.039\ +0.016}_{-0.052\ -0.017}$	2.126
		25	$0.013^{-0.002\ -0.001}_{+0.003\ +0.001}$	$-0.185^{+0.031\ +0.013}_{-0.041\ -0.014}$	2.127
		50	$0.006^{-0.001\ -0.001}_{+0.001\ +0.001}$	$-0.137^{+0.023\ +0.010}_{-0.030\ -0.011}$	2.128
	500	2.5	$0.191^{-0.031\ -0.014}_{+0.042\ +0.016}$	$-0.113^{+0.019\ +0.008}_{-0.025\ -0.009}$	2.022
		5	$0.092^{-0.015\ -0.007}_{+0.020\ +0.008}$	$-0.112^{+0.019\ +0.008}_{-0.025\ -0.009}$	2.025
		10	$0.043^{-0.007\ -0.003}_{+0.009\ +0.004}$	$-0.114^{+0.019\ +0.008}_{-0.025\ -0.009}$	2.027
		25	$0.014^{-0.002\ -0.001}_{+0.003\ +0.001}$	$-0.103^{+0.017\ +0.008}_{-0.023\ -0.009}$	2.028
		50	$0.006^{-0.001\ -0.001}_{+0.001\ +0.001}$	$-0.085^{+0.014\ +0.007}_{-0.018\ -0.007}$	2.028
	600	2.5	$0.123^{-0.020\ -0.010}_{+0.026\ +0.012}$	$-0.027^{+0.004\ +0.002}_{-0.006\ -0.002}$	1.971
		5	$0.060^{-0.010\ -0.005}_{+0.013\ +0.006}$	$-0.031^{+0.005\ +0.002}_{-0.007\ -0.003}$	1.973
		10	$0.028^{-0.005\ -0.002}_{+0.006\ +0.003}$	$-0.036^{+0.006\ +0.003}_{-0.008\ -0.003}$	1.975
		25	$0.009^{-0.002\ -0.001}_{+0.002\ +0.001}$	$-0.043^{+0.007\ +0.003}_{-0.009\ -0.004}$	1.976
		50	$0.004^{-0.001\ -0.001}_{+0.001\ +0.001}$	$-0.045^{+0.007\ +0.004}_{-0.010\ -0.004}$	1.976
	750	2.5	$0.050^{-0.008\ -0.005}_{+0.010\ +0.006}$	$0.011^{-0.002\ -0.001}_{+0.002\ +0.001}$	1.926
		5	$0.025^{-0.004\ -0.002}_{+0.005\ +0.003}$	$0.009^{-0.001\ -0.001}_{+0.002\ +0.001}$	1.928
		10	$0.012^{-0.002\ -0.001}_{+0.002\ +0.001}$	$0.003^{-0.001\ -0.001}_{+0.001\ +0.001}$	1.929
		25	$0.004^{-0.001\ -0.001}_{+0.001\ +0.001}$	$-0.007^{+0.001\ +0.001}_{-0.002\ -0.001}$	1.929
		50	$0.002^{-0.001\ -0.001}_{+0.001\ +0.001}$	$-0.016^{+0.003\ +0.001}_{-0.003\ -0.001}$	1.930

7.2.2 Top pair invariant mass binning

Having decided on the coupling modifier $g_{A/H}$ as the POI in our search, we now focus on the search observables. Since the signal introduces both an excess and a deficit on the total event yield, it is crucial that the search is performed over a distribution where these contributions do not overlap. Figure 2.5 strongly suggests $m_{t\bar{t}}$ as one of our search observables, in which the signal manifests itself as a peak-dip structure. However, considering the difference between signal and background cross sections (c.f. Tables 7.1, 7.2 and 6.2), it is clear that our sought after signal is only a tiny wiggle within a large continuum. If we are to have a chance at making conclusive statements on the presence of the signal, this wiggle must be made more striking.

As all distributions that we are exploiting will be presented as histograms, a binning scheme has to be defined. A narrower binning allows us to retain more shape information in the distribution; this is important in retaining the peak-dip structure in $m_{t\bar{t}}$ especially for A/H at narrow widths. To determine the appropriate binning, we turn to the estimated experimental resolution as a function of generated $m_{t\bar{t}}$, shown in Figure 7.1, together with its bias. The bias and resolution are estimated using the SM $t\bar{t}$ simulation as the mean and RMS of the distribution of the following quantity:

$$\frac{m_{t\bar{t}}^{\text{reco.}} - m_{t\bar{t}}^{\text{gen.}}}{m_{t\bar{t}}^{\text{gen.}}} \tag{7.3}$$

with the superscripts referring to the reconstructed and generated values of $m_{t\bar{t}}$, respectively. Although we are primarily interested in the overall bias and resolution with no selection applied at the generator level, the resolution and bias of two other scenarios are shown to give us an estimate of the performance of our methods in the ideal limit of all required inputs being present and correctly assigned.

From Figure 7.1 (b), the best overall resolution is around 20%, giving us the upper bound on the bin widths to be adopted. The lower bound on the other hand is simply bins that are sufficiently wide that the features in the distributions are driven by physical properties of the investigated process instead of statistical fluctuations. This requirement is fullfilled if the bins in the distribution are sufficiently populated, where in our case 'sufficient' is taken to be of $\mathcal{O}(100)$ unweighted simulated events on average. As can be seen in Figure 7.2, this requirement is well fulfilled by the investigated A and H points assuming the chosen binning scheme, where for this check the widest resonance points are chosen as they are most spread out in the $m_{t\bar{t}}$ spectrum resulting in the weakest statistical power per bin.

The $m_{t\bar{t}}$ binning scheme adopted in this work is non-uniform with 23 bins in total, the edges of which is given in Equation 7.4. The binning is inclusive over the full $m_{t\bar{t}}$ spectrum in that underflow and overflow contributions are added to the first and last bins.

$$\begin{aligned} m_{t\bar{t}} \in [\ &325, 355, 385, 415, 445, 475, 505, 535, 565, 595, 625, 655, \\ &685, 715, 745, 775, 805, 837, 872, 911, 957, 1014, 1094, 1200\ ] \text{ GeV} \end{aligned} \tag{7.4}$$

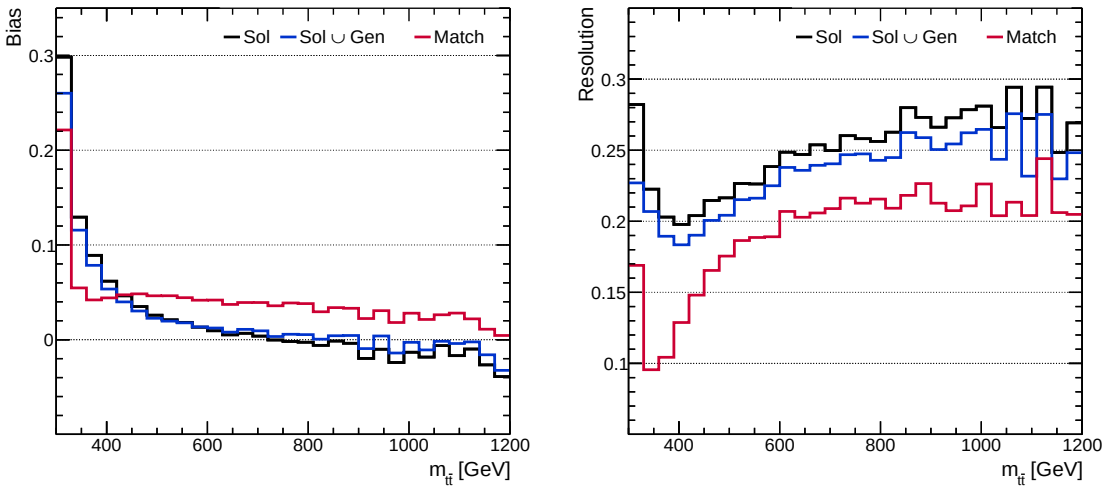

(a) Bias (b) Resolution

Figure 7.1: Bias and resolution of the reconstructed top pair invariant mass as functions of the generated top pair in variant mass. The labeling for each scenario follows that of the generator-oriented evaluation discussed in Section 6.5.

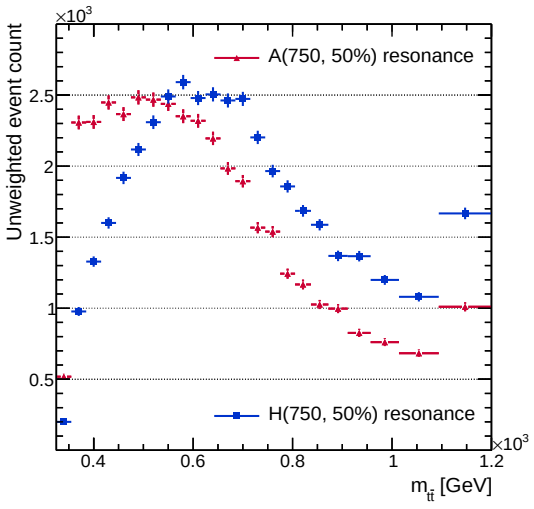

Figure 7.2: The reconstructed top pair invariant mass distribution for the resonant $\mathrm{A}(750, 50\%)$ and $\mathrm{H}(750, 50\%)$ points adopting the analysis binning scheme. The uncertainties are statistical due to the finite simulation size.

7.2.3 Spin correlation observable

While $m_{t\bar{t}}$ is our primary search observable, the presence of signal is only a tiny feature within its distribution. The sensitivity of our search has to be increased in order to strengthen whatever conclusions we may extract regarding the presence of the signal in our data. Broadly speaking, this can be done in two (not necessarily mutually exclusive) ways; the use of higher-dimensional histograms or a multivariate classifier. The former has the advantage of fully exploiting both the information in individual observables and the correlations in a straightforward way. However, it has the drawback that the number of bins grow exponentially for every added observable, reducing the statistical power of each bin. Trying to compensate for this by reducing the number of bins may be counter-productive as in doing so one also sacrifices the available shape information in each observable. The multivariate classifier method seeks to solve exactly this problem by mapping the differences in features between signal and background processes in many observables into a single discriminator - a quantity that takes on higher values for events that are more signal-like and lower for those that are more background-like. In principle at least, a multivariate classifier is able to exploit all the features that differentiate between signal and background processes. However, in practice this may not be the case; the available algorithms need some input variables which are used to compute the discriminator, the choice of which can be as tricky as for the high-dimensional histograms. Furthermore, these inputs are often passed through complex layers of neural networks or other architechtures; rendering the final discriminators not as intuitive as their physically-motivated counterparts.

In this work, we adopt the first method of using a higher dimensional histogram to enhance our sensitivity[1]. Exploiting the different spins of the propagators of the s-channel diagrams of signal and background processes, we add a spin correlation observable as the second dimension to the $m_{t\bar{t}}$ spectrum. Since we are quite close to the limit of sufficient statistical power per bin from the $m_{t\bar{t}}$ binning alone (see Figure 7.2), for the second dimension we choose 5 equidistant bins as our binning scheme a priori in order to avoid reducing the number of bins of and therefore the shape information in the $m_{t\bar{t}}$ distribution.

The remaining problem is the choice of spin correlation observable. In Appendix C, the generated distributions of all spin correlation observables for signal and background are shown. There we see only a few are useful for signal against background discrimation: c_{ii}, c_{hel} and the laboratory frame observables. We shall confine our choice between c_{hel} and $\Delta\phi_{\ell\ell}$ as c_{hel} encapsulates the information in c_{ii} (see Table 2.2) while c_{lab} is expected to be significantly affected by the PDF systematic source. To determine which of the two to be used in later steps of the analysis, we analyze their respective unrolled[2] 2D reconstructed-level signal + background and background-only distributions. The distributions in the combined channel, obtained from summing the ee, eμ and $\mu\mu$ channels, are shown in Figure 7.3 for A and Figure 7.4 for H, both at 2.5% width and taking into account both the resonance and interference parts. In these Figures, the bands defined by the gray histograms in the ratio pad

[1] A boosted decision tree approach was explored at some point during the course of the search, but it was found to be no more sensitive than the $m_{t\bar{t}}$ × spin correlation approach used in this work while requiring a higher computational cost and processing time.

[2] To unroll a 2D distribution is to present one dimension in bins of the other. In our current case, it means presenting the $m_{t\bar{t}}$ distributions in bins of the respective spin correlation observable.

denote the total impact of statistical and systematic uncertainties; loosely estimated as the sum in quadrature of the symmetrized impact of each source of uncertainties. All systematic sources affecting the background[3] are taken into account in this estimate.

From these Figures, the sensitivity is estimated utilizing the χ^2 between the signal + background and background-only distribution, where the uncertainty is taken to be the estimated total uncertainty above. The χ^2 for each A/H mass points at 2.5% width are shown in Table 7.3 where for the sake of comparison, the same χ^2 considering only the $m_{t\bar{t}}$ distribution are also shown. From these results, we see that $\Delta\phi_{\ell\ell}$ is the slightly more sensitive observable for A at low mass, while c_{hel} takes over from 600 GeV onwards. For H, c_{hel} is consistently more sensitive than $\Delta\phi_{\ell\ell}$. We also see that both 2D search strategies vastly outperform the strategy using only $m_{t\bar{t}}$. A single search strategy would greatly simplify the overall analysis workflow, so c_{hel} is chosen as the second search observable for both A and H.

Table 7.3: The sensitivity χ^2 for several A/H points comparing different search strategies.

Point	Search strategy		
	$m_{t\bar{t}}$	$m_{t\bar{t}} \times c_{hel}$	$m_{t\bar{t}} \times \Delta\phi_{\ell\ell}$
A(400, 2.5%)	1.117	5.376	5.390
A(500, 2.5%)	0.253	1.247	1.358
A(600, 2.5%)	0.085	0.438	0.435
A(750, 2.5%)	0.025	0.137	0.115
H(400, 2.5%)	0.019	0.112	0.087
H(500, 2.5%)	0.018	0.109	0.090
H(600, 2.5%)	0.015	0.092	0.069
H(750, 2.5%)	0.009	0.049	0.035

7.3 Template Smoothing

While the general outline of the treatment of systematic uncertainties has been provided in Section 6.6, in this search some of the systematic templates are smoothed. The motivation is to suppress statistical fluctuations within these templates; a discussion on why this is necessary is deferred to Section 7.4. Here we will be focusing on the smoothing procedures instead. The approach that is adopted in this work is based on the LOWESS (LOcally WEighted Scatterplot Smoothing) approach. The algorithm is described in detail in Reference [9]; only its essential features that are directly relevant to this work will be discussed here.

[3] As a reminder, the background estimation procedure in this search has been discussed in Section 6.4.

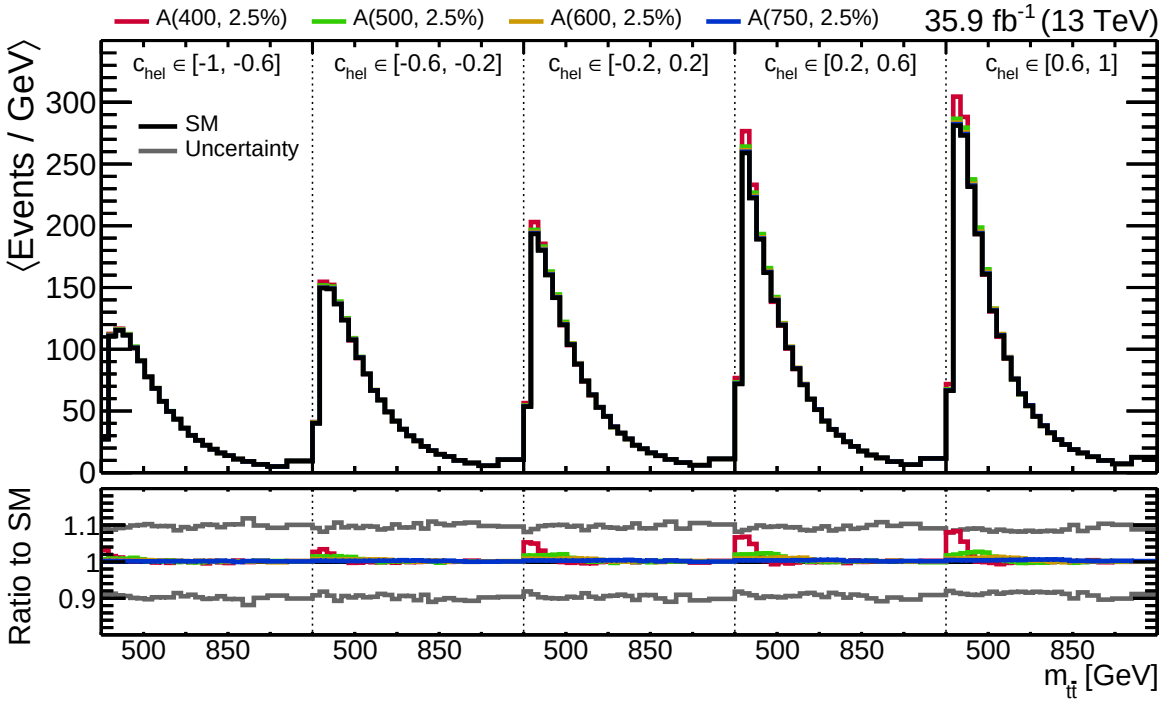

(a) Unrolled $m_{t\bar{t}}$ - c_{hel} distribution

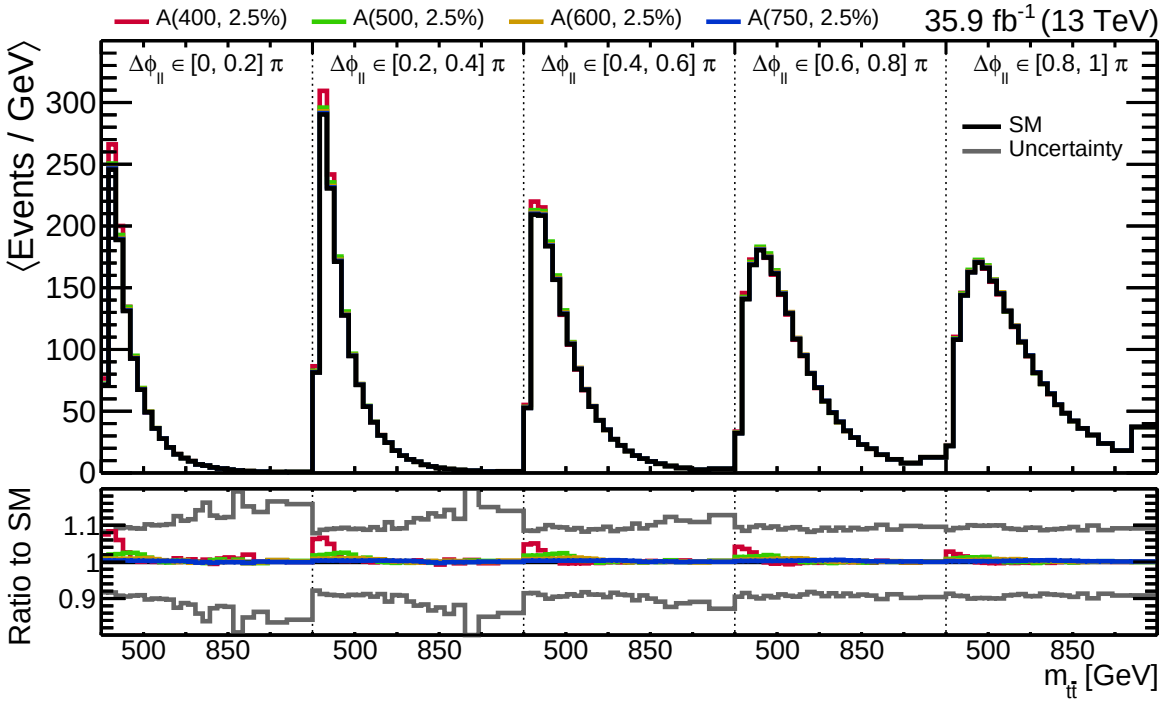

(b) Unrolled $m_{t\bar{t}}$ - $\Delta\phi_{\ell\ell}$ distribution

Figure 7.3: Unrolled 2D $m_{t\bar{t}}$ and a spin correlation observable distributions comparing the A at 2.5% width signal + background and background only distributions.

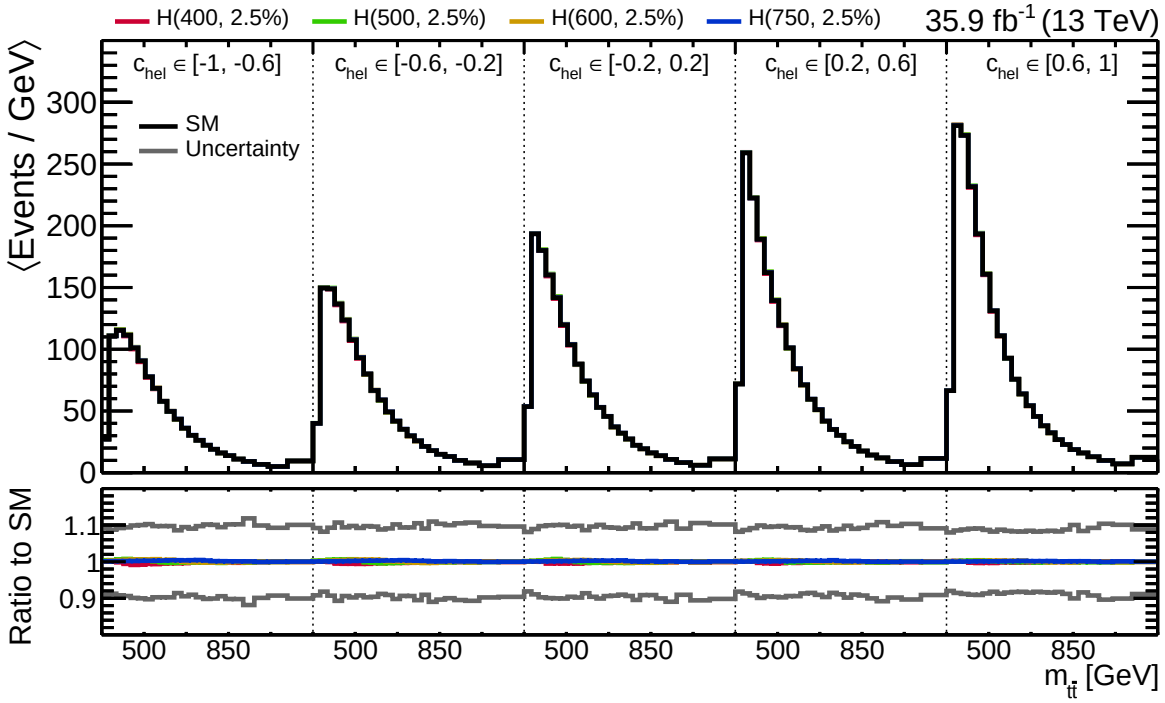

(a) Unrolled $m_{t\bar{t}}$ - c_{hel} distribution

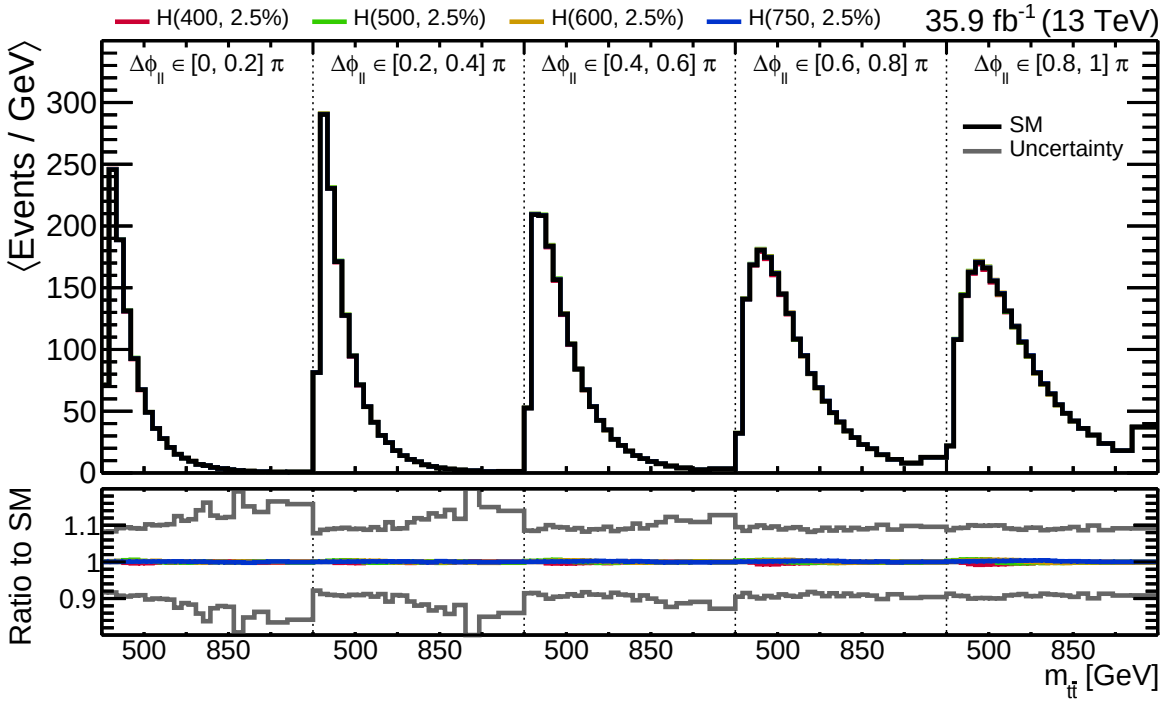

(b) Unrolled $m_{t\bar{t}}$ - $\Delta\phi_{\ell\ell}$ distribution

Figure 7.4: Unrolled 2D $m_{t\bar{t}}$ and a spin correlation observable distributions comparing the H at 2.5% width signal + background and background only distributions.

The LOWESS algorithm operates on the symmetrized relative deviation $\hat{r}$ of a given systematic source with respect to the nominal template. The relative deviation of a given variation is defined as $r_{\pm} = \frac{\lambda^{\pm}}{\lambda^{0}} - 1$ where λ is the (per-bin vector of the) expected yields of the total background or only SM $\mathrm{t\bar{t}}$ contribution, depending on the systematic source that is being smoothed. The superscripts $+$, 0 and $-$ on the other hand denote the up, nominal and down variations, respectively. In order to prevent the rather coarse analysis binning to introduce potential artefacts in the smoothing step, a fine binning of approximately equal statistical power (10 bins in $\mathrm{c_{hel}}$ and 90 bins in $\mathrm{m_{t\bar{t}}}$) for the nominal template of total background contribution is used. The higher bin count in $\mathrm{m_{t\bar{t}}}$ is to account for the higher degree of shape variation that is possible along this axis.

The relative deviation is smoothed locally by performing a weighted least squares fit within a sliding window of size $2h_x \times 2h_y$, where h_i is the bandwidth along a given axis. x and y are identified as $\mathrm{c_{hel}}$ and $\mathrm{m_{t\bar{t}}}$ respectively. h_i is expressed as a ratio to the number of bins used, for example when $h_{\mathrm{m_{t\bar{t}}}} = 0.1$, a point may be up to 9 bins away along $\mathrm{m_{t\bar{t}}}$ in a given window. Let w_{ij} be the weight assigned to any point $p_j \equiv (x_j, y_j)$ within the plane centered at p_i. w_{ij} is given by a tricubic function of the distance between p_j and p_i, d_{ij}:

$$w_{ij} = \left(1 - d_{ij}^3\right)^3, \; d_{ij}^2 = \left(\frac{x_j - x_i}{2h_x}\right)^2 + \left(\frac{y_j - y_i}{2h_y}\right)^2$$

Since $d_{ij} \in [0, 1]$, points that are further away from plane center are assigned smaller weights. The smoothed value of a point p_j is then simply given as the weighted average of the fits over all planes. An example of the smoothed template for the $\mathrm{m_t}$ systematic source in a particular $\mathrm{c_{hel}}$ bin, for a particular choice of bandwidth is shown in Figure 7.5. It can be seen that the algorithm successfully reproduces the main features of the relative deviation while at the same time suppressing the high-frequency fluctuations in the raw template.

While the up and down variations are assumed to be symmetric in shape, their normalizations are allowed to differ. Let $s_{\pm}$ be the independent scaling factors used to construct the smoothed systematic template: $\lambda^{\pm} \to \lambda'^{\pm} = \lambda^{0}(1 + s_{\pm}\hat{r})$. The $s_{\pm}$ are determined by a least squares fit minimizing the difference between original $\lambda^{\pm}$ and smoothed $\lambda'^{\pm}$:

$$\chi^2_{\pm} = \frac{\lambda'^{\pm} - \lambda^{\pm}}{\sigma}$$

where σ is the combined statistical uncertainties of the nominal and systematic templates in the analysis binning.

One remaining problem is the choice of $h_{\mathrm{c_{hel}}}$ and $h_{\mathrm{m_{t\bar{t}}}}$, which are free parameters of the algorithm. This is done by a cross-validation procedure over a $h_{\mathrm{c_{hel}}} \times h_{\mathrm{m_{t\bar{t}}}}$ grid of (0.2, 0.5, 1) $\times$ (0.05, 0.1, 0.2, 0.3, 0.5, 1). For a given choice of $\left(h_{\mathrm{c_{hel}}} \times h_{\mathrm{m_{t\bar{t}}}}\right)$, the events that are filled into the input templates are randomly split into ten partitions, nine of which are used as the training set to determine $s_{\pm}$ which are then applied to the testing set. An approximation error is computed on this set as $\chi^2 = \chi^2_{+} + \chi^2_{-}$. This procedure is repeated until all partitions have been used as a testing set, at which point the mean approximation error is available. The

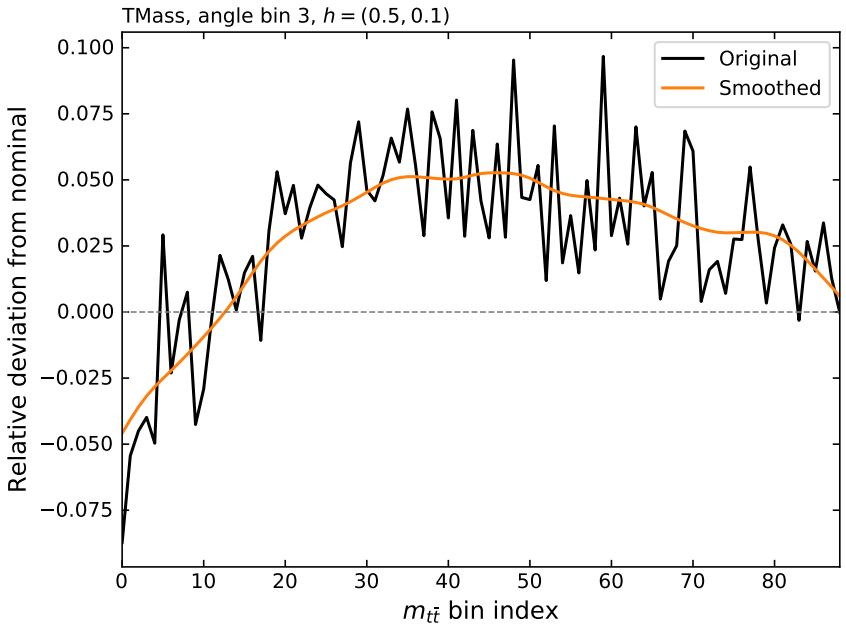

Figure 7.5: Comparison between the smoothed and raw relative deviation of the m_t systematic source as a function of $m_{t\bar{t}}$ in a particular c_{hel} bin.

choice of $(h_{c_{hel}} \times h_{m_{t\bar{t}}})$ that results in the smallest mean error is chosen to be the bandwidth for that particular systematic source, which is then used to smooth the templates containing all events. Figure 7.6 shows the mean error for different choices of $(h_{c_{hel}} \times h_{m_{t\bar{t}}})$ for two systematic sources. In the PS FSR case, there is a clear minimum at $(h_{c_{hel}}, h_{m_{t\bar{t}}}) = (0.5, 0.3)$. In the JEC PileUpPtRef case, the mean error slowly levels off until the edge of the tested grid as a function of $h_{m_{t\bar{t}}}$, so the maximum value of 1 in this direction is chosen in the final smoothing. The bandwidth that is used for each systematic source in the background template smoothing is given in Table 7.4. It is remarked that during the course of this study, the variation induced by the PS ISR source is found to be smaller than the statistical uncertainties of the nominal template. For this reason, it is not further considered in this search. The impact of each systematic source on the background is shown in Appendix D.

7.4 Model-Independent Interpretation

In this section, the results of the search in the dileptonic channel are shown. We begin with a discussion of the statistical analysis with which the results are obtained, before moving to the checks performed to ensure the reliability of the results. As mentioned in Section 7.2, the presence of the signal in the data is quantified in terms of $g_{A/H}$, considering at a time only one signal point A or H of a given mass and width. Since $g_{A/H}$ in the current context is only a multiplicative factor to the Yukawa coupling of the top quark, in contrast to e.g. 2HDM where $g_A = \tan^{-1}\beta$, for the sake of brevity we will refer to this set of results as the

Table 7.4: The bandwith used in the background systematic template smoothing and its associated mean approximation errors.

Systematic source	Bandwidth and mean approximation error ($N_{DF} = 115$)		
	$\left(h_{c_{hel}}, h_{m_{t\bar{t}}}\right)$	Variation 'up' χ^2_+	Variation 'down' χ^2_-
JER	(1, 1)	136.8	114.1
Unclustered $\not{p}_T$	(1, 1)	47.3	50.9
JEC PileUpDataMC	(1, 0.5)	75.5	111.6
JEC PileUpPtRef	(0.2, 1)	96.7	93.8
JEC PileUpPtBB	(1, 1)	79.0	134.5
JEC PileUpPtEC1	(1, 1)	49.7	44.6
JEC RelativeBal	(1, 0.5)	107.1	111.6
JEC RelativeFSR	(0.2, 1)	131.5	109.4
JEC RelativeJEREC1	(0.5, 1)	56.7	47.5
JEC RelativePtBB	(0.2, 0.5)	120.2	84.2
JEC RelativePtEC1	(0.5, 0.2)	50.4	46.4
JEC RelativeStatEC	(1, 0.5)	47.6	54.1
JEC RelativeStatFSR	(1, 1)	92.1	78.0
JEC TimePtEta	(1, 1)	132.8	100.1
JEC AbsoluteMPFBias	(1, 0.5)	104.0	123.3
JEC AbsoluteScale	(1, 1)	115.9	125.2
JEC AbsoluteStat	(1, 1)	91.4	78.1
JEC SinglePionECAL	(1, 1)	109.0	114.8
JEC SinglePionHCAL	(1, 1)	100.0	122.8
JEC FlavorQCD	(0.5, 0.3)	113.6	101.7
JEC Fragmentation	(1, 1)	109.5	117.2
m_t	(0.5, 0.1)	86.4	71.9
h_{damp}	(1, 1)	80.7	73.2
PS FSR	(0.5, 0.3)	68.4	89.8

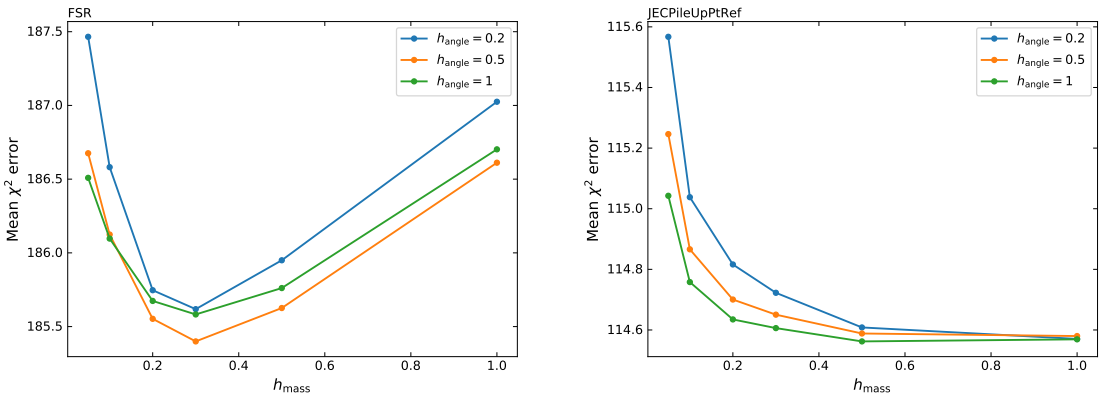

(a) PS FSR

(b) JEC PileUpPtRef

Figure 7.6: Average approximation error for each choice of bandwidths for PS FSR and JEC PileUpPtRef systematic sources. h_{mass} in these plots refer to $h_{\text{m}_{\text{t}\bar{\text{t}}}}$, and h_{angle} refers to $h_{\text{c}_{\text{hel}}}$.

model-independent interpretation[4].

7.4.1 Statistical analysis

The presence of A/H signal in the data is established by performing a statistical analysis based on the following likelihood function L:

$$L\Big(\mu,\, \vec{\text{p}}_{\text{A/H}},\, \vec{\nu}\Big) = \prod_i \frac{\lambda_i^{\text{N}_i}\Big(\mu,\, \vec{\text{p}}_{\text{A/H}},\, \vec{\nu}\Big)}{\text{N}_i!} e^{-\lambda_i\left(\mu,\, \vec{\text{p}}_{\text{A/H}},\, \vec{\nu}\right)} \times G(\vec{\nu}) \tag{7.5}$$

which is evaluated for every bin i. N_i is the observed event yield and $\vec{\nu}$ is a vector of nuisance parameters denoting the impact of systematic uncertainties. In addition to the systematic sources described in Section 6.6, some of which are smoothed as discussed in Section 7.3, $\vec{\nu}$ also includes the impact of finite simulation size on $\lambda\Big(\mu,\, \vec{\text{p}}_{\text{A/H}},\, \vec{\nu}\Big)$. This is done by assigning one nuisance parameter per bin following the 'light Barlow-Beeston' prescription [10]. Finally, $G(\vec{\nu})$ encode the external constraints on the nuisance parameters. For nuisance parameters corresponding to systematic sources, they are constrained by a Gaussian distribution of mean 0 and width 1. The background-only systematic templates at one standard deviation are as shown in Appendix D. Nuisance parameters corresponding to finite simulation size is constrained by a Poisson distribution.

[4]Although, as we will later see, in the parameter scan we impose an upper bound on $\text{g}_{\text{A/H}}$ - the choice of which is motivated by the 2HDM - so calling this set of results a 'model-independent interpretation' is strictly for the sake of brevity and is not to be taken literally. One may argue that '2HDM-inspired interpretation' might have been a better name, but this name is not chosen because the 2HDM contains a specific set of free parameters, most of which are irrelevant in our $\text{gg} \to \text{A/H} \to \text{t}\bar{\text{t}}$ simulation (see Section 7.1). As far as the signal simulation is concerned, the only free parameters in addition to those of the SM are $\vec{\text{p}}_{\text{A/H}}$ (with one of g_{A} or g_{H} set to 0 in all simulations), so 'model-independent interpretation' is deemed to be more appropriate.

From the likelihood, a profiled likelihood ratio is constructed as the test statistic $\tilde{q}_\mu$ [11]:

$$\tilde{q}_\mu = -2 \ln \frac{L(\vec{\nu})}{L(\mu, \vec{\nu})}, \ \mu \in [0, 1] \tag{7.6}$$

where we have suppressed the arguments of L that are kept fixed in the likelihood maximization. The full arguments of L are given in Equation 7.5. In other words, in computing $\tilde{q}_\mu$, the numerator of the logarithm of the likelihood ratio is maximized with respect to $\vec{\nu}$ with μ and $\vec{\mathrm{p}}_{\mathrm{A/H}}$ kept fixed (to 1 and the value of $\mathrm{g_{A/H}}$ that is being probed), while the denominator is maximized with respect to μ and $\vec{\nu}$, keeping only $\vec{\mathrm{p}}_{\mathrm{A/H}}$ fixed. The additional constraint on the minimum allowed value of μ is imposed to exclude cases when the signal shape is flipped with respect to the expectation (i.e. dip-peak instead of peak-dip for the A$(400, 2.5\%)$ point) while the maximum value constraint is to prevent the exclusion of a signal hypothesis in cases when the data is compatible with a contribution similar in shape but larger in size.

Exclusion regions are obtained using the CL_s technique[12, 13]. For a given $\mathrm{m_{A/H}}$ and $\Gamma_{\mathrm{A/H}}$, $\tilde{q}_\mu$ is computed for different values of $\mathrm{g_{A/H}}$. A CL_s value is computed for each of $\tilde{q}_\mu$, and the range of $\mathrm{g_{A/H}}$ for which the $\mathrm{CL}_s < 0.05$ is said to be excluded. In performing the scan, only the range of $\mathrm{g_{A/H}} < 3$ is considered; this choice is made to conserve perturbative unitarity within the context of 2HDM, which is only the case within the limit of $\tan^{-1}\beta = \mathrm{g_A} \gtrsim 0.3$ [2]. As the signal points with 50% width result in expected exclusion regions that are above this limit, they are considered to be physically ill-motivated and therefore dropped from this search.

The scan over fixed values of $\vec{\mathrm{p}}_{\mathrm{A/H}}$ relies on the asymptotic approximation in order to be computationally efficient [11]. For our analysis to be reliable, it is crucial that all the assumptions in the approximation is satisfied. The non-linear dependence of $\mathrm{g_{A/H}}$ to the predicted event yield (see Equation 7.1) means that the signal distibution may change in shape at different values of $\mathrm{g_{A/H}}$, leading to the possibility that multiple minima exists in $\tilde{q}_\mu$. Since this may invalidate the asymptotic approximation, μ is introduced as an auxiliary parameter with respect to which the likelihood is maximized. Nevertheless, it is mentioned that consistent results are obtained when identifying $\mathrm{g_{A/H}}$ as the signal strength parameter (i.e. using $\lambda\left(\vec{\mathrm{p}}_{\mathrm{A/H}}, \vec{\nu}\right)$ in the $\tilde{q}_\mu$ definition) with respect to those obtained using the μ-based $\mathrm{g_{A/H}}$ scan described here.

7.4.2 Impact of nuisance parameters

Before reporting the results, several cross checks that are performed to ensure the reliability of the statistical analysis are reported. They are conducted using the so-called Asimov data. It is a pseudodata that is constructed from simulation in such a way that when it is used to estimate the values of a set of parameters, the estimate results in the true values of those parameters [11]. The first cross check is therefore the pull distribution of each nuisance parameter [14]. Given the use of the Asimov dataset, if the initial estimate of the size of uncertainties are correct, the fit should result in pulls with mean 0 and width 1. The resulting pulls from a fit of a benchmark signal point of A$(500, 10\%)$ are shown in Figure 7.7. Two different cases are shown; with and without the template smoothing (see Section 7.3) applied. For the sake of readibility, all nuisance parameters related to finite simulation size

are suppressed, as they are all consistent with the expectation above.

As can be seen in Figure 7.7, all pulls are consistent with 0, as would be expected from the use of the Asimov data. However, the pull widths for some systematic sources are significantly lower than 1, contrary to our earlier expectation. Such sources are said to be constrained. In some cases this is acceptable, e.g. the PS FSR scale is expected to be constrained from the fact that the uncertainties in the relevant parameters used in simulation are larger than the uncertainties as obtained by dedicated studies using $t\bar{t}$ events [15]. However, the same cannot be said for many of the constraints, especially those related to the experimental systematic sources. The source of the constraints is traced to the fit constraining the statistical fluctuations within these templates, thus motivating the choice to smooth them. An analytical discussion on how such contraints can arise is available in Reference [9].

The second cross check is to look at the impact of each nuisance parameter. Impact is defined as the change in the POI (which is the signal strength μ in this case) that is induced when a nuisance parameter is fixed at its $\pm 1\sigma$ post-fit[5] value, with all the others profiled as usual. This gives a rough indication of the relevance of a given nuisance parameter. However, it is worth noting that the impact is different for a given nuisance parameter over different signal points. The impacts for four different points - A/H$(400, 10\%)$ and A/H$(750, 10\%)$ - are shown in Figures 7.8 and 7.9.

From these results, several observations are noted. First, variations in the ME scale choices for the SM $t\bar{t}$ process are usually among the nuisance parameters with the largest impacts in all the signal points shown. This is understood as these variations affecting the shape of the search templates (see Figure D.7), particularly along $m_{t\bar{t}}$. The ME scale choice for the signal on the other hand has a larger impact for A than H; in both cases the choice in the interference part is more relevant. Variations in the p_T^t reweighting parameters tend to affect the signal at higher masses, which is expected considering that, as shown in Reference [5], the reweighting improves the description of the data more in the higher $m_{t\bar{t}}$ values. On the experimental side, variations in JEC have the largest impact; this is true of all points that are shown. This is also expected considering the crucial role of JEC in the reconstruction of $m_{t\bar{t}}$ and c_{hel}. Finally, that the nuisance parameters representing finite simulation size being relevant whenever they affect the bins where the signal is reconstructed is straightforward.

It should be noted that in general the nuisance parameters are correlated. Therefore, the impacts can not illustrate all the features of the fit, as they ignore the correlations by definition. The correlations between 20 nuisance parameters with the largest impacts in Figures 7.8 and 7.9 are shown in Figures 7.10 and 7.11. As shown, the nuisance parameters are typically uncorrelated in the fit, in line with the initial assumption. The H$(750, 10\%)$ point is an exception among the points shown; the anticorrelations between the h_{damp} and JEC FlavorQCD parameters with the others is likely because their shapes are more similar to the H$(750, 10\%)$ point compared to other nuisance parameters.

[5]The *post-fit* value of a parameter refers to its value *after* the likelihood maximization that is performed in computing $\tilde{q}_\mu$ (see Equation 7.6). This is contrasted with the *pre-fit* value, which is the value *before* the maximization. For nuisance parameters the pre-fit values are always 0.

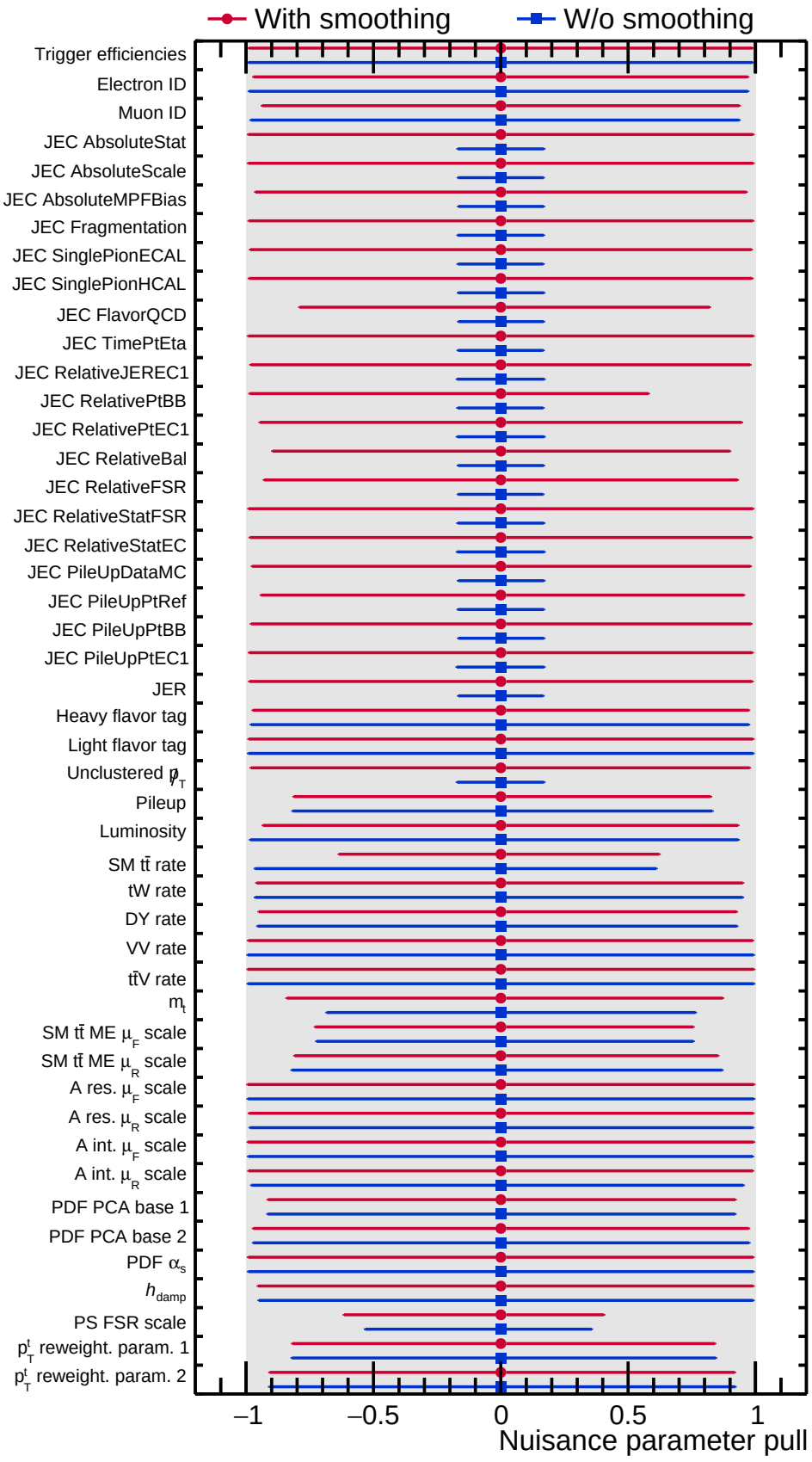

Figure 7.7: Nuisance parameter pulls from fitting the A(500, 10%) point to the Asimov data with and without the template smoothing applied.

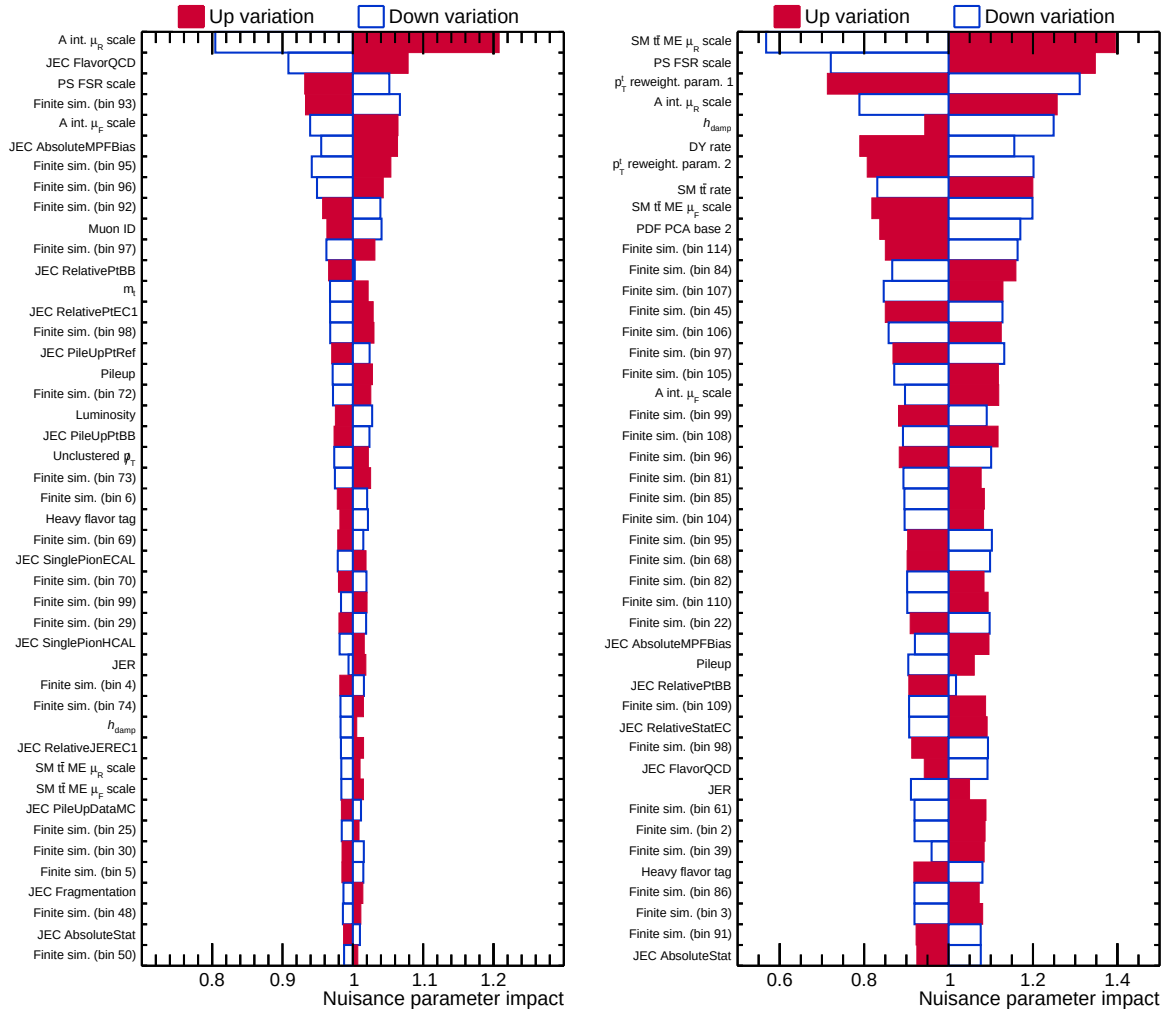

(a) A$(400, 10\%)$ (b) A$(750, 10\%)$

Figure 7.8: Nuisance parameter impacts from fitting the A$(400, 10\%)$ and A$(750, 10\%)$ points to the Asimov data. Only the 45 largest impacts are shown.

7.4.3 Comparison between data and background expectation

Considering that the presence of signal would cause only a small distortion on the search template, a good agreement between data and SM simulation is expected. As shown in Section 6.7 and Appendix B, this is observed for the control distributions that are inspected prior to the construction of the search templates. In addition, a similar agreement is qualitatively observed in both the pre-fit and background post-fit search templates shown in Figure 7.12. While there is some difference between the data and the SM simulation in the pre-fit template, this difference is covered by the uncertainties. In the background post-fit template, where all the nuisance parameters are profiled according to the observed data, a good agreement is also seen.

This agreement is quantified by goodness of fit tests. A distribution of the test statistic

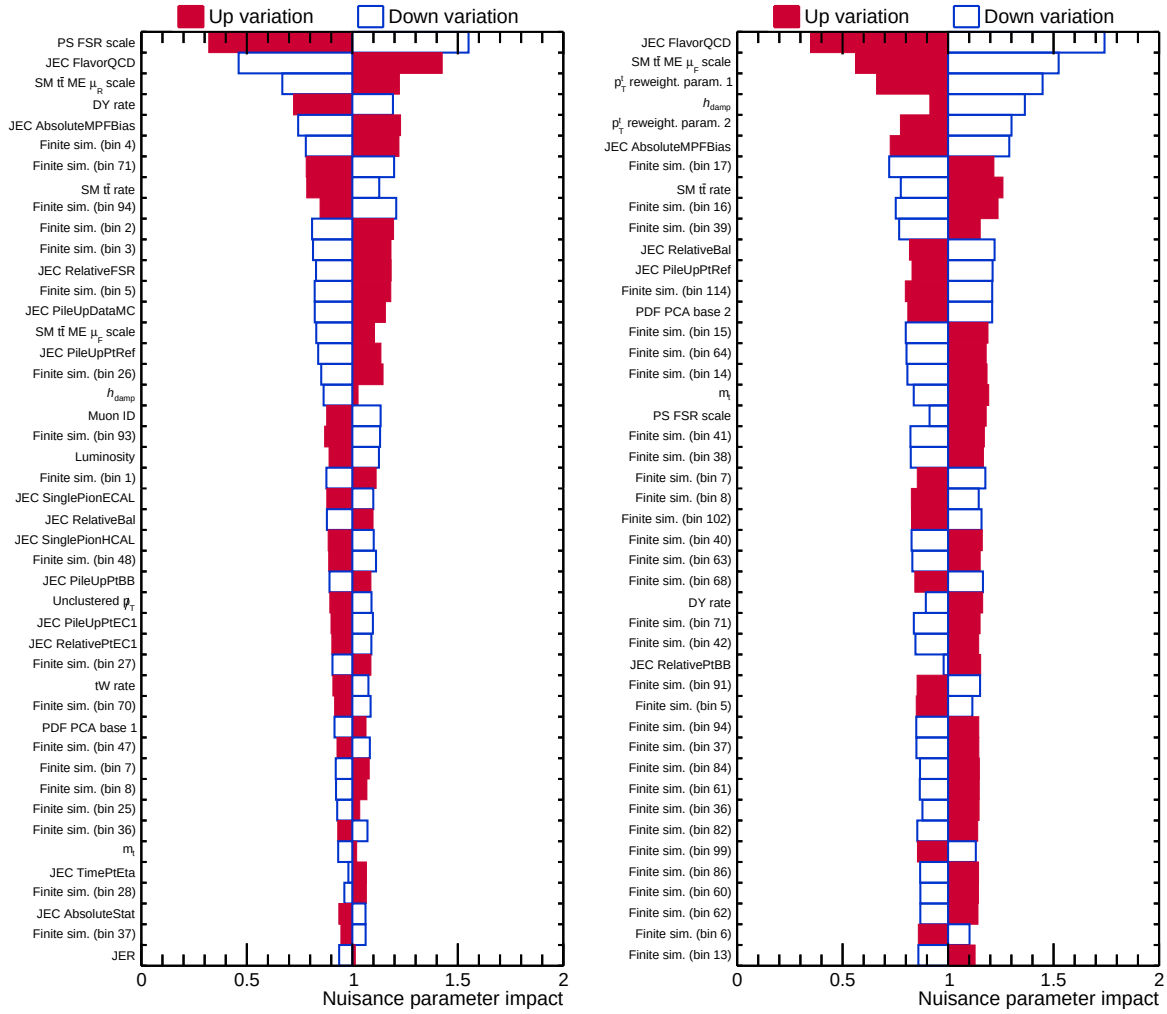

(a) H(400, 10%) (b) H(750, 10%)

Figure 7.9: Nuisance parameter impacts from fitting the H(400, 10%) and H(750, 10%) points to the Asimov data. Only the 45 largest impacts are shown.

is obtained by performing toy fits i.e. fits on pseudoexperiments which are obtained by randomly sampling the background-only search template. The distribution is then compared with the expected distribution through three different tests; the saturated model test [16], Kolmogorov-Smirnov (KS) test [17, 18] and the Anderson-Darling (AD) test [19, 20], which convert this distribution into distributions of 'scores' that express the degree of agreement between the data and the model. The score that is obtained when using the observed data is then compared with the toy score distribution. A good agreement between the data and the model within a given test is declared if the resulting p-value is not too small i.e. if the data score lies within the bulk of the toy distribution. The results of the goodness of fit tests are shown in Figure 7.13. As can be seen, for all three tests the p-values are reasonable, indicating a good agreement between the data and the background-only hypothesis.

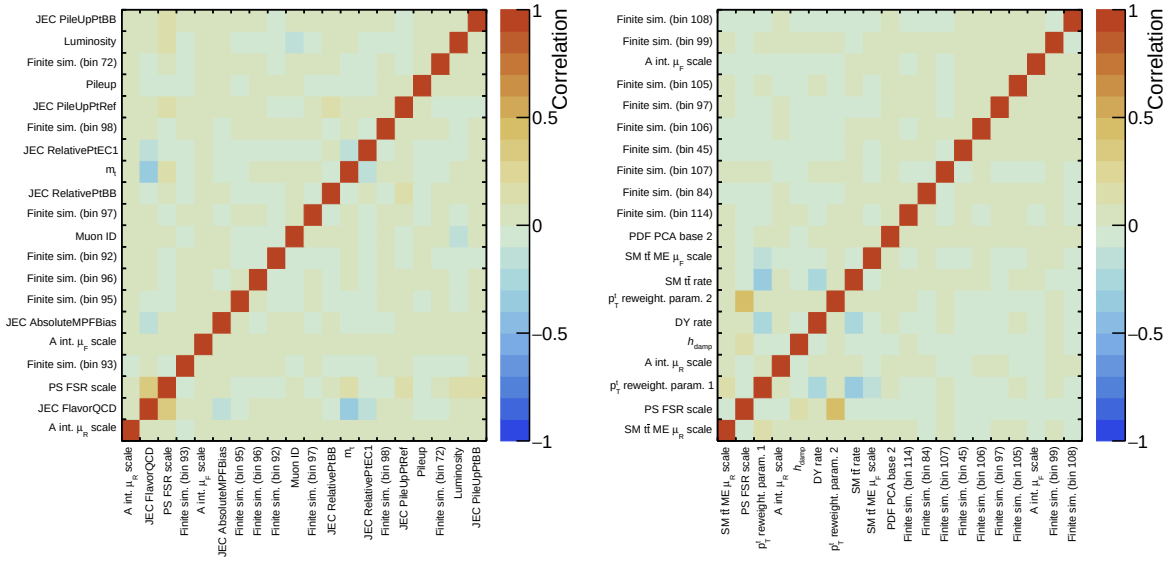

(a) A(400, 10%) (b) A(750, 10%)

Figure 7.10: Correlation between nuisance parameters from fitting the A(400, 10%) and A(750, 10%) points to the Asimov data.

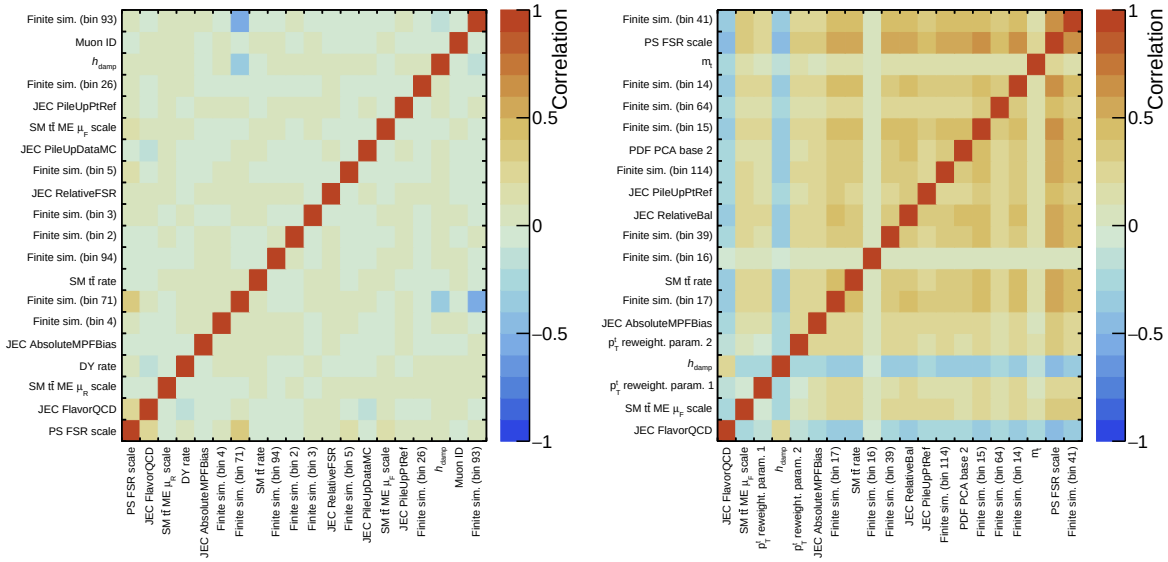

(a) H(400, 10%) (b) H(750, 10%)

Figure 7.11: Correlation between nuisance parameters from fitting the H(400, 10%) and H(750, 10%) points to the Asimov data.

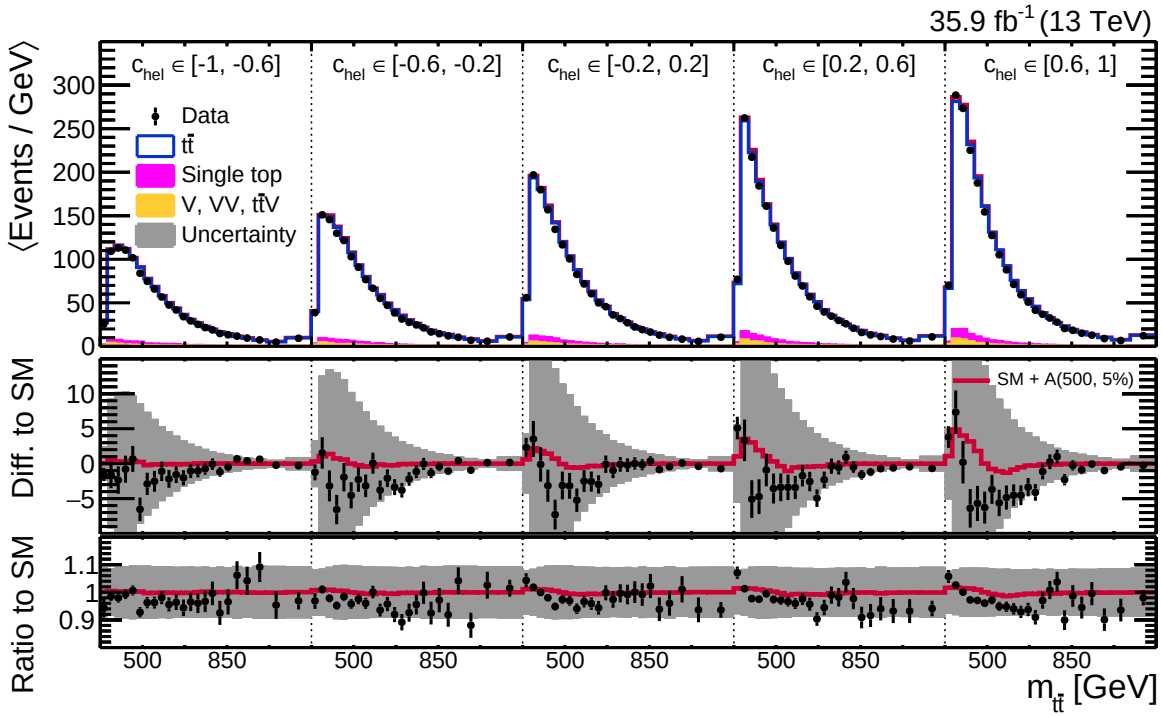

(a) Pre-fit

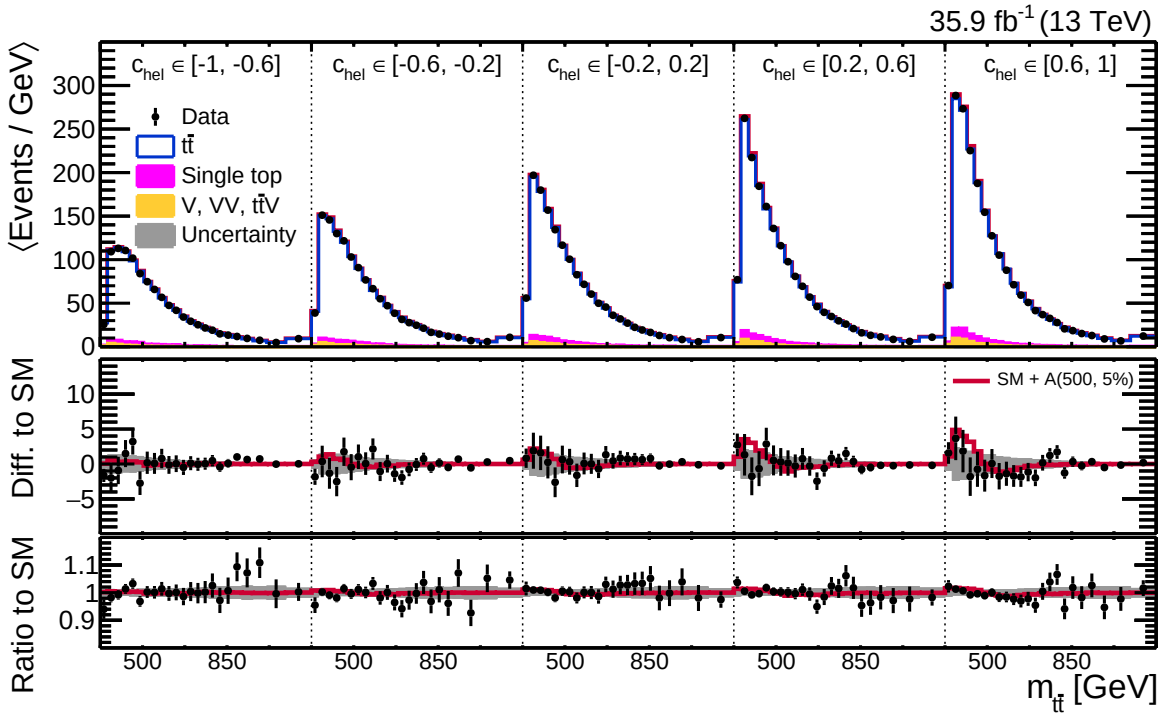

(b) Background-only post-fit

Figure 7.12: Pre-fit and background-only post-fit search templates compared to the data. The A(500, 10%) signal point is shown as an illustration. Only the dileptonic channel templates are used in the fit.

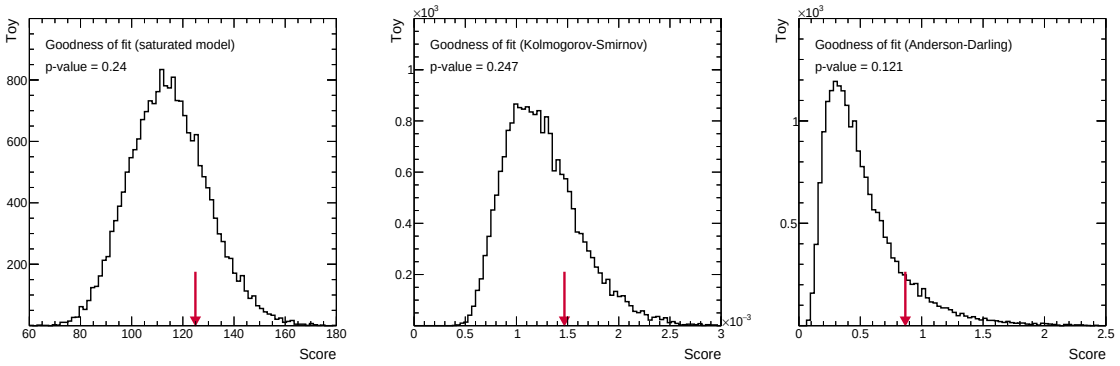

(a) Saturated model (b) KS test (c) AD test

Figure 7.13: Results of the goodness of fit test. The black histogram is the score distribution obtained with toys while the red arrow shows the score obtained with the data.

7.4.4 Exclusion regions on the A/H coupling modifier

Having discussed the checks that are performed to ensure the consistency of the fit, we now turn to the first set of results of the search. Exclusion regions on the signal production are set considering only one state of fixed mass and width at a time. The results are shown as a function of m_A and m_H at fixed width values in Figures 7.14 and 7.15.

In all the exclusion region plots, the boundary of the unphysical region where the values of $g_{A/H}$ would induce a partial A/H width to top quarks, $\Gamma_{A/H\to t\bar{t}}$, that exceeds the $\Gamma_{A/H}$ value assumed in simulation, is denoted with a hatched gray line. $\Gamma_{A/H\to t\bar{t}}$ is given as [21]:

$$\Gamma_{A/H\to t\bar{t}} = g^2_{A/H}\frac{3G_F m_t^2 m_{A/H}}{4\pi\sqrt{2}}\left(1-\frac{4m_t^2}{m^2_{A/H}}\right)^X \tag{7.7}$$

where X is 1/2 and 3/2 for A and H respectively. Looking at the expected exclusion regions, which represent the senstivity of the analysis, we see that at low $\Gamma_{A/H}$ values, for most of the $m_{A/H}$ values they lie within the unphysical region. This is because the $m_{t\bar{t}}$ resolution, as shown in Figure 7.1, is significantly worse than the assumed $\Gamma_{A/H}$ values. On the other hand, since the unphysical region lie well within $g_{A/H} < 1$ for much of the mass range (especially for A), it can be argued that such narrow states are physically ill-motivated and are therefore self-excluding. As we go to wider A/H states, the analysis begins to be sensitive to a larger part of the parameter space. However, at even larger width values the expected exclusion gets weaker again; this is because the production rate is inversely proportional to $\Gamma_{A/H}$. Additionally, the higher width means the signal is more smeared out along $m_{t\bar{t}}$, leading to a smaller deviation with respect to SM predictions and therefore lower sensitivity. In general the search is more sensitive to A rather than H, this follows from the larger inclusive A cross section (see Tables 7.1 and 7.2) and the more prominent deviation in the shape of $m_{t\bar{t}}$ and c_{hel} with respect to the SM $t\bar{t}$ shape (see Figures 2.5 and C.2).

The observed exclusion region based on the data is shown by a shaded blue area. As

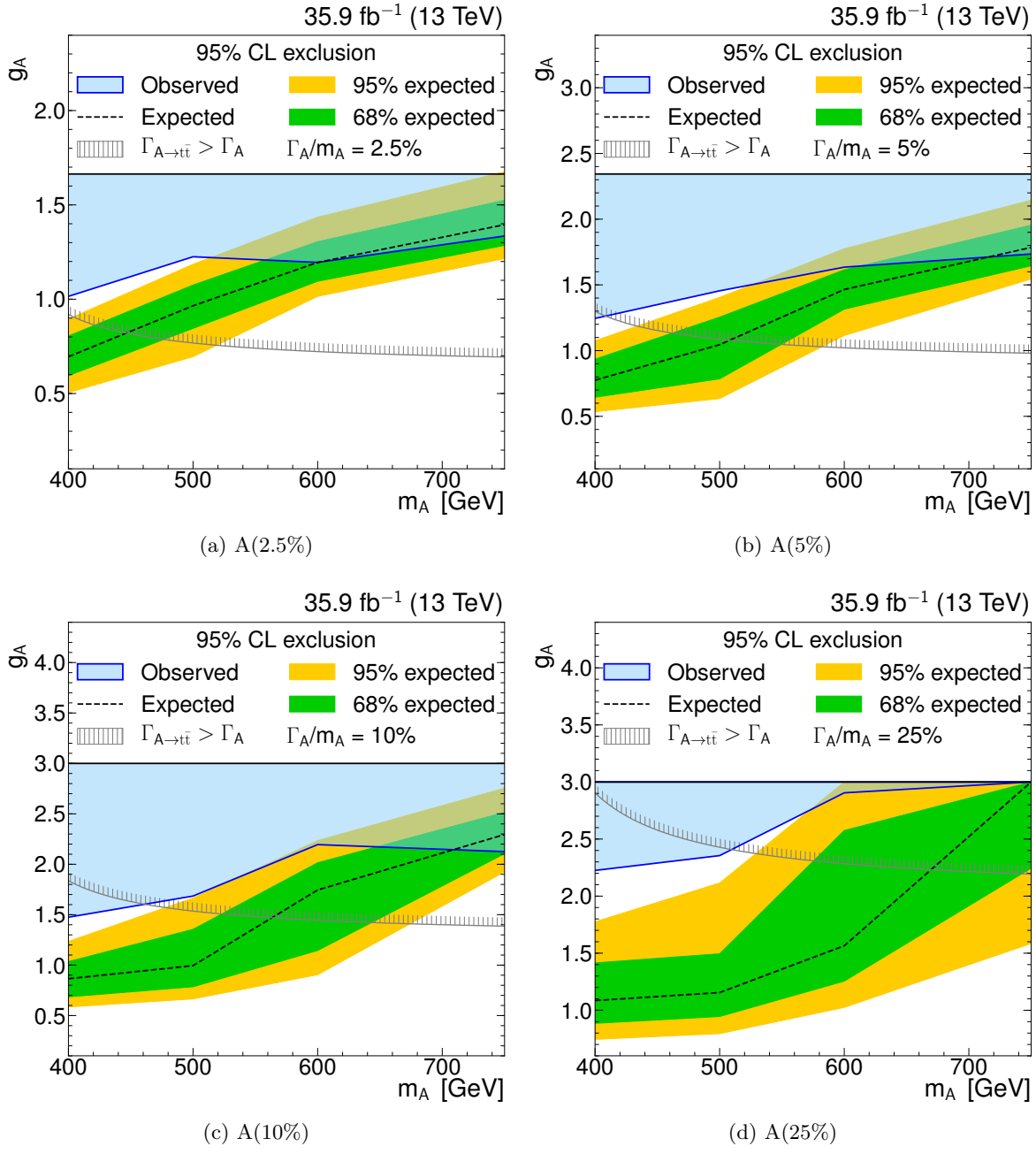

(a) A(2.5%)

(b) A(5%)

(c) A(10%)

(d) A(25%)

Figure 7.14: Exclusion region on g_A as a function of m_A at fixed Γ_A/m_A values in the dileptonic channel.

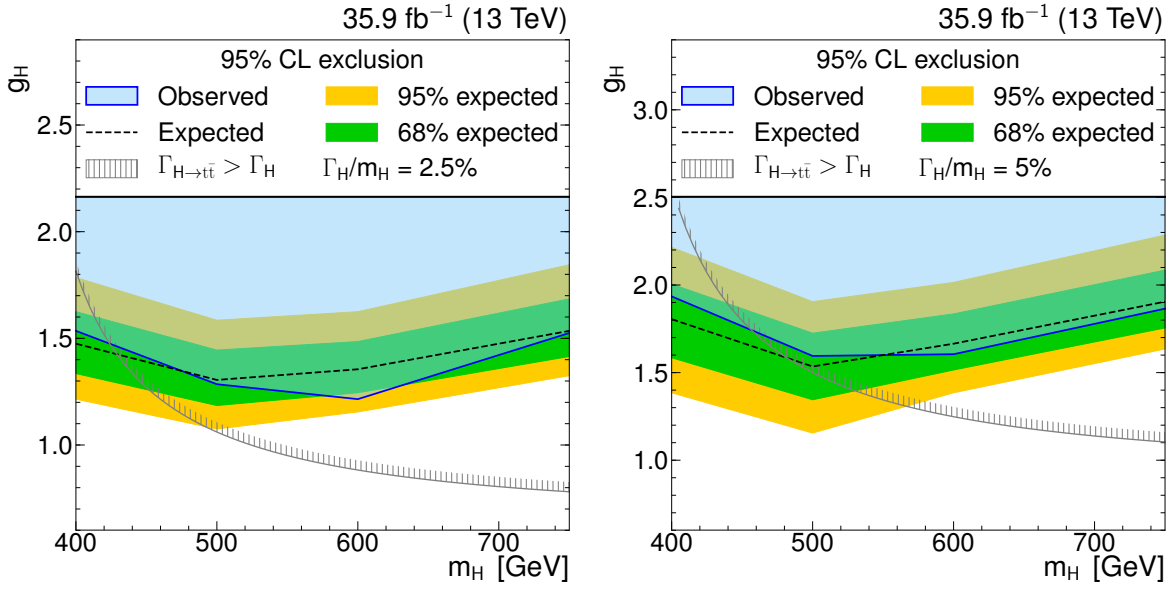

(a) H(2.5%)

(b) H(5%)

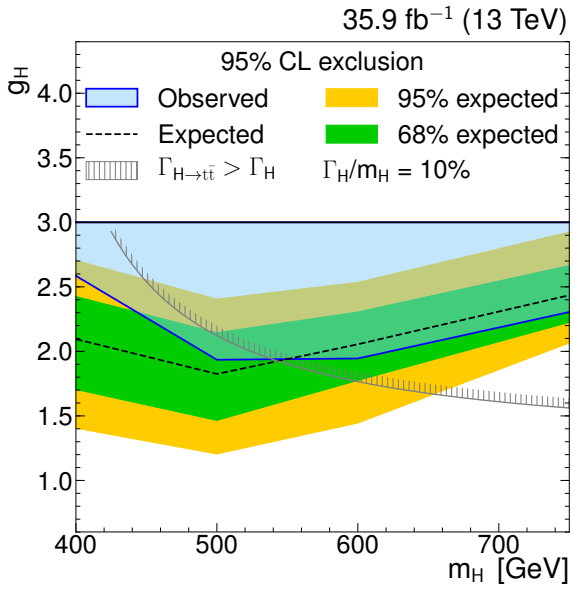

(c) H(10%)

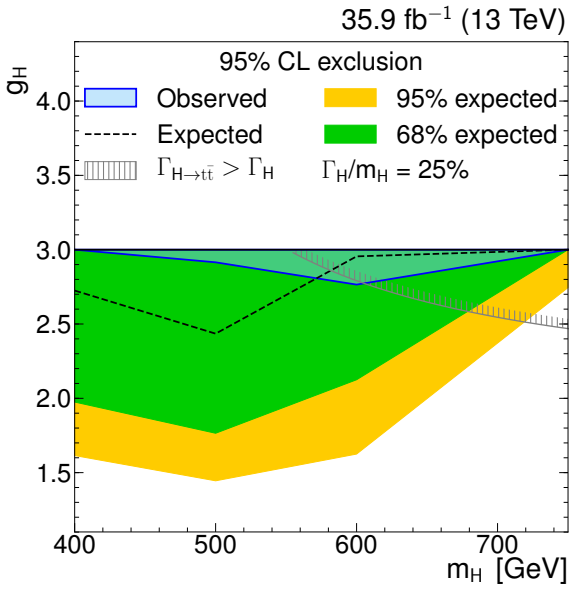

(d) H(25%)

Figure 7.15: Exclusion region on g_H as a function of m_H at fixed Γ_H/m_H values in the dileptonic channel.

can be seen Figure 7.14, the observed exclusion is consistent with the expected one at all m_H and Γ_H values, and also at high values of m_A. However, it is weaker than the expected exclusion for low m_A. This is interpreted as the data being consistent with the presence of an A boson with m_A of around 400 GeV, where the discrepancy between the observed and expected exclusion is the largest. The local significance of this excess is estimated using the asymptotic approximation from the minimum of $\tilde{q}_\mu$, where the likelihood ratio is defined using $g_{A/H} = 0$ in the numerator and the best fit value of $g_{A/H}$ in the denominator. The point with the highest local significance is found to be $A(400, 5\%)$ at 4σ. Another hint for the excess is given by the post-fit nuisance parameter pulls on data, which is shown for the $A(400, 5\%)$ point in Figure 7.16. In the background-only fit, a signal-like feature in the data must be compensated by the nuisance parameters, which means that they would be more strongly pulled away from zero compared to the signal + background fit. As can be seen in Figure 7.16, this is indeed the case. This is also understood to be the explanation of the apparent contradiction between the observation of the excess and good agreement observed in the goodness of fit tests (see Figure 7.13). In the background-only fits, $g_{A/H}$ is fixed to zero, so the toys are sampled using the pulled values of nuisance parameters. When $g_{A/H}$ is allowed to float in the signal + background fit, the likelihood is instead maximized at a nonzero value of $g_{A/H}$ and the nuisance parameters are pulled less strongly.

7.5 Combined A/H Search

The combined A/H search, where the combination is between the dileptonic and semileptonic $t\bar{t}$ channels, is the subject of this section. A brief overview of the semileptonic channel analysis, which is described in detail in Reference [5], is provided with an emphasis on the similarities and differences with respect to our search in the dileptonic channel. The model-independent interpretation is once again derived, demonstrating the increased sensitivity that is brought by the complementary analyses. As additional signal points are probed in the scan, part of the discussion will cover the procedure with which they are obtained.

7.5.1 Combination with the semileptonic channel

The search in the semileptonic channel targets the case when only one of the top quarks decay leptonically. As such, events containing exactly one electron or one muon together with at least four jets, at least two of which are b-tagged, are selected. Similar to our search, a kinematic reconstruction algorithm is adopted to reconstruct the $t\bar{t}$ system, and the search template is also a 2D histogram of $m_{t\bar{t}}$ and an angular observable. Due to the presence of only one neutrino in the event, the $m_{t\bar{t}}$ resolution in this search is $\in [15, 20]$ %, which is better than ours (c.f. Figure 7.1). The angular observable is $\left|\cos\theta^*_{t^\ell}\right|$, which is the absolute value of the angle between the direction of the leptonically decaying top quark in the $t\bar{t}$ ZMF and the direction of the $t\bar{t}$ system in the laboratory frame. This angle exploits the fact that in scalar resonance decays the top quarks are emitted isotropically, leading to a flat distribution if no other cuts are applied. The SM $gg \to t\bar{t}$ production on the other hand is a mixture of states of different angular momenta, resulting in a distribution that peaks at high values of $\left|\cos\theta^*_{t^\ell}\right|$ i.e. the top quarks are emitted preferentially parallel to the momentum direction of the $t\bar{t}$ system.

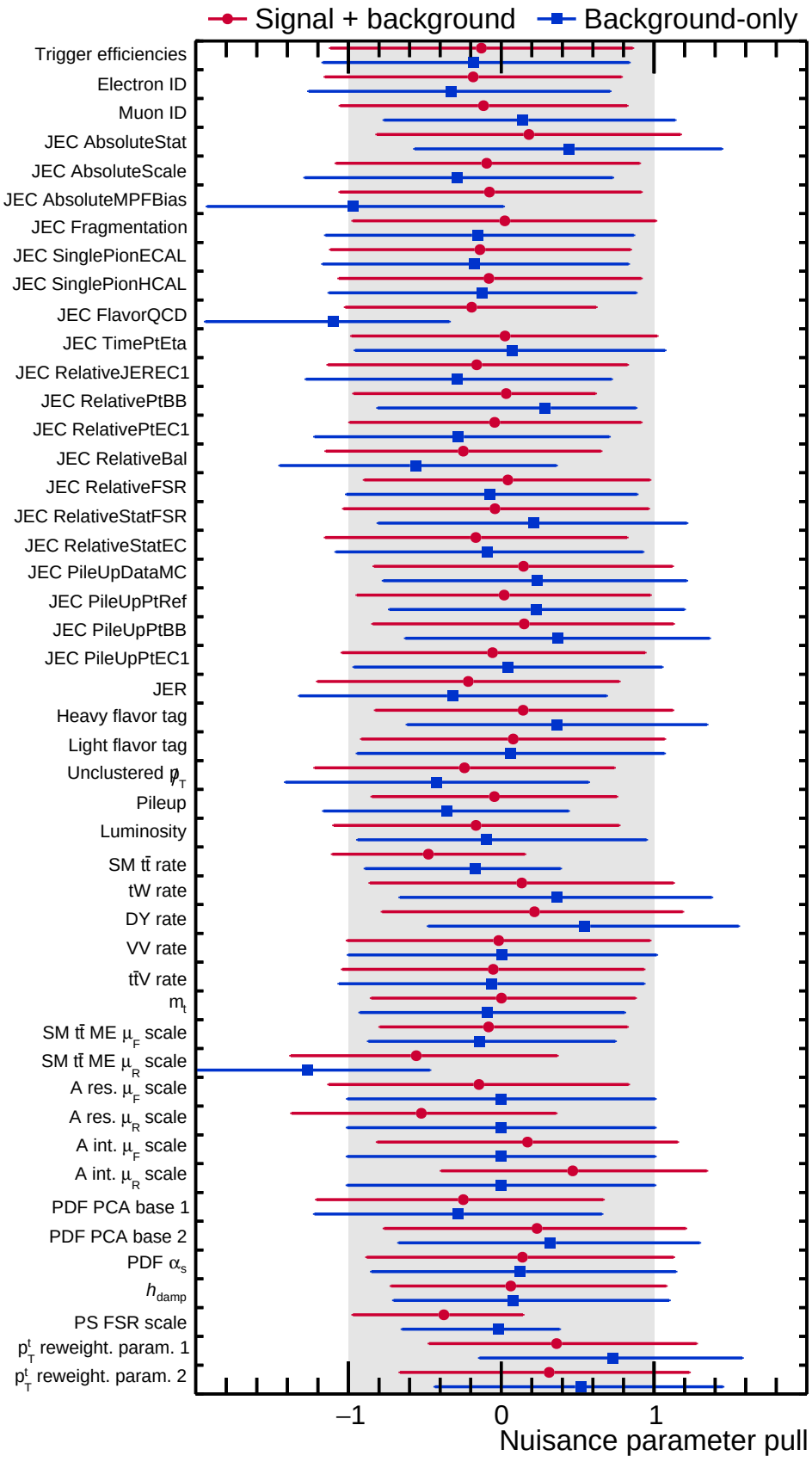

Figure 7.16: Nuisance parameter pulls from signal + background and background-only fits of the A$(400, 5\%)$ point to the data.

The systematic sources taken into account in the semileptonic search are mostly the same as in this search, as described in Section 6.6. The main difference is in the treatment of DY background, which is estimated using simulation. The multijet QCD background is present in this channel and is estimated using a data-driven method. Since it affects the electron and muon channel differently, the two channels are not combined in the statistical analysis step.

7.5.2 Interpolation and extrapolation of search templates

In the combined search, the scan described in Section 7.4 is performed over a finer $m_{A/H}$ and $\Gamma_{A/H}$ grid than the available simulated signal points. The remaining points are obtained through an interpolation procedure along the $m_{t\bar{t}}$ axis, separately in each c_{hel} and $\left|\cos\theta^*_{t^\ell}\right|$ bin of the three search templates. Resonance and inteference parts of the signal are separately interpolated. The horizontal shift along the $m_{t\bar{t}}$ axis is implemented as non-linear morphing along simulated mass points with the same width [22]. The change in width for the same mass values is separatedly implemented as hyperbolic interpolation for the resonance part of the signal and a linear interpolation for the interference part.

Additionally, the scan also probes $\Gamma_{A/H}$ values that are narrower than 2.5%. As the $m_{t\bar{t}}$ resolution in this analysis is significantly worse than this, the search template for 2.5% width points are simply taken and rescaled to the cross section of the desired width points. Both the interpolation and extrapolation procedures are discussed in more detail and validated in Reference [7].

7.5.3 Combined model-independent interpretation

We now turn to the exclusion region on $g_{A/H}$ that is set in the combined analysis, shown for a few representative width points in Figures 7.17 and 7.18. Compared to Figures 7.14 and 7.15, the improvement from adding the semileptonic search templates is clear; the expected exclusion improve by 30% or more. Correspondingly, a larger set of $g_{A/H}$ values are now excluded by the data. It is noted that at high mass and width values, the observed exclusion regions contain 'islands' where specific values of $g_{A/H}$ are not excluded, for both A and H. Since the event yield is not a linear function of the POI, the per-bin yields also change non-linearly. In particular, there can be a value of $g_{A/H} \neq 0$ where the total resonance and interference contributions cancel. If this occurs for many bins in the search template, this value of $g_{A/H}$ would be consistent with the $g_{A/H} = 0$ case and therefore is excluded. The high width points are more prone to this effect since they are more smeared out along $m_{t\bar{t}}$, increasing the overlap between the positive and negative signal contributions.

As with the dileptonic-only results, there is an excess consistent with the presence of A at low mass. The point with the highest local significance is once again found to be $A(400, 5\%)$, with a mild reduction at 3.7σ. In addition, the excess is illustrated by comparing the background-only and signal + background post-fit search templates. They are shown in Figure 7.19 for the dileptonic channel, Figure 7.20 for the electron channel and Figure 7.21 for the muon channel. Comparing the three search templates, one sees that the presence of the excess is more visible in the dileptonic channel; this explains the degradation of the local significance when all three channels are fitted together. One possible explanation for this

is that the impact of the signal is compensated by nuisance parameters in the semileptonic channel. This possibility is not investigated further as it is beyond the scope of this work.

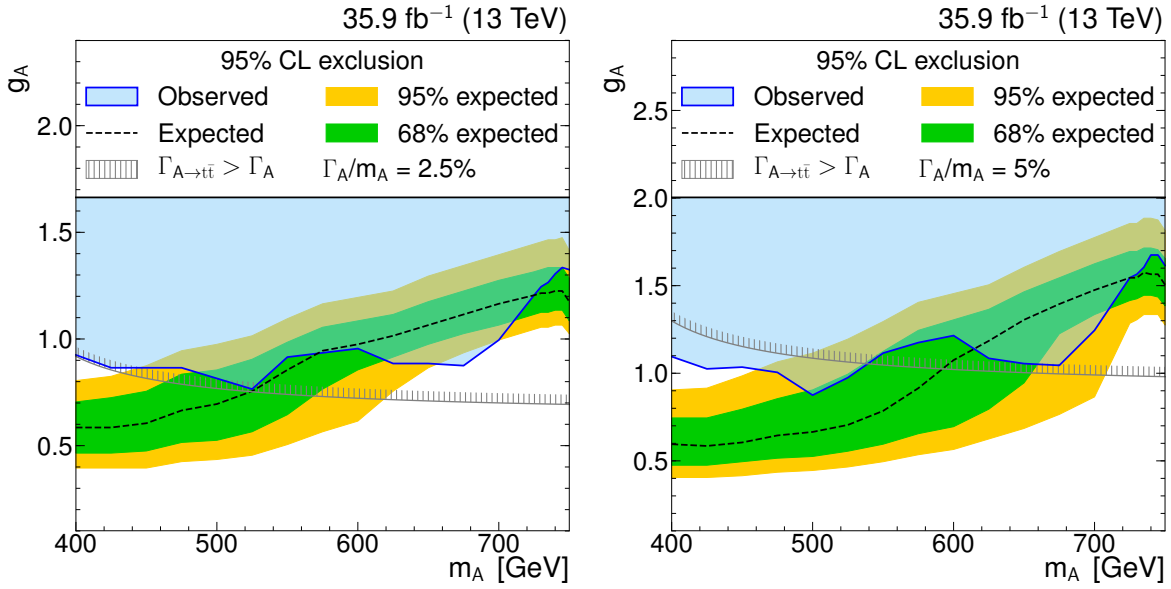

(a) A(2.5%)

(b) A(5%)

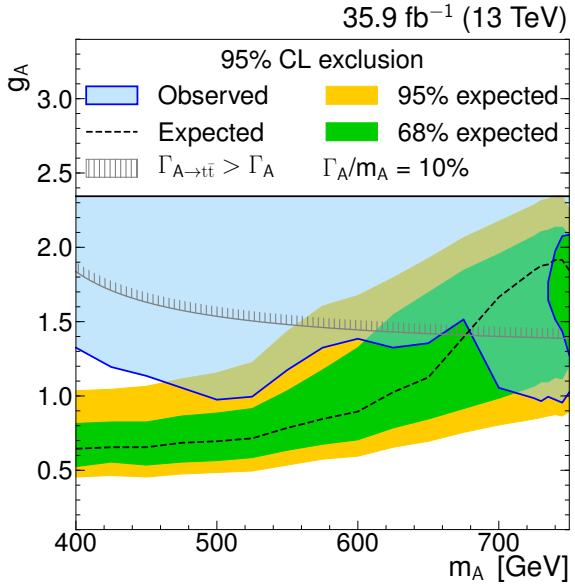

(c) A(10%)

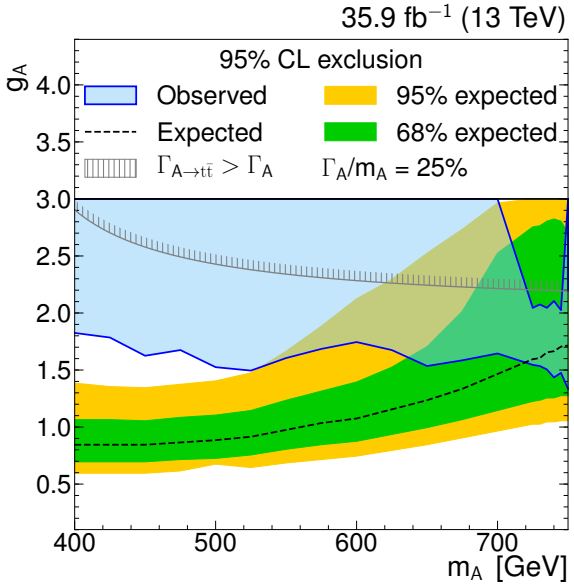

(d) A(25%)

Figure 7.17: Exclusion region on g_A as a function of m_A at fixed Γ_A/m_A values in the combination of dileptonic and semileptonic channels.

Another explanation for the difference between the channels is that it is caused by statistical fluctuations. In order to explore this possibility, the global significance of this excess is evaluated as the p-value of the asymptotic local significance being at least as large as the

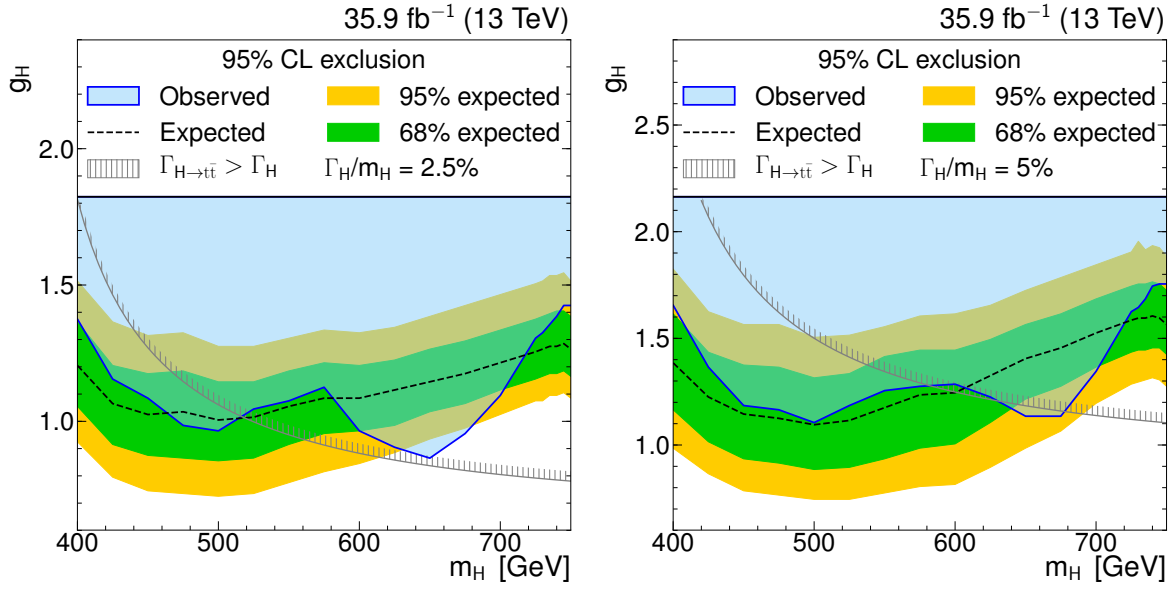

(a) H(2.5%)

(b) H(5%)

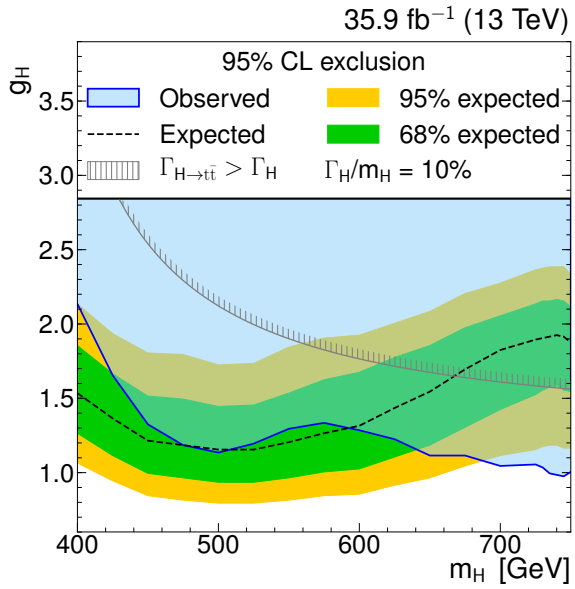

(c) H(10%)

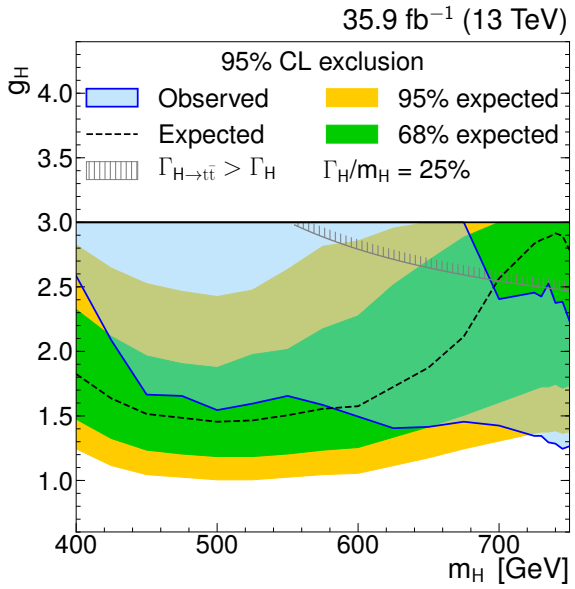

(d) H(25%)

Figure 7.18: Exclusion region on g_H as a function of m_H at fixed Γ_H/m_H values in the combination of dileptonic and semileptonic channels.

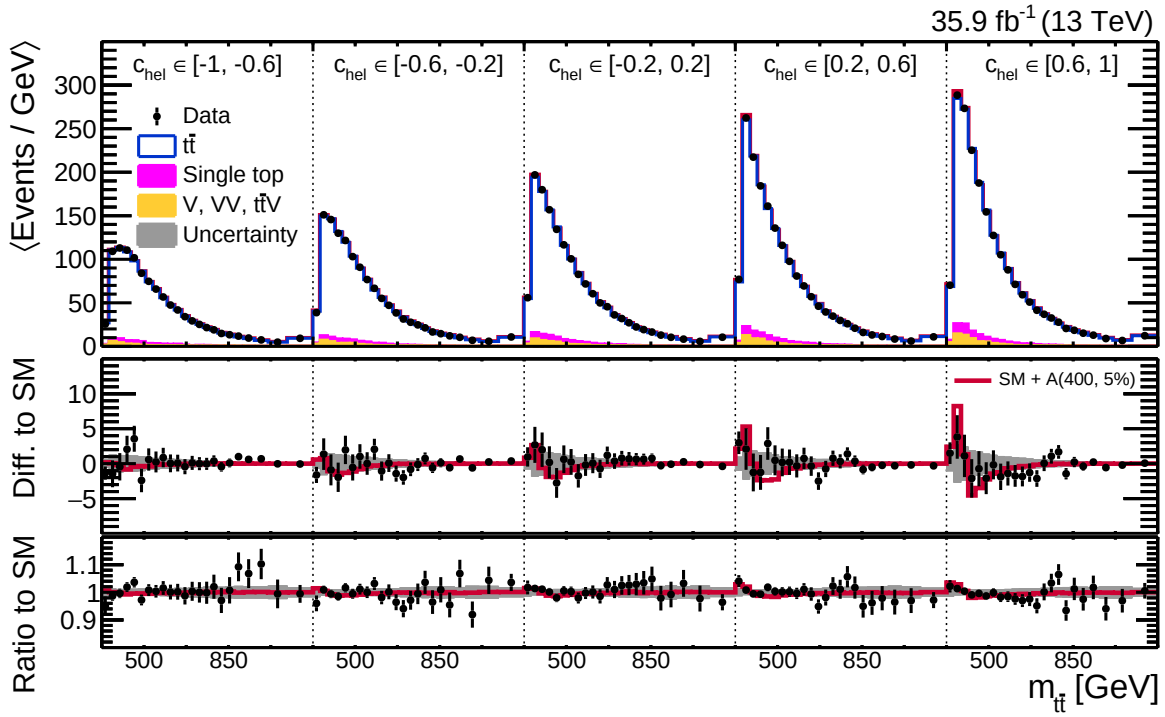

(a) Background-only post-fit

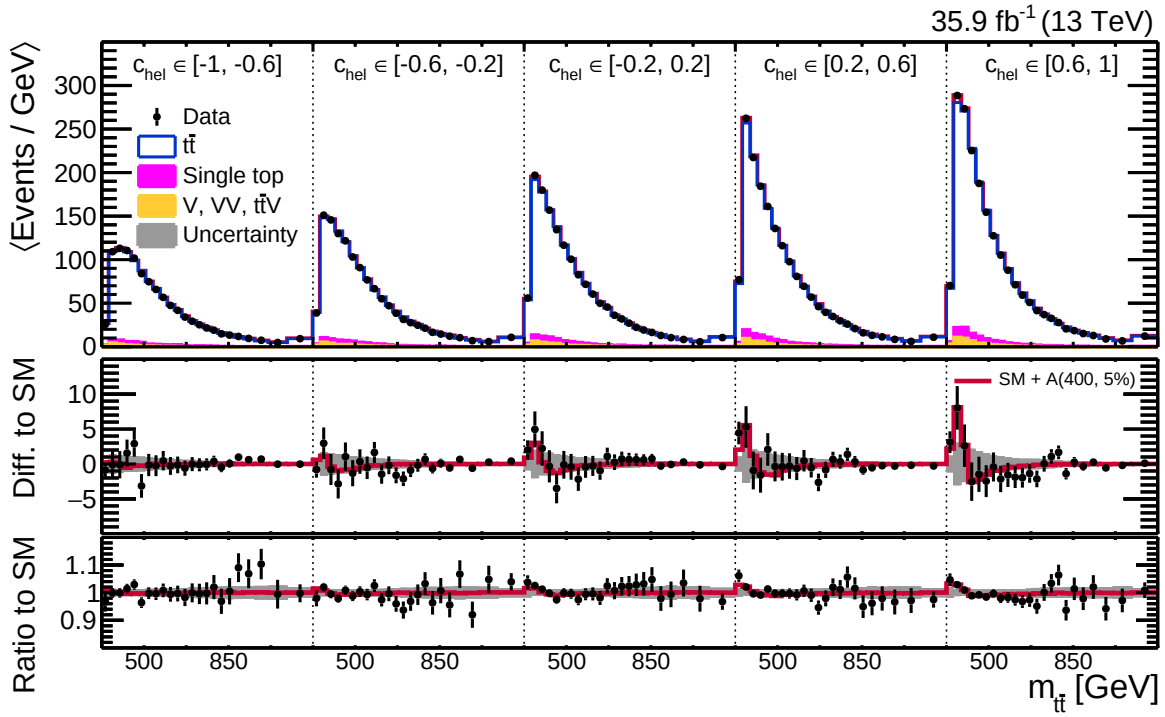

(b) Signal + background post-fit

Figure 7.19: Background-only and signal + background post-fit search templates to the data in the dileptonic channel, illustrating the presence of the A$(400, 5\%)$ excess. The dileptonic and semileptonic channel templates are fitted together.

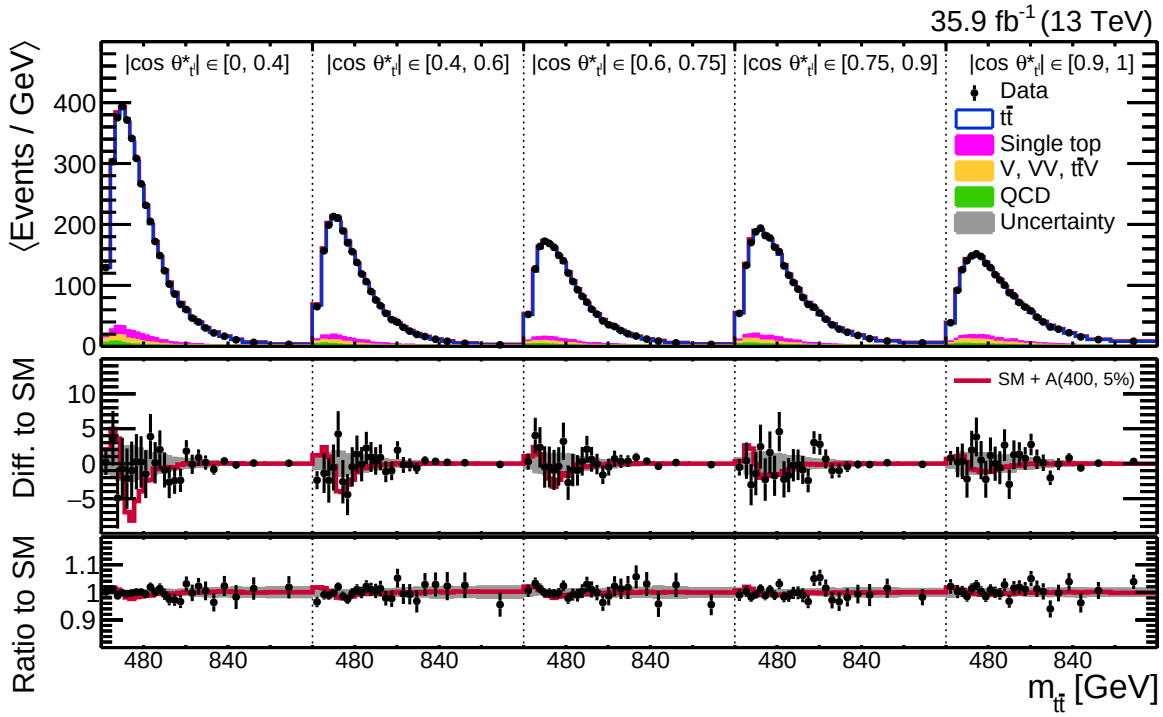

(a) Background-only post-fit

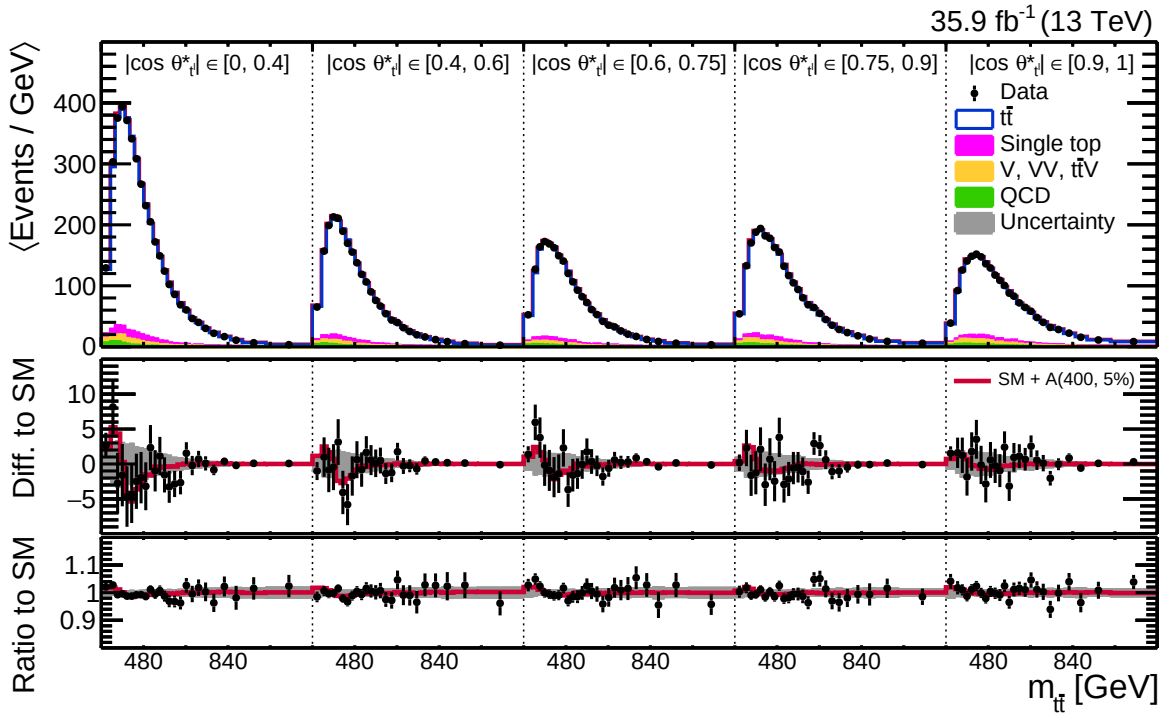

(b) Signal + background post-fit

Figure 7.20: Background-only and signal + background post-fit search templates to the data in the electron channel, illustrating the presence of the A(400, 5%) excess. The dileptonic and semileptonic channel templates are fitted together.

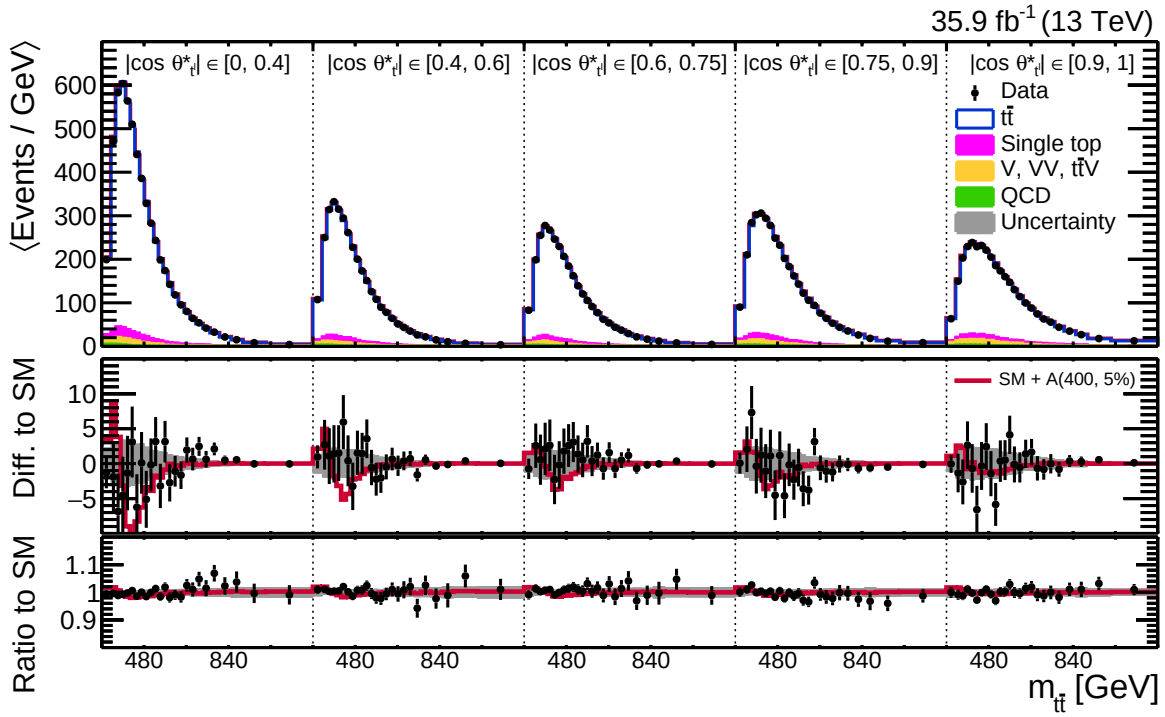

(a) Background-only post-fit

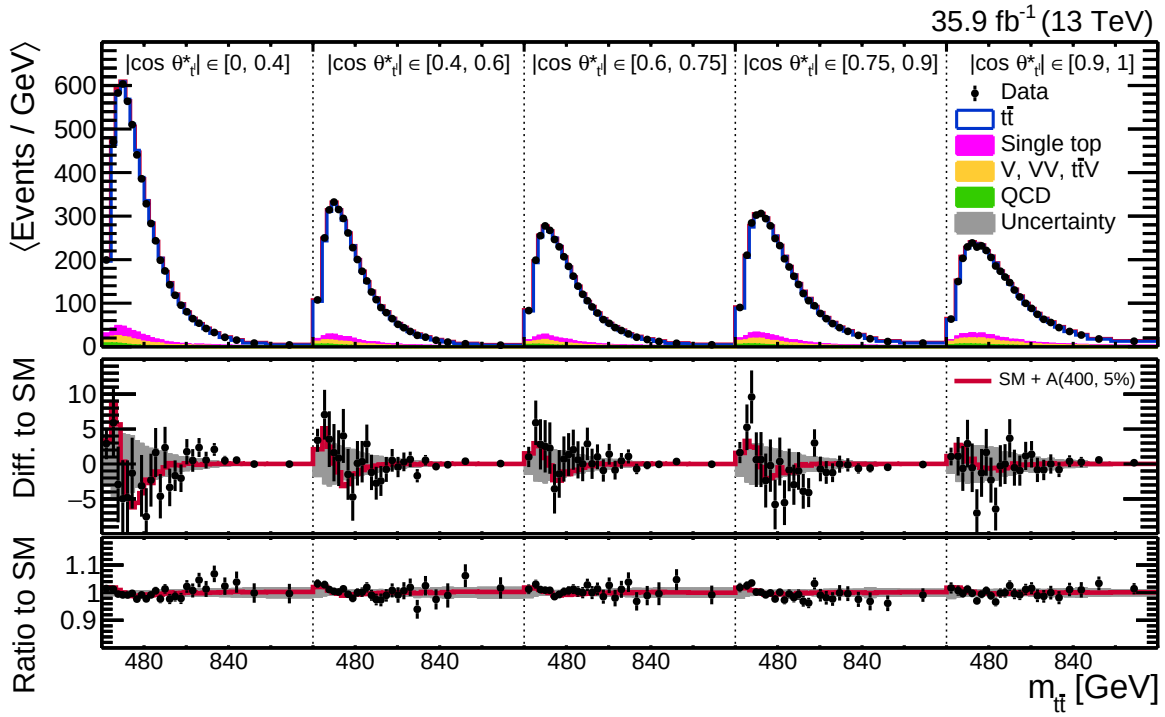

(b) Signal + background post-fit

Figure 7.21: Background-only and signal + background post-fit search templates to the data in the muon channel, illustrating the presence of the A(400, 5%) excess. The dileptonic and semileptonic channel templates are fitted together.

observed significance when background-only toys are fitted to each of the considered signal points. It is found to be 2σ.

7.6 hMSSM Interpretation

The final set of results of this search is its interpretation in the hMSSM context. Unlike the model-independent interpretation that considers one signal state at a time, in the hMSSM both states are present, and $\vec{p}_{A/H}$ is completely specified by two parameters, conventionally chosen to be m_A and $\tan\beta$. Therefore, the exclusion regions on $g_{A/H}$ presented earlier in Figures 7.17, 7.18, 7.17 and 7.18 can be turned into exclusion regions within the m_A-$\tan\beta$ plane, which is the subject of this section.

7.6.1 A/H relations within the hMSSM

In order to set an exclusion region in the hMSSM parameter space, $\vec{p}_{A/H}$ have to be obtained according to the relationship set by the model. Parts of this relationship are shown in Figure 7.22, where the left figure shows the values of m_H as a function of m_A, the middle A/H width values and the right branching ratios of $A/H \to t\bar{t}$ at different values of $\tan\beta$.

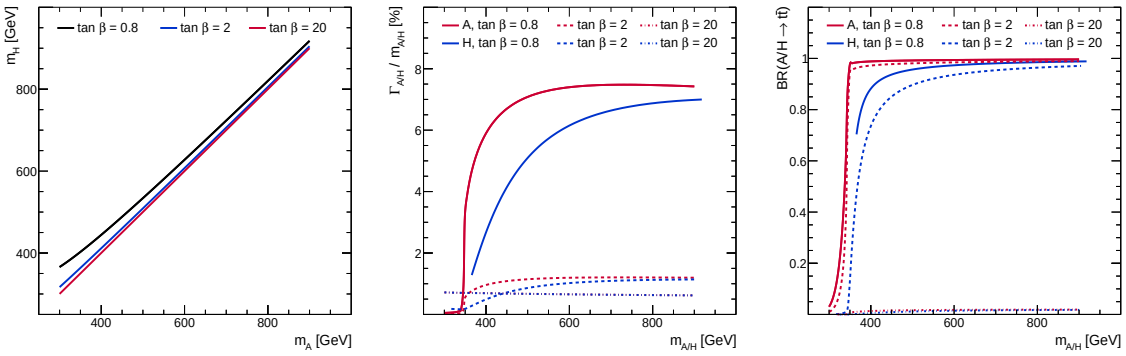

(a) $m_H(m_A)$ (b) A/H width values (c) $\mathrm{BR}\left(A/H \to t\bar{t}\right)$

Figure 7.22: m_H as a fuction of m_A, $\Gamma_{A/H}$ and branching ratios of $A/H \to t\bar{t}$ at different values of $\tan\beta$. Adapted from Reference [6].

From Figure 7.22, one can see that the assumption that A and H are mass-degenerate is valid only in the high-$\tan\beta$ region. As this search probes the low-$\tan\beta$ region, the search templates for A and H at the correct mass and width values have to be obtained. The generation of signal points over a fine grid is not computationally feasible, which motivates the use of the interpolation procedure discussed in Section 7.5. In addition, we see that for a sufficiently low value of $\tan\beta$ and for $m_{A/H} > m_{t\bar{t}}$, the search of A/H is only viable in the $t\bar{t}$ channel due to their BRs that are close to 1 over a very large mass range.

Figure 7.23 illustrates the procedure to set a hMSSM exclusion region for two different values of m_A. The black line indicates its total width predicted by the hMSSM as a function

of $\tan^{-2}\beta$, while the blue line indicates the partial $A \to t\bar{t}$ width also as predicted by the hMSSM. The signal, which is simulated at fixed total width values and $g_A = 1$, are shown as points. The horizontal lines along these points correspond to the allowed range of $\tan^{-2}\beta$ for a given signal hypothesis. The shaded area indicates the unphysical region where the partial width predicted by the hMSSM exceeds the $\Gamma_{A/H}$ value assumed in simulation. A particular point in the m_A-$\tan\beta$ space is said to be excluded if it results in $g_{A/H}$ values that lie within the observed exclusion region.

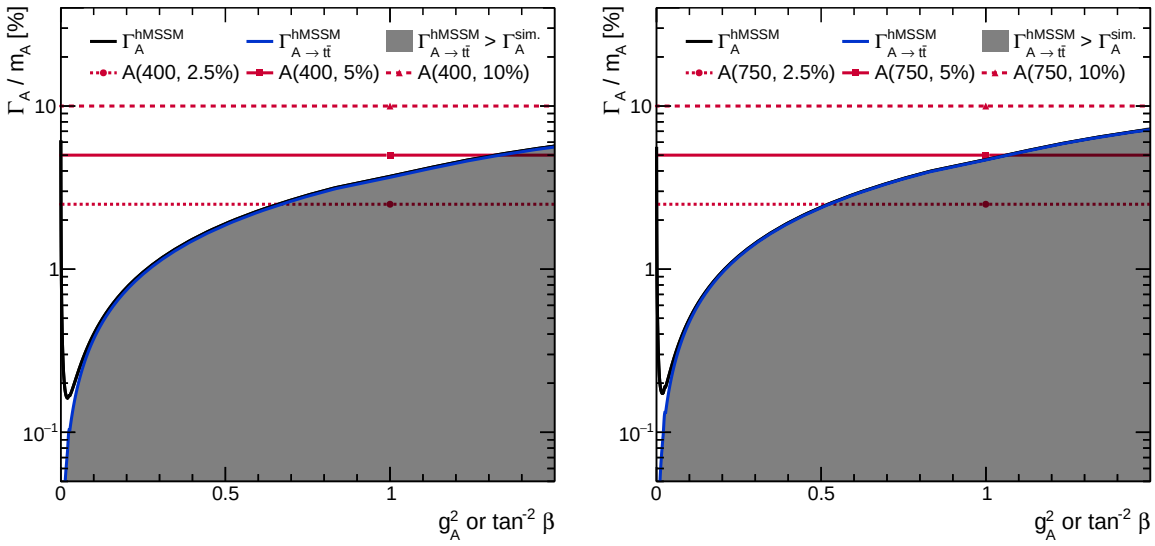

(a) A(400) (b) A(750)

Figure 7.23: Total and partial width values of A as functions of g_A^2 i.e. $\tan^{-2}\beta$ as predicted by the hMSSM for two different m_A values. Also shown are the simulated width points indicating the allowed ranges of $\tan^{-2}\beta$. Adapted from Reference [6].

7.6.2 Result

An exclusion region in the m_A-$\tan\beta$ space is set by performing a grid scan in steps of 10 GeV in the $m_A \in [400, 700]$ GeV and 0.1 in the $\tan\beta \in [0.4, 4]$ ranges using the procedure outlined earlier. As in the model-independent interpretation, the lower limit on $\tan\beta$ is imposed to conserve perturbative unitarity. For each point in the scan, the values of the remaining parameters in $\vec{p}_{A/H}$ are obtained using the 2HDMC program [23]. As there is no interference between A and H states, the signal search templates, either simulated or interpolated, are trivially added together to the background search template.

The result of the scan, taking into account only the dileptonic channel, is shown in Figure 7.24. The expected exclusion indicates that there is sensitivity to exclude up to $\tan\beta$ of 1.7 at low m_A, while we have essentially no sensitivity in the considered $\tan\beta$ range above m_A of 650 GeV. However, due to the excess of $A(400, 5\%)$ we first encountered in Section 7.4, we observe very little exclusion in the m_A-$\tan\beta$ plane. The result of the combined scan are shown in Figure 7.25. Similar to the model-independent interpretation, the sensitivity of the

combined search is considerably higher; the expected exclusion range from $\tan\beta$ of 2.5 to 0.8 from m_A of 400 to 700 GeV. The observed exclusion is between $\tan\beta$ of 1 and 1.5.

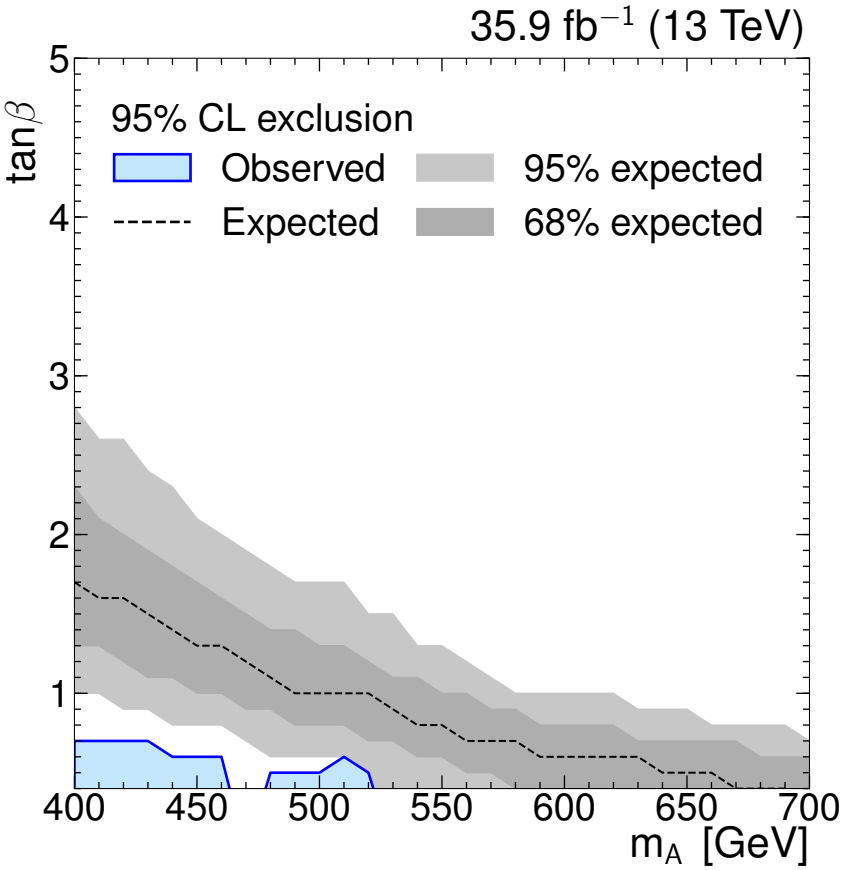

Figure 7.24: Exclusion region in the hMSSM parameter space set from the A/H search in the dileptonic channel.

7.7 Summary and Outlook

A search for heavy Higgs bosons decaying to $t\bar{t}$, performed using 35.9 /fb of data recorded by the CMS experiment in 2016, has been presented. The dileptonic $t\bar{t}$ final state is targeted in this measurement. Events containing two isolated, oppositely charged electrons or muons and at least two jets, at least one of which is consistent with having been initiated by a b quark, are selected. A kinematic reconstruction algorithm is used to reconstruct the kinematics of the top quarks, which is based on a polynomial to recover the longitudinal momenta of the two neutrinos. CP conservation in the extended Higgs sector is assumed in this search, which means the pure pseudoscalar A and the pure scalar H are considered, without a mixing between the two. This is done over a mass range of 400 - 750 GeV and a relative width range of 0.5% - 50%. The interference between the A/H and SM $t\bar{t}$ production amplitudes is taken into account. Exclusion regions are set on the coupling modifier $g_{A/H}$ of the A/H bosons to top quarks. An excess with a local significance of 4σ is observed for the A$(400, 5\%)$ signal hy-

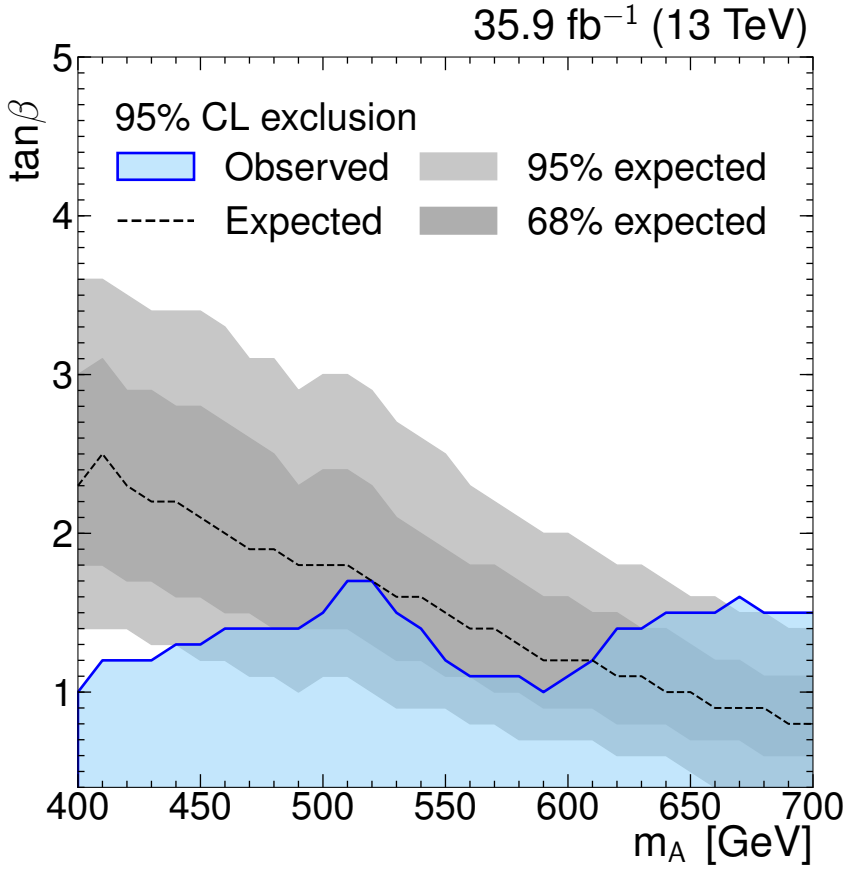

Figure 7.25: Exclusion region in the hMSSM parameter space set from the A/H search in the combination of dileptonic and semileptonic channels.

pothesis. When the results of the analysis are combined with the respective search performed in the semileptonic channel, the local significance of this excess is reduced to 3.7σ. The global significance of this excess is found to be 2σ over all parity, mass and width hypotheses. The exclusion regions on $g_{A/H}$ obtained in this search are converted into exclusion regions in the hMSSM parameter space m_A-$\tan\beta$ without assuming mass degeneracy between the A and H bosons. Values of $\tan\beta$ up to 1 and 1.5 are excluded for m_A of 400 GeV and 700 GeV, respectively, with the expected exclusion being 2.5 and 0.8 for the same values of m_A. The work presented here is submitted for publication by the CMS collaboration as Reference [3].

The two-dimensional spectrum of $m_{t\bar{t}}$ and c_{hel} is used as the search template. It exploits the fact that the signal manifests itself as a local peak-dip structure in the $m_{t\bar{t}}$ distribution (see Figure 2.5), and that the $t\bar{t}$ spin correlation is different between the resonant A/H and SM $t\bar{t}$ production (see Appendix C). The semileptonic search on the other hand uses the two-dimensional spectrum of $m_{t\bar{t}}$ and $\left|\cos\theta^*_{t^\ell}\right|$ as the search template. $\left|\cos\theta^*_{t^\ell}\right|$ is an angle that exploits the isotropic emission of the top quarks in scalar resonance decays, whereas in the SM $t\bar{t}$ production the top quarks are emitted preferentially parallel to the momentum direction of the $t\bar{t}$ system. In both analyses, a template smoothing approach is used to sup-

press the statistical fluctuations in the systematic templates (see Section 7.3).

From the experience of the analysis, a number of observations are made. The modelling of the signal can be improved by simulating the signal at NLO accuracy. The main obstacle against doing so in this search has been the unknown NLO QCD corrections to the interference between the A/H and SM amplitudes, but recently an approach that approximates the gluon loop as an effective vertex has become available [24]. In an extension of this search, it may also be interesting to explore the possibility of CP violation in the Higgs sector. Considering that the $t\bar{t}$ spin density matrix is a crucial part of our search strategy, and that it is also sensitive to CP violating effects (see Section 2.5), we are already in a good position to explore this line of research. The primary challenge in this case is that there is an additional interference between A and H amplitudes to be taken into account, on top of the interference between A/H and SM $t\bar{t}$ production [25, 26]. On the simulation side, the large number of signal hypotheses to be probed require the use of an interpolation procedure, indicating the infeasibility of simulating a sufficiently fine grid of signal points. This problem can be circumvented through a reweighting approach. A large sample of SM $t\bar{t}$ events can be reweighted into arbitrary signal hypotheses, removing the need for large computational resources in simulating the signal and storing the events. Such an approach is currently being explored for use in future iterations of the search; first studies indicated that this approach is indeed promising.

Other improvements that the search can benefit from include the use of a more accurate kinematic reconstruction algorithm. As shown in Figure 6.4, the algorithm picks up a wrong jet assignment in a non-negligible fraction of simulated events, especially at low values of $m_{t\bar{t}}$. This results in a correspondingly high bias and poor resolution in the reconstructed $m_{t\bar{t}}$, as shown in Figure 7.1. Another behavior of the algorithm is that there is some sensitivity to the spin and parity of the $t\bar{t}$ system. This can be seen for example when comparing Figures 2.5 and 7.2. Both the A and H resonances are of Breit-Wigner shape at the truth level, but the reconstructed $m_{t\bar{t}}$ tend to be lower on average for the pseudoscalar case. An algorithm that can reconstruct the kinematic properties of the $t\bar{t}$ system more accurately, and responds more uniformly to different kinds of input, is expected to considerably improve the sensitivity of the search. There are many alternative approaches in the literature - one example of which is described in Reference [27] - it is interesting to compare their performances. As many of these algorithms return multiple solutions for each event, one can also envision employing a kind of a majority vote method to reduce the combinatorial ambiguities. Regarding the algorithm that is used in this work, we stress that its suboptimal features that we discussed can not introduce a spurious A excess to the search. The reason for this is simple; the same algorithm is used to reconstruct the kinematic properties of the $t\bar{t}$ system in both data and simulation, so, provided that the two agree with each other (which is the case, as demonstrated in e.g. Section 6.7 and Figure 7.13), it does not introduce any discrepancy between them. This can also be seen in the reconstruction-oriented evaluation of the algorithm in Figure 6.3; the flat SFs suggest that the algorithm indeed performs similarly in data and simulation.

Let us briefly discuss how our search fits into the wider context of searches for BSM phenomena. Within the hMSSM context, it contributes to the ongoing search for additional Higgs bosons by extending the available exclusion regions into the low $\tan\beta$ region with m_A

beyond the $t\bar{t}$ production threshold. While it is not the first search to do so at the LHC - that honor belongs to Reference [28] - our search is at once the first such search at $\sqrt{s} = 13$ TeV and also the first that does so without a minimum bound on $m_{t\bar{t}}$, extending the search to the case when $m_{A/H}$ is not too far from the $t\bar{t}$ production threshold. In comparison to Reference [29], where a search of charged Higgs bosons decaying into top and bottom quarks is also interpreted in the hMSSM context, this search is more sensitive, resulting in a larger expected exclusion in the m_A-tan β plane.

The excess, which is consistent with the presence of $A(400, 5\%)$, provides a tantalizing hint of the existence of BSM phenomena. Although its significance in this search is not at a level that allows concrete statements to be made, it is interesting that the $A \to Zh$ searches that are reported in References [30] and [31] also hint at the existence of a potential A boson with mass of about 400 GeV. Going back to our channel of interest, the existence of A may only be established by using a larger data sample and an increased search sensitivity beyond what has been attained in this work. Furthermore, an improved theoretical description of the $t\bar{t}$ production processes will be essential in this effort; in the SM particularly in the region close to the $t\bar{t}$ production threshold, and the higher-order corrections to the resonant and interference contributions of A/H to the former.

7.8 Bibliography

[1] P. Langacker, "The Physics of Heavy Z' Gauge Bosons", *Rev. Mod. Phys.* **81** (2009) 1199–1228, doi:10.1103/RevModPhys.81.1199, arXiv:0801.1345.

[2] G. C. Branco et al., "Theory and phenomenology of two-Higgs-doublet models", *Phys. Rept.* **516** (2012) 1–102, doi:10.1016/j.physrep.2012.02.002, arXiv:1106.0034.

[3] CMS Collaboration, "Search for heavy Higgs bosons decaying to a top quark pair in proton-proton collisions at $\sqrt{s} = 13$ TeV", arXiv:1908.01115. Submitted to JHEP.

[4] B. Hespel, F. Maltoni, and E. Vryonidou, "Signal background interference effects in heavy scalar production and decay to a top-anti-top pair", *JHEP* **10** (2016) 016, doi:10.1007/JHEP10(2016)016, arXiv:1606.04149.

[5] M. Gul et al., "Search for a scalar particle decaying to top quarks in the semileptonic final state with 2016 pp dataset", CMS Analysis Note AN-2016-272, 2017.

[6] LHC Higgs Cross Section Working Group Collaboration, "Handbook of LHC Higgs Cross Sections: 4. Deciphering the Nature of the Higgs Sector", doi:10.23731/CYRM-2017-002, arXiv:1610.07922.

[7] A. Cheng et al., "Statistical evaluation, combination, and interpretation of searches for additional heavy Higgs bosons in top quark pair final states", CMS Analysis Note AN-17-202, 2017.

[8] M. Czakon, P. Fiedler, and A. Mitov, "Total Top-Quark Pair-Production Cross Section at Hadron Colliders Through $O(\alpha_S^4)$", *Phys. Rev. Lett.* **110** (2013) 252004, doi:10.1103/PhysRevLett.110.252004, arXiv:1303.6254.

[9] A. Popov, J. Steggemann, and M. Verzetti, "Artificial constraints from statistical fluctuations in systematic variations", CMS Analysis Note AN-18-077, 2018.

[10] R. Barlow and C. Beeston, "Fitting using finite Monte Carlo samples", *Comput. Phys. Commun.* **77** (1993) 219, doi:https://doi.org/10.1016/0010-4655(93)90005-W.

[11] G. Cowan, K. Cranmer, E. Gross, and O. Vitells, "Asymptotic formulae for likelihood-based tests of new physics", *Eur. Phys. J. C* **71** (2011) 1554, doi:10.1140/epjc/s10052-011-1554-0, arXiv:1007.1727. [Erratum: *Eur. Phys. J. C* **73** (2013) 2501].

[12] T. Junk, "Confidence level computation for combining searches with small statistics", *Nucl. Instrum. Meth. A* **434** (1999) 435, doi:10.1016/S0168-9002(99)00498-2, arXiv:hep-ex/9902006.

[13] A. L. Read, "Presentation of search results: The CL_s technique", *J. Phys. G* **28** (2002) 2693, doi:10.1088/0954-3899/28/10/313.

[14] L. Demortier and L. Lyons, "Everything you always wanted to know about pulls", CDF Note 5776, 2002.

[15] CMS Collaboration Collaboration, "Investigations of the impact of the parton shower tuning in Pythia 8 in the modelling of $t\bar{t}$ at $\sqrt{s} = 8$ and 13 TeV", Technical Report CMS-PAS-TOP-16-021, CERN, Geneva, 2016.

[16] R. D. Cousins, "Generalization of chisquare goodness-of-fit test for binned data using saturated models, with application to histograms", Technical Report, 2010.

[17] A. Kolmogorov, "Sulla determinazione empirica di una lgge di distribuzione", *Inst. Ital. Attuari, Giorn.* **4** (1933) 83–91.

[18] N. Smirnov, "Table for Estimating the Goodness of Fit of Empirical Distributions", *Ann. Math. Statist.* **19** (06, 1948) 279–281, doi:10.1214/aoms/1177730256.

[19] T. W. Anderson and D. A. Darling, "Asymptotic Theory of Certain Goodness of Fit Criteria Based on Stochastic Processes", *Ann. Math. Statist.* **23** (1952) 193–212, doi:10.1214/aoms/1177729437.

[20] T. W. Anderson and D. A. Darling, "A Test of Goodness of Fit", *J. Amer. Stat. Assoc.* **49** (1954) 765–769, doi:10.1080/01621459.1954.10501232.

[21] D. Dicus, A. Stange, and S. Willenbrock, "Higgs decay to top quarks at hadron colliders", *Phys. Lett. B* **333** (1994) 126–131, doi:10.1016/0370-2693(94)91017-0, arXiv:hep-ph/9404359.

[22] M. Baak, S. Gadatsch, R. Harrington, and W. Verkerke, "Interpolation between multi-dimensional histograms using a new non-linear moment morphing method", *Nucl. Instrum. Meth. A* **771** (2015) 39, doi:10.1016/j.nima.2014.10.033, arXiv:1410.7388.

[23] D. Eriksson, J. Rathsman, and O. Stal, "2HDMC: Two-Higgs-Doublet Model Calculator Physics and Manual", *Comput. Phys. Commun.* **181** (2010) 189–205, doi:10.1016/j.cpc.2009.09.011, arXiv:0902.0851.

[24] D. Buarque Franzosi, E. Vryonidou, and C. Zhang, "Scalar production and decay to top quarks including interference effects at NLO in QCD in an EFT approach", *JHEP* **10** (2017) 096, doi:10.1007/JHEP10(2017)096, arXiv:1707.06760.

[25] W. Bernreuther and A. Brandenburg, "Tracing CP violation in the production of top quark pairs by multiple TeV proton proton collisions", *Phys. Rev.* **D49** (1994) 4481–4492, doi:10.1103/PhysRevD.49.4481, arXiv:hep-ph/9312210.

[26] W. Bernreuther, A. Brandenburg, and M. Flesch, "Effects of Higgs sector CP violation in top quark pair production at the LHC", arXiv:hep-ph/9812387.

[27] B. A. Betchart, R. Demina, and A. Harel, "Analytic solutions for neutrino momenta in decay of top quarks", *Nucl. Instrum. Meth.* **A736** (2014) 169–178, doi:10.1016/j.nima.2013.10.039, arXiv:1305.1878.

[28] ATLAS Collaboration, "Search for Heavy Higgs Bosons A/H Decaying to a Top Quark Pair in pp Collisions at $\sqrt{s} = 8$ TeV with the ATLAS Detector", *Phys. Rev. Lett.* **119** (2017), no. 19, 191803, doi:10.1103/PhysRevLett.119.191803, arXiv:1707.06025.

[29] ATLAS Collaboration, "Search for charged Higgs bosons decaying into top and bottom quarks at $\sqrt{s} = 13$ TeV with the ATLAS detector", *JHEP* **11** (2018) 085, doi:10.1007/JHEP11(2018)085, arXiv:1808.03599.

[30] ATLAS Collaboration, "Search for heavy resonances decaying into a W or Z boson and a Higgs boson in final states with leptons and b-jets in 36 fb^{-1} of $\sqrt{s} = 13$ TeV pp collisions with the ATLAS detector", *JHEP* **03** (2018) 174, doi:10.1007/JHEP11(2018)051,10.1007/JHEP03(2018)174, arXiv:1712.06518. [Erratum: JHEP11, 051 (2018)].

[31] CMS Collaboration, "Search for a heavy pseudoscalar boson decaying to a Z and a Higgs boson at $\sqrt{s} = 13$ TeV", *Eur. Phys. J.* **C79** (2019), no. 7, 564, doi:10.1140/epjc/s10052-019-7058-z, arXiv:1903.00941.

CHAPTER

8

TOP POLARIZATION AND SPIN CORRELATION MEASUREMENT

Contents

Polarization and spin correlation are powerful probes for the underlying production mechanisms for any pair of particles. However, getting access to this information is often a challenge. Consider for example the decay of a Higgs boson to a bottom quark pair. While the spin of the $b\bar{b}$ system is zero in its own ZMF, in other words the spins of the b and $\bar{b}$ quarks are anticorrelated, this information is lost in their subsequent showering and hadronization. As discussed in Section 2.3, the top quark is special in that it is the only quark where this information remains accessible. Due to its short lifetime, its spin orientation is transferred to the momentum direction of the down-type daughter of the W boson decay. By exploiting this fact we are in the unique position to study the the spin structure of a primarily QCD process, the top quark pair production. We have done so to an extent by using c_{hel} as one of our search observables in the A/H search that is described in Chapter 7, and here we focus more closely on this topic.

In this chapter, the measurement of top polarization and $t\bar{t}$ spin correlation is discussed. All the coefficients of the spin density matrix R, introduced in Section 2.5, are measured. The distributions of observables associated with the coefficients are unfolded to the parton level and extrapolated to the full phase space. The measurements are compared to the SM predictions derived from Monte Carlo generators and analytical calculations at NLO QCD (+ weak) and NNLO accuracies. They are then used to constrain the contributions of EFT operators relevant to the hadronic $t\bar{t}$ production.

The work presented here has been published as Reference [1] in the Physical Review D journal.

8.1 Signal and Background Definition

The processes that are taken into account in this measurement are those listed in Table 6.2.The procedure for background estimation is outlined in Section 6.4. The $t\bar{t}$ contributions are split into two categories; '$t\bar{t}$ dilepton' is the category for prompt dileptonic $t\bar{t}$ events, where prompt means the event contains two generator leptons as defined in Section 4.6. No acceptance cuts are imposed on the generator leptons in the $t\bar{t}$ dilepton categorization. This is the process that is treated as signal in this measurement. Any $t\bar{t}$ contribution not belonging to the $t\bar{t}$ dilepton category is categorized as '$t\bar{t}$ other' and is treated as background.

With this categorization, $t\bar{t}$ events with τs that decay leptonically ($\tau(\ell)$) constitute an irreducible background. In order to avoid biasing the measured $t\bar{t}$ rate, this background is estimated in a slightly different way than the procedure described in Section 6.4. Instead of obtaining the $t\bar{t} \to \tau(\ell) + (\tau(\ell)/\ell) + 2j \to 2\ell + 2j$ contribution directly from simulation, only the per-bin ratio of its contribution to the full $t\bar{t} \to 2\ell + 2j$ is taken. This is then fractionally subtracted from the data after all other background contributions have been subtracted.

8.2 Reconstructed Spin Correlation Observables

The distributions of polarization and spin correlation observables at the reconstructed level in the combined channel are shown in Figures 8.1 (b_i^a), 8.2 (c_{ii} and $c_{ij} \pm c_{ji}$) and 8.3

(c_{hel}, c_{lab} and $\Delta\phi_{\ell\ell}$). The full event selection has been imposed, and all the corrections have been applied as described in Chapter 6. The uncertainty bands indicate the total impact of statistical and systematic uncertainties; however in all distributions the latter dominate.

Prior to the measurement, the reconstructed distributions are inspected for any possible discrepancies between data and simulation. This is done in a blind way (see Section 6.7 for a definition of the term) by symmetrizing the distributions in both data and simulation. Since for all the polarization and spin correlation observables, the information is contained in the spin coefficients (which is directly related to the asymmetry of the distribution, see Table 2.2), this is sufficient to be blind from any possible effects of BSM physics within the scope of this measurement.

8.3 Distribution Unfolding

The aim of most differential cross section measurements is to extract the underlying distribution of some observable x, which is typically represented in the form of a histogram. However, a real detector comes with a number of limitations such as a coverage that is not perfectly hermetic, non-linear responses that commonly also vary between different particle species, and finite resolution introducing a smearing effect, among others. The procedure to correct for the effects of the detector to recover the underlying distribution is called unfolding, which is the subject of this section.

8.3.1 Unfolding as a recovery procedure

Consider a histogram of a quantity x, $\vec{x}$ and the histogram of the corresponding measured quantity y, $\vec{y}$. Even after background subtraction, $\vec{y}$ is usually different from $\vec{x}$ due to the aforementioned detector effects. Introducing the response matrix M, the relationship between the two can be written as:

$$\vec{y} = M\vec{x} \tag{8.1}$$

Given the myriad of effects that can possibly affect M, its exact value is almost never known a priori for an arbitrary $\vec{x}$. This means that M has to be determined from simulation. In our case, the SM $t\bar{t}$ simulation is used, considering only $t\bar{t}$ dilepton events. The determination of M then starts by defining the level and phase space region to which $\vec{x}$ is to be unfolded. As mentioned at the beginning of the chapter, the spin correlation observables are to be unfolded to the parton level, which means that the distributions are obtained using the inputs defined at the generator level as defined in Section 4.6. They are to be extrapolated to the full phase space, meaning no acceptance cuts are imposed in obtaining the generator-level distributions which are shown in Appendix C. This choice is made to preserve the form of the observables as given in Table 2.2, leading to a straightforward extraction and interpretation of the relevant spin density matrix coefficients. The unfolding in this work is performed by using the `TUnfold` software [2], which is one of the standard tools for unfolding based on matrix inversion in the field.

The unfolded distributions will be reported as differential cross sections, which requires a transformation from the event yields. Two types of transformations are considered; absolute

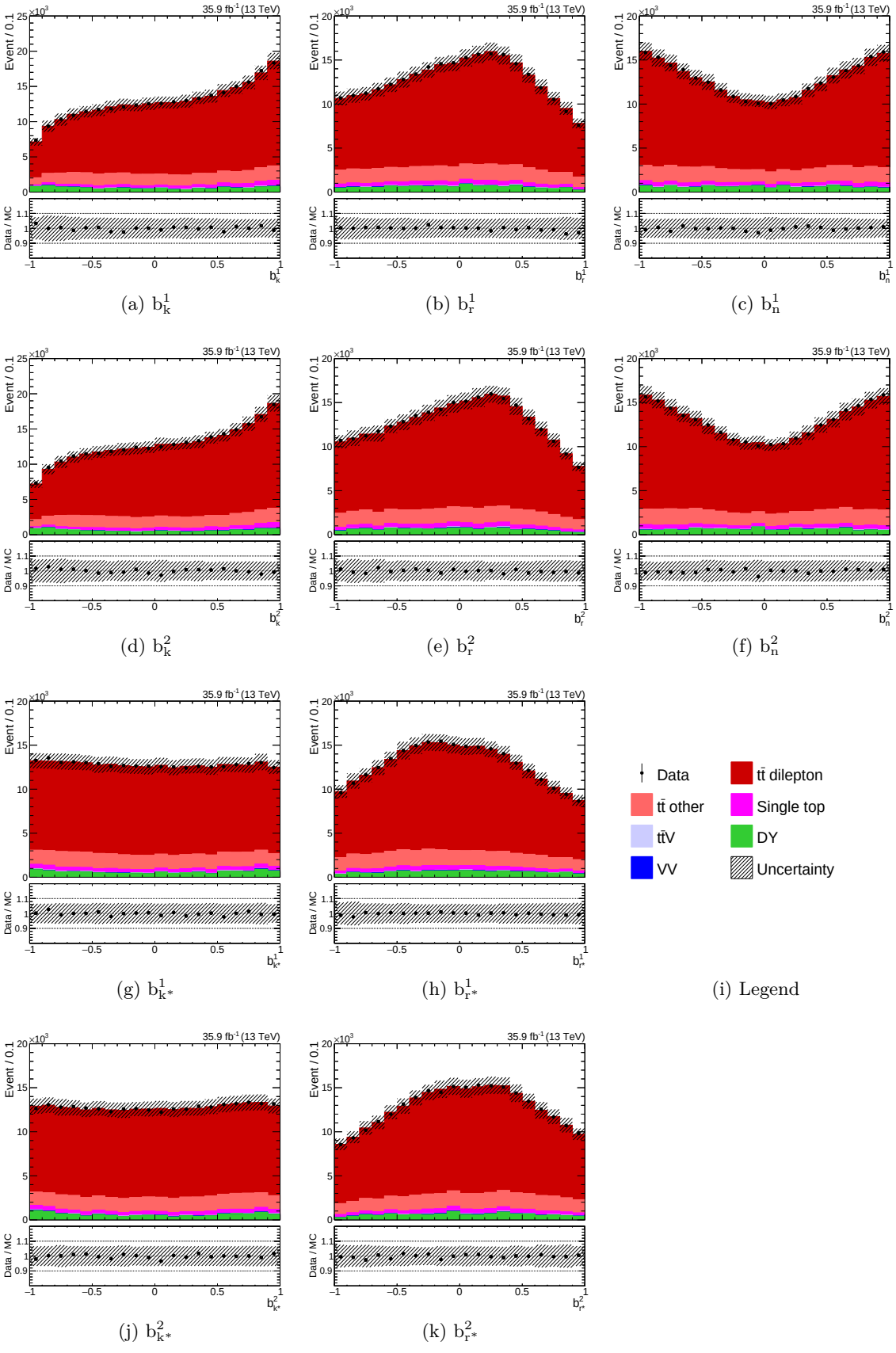

(a) b^1_k (b) b^1_r (c) b^1_n

(d) b^2_k (e) b^2_r (f) b^2_n

(g) b^1_{k*} (h) b^1_{r*} (i) Legend

(j) b^2_{k*} (k) b^2_{r*}

Figure 8.1: Reconstructed b^a_i distributions.

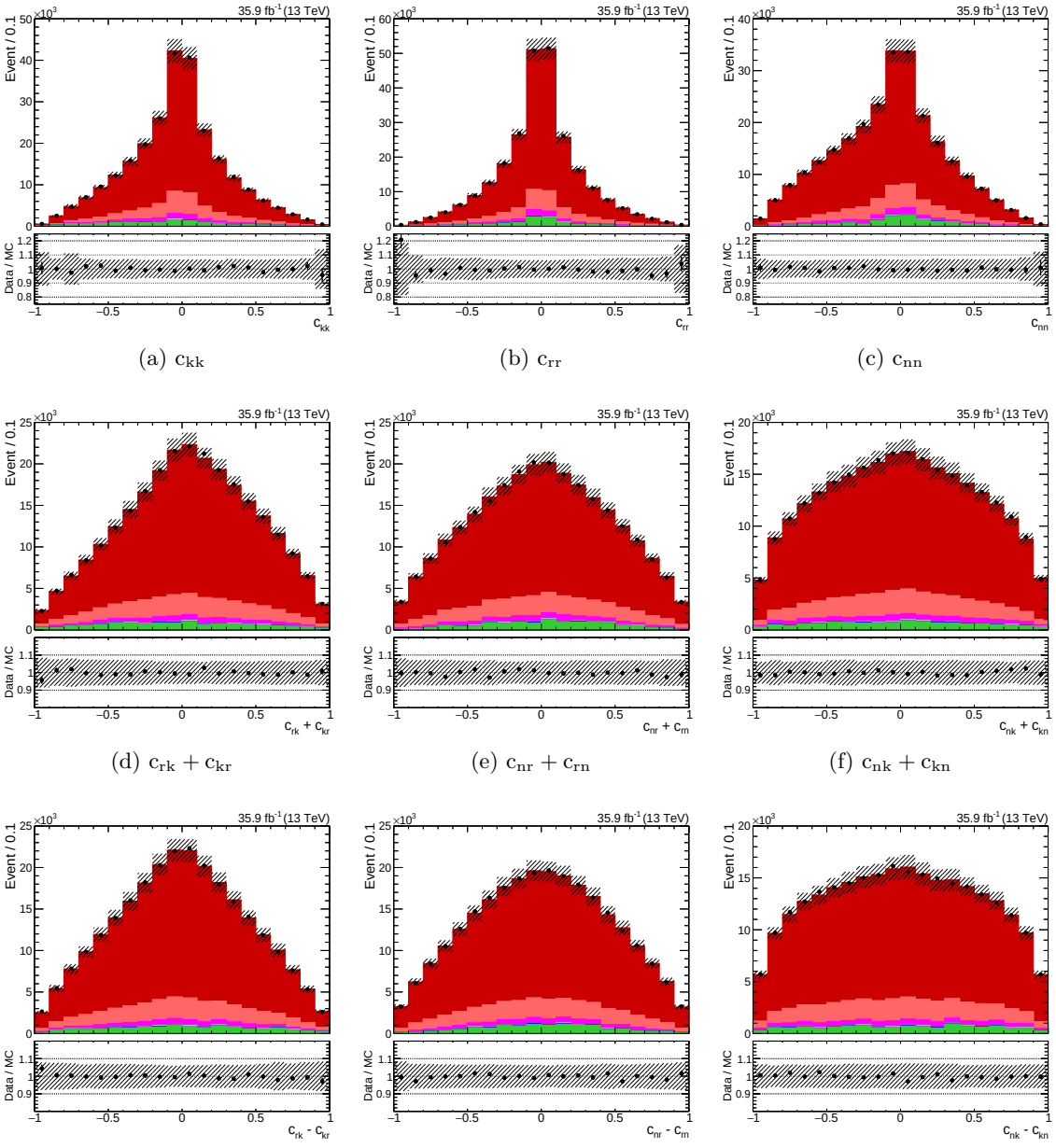

(a) c_{kk} (b) c_{rr} (c) c_{nn}

(d) $c_{rk} + c_{kr}$ (e) $c_{nr} + c_{rn}$ (f) $c_{nk} + c_{kn}$

(g) $c_{rk} - c_{kr}$ (h) $c_{nr} - c_{rn}$ (i) $c_{nk} - c_{kn}$

Figure 8.2: Reconstructed c_{ii} and $c_{ij} \pm c_{ji}$ distributions. The legend of the plots is the same as shown in Figure 8.1.

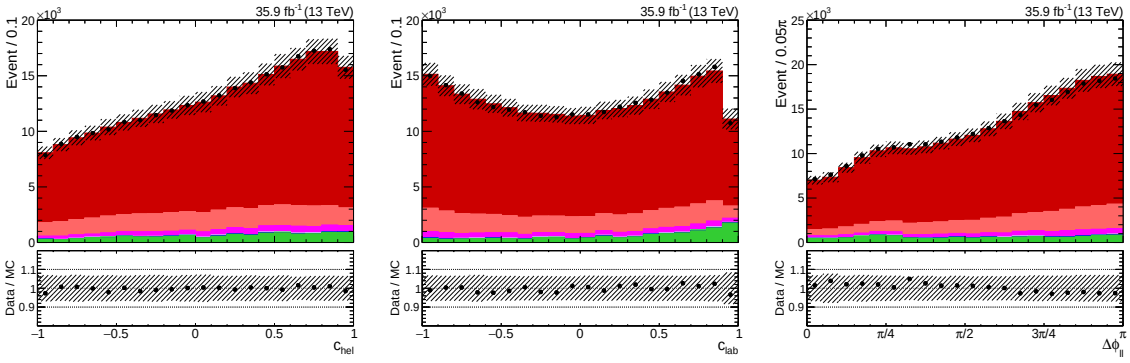

(a) c_{hel} (b) c_{lab} (c) $\Delta\phi_{\ell\ell}$

Figure 8.3: Reconstructed c_{hel}, c_{lab} and $\Delta\phi_{\ell\ell}$ distributions. The legend of the plots is the same as shown in Figure 8.1.

and normalized. The absolute differential cross section is defined as:

$$\frac{d\sigma}{dx} = \frac{\vec{x}}{\vec{\Delta}_{bin} \cdot L} \tag{8.2}$$

where $\vec{\Delta}_{bin}$ is the vector of bin widths associated to the distribution $\vec{x}$ and L is the integrated luminosity. The normalized differential cross section is then simply the absolute differential cross section divided by σ. This definition of the normalized differential cross section is such that in absence of the $\vec{\Delta}_{bin}^{-1}$ correction factor, the sum of all bin contents equals 1 i.e. each bin content is the ratio between the integral of the function within the bin boundaries and the integral of the function over its domain. For the sake of brevity, we shall be dropping the arrow on x and y from now on when discussing the unfolding procedure.

8.3.2 Binning scheme

Prior to the unfolding, a binning scheme has to be defined. The measurement resolution of each observable is one of the most relevant factors in doing so, since it places a limit on the precision of the information that can be extracted from the data. The resolution of each observable is measured by taking the difference between its reconstructed and generated values as a function of the latter. This is then quantified in the optimistic scenario as the width of the Gaussian fit on the peak of this distribution, and in the pessimistic scenario as the RMS of the entire distribution. This is shown in Figure 8.4. The resolutions of b_i^2 are not shown as they are the same as b_i^1 resolutions in the reference SM simulation.

Based on these results in Figure 8.4, it is clear that the two estimated resolutions do not agree with each other, especially near the edge of the distributions. Due to the bounded nature of these observables, the distributions of differences between reconstructed and generated values are highly skewed. This affects the two estimates differently since the RMS-based estimate takes the entire distribution - including the long tail - which is ignored in the Gaussian fit. The distributions of differences in three generated c_{hel} bins - first, center and last -

are shown in Figure 8.5, together with the estimated resolutions in those bins to illustrate this effect. The choice of six uniform bins across the full range is found to be a good compromise between the two approaches for all observables and is adopted as the binning scheme for the final measured distributions.

The resolutions of the observables defined in the laboratory frame are not shown as they are far smaller than the resolutions of any observables defined in the $\{\mathrm{k}, \mathrm{r}, \mathrm{n}\}$ system. However, the same binning scheme is adopted for these observables for the sake of simplicity.

One way of checking if the chosen binning scheme is suitable is to compute the purity p_{bin} and stability s_{bin} within each bin of the generated observables. Considering only events within the reconstructed - generated space[1], they are defined as:

$$p_{\mathrm{bin}} = \frac{\mathrm{N}_{\mathrm{reco.\,\&\,gen.} \in \mathrm{bin}}}{\mathrm{N}_{\mathrm{reco.} \in \mathrm{bin},\ \mathrm{gen.} \in \mathrm{any}}},\ s_{\mathrm{bin}} = \frac{\mathrm{N}_{\mathrm{reco.\,\&\,gen.} \in \mathrm{bin}}}{\mathrm{N}_{\mathrm{gen.} \in \mathrm{bin},\ \mathrm{reco.} \in \mathrm{any}}} \tag{8.3}$$

where 'reco. & gen. $\in$ bin' means that both the reconstructed and generated values of the observable are within the range defined by the bin. 'gen. $\in$ any' on the other hand refers to the case when the generated value of the observable taking any value, not necessarily within the bin range. The other cases in Equation 8.3 are similarly defined. From these definitions it can be seen that purity is sensitive to the influx of events into a given bin of the reconstructed observable, while stability is sensitive to the outflux of events from a given bin of the generated observable; both with respect to the entire reconstructed-generated observable space. They are both clearly related to the measurement resolution, as a binning scheme finer than the resolution introduces an additional smearing to the reconstructed observable, further lowering the values of both purity and stability. The purities and stabilities of each observable are shown in Figure 8.6. As with the resolutions, the purities and stabilities of b_i^2 are not shown, being very similar to those of b_i^1. As can be seen in Figure 8.6, both purity and stability values for the $\{\mathrm{k}, \mathrm{r}, \mathrm{n}\}$ system observables are typically in the 0.3 - 0.5 range - in no case lower than 0.15 - indicating that the chosen binning scheme is robust.

8.3.3 Response matrix derivation

Having established the binning scheme, the next step is to derive the response matrix M. As we are unfolding the data to the parton level and extrapolating to the full phase space, it means that M is expected to express both the loss of events due to limited acceptance and the migration of events within the reconstructed-generated space. Based on this, M is decomposed as $M \rightarrow S \cdot A$, where A is the acceptance matrix and S is the migration (or smearing) matrix. The entries of A and S are given by:

$$A_{ij} = \delta_{ij} \frac{\mathrm{N}_{\mathrm{reco.} \in \mathrm{any}}}{\mathrm{N}_{\mathrm{gen.} \in \mathrm{i}}},\quad S_{ij} \propto \frac{\mathrm{N}_{\mathrm{reco.} \in \mathrm{j}}}{\mathrm{N}_{\mathrm{gen.} \in \mathrm{i}}} \tag{8.4}$$

Here i and j refer to bins in the reconstructed-generated space. In deriving A and S, the generator level distributions are split into 24 equidistant bins while the reconstructed distri-

[1] In contrast to background events which are only reconstructed or signal events that fall outside detector acceptance and therefore are only generated.

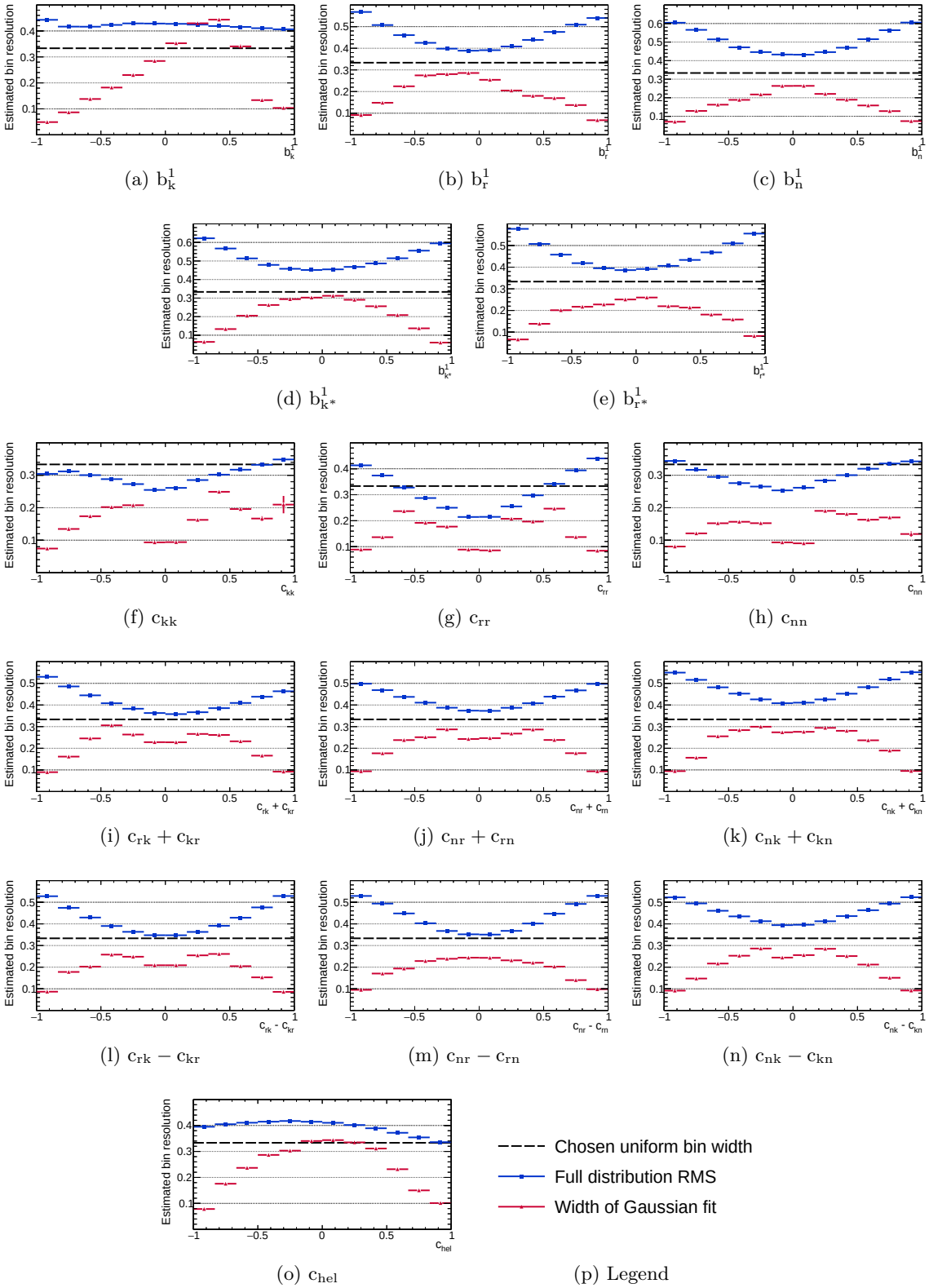

(a) b^1_k (b) b^1_r (c) b^1_n

(d) b^1_{k*} (e) b^1_{r*}

(f) c_{kk} (g) c_{rr} (h) c_{nn}

(i) $c_{rk} + c_{kr}$ (j) $c_{nr} + c_{rn}$ (k) $c_{nk} + c_{kn}$

(l) $c_{rk} - c_{kr}$ (m) $c_{nr} - c_{rn}$ (n) $c_{nk} - c_{kn}$

(o) c_{hel} (p) Legend

Figure 8.4: The estimated resolution as functions of the generated polarization and spin correlation observables.

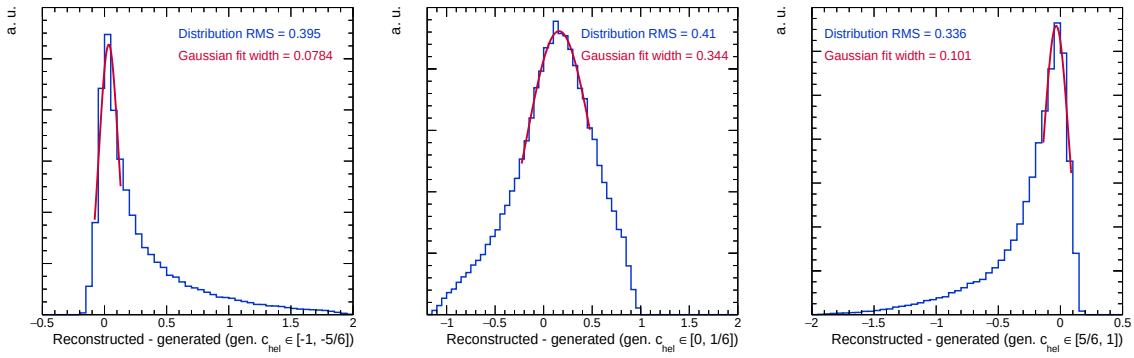

(a) First bin (b) Center bin (c) Last bin

Figure 8.5: Distributions of the differences between reconstructed and generated c_{hel} values in the first, center and last bins (blue) and the Gaussian fits on the peak of the distributions (red) to estimate c_{hel} resolution within the bin.

butions are split into 48 equidistant bins. The reason for this choice is as follows. A is a diagonal matrix approximating the acceptance as a function of the generator level observable. With the adopted binning scheme, the approximate acceptance functions are rather crude since they are averaged over large bin ranges. This motivates a finer splitting for the generator level distributions, with 24 bins taken to be a good compromise between the final binning scheme and the unbinned case. The impact of these schemes on the unfolded results will be compared later in this section. The 48 bins of reconstructed distributions is simply to have twice as many bins with respect to the generator level distributions, following the recommendation in Reference [2]. This recommendation is motivated by the fact that the least squares fit is used in the unfolding; using the same number of bins between reconstructed and generated distributions leaves the fit with zero degrees of freedom in determining the best fit between the folded output Mx and the original data y. Only at the end of the unfolding step is the final binning scheme applied through a simple rebinning of the unfolded output.

The matrices A are shown in Figure 8.7, and S are shown in Figures 8.8 (b_i^1), 8.9 (c_{ii} and $c_{ij} \pm c_{ji}$) and 8.10 (c_{hel}, c_{lab} and $\Delta\phi_{\ell\ell}$). The b_i^2 matrices are very similar to their b_i^1 counterparts. In Figure 8.10 one sees that the smearing matrices for laboratory frame observables are very highly diagonal as a result of the excellent experimental resolutions and leads to their very high purities and stabilities (see Figure 8.6).

8.3.4 Naive least squares unfolding

From Equation 8.1, the 'underlying generator-level' distribution of the data x_{data} can be obtained using the matrix M we derived earlier:

$$x_{data} = M^{-1} y_{data} \tag{8.5}$$

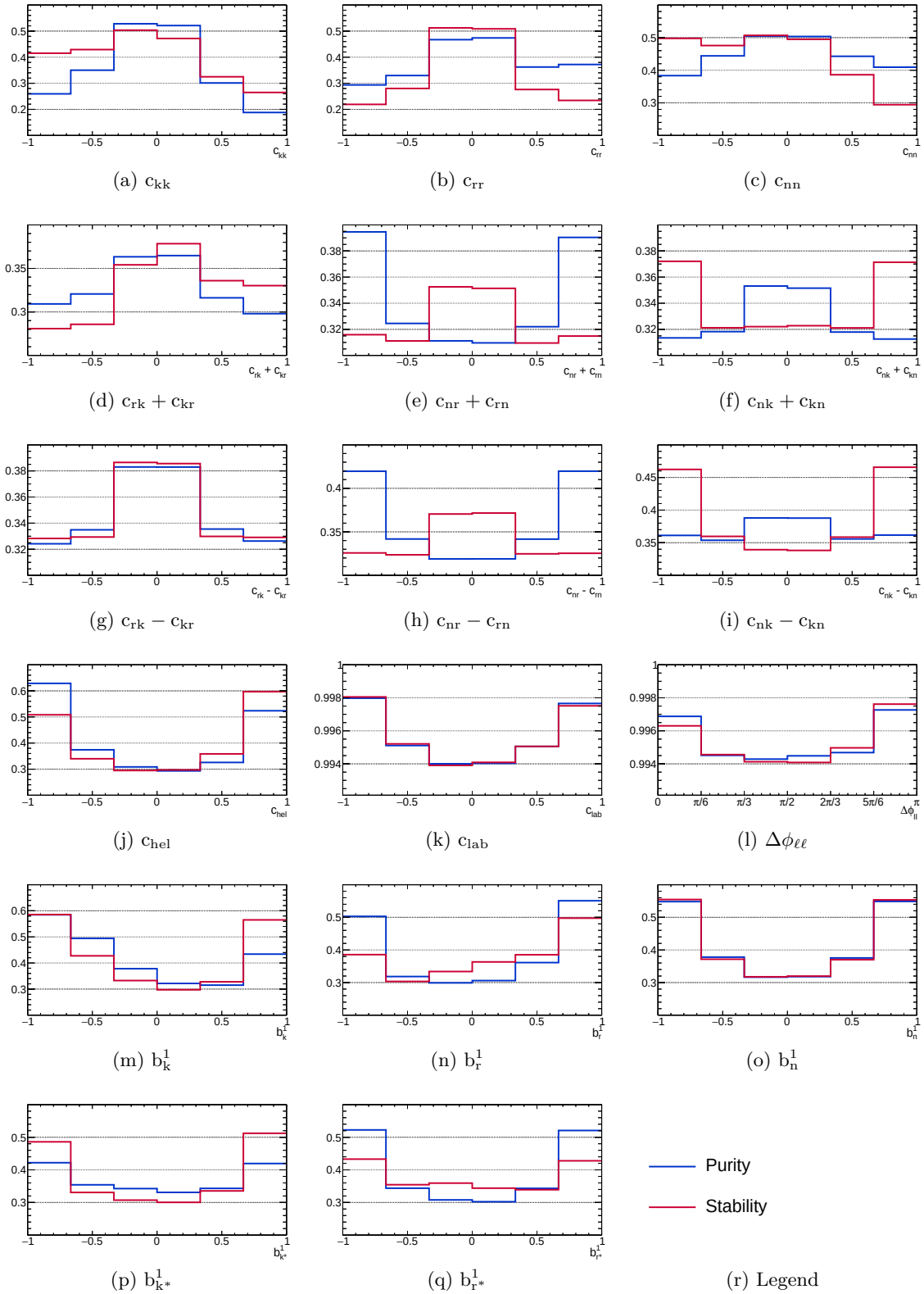

(a) c_{kk} (b) c_{rr} (c) c_{nn}

(d) $c_{rk} + c_{kr}$ (e) $c_{nr} + c_{rn}$ (f) $c_{nk} + c_{kn}$

(g) $c_{rk} - c_{kr}$ (h) $c_{nr} - c_{rn}$ (i) $c_{nk} - c_{kn}$

(j) c_{hel} (k) c_{lab} (l) $\Delta\phi_{\ell\ell}$

(m) b^1_k (n) b^1_r (o) b^1_n

(p) b^1_{k*} (q) b^1_{r*} (r) Legend

Figure 8.6: Purity and stability within each bin of the generated polarization and spin correlation observables in the chosen binning scheme.

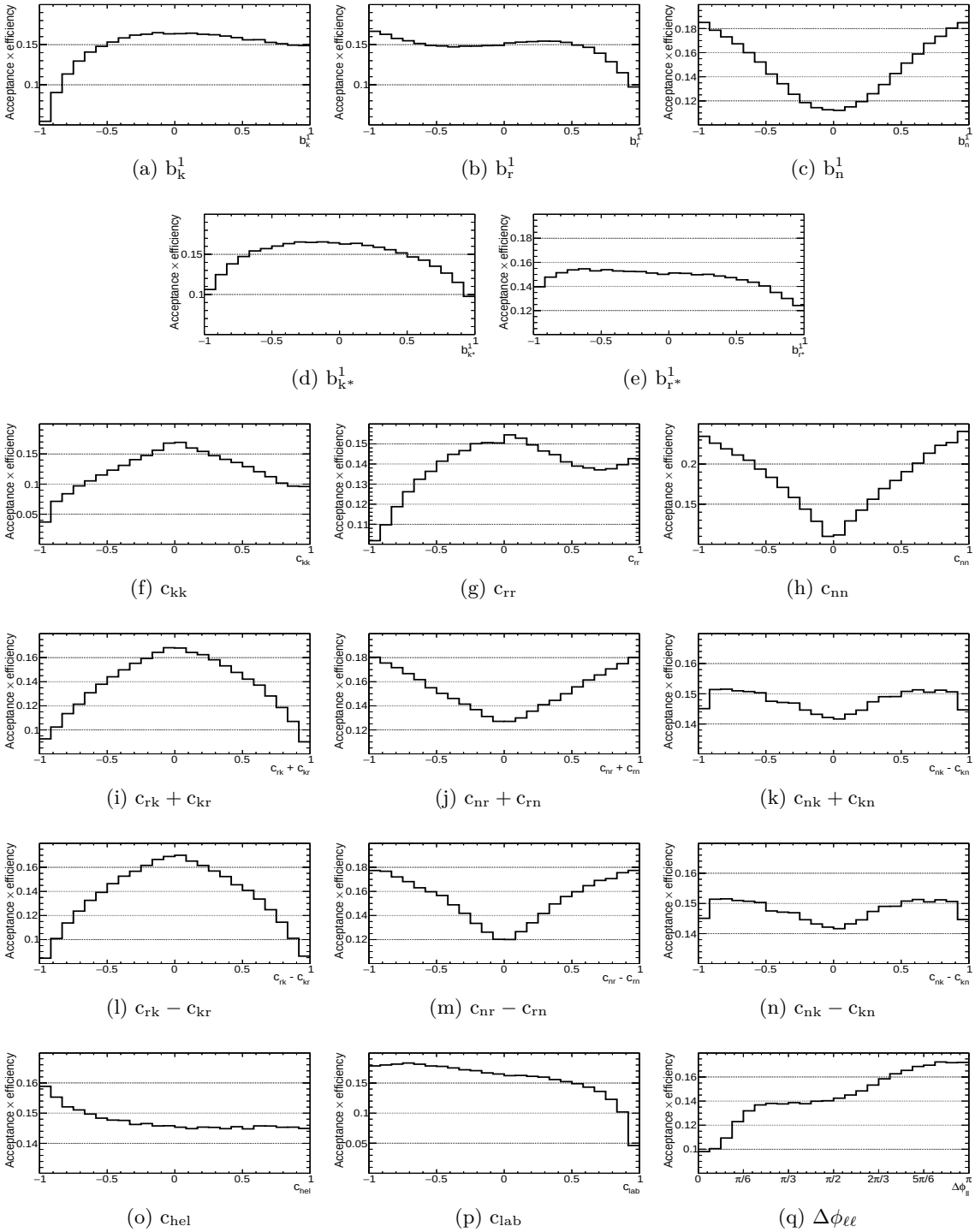

(a) b^1_k (b) b^1_r (c) b^1_n

(d) b^1_{k*} (e) b^1_{r*}

(f) c_{kk} (g) c_{rr} (h) c_{nn}

(i) $c_{rk} + c_{kr}$ (j) $c_{nr} + c_{rn}$ (k) $c_{nk} + c_{kn}$

(l) $c_{rk} - c_{kr}$ (m) $c_{nr} - c_{rn}$ (n) $c_{nk} - c_{kn}$

(o) c_{hel} (p) c_{lab} (q) $\Delta\phi_{\ell\ell}$

Figure 8.7: Acceptance matrices in bins of the generated polarization and spin correlation observables.

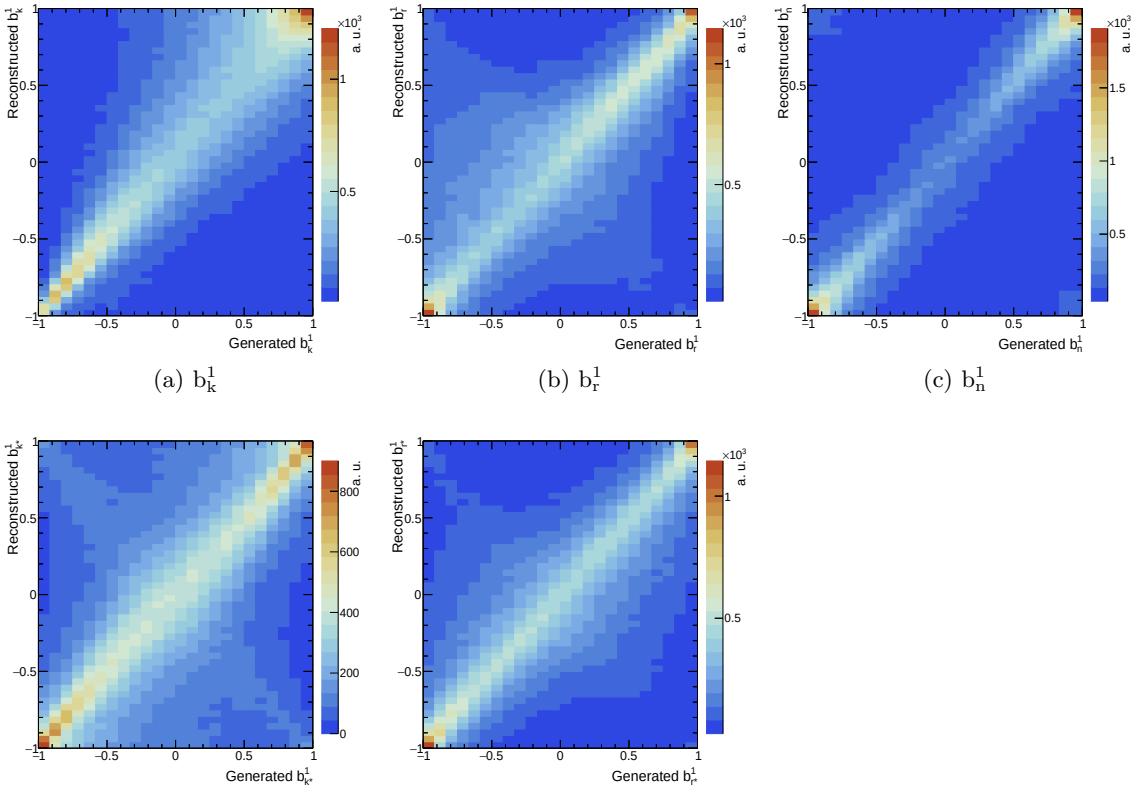

(a) b^1_k (b) b^1_r (c) b^1_n

(d) b^1_{k*} (e) b^1_{r*}

Figure 8.8: Two-dimensional distributions of reconstructed vs generated b^1_i used to derive their respective smearing matrices.

This relationship[2] necessarily holds for the simulated distributions x_{MC} and y_{MC}, since it is with these distributions M is derived. However, the data is affected by statistical uncertainties, expressed as a covariance matrix $V_{y,\,\text{data}}$, which have to be taken into account. This is done by finding the distribution x that best fits y_{data} through the least squares method:

$$\chi^2_{\text{unfold}} = \chi^2_M + \lambda \sum_i (Mx - y)_i \tag{8.6}$$

where χ^2_M is the standard least squares term:

$$\chi^2_M = (Mx - y)^T V_y^{-1} (Mx - y) \tag{8.7}$$

while $\lambda \sum_i (Mx - y)_i$ is the constraint term with a Lagrange multiplier λ used to force the re-folded distribution to have the same area as the input reconstructed distribution.

[2] In some cases - like ours - the matrix M is rectangular, so the regular inverse matrix M^{-1} does not exist. Instead the so-called pseudoinverse matrix M^+ is used; it is a generalization of matrix inversion to rectangular matrices [3, 4]. In particular, it solves the linear system of Equation 8.1 that we are interested in; Equation 8.5 holds with the simple replacement $M^{-1} \to M^+$. For this reason, in this work we do not distinguish between regular and pseudoinverses; both will be labeled as M^{-1}.

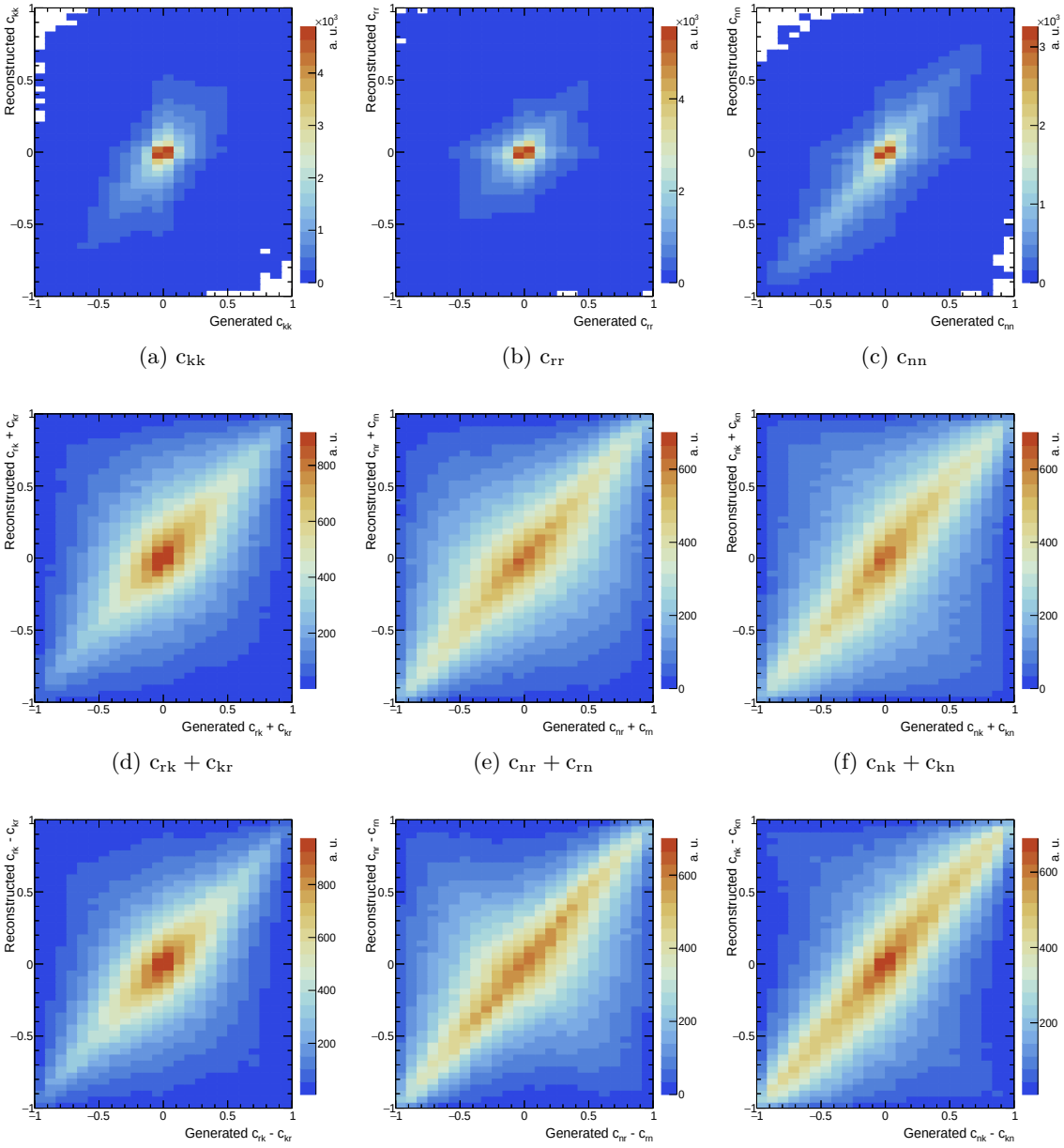

(a) c_{kk} (b) c_{rr} (c) c_{nn}

(d) $c_{rk} + c_{kr}$ (e) $c_{nr} + c_{rn}$ (f) $c_{nk} + c_{kn}$

(g) $c_{rk} - c_{kr}$ (h) $c_{nr} - c_{rn}$ (i) $c_{nk} - c_{kn}$

Figure 8.9: Two-dimensional distributions of reconstructed vs generated c_{ii} and $c_{ij} \pm c_{ji}$ used to derive their respective smearing matrices.

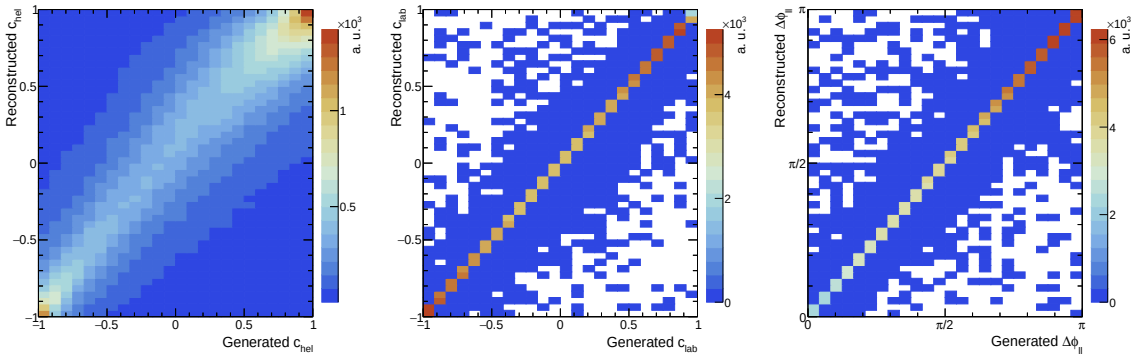

(a) c_{hel} (b) c_{lab} (c) $\Delta\phi_{\ell\ell}$

Figure 8.10: Two-dimensional distributions of reconstructed vs generated c_{hel}, c_{lab} and $\Delta\phi_{\ell\ell}$ used to derive their respective smearing matrices.

8.3.5 Regularization

Strictly speaking, the distribution x as determined from Equation 8.6 can be treated as the underlying generated distribution of y. However, this x often contains unphysically large oscillations due to magnification of small fluctuations by M and is therefore unsatisfactory [5]. A procedure to enforce a degree of smoothness on the unfolding output is hence desired; this is called regularization. It is done by introducting an additional term χ^2_L:

$$\chi^2_L = (x - cx_0)^T L^T L (x - cx_0) \tag{8.8}$$

where x_0 is the expected distribution as determined from simulation, c is a normalization factor that is ~ 1 - following from the fact that the background subtracted data yield agrees closely with the reference simulation - and L is a matrix so chosen that the second derivative, or curvature, of $x - cx_0$ is minimized[3]. Including this new term, Equation 8.6 now reads:

$$\chi^2_{\text{unfold}} = \chi^2_M + \tau^2 \chi^2_L + \lambda \sum_i (Mx - y)_i \tag{8.9}$$

where the regularization strength τ^2 is a free parameter controlling the degree of regularization to be applied. χ^2_L therefore has the effect of penalizing large deviations of x from x_0.

While adding χ^2_L to Equation 8.6 achieves the goal of suppressing the unphysical oscillations in x, it has the problem that it introduces a bias towards x_0. Only when x differs by a constant factor with respect to x_0 this is not the case. In our case, this is especially undesirable as the unfolding may change the shape of x to be different than those dictated by Table 2.2. Since the regularization can be made unbiased if a transformation is applied to $x - cx_0$ such that their difference is a constant factor, we do so by multiplying $x - cx_0$ with the so-called the bin factor f_{bin}:

$$(x - cx_0) \to z \equiv f_{\text{bin}} \cdot (x - cx_0) \tag{8.10}$$

[3]For this reason, L is also known as the curvature matrix. Its exact definition is provided in Reference [2].

Taking $g(x)$ to be the continuous analog of the histogram x, the continuous analog of f_{bin}, $f(x)$, is computed such that:

$$z(x) \equiv f(x) \cdot (g(x) - g_0(x)) = \text{const} \cdot x \tag{8.11}$$

Here $g_0(x)$ is simply the special case where all the spin density matrix elements take on the values as in the reference simulation i.e. it is the continuous analog of x_0. We recall that for spin correlation observables, their respective $g(x)$ are given in Table 2.2; they all depend only on one coefficient. The difference $g(x) - g_0(x)$ for each observable is given as:

$$\begin{aligned}
x = \mathrm{b}_i^a: \;\; g(x) - g_0(x) &= \frac{1}{2}\Delta\mathrm{C}x \\
x = \mathrm{c}_{ii}: \;\; g(x) - g_0(x) &= -\frac{1}{2}\Delta\mathrm{C}x \ln\frac{1}{|x|} \\
x = \mathrm{c}_{ij} \pm \mathrm{c}_{ji}: \;\; g(x) - g_0(x) &= -\frac{1}{4}\Delta\mathrm{C}x \cos^{-1}|x| \\
x = \mathrm{c}_{\text{hel}}: \;\; g(x) - g_0(x) &= -\frac{1}{2}\Delta\mathrm{C}x
\end{aligned} \tag{8.12}$$

where $\Delta\mathrm{C}$ is the change in the relevant spin coefficient with respect to the reference simulation. Substituting Equation 8.12 back into Equation 8.11, we obtain:

$$\begin{aligned}
x = \mathrm{b}_i^a,\, \mathrm{c}_{\text{hel}}: \;\; f(x) &= 1 \\
x = \mathrm{c}_{ii}: \;\; f(x) &= \left(\ln\frac{1}{|x|}\right)^{-1} \\
x = \mathrm{c}_{ij} \pm \mathrm{c}_{ji}: \;\; f(x) &= \left(\cos^{-1}|x|\right)^{-1}
\end{aligned} \tag{8.13}$$

As we are dealing with histograms rather than functions, the bin factors f_{bin} are obtained by integrating $f(x)$ within the range bounded by the bin; $f_{\text{bin}} = \int_{\text{bin}} f(x)$. Regarding laboratory frame observables, their unknown forms prevent any $f(x)$ to be derived. Instead, since in this measurement they are also characterized by asymmetries about their distribution centers like the other observables, the f_{bin} assigned to them is $x|^{-1}_{\mathrm{A}^x=0}$, where $x|_{\mathrm{A}^x=0}$ is the symmetrized distribution of these observables. While this choice is made to make the regularization unbiased to variations linear in $x|_{\mathrm{A}^x=0}$, it has very little effect on the final result due to the highly diagonal response matrices of these observables.

We are now in a position to answer the question we raised before. Near the end of Section 2.5, it is mentioned that the choice to measure b_i^a separately is made because it is better from the measurement point of view. The explanation for this lies in the form of the $\mathrm{b}_i^1 \pm \mathrm{b}_i^2$ distribution (where only here the shorthand $\mathrm{b}_\pm = \mathrm{b}_i^1 \pm \mathrm{b}_i^2$ will be used, ditto for $\mathrm{B}_\pm$):

$$\frac{1}{\sigma}\frac{\mathrm{d}\sigma}{\mathrm{d}\mathrm{b}_\pm} = \frac{1}{24}(2 - |\mathrm{b}_\pm|)\Big(6 + 3\mathrm{B}_\pm\mathrm{b}_\pm \pm \mathrm{C}_{ii}\Big(2 - 2|\mathrm{b}_\pm| - \mathrm{b}_\pm^2\Big)\Big) \tag{8.14}$$

which depends on both $\mathrm{B}_\pm$ and C_{ii}. The regularization can only be made unbiased if the condition stated in Equation 8.11 holds. For $\mathrm{b}_\pm$, the condition can only hold with respect to either $\mathrm{B}_\pm$ or C_{ii} by deriving the corresponding f_{bin} with the other coefficient fixed to its reference value (and the regularization is unbiased only if its value in the data matches the

reference simulation). Compared to the apparent simplicity such a direct measurement would have, the advantage offered by unbiased regularization irrespective of the values of all spin density matrix elements is far more significant, justifying the choice to measure b_i^a separately.

Before proceeding further, let us discuss the uncertainties on the unfolded distribution x. One way to obtain them is by error propagation due to Equation 8.9 on V_y, the complete expression of which is provided in Reference [2]. The covariance matrix obtained in this way will be denoted as V'_x and referred to as the propagation matrix. While in this work this is not the method used to estimate the final covariance matrix of x, as we will later see, the propagation matrix nevertheless serves as input for some of the unfolding steps, including the estimation of the final covariance matrix.

Returning to the regularization, τ^2 is chosen such that the mean of the square of the global correlation coefficients between bins of x, ρ^2_{avg} is minimized. The global correlation coefficient of a bin i is given by:

$$\rho_i^2 = 1 - \frac{1}{V'^{-1}_{x,ii} V'_{x,ii}} \tag{8.15}$$

It is to be noted that ρ_i^2 is computed after x is rebinned to the final binning scheme in order to prevent the choice of τ^2 to be driven by features finer than the achievable resolution. The result of the τ^2 scan as functions of ρ_{avg} for the representative observables are shown in Figure 8.11. Note the significantly lower values of ρ_{avg} for laboratory frame observables, leading to much weaker regularization applied in their unfolding.

8.3.6 Linearity test

Although the regularization is unbiased, this is not the only the possible source of bias in the unfolding. A bias can be introduced through the loss of shape information inherent in any binning. While this is mitigated to an extent by the use fine binning during the unfolding, the impact of this bias still has to be quantified. This is done by unfolding injected distributions at different coefficient values, where the sampling is done within an interval of $\Delta C \in [-0.5, 0.5]$[4]. This is done at the generator level by reweighting the distributions to the desired coefficient values, and the corresponding reconstructed distributions are obtained by propagating this reweighting to the matrix M. In this way the unfolding of the injected distributions is the same for all coefficient values, as the matrix M is by construction the same, while the χ^2_L term also stays the same due to the inclusion of f_{bin} as the curvature vector. The comparison therefore explicitly tests the binning-induced bias in the unfolding.

The comparison between the injected and measured distributions in terms of the raw yield difference per unit change in spin coefficient values are shown in Figure 8.12. For the laboratory frame observables, due to their unknown analytical forms the injection is done by changing their asymmetries within the same range. To motivate the choice of unfolding with

[4]Note that this range is far bigger than any expected change in the coefficient values with respect to the SM, even in the presence of new physics. To provide an idea on how big the range is, consider a purely additive new physics process whose impact to D is consistent with that of resonance-only A. For it to alter D by -0.5, its rate needs to be 1589 pb; almost double the SM $t\bar{t}$ production rate!

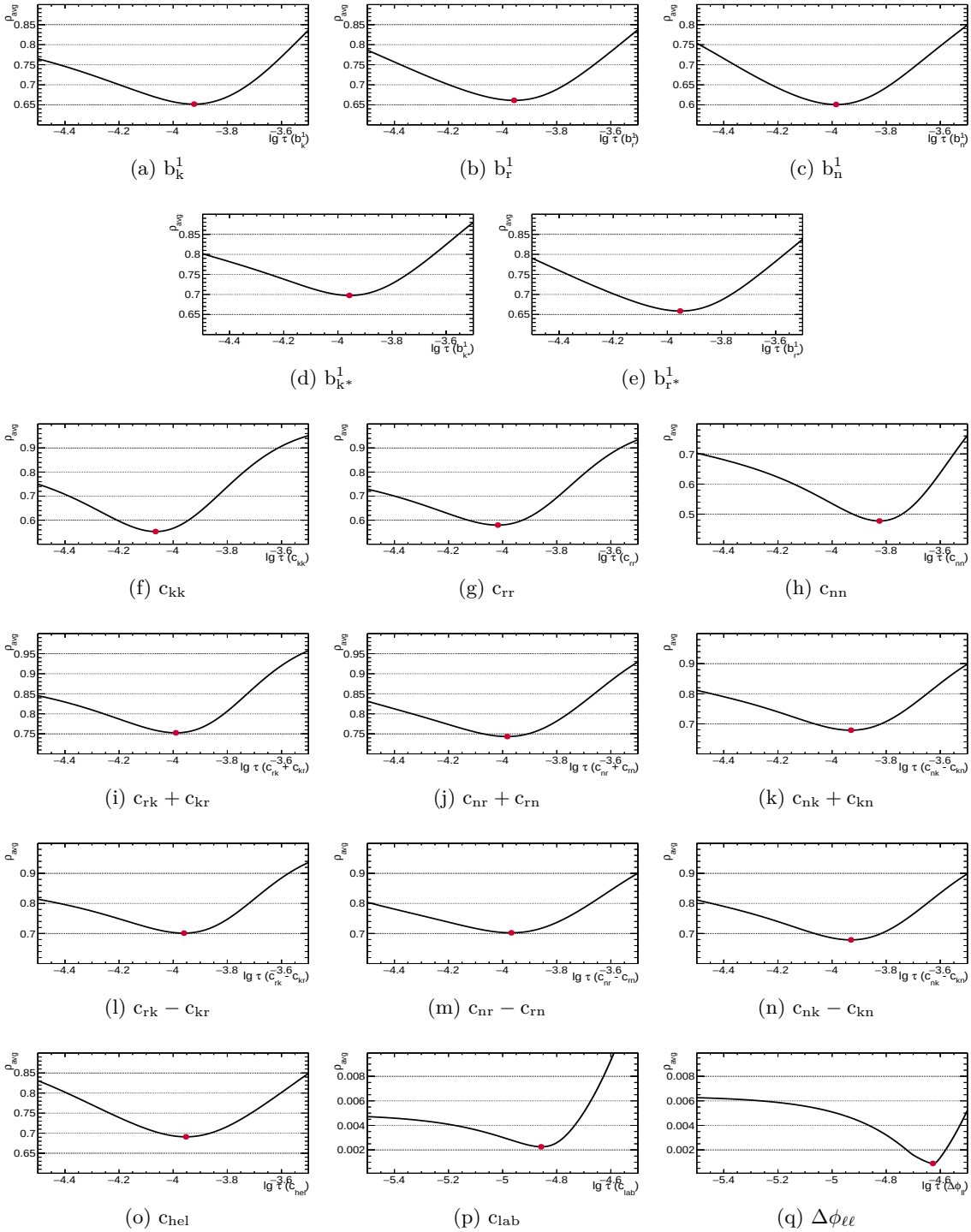

(a) b^1_k (b) b^1_r (c) b^1_n

(d) b^1_{k*} (e) b^1_{r*}

(f) c_{kk} (g) c_{rr} (h) c_{nn}

(i) $c_{rk} + c_{kr}$ (j) $c_{nr} + c_{rn}$ (k) $c_{nk} + c_{kn}$

(l) $c_{rk} - c_{kr}$ (m) $c_{nr} - c_{rn}$ (n) $c_{nk} - c_{kn}$

(o) c_{hel} (p) c_{lab} (q) $\Delta\phi_{\ell\ell}$

Figure 8.11: The scan of regularization strength as functions of the average global correlation coefficients for each observable, with the minimum points marked with red dots.

24 bins at the generator level instead of 6 bins as in the final binning, the same comparison is also shown when the unfolding is done with 6 bins from the beginning. One sees that there is a difference between the injected and measured distributions in this case, this is a direct manifestation of the binning-induced bias that is stronger when a coarser binning is used.

Another way to estimate the bias is to check the slope of a linear fit on the injected vs measured differences with respect to reference values. The slope of such fits for each bin of the observables are shown in Figure 8.13. For an unfolding that is completely free of bias, the slope of such fits would be 1, while a higher (lower) slope means that the bias is inflating (deflating) the deviation of the true values with respect to that of the reference. We see that the non-linearities are most apparent when the underlying distribution varies strongly within the bin, such as the center bins of the c_{ii} distributions or the last bin of the c_{lab} distribution; this due to the larger loss of shape information when the bins are coarse.

8.3.7 Statistical covariance matrix through ensemble tests

To further test the behavior of the unfolding procedure, ensemble tests are performed through bootstrapping [6]. 6500 pseudoexperiments are generated where in each, the events are sampled from the reconstructed distributions N times; N is Poisson-distributed with mean 1. These sampled distributions are unfolded and the pull distributions of each bin are inspected [7]. The results when sampling simulated events are summarized in Figure 8.14. All the pulls are compatible with having a mean of 0 and width of 1, which would be the case if the unfolding procedure is unbiased.

While V'_x is a reliable estimate of the uncertainties of the unfolded distributions, it is limited to the covariances between bins of one distribution. As in this work 22 observables are unfolded, it would be ideal to provide one covariance matrix that expresses the correlations between all bins, including those that do not belong to the same observables. This would allow the use of multiple distributions in a single fit. Such a matrix can be constructed also using the pseudoexperiments. For each pair of parameters - denoted as p_1 and p_2 respectively - whose correlations are to be estimated, two quantities sensitive to their covariance are defined:

$$\Delta^{\pm} = \frac{p_1^{\text{p.e.}} - p_1^0}{\sigma_1^{\text{p.e.}}} \pm \frac{p_2^{\text{p.e.}} - p_2^0}{\sigma_2^{\text{p.e.}}} \tag{8.16}$$

where σ_i is the estimated uncertainty of p_i and the superscript refers to pseudoexperiments or reference simulation respectively. In the case of p_i being the bin contents of the unfolded distributions, σ_i is simply $V'_{x,ii}$ (and for subsequent transformations from the unfolded distributions, their uncertainties are propagated from V'_x accordingly). From this, it follows that if p_1 and p_2 are perfectly correlated, $\Delta^- = 0$ and $\Delta^+ = 2$; vice versa for perfectly anti-correlated p_1 and p_2. In general, the variance of the $\Delta^{\pm}$ distributions are given as:

$$\sigma^2_{\Delta^{\pm}} = 2 \pm 2\rho_{12} \tag{8.17}$$

from which the correlations between p_1 and p_2, ρ_{12} and therefore the statistical covariance matrix V_x^{stat} are readily available. In order to minimize the uncertainties in the estimation,

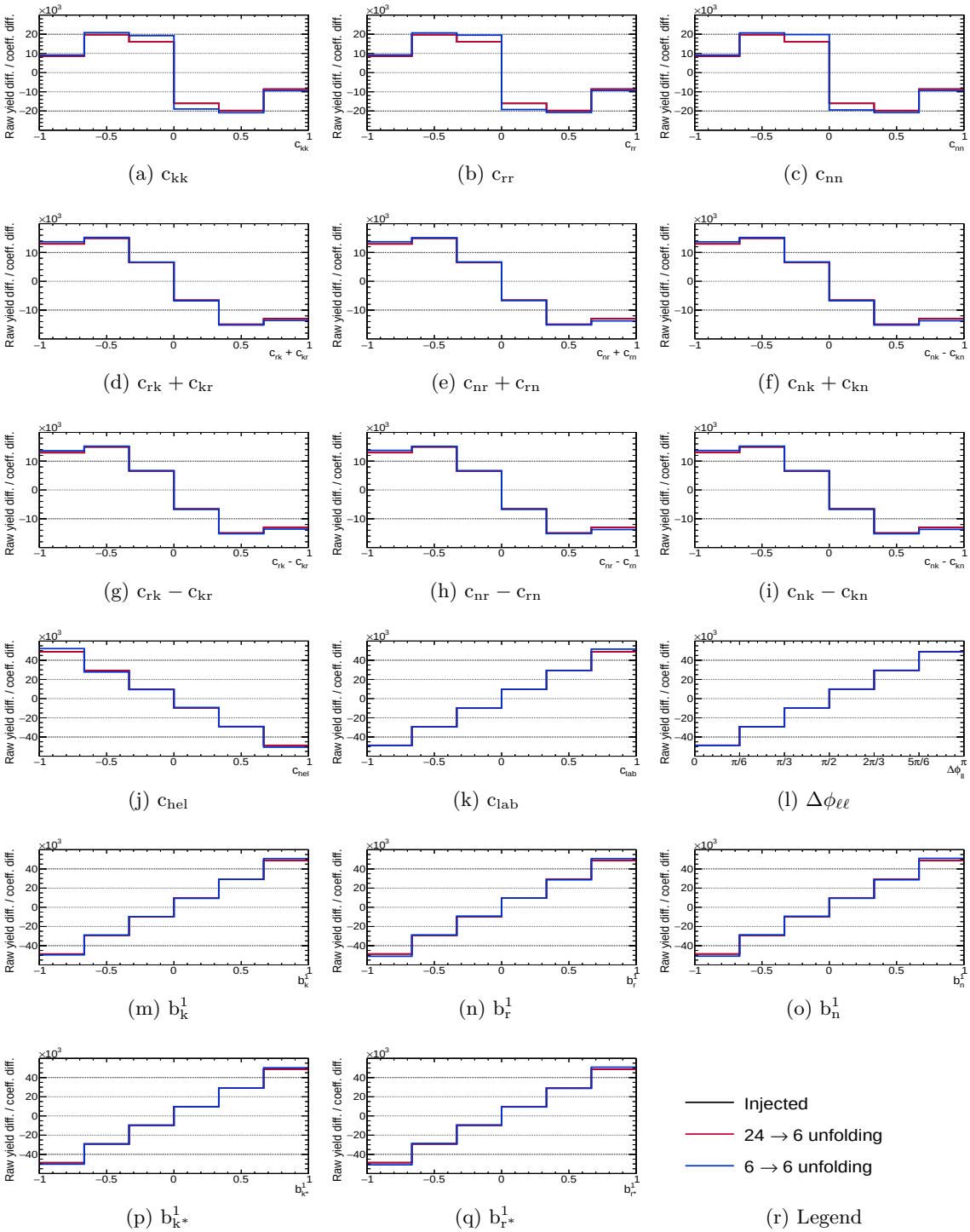

(a) c_{kk} (b) c_{rr} (c) c_{nn}

(d) $c_{rk} + c_{kr}$ (e) $c_{nr} + c_{rn}$ (f) $c_{nk} + c_{kn}$

(g) $c_{rk} - c_{kr}$ (h) $c_{nr} - c_{rn}$ (i) $c_{nk} - c_{kn}$

(j) c_{hel} (k) c_{lab} (l) $\Delta\phi_{\ell\ell}$

(m) b^1_k (n) b^1_r (o) b^1_n

(p) b^1_{k*} (q) b^1_{r*} (r) Legend

Figure 8.12: Differences in raw yields between injected and measured shapes per unit change in spin coefficient values.

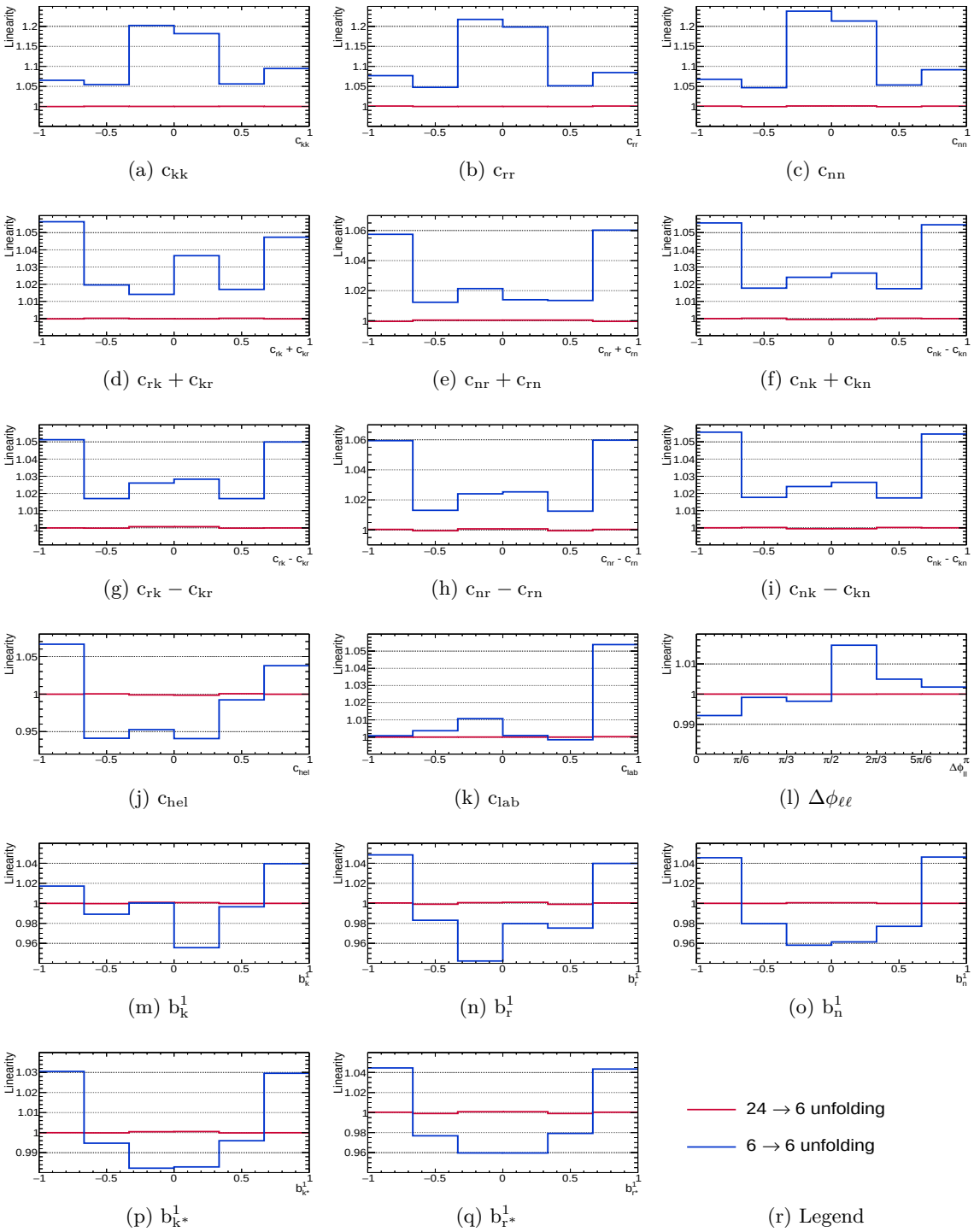

(a) c_{kk} (b) c_{rr} (c) c_{nn}

(d) $c_{rk} + c_{kr}$ (e) $c_{nr} + c_{rn}$ (f) $c_{nk} + c_{kn}$

(g) $c_{rk} - c_{kr}$ (h) $c_{nr} - c_{rn}$ (i) $c_{nk} - c_{kn}$

(j) c_{hel} (k) c_{lab} (l) $\Delta\phi_{\ell\ell}$

(m) b_k^1 (n) b_r^1 (o) b_n^1

(p) b_{k*}^1 (q) b_{r*}^1 (r) Legend

Figure 8.13: Linearities between injected and measured values.

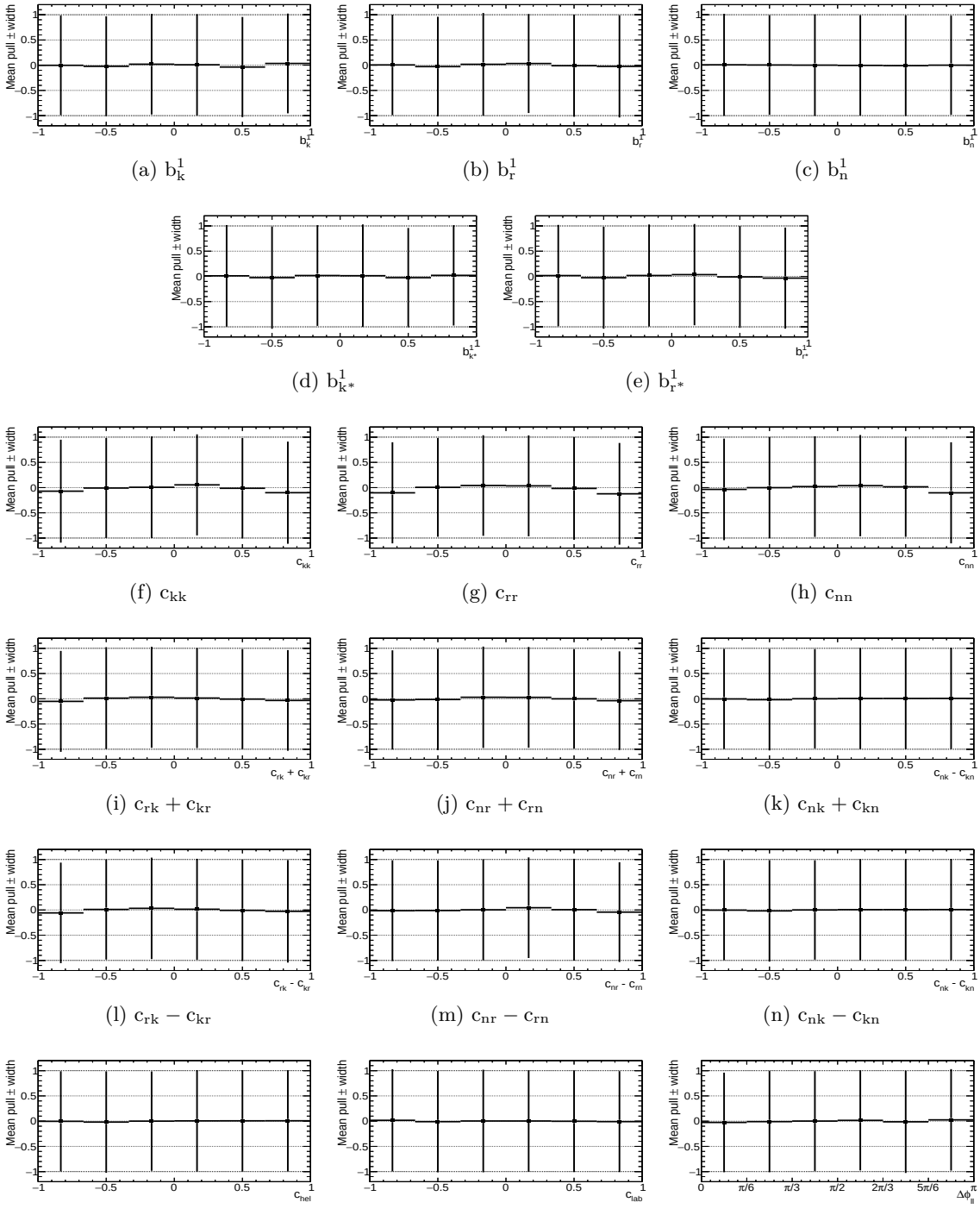

(a) b^1_k (b) b^1_r (c) b^1_n

(d) $b^1_{k^*}$ (e) $b^1_{r^*}$

(f) c_{kk} (g) c_{rr} (h) c_{nn}

(i) $c_{rk} + c_{kr}$ (j) $c_{nr} + c_{rn}$ (k) $c_{nk} + c_{kn}$

(l) $c_{rk} - c_{kr}$ (m) $c_{nr} - c_{rn}$ (n) $c_{nk} - c_{kn}$

(o) c_{hel} (p) c_{lab} (q) $\Delta\phi_{\ell\ell}$

Figure 8.14: Summary of the pull test using simulated events: the mean and width of pull distributions for each bin of the unfolded distributions.

$\sigma_i^{\text{p.e.}}$ are corrected using the data pull widths. The final estimate of ρ_{12} is taken as the average of the Δ^+ and Δ^- estimates. The Pearson correlation coefficient [8] is computed for every p_1 and p_2 pair as a cross check and found to be compatible with the estimated ρ_{12}.

8.3.8 Systematic uncertainties breakdown and covariance matrices

Each source of systematic uncertainties is treated as an alternative reference hypothesis for the unfolding. In each case the complete procedure, starting from the derivation of the response matrix, is repeated, resulting in one alternative unfolded distribution for each. Taking Δx_{syst} to be the difference between the alternative unfolded distribution of a given source and the nominal one, the systematic covariance matrix for this source is:

$$V_x^{\text{syst}} = \Delta x_{\text{syst}}^T \Delta x_{\text{syst}} \tag{8.18}$$

For the envelope-based systematic sources e.g. the ME + PS systematic, first the Δx_{env} due to the combined effect of all contributing sources is evaluated. In order to preserve the correlations that would otherwise be washed out by the envelope, a V_x^{syst} is computed for each of the contributing sources and converted into a correlation matrix. The correlation matrices due to all contributing sources are summed up, from which the covariance matrix is constructed by multiplication with Δx_{env}.

The total systematic covariance matrix is taken to be the sum of all V_x^{syst} and V_x^{env} sources that are taken into account as described in Section 6.6. In the absolute differential measurement, the dominant uncertainties are the experimental systematic sources, as they mainly affect the acceptance matrix, which is propagated to the total rate. The normalized differential measurements on the other hand are mainly affected by sources related to modelling of the process, since they induce a larger change in distribution shapes, while the impact of experimental sources are reduced, as their impact on total rates cancel out. However their overall contribution can still be significant, e.g. the JEC systematics since uncertainties related to the b jet energies directly affect the reconstructed position of the $\mathrm{t\bar{t}}$ scattering plane. Background normalization affects $\mathrm{c_{lab}}$ the most due to the increase in DY contribution at high $\mathrm{c_{lab}}$[5]. The $\mathrm{p_T^t}$ reweighting source has a relatively minor impact in all observables except for $\Delta\phi_{\ell\ell}$, an observable that is particularly difficult to model accurately [9]. The relative contribution of different systematic sources to each of the measured absolute and normalized measurements are shown in Appendix E.

8.4 Result

We now turn to the results of the measurement. The first set of results are the distributions of all the observables, from which the second set of results, the spin coefficients, are extracted. Both sets are compared to state of the art theoretical predictions.

[5]The resulting total uncertainties on $\mathrm{A^{c_{lab}}}$ is lower if the analysis considers only the eμ channel for this reason. However, since the total uncertainties of all other coefficients are higher compared to the combined channel, this option will not be discussed further in this work.

8.4.1 Spin observables distributions

The absolute differential measurements are shown in Figure 8.15 for b_i^a, Figure 8.16 for $c_{ij} \pm c_{ji}$ and Figure 8.17 for c_{ii}, c_{hel} and the laboratory frame observables. The corresponding results for the normalized differential measurements are shown in Figures 8.18 (b_i^a), 8.19 ($c_{ij} \pm c_{ji}$) and 8.20 (c_{ii}, c_{hel}, and laboratory frame observables). It can be seen that the absolute measurements are significantly less precise; this is because the normalized measurements benefit from cancellation in rate-changing uncertainties, which is not present in the absolute measurements. The measurements are compared to several different theoretical predictions. The first set of predictions are the generator-level distributions from two MC generators, POWHEGV2 and MG5_aMC@NLO. The MG5_aMC@NLO sample is simulated with up to two additional partons at NLO accuracy using the same PDF set, parton showering and hadronization configuration as the POWHEGV2 sample, as well as using the same tune (see Section 6.1). The top quark decays are modeled with MADSPIN [10] and the partons are matched using the FxFx prescription [11] as with other NLO MG5_aMC@NLO samples. Second is a calculation performed at the NLO QCD + weak accuracy (+ EWK in the case of $b_{\mathrm{n}}^1 \pm b_{\mathrm{n}}^2$) [12]. Third is also a calculation at the NLO QCD + weak accuracy, but it assumes that all the polarization and spin correlation coefficients are zero, the so-called unpolarized and uncorrelated case. As this prediction is primarily of historical interest and is already ruled out prior to this measurement [13][6], it is included only in the upper panels of the Figures and not the lower panels. Fourth is also a calculation; it differs from the previous two in that it is calculated at the NNLO QCD accuracy and is available only for the $\Delta\phi_{\ell\ell}$ distribution [9]. The χ^2 expressing the agreement between data and the predictions are evaluated only for the normalized differential measurements and are shown in Table 8.1. Further discussion on the agreement is deferred to the next subsection, when we have at our disposal also the measured and predicted values of the spin coefficients.

The statistical correlation matrices are shown in Figures 8.21 and 8.22 for absolute and normalized measurements respectively. The systematic correlation matrices on the other hand are shown in Figures 8.23 (absolute) and 8.24 (normalized). In these matrices the same effect that leads to higher precision in the normalized measurements, which is discussed at the end of Section 8.3, is also manifest; while the statistical correlation matrices are similar between the two measurements, the systematic correlations are significantly higher across all bins in the absolute measurement.

8.4.2 Spin coefficients extraction

Having obtained the unfolded distributions, the next step is to extract the spin coefficients. There are several ways this can be done; two of them are from the distribution means or asymmetries as suggested in Table 2.2. The mean - since it requires bin center corrections - is not suitable for our purposes, so we resort to asymmetries. However, instead of the full left-right asymmetry, we use the i-pair asymmetries A_i^x, considering only the two i-th bins to the left and right from distribution center. Specifically, given our 6 bins scheme and using the same notation as Equation 2.15: A_1^x considers the first (leftmost) and sixth (rightmost) bins

[6] One may wonder why is it included *at all* in our case; the reason is that it also establishes a convenient benchmark for us to define the f_{SM} parameter with, which we will soon encounter.

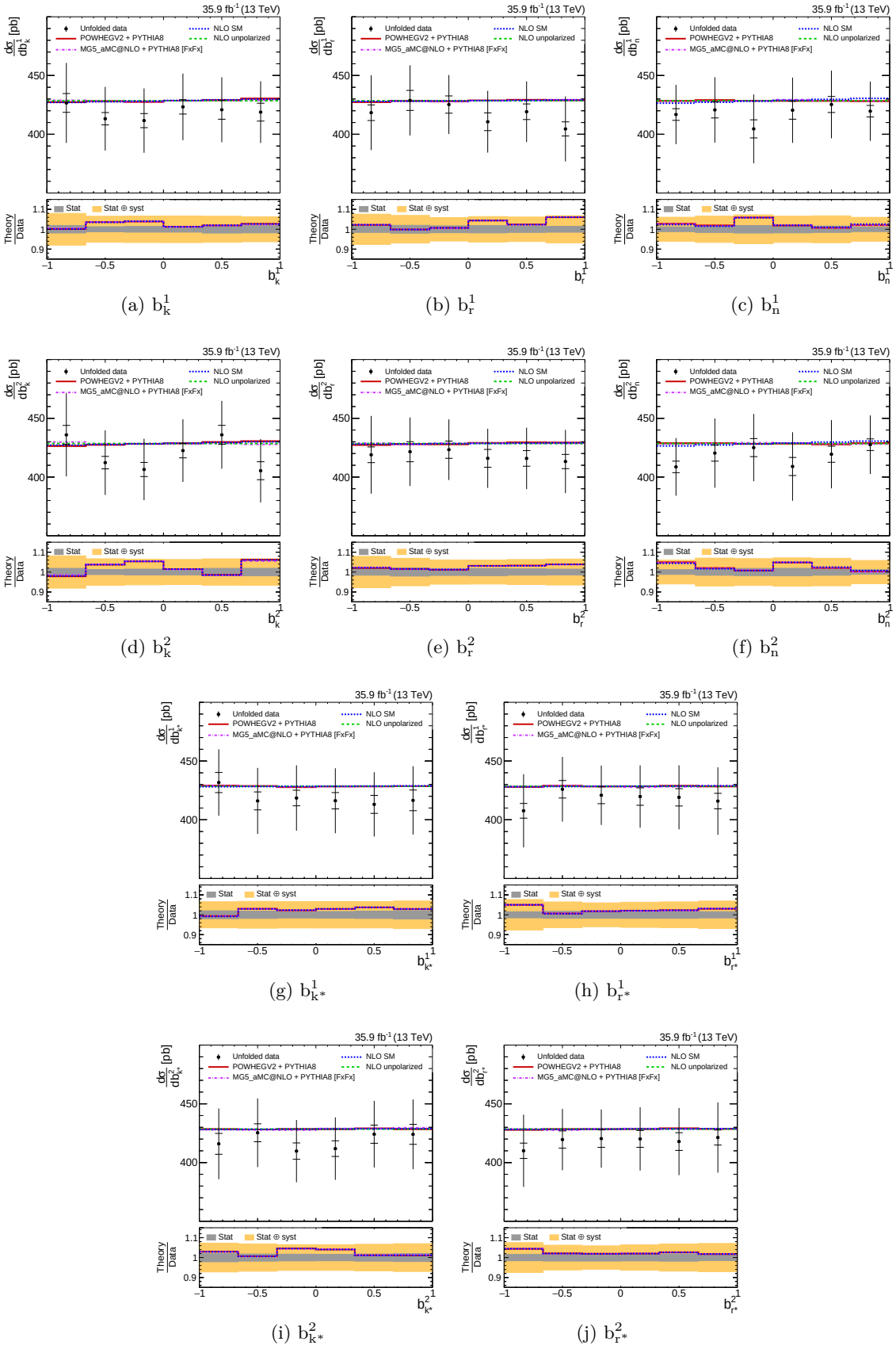

(a) b_k^1 (b) b_r^1 (c) b_n^1

(d) b_k^2 (e) b_r^2 (f) b_n^2

(g) $b_{k^*}^1$ (h) $b_{r^*}^1$

(i) $b_{k^*}^2$ (j) $b_{r^*}^2$

Figure 8.15: Unfolded absolute differential b_i^a distributions together with the simulated and calculated predictions at NLO QCD (+ weak) accuracy.

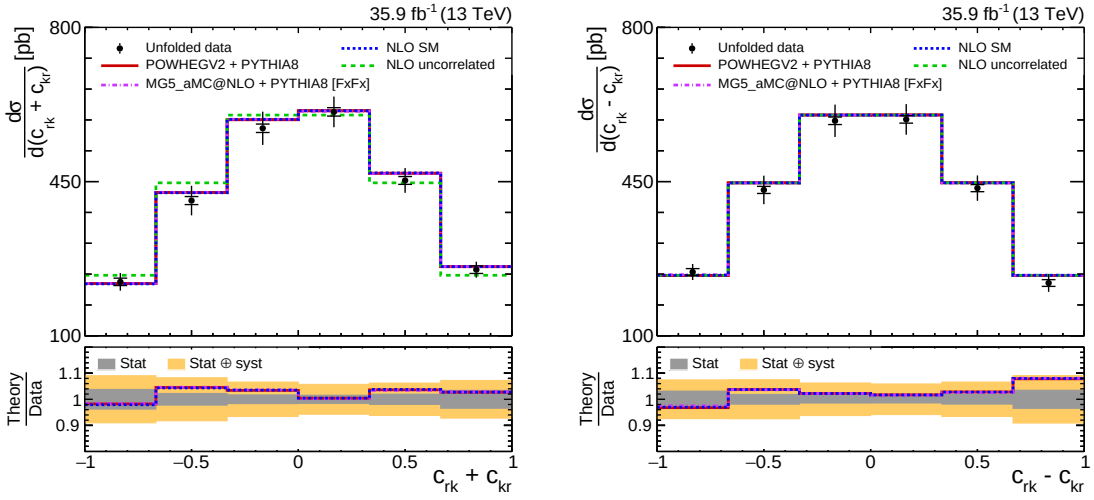

(a) $c_{rk} + c_{kr}$ (b) $c_{rk} - c_{kr}$

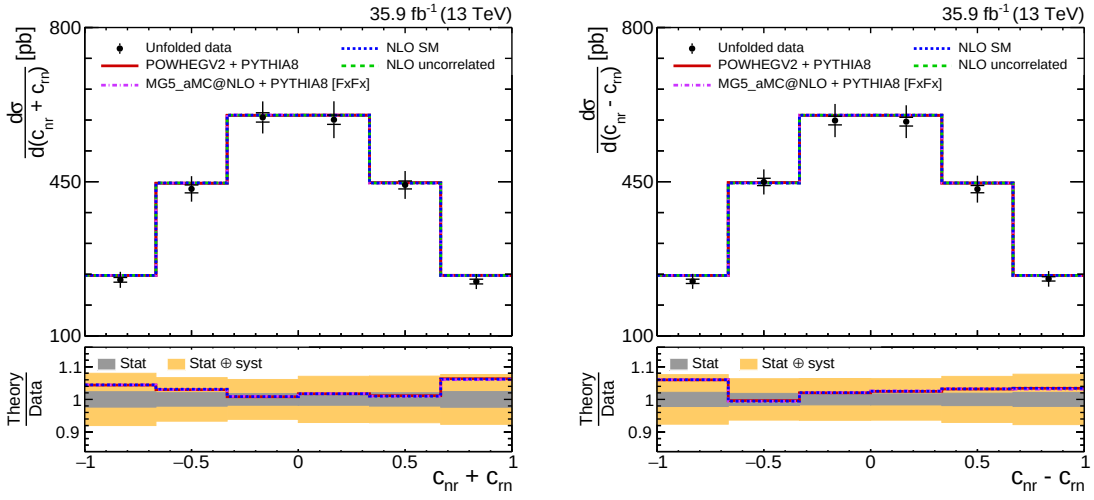

(c) $c_{nr} + c_{rn}$ (d) $c_{nr} - c_{rn}$

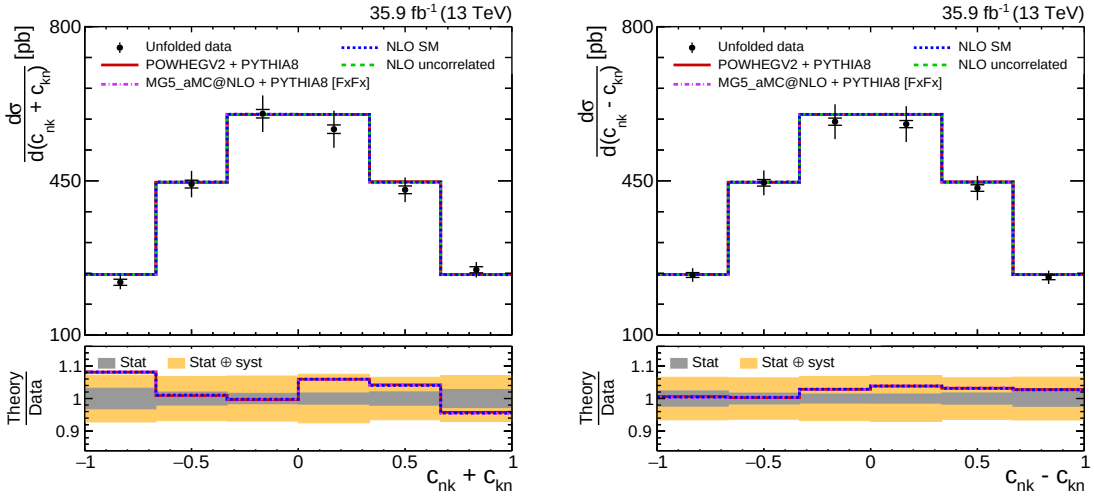

(e) $c_{nk} + c_{kn}$ (f) $c_{nk} - c_{kn}$

Figure 8.16: Unfolded absolute differential $c_{ij} \pm c_{ji}$ distributions together with the simulated and calculated predictions at NLO QCD (+ weak) accuracy.

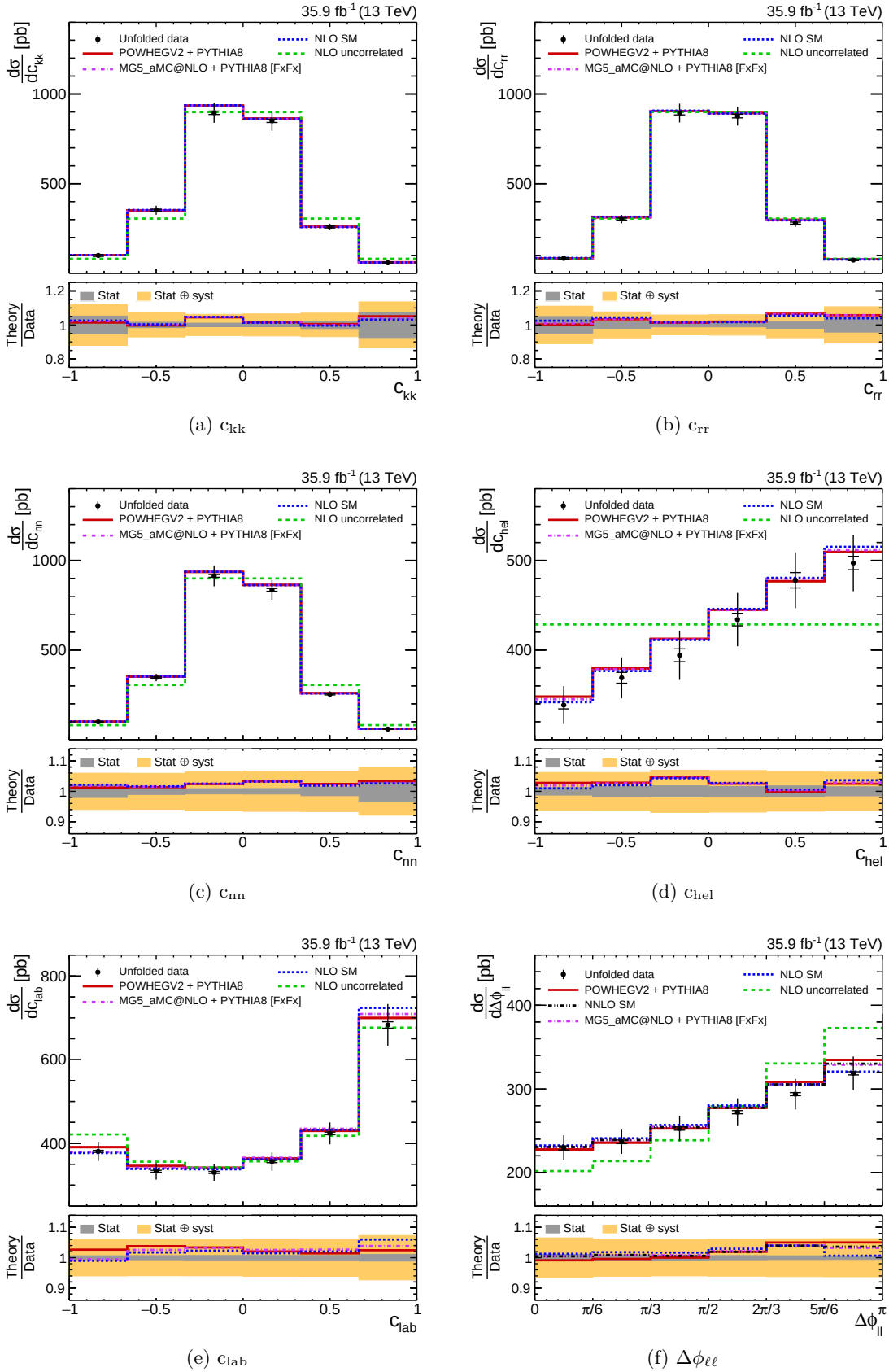

(a) c_{kk} (b) c_{rr}

(c) c_{nn} (d) c_{hel}

(e) c_{lab} (f) $\Delta\phi_{\ell\ell}$

Figure 8.17: Unfolded absolute differential c_{ii}, c_{hel}, c_{lab} and $\Delta\phi_{\ell\ell}$ distributions together with the simulated and calculated predictions at NLO QCD (+ weak) accuracy.

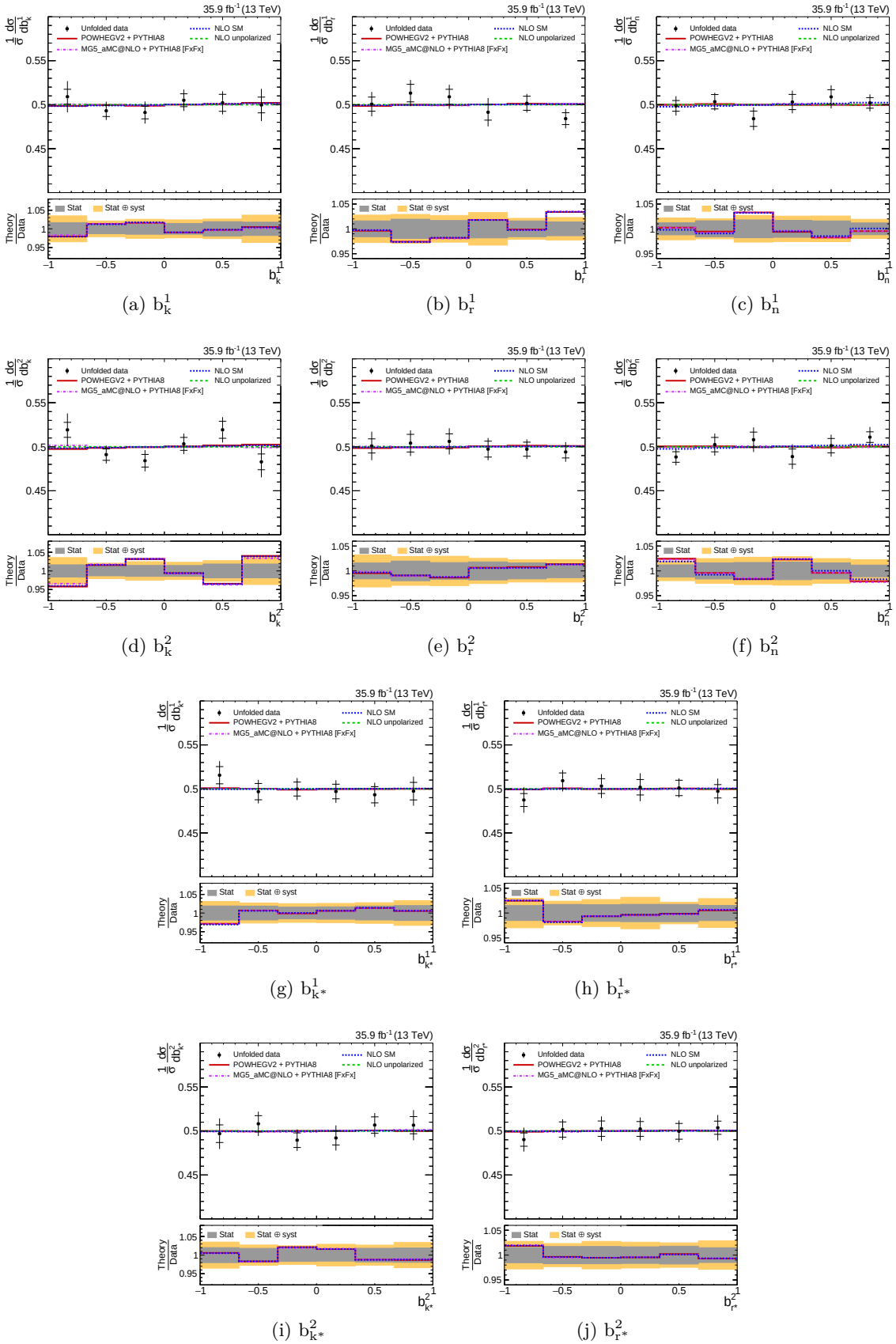

(a) b_k^1 (b) b_r^1 (c) b_n^1

(d) b_k^2 (e) b_r^2 (f) b_n^2

(g) $b_{k^*}^1$ (h) $b_{r^*}^1$

(i) $b_{k^*}^2$ (j) $b_{r^*}^2$

Figure 8.18: Unfolded normalized differential b_i^a distributions together with the simulated and calculated predictions at NLO QCD (+ weak) accuracy.

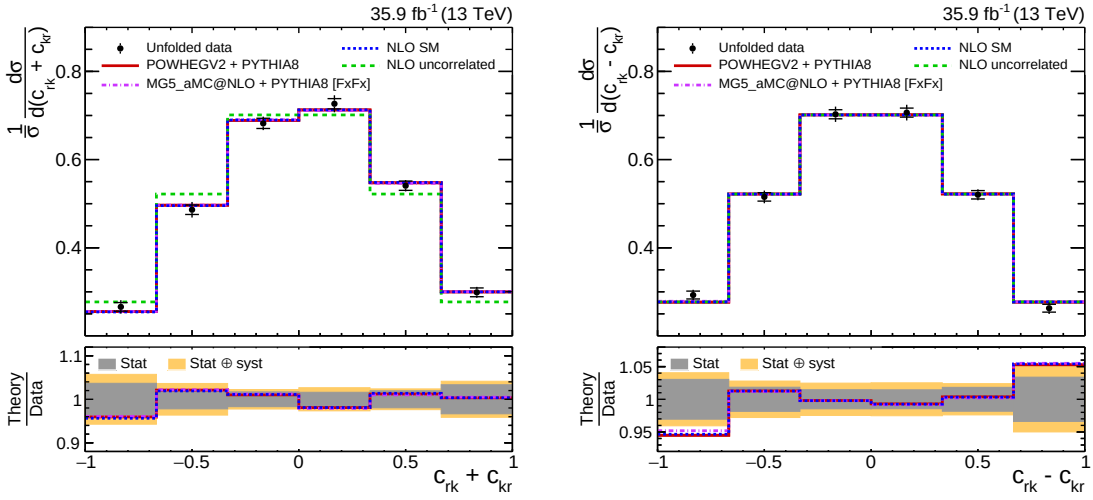

(a) $c_{rk} + c_{kr}$ (b) $c_{rk} - c_{kr}$

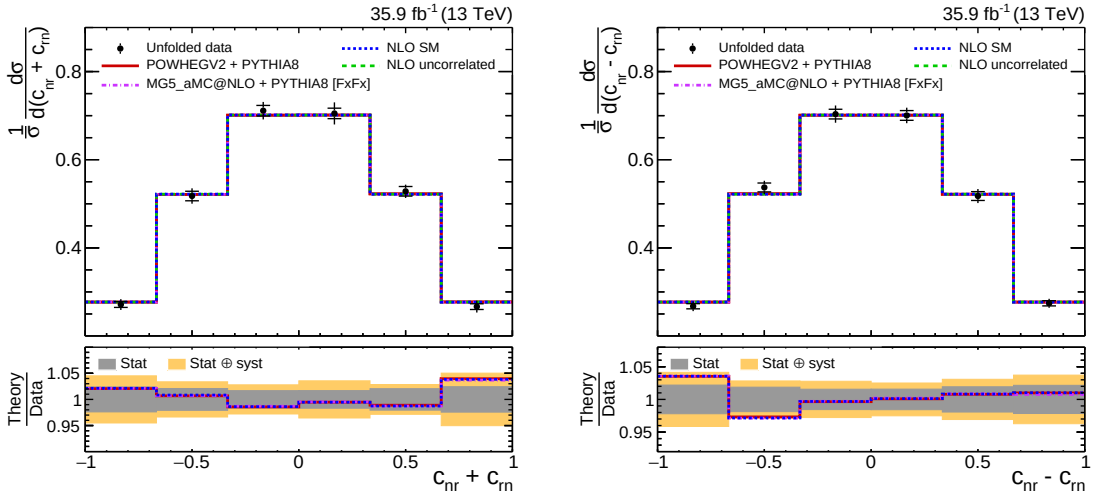

(c) $c_{nr} + c_{rn}$ (d) $c_{nr} - c_{rn}$

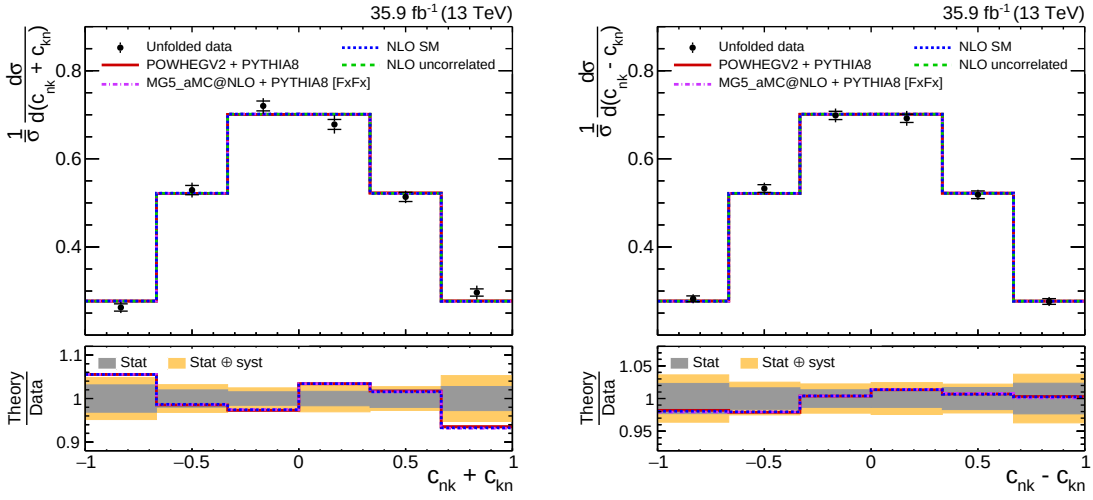

(e) $c_{nk} + c_{kn}$ (f) $c_{nk} - c_{kn}$

Figure 8.19: Unfolded normalized differential $c_{ij} \pm c_{ji}$ distributions together with the simulated and calculated predictions at NLO QCD (+ weak) accuracy.

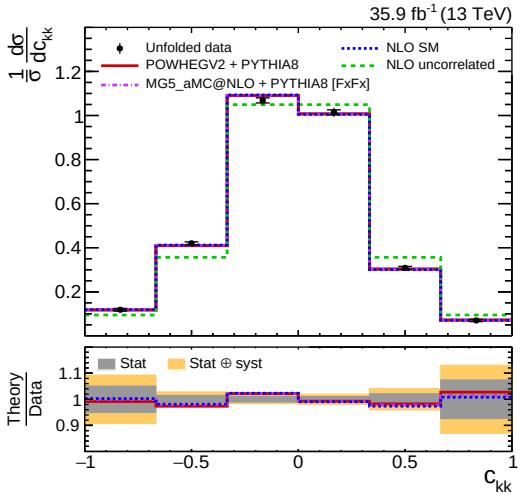

(a) c_{kk}

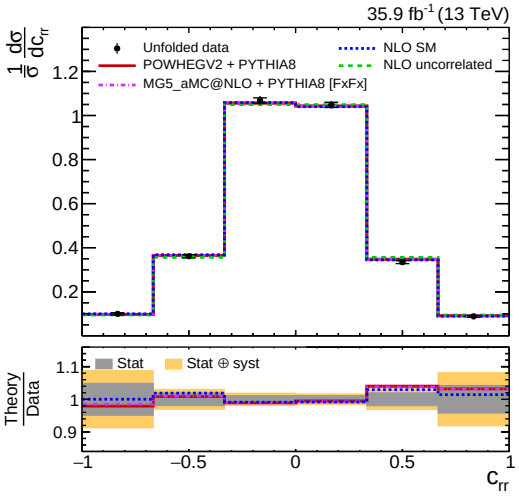

(b) c_{rr}

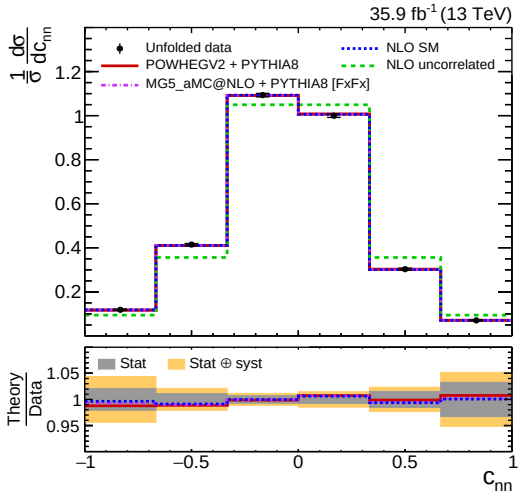

(c) c_{nn}

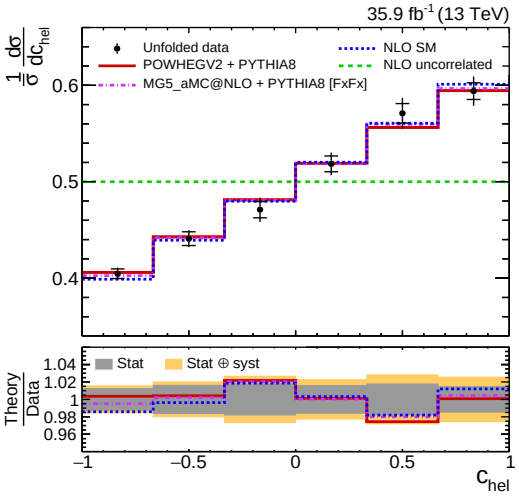

(d) c_{hel}

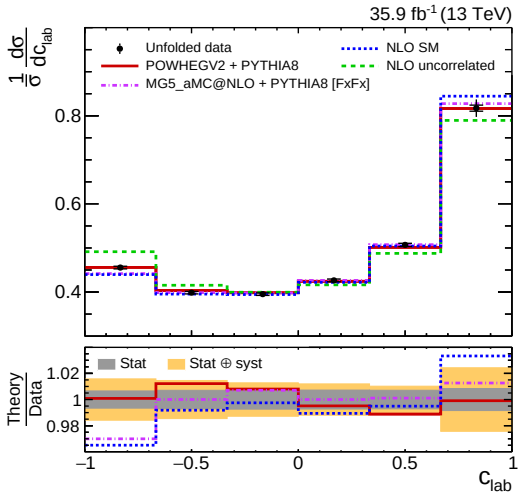

(e) c_{lab}

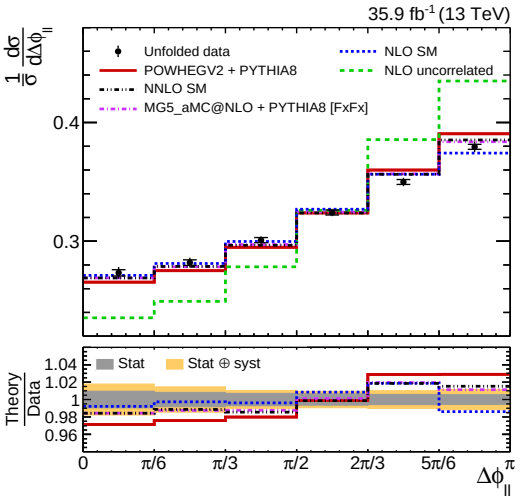

(f) $\Delta\phi_{\ell\ell}$

Figure 8.20: Unfolded normalized differential c_{ii}, c_{hel}, c_{lab} and $\Delta\phi_{\ell\ell}$ distributions together with the simulated and calculated predictions at NLO QCD (+ weak) accuracy.

Table 8.1: χ^2 between measured and predicted normalized differential distributions.

Observable	χ^2 between data and prediction [N_{DF} = 5 (single obs.) or 110 (all)]			
	POWHEGV2	MG5_aMC@NLO	NLO calculation	NNLO calculation
b_k^1	1.1	1.0	1.1	-
b_k^2	5.2	5.0	5.2	-
b_r^1	4.3	4.4	4.2	-
b_r^2	0.7	0.5	0.6	-
b_n^1	1.9	1.8	1.8	-
b_n^2	3.2	3.1	2.1	-
$b_{k^*}^1$	1.3	1.3	1.4	-
$b_{k^*}^2$	1.8	1.6	1.7	-
$b_{r^*}^1$	1.5	1.5	1.6	-
$b_{r^*}^2$	0.5	0.6	0.6	-
c_{kk}	3.1	3.2	3.5	-
c_{rr}	2.0	1.7	1.1	-
c_{nn}	0.6	0.3	0.3	-
$c_{rk} + c_{kr}$	1.5	1.6	1.7	-
$c_{rk} - c_{kr}$	3.6	3.1	3.6	-
$c_{nr} + c_{rn}$	1.7	1.7	1.8	-
$c_{nr} - c_{rn}$	1.8	1.9	1.9	-
$c_{nk} + c_{kn}$	3.8	4.0	4.0	-
$c_{nk} - c_{kn}$	2.3	2.4	2.2	-
c_{hel}	1.5	0.7	1.4	-
c_{lab}	3.9	7.6	7.0	-
$\Delta\phi_{\ell\ell}$	10.8	4.0	9.2	4.3
All	88.4	89.7	88.6	-

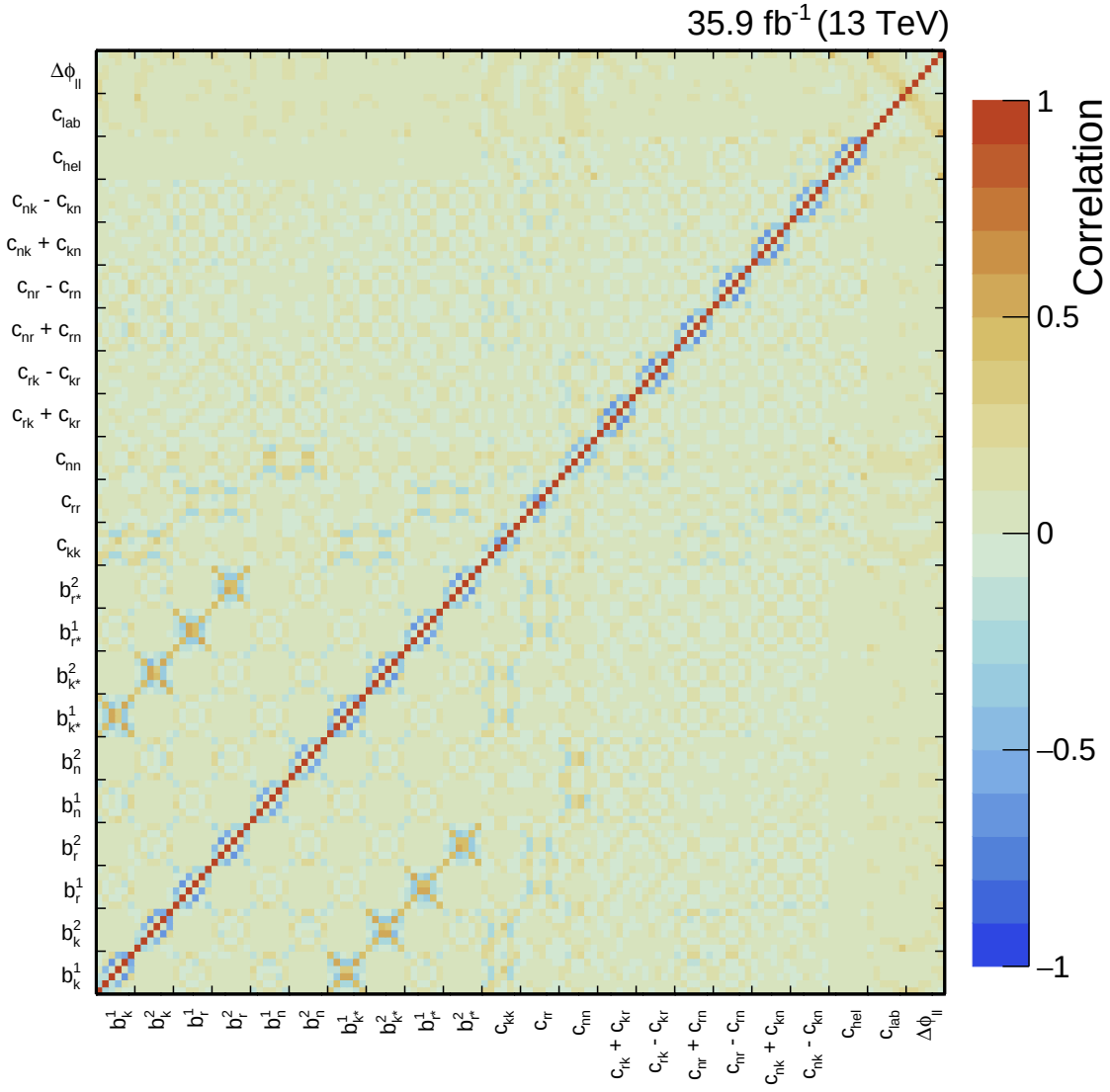

Figure 8.21: The statistical correlation matrix for the absolute differential distributions.

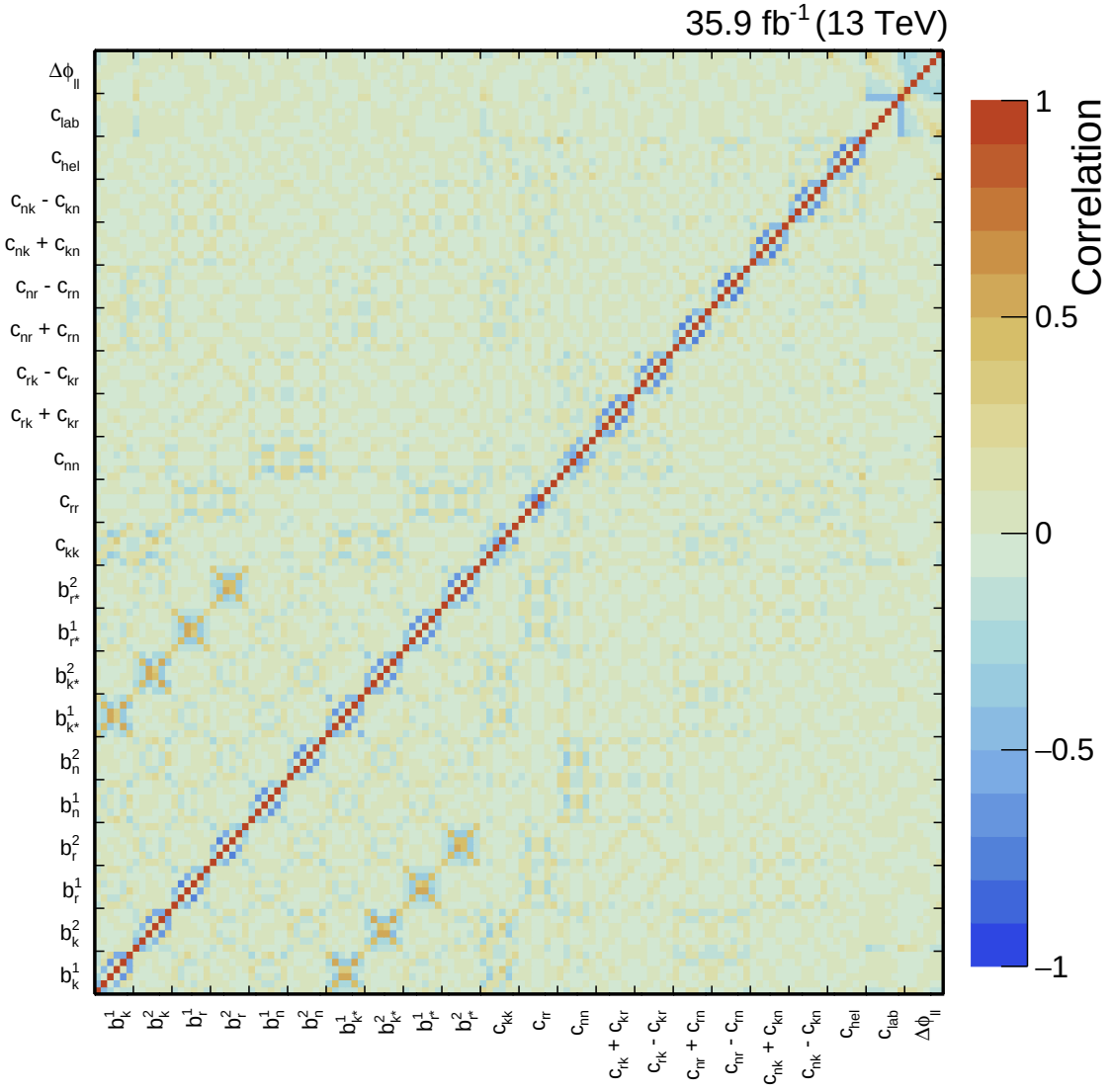

Figure 8.22: The statistical correlation matrix for the normalized differential distributions.

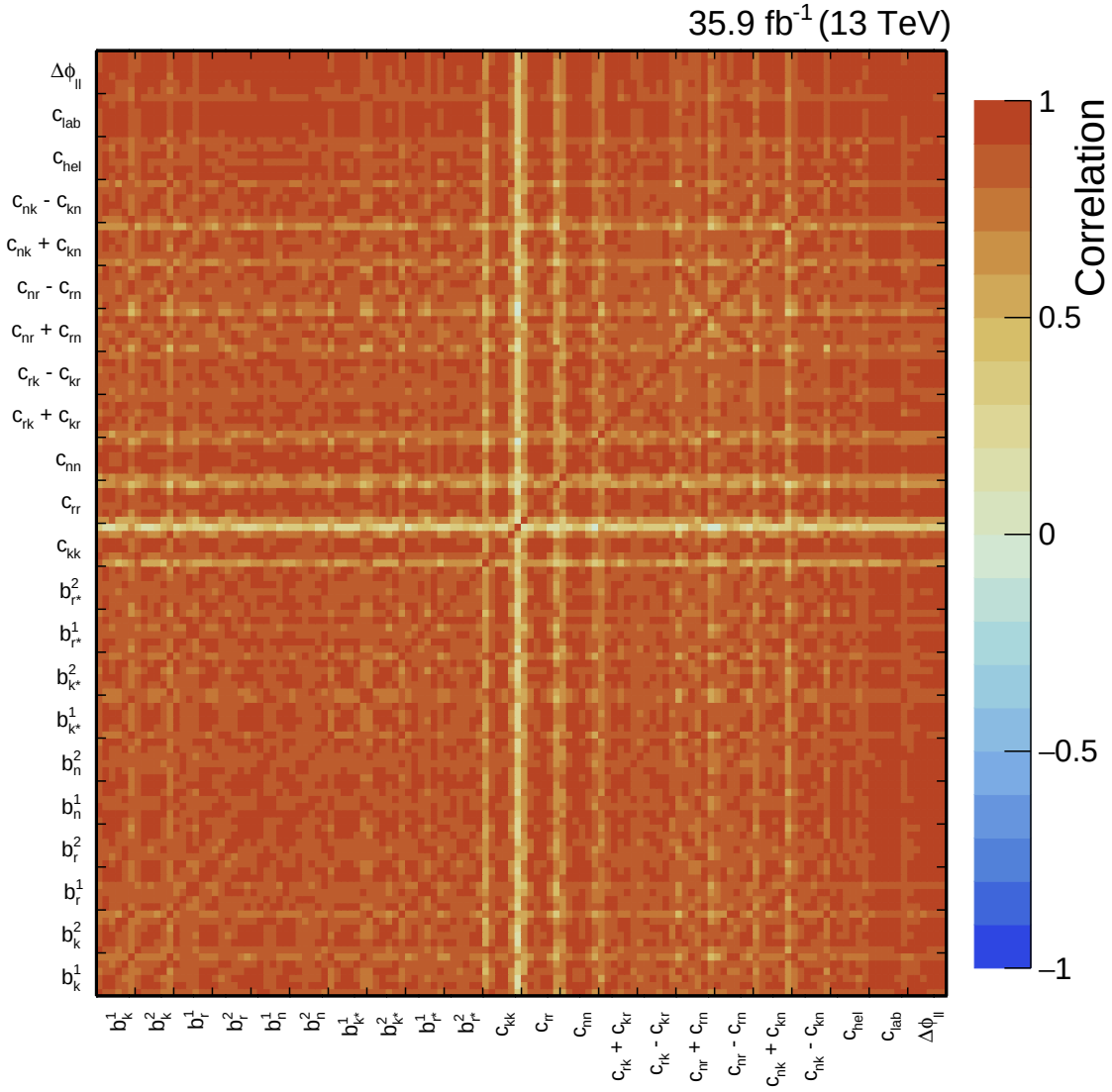

Figure 8.23: The systematic correlation matrix for the absolute differential distributions.

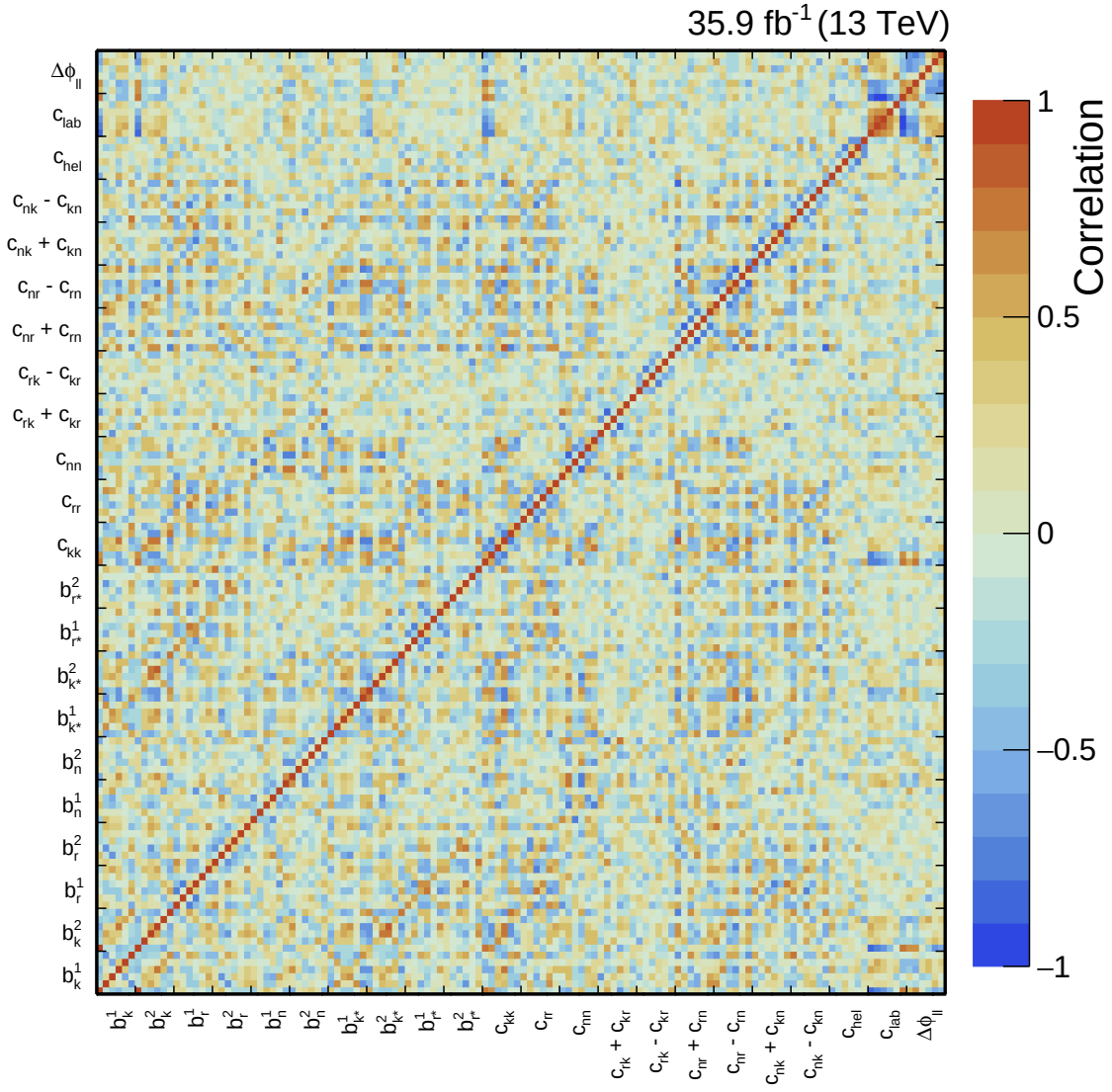

Figure 8.24: The systematic correlation matrix for the normalized differential distributions.

as the $\leftarrow$ and $\rightarrow$ bins, A_2^x the second and fifth bin respectively and finally A_3^x the third and fourth bins of a given distribution. Let $g(x;C)$ be the form of our spin correlation observables at a particular value of spin coefficient C. Since $N_{\rightarrow}^x = \int_i g(x;C)\ dx = \int_i (1 \pm C) g(x;0)\ dx$, A_i^x is related to C_i, the spin coefficient extracted using this i-pair asymmetry by:

$$C_i = \pm A_i^x \frac{\int_i g(x;0)\ dx}{\int_i x g(x;0)\ dx} \tag{8.19}$$

where the signs are observable-dependent (see Table 2.2) and term following A_i^x are constants that are analytically evaluated. In fact, the above equation is the general form of the relationship between coefficients and asymmetries that are given in Table 2.2. C is then given by a combination of the three C_i using the BLUE method [14]. The spin coefficients extracted from the unfolded data and predictions are shown in Table 8.2. They also shown in graphical form in Figures 8.25 (B_i^a), 8.26 ($C_{ij} \pm C_{ji}$) and 8.27 (C_{ii}, D, $A^{c_{lab}}$ and $A^{\Delta\phi_{\ell\ell}}$).

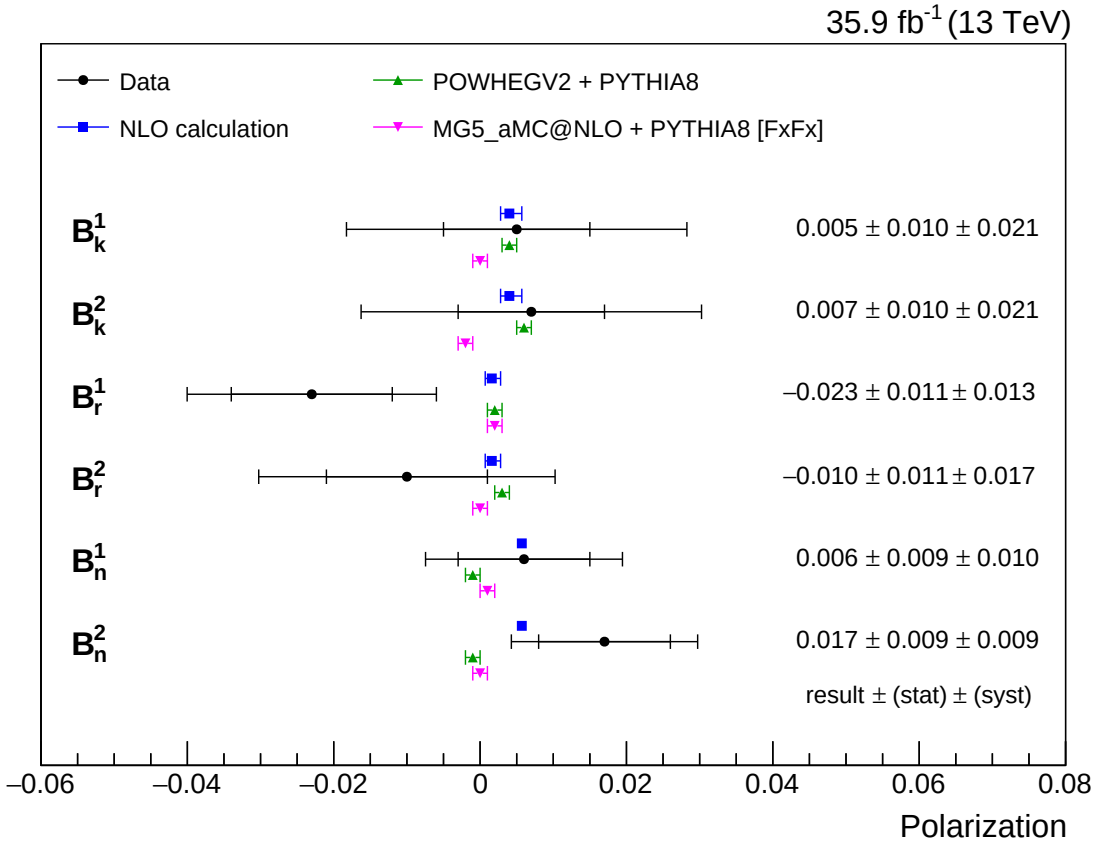

Figure 8.25: Measured and predicted values of B_i^a. Simulation-based predictions are quoted with a combination of statistical and scale uncertainties. The NLO calculations are quoted with scale uncertainties [12].

The contributions of each systematic source to the spin coefficients are shown in Table 8.3 and Table 8.4. The correlation matrices between them are shown in Figure 8.28 (statistical) and Figure 8.29 (systematic). It is worth noting that the statistical correlation matrix

Table 8.2: Measured and predicted spin coefficients. Simulation-based predictions are quoted with a combination of statistical and scale uncertainties. The NLO calculations are quoted with scale uncertainties [12]. The value of $A^{\Delta\phi_{\ell\ell}}$ predicted by the NNLO calculation is $0.115^{+0.005}_{-0.001}$; the uncertainties are from scale variations [9].

Coefficient	Data	POWHEGV2	MG5_aMC@NLO	NLO calculation
B_k^1	0.005 ± 0.023	$0.004^{+0.001}_{-0.001}$	$0.000^{+0.001}_{-0.001}$	$4.0^{+1.7}_{-1.2} \times 10^{-3}$
B_k^2	0.007 ± 0.023	$0.006^{+0.001}_{-0.001}$	$-0.002^{+0.001}_{-0.001}$	$4.0^{+1.7}_{-1.2} \times 10^{-3}$
B_r^1	-0.023 ± 0.017	$0.002^{+0.001}_{-0.001}$	$0.002^{+0.001}_{-0.001}$	$1.6^{+1.2}_{-0.9} \times 10^{-3}$
B_r^2	-0.010 ± 0.020	$0.003^{+0.001}_{-0.001}$	$0.000^{+0.001}_{-0.001}$	$1.6^{+1.2}_{-0.9} \times 10^{-3}$
B_n^1	0.006 ± 0.013	$-0.001^{+0.001}_{-0.001}$	$0.001^{+0.001}_{-0.001}$	$5.7^{+0.5}_{-0.4} \times 10^{-3}$
B_n^2	0.017 ± 0.013	$-0.001^{+0.001}_{-0.001}$	$0.000^{+0.001}_{-0.001}$	$5.7^{+0.5}_{-0.4} \times 10^{-3}$
$B_{k^*}^1$	-0.016 ± 0.018	$-0.001^{+0.001}_{-0.001}$	$0.000^{+0.001}_{-0.001}$	$< 10^{-3}$
$B_{k^*}^2$	0.007 ± 0.019	$0.001^{+0.001}_{-0.001}$	$0.003^{+0.002}_{-0.001}$	$< 10^{-3}$
$B_{r^*}^1$	0.001 ± 0.017	$0.000^{+0.001}_{-0.001}$	$0.000^{+0.001}_{-0.001}$	$< 10^{-3}$
$B_{r^*}^2$	0.010 ± 0.017	$0.001^{+0.001}_{-0.001}$	$0.001^{+0.001}_{-0.001}$	$< 10^{-3}$
C_{kk}	0.300 ± 0.038	$0.314^{+0.005}_{-0.004}$	$0.325^{+0.011}_{-0.006}$	$0.331^{+0.002}_{-0.002}$
C_{rr}	0.081 ± 0.032	$0.048^{+0.007}_{-0.006}$	$0.052^{+0.007}_{-0.005}$	$0.071^{+0.008}_{-0.006}$
C_{nn}	0.329 ± 0.020	$0.317^{+0.001}_{-0.001}$	$0.324^{+0.002}_{-0.002}$	$0.326^{+0.002}_{-0.002}$
$C_{rk} + C_{kr}$	-0.193 ± 0.064	$-0.201^{+0.004}_{-0.003}$	$-0.198^{+0.004}_{-0.005}$	$-0.206^{+0.002}_{-0.002}$
$C_{rk} - C_{kr}$	0.057 ± 0.046	$-0.001^{+0.002}_{-0.002}$	$0.004^{+0.002}_{-0.002}$	0
$C_{nr} + C_{rn}$	-0.004 ± 0.037	$-0.003^{+0.002}_{-0.002}$	$0.001^{+0.002}_{-0.002}$	$1.06^{+0.01}_{-0.01} \times 10^{-3}$
$C_{nr} - C_{rn}$	-0.001 ± 0.038	$0.002^{+0.002}_{-0.002}$	$0.001^{+0.003}_{-0.002}$	0
$C_{nk} + C_{kn}$	-0.043 ± 0.041	$-0.002^{+0.002}_{-0.002}$	$0.003^{+0.002}_{-0.002}$	$2.15^{+0.04}_{-0.07} \times 10^{-3}$
$C_{nk} - C_{kn}$	0.040 ± 0.029	$-0.001^{+0.002}_{-0.002}$	$-0.001^{+0.002}_{-0.002}$	0
D	-0.237 ± 0.011	$-0.226^{+0.003}_{-0.004}$	$-0.233^{+0.004}_{-0.006}$	$-0.243^{+0.001}_{-0.001}$
$A^{c_{lab}}$	0.167 ± 0.010	$0.161^{+0.002}_{-0.002}$	$0.174^{+0.004}_{-0.003}$	$0.181^{+0.004}_{-0.003}$
$A^{\Delta\phi_{\ell\ell}}$	0.103 ± 0.008	$0.125^{+0.004}_{-0.005}$	$0.115^{+0.003}_{-0.005}$	$0.112^{+0.009}_{-0.012}$

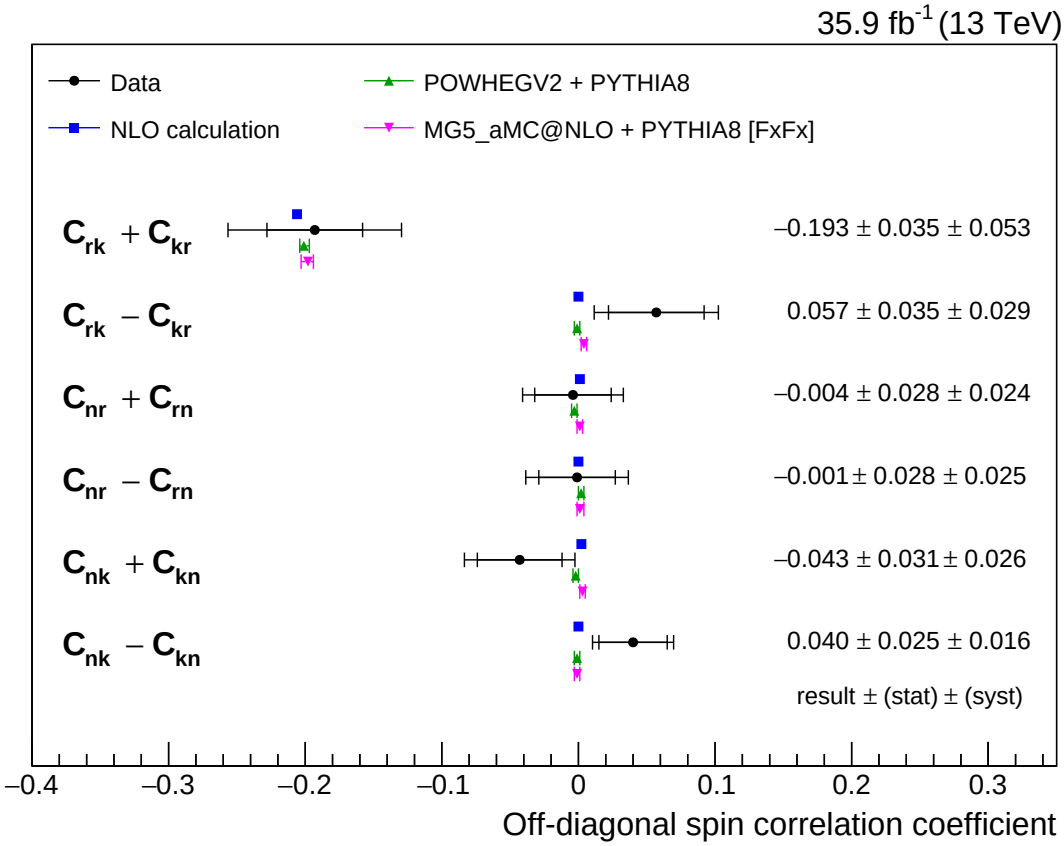

Figure 8.26: Measured and predicted values of $C_{ij} \pm C_{ji}$. Simulation-based predictions are quoted with a combination of statistical and scale uncertainties. The NLO calculations are quoted with scale uncertainties [12].

reflects our initial expectation that the spin coefficients are uncorrelated, except for D and C_{ii} whose relationship is also present in the matrix. Systematic-induced correlations are in general stronger and more structured; variations in the choice of scales for example affect B_k^1 and B_k^2 in the same way within the SM, inducing a positive correlation between the two coefficients.

Judging by the χ^2 between measured and predicted distributions (Table 8.1), all predictions are consistent with the measurements. The most notable deviation is seen in the $\Delta\phi_{\ell\ell}$ distribution, with POWHEGV2 being the most discrepant. However, POWHEGV2 is also the prediction that describes the c_{lab} distribution the best. We recall from Section 2.5 that the laboratory frame observables are theoretically complicated, as they are affected also by any boosts to the top and antitop quarks. As such, their distributions are a convolution of both spin correlation and kinematical effects. The best description of the $\Delta\phi_{\ell\ell}$ distribution is achieved by the MG5_aMC@NLO simulation and the NNLO calculation, this may be due to an improved description of the kinematical effects in $t\bar{t}$ events in them, through the inclusion of up to two additonal partons in the MG5_aMC@NLO simulation and in going to a higher order in QCD for the NNLO calculation. This is corroborated by the fact that

Table 8.3: Contribution of each systematic sources to the uncertainty in the measured values of B_i^a. A dash (-) is written instead when the uncertainties have values < 0.0005.

Source	Uncertainty									
	B_k^1	B_k^2	B_r^1	B_r^2	B_n^1	B_n^2	$B_{k^*}^1$	$B_{k^*}^2$	$B_{r^*}^1$	$B_{r^*}^2$
JER	0.001	0.002	0.001	0.001	0.001	0.001	-	0.001	0.001	0.001
JEC	0.011	0.012	0.007	0.009	0.003	0.003	0.009	0.008	0.007	0.007
Unclustered $\not{p}_T$	0.001	0.002	0.001	0.001	-	0.001	0.001	-	0.001	0.002
Pileup	-	-	0.002	0.002	-	0.001	0.001	0.001	-	-
Trigger efficiency	0.001	0.001	0.001	0.001	-	-	0.001	0.001	0.002	0.002
Lepton ID	0.001	-	-	-	-	-	-	-	-	-
Kinematic reconstruction	-	-	-	-	-	-	-	-	-	-
b-tagging	0.003	0.004	0.003	0.003	-	-	0.002	0.002	0.001	0.001
Background normalization	0.008	0.008	0.005	0.008	0.001	0.001	0.004	0.005	0.002	0.002
ME + PS scale	0.005	0.004	0.004	0.009	0.003	0.004	0.003	0.004	0.006	0.005
b quark fragmentation	0.009	0.009	0.004	0.005	-	0.001	0.001	0.001	0.001	0.001
B hadron leptonic BR	0.001	0.001	-	-	-	-	-	-	-	-
Color reconnection	0.005	0.003	0.003	0.004	0.008	0.005	0.006	0.008	0.006	0.008
UE tune	0.001	0.003	0.001	0.003	0.002	0.003	0.003	0.002	0.004	0.004
h_{damp}	0.006	0.006	0.004	0.001	0.003	0.004	0.003	0.003	0.004	0.004
Top quark mass	0.007	0.007	-	0.001	0.001	0.002	0.002	0.001	0.002	0.002
PDF	0.001	0.001	-	-	-	-	0.001	0.001	0.001	0.001
p_T^t reweighting	0.003	0.004	0.001	0.001	-	-	0.001	0.001	-	-
Total systematic	0.021	0.021	0.013	0.017	0.010	0.009	0.013	0.014	0.013	0.013
Data	0.009	0.008	0.009	0.009	0.007	0.008	0.010	0.010	0.010	0.009
Signal simulation	0.003	0.003	0.003	0.003	0.003	0.003	0.004	0.004	0.004	0.003
Background simulation	0.005	0.005	0.005	0.005	0.004	0.004	0.006	0.006	0.005	0.005
Total statistical	0.010	0.010	0.011	0.011	0.009	0.009	0.012	0.012	0.012	0.011
Total	0.023	0.023	0.017	0.020	0.013	0.013	0.018	0.019	0.017	0.017

Table 8.4: Contribution of each systematic sources to the uncertainty in the measured values of C_{ii}, $C_{ij} \pm C_{ji}$, D, $A^{c_{lab}}$ and $A^{\Delta\phi_{\ell\ell}}$. A dash (-) is written instead when the uncertainties have values < 0.0005.

Source	Uncertainty											
	C_{kk}	C_{rr}	C_{nn}	$C_{rk}+C_{kr}$	$C_{rk}-C_{kr}$	$C_{nr}+C_{rn}$	$C_{nr}-C_{rn}$	$C_{nk}+C_{kn}$	$C_{nk}-C_{kn}$	D	$A^{c_{lab}}$	$A^{\Delta\phi_{\ell\ell}}$
JER	0.001	0.002	0.001	0.004	0.002	0.001	0.001	0.003	0.001	-	-	-
JEC	0.012	0.009	0.005	0.022	0.011	0.011	0.009	0.012	0.007	0.002	-	0.001
Unclustered $\not{p}_T$	0.001	0.001	0.001	0.004	0.001	0.001	0.002	0.001	0.001	-	-	0.001
Pileup	0.002	-	0.001	0.004	0.001	0.001	0.002	0.001	0.001	0.001	-	0.001
Trigger efficiency	0.001	0.001	-	0.002	-	-	-	-	-	-	0.001	-
Lepton ID	0.001	0.001	-	0.001	-	-	-	-	-	-	-	-
Kinematic reconstruction	-	-	-	-	-	-	-	-	-	-	-	-
b-tagging	0.004	0.001	0.002	0.005	0.001	0.001	0.001	0.001	0.001	0.001	-	-
Background normalization	0.017	0.009	0.008	0.025	0.006	0.004	0.004	0.007	0.003	0.004	0.008	0.002
ME + PS scale	0.012	0.006	0.007	0.026	0.011	0.007	0.014	0.011	0.007	0.003	0.002	0.003
b quark fragmentation	0.014	0.002	0.005	0.017	0.001	0.001	0.001	0.002	0.001	0.003	-	0.001
B hadron leptonic BR	-	0.001	0.001	0.002	-	0.001	-	-	-	0.001	-	-
Color reconnection	0.005	0.013	0.006	0.013	0.011	0.014	0.017	0.009	0.008	0.002	0.001	0.001
UE tune	0.008	0.002	0.002	0.004	0.010	0.007	0.005	0.007	0.002	0.003	0.001	0.001
h_{damp}	0.004	0.003	0.001	0.009	0.016	0.011	0.001	0.012	0.009	0.002	0.002	0.004
Top quark mass	0.001	0.002	0.006	0.006	0.009	0.002	0.002	0.009	0.001	0.002	0.001	-
PDF	0.002	0.002	0.001	0.002	-	-	-	-	-	0.001	0.003	0.001
p_T^t reweighting	0.008	0.011	0.005	0.019	-	0.001	-	0.001	-	0.004	0.003	0.005
Total systematic	0.031	0.023	0.016	0.053	0.029	0.024	0.025	0.026	0.016	0.009	0.010	0.007
Data	0.018	0.019	0.010	0.029	0.029	0.024	0.025	0.025	0.020	0.006	0.003	0.003
Signal simulation	0.007	0.007	0.004	0.011	0.011	0.009	0.009	0.010	0.008	0.002	0.001	0.001
Background simulation	0.010	0.010	0.005	0.018	0.017	0.012	0.010	0.015	0.012	0.003	0.002	0.002
Total statistical	0.022	0.023	0.012	0.035	0.035	0.028	0.028	0.031	0.025	0.007	0.003	0.003
Total	0.038	0.032	0.020	0.064	0.046	0.037	0.038	0.041	0.029	0.011	0.010	0.008

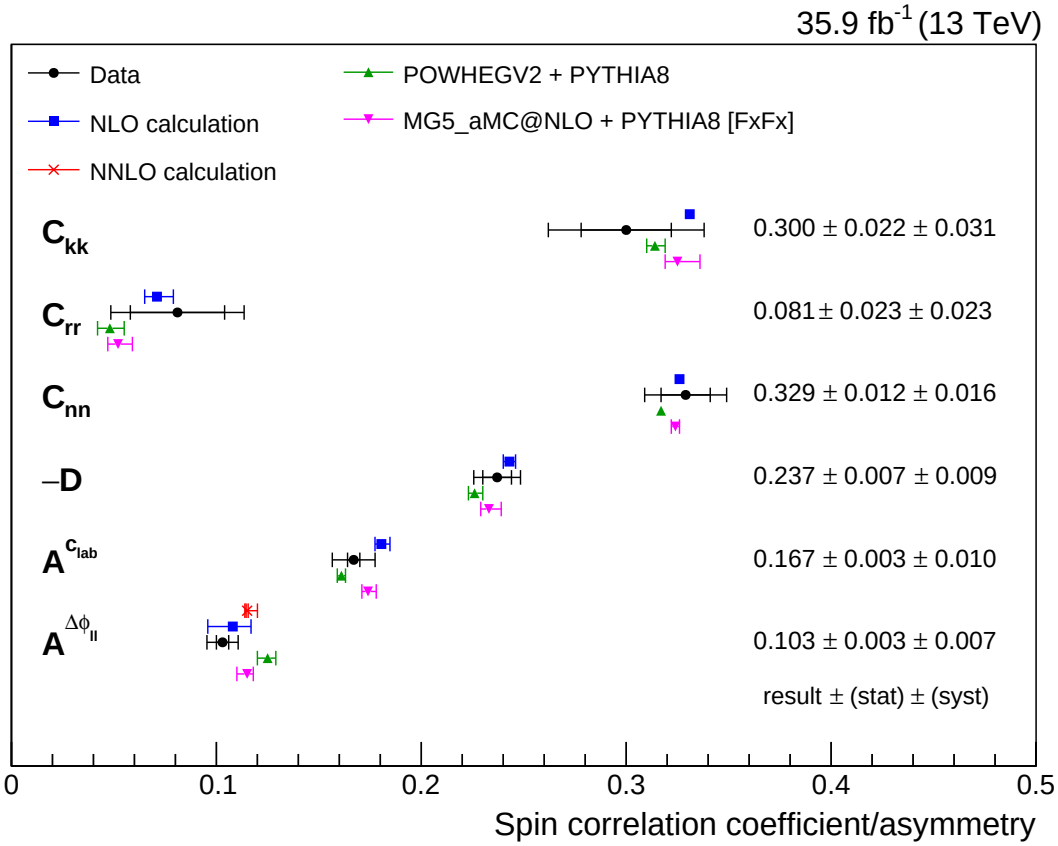

Figure 8.27: Measured and predicted values of C_{ii}, D, $A^{c_{lab}}$ and $A^{\Delta\phi_{\ell\ell}}$. Simulation-based predictions are quoted with a combination of statistical and scale uncertainties. The NLO calculations are quoted with scale uncertainties [12]. The value of $A^{\Delta\phi_{\ell\ell}}$ predicted by the NNLO calculation is $0.115^{+0.005}_{-0.001}$; the uncertainties are from scale variations [9].

the agreement between the POWHEGV2 $\Delta\phi_{\ell\ell}$ predictions and the data improves when the p_T^t reweighting (described in Section 6.6) is applied. However, the reweighting also deteriorates the agreement in the c_{kk} distribution. This fact, together with its empirical origin, means that the reweighting is not seen as of particular relevance in clarifying the origin of the observed discrepancy. The description of the other distributions are in general good by all predictions, which shows in the p-value of around 0.9 by all predictions in the global χ^2.

Comparing the spin coefficients, one sees a slightly different picture. The MC generators both predict lower values of C_{ii} in comparison to the NLO calculation, which might be related to the missing weak corrections in the generators. However, the impact of the weak corrections, as evaluated by the authors of References [12] and [15], is found to be around 2% for $A^{\Delta\phi_{\ell\ell}}$, and so is unlikely to be the sole explanation of the discrepancy. Another difference between the predictions is that in all cases, the numerator and denominator of the normalized differential cross sections are computed at their quoted accuracy. However, the ratio between the two is also expanded to this accuracy only in the NLO calculation [12]. This leads to a difference of $\mathcal{O}(\alpha_s^2)$ in comparison to the simulations. In the NNLO calculation,

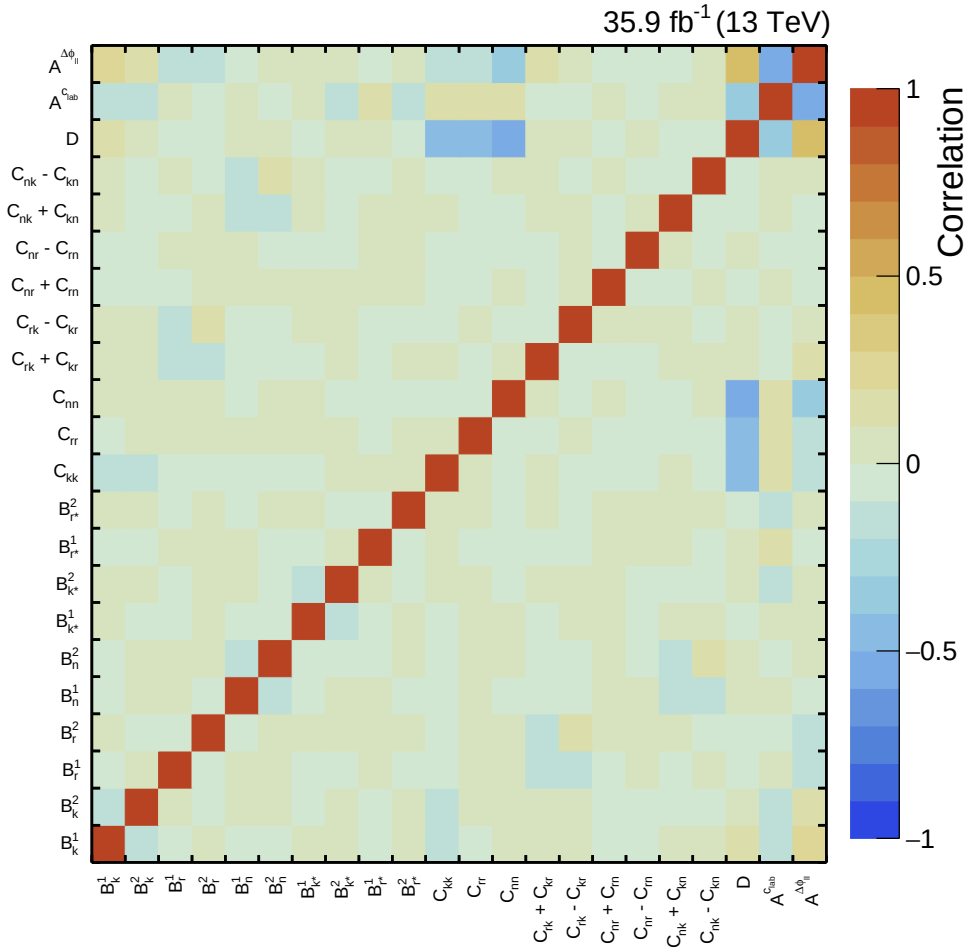

Figure 8.28: The statistical correlation matrix for the measured coefficients.

this expansion is not performed [9]. However, as shown by the authors of Reference [9] in Reference [16], this expansion has a larger impact at the NLO accuracy compared to NNLO, and so in the NNLO calculation with the expansion performed, some residual discrepancy still remains. While it is clear that more work is needed to fully understand the situation, given the precision of this measurement and taking the global picture over all observables and coefficients, we conclude that at the moment no significant deviations with respect to the SM is seen, especially when the calculation-based predictions are considered.

The measured values of C_{ii}, $C_{rk}+C_{kr}$, D, $A^{c_{lab}}$ and $A^{\Delta\phi_{\ell\ell}}$ are transformed into a measurement of the spin correlation fraction f_{SM} which expresses the spin correlation strength relative to the SM. In our case the SM prediction is taken to be the NLO calculation. f_{SM} linearly interpolates between 0, the unpolarized/uncorrelated case and 1, the SM case. The result of this measurement is shown in Figure 8.30. It is to be noted that there is some correlation between the theoretical and the ME + PS source of the systematic uncertainties. The same may apply to the systematic source due to p_T^t reweighting whose cause is attributed to the missing higher-order corrections. In both cases the effect of these correlations are neglected

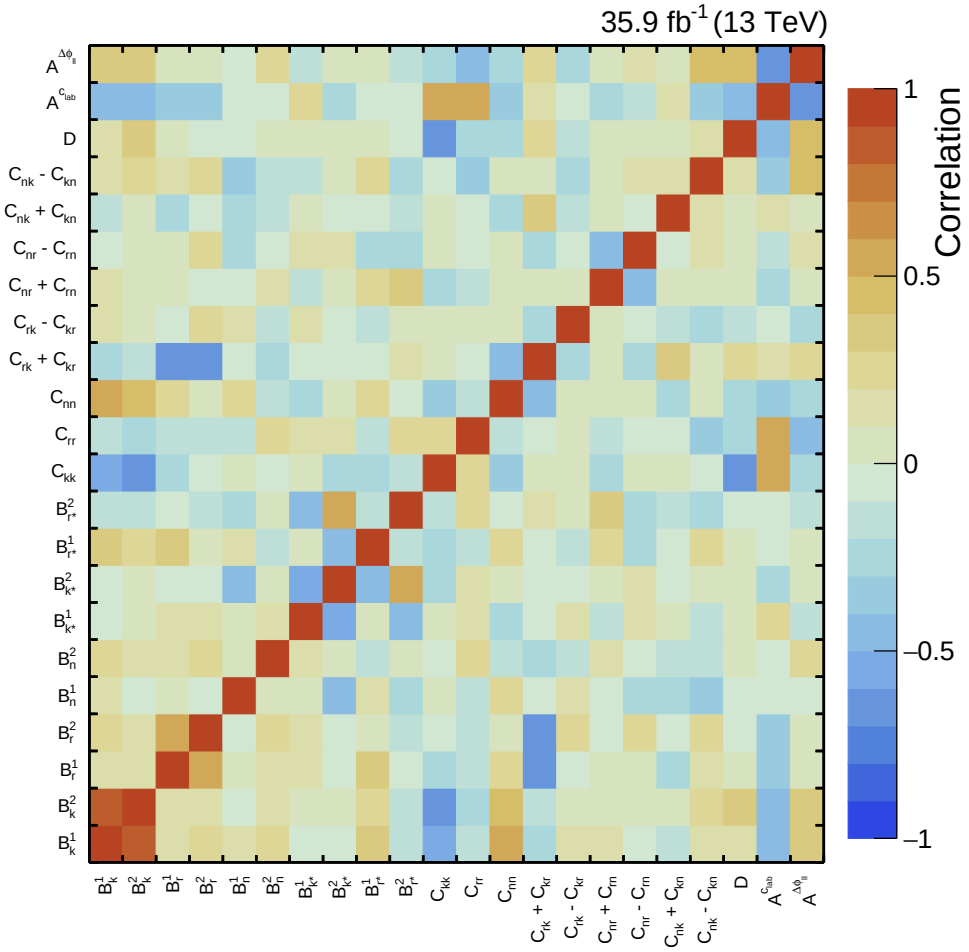

Figure 8.29: The systematic correlation matrix for the measured coefficients.

as they are expected to be small. The measured f_{SM} values are all compatible with 1, as expected considering the spin coefficient values presented in Table 8.2.

8.5 Constraints on Effective Field Theory Operators

As discussed in Section 2.4, one approach to probing BSM physics is the EFT. Due to the assumed higher scale where BSM effects are directly manifested in this approach, only subtle deviations from the SM predictions are accessible to us. In this section, constraints placed on EFT operators that are relevant to hadronic $t\bar{t}$ production using the polarization and spin correlation measurements are discussed. We will be encountering two kinds of fit; simulation-based and analytical, based on the source of the EFT predictions that are used in the fit. As the simulation-based fit is chronologically the first one pursued, some of the discussion will be dedicated to setting up the final fit procedure that makes the most of our measurement, which is then directly adopted in the analytical fit.

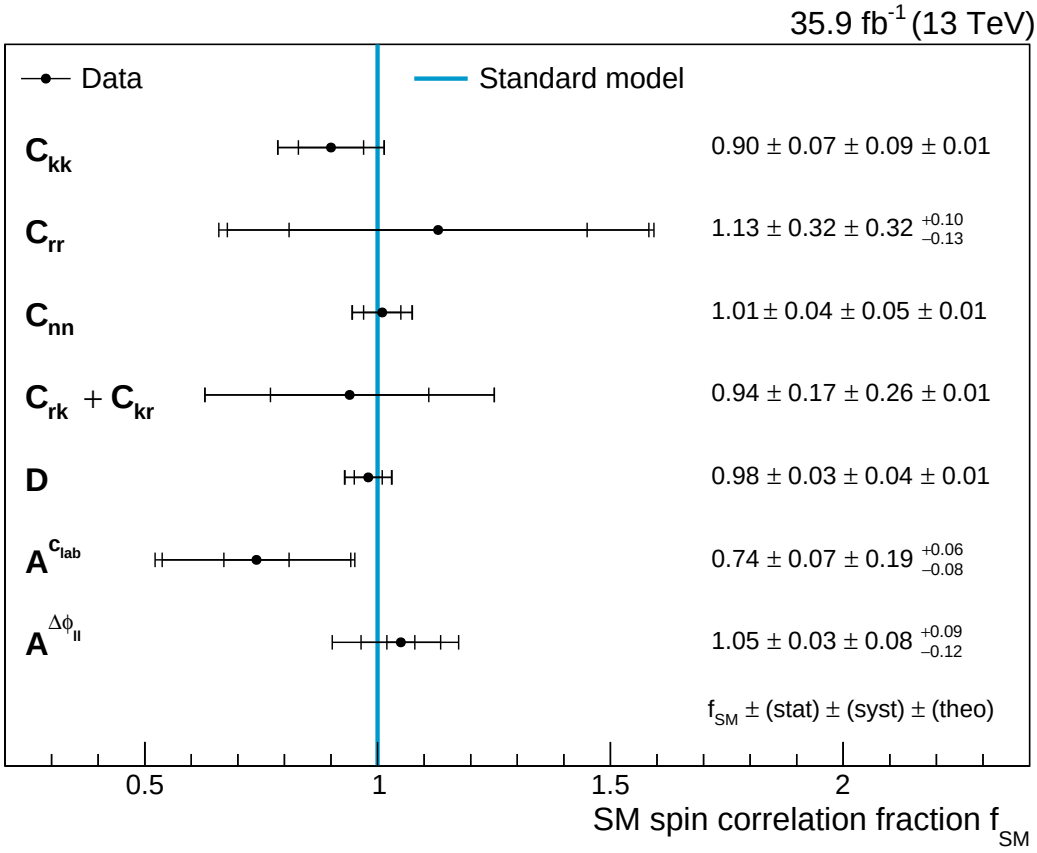

Figure 8.30: Measured values of f_{SM}, obtained from the measured values of C_{ii}, $C_{rk} + C_{kr}$, D and laboratory frame asymmetries.

8.5.1 Simulation

The operator to be constrained in the simulation-based fit is called $\mathcal{O}_{tG}$, whose contribution is parametrized by the complex Wilson coefficient C_{tG}. The real part of $\mathcal{O}_{tG}$ models the chromomagnetic dipole moment (CMDM) of the top quark that arises from the interplay of its spin and color charge [12, 15]. At the observable level, this operator modifies the $t\bar{t}$ production rate and spin coefficients, making our measurement ideal to constrain its contribution. In this fit we make the assumption that the imaginary part of C_{tG} that models the top quark chromoelectric dipole moment (CEDM) is zero[7]. For the sake of simplicity, from this point onwards we will use C_{tG} to refer only to the real part of the Wilson coefficient. The imaginary part will be referred to as C_{tG}^{I}. $\mathcal{O}_{tG}$ takes the form [17]:

$$\mathcal{O}_{tG} = Y_t g_s \left(\bar{Q}\sigma^{\mu\nu}T^a t\right)\tilde{\phi}\, G^a_{\mu\nu} \tag{8.20}$$

where Y_t denotes the Yukawa coupling of the top quark, g_s the strong coupling constant ($g_s = 2\sqrt{\pi\alpha_s}$), Q the left-handed third-generation quark doublet, T^a the Gell-Mann matrices divided by 2, t the right-handed top quark singlet, $\tilde{\phi}$ the charge-conjugated Higgs doublet

[7] We do not make this assumption in the analytical fit and there we will see that this assumption is compatible with its results.

field and $G^a_{\mu\nu}$ the gluon field strength tensor. As the contribution of any EFT operator is affected also by the EFT scale Λ, it is C_{tG}/Λ^2 that is constrained in this analysis.

The simulation is done using MG5_aMC@NLO with both the SM and $\mathcal{O}_{tG}$ contributions evaluated at NLO QCD accuracy, with the value of Λ set to 1 TeV. The PDF set used is `NNPDF30_nlo_as_0118`. Showering and hadronization are handled by PYTHIA8. SM + $\mathcal{O}_{tG}$ samples at three different C_{tG}/Λ^2 points are generated, from which the predictions at any value of C_{tG}/Λ^2 are obtained through an interpolation procedure. The SM + $\mathcal{O}_{tG}$ samples are assigned rates as provided by the generator multiplied by 1.22; this factor is obtained by taking the ratio between the NNLO $t\bar{t}$ rate of 831.76 pb [18] and the rate according to the generator. The $t\bar{t}$ rate as a function of C_{tG}/Λ^2 is shown in Figure 8.31 together with the rate measured in this analysis.

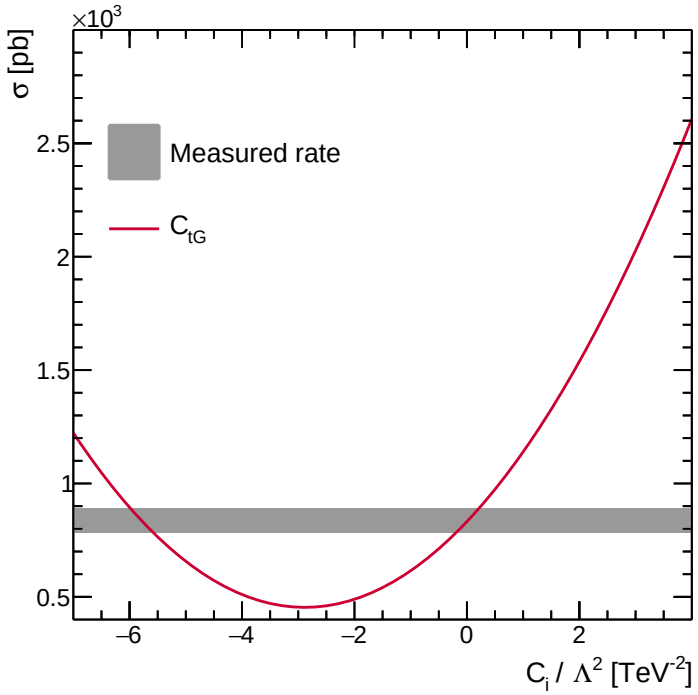

Figure 8.31: $t\bar{t}$ production rate as a function of C_{tG}/Λ^2 in comparison to the measured rate.

8.5.2 Template interpolation

Let us consider a process that is affected by N dimension-6 operators $\mathcal{O}_i$, which are limited to one EFT vertex insertion per diagram. The rate of the process is given by:

$$\sigma_{\text{SM+EFT}} = \sigma_{\text{SM}} + \sum_i \frac{C_i}{\Lambda^2}\sigma_i + \sum_{i,j} \frac{C_i C_j}{\Lambda^4}\sigma_{ij} \tag{8.21}$$

where σ_{SM} refers to the SM prediction of the rate and σ_i is the contribution due to $\mathcal{O}_i$. When N = 1, Equation 8.21 reduces to the familiar quadratic function of C_i/Λ^2. σ_i and σ_{ii} contributions that are linear and quadratic in C_i/Λ^2 can easily be determined if we have

the predicted $\sigma_{\mathrm{SM+EFT}}$ at three different values of C_i/Λ^2, which we denote as σ_0, σ_1 and σ_2 respectively. For technical convenience we restrict σ_0 to be the point where C_i/Λ^2 equals 0 TeV^{-2} i.e. the SM case. We then have:

$$\begin{aligned}\sigma_{\mathrm{SM}} &= \sigma_0 \\ \sigma_i &= \frac{\Lambda^2}{\mathrm{C}_1\mathrm{C}_2}\left[\frac{\mathrm{C}_2^2\sigma_1 - \mathrm{C}_1^2\sigma_2}{\mathrm{C}_2 - \mathrm{C}_1} - (\mathrm{C}_2 + \mathrm{C}_1)\,\sigma_0\right] \\ \sigma_{ii} &= \frac{\Lambda^4}{\mathrm{C}_1\mathrm{C}_2}\left[\sigma_0 - \frac{\mathrm{C}_2\sigma_1 - \mathrm{C}_1\sigma_2}{\mathrm{C}_2 - \mathrm{C}_1}\right]\end{aligned} \tag{8.22}$$

which can be scaled to obtain the prediction for $\sigma_{\mathrm{SM+EFT}}$ at any desired C_i/Λ^2 value. The values of σ_i and σ_{ii} for $\mathcal{O}_{\mathrm{tG}}$ used in the fits are reported in Table 8.5. When there are two operators to be interpolated one sees that, in addition to the five points needed to determine the linear and quadratic contributions of each operator, only one point is needed at nonzero $\mathrm{C}_i\mathrm{C}_j/\Lambda^4$ to account for the interference between $\mathcal{O}_i$ and $\mathcal{O}_j$. It is straightforward to see that (N + 1)(N + 2) / 2 predictions are needed to completely specify the contribution of N operators. When dealing with differential distributions, the interpolation simply needs to be done separately for each bin to account for the possibly different kinematical effects induced by each operator.

Table 8.5: Values of the linear and quadratic contribution of $\mathcal{O}_{\mathrm{tG}}$ used in the simulation-based fit.

Contribution	Cross section
SM	831.76 pb
σ_i	262.08 pb TeV^2
σ_{ii}	45.42 pb TeV^4

Two fits on $\mathrm{C}_{\mathrm{tG}}/\Lambda^2$ are performed; taking into account all contributions due to $\mathrm{C}_{\mathrm{tG}}/\Lambda^2$ and also only the one linear in $\mathrm{C}_{\mathrm{tG}}/\Lambda^2$. From order-of-magnitude estimates, one expects that the quadratic contribution to be suppressed by $1/\Lambda^2$ in comparison to the linear contribution. Furthermore, the quadratic contribution is of dimension 8 and one might be wary of including it while ignoring all other dimension-8 contributions. The choice to set two separate constraints is made out of the desire to refrain from making any assumption on the relative size of the linear and quadratic contributions[8]; the resulting constraints will inform us of that. If the initial estimate is correct, then the quadratic term will have a negligible impact on the result, while a significant difference in the two constraints indicates the need for a more complete picture before any conclusion can be drawn. In addition, the quadratic term guarantees that the rate is positive everywhere in the phase space. The fit taking both

[8]Recall that the linear contribution is due to the interference between the SM and EFT diagrams; the $1/\Lambda^2$-based estimate of the suppression implicitly assumes that the SM contribution is large. When it is not - e.g. for some operators affecting non-QCD $\mathrm{t\bar{t}}$ production - the quadratic contributions can be and often are significant with respect to the linear one.

the linear and quadratic contributions into account will be labeled as the 'all' fit, while the fit that neglects the quadratic contribution will be labeled as 'linear'.

8.5.3 Fit strategy and result

C_{tG}/Λ^2 is constrained through χ^2 minimazation i.e. least squares method:

$$\chi^2 = \sum_i^N \sum_j^N \Big(\text{data}_i - \text{pred}_i\Big) \cdot \Big(\text{data}_j - \text{pred}_j\Big) \cdot V_{ij}^{-1} \tag{8.23}$$

where data_i and pred_i are the measured and predicted differential cross sections in bin i - either absolute or normalized - and V_{ij}^{-1} is the relevant element of the inverse of the corresponding total covariance matrix. Assuming Gaussian probability density functions for the uncertainties in the unfolded data, constraints at given CLs can be estimated from the values of C_{tG}/Λ^2 for which the $\Delta\chi^2$ reaches certain values. The $\Delta\chi^2$ is defined as the change in χ^2 from its minimum value.

As $\mathcal{O}_{tG}$ alters both the rate and spin coefficients, it seems natural to constrain it using the absolute differential measurement. However, we will exclude the laboratory frame observables right from the beginning. This decision is made considering the unknown analytical forms of these observables, which prevents an analytical fit to be made. Among the remaining observables, which is the most sensitive to C_{tG}/Λ^2 can be idenfitied by performing the fit, considering only one distribution at a time. The result when using the SM pseudodata is shown in Figure 8.32.

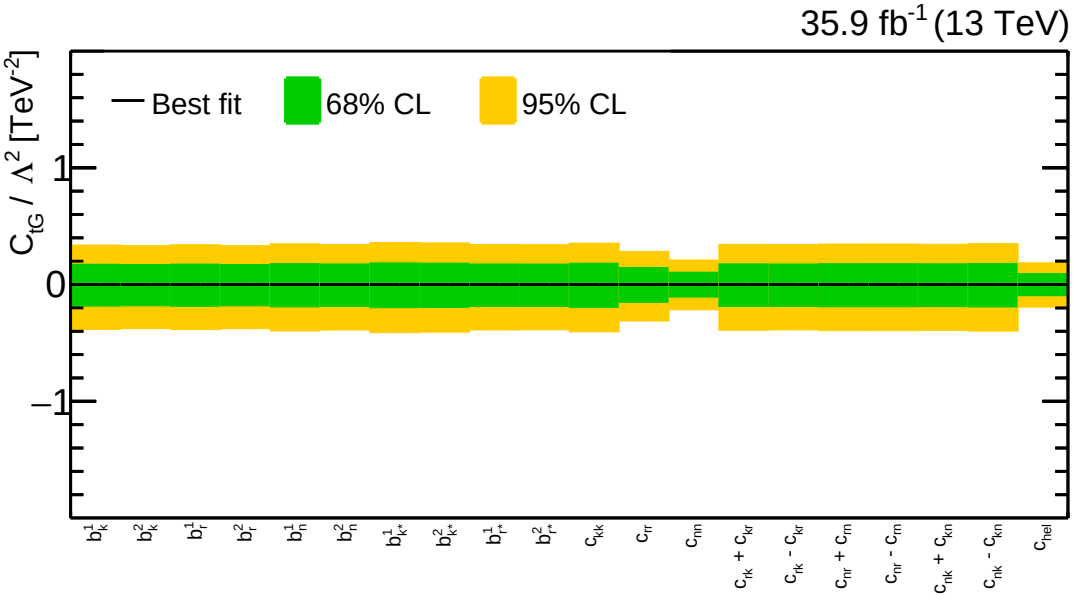

Figure 8.32: Fits on C_{tG}/Λ^2 ('all') using individual distributions of the absolute differential measurement and pseudodata.

From Figure 8.32, it is clear that c_{hel} distribution is the most sensitive observable (fit

result: $C_{tG}/\Lambda^2 = 0\ ^{+0.09}_{-0.10} \pm 0.19\ \text{TeV}^{-2}$ where the first uncertainties are from the 68% CL band and the second from the 95% CL band). However, we recall that the covariance matrices estimated in this measurement encode the correlations between all pair of bins in all distributions. This allows more than one distributions to be used in the fit, increasing our sensitivity. However, before we go into combining all 20 distributions into one fit, let us ponder for a moment on the proper way for measurements to be combined.

Since the considered observables are all angles constructed in the $\{k, r, n\}$ system and sums and products thereof, they are not entirely independent from each other. For example, b^a_k, b^a_r and b^a_n are related to each other by $\sum_{i\in\{k,r,n\}}(b^a_i)^2 = 1$. Similarly, $c_{hel} = -\sum c_{ii}$. To ensure that the set consists only of independent observables, four distributions are chosen from the predictions corresponding to the four dimensions in Equation 2.9, excluding the known intradependent combinations. The motivation for doing so and the procedure for choosing the distributions to be used in the fit is described in Appendix F. In the C_{tG} fit, the distributions used are c_{kk}, c_{nn}, $c_{rk} + c_{kr}$ and c_{hel}.

Another consideration is the following. When combining measurements e.g. by using the BLUE method, it is important that their correlations are correctly accounted for. When correlations are high, it is very important that the correlations are correctly estimated. This is because, as shown in Reference [19], combinations of measurements yield a more precise result only when the individual measurements are not perfectly correlated. As indicated by the systematic covariance matrix of the absolute measurement (see Figure 8.23), the correlations between pairs of bins are high. Since they are mostly due to the effect the systematic sources have on total rates, it is instructive to look at the correlation between the total rates measured through individual distributions of the absolute measurement. The total correlation matrix is shown in Figure 8.33.

The correlations are extremely high, but not perfect as would be expected when considering the reconstructed distributions all share the same set of events. This can be understood when considering that the response matrix M is estimated using simulation of finite size. This means that all components of M are estimated at less-than-perfect accuracy, which is then propagated through the unfolding procedure to the covariance matrices. Since combinations of measurements lead to improvements only if the individual measurements are not perfectly correlated, it is certain that any improvements obtained in combining the absolute measurements are partially spurious, being an artifact of the unfolding procedure.

The normalized measurements do not suffer from this problem, making it suitable for combinations of distributions[9]. Rate information can be incorporated easily by adding a term in Equation 8.23, which is assumed to be uncorrelated with all terms corresponding to the fraction of events in the bin. The result of such a combined shape + rate fit using real data is shown in Figure 8.34.

[9]In using the normalized measurements, one bin has to be dropped from the fit for the covariance matrix to be invertible. This is because the distributions sum up to 1 by construction; any given bin is linearly dependent on the others. While the choice of which bin that is dropped does not affect the result, for specificity we mention that the second bin of each distribution is dropped when normalized measurements are used.

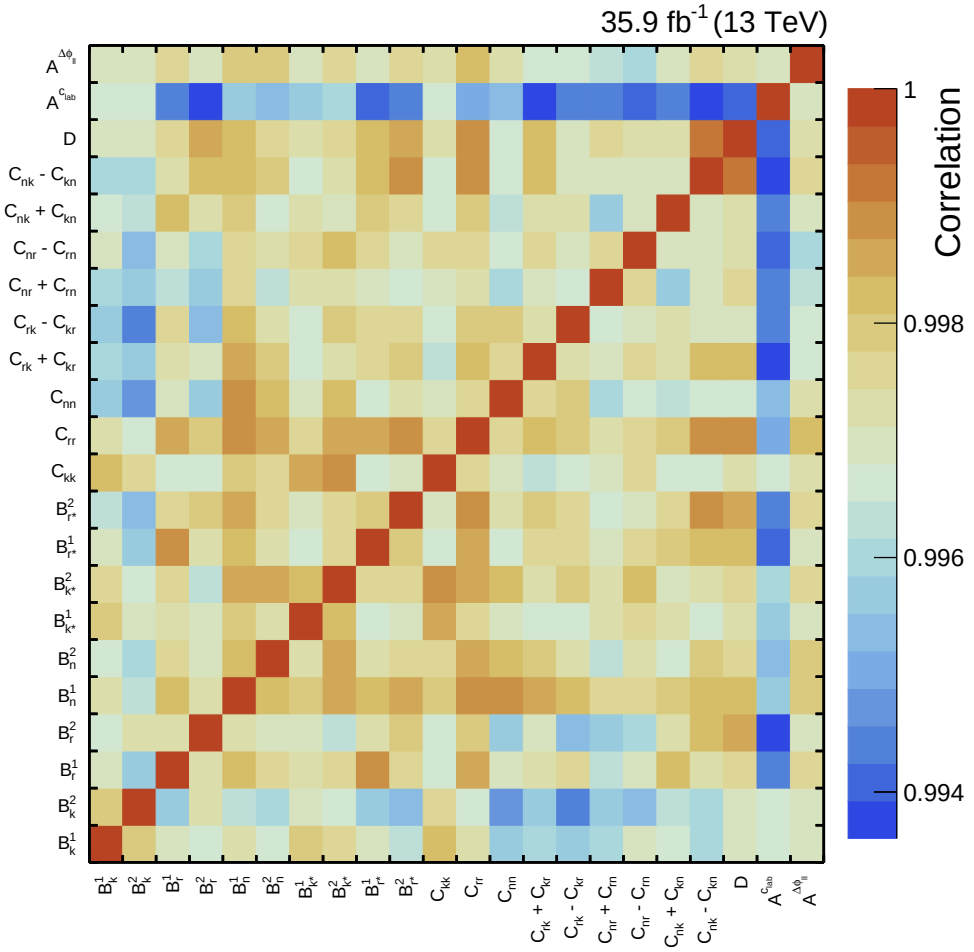

Figure 8.33: The correlation matrix between measured total rates in the absolute differential measurement.

Before commenting on the result, let us comment on the two additional curves with label 'theory' in addition to the nominal parabolas in Figure 8.34. Since the theoretical uncertainties do not have a clear frequentist interpretation, we choose to report their impacts in the form of separate fits instead. Six scenarios where μ_R and μ_F are varied[10] by factors of 2 and 0.5 are separatedly fitted and the fits that lead to the largest deviation in the best fit value with respect to the nominal one in both directions are taken to be the impact of theoretical uncertainties on C_{tG}/Λ^2. The theoretical uncertainties on the rate is accounted for by varying the rate by $+5.8\%$ and -6.1%, which is assumed to vary in the same way for the SM and C_{tG}/Λ^2 contributions.

The result of the 'all' part, where the third uncertainties are theoretical, is $C_{tG}/\Lambda^2 = 0.05\ ^{+0.08}_{-0.07} \pm 0.15\ ^{+0.05}_{-0.06}$ TeV^{-2} (with χ^2 / N_{DF} of 8.0 / 20). This is significantly more sensitive than the fit using single distributions. The result of the 'all' fit is very close to the 'linear' one, demonstrating the small impact of the quadratic C_{tG}/Λ^2 contribution. However, we

[10] As before, we do not consider variations where μ_R and μ_F are simultaneously varied in opposite directions.

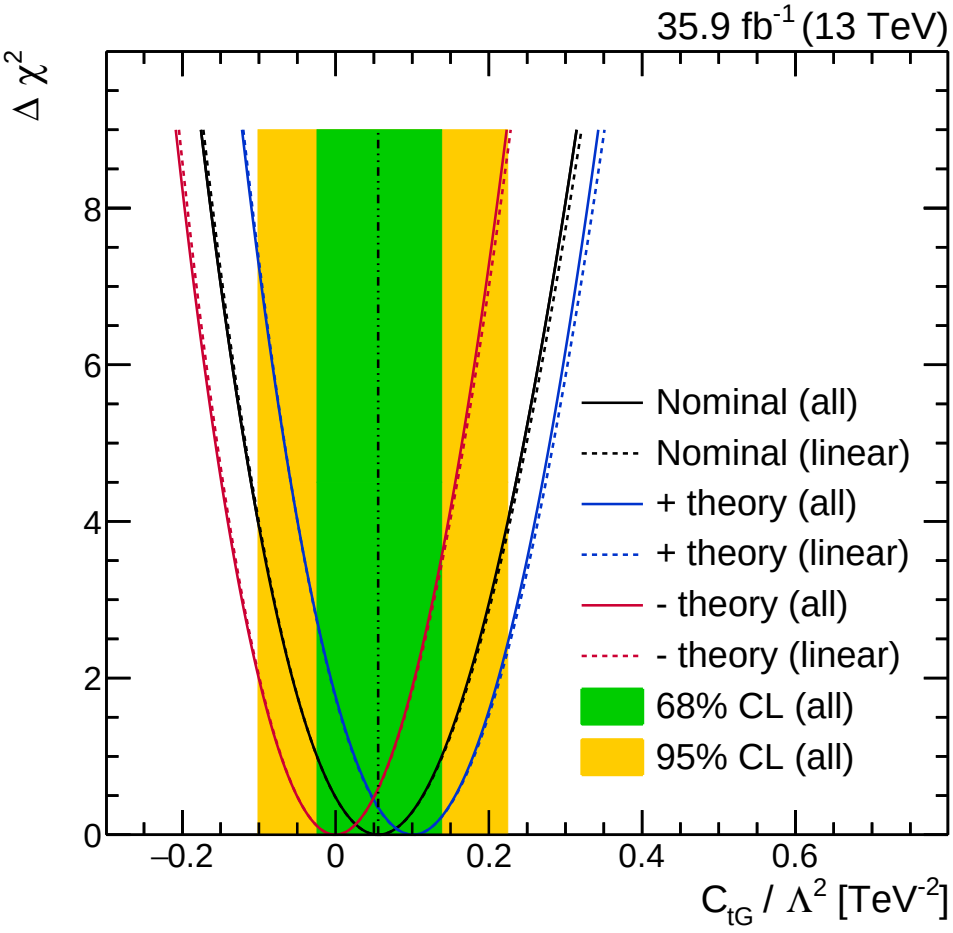

Figure 8.34: Result of combined shape + rate fit on C_{tG}/Λ^2.

note that the theoretical uncertainties are consistent with having being caused by the rate variation alone. It is therefore interesting to check how much the rate information contributes to our sensitivity. The result of the shape fit is shown in Figure 8.35. The result of the 'all' part of this fit is $C_{tG}/\Lambda^2 = 0.06 \pm 0.08\ ^{+0.17}_{-0.16}\ ^{+0.02}_{-0.03}$ TeV^{-2} (with χ^2 / N_{DF} of 8.0 / 19), from which it can be seen that the rate information provides only a small gain in sensitivity while at the same time increases the theoretical uncertainties. From this we conclude that the fit is best performed using the normalized differential measurements alone, without the inclusion of rate information.

8.5.4 Analytical fit

$\mathcal{O}_{tG}$ is not the only dimension-6 operator that is relevant to hadronic $t\bar{t}$ production. There are eleven independent operators, whose properties are summarized in Table 8.6. A more detailed discussion of these operators and predictions of their contributions can be found in Reference [12]. All of them except $\hat{c}_{AA}$ affect the $t\bar{t}$ spin density matrix, allowing constraints to be set using our measurements.

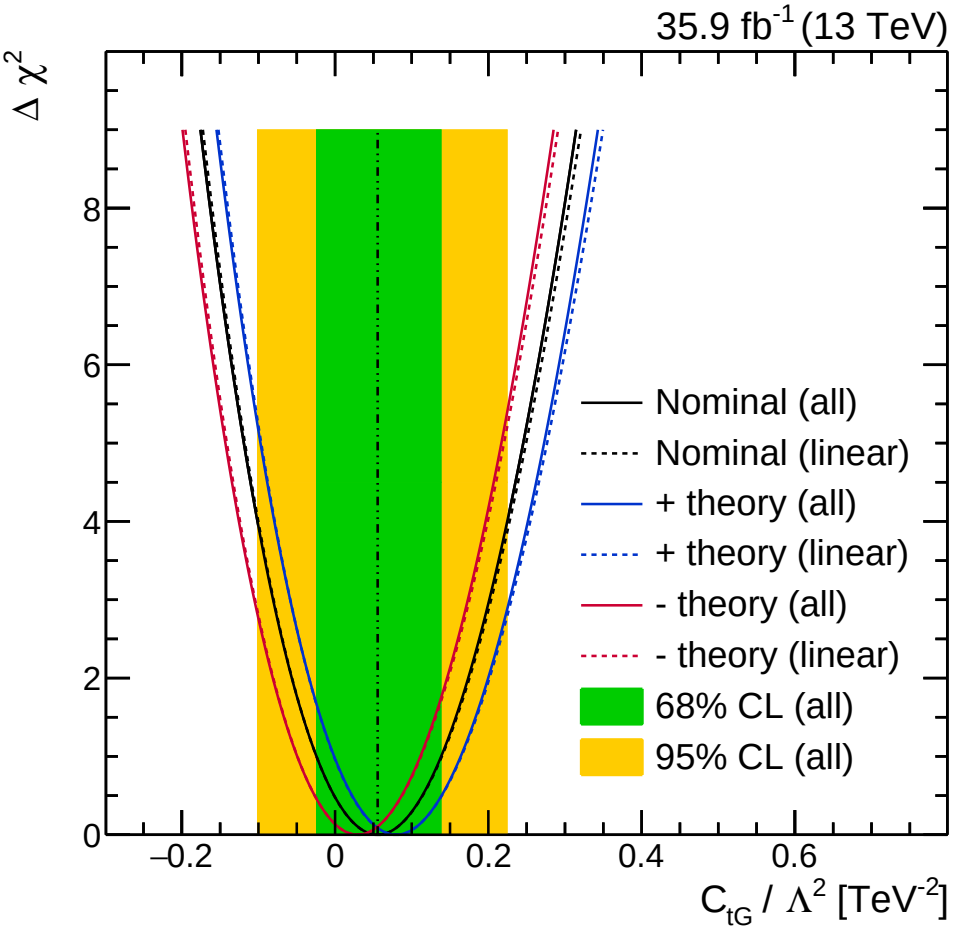

Figure 8.35: Result of combined shape fit on C_{tG}/Λ^2.

$\hat{\mu}_t$ and $\hat{d}_t$ are the coupling parameters that model the top quark CMDM and CEDM contributions; they can be directly translated into C_{tG} and C^I_{tG} using the relationships $C_{tG}/\Lambda^2 = \hat{\mu}_t/(2m_t^2)$ and $C^I_{tG}/\Lambda^2 = \hat{d}_t/(2m_t^2)$ respectively. There are two further CP-odd operators involving two top quarks and up to three gluons ($\hat{c}_{--}$ and $\hat{c}_{-+}$). The operators associated with the remaining couplings represent CP-even four-quark interactions with weak isospin quantum numbers either 0 or 1. $\hat{c}_{AA}$ is constrained by measurements of the $t\bar{t}$ charge asymmetry and is not relevant for our purposes [12].

In Reference [12], the predictions are provided as conversion factors that modify a set of spin coefficients affected by the operator, considering only their linear contributions. We start by computing the value of the spin coefficients receiving a contribution c_i with a spin scaling factor s_i as:

$$C^{SM+EFT} = C^{SM} + \sum c_i s_i \tag{8.24}$$

The predicted values of s_i for each operator, reproduced from Reference [12], are given in Tables 8.7 and Table 8.8. Constraints are then set through deviations of the measured coefficients with respect to the SM prediction, where in this case the NLO calculation is used.

Table 8.6: Coupling parameters of dimension-6 operators relevant to hadronic $t\bar{t}$ production and their properties.

Operator	Type	Symmetry properties
$\hat{\mu}_t$	2 quark plus gluon	P-even, CP-even
$\hat{d}_t$	2 quark plus gluon	P-odd, CP-odd
$\hat{c}_{--}$	2 quark plus gluon	P-odd, CP-odd
$\hat{c}_{-+}$	2 quark plus gluon	P-even, CP-odd
$\hat{c}_{VV}$	4 quark (weak isospin 0)	P-even, CP-even
$\hat{c}_{VA}$	4 quark (weak isospin 0)	P-odd, CP-even
$\hat{c}_{AV}$	4 quark (weak isospin 0)	P-odd, CP-even
$\hat{c}_{AA}$	4 quark (weak isospin 0)	P-even, CP-even
$\hat{c}_1$	4 quark (weak isospin 1)	CP-even
$\hat{c}_3$	4 quark (weak isospin 1)	CP-even
$\hat{c}_1 - \hat{c}_2 + \hat{c}_3$	4 quark (weak isospin 1)	CP-even

The constraints obtained in this way is reported in Table 8.9, where in all cases only the spin coefficient that results in the tightest constraint on a given operator is used. The theoretical uncertainties are due to simultaneous μ_R and μ_F scale variations by factors of 2 and 0.5, with the default scale choice being $\mu_R = \mu_F = m_t$.

Before moving into the interpretation of these results, let us first discuss ways to improve the constraints. From the simulation-based C_{tG} fit we saw that this can be done by fitting multiple distributions simultaneously instead of only the most sensitive coefficient. To do this, the coefficients are expanded into shapes by assigning to each bin a content of:

$$\frac{\int_{\text{bin}} g(x;\text{C})\ \text{d}x}{\Delta_{\text{bin}} \int_{\text{full}} g(x;\text{C})\ \text{d}x} \tag{8.25}$$

where $g(x;\text{C})$ is the familar form of spin correlation observables (see Table 2.2). In this approach, no simulated samples are necessary for setting the constraints. We can expand the predictions on the spin coefficients analytically due to the particularly simple form of our observables, avoiding issues such as costly generation and storage resources or finite sample size while at the same time benefiting from the full power of the combined shape fits. This benefit is particularly significant for many of the operators listed in Table 8.6 for whom no MC generator is available at NLO QCD accuracy e.g. all the CP-odd operators. For consistency's sake, in these fits the prediction for SM is also expanded from the analytical predictions instead of taken from simulation.

Table 8.7: The predicted spin scaling factors for operators in Table 8.6 that affect the $\vec{B}_a$ vectors. The upper and lower uncertainties are from varying the default scales $\mu_R = \mu_F = m_t$ by factors of 2 and 0.5 respectively.

Coefficient	$\hat{c}_{VA}$	$\hat{c}_3$	$\hat{c}_{AV}$	$\hat{c}_1 - \hat{c}_2 + \hat{c}_3$	$\hat{c}_{-+}$
B^1_k	$0.8035^{+0.0255}_{-0.0260}$	0.1005 ± 0.0045	-	-	-
B^2_k	$0.8035^{+0.0255}_{-0.0260}$	0.1005 ± 0.0045	-	-	-
B^1_r	0.1050 ± 0.0045	0.01275 ± 0.0007	-	-	-
B^2_r	0.1050 ± 0.0045	0.01275 ± 0.0007	-	-	-
B^1_n	-	-	-	-	$2.438^{-0.062}_{+0.054}$
B^2_n	-	-	-	-	$-2.438^{+0.062}_{-0.054}$
$B^1_{k^*}$	-	-	0.4415 ± 0.0170	0.0915 ± 0.0040	-
$B^2_{k^*}$	-	-	0.4415 ± 0.0170	0.0915 ± 0.0040	-
$B^1_{r^*}$	-	-	$0.3960^{+0.0200}_{-0.0195}$	0.0820 ± 0.0045	-
$B^2_{r^*}$	-	-	$0.3960^{+0.0200}_{-0.0195}$	0.0820 ± 0.0045	-

Table 8.8: The predicted spin scaling factors for operators in Table 8.6 that affect the elements of C matrix. The upper and lower uncertainties are from varying the default scales $\mu_R = \mu_F = m_t$ by factors of 2 and 0.5 respectively. The spin scaling factors for D of all operators are computed as in Table 2.2.

Coefficient	$\hat{\mu}_t$	$\hat{c}_{VV}$	$\hat{c}_1$	$\hat{d}_t$	$\hat{c}_{--}$
C_{kk}	0.917 ± 0.006	$-1.218^{-0.040}_{+0.039}$	-0.151 ∓ 0.007	-	-
C_{rr}	$2.475^{-0.019}_{+0.020}$	-0.697 ∓ 0.027	$-0.0846^{-0.0043}_{+0.0041}$	-	-
C_{nn}	$2.025^{-0.024}_{+0.025}$	$-0.0799^{-0.0085}_{+0.0080}$	$-0.00821^{-0.00108}_{+0.00099}$	-	-
$C_{rk} + C_{kr}$	$0.740^{+0.001}_{-0.002}$	-0.306 ∓ 0.014	-0.0358 ∓ 0.0020	-	-
$C_{rk} - C_{kr}$	-	-	-	-	-
$C_{nr} + C_{rn}$	-	-	-	-	-
$C_{nr} - C_{rn}$	-	-	-	$-4.143^{+0.053}_{-0.056}$	$-1.226^{-0.004}_{+0.007}$
$C_{nk} + C_{kn}$	-	-	-	-	-
$C_{nk} - C_{kn}$	-	-	-	$-0.800^{+0.006}_{-0.003}$	$-2.157^{+0.108}_{-0.087}$

Table 8.9: Constraints on operators from Table 8.6 using the measured spin coefficients from Table 8.2. Theoretical uncertainties that are much smaller than experimental uncertainties are reported as 0.

Operator	Coefficient	Best fit ± stat. ± syst. ± theo.	95% CL
$\hat{\mu}_{\mathrm{t}}$	D	$-0.0032 \pm 0.0040 \pm 0.0048\ ^{+0.0004}_{-0.0007}$	$-0.0157 < \hat{\mu}_{\mathrm{t}} < 0.0093$
$\hat{d}_{\mathrm{t}}$	$\mathrm{C_{nr}} - \mathrm{C_{rn}}$	$0.0002 \pm 0.0068 \pm 0.0060 \pm 0$	$-0.0180 < \hat{d}_{\mathrm{t}} < 0.0184$
$\hat{c}_{--}$	$\mathrm{C_{nk}} - \mathrm{C_{kn}}$	$-0.0187 \pm 0.0114 \pm 0.0076\ ^{+0.0008}_{-0.0009}$	$-0.0460 < \hat{c}_{--} < 0.0086$
$\hat{c}_{-+}$	$\mathrm{B^1_n}$- $\mathrm{B^2_n}$	$-0.002 \pm 0.003 \pm 0.003 \pm 0$	$-0.010 < \hat{c}_{-+} < 0.006$
$\hat{c}_{\mathrm{VV}}$	D	$0.009 \pm 0.011 \pm 0.013\ ^{+0.002}_{-0.001}$	$-0.025 < \hat{c}_{\mathrm{VV}} < 0.043$
$\hat{c}_{\mathrm{VA}}$	$\mathrm{B^1_k} + \mathrm{B^2_k}$	$0.003 \pm 0.008 \pm 0.025\ ^{+0.001}_{-0.002}$	$-0.050 < \hat{c}_{\mathrm{VA}} < 0.056$
$\hat{c}_{\mathrm{AV}}$	$\mathrm{B^1_{k^*}} + \mathrm{B^2_{k^*}}$	$-0.011 \pm 0.018 \pm 0.014\ ^{+0.001}_{-0.001}$	$-0.057 < \hat{c}_{\mathrm{AV}} < 0.035$
$\hat{c}_1$	D	$0.07 \pm 0.09 \pm 0.11\ ^{+0.02}_{-0.01}$	$-0.21 < \hat{c}_1 < 0.35$
$\hat{c}_3$	$\mathrm{B^1_k} + \mathrm{B^2_k}$	$0.02 \pm 0.07 \pm 0.21\ ^{+0.01}_{-0.02}$	$-0.40 < \hat{c}_3 < 0.44$
$\hat{c}_1 - \hat{c}_2 + \hat{c}_3$	$\mathrm{B^1_{k^*}} + \mathrm{B^2_{k^*}}$	$-0.052 \pm 0.088 \pm 0.067\ ^{+0.006}_{-0.006}$	$-0.274 < \hat{c}_1 - \hat{c}_2 + \hat{c}_3 < 0.169$

The results of the 1D fits, considering one operator at a time, are shown in tabular and graphical forms in Table 8.10 and Figure 8.36. Converting the $\hat{\mu}_t$ result to C_{tG}/Λ^2 using m_t of 173.34 GeV (to be consistent with the computations in Reference [12]), we find a constraint of $C_{tG}/\Lambda^2 = -0.09 \pm 0.08 \pm 0.15\ ^{+0.01}_{-0.02}$ TeV^{-2}, in agreement with the simulation-based fit in Figure 8.35. The single-coefficient $\hat{\mu}_t$ fit similarly agrees with the c_{hel} fit. This is expected since for single distributions the information content of the shapes and the coefficients is the same. The fact that the central values of both fits differ is due to the different SM predictions they use; the analytical fit uses the NLO calculation which includes the weak corrections, that the MG5_aMC@NLO simulation does not. For this reason, the NLO calculation is of greater accuracy, so we quote the C_{tG}/Λ^2 constraint from the analytical fit as our nominal constraint on C_{tG}/Λ^2. Our constraint on $\hat{d}_t$ translates to $C^I_{tG}/\Lambda^2 = -0.066 \pm 0.133\ ^{+0.265}_{-0.266} \pm 0.003$ TeV^{-2}. Another thing worth noting is that the theoretical uncertainties are typically smaller for the CP-odd operators when they are constrained using single coefficients. This is because the relevant coefficients are all predicted to be zero in the NLO calculation (see Table 8.2), meaning the theoretical uncertainties are purely from the EFT part which also approach zero together with the operator's best fit value. In the shape fits this is not the case as correlations between distributions are taken into account, leading to non-negligible theoretical uncertainties. Nevertheless the improved sensitivity from going to the shape fits still outweigh the increase in theoretical uncertainties as can be seen from the confidence interval (CI) width ratios in Table 8.10.

Having set the constraints for the cases of only one active operator at a time, we now turn to the higher dimensional scenarios. Setting the constraints allowing all ten to be active at once is an option, but we note that all the operators alter only a limited set of the spin coefficients, leaving the others unchanged from their SM values. Any operator combinations that alter different sets of coefficients (see Tables 8.7 and 8.8) would result in uncorrelated contraints when fitted together, in these cases the higher dimensional constraints offer us no additional insights beyond what we already learn from 1D fits. Two examples of such uncorrelated combinations are shown in Figure 8.37.

After removing all the uncorrelated combinations, we are left with six 2-operator combinations and one 3-operator combination. Focusing on the 2D combinations first, we see that three of them suffer from the opposite problem of high (anti-)correlation. One example, the $\hat{c}_{VV}$ - $\hat{c}_1$ pair, is shown in Figure 8.38. To understand how such high correlations arise, we consult the ratio between the contributions of this pairing, which are listed in Table 8.11. We see that $\hat{c}_{VV}$ and $\hat{c}_1$ are almost degenerate. When fitted together, contributions from one operator can cancel the other over a very wide range of both, leading to a very loose constraint.

Removing these 'blind directions'[11], only three 2-operator combinations remain. The 3-operator combination contains as its subset the highly correlated combination shown above and is sufficiently described by its constituent two 2-operator combinations. The results for the three combinations are shown in Figures 8.39, 8.40 and 8.41. These 2D constraints, together with the fits on individual operators reported in Table 8.10 and Figure 8.36, are considered to be a sufficient description of all ten operators relevant to hadronic $t\bar{t}$ production

[11] Specifically, they are the ($\hat{c}_{VV}$ - $\hat{c}_1$), ($\hat{c}_{VA}$ - $\hat{c}_3$) and ($\hat{c}_{AV}$ - $\hat{c}_1 - \hat{c}_2 + \hat{c}_3$) combinations.

Table 8.10: Results of the 1D shape fits considering one operator from Table 8.6 at a time and the improvement in sensitivity with respect to the single coefficient constraints (Table 8.9). The uncertainties are 68% and 95% CLs and theoretical. Theoretical uncertainties that are much smaller than experimental uncertainties are reported as 0.

Operator	Distribution	Constraint	χ^2 ($N_{DF} = 19$)	CI width ratio
$\hat{\mu}_t$	c_{kk}, c_{nn}, $c_{rk} + c_{kr}$, c_{hel}	$-0.0052 \pm 0.0046\ ^{+0.0092\ +0.0007}_{-0.0093\ -0.0011}$	7.2	1.35
$\hat{d}_t$	b^2_r, b^1_n, $c_{nr} - c_{rn}$, $c_{nk} - c_{kn}$	$-0.0040 \pm 0.0080 \pm 0.0160 \pm 0.0002$	8.5	1.14
$\hat{c}_{--}$	b^2_r, b^1_n, $c_{nr} - c_{rn}$, $c_{nk} - c_{kn}$	$-0.0169 \pm 0.0115 \pm 0.0230\ ^{+0.0006}_{-0.0008}$	6.6	1.19
$\hat{c}_{-+}$	b^1_n, b^2_n, $b^1_{r^*}$, $c_{nk} + c_{kn}$	$-0.002 \pm 0.003 \pm 0.007 \pm 0$	10.7	1.17
$\hat{c}_{VV}$	c_{kk}, c_{nn}, $c_{rk} + c_{kr}$, c_{hel}	$0.016 \pm 0.013 \pm 0.026\ ^{+0.005}_{-0.003}$	7.1	1.30
$\hat{c}_{VA}$	b^2_k, b^2_r, c_{kk}, $c_{nr} + c_{rn}$	$-0.009 \pm 0.018 \pm 0.035\ ^{+0.002}_{-0.003}$	9.3	1.50
$\hat{c}_{AV}$	$b^1_{k^*}$, $b^2_{k^*}$, $b^1_{r^*}$, $b^2_{r^*}$	$-0.001 \pm 0.017 \pm 0.033 \pm 0.001$	5.9	1.38
$\hat{c}_1$	c_{kk}, c_{nn}, $c_{rk} + c_{kr}$, c_{hel}	$0.13 \pm 0.11 \pm 0.21\ ^{+0.04}_{-0.03}$	7.1	1.31
$\hat{c}_3$	b^2_k, b^2_r, c_{kk}, $c_{nr} + c_{rn}$	$-0.07 \pm 0.14 \pm 0.28 \pm 0.02$	9.3	1.48
$\hat{c}_1 - \hat{c}_2 + \hat{c}_3$	$b^1_{k^*}$, $b^2_{k^*}$, $b^1_{r^*}$, $b^2_{r^*}$	$-0.007\ ^{+0.080}_{-0.081} \pm 0.161 \pm 0.005$	5.9	1.38

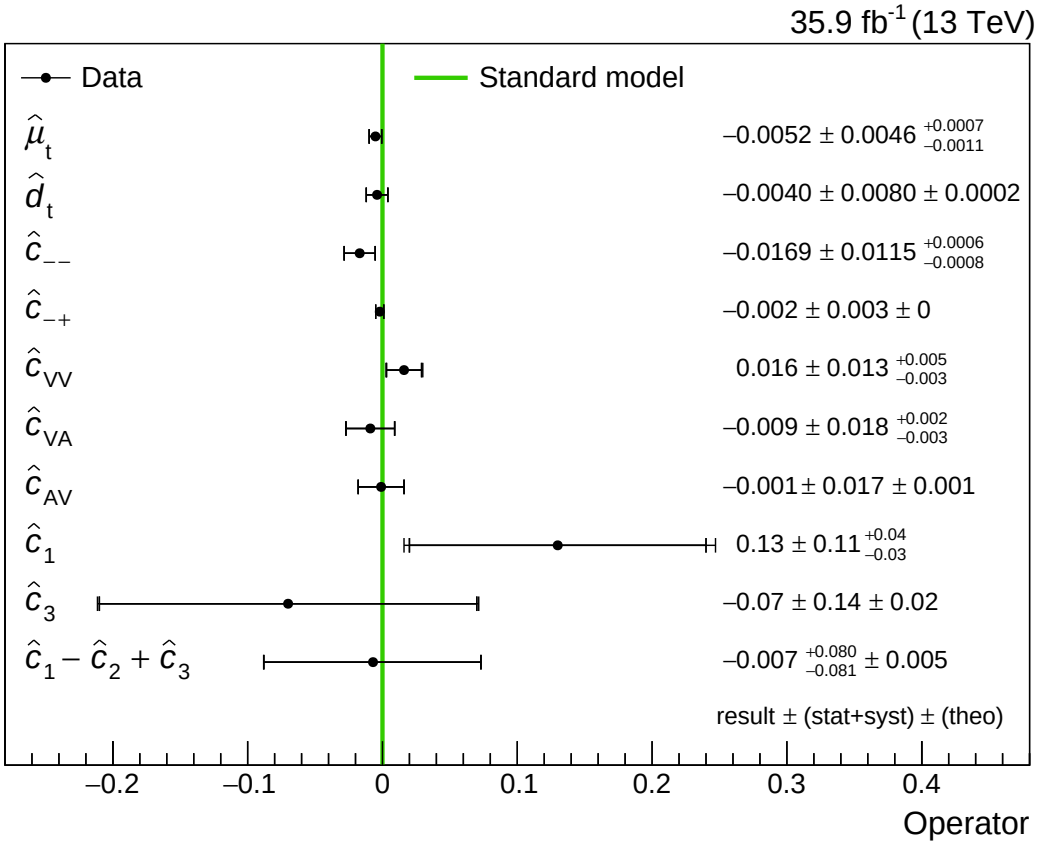

Figure 8.36: Results of the 1D shape fits considering one operator from Table 8.6 at a time. The uncertainties are 68% CL and theoretical. Theoretical uncertainties that are much smaller than experimental uncertainties are reported as 0.

Table 8.11: Ratio of contributions of the $\hat{c}_{VV}$ and $\hat{c}_1$ to the spin coefficients indicating the degeneracy between them.

Observable	$\hat{c}_{VV}/\hat{c}_1$
C_{kk}	8.1
C_{rr}	8.2
C_{nn}	9.7
D	8.2
$C_{rk} + C_{kr}$	8.5

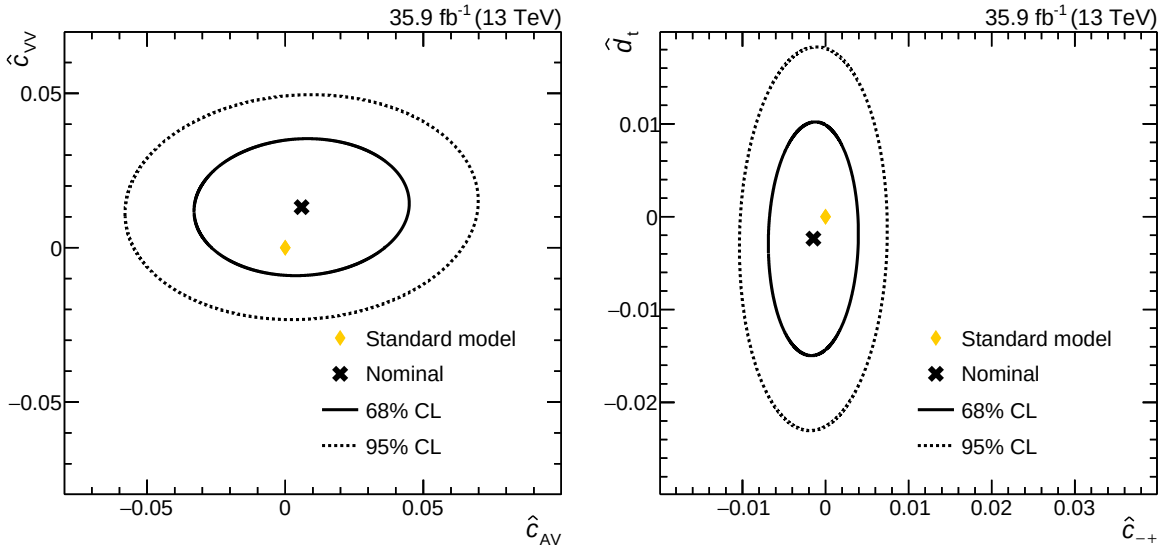

(a) Constraint on $\hat{c}_{\mathrm{VV}}$ - $\hat{c}_{\mathrm{AV}}$ plane

(b) Constraint on $\hat{d}_{\mathrm{t}}$ - $\hat{c}_{-+}$ plane

Figure 8.37: Example constraints on two 2-operator combinations that alter different sets of spin coefficients and are thus uncorrelated.

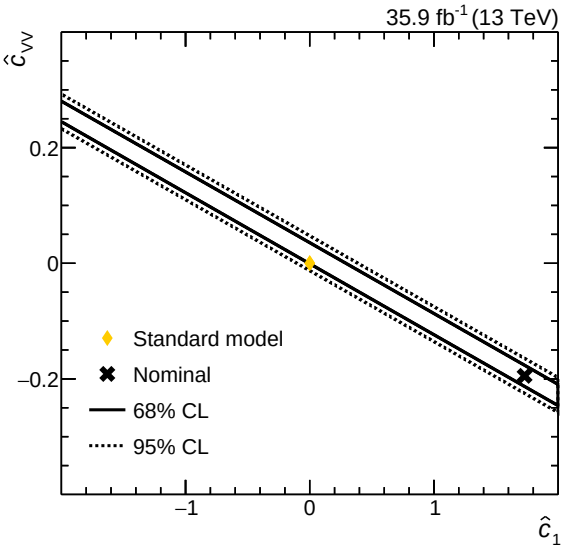

Figure 8.38: Constraint on $\hat{c}_{\mathrm{VV}}$ - $\hat{c}_1$ plane, one of the 2-operator combinations that alter the same set of spin coefficients in similar ways such that they are almost degenerate.

considered within the scope of our measurement.

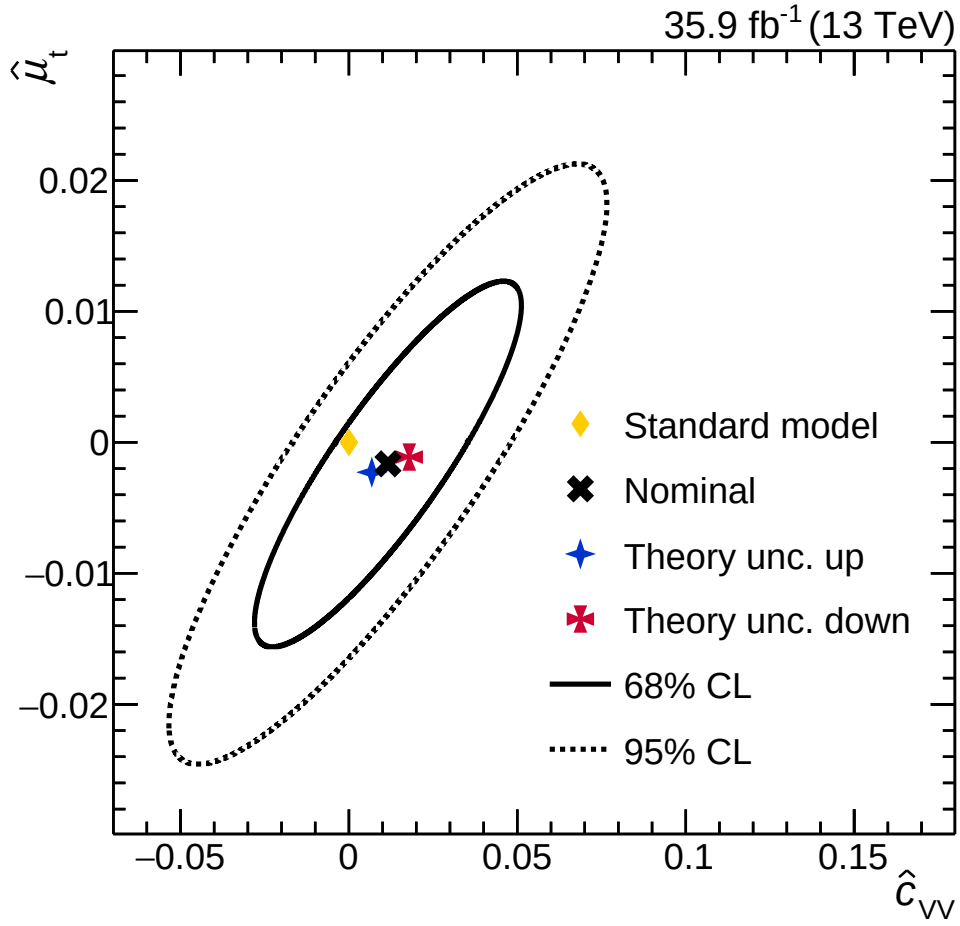

Figure 8.39: Constraint on the $\hat{\mu}_t$ - $\hat{c}_{VV}$ plane. 'Theory unc. up' and 'theory unc. down' refer to the best fit value when μ_R and μ_F are simultaneously increased or decreased by a factor of two. The distributions used in the fit are c_{kk}, c_{nn}, $c_{rk} + c_{kr}$ and c_{hel}.

8.5.5 Comparison with existing top quark CMDM and CEDM constraints

$\hat{\mu}_t$ and $\hat{d}_t$ have been the subject of investigation on many occassions since the discovery of the top quark in 1995 [20, 21]. The constraints on these two operators that we report in Figure 8.36 are therefore the latest in a series of effort to conclusively establish or rule out the existence of the top quark CMDM and CEDM. Here we make a comparison between our results and the constraints and projections that are available in the literature.

Given that our constraints are direct i.e. they are derived from direct measurements of the properties of the top quark, we start by comparing with other direct constraints. Through a fit on $t\bar{t}$ rate measurements, Reference [22] derived limits of $-0.007 < d_V < 0.002$ and $|d_A| < 0.038$ in the 5% LHC14 virtual-experiment scenario, which assumes that the $t\bar{t}$ rate will be measured with a precision of 5% in a future run of the LHC at $\sqrt{s}$ of 14 TeV. LHC 7 and 8

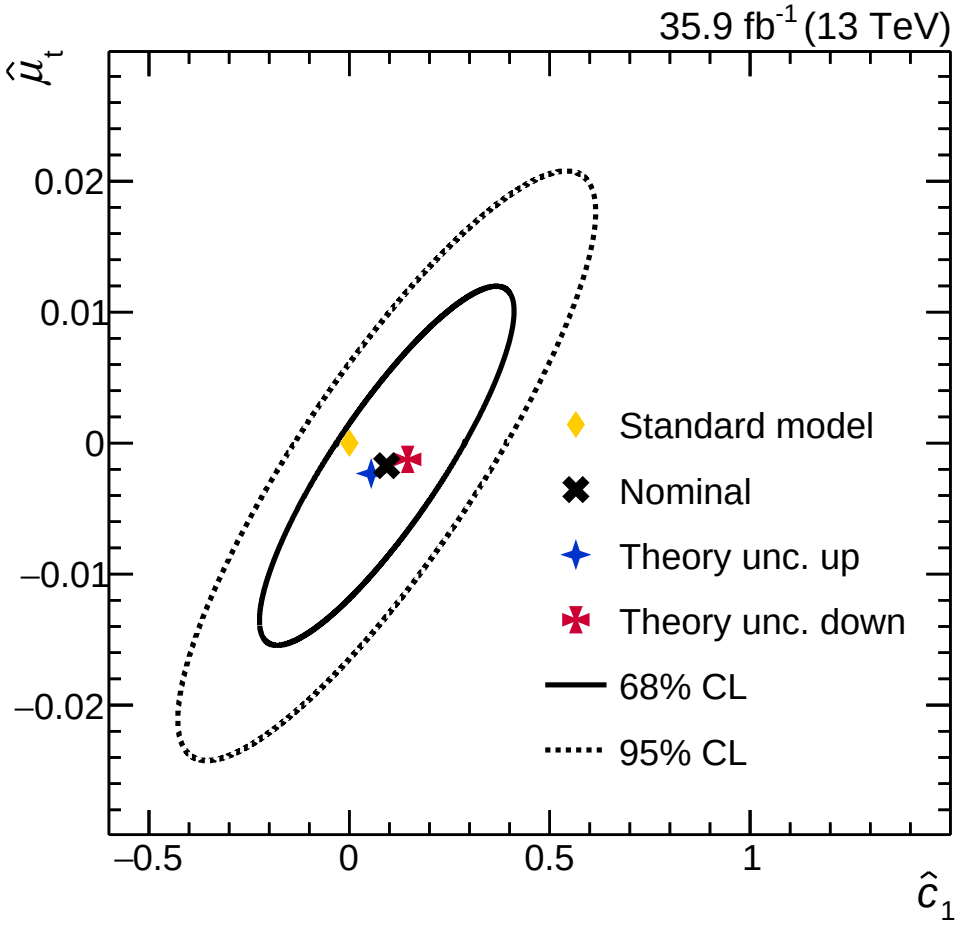

Figure 8.40: Constraint on the $\hat{\mu}_t$ - $\hat{c}_1$ plane. 'Theory unc. up' and 'theory unc. down' refer to the best fit value when μ_R and μ_F are simultaneously increased or decreased by a factor of two. The distributions used in the fit are c_{kk}, c_{nn}, $c_{rk} + c_{kr}$ and c_{hel}.

TeV data from the CMS and ATLAS experiments, together with the Tevatron data, are also used in the fit. Using the relationship $\hat{\mu}_t = -2d_V$ and $\hat{d}_t = -2d_A$, their results translate to limits of $-0.004 < \hat{\mu}_t < 0.014$ and $\left|\hat{d}_t\right| < 0.076$. Our $\hat{\mu}_t$ constraint of $-0.0145 < \hat{\mu}_t < 0.0040$ at 95% CL is of similar sensitivity, but is strictly within the scope of one measurement, without making any assumptions on the performance of a future machine. Our $\hat{d}_t$ constraint of $-0.020 < \hat{d}_t < 0.012$ on the other hand is almost four times stronger. This is easily understood; within the linear approximation $\hat{\mu}_t$ has a large impact on $t\bar{t}$ rate (see Table 8.5), which is not the case for $\hat{d}_t$.

Also through a fit on $t\bar{t}$ rate measurements, Reference [23] derived in the inclusive 14 TeV scenario, which is defined in a similar way as the above, limits of $-0.0086 < d_V < 0.0012$ and $|d_A| < 0.019$, which translates to $-0.0024 < \hat{\mu}_t < 0.0172$ and $\left|\hat{d}_t\right| < 0.038$. It has to be noted that contributions up to fourth order in d_V and d_A are taken into account in their fit, since they consider up to two insertion of EFT operators into a single diagram. As with the above, their $\hat{\mu}_t$ sensitivity is similar as ours, while our $\hat{d}_t$ constraint is stronger only by a factor of

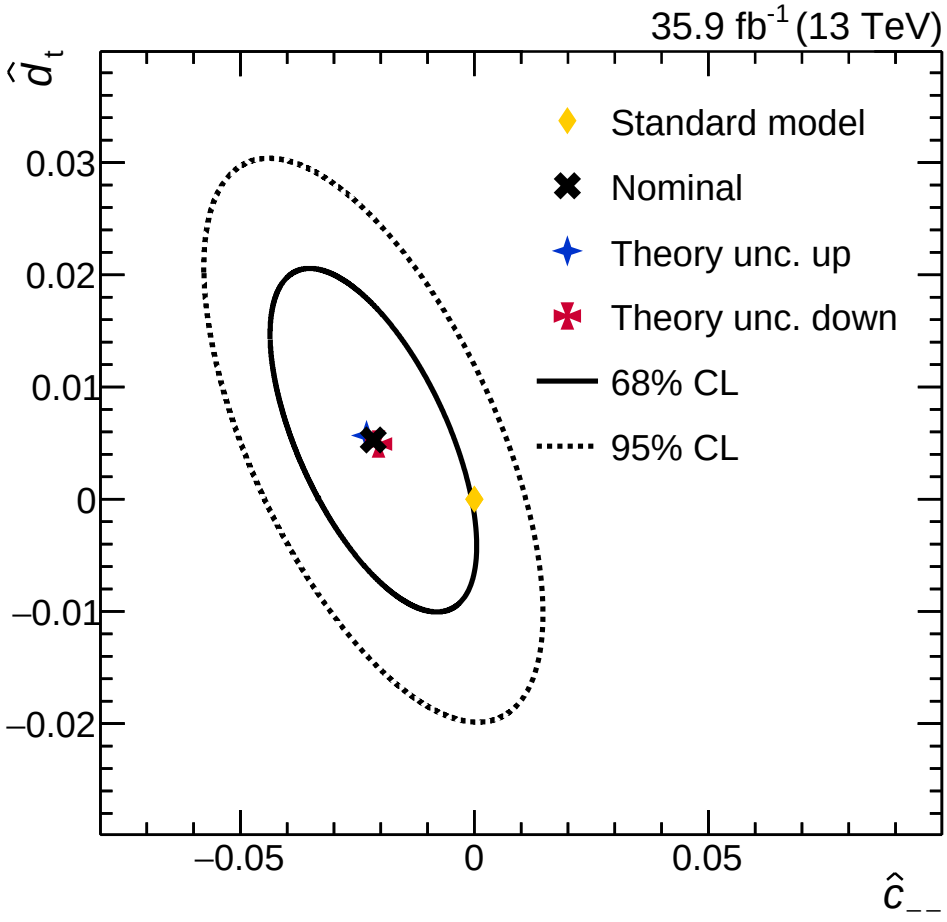

Figure 8.41: Constraint on the $\hat{d}_t$ - $\hat{c}_{--}$ plane. 'Theory unc. up' and 'theory unc. down' refer to the best fit value when μ_R and μ_F are simultaneously increased or decreased by a factor of two. The distributions used in the fit are b^2_r, b^1_n, $c_{nr} - c_{rn}$ and $c_{nk} - c_{kn}$.

two, since the inclusion of up to the quartic term increases their $\hat{d}_t$ sensitivity.

Reference [24] derived a limit of $D_5 < 5{\times}10^{-18}$ $g_s$cm through an analysis exploiting CP-odd observables that are similar to $c_{nk} - c_{kn}$ and $c_{nr} - c_{rn}$ that we measure in this work. D_5 is related to $\hat{d}_t$ by a factor of $1/m_t$. Using 1 /GeV $= 1.97327{\times}10^{-14}$ cm, our results translate to $(-2.26 < D_5 < 1.36) \times 10^{-18}$ g_s cm, which is more than two times stronger. Similarly, we find a limit on the parameter C_5 that is related to $\hat{\mu}_t$ as $(-1.64 < C_5 < 0.46) \times 10^{-18}$ g_s cm.

Finally, in regards to indirect constraints, our result of $-0.33 < C^I_{tG}/\Lambda^2 < 0.20$ TeV^{-2} is significantly weaker than the constraint of $\left|C^I_{tG}/\Lambda^2\right| < 0.007$ TeV^{-2} [25] that is derived from the experimental limit on the neutron electric dipole moment [26, 27]. However, given the indirect nature of the constraint, it is very sensitive to the assumptions made in deriving it, which may well be revised as new measurements become available. For completeness' sake, we mention that our C_{tG}/Λ^2 constraint is $-0.24 < C_{tG}/\Lambda^2 < 0.07$ TeV^{-2}.

From these comparisons it is seen that our results are the strongest direct constraints on $\hat{\mu}_t$ and $\hat{d}_t$ to date. Thus our measurement constitutes a substantial improvement over existing direct constraints, with improvements up to a factor of four compared to fits that include also projected future measurements among their inputs.

8.6 Summary and Outlook

A measurement of the top quark polarization and $t\bar{t}$ spin correlation, performed using 35.9 /fb of data recorded by the CMS experiment in 2016, has been presented. The dileptonic $t\bar{t}$ final state is targeted in this measurement because the spin analyzing power of the charged leptons from the top and antitop quark decay, respectively, is almost 100%. Events containing two isolated, oppositely charged electrons or muons and at least two jets, at least one of which is consistent with having been initiated by a b quark, are selected. A kinematic reconstruction algorithm is used to reconstruct the kinematics of the top quarks, which is based on a polynomial to recover the longitudinal momenta of the two neutrinos. The distributions of all observables that are directly sensitive to the elements of the top quark polarization vector and $t\bar{t}$ spin density matrix are measured, unfolded to the parton level and extrapolated to the full phase space. In addition, two angles between the charged leptons in the laboratory frame that are indirectly sensitive to $t\bar{t}$ spin correlation, but are measurable with excellent experimental resolution, are also measured. No significant deviation with respect to the SM is found, and the results of the measurements are used to constrain anomalous contributions within the EFT framework. The work presented here has been published as Reference [1] in the Physical Review D journal.

At a more detailed level, a discrepancy between the different predictions of the $\Delta\phi_{\ell\ell}$ distribution is observed (see Figure 8.20 and Table 8.1). Judging by the χ^2 fits of the predictions to the data, the best description is achieved by the MG5_aMC@NLO simulation [10, 11] and by the NNLO calculation [9]. This may be due to an improved description of kinematical effects in $t\bar{t}$ events in these two predictions, through the inclusion of up to two additonal partons in the MG5_aMC@NLO simulation and in going to a higher order in QCD for the NNLO calculation. When considering only the asymmetry of this distribution, the best agreement is achieved instead by the NLO calculation [12]. The theoretical uncertainties are also different between the predictions. One possible explanation for this discrepancy between them is that, only for the NLO calculation the ratio in the normalized distribution is perturbatively expanded [12], in contrast to the MC simulations, where denominator and numerator are expanded separately. This introduces a difference of $\mathcal{O}(\alpha_s^2)$ in comparison between the NLO calculation and MC simulations. It has been demonstrated that the proper expansion of the ratio leads to a better agreement with the data [16]. For the NNLO calculation, where the denominator and numerator are expanded separately as in the MC simulations, the difference to the expanded ratio is, however, suppressed by another order of magnitude, leading to the expansion having only a limited impact. Therefore the tension with the data remains. While at present the $\Delta\phi_{\ell\ell}$ stands out as being the only observable whose distribution deviate from the SM expectation, it is also more theoretically challenging, being a convolution of spin correlation and kinematical effects. It is also possible that the observed $\Delta\phi_{\ell\ell}$ discrepancy

between data and predictions is BSM in origin, and that the agreement observed in the other observables such as c_{hel} is simply due to the lower precision that has been achieved for them (see e.g. Table 8.2). Clearly, more work is required on both the theoretical and experimental sides for the discrepancy between data and the simulated predictions to be fully understood.

Ten out of eleven operators that affect the hadronic $t\bar{t}$ production are constrained by our measurement. As expected from the discussion in the previous paragraph, the results of the EFT fits, shown in Figure 8.36, are compatible with the case of zero contribution from all of the considered operators, as expected in the SM. One of the great advantages of this measurement is that the observables considered have definite properties with respect to discrete symmetries. This means that they are sensitive to different kinds of BSM contributions (see Table 8.6), leading to the ten operators affecting disjoint parts of the $t\bar{t}$ spin density matrix (see Tables 8.7 and 8.8). As such, the ten-dimensional space spanned by these operators is sufficiently characterized by ten one-dimensional (see Figure 8.36) and three two-dimensional constraints (see Figures 8.39, 8.40 and 8.41); this vastly simplifies the task of constraining them. In addition, the observables have particularly simple analytical forms when no acceptance cuts are imposed (see Table 2.2), allowing the predictions on the distributions to be obtained in an analytical way without the need of CPU-intensive event generation. This is a testament to the power of the $t\bar{t}$ spin density matrix in characterizing the nature of BSM physics, even when their specific forms are not known a priori. Comparing the results of our top quark CMDM and CEDM constraints with others in the literature, as outlined in Section 8.5, we find that ours are the strongest direct constraints to date, improving also upon contraints that take into account projected future measurements among their inputs.

Looking to the future, this measurement can be improved in a number of ways. DY background is one of the major source of uncertainties, particularly in the same-flavor channels. In the next iteration of this measurement, where a larger data sample is expected to be available, it might be worth performing it only in the eμ channel, where the DY background contamination is small. It is also interesting to provide the measurements within the fiducial phase space. The reason for this is that the uncertainties in the extrapolation to the full phase space are thought to partially contribute to the $\Delta\phi_{\ell\ell}$ discrepancy between theory and measurement [9]. A measurement performed within the fiducial phase space would result in smaller extrapolation uncertainties, thus helping to clarify the origin of the discrepancy. However, since in doing so the advantage of simple analytical forms of the observables would be lost, the ideal approach is to report both results in a future analysis; the extrapolated measurement for a straightforward comparison between the data and the predictions, and the fiducial one for determining the reliability of the extrapolation. On the experimental side, the JEC has always been a dominant source of uncertainty of most measured coefficients (see Table 8.3, Table 8.4 and Appendix E). This is easily understood; the observables are defined in a coordinate system that involves boosting to the $t\bar{t}$ ZMF, and the jet energies directly affect the precision of this step. As with the A/H search described in Chapter 7, this measurement can also benefit from improvements in the kinematic reconstruction algorithm. Although the benefit in this case is lower, since the inaccuracies of the algorithm can be corrected by the response matrices, the algorithm also plays a part in the resolution that can be achieved, and therefore the degree of the corrections that has to be imposed by the unfolding procedure.

The EFT fits demonstrate that one-dimensional measurements are not sufficient to describe the observable space as some of them are related to each other in ways that cannot be described by the covariance matrix (see Appendix F). Thus, measurements in two dimensions, e.g. of b_k^1 and $b_{k^*}^1$, are necessary in order to fully exploit the power of the spin density matrix in probing BSM physics. Such two-dimensional measurements may also be relevant in other physics contexts. For example, a measurement of the two-dimensional c_{hel} and c_{lab} distribution may be used to constrain the PDF. In addition, as mentioned in Section 2.5, the spin coefficients are all functions of $m_{t\bar{t}}$. It is crucial that this prediction of the SM is tested, and this is only possible by going beyond one-dimensional measurements.

8.7 Bibliography

[1] CMS Collaboration, "Measurement of the top quark polarization and $t\bar{t}$ spin correlations using dilepton final states in proton-proton collisions at $\sqrt{s} = 13$ TeV", *Phys. Rev.* **D100** (2019) 072002, doi:10.1103/PhysRevD.100.072002, arXiv:1907.03729.

[2] S. Schmitt, "TUnfold, an algorithm for correcting migration effects in high energy physics", *JINST* **7** (2012) T10003, doi:10.1088/1748-0221/7/10/T10003, arXiv:1205.6201.

[3] E. H. Moore, "On the reciprocal of the general algebraic matrix", *Bulletin of the American Mathematical Society* **26** (06, 1920) 394–395, doi:10.1090/S0002-9904-1920-03322-7.

[4] R. Penrose, "A generalized inverse for matrices", *Mathematical Proceedings of the Cambridge Philosophical Society* **51** (1955), no. 3, 406–413, doi:10.1017/S0305004100030401.

[5] V. Blobel, "An Unfolding method for high-energy physics experiments", in *Advanced Statistical Techniques in Particle Physics. Proceedings, Conference, Durham, UK, March 18-22, 2002*, pp. 258–267. 2002. arXiv:hep-ex/0208022.

[6] B. Efron, "Bootstrap Methods: Another Look at the Jackknife", *The Annals of Statistics* **7** (01, 1979) 1–26, doi:10.1214/aos/1176344552.

[7] L. Demortier and L. Lyons, "Everything you always wanted to know about pulls", CDF Note 5776, 2002.

[8] K. Pearson and F. Galton, "VII. Note on regression and inheritance in the case of two parents", *Proceedings of the Royal Society of London* **58** (1895), no. 347-352, 240–242, doi:10.1098/rspl.1895.0041.

[9] A. Behring et al., "Higher order corrections to spin correlations in top quark pair production at the LHC", *Phys. Rev. Lett.* **123** (2019), no. 8, 082001, doi:10.1103/PhysRevLett.123.082001, arXiv:1901.05407.

[10] J. Alwall et al., "The automated computation of tree-level and next-to-leading order differential cross sections, and their matching to parton shower simulations", *JHEP* **07** (2014) 079, doi:10.1007/JHEP07(2014)079, arXiv:1405.0301.

[11] R. Frederix and S. Frixione, "Merging meets matching in MC@NLO", *JHEP* **12** (2012) 061, doi:10.1007/JHEP12(2012)061, arXiv:1209.6215.

[12] W. Bernreuther, D. Heisler, and Z.-G. Si, "A set of top quark spin correlation and polarization observables for the LHC: Standard Model predictions and new physics contributions", *JHEP* **12** (2015) 026, doi:10.1007/JHEP12(2015)026, arXiv:1508.05271.

[13] ATLAS Collaboration, "Observation of spin correlation in $t\bar{t}$ events from pp collisions at sqrt(s) = 7 TeV using the ATLAS detector", *Phys. Rev. Lett.* **108** (2012) 212001, doi:10.1103/PhysRevLett.108.212001, arXiv:1203.4081.

[14] L. Lista, "Combination of measurements and the BLUE method", *EPJ Web Conf.* **137** (2017) 11006, doi:10.1051/epjconf/201713711006, arXiv:1610.00422.

[15] W. Bernreuther and Z.-G. Si, "Top quark spin correlations and polarization at the LHC: standard model predictions and effects of anomalous top chromo moments", *Phys. Lett.* **B725** (2013) 115–122, doi:10.1016/j.physletb.2013.06.051, arXiv:1305.2066. [Erratum: Phys. Lett. B744, 413 (2015)].

[16] "Spin correlations in top-pair production at the LHC". http://www.precision.hep.phy.cam.ac.uk/results/ttbar-decay/.

[17] D. Buarque Franzosi and C. Zhang, "Probing the top-quark chromomagnetic dipole moment at next-to-leading order in QCD", *Phys. Rev. D* **91** (2015) 114010, doi:10.1103/PhysRevD.91.114010, arXiv:1503.08841.

[18] "NNLO+NNLL top-quark-pair cross sections". https://twiki.cern.ch/twiki/bin/view/LHCPhysics/TtbarNNLO.

[19] L. Lyons, D. Gibaut, and P. Clifford, "How to combine correlated estimates of a single physical quantity", Technical Report OUNP-88-5, Oxford Univ., Oxford, 1987.

[20] CDF Collaboration, "Observation of top quark production in $\bar{p}p$ collisions", *Phys. Rev. Lett.* **74** (1995) 2626–2631, doi:10.1103/PhysRevLett.74.2626, arXiv:hep-ex/9503002.

[21] D0 Collaboration, "Search for high mass top quark production in $p\bar{p}$ collisions at $\sqrt{s} = 1.8$ TeV", *Phys. Rev. Lett.* **74** (1995) 2422–2426, doi:10.1103/PhysRevLett.74.2422, arXiv:hep-ex/9411001.

[22] Z. Hioki and K. Ohkuma, "Latest constraint on nonstandard top-gluon couplings at hadron colliders and its future prospect", *Phys. Rev.* **D88** (2013) 017503, doi:10.1103/PhysRevD.88.017503, arXiv:1306.5387.

[23] J. A. Aguilar-Saavedra, B. Fuks, and M. L. Mangano, "Pinning down top dipole moments with ultra-boosted tops", *Phys. Rev.* **D91** (2015) 094021, doi:10.1103/PhysRevD.91.094021, arXiv:1412.6654.

[24] J. Sjolin, "LHC experimental sensitivity to CP violating g t anti-t couplings", *J. Phys.* **G29** (2003) 543–560, doi:10.1088/0954-3899/29/3/308.

[25] D. Barducci et al., "Interpreting top-quark LHC measurements in the standard-model effective field theory", (2018). arXiv:1802.07237.

[26] C. A. Baker et al., "An improved experimental limit on the electric dipole moment of the neutron", *Phys. Rev. Lett.* **97** (2006) 131801, doi:10.1103/PhysRevLett.97.131801, arXiv:hep-ex/0602020.

[27] J. M. Pendlebury et al., "Revised experimental upper limit on the electric dipole moment of the neutron", *Phys. Rev. D* **92** (2015) 092003, doi:10.1103/PhysRevD.92.092003, arXiv:1509.04411.

CHAPTER

9

SUMMARY

A search for heavy Higgs bosons decaying to $t\bar{t}$ and a measurement of the top quark polarization and $t\bar{t}$ spin correlation have been presented. Both analyses are performed using 35.9 /fb of data recorded by the CMS experiment in 2016, targeting the dileptonic $t\bar{t}$ final state. Events containing two isolated, oppositely charged electrons or muons and at least two jets, at least one of which is consistent with having been initiated by a b quark, are selected. A kinematic reconstruction algorithm is used to reconstruct the kinematics of the top quarks, which is based on a polynomial to recover the longitudinal momenta of the two neutrinos. Both analyses have been submitted for publication by the CMS collaboration.

The heavy Higgs search considers both the pure pseudoscalar A and the pure scalar H, over a mass range of 400 - 750 GeV and a relative width range of 0.5% - 50%. Interference between the A/H and SM $t\bar{t}$ production is taken into account. Exclusion regions are set on the coupling modifier $g_{A/H}$ of the A/H bosons to top quark pairs. An excess with a local significance of 4σ is observed for the $A(400, 5\%)$ signal hypothesis. When the results of the analysis is combined with the same search performed in the semileptonic channel, the local significance of this excess is degraded to 3.7σ. The global significance of this excess is found to be 2σ over all parity, mass and width hypotheses. The existence of the signal may only be established in a future analysis with a larger data sample, an increased search sensitivity and an improved description of the SM $t\bar{t}$ process, particularly in the region close to the $t\bar{t}$ production threshold. The exclusion regions on $g_{A/H}$ obtained in this search is converted into an exclusion region in the hMSSM parameter space m_A-$\tan\beta$ without assuming mass degeneracy between the A and H bosons. Values of $\tan\beta$ up to 1 and 1.5 are excluded for m_A of 400 GeV and 700 GeV respectively, with the expected exclusion being 2.5 and 0.8 for the same m_A. This is the first search for additional Higgs bosons in the low $\tan\beta$ region with m_A beyond the $t\bar{t}$ production threshold at $\sqrt{s} = 13$ TeV. It is also the first such search to be performed without imposing a minimum value on the $t\bar{t}$ invariant mass, extending the search to the case when $m_{A/H}$ is not too far from the $t\bar{t}$ production threshold.

In the top quark polarization and $t\bar{t}$ spin correlation measurement, distributions of all

observables that are directly sensitive to the elements of top quark polarization vector and $t\bar{t}$ spin density matrix are measured, unfolded to the parton level and extrapolated to the full phase space. In addition, two angles between the charged leptons in the laboratory frame that are indirectly sensitive to $t\bar{t}$ spin correlation, but are measurable with excellent experimental resolution, are also measured. No significant deviation with respect to the SM is found. However, there is some tension between the data and the SM predictions in the distribution of the azimuthal gap between the charged leptons in the laboratory frame. The results of the measurements are used to constrain anomalous contributions within the EFT framework. Ten out of eleven operators that affect the hadronic $t\bar{t}$ production are constrained. The ten-dimensional space spanned by these operators is sufficiently characterized by ten one-dimensional and three two-dimensional constraints, due to them affecting disjoint parts of the $t\bar{t}$ spin density matrix. The constraints are compatible with the case of zero contribution from all ten operators. Constraints on the top quark chromomagnetic and chromoelectric dipole moments derived in this measurement are the strongest direct constraints to date.

In both analyses, some tension with respect to the SM predictions are observed. While the precision that has been achieved prevents any concrete statements from being made, it is remarkable that they are both consistent with the presence of A with a mass of around 400 GeV. Furthermore, as mentioned in Section 7.7, the analyses performed in this work are not the only ones that point in this general direction. Although caution is urged in interpreting these results, they remain tantalizing as direct hints of BSM phenomena in the high p_T sector and ought to be explored further. In doing so it is crucial that the theoretical description of the $t\bar{t}$ production processes and the uncertainties affecting them - in SM and BSM - are improved. For example, a modification to the Yukawa coupling of the top quark affects the shape of the $m_{t\bar{t}}$ distribution near the $t\bar{t}$ production threshold. That this is not taken into account in this work is a matter of timing; the degree of modification is quantitatively known only at very late stages of our search. The spin correlation measurement on the other hand would benefit from an improved description of the kinematical aspects of $t\bar{t}$ events; this can be seen from the fact that the empirical top p_T reweighting is one of the more significant systematic sources in many spin correlation coefficients in Table 8.4. As discussed in Sections 7.7 and 8.6, the list of desiderata is no shorter on the experimental side. A more precise jet energy measurement, a more accurate kinematic reconstruction algorithm and a better control over the DY backgrounds are the three important systematic sources common to both analyses. A more sensitive A/H search strategy also has to be explored, and the viability of higher-dimensional spin correlation measurements has to be evaluated...

It is a given that the SM is not all there is to physics. That said, it has withstood many different experimental tests so far. Are we on the right track to discover the first cracks on this extremely tough theory? Only by moving forward we will find out.

Appendices

APPENDIX

A

ELECTRON IDENTIFICATION VARIABLES AT THE HLT

In this appendix, the distributions of all electron identification variables that are considered in the single electron trigger tuning in Chapter 5 are shown together with their efficiency profiles. All distributions are normalized to unity and the uncertainties are due to finite simulation size. The efficiency profiles of all variables are obtained as the ratio between the integral of the distribution up to a given bin in the distribution and the integral of the entire distribution.

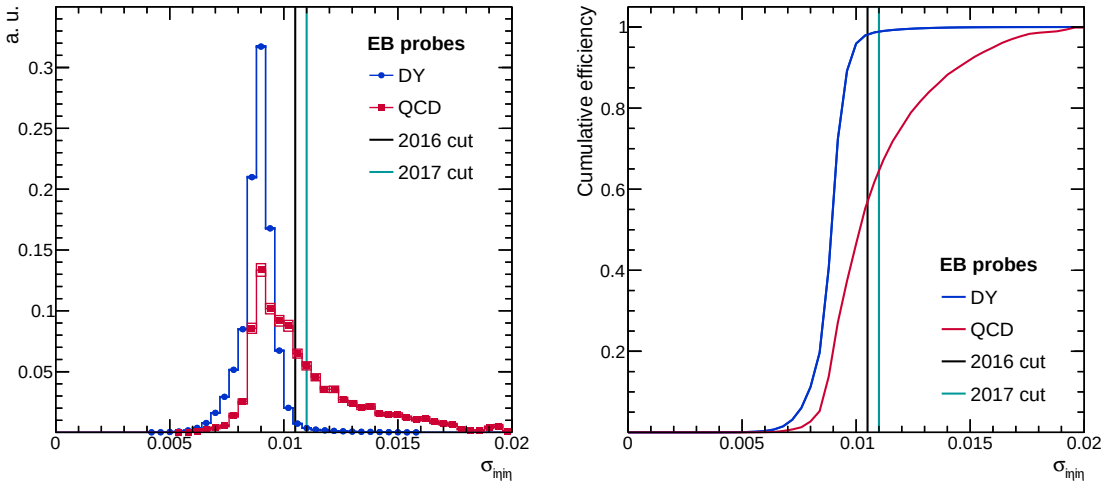

(a) EB $\sigma_{i\eta i\eta}$ distribution

(b) EB $\sigma_{i\eta i\eta}$ efficiency profile

(c) EE $\sigma_{i\eta i\eta}$ distribution

(d) EE $\sigma_{i\eta i\eta}$ efficiency profile

Figure A.1: EB and EE distributions and efficiency profiles for $\sigma_{i\eta i\eta}$. The black vertical line indicates the cut value in the 2016 WP and the cyan vertical line indicates the cut value derived in this tuning.

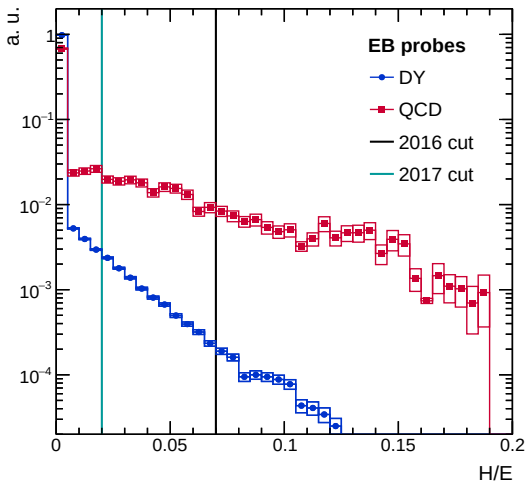

(a) EB H/E distribution

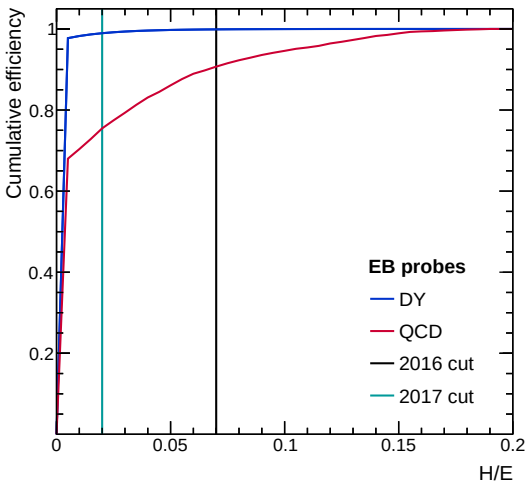

(b) EB H/E efficiency profile

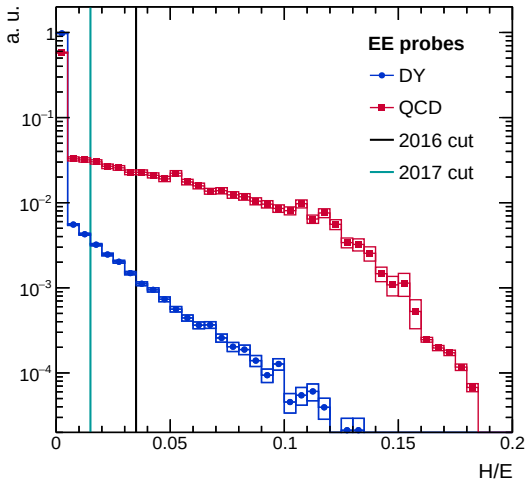

(c) EE H/E distribution

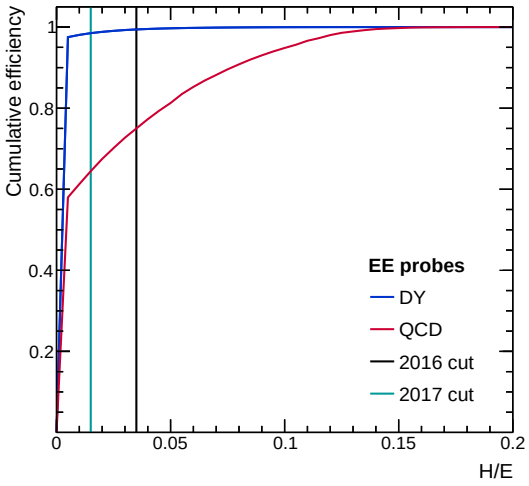

(d) EE H/E efficiency profile

Figure A.2: EB and EE distributions and efficiency profiles for H/E (applying the ρ-correction with EA and NT as in Table 5.13 and Table 5.14). The black vertical line indicates the cut value in the 2016 WP and the cyan vertical line indicates the cut value derived in this tuning.

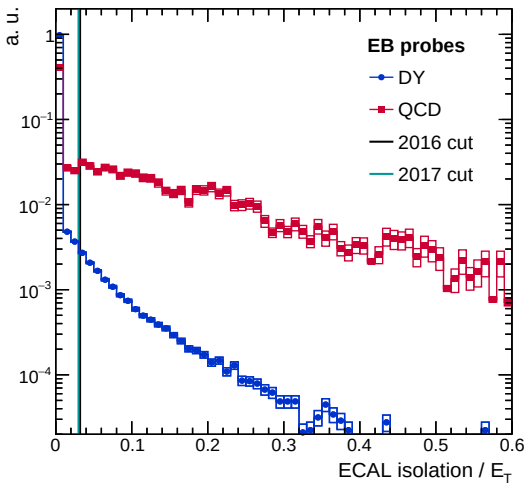

(a) EB relative ECAL isolation distribution

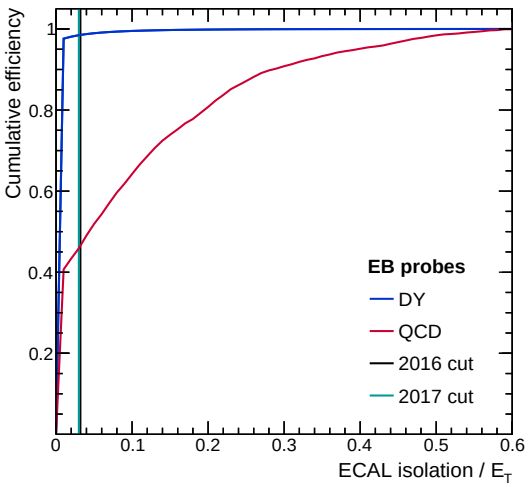

(b) EB relative ECAL isolation efficiency profile

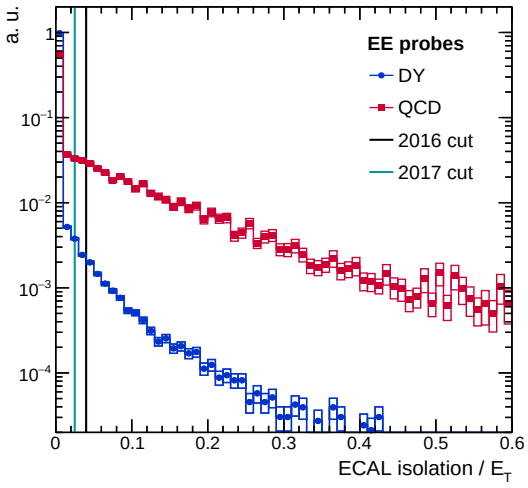

(c) EE relative ECAL isolation distribution

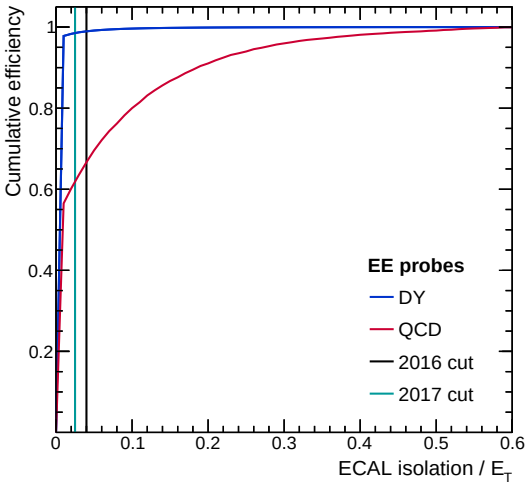

(d) EE relative ECAL isolation efficiency profile

Figure A.3: EB and EE distributions and efficiency profiles for relative ECAL isolation (applying the ρ-correction with EA and NT as in Table 5.13 and Table 5.14). The black vertical line indicates the cut value in the 2016 WP and the cyan vertical line indicates the cut value derived in this tuning.

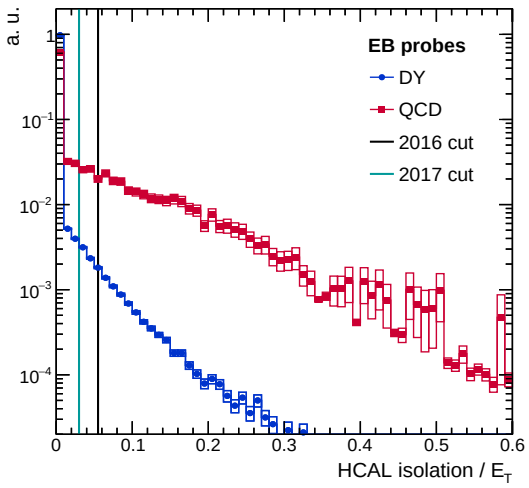

(a) EB relative HCAL isolation distribution

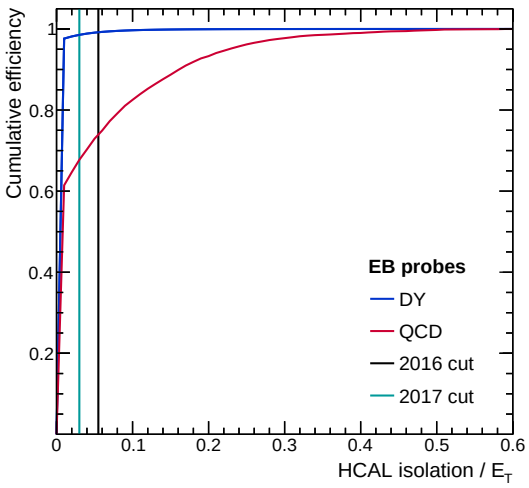

(b) EB relative HCAL isolation efficiency profile

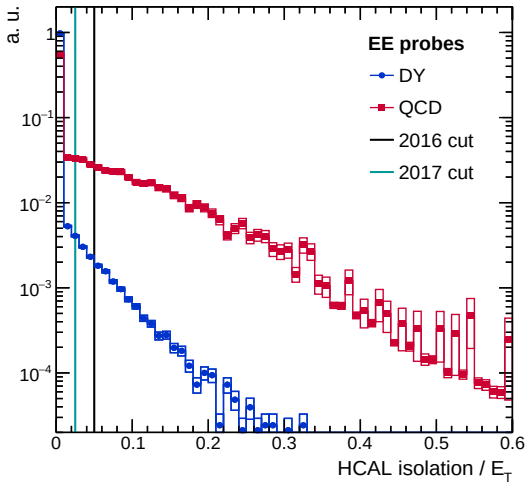

(c) EE relative HCAL isolation distribution

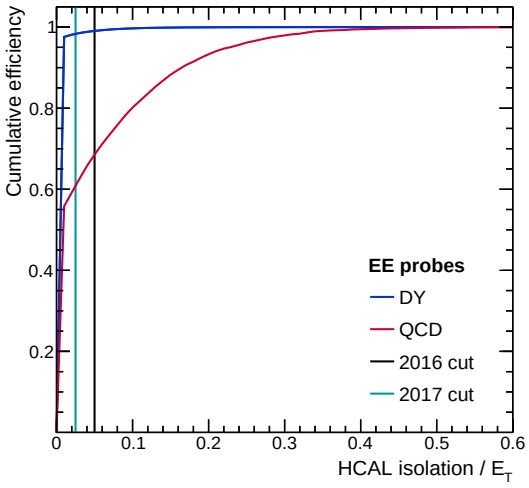

(d) EE relative HCAL isolation efficiency profile

Figure A.4: EB and EE distributions and efficiency profiles for relative HCAL isolation (applying the ρ-correction with EA and NT as in Table 5.13 and Table 5.14). The black vertical line indicates the cut value in the 2016 WP and the cyan vertical line indicates the cut value derived in this tuning.

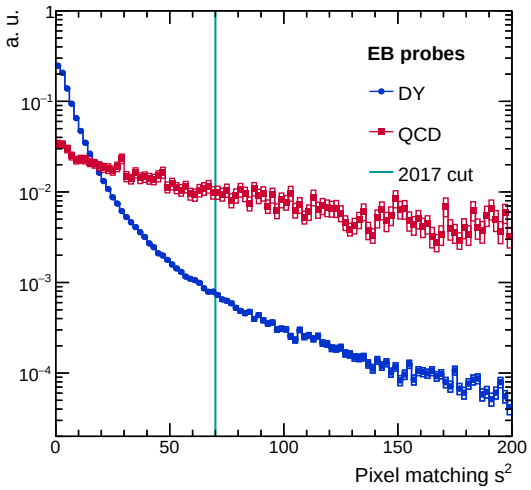

(a) EB pixel matching s^2 distribution

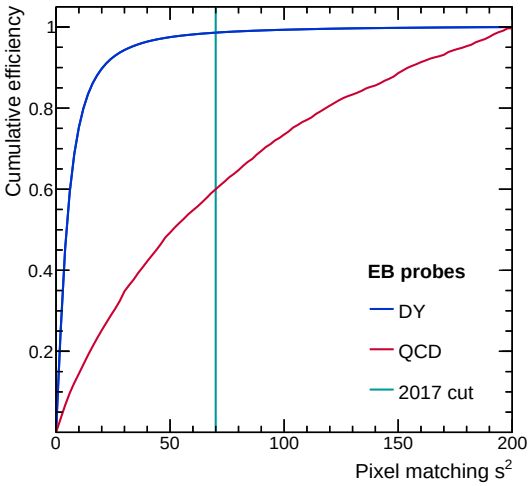

(b) EB pixel matching s^2 efficiency profile

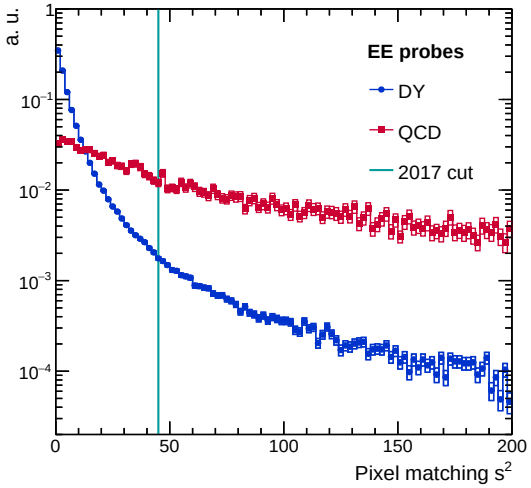

(c) EE pixel matching s^2 distribution

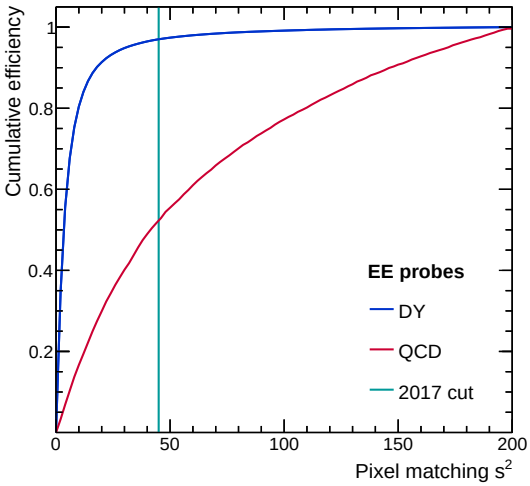

(d) EE pixel matching s^2 efficiency profile

Figure A.5: EB and EE distributions and efficiency profiles for pixel matching s^2. In anticipation of the conclusion of this section, the cyan vertical line indicates the cut value derived in this tuning.

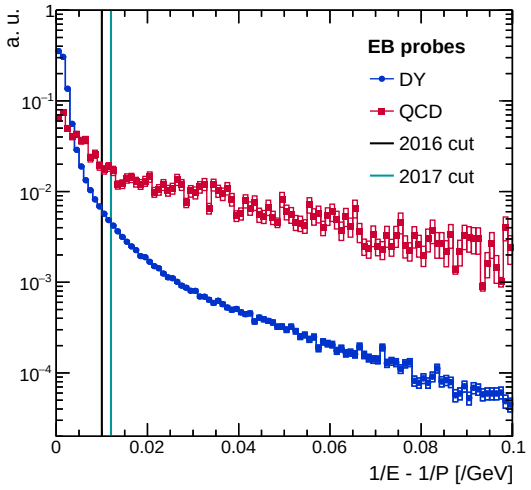

(a) EB $1/E - 1/P$ distribution

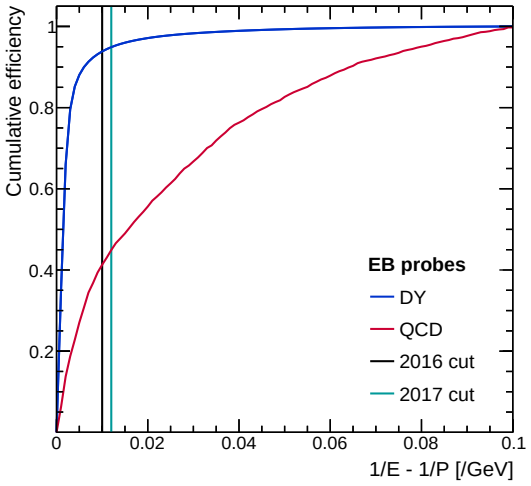

(b) EB $1/E - 1/P$ efficiency profile

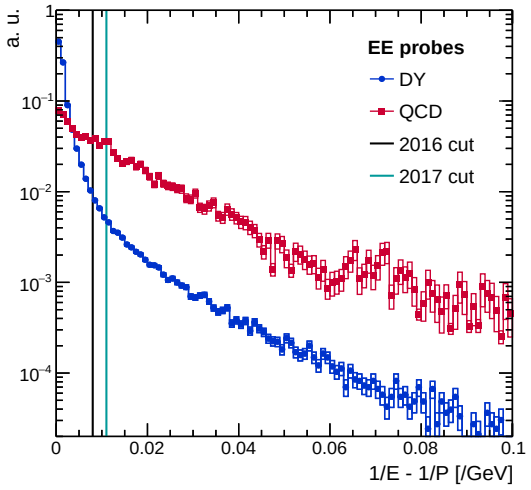

(c) EE $1/E - 1/P$ distribution

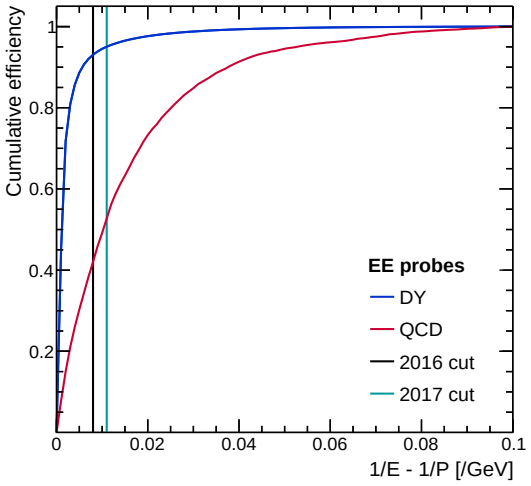

(d) EE $1/E - 1/P$ efficiency profile

Figure A.6: EB and EE distributions and efficiency profiles for $1/E - 1/P$. The black vertical line indicates the cut value in the 2016 WP and the cyan vertical line indicates the cut value derived in this tuning.

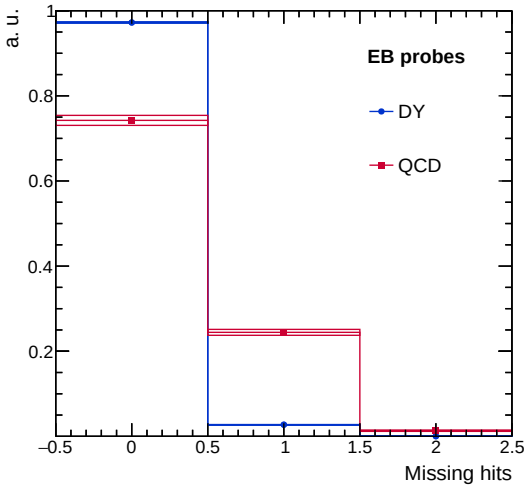

(a) EB missing hits distribution

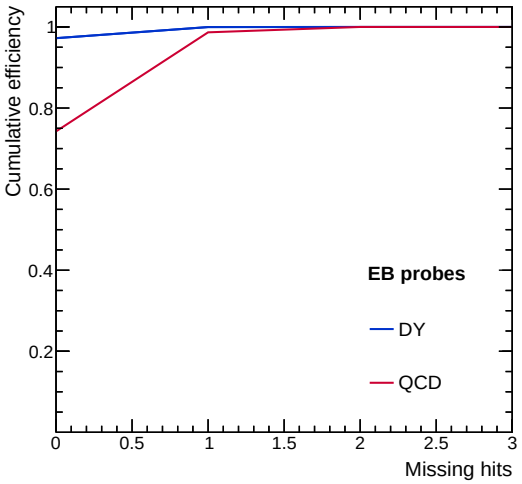

(b) EB missing hits efficiency profile

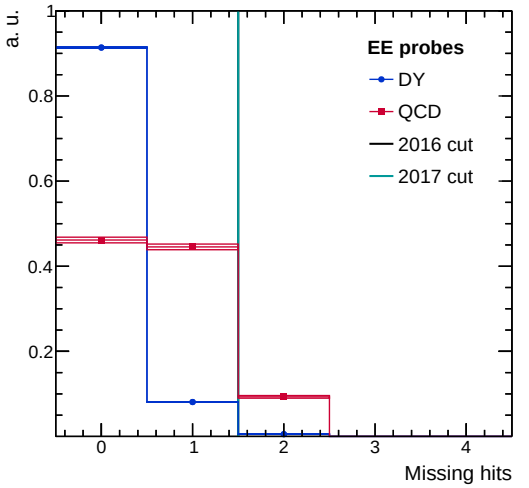

(c) EE missing hits distribution

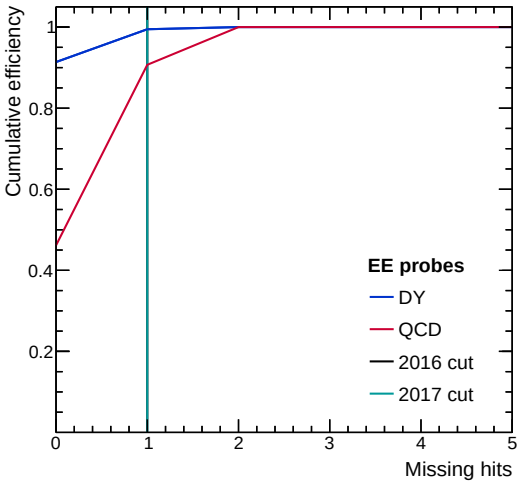

(d) EE missing hits efficiency profile

Figure A.7: EB and EE distributions and efficiency profiles for missing hits. The black vertical line indicates the cut value in the 2016 WP and the cyan vertical line indicates the cut value derived in this tuning. For the histograms, the lines are shifted to the end of the bin to indicate that the cut is inclusive of the bin of this discrete variable.

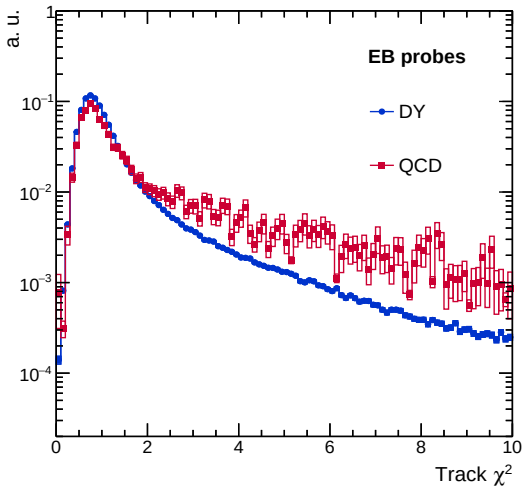

(a) EB track χ^2 distribution

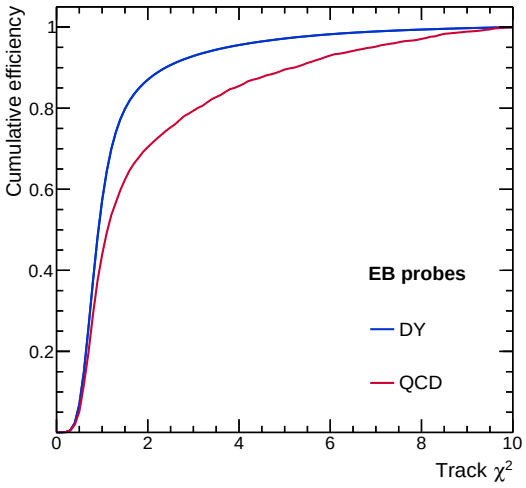

(b) EB track χ^2 efficiency profile

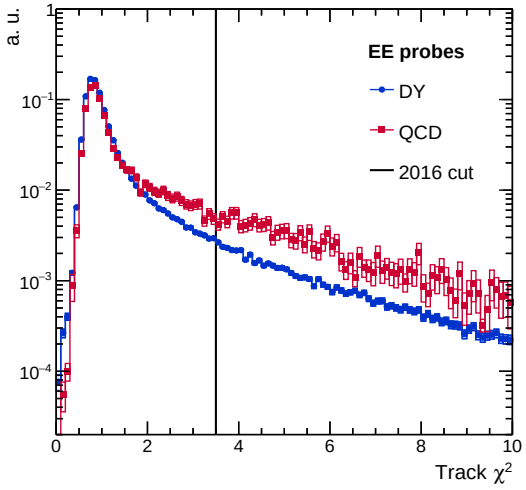

(c) EE track χ^2 distribution

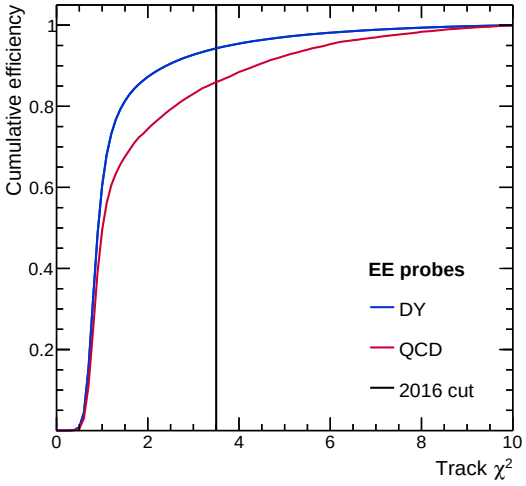

(d) EE track χ^2 efficiency profile

Figure A.8: EB and EE distributions and efficiency profiles for track χ^2. The black vertical line indicates the cut value in the 2016 WP.

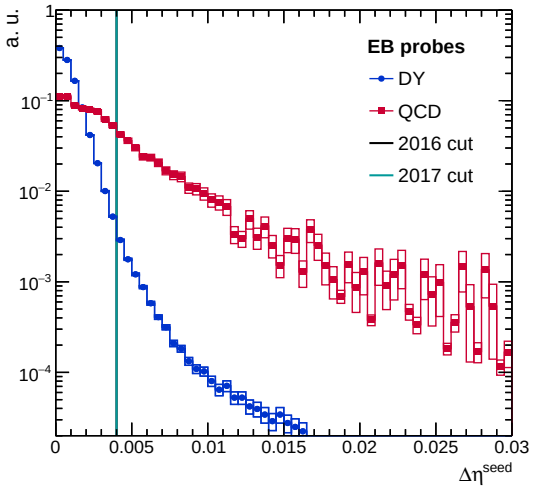

(a) EB $\Delta\eta^{\text{seed}}$ distribution

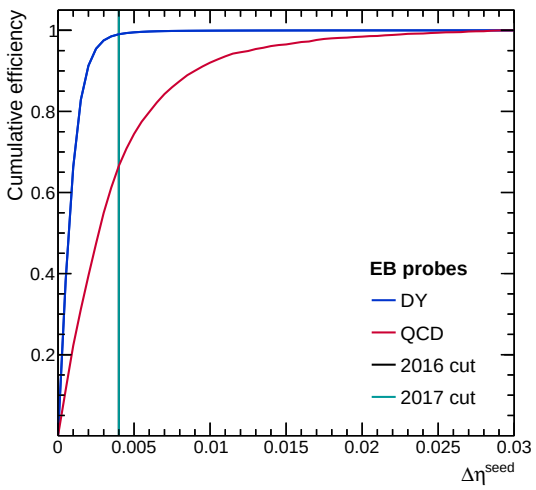

(b) EB $\Delta\eta^{\text{seed}}$ efficiency profile

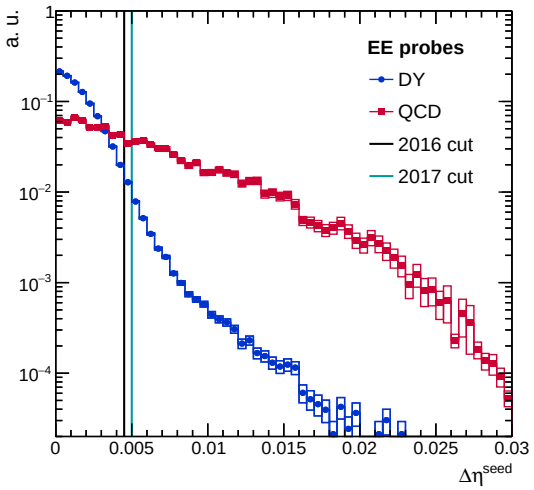

(c) EE $\Delta\eta^{\text{seed}}$ distribution

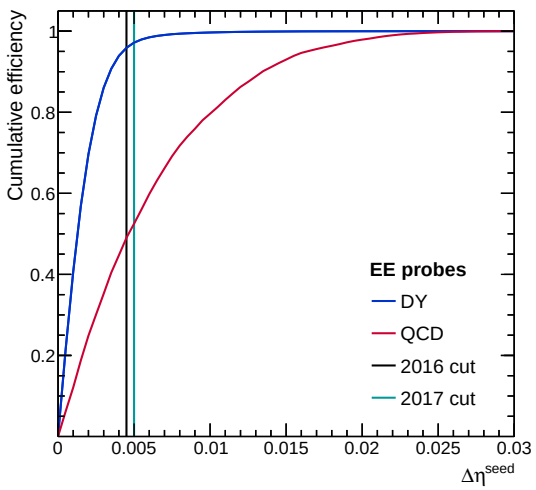

(d) EE $\Delta\eta^{\text{seed}}$ efficiency profile

Figure A.9: EB and EE distributions and efficiency profiles for $\Delta\eta^{\text{seed}}$. The black vertical line indicates the cut value in the 2016 WP and the cyan vertical line indicates the cut value derived in this tuning.

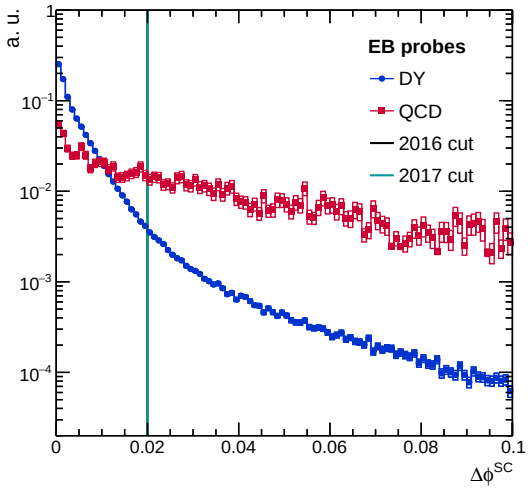

(a) EB $\Delta\phi^{SC}$ distribution

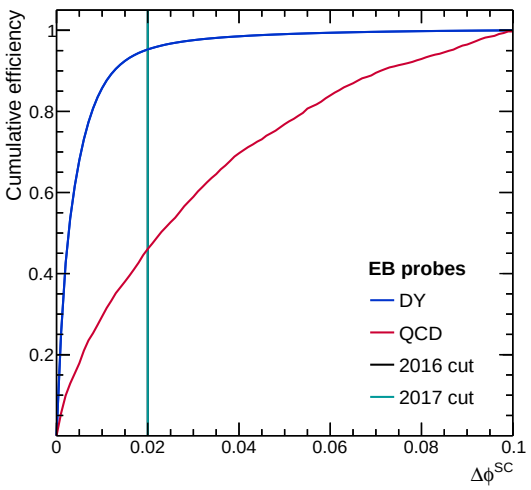

(b) EB $\Delta\phi^{SC}$ efficiency profile

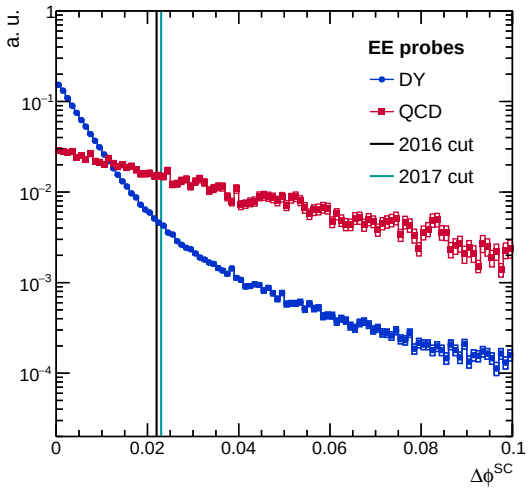

(c) EE $\Delta\phi^{SC}$ distribution

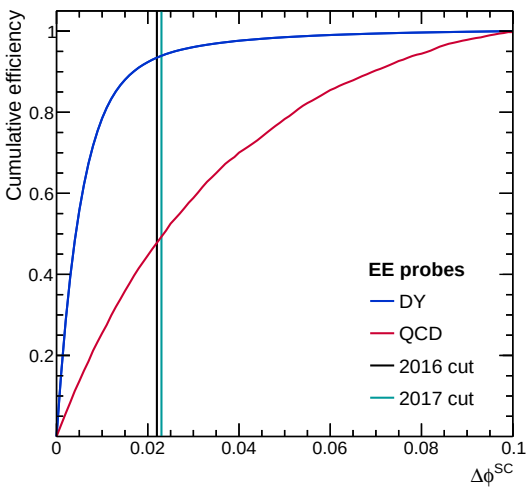

(d) EE $\Delta\phi^{SC}$ efficiency profile

Figure A.10: EB and EE distributions and efficiency profiles for $\Delta\phi^{SC}$. The black vertical line indicates the cut value in the 2016 WP and the cyan vertical line indicates the cut value derived in this tuning.

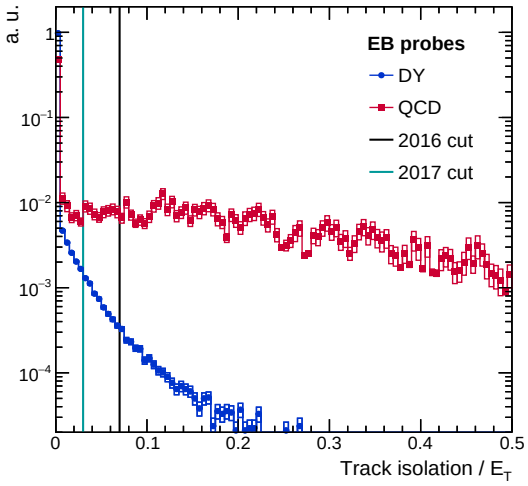

(a) EB relative track isolation distribution

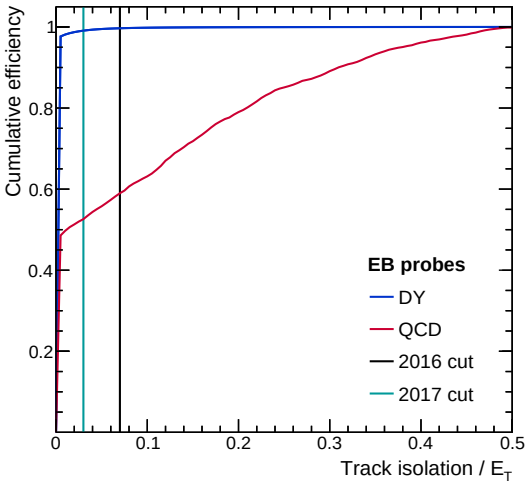

(b) EB relative track isolation efficiency profile

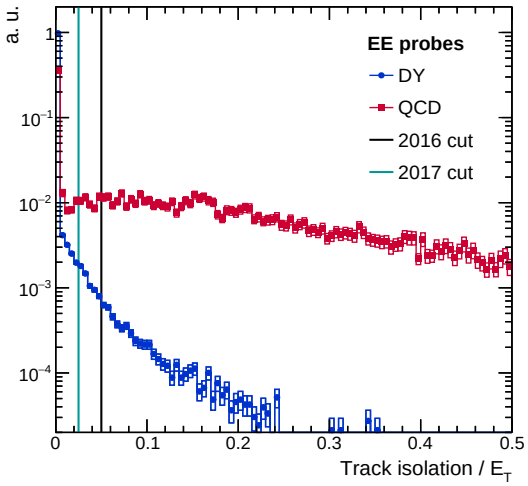

(c) EE relative track isolation distribution

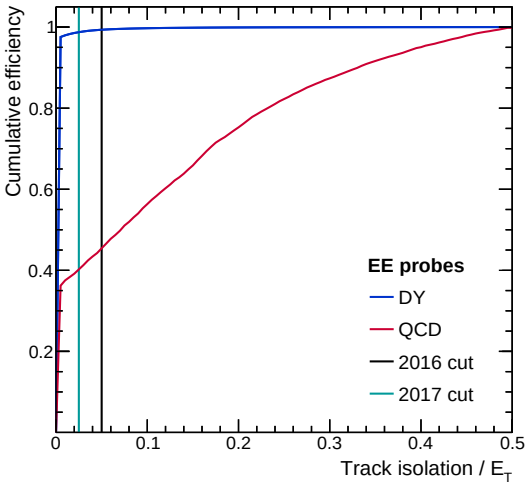

(d) EE relative track isolation efficiency profile

Figure A.11: EB and EE distributions and efficiency profiles for relative track isolation (applying the ρ-correction with EA and NT as in Table 5.13 and Table 5.14). The black vertical line indicates the cut value in the 2016 WP and the cyan vertical line indicates the cut value derived in this tuning.

APPENDIX

B

EVENT YIELDS AND CONTROL DISTRIBUTIONS

This appendix shows the event yields and control distributions in all three channels within the context of the A/H search, as a follow-up to the discussion in Section 6.7. This is done at each step of the event selection up to the $\not{p}_T$ cut (see Section 6.3). Non-DY background contributions are estimated from simulation, while the DY background contribution is estimated using a data-driven procedure discussed in Section 6.4. All the corrections discussed in Section 6.2 and Section 6.6 are applied.

For the event yields, only uncertainties of statistical nature i.e. those due to finite data or simulation size are considered. They are shown in Tables B.1, B.2, B.3, B.4, B.5 and B.6. Although there appears to be an underestimation of yields at all selection steps, as will be seen in the control distributions, the differences are well within the total uncertainties.

In the control distributions, the impact of statistical and systematic uncertainties are shown together, however in all cases the latter dominate. Underflow and overflow entries are added to the first and last bins respectively. Since all distributions share a common legend, for the sake of brevity it is shown only once in Figure B.1. The control distributions are shown in Figures B.2, B.3 and B.4 with up to the 2 lepton cut applied, and in Figures B.5 and B.6 with up to the Z window cut applied. In these distributions we see that the yield underestimation appear to be a systematic effect due to a poor description of DY contributions, particularly around the Z peak and low N_j regions. However, the systematic uncertainties are large, particularly in the same flavor channels that are dominated by DY and are therefore significantly affected by lepton ID uncertainties. Applying the 2 jet cut, we see that the data description is improved (Figures B.7, B.8 and B.9), although in the same flavor channels the uncertainty is still large in the low $\not{p}_T$ region. The $\not{p}_T$ cut further supresses the DY contribution (Figures B.10 and B.11), thus avoiding this problem. Finally, as mentioned in Section 6.7, a reasonable agreement between the data and simulation is reached when 1-btag cut is imposed.

Table B.1: Event yields up to the 2 lepton cut. The uncertainties are due to the finite simulation statistics and for DY includes the uncertainties from the data-driven estimation described in Section 6.4.

Process	Event yield			
	ee	eμ	$\mu\mu$	Combined
A$(400, 5\%) \rightarrow t\bar{t}$	-188 $\pm$ 31	-693 $\pm$ 53	-415 $\pm$ 45	-1297 $\pm$ 76
A$(500, 5\%) \rightarrow t\bar{t}$	231 $\pm$ 17	713 $\pm$ 29	570 $\pm$ 24	1515 $\pm$ 41
A$(600, 5\%) \rightarrow t\bar{t}$	222 $\pm$ 9	626 $\pm$ 14	464 $\pm$ 12	1312 $\pm$ 21
A$(750, 5\%) \rightarrow t\bar{t}$	144 $\pm$ 4	418 $\pm$ 6	288 $\pm$ 5	850 $\pm$ 9
$t\bar{t}$	82316 $\pm$ 124	233837 $\pm$ 212	166931 $\pm$ 181	483085 $\pm$ 305
Single top	8130 $\pm$ 101	23485 $\pm$ 174	16542 $\pm$ 147	48156 $\pm$ 250
DY	$(11767 \pm 4) \times 10^3$	61991 $\pm$ 259	$(26131 \pm 6) \times 10^3$	$(37960 \pm 7) \times 10^3$
$t\bar{t}$V	381 $\pm$ 3	544 $\pm$ 5	694 $\pm$ 4	1619 $\pm$ 7
VV	25600 $\pm$ 103	27023 $\pm$ 119	53648 $\pm$ 153	106270 $\pm$ 220
Total background	$(11883 \pm 4) \times 10^3$	346879 $\pm$ 396	$(26369 \pm 6) \times 10^3$	$(38599 \pm 7) \times 10^3$
Data	10359×10^3	351338	23203×10^3	33913×10^3

Table B.2: Event yields up to the Z window cut. The uncertainties are due to the finite simulation statistics and for DY includes the uncertainties from the data-driven estimation described in Section 6.4.

Process	Event yield			
	ee	eμ	$\mu\mu$	Combined
A$(400, 5\%) \to t\bar{t}$	-132 $\pm$ 27	-693 $\pm$ 53	-254 $\pm$ 39	-1080 $\pm$ 71
A$(500, 5\%) \to t\bar{t}$	163 $\pm$ 15	713 $\pm$ 29	405 $\pm$ 21	1281 $\pm$ 39
A$(600, 5\%) \to t\bar{t}$	150 $\pm$ 8	626 $\pm$ 14	331 $\pm$ 11	1107 $\pm$ 20
A$(750, 5\%) \to t\bar{t}$	104 $\pm$ 3	418 $\pm$ 6	208 $\pm$ 5	730 $\pm$ 8
$t\bar{t}$	65016 $\pm$ 110	233837 $\pm$ 212	130434 $\pm$ 160	429287 $\pm$ 288
Single top	6557 $\pm$ 91	23485 $\pm$ 174	13007 $\pm$ 131	43049 $\pm$ 236
DY	870006 $\pm$ 1171	61991 $\pm$ 259	$(2058 \pm 2) \times 10^3$	$(2990 \pm 2) \times 10^3$
$t\bar{t}V$	182 $\pm$ 3	544 $\pm$ 5	328 $\pm$ 4	1053 $\pm$ 7
VV	8511 $\pm$ 65	27023 $\pm$ 119	17726 $\pm$ 95	53259 $\pm$ 166
Total background	950272 $\pm$ 1181	346879 $\pm$ 396	$(2219 \pm 2) \times 10^3$	$(3516 \pm 2) \times 10^3$
Data	866632	351338	2029×10^3	3247×10^3

Table B.3: Event yields up to the 2 jet cut. The uncertainties are due to the finite simulation statistics and for DY includes the uncertainties from the data-driven estimation described in Section 6.4.

Process	Event yield			
	ee	eμ	$\mu\mu$	Combined
A$(400, 5\%) \rightarrow \mathrm{t\bar{t}}$	-67 ± 23	-407 ± 45	-98 ± 33	-572 ± 60
A$(500, 5\%) \rightarrow \mathrm{t\bar{t}}$	134 ± 13	534 ± 25	310 ± 18	978 ± 33
A$(600, 5\%) \rightarrow \mathrm{t\bar{t}}$	109 ± 7	463 ± 13	237 ± 9	809 ± 17
A$(750, 5\%) \rightarrow \mathrm{t\bar{t}}$	77 ± 3	308 ± 5	154 ± 4	539 ± 7
$\mathrm{t\bar{t}}$	47347 ± 94	170587 ± 181	94530 ± 136	312463 ± 245
Single top	2554 ± 57	9109 ± 109	4960 ± 81	16623 ± 147
DY	47617 ± 179	3809 ± 42	104765 ± 265	156192 ± 323
$\mathrm{t\bar{t}V}$	170 ± 3	506 ± 5	307 ± 4	983 ± 7
VV	1089 ± 22	2090 ± 33	2009 ± 30	5189 ± 50
Total background	98778 ± 211	186101 ± 218	206572 ± 310	491450 ± 434
Data	99858	183616	208005	491479

Table B.4: Event yields up to the $\not{p}_T$ cut. The uncertainties are due to the finite simulation statistics and for DY includes the uncertainties from the data-driven estimation described in Section 6.4.

Process	Event yield			
	ee	eμ	$\mu\mu$	Combined
A$(400, 5\%) \to t\bar{t}$	-46 $\pm$ 20	-407 $\pm$ 45	-54 $\pm$ 29	-508 $\pm$ 57
A$(500, 5\%) \to t\bar{t}$	107 $\pm$ 11	534 $\pm$ 25	241 $\pm$ 16	882 $\pm$ 32
A$(600, 5\%) \to t\bar{t}$	83 $\pm$ 6	463 $\pm$ 13	184 $\pm$ 8	730 $\pm$ 16
A$(750, 5\%) \to t\bar{t}$	60 $\pm$ 3	308 $\pm$ 5	118 $\pm$ 4	486 $\pm$ 7
$t\bar{t}$	37318 $\pm$ 83	170587 $\pm$ 181	74660 $\pm$ 121	282564 $\pm$ 233
Single top	2043 $\pm$ 51	9109 $\pm$ 109	3906 $\pm$ 72	15058 $\pm$ 140
DY	11392 $\pm$ 86	3809 $\pm$ 42	25696 $\pm$ 129	40897 $\pm$ 161
$t\bar{t}$V	139 $\pm$ 2	506 $\pm$ 5	251 $\pm$ 3	896 $\pm$ 6
VV	591 $\pm$ 17	2090 $\pm$ 33	1082 $\pm$ 23	3763 $\pm$ 43
Total background	51482 $\pm$ 131	186101 $\pm$ 218	105595 $\pm$ 192	343178 $\pm$ 319
Data	51141	183616	103982	338739

Table B.5: Event yields up to the 1 b-tag cut. The uncertainties are due to the finite simulation statistics and for DY includes the uncertainties from the data-driven estimation described in Section 6.4.

Process	Event yield			
	ee	eμ	$\mu\mu$	Combined
A$(400, 5\%) \rightarrow t\bar{t}$	-38 $\pm$ 18	-375 $\pm$ 40	-59 $\pm$ 26	-472 $\pm$ 51
A$(500, 5\%) \rightarrow t\bar{t}$	78 $\pm$ 10	446 $\pm$ 22	204 $\pm$ 14	727 $\pm$ 29
A$(600, 5\%) \rightarrow t\bar{t}$	71 $\pm$ 5	380 $\pm$ 11	148 $\pm$ 8	599 $\pm$ 15
A$(750, 5\%) \rightarrow t\bar{t}$	49 $\pm$ 2	256 $\pm$ 5	97 $\pm$ 3	401 $\pm$ 6
$t\bar{t}$	30625 $\pm$ 75	140178 $\pm$ 162	61212 $\pm$ 108	232015 $\pm$ 209
Single top	1487 $\pm$ 43	6591 $\pm$ 91	2803 $\pm$ 60	10880 $\pm$ 117
DY	1260 $\pm$ 27	426 $\pm$ 14	2896 $\pm$ 42	4582 $\pm$ 52
$t\bar{t}$V	112 $\pm$ 2	406 $\pm$ 4	200 $\pm$ 3	717 $\pm$ 6
VV	56 $\pm$ 5	198 $\pm$ 10	118 $\pm$ 7	372 $\pm$ 13
Total background	33539 $\pm$ 90	147798 $\pm$ 187	67230 $\pm$ 131	248567 $\pm$ 245
Data	33066	144396	65561	243023

Table B.6: Event yields after the full event selection. The uncertainties are due to the finite simulation statistics and for DY includes the uncertainties from the data-driven estimation described in Section 6.4.

Process	Event yield			
	ee	eμ	$\mu\mu$	Combined
A$(400, 5\%) \to t\bar{t}$	-38 $\pm$ 18	-379 $\pm$ 40	-65 $\pm$ 26	-481 $\pm$ 50
A$(500, 5\%) \to t\bar{t}$	71 $\pm$ 10	429 $\pm$ 22	191 $\pm$ 14	692 $\pm$ 28
A$(600, 5\%) \to t\bar{t}$	68 $\pm$ 5	368 $\pm$ 11	144 $\pm$ 7	579 $\pm$ 14
A$(750, 5\%) \to t\bar{t}$	48 $\pm$ 2	248 $\pm$ 5	93 $\pm$ 3	389 $\pm$ 6
$t\bar{t}$	29436 $\pm$ 73	135077 $\pm$ 159	58575 $\pm$ 106	223088 $\pm$ 205
Single top	1103 $\pm$ 37	5135 $\pm$ 80	2094 $\pm$ 52	8332 $\pm$ 102
DY	928 $\pm$ 24	353 $\pm$ 13	2169 $\pm$ 37	3451 $\pm$ 45
$t\bar{t}$V	95 $\pm$ 2	363 $\pm$ 4	172 $\pm$ 3	630 $\pm$ 6
VV	37 $\pm$ 4	117 $\pm$ 8	70 $\pm$ 6	224 $\pm$ 10
Total background	31599 $\pm$ 86	141045 $\pm$ 179	63080 $\pm$ 123	235724 $\pm$ 234
Data	30953	137852	61428	230233

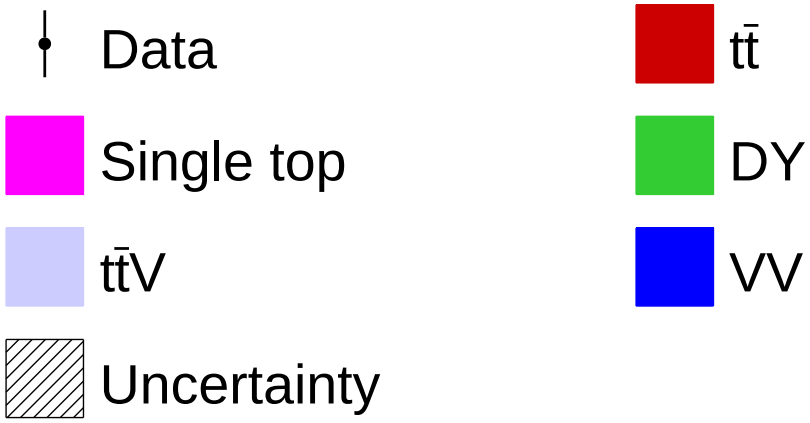

Figure B.1: Legend for all control distributions in this appendix. The legend also represents the stack order i.e. $t\bar{t}$ is always at the top of the stack, followed by single top, DY and so on. Uncertainty is the combination of statistical and systematic uncertainties.

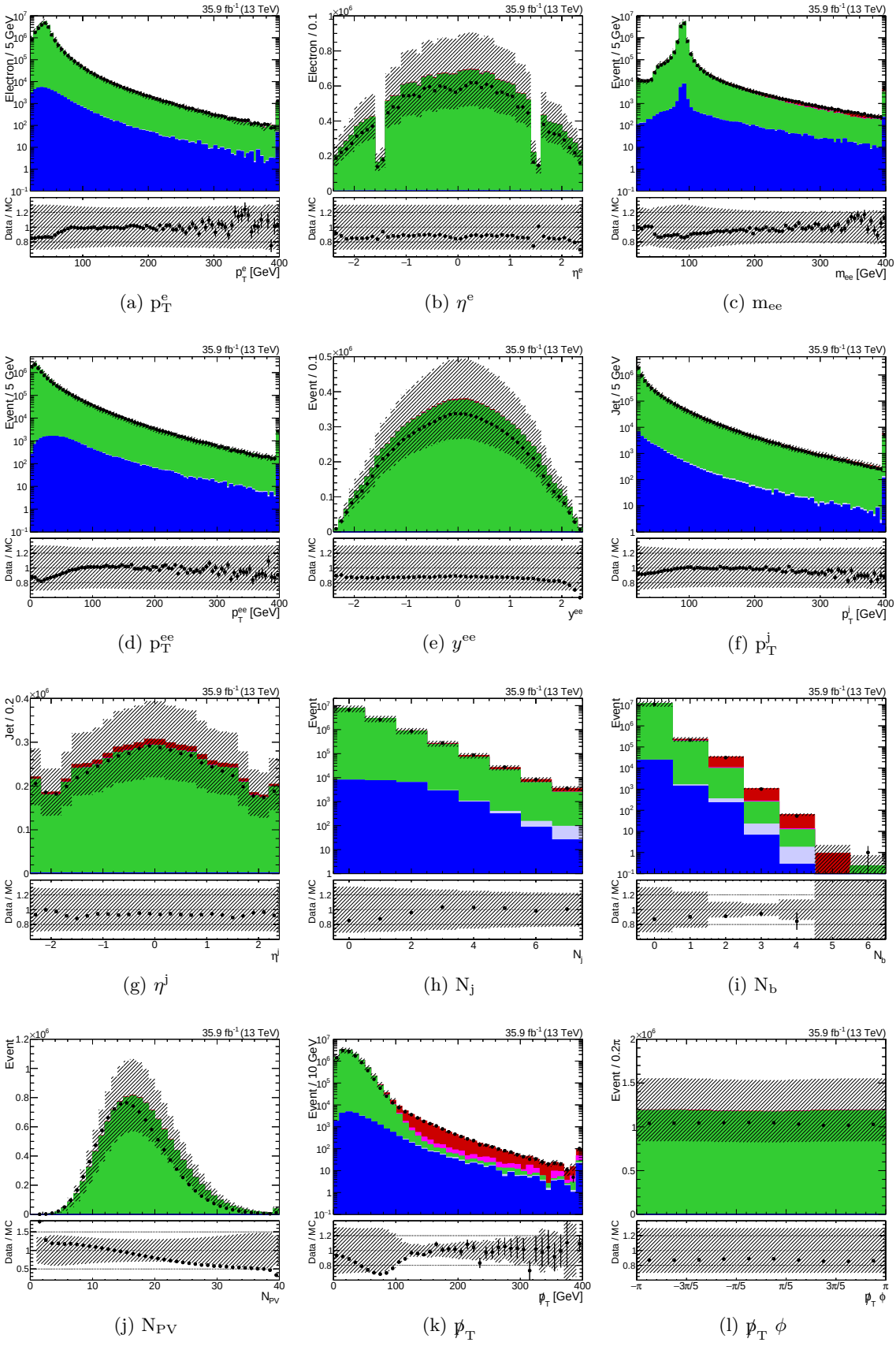

Figure B.2: Control distributions with up to the 2 lepton cut applied in the ee channel.

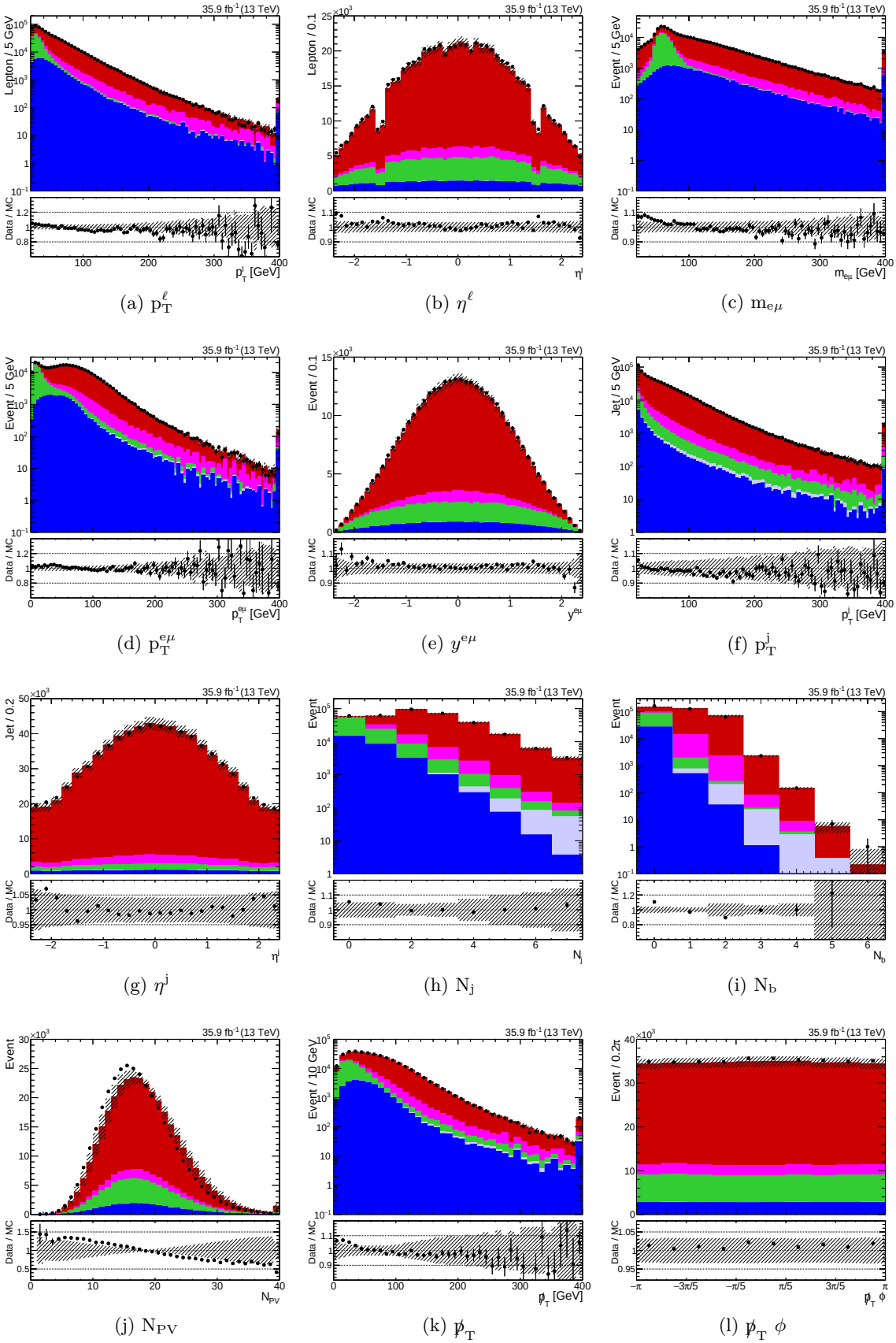

Figure B.3: Control distributions with up to the 2 lepton cut applied in the eμ channel.

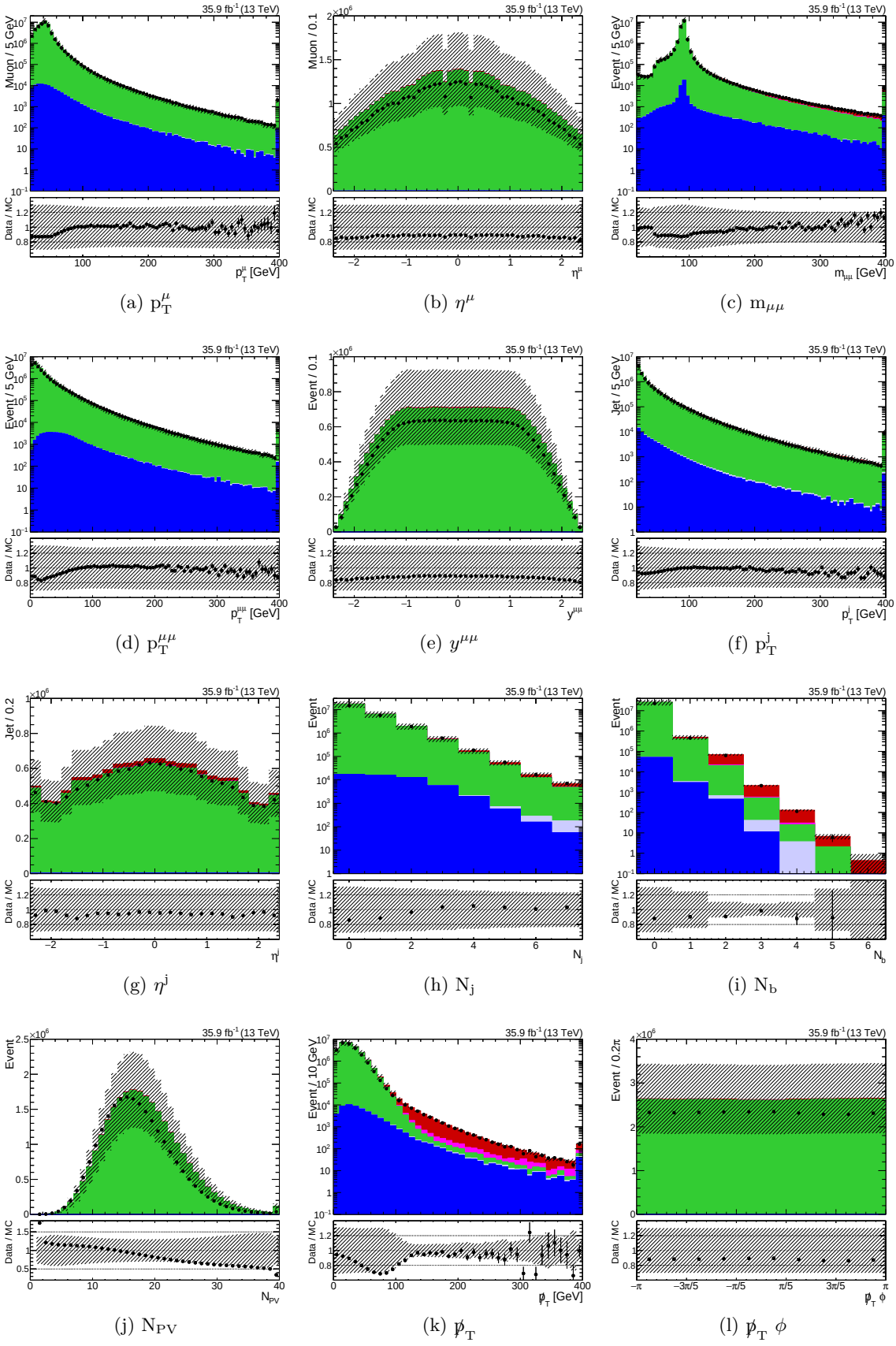

Figure B.4: Control distributions with up to the 2 lepton cut applied in the $\mu\mu$ channel.

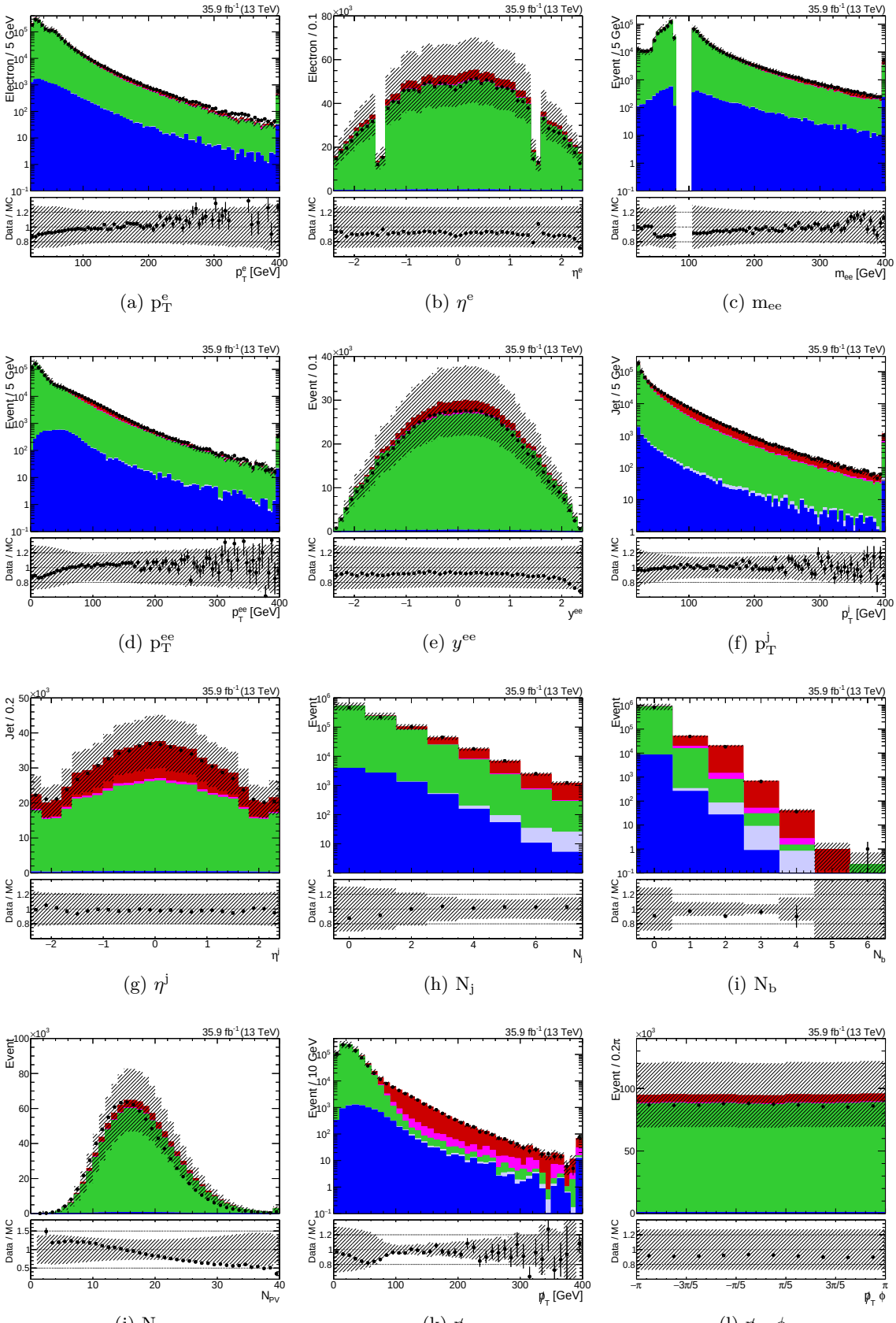

Figure B.5: Control distributions with up to the Z window cut applied in the ee channel.

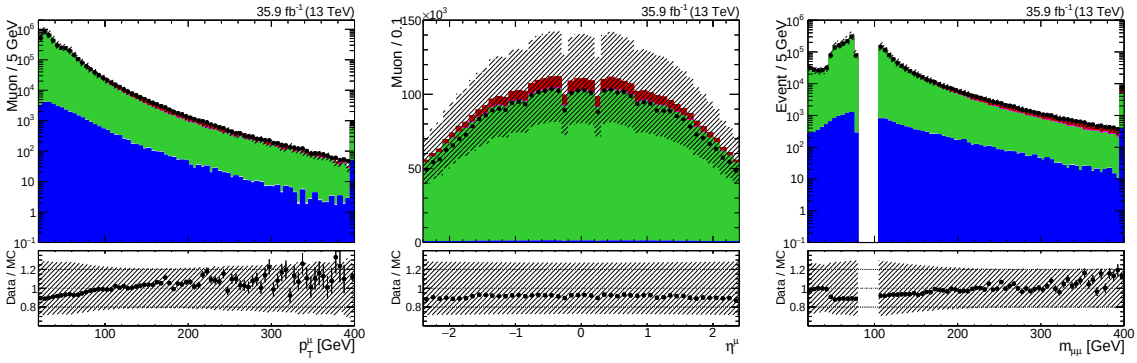

(a) p_T^{μ}

(b) η^{μ}

(c) $m_{\mu\mu}$

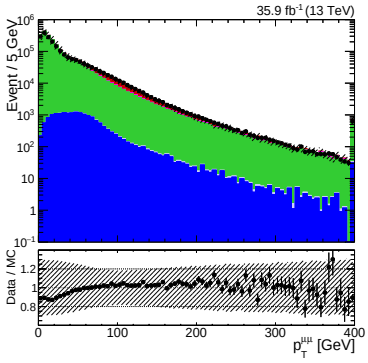

(d) $p_T^{\mu\mu}$

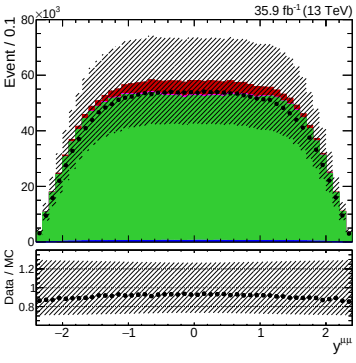

(e) $y^{\mu\mu}$

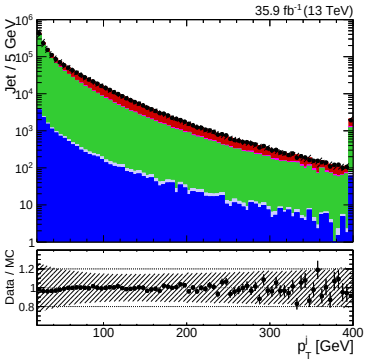

(f) p_T^{j}

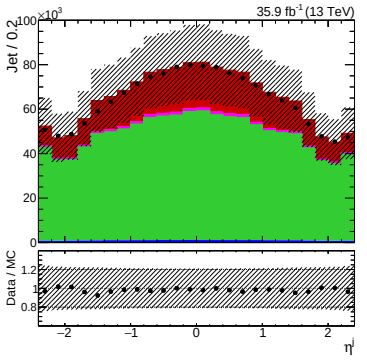

(g) η^{j}

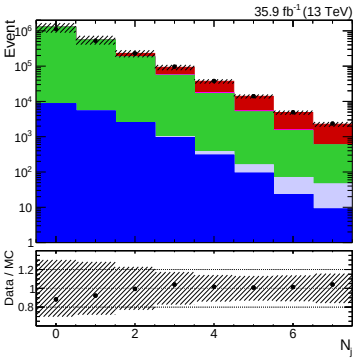

(h) N_j

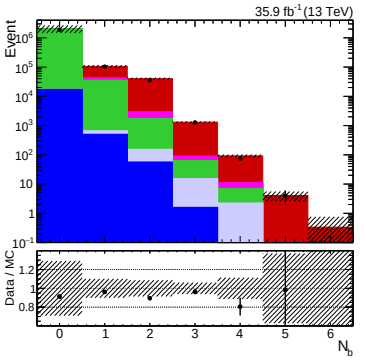

(i) N_b

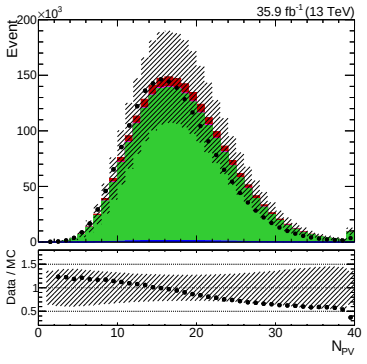

(j) N_{PV}

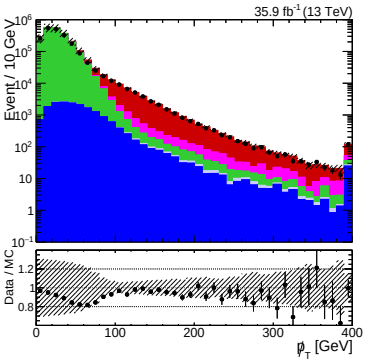

(k) $\not{p}_T$

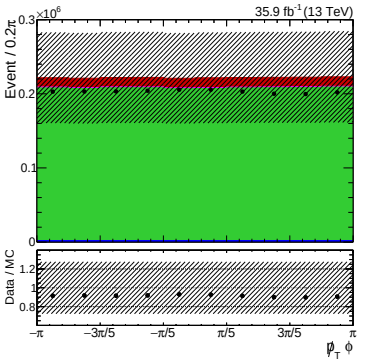

(l) $\not{p}_T$ ϕ

Figure B.6: Control distributions with up to the Z window cut applied in the $\mu\mu$ channel.

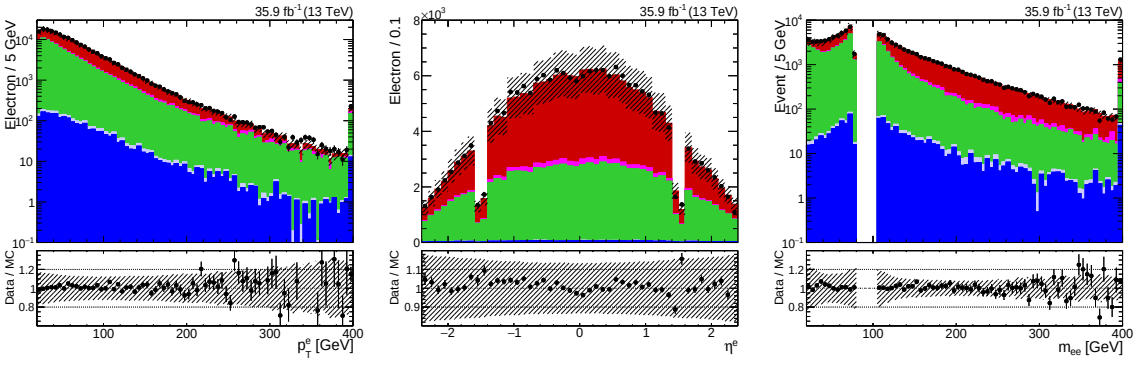

(a) p_T^e

(b) η^e

(c) m_{ee}

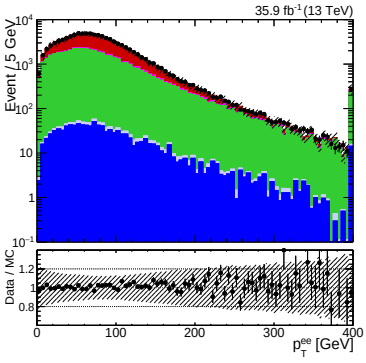

(d) p_T^{ee}

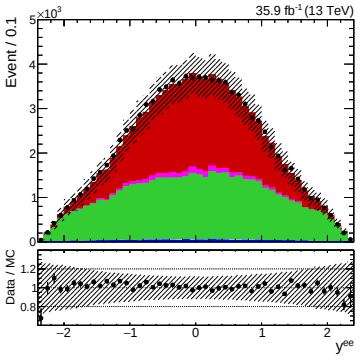

(e) y^{ee}

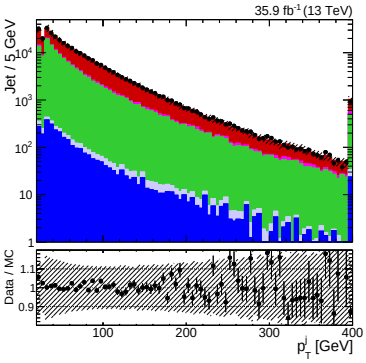

(f) p_T^j

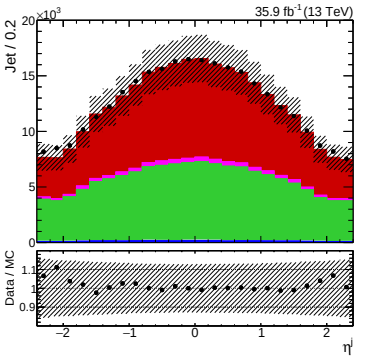

(g) η^j

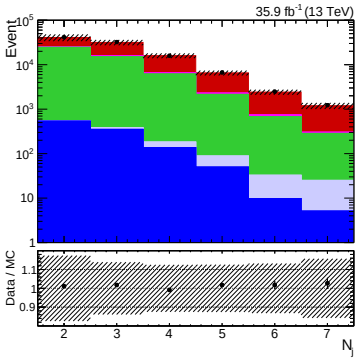

(h) N_j

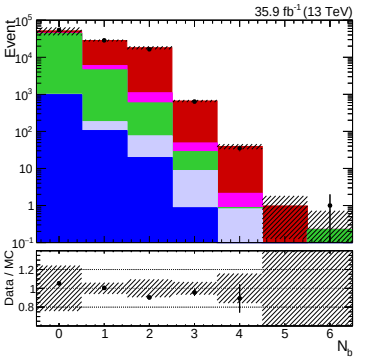

(i) N_b

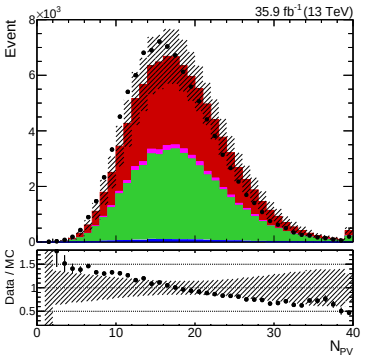

(j) N_{PV}

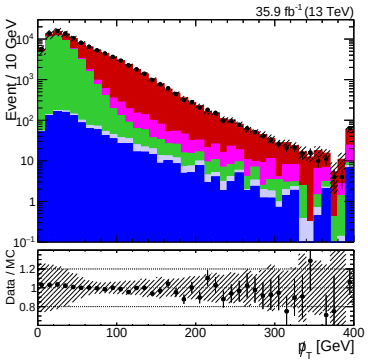

(k) $\not{p}_T$

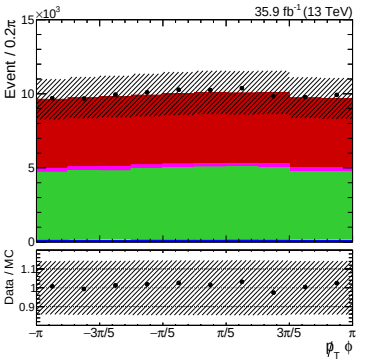

(l) $\not{p}_T$ ϕ

Figure B.7: Control distributions with up to the 2 jet cut applied in the ee channel.

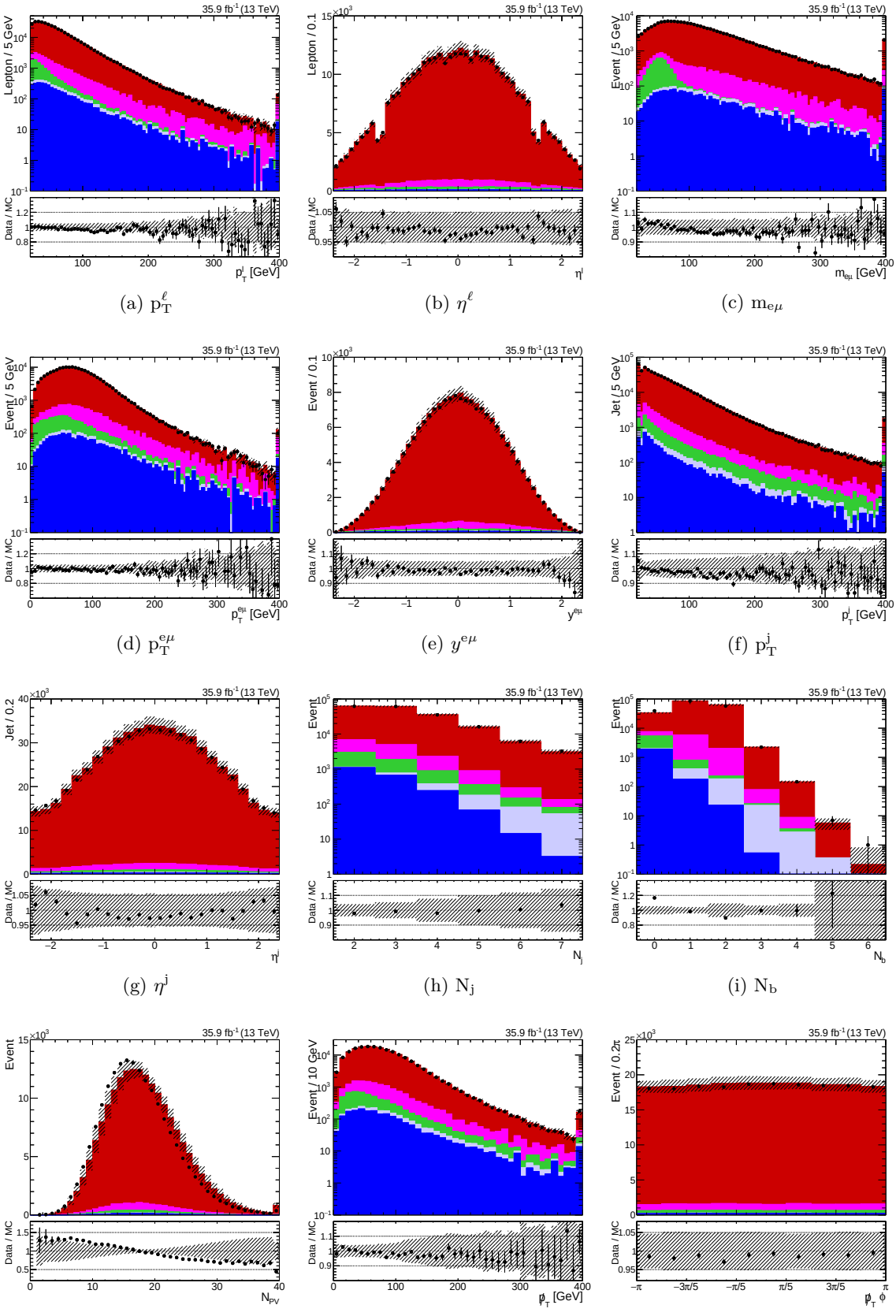

(a) p_T^{ℓ} (b) η^{ℓ} (c) $m_{e\mu}$

(d) $p_T^{e\mu}$ (e) $y^{e\mu}$ (f) p_T^{j}

(g) η^{j} (h) N_j (i) N_b

(j) N_{PV} (k) $\not{p}_T$ (l) $\not{p}_T$ ϕ

Figure B.8: Control distributions with up to the 2 jet cut applied in the eμ channel.

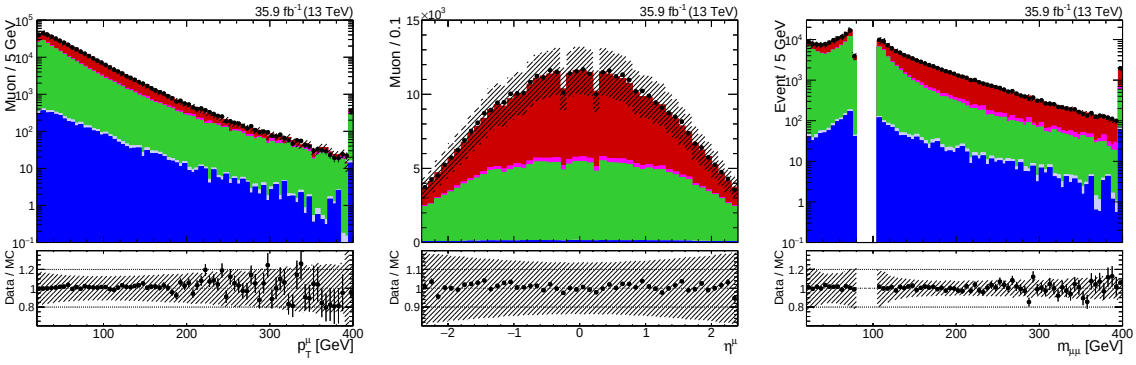

(a) p_T^{μ}

(b) η^{μ}

(c) $m_{\mu\mu}$

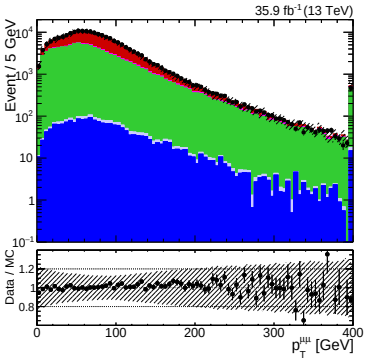

(d) $p_T^{\mu\mu}$

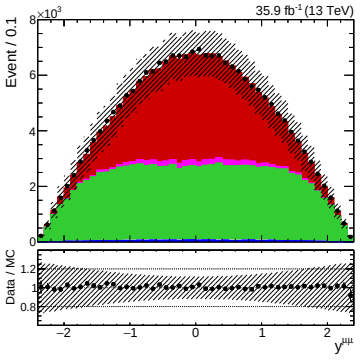

(e) $y^{\mu\mu}$

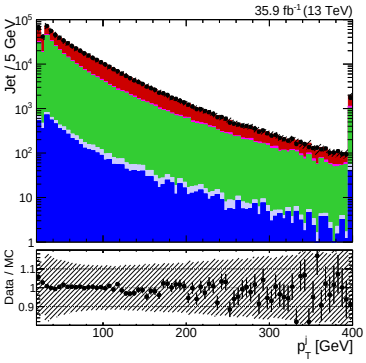

(f) p_T^{j}

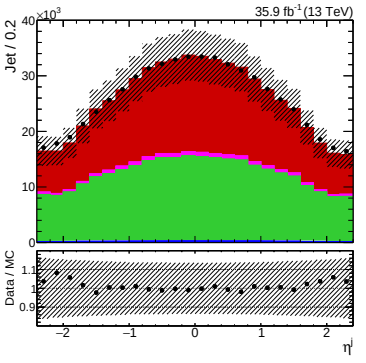

(g) η^{j}

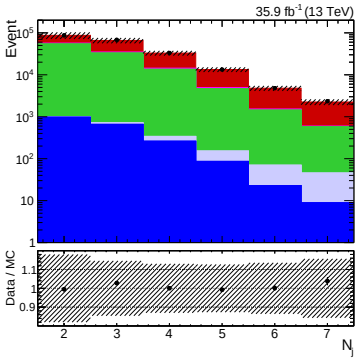

(h) N_j

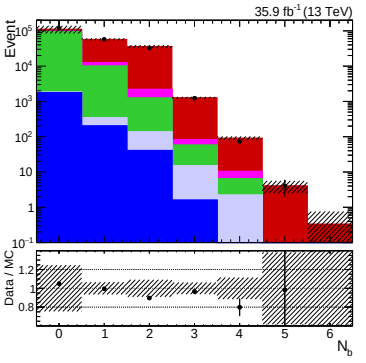

(i) N_b

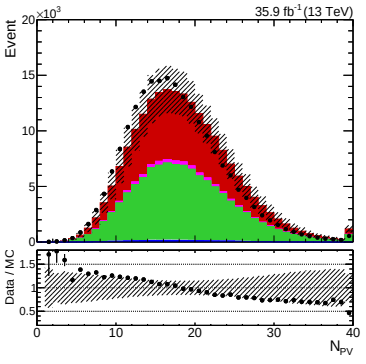

(j) N_{PV}

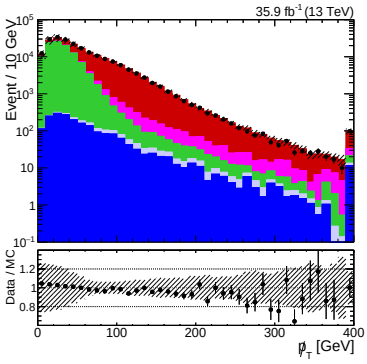

(k) $\not{p}_T$

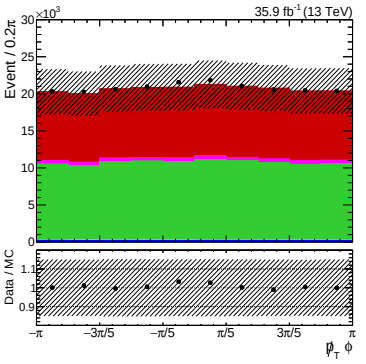

(l) $\not{p}_T$ ϕ

Figure B.9: Control distributions with up to the 2 jet cut applied in the $\mu\mu$ channel.

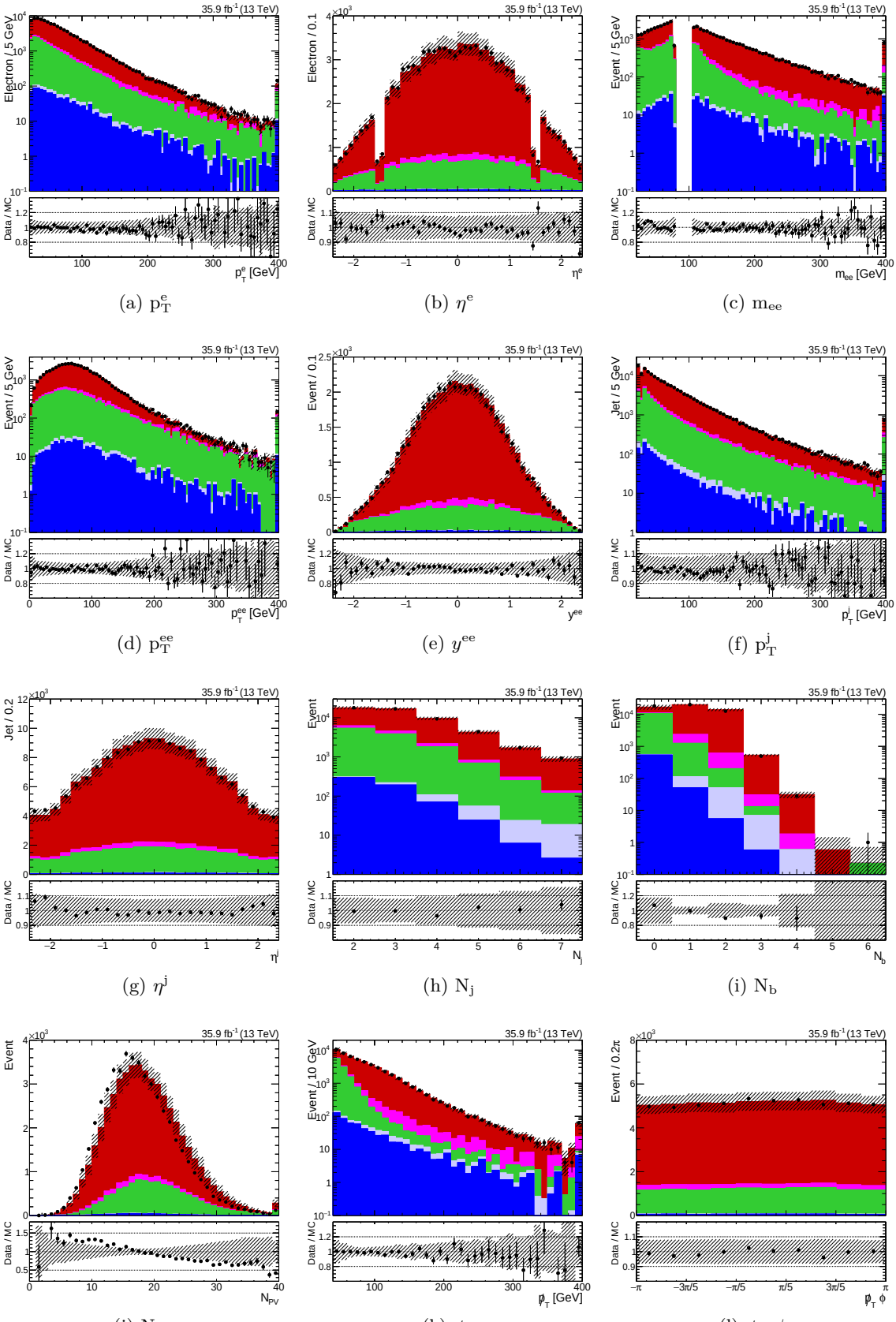

Figure B.10: Control distributions with up to the $\not{p}_{\mathrm{T}}$ cut applied in the ee channel.

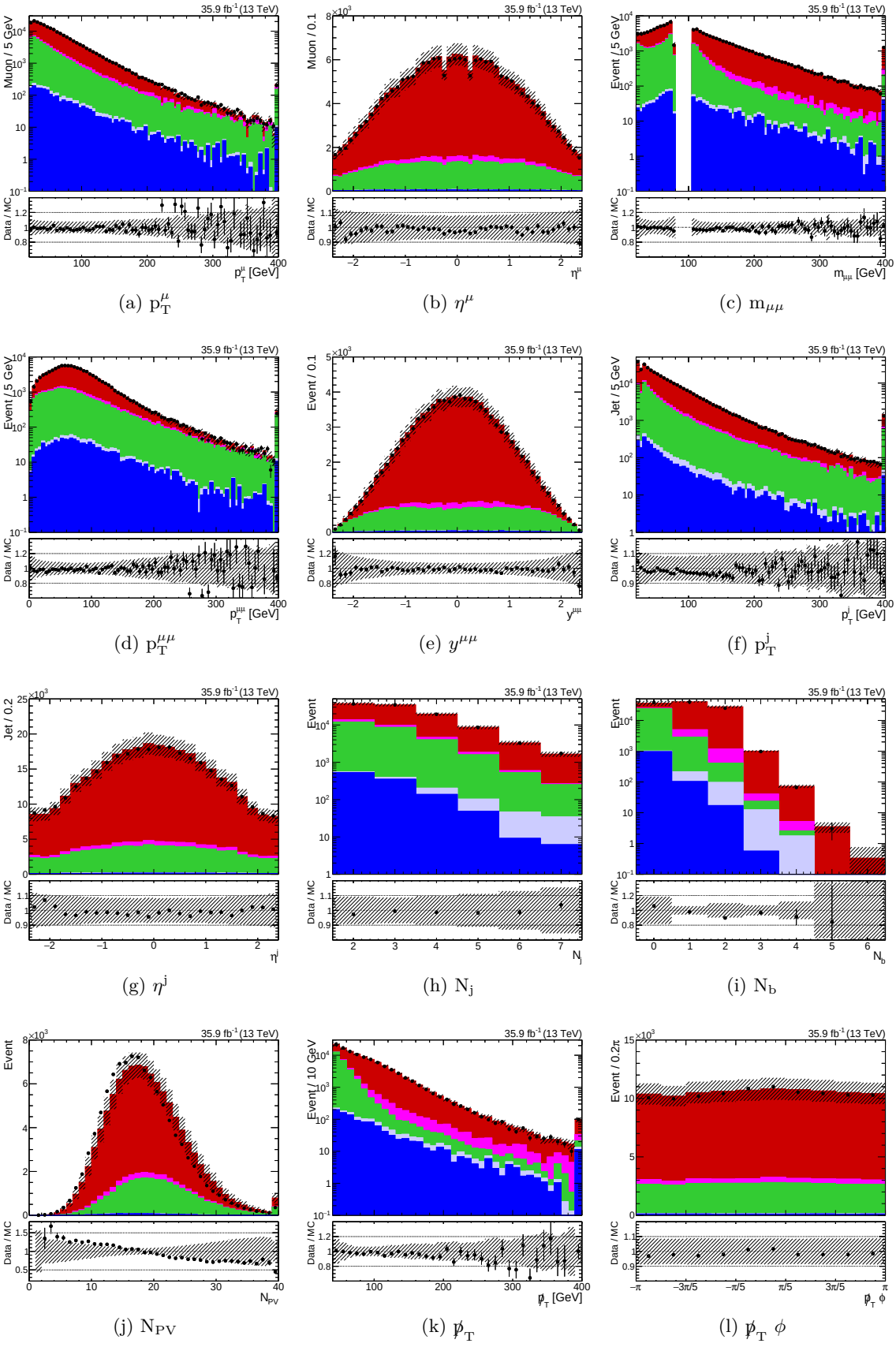

(a) p_T^{μ} (b) η^{μ} (c) $m_{\mu\mu}$

(d) $p_T^{\mu\mu}$ (e) $y^{\mu\mu}$ (f) p_T^{j}

(g) η^{j} (h) N_j (i) N_b

(j) N_{PV} (k) $\not{p}_T$ (l) $\not{p}_T$ ϕ

Figure B.11: Control distributions with up to the $\not{p}_T$ cut applied in the $\mu\mu$ channel.

APPENDIX

C

GENERATED DISTRIBUTIONS OF SPIN CORRELATION OBSERVABLES

In this appendix, the distributions of spin correlation variables at the generator level for both SM and A/H resonance production are shown; for the latter the A/H$(500, 10\%)$ points are chosen as representative signal points. No acceptance cuts are imposed in making the distributions. For the observables defined in the $\{\mathrm{k}, \mathrm{r}, \mathrm{n}\}$ system, the distributions are the same for A/H resonances of all mass and width values. All distributions are normalized to unit area and the uncertainties are only due to finite simulation size.

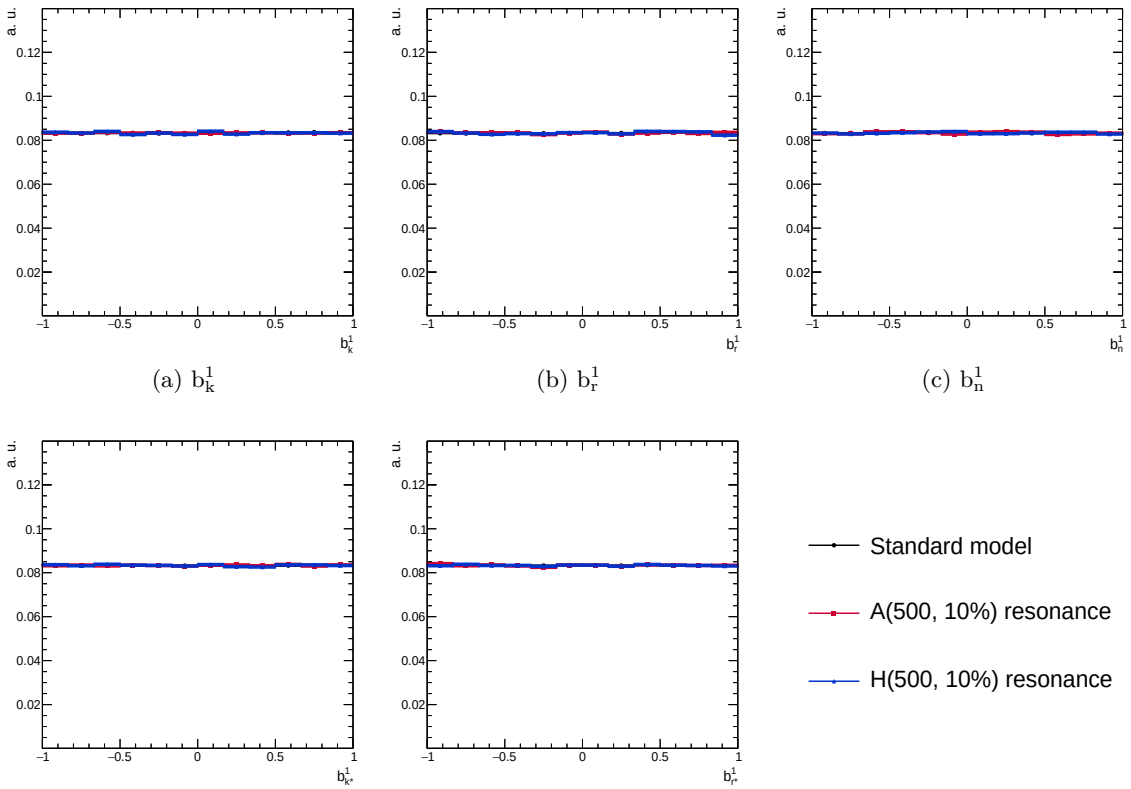

(a) b^1_k (b) b^1_r (c) b^1_n

(d) b^1_{k*} (e) b^1_{r*} (f) Legend

Figure C.1: Generated distributions of the polarization angles b^1_i. b^2_i distributions are the same as b^1_i for all the three cases shown here.

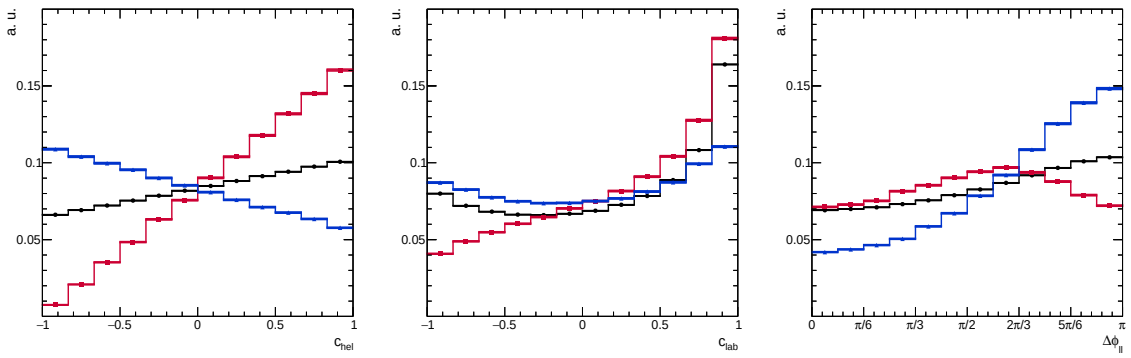

(a) c_{hel} (b) c_{lab} (c) $\Delta\phi_{\ell\ell}$

Figure C.2: Generated distributions of c_{hel}, c_{lab} and $\Delta\phi_{\ell\ell}$. The legend of the plots is the same as shown in Figure C.1.

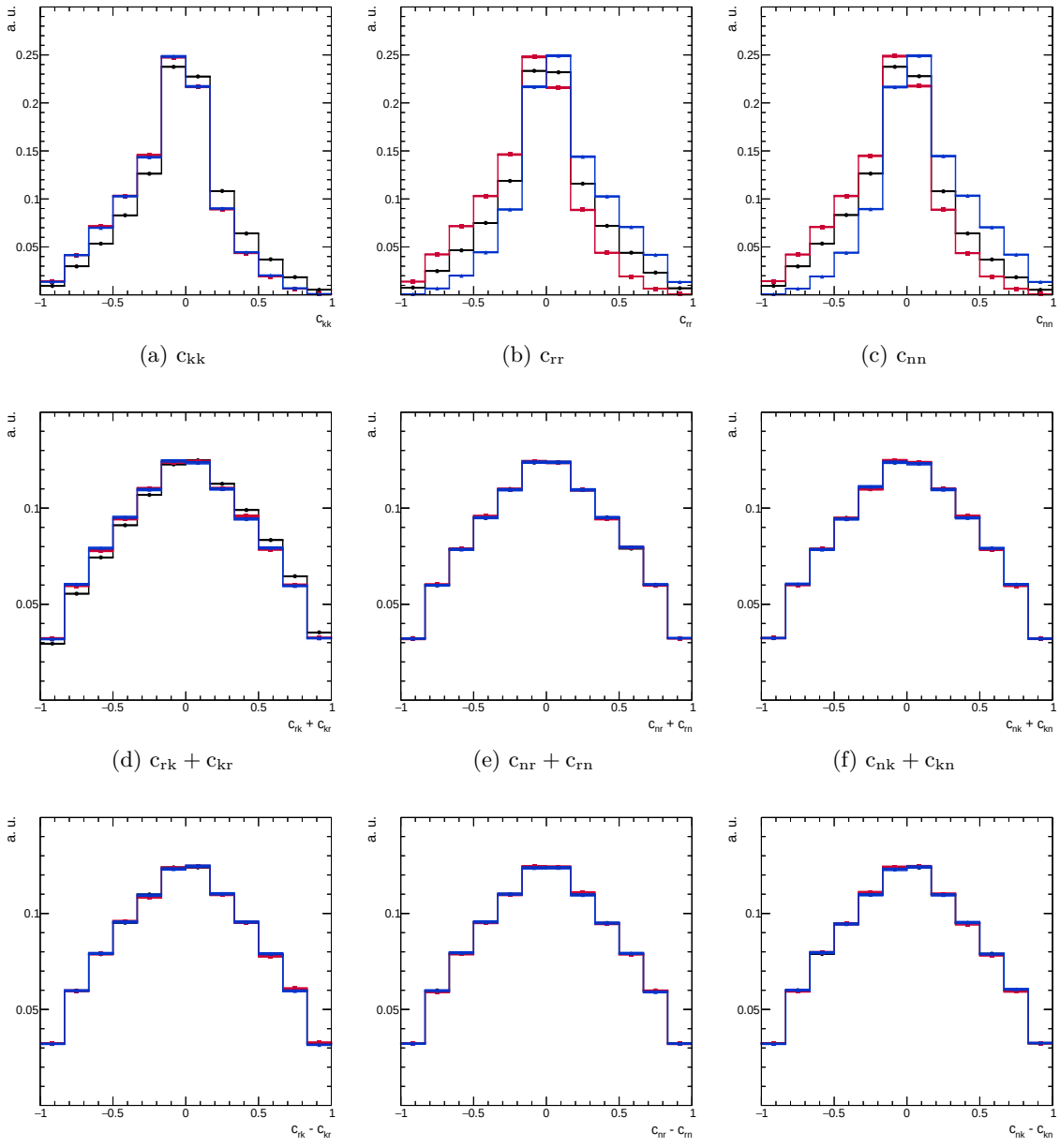

(a) c_{kk} (b) c_{rr} (c) c_{nn}

(d) $c_{rk} + c_{kr}$ (e) $c_{nr} + c_{rn}$ (f) $c_{nk} + c_{kn}$

(g) $c_{rk} - c_{kr}$ (h) $c_{nr} - c_{rn}$ (i) $c_{nk} - c_{kn}$

Figure C.3: Generated distributions of c_{ii} and $c_{ij} \pm c_{ji}$. The legend of the plots is the same as shown in Figure C.1.

APPENDIX

D

SYSTEMATIC TEMPLATES IN A/H SEARCH

This appendix shows the systematic templates in the A/H search in Figure D.1 to Figure D.8. The systematic sources are discussed in Section 6.6. Only their impact on the background are shown, which is either the total SM background or only SM $t\bar{t}$, depending on which processes are affected by the source in question. For sources that are smoothed (see Section 7.3), both the smoothed and original templates are shown as solid and dashed lines respectively. The up and down variations are not specified as it is the envelope formed by these variations that are of relevance in the statistical analysis (see Section 7.4).

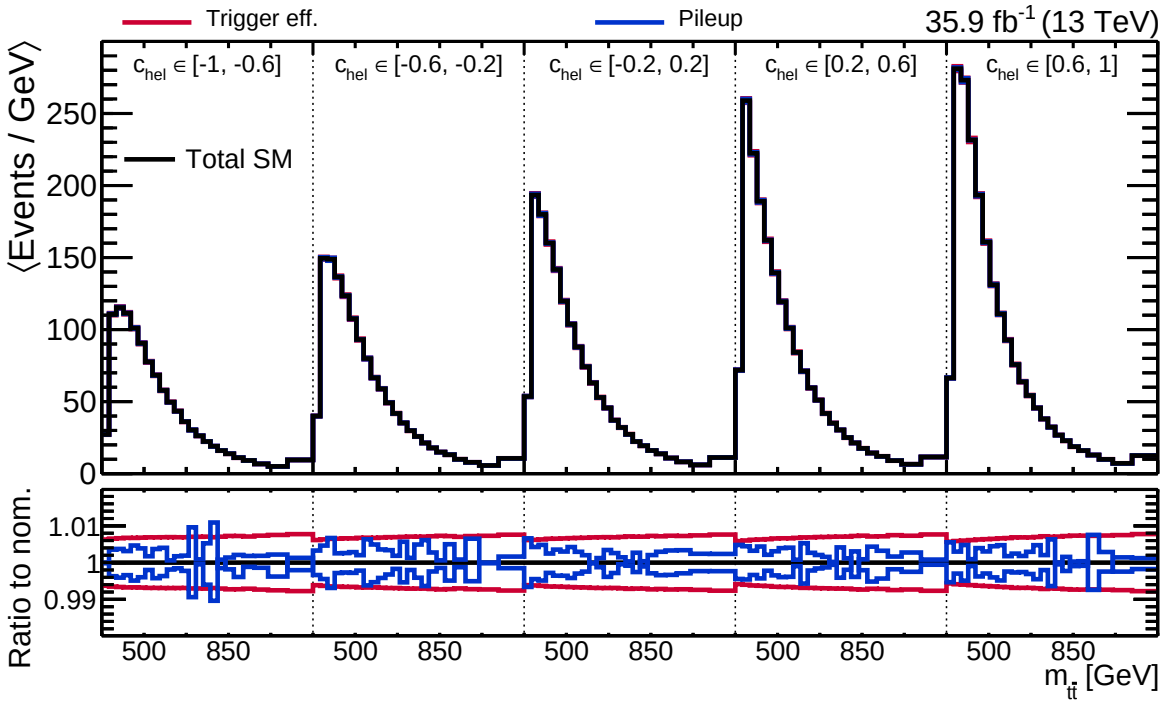

(a) Trigger SF and PU reweighting

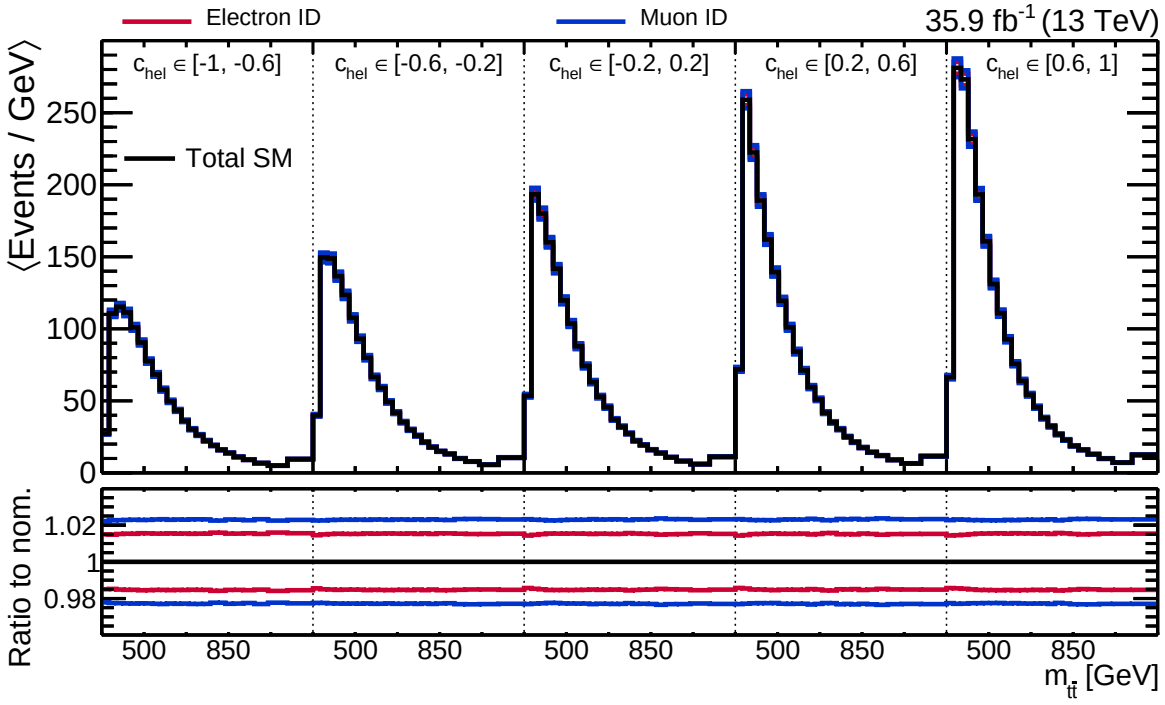

(b) Lepton ID SFs

Figure D.1: Search template comparison between the nominal case and the systematic sources due to trigger efficiencies, pileup and lepton ID. All background contributions are considered.

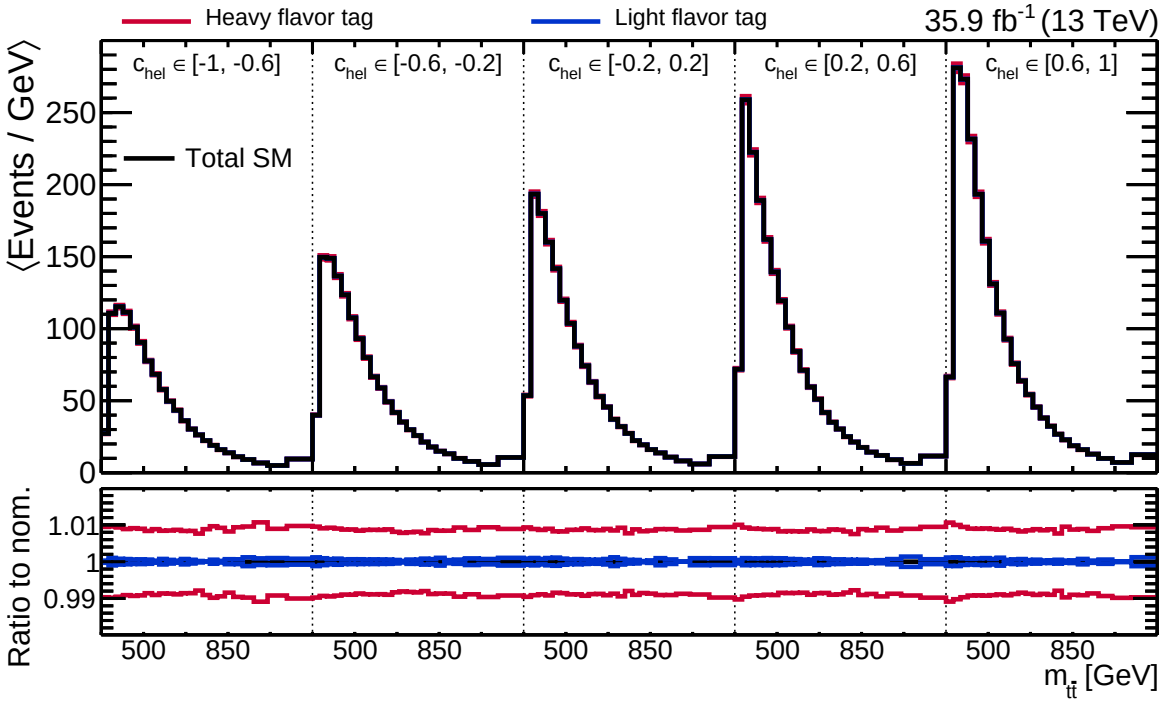

(a) b- and mis-tagging SFs

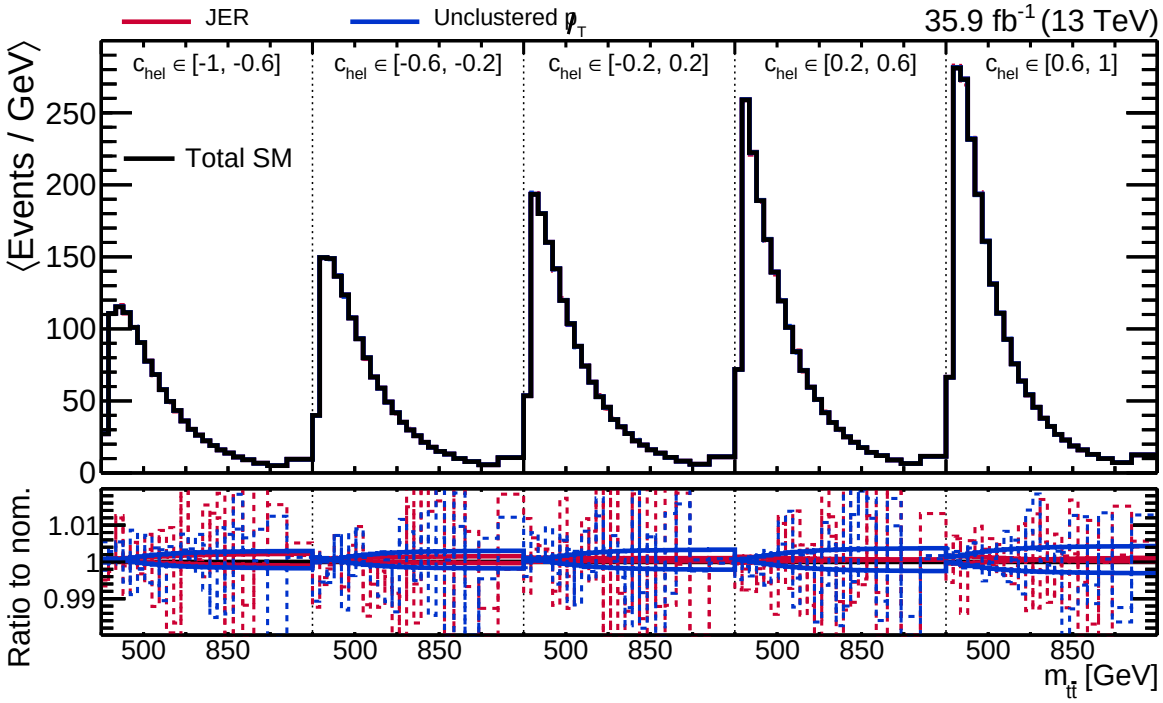

(b) JER and unclustered $\not{p}_T$

Figure D.2: Search template comparison between the nominal case and the systematic sources due to heavy and light flavor tag, JER and unclustered $\not{p}_T$. All background contributions are considered. The dashed lines show the original unsmoothed systematic templates.

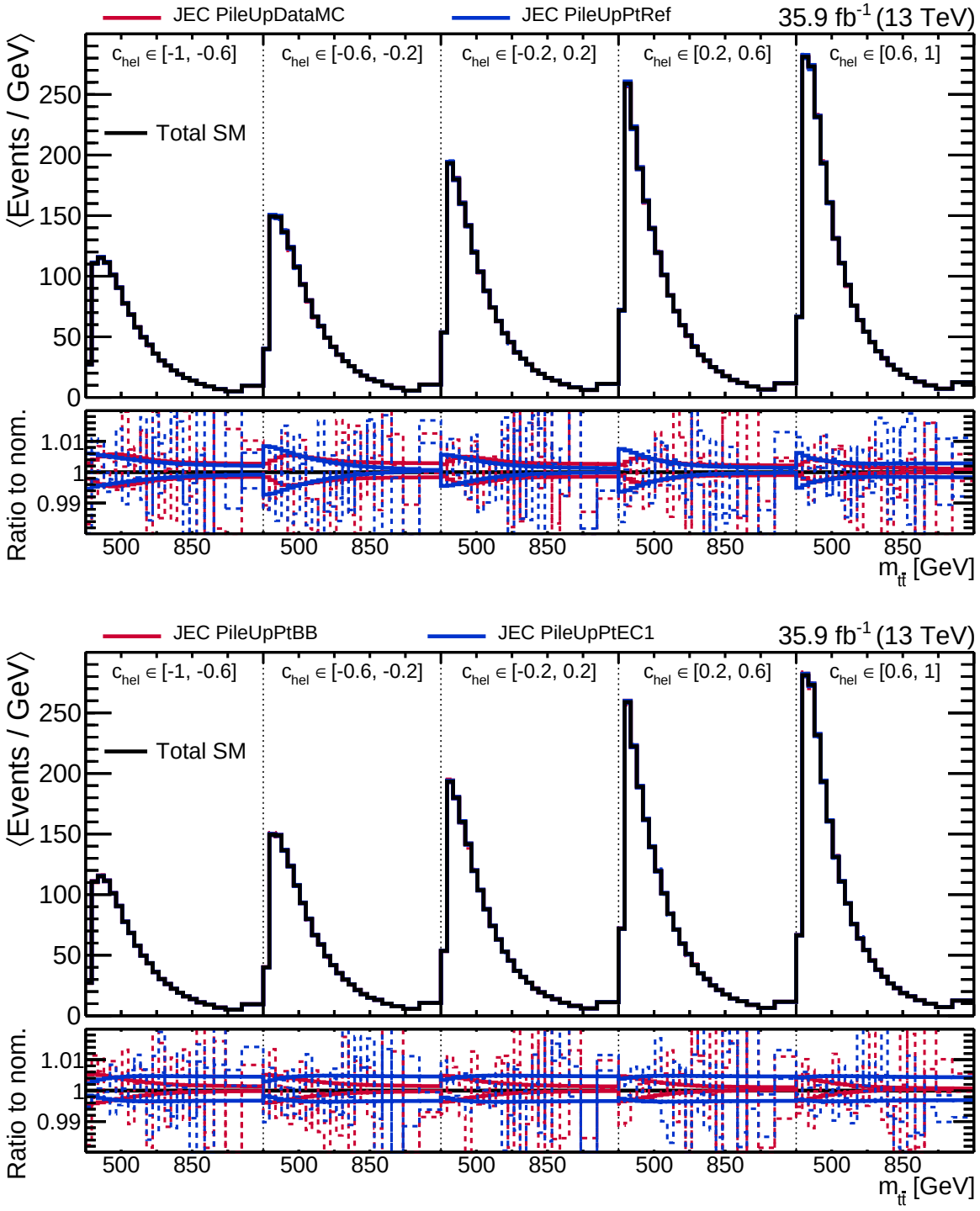

Figure D.3: Search template comparison between the nominal case and the systematic sources due to JEC subsources related to PU. All background contributions are considered. The dashed lines show the original unsmoothed systematic templates.

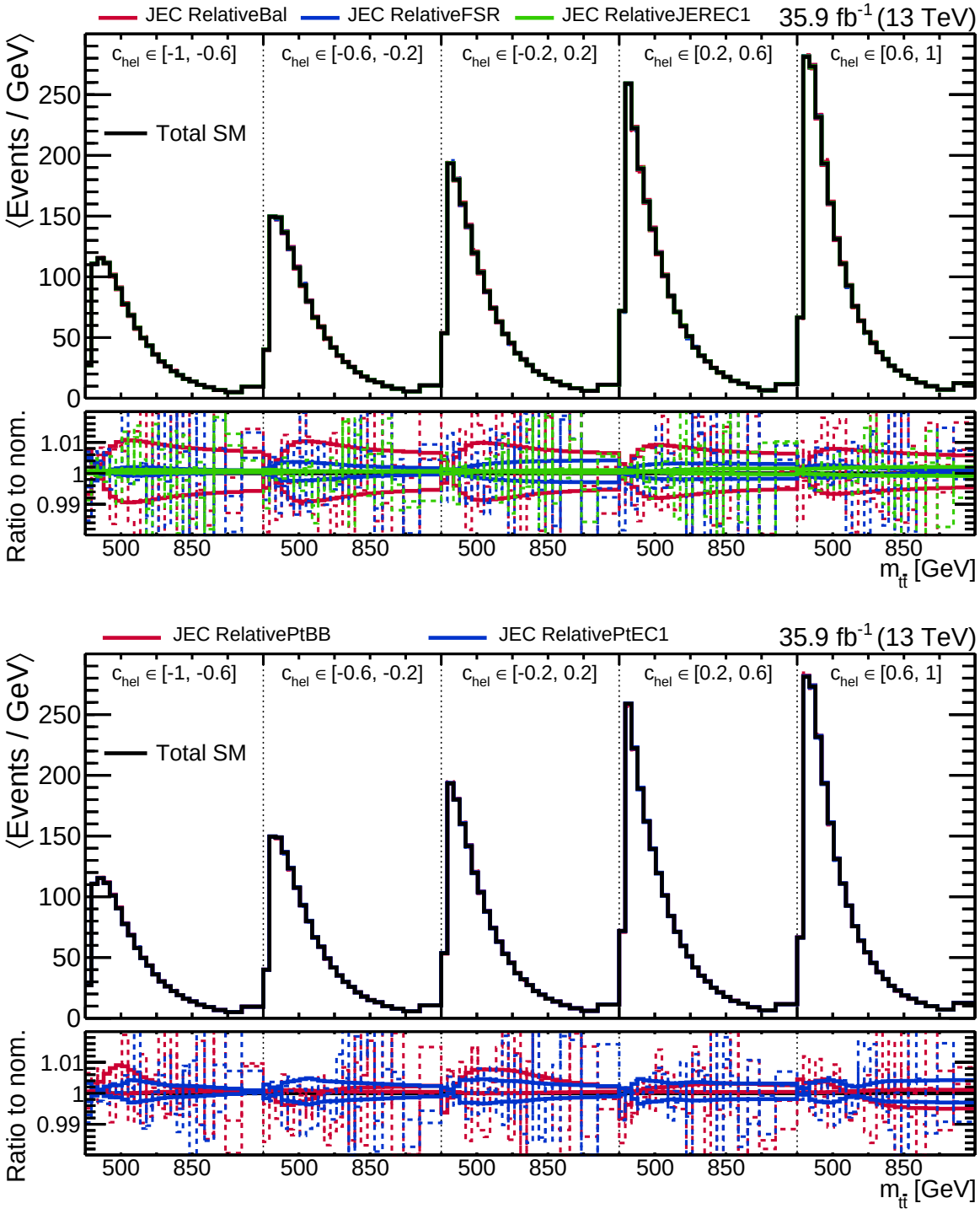

Figure D.4: Search template comparison between the nominal case and the systematic sources due to JEC subsources related to jet response relative to jets within the HB i.e. $|\eta^{j}| < 1.26$. All background contributions are considered. The dashed lines show the original unsmoothed systematic templates.

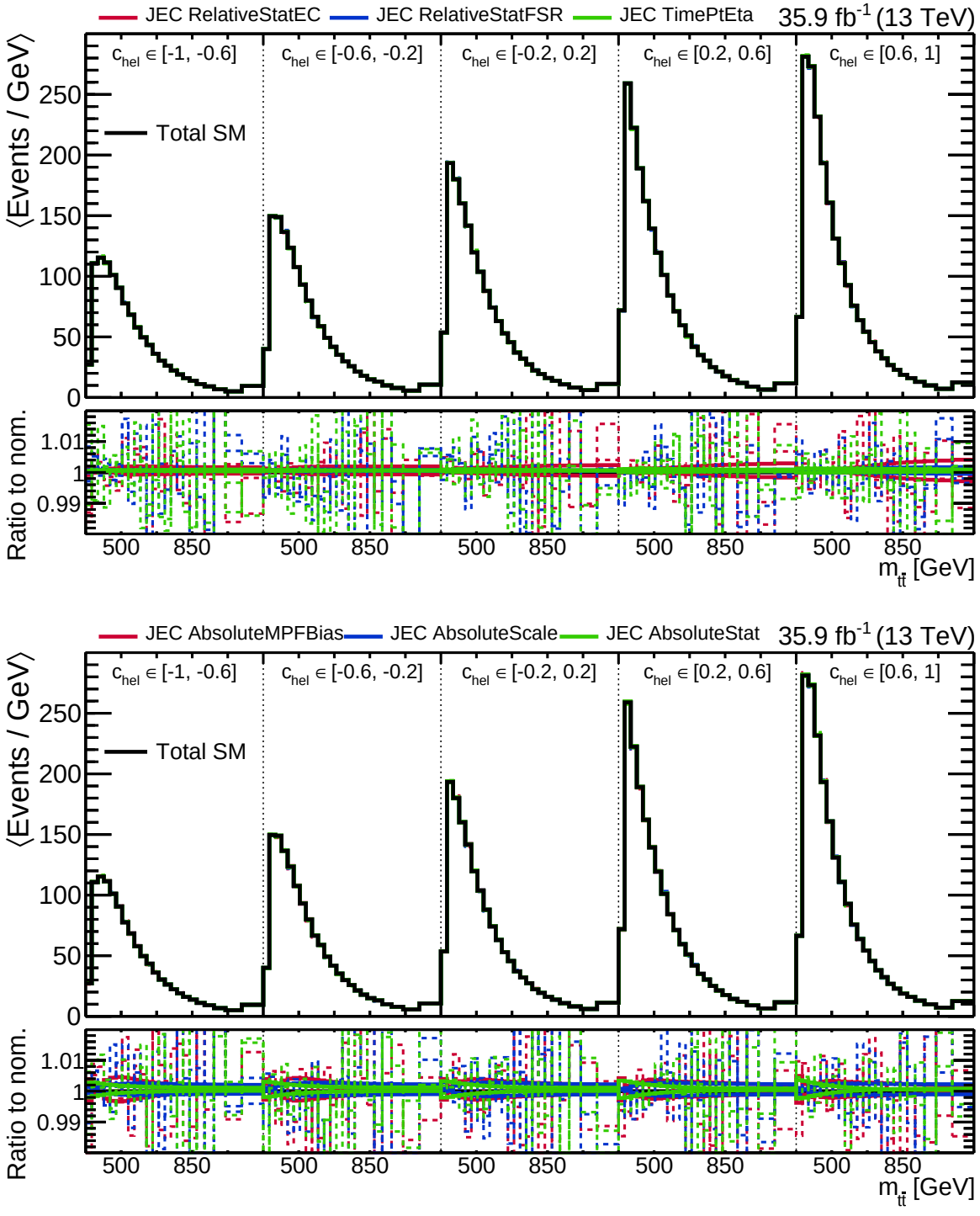

Figure D.5: Search template comparison between the nominal case and the systematic sources due to JEC subsources related to statistical uncertainties in relative response estimation (Figure D.4), time dependence of jet response and absolute response estimation using DY events. All background contributions are considered. The dashed lines show the original unsmoothed systematic templates.

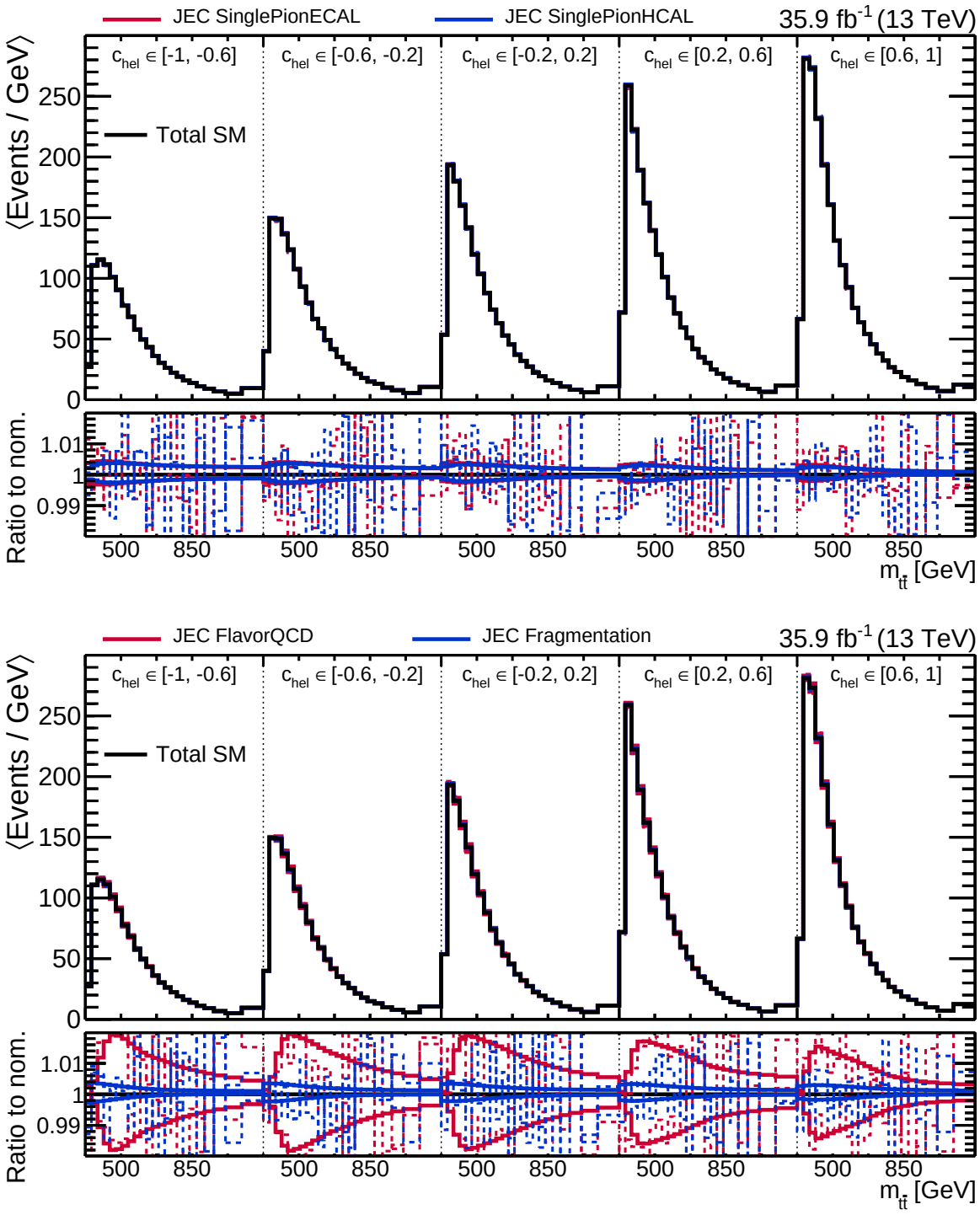

Figure D.6: Search template comparison between the nominal case and the systematic sources due to JEC subsources related to calorimeter response to single pions and parton composition and fragmentation within jets. All background contributions are considered. The dashed lines show the original unsmoothed systematic templates.

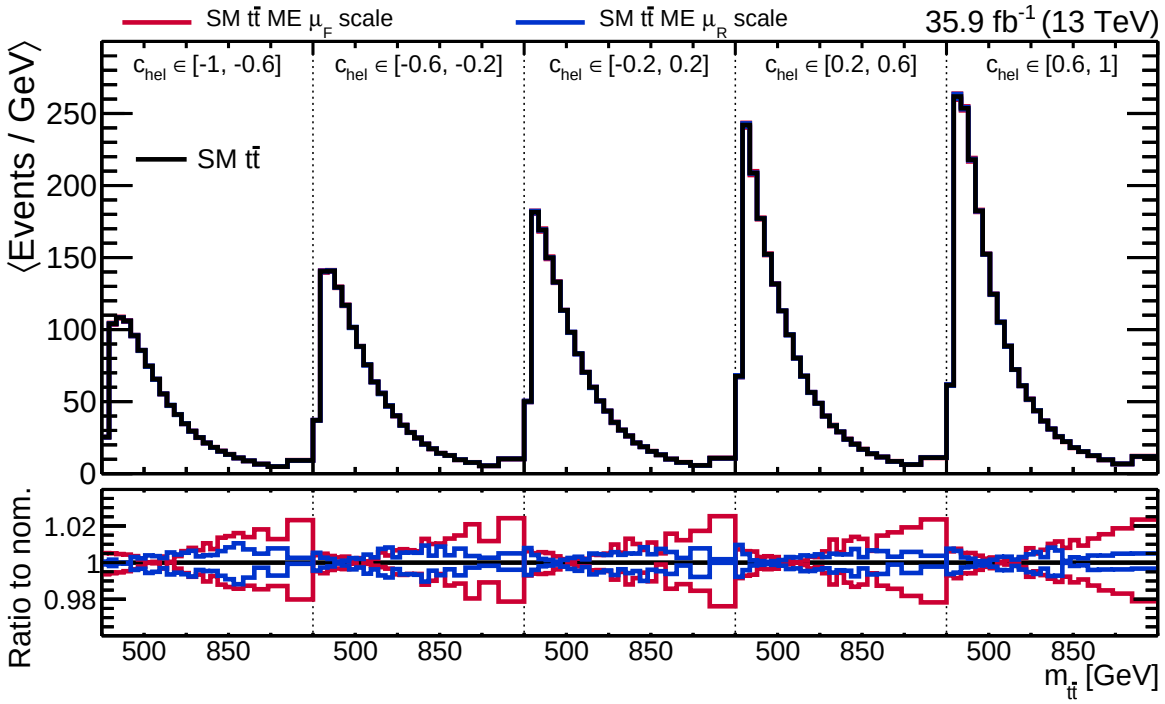

(a) ME scales

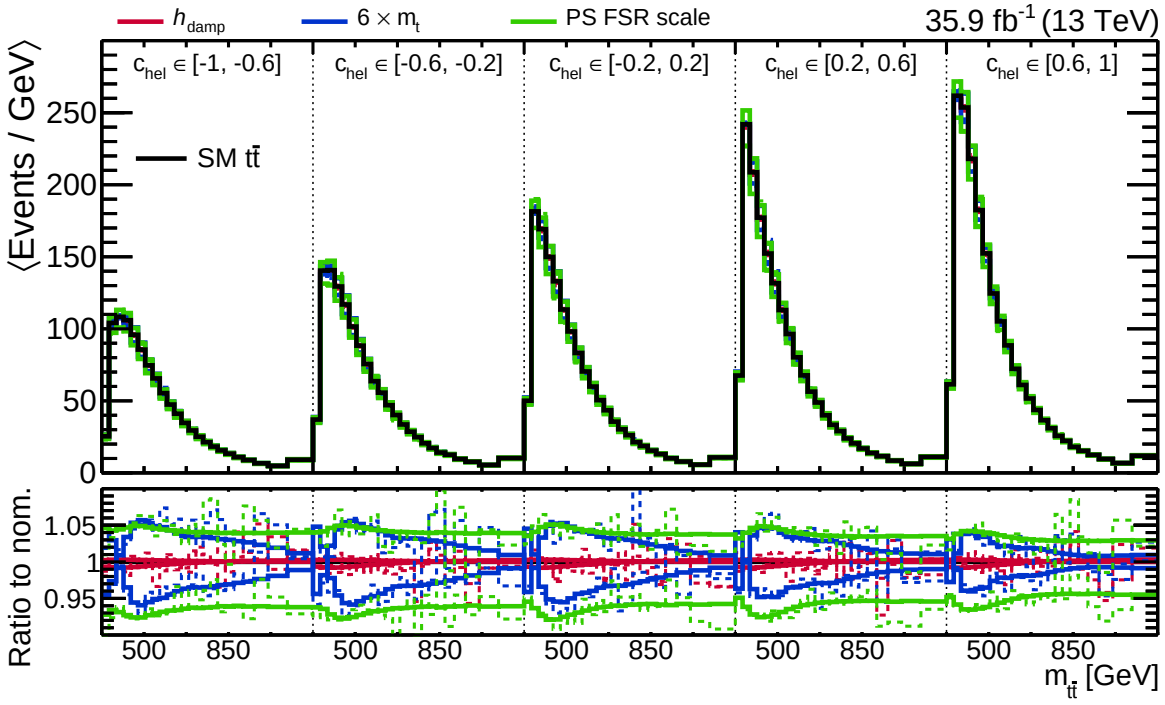

(b) h_{damp}, $\mathrm{m_t}$ and PS FSR

Figure D.7: Search template comparison between the nominal case and the systematic sources due to ME scales, h_{damp}, $\mathrm{m_t}$ and PS FSR. Only the SM $\mathrm{t\bar{t}}$ background is considered. The dashed lines show the original unsmoothed systematic templates.

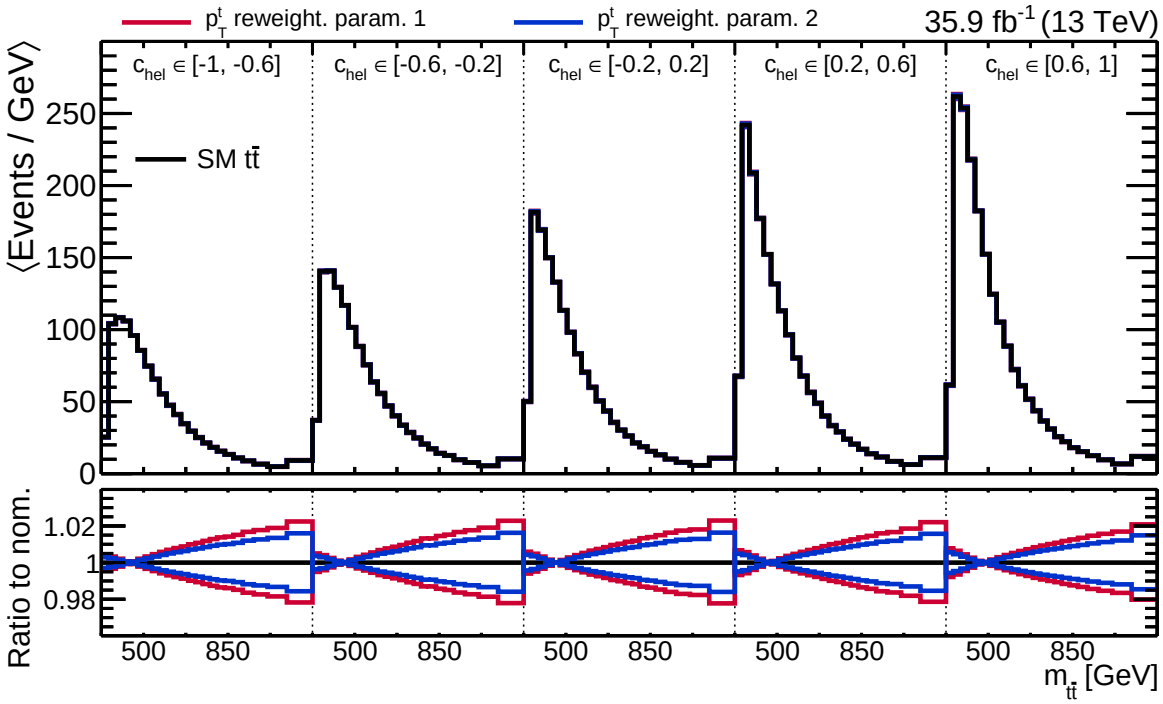

(a) p_T^t reweighting parameters

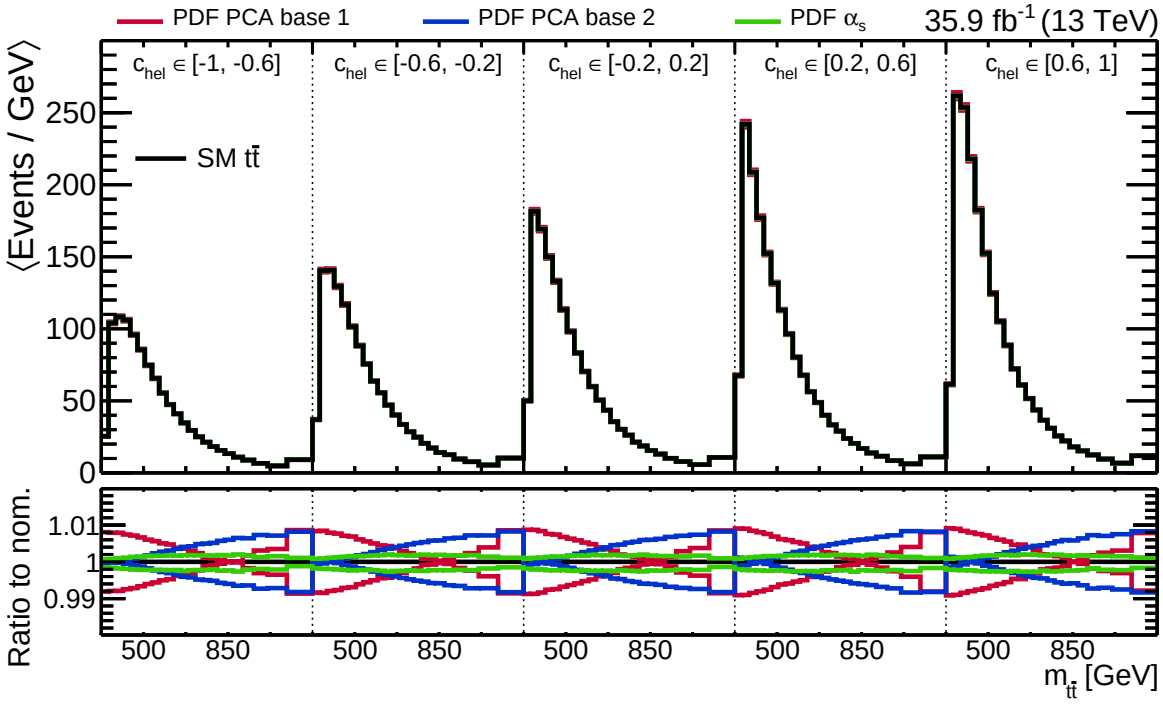

(b) PDF bases and α_s value

Figure D.8: Search template comparison between the nominal case and the systematic sources due to p_T^t reweighting parameters, PDF bases and its α_s value. Only the SM $t\bar{t}$ background is considered.

APPENDIX

E

IMPACT OF SYSTEMATIC SOURCES ON SPIN CORRELATION OBSERVABLES

In this appendix, the impact of individual systematic sources to the measured distributions of spin correlation observables are shown. The cumulative fractional contribution of different systematic sources with respect to the total systematic uncertainties are shown in Figures E.1, E.2 and E.5 for the absolute differential measurement, and Figures E.3, E.4 and E.6 for the normalized differential measurement. For the sake of readability, some systematic sources are grouped together in these plots e.g. all JEC sources are shown under a single JEC source and both b-tagging and mistagging are also merged.

In the absolute differential measurement, the dominant uncertainties are the experimental systematic sources, as they mainly affect the acceptance matrix, which is propagated to the total rate. The normalized differential measurements on the other hand are mainly affected by sources related to modelling of the process, since they induce a larger change in distribution shapes, while the impact of experimental sources are reduced, as their impact on total rates cancel out. However their overall contribution can still be significant, e.g. the JEC systematics since uncertainties related to the b jet energies directly affect the reconstructed position of the $t\bar{t}$ scattering plane. Background normalization affects c_{lab} the most due to the increase in DY contribution at high c_{lab}. The p_T^t reweighting source has a relatively minor impact in all observables except for $\Delta\phi_{\ell\ell}$.

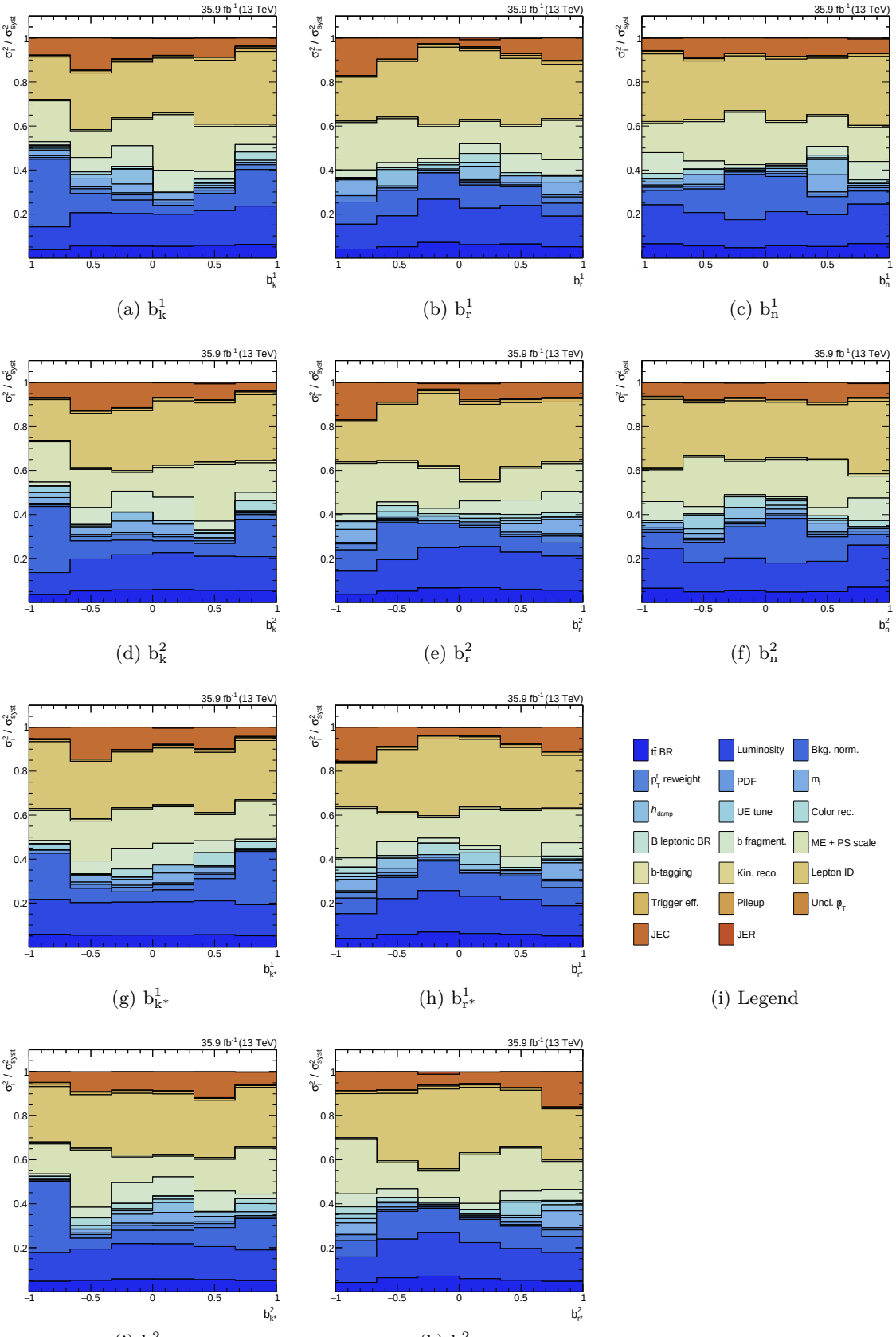

(a) b_k^1 (b) b_r^1 (c) b_n^1

(d) b_k^2 (e) b_r^2 (f) b_n^2

(g) $b_{k^*}^1$ (h) $b_{r^*}^1$ (i) Legend

(j) $b_{k^*}^2$ (k) $b_{r^*}^2$

Figure E.1: Cumulative fractional systematic contributions to the total systematic uncertainties for unfolded b_i^a distributions in the absolute differential measurement.

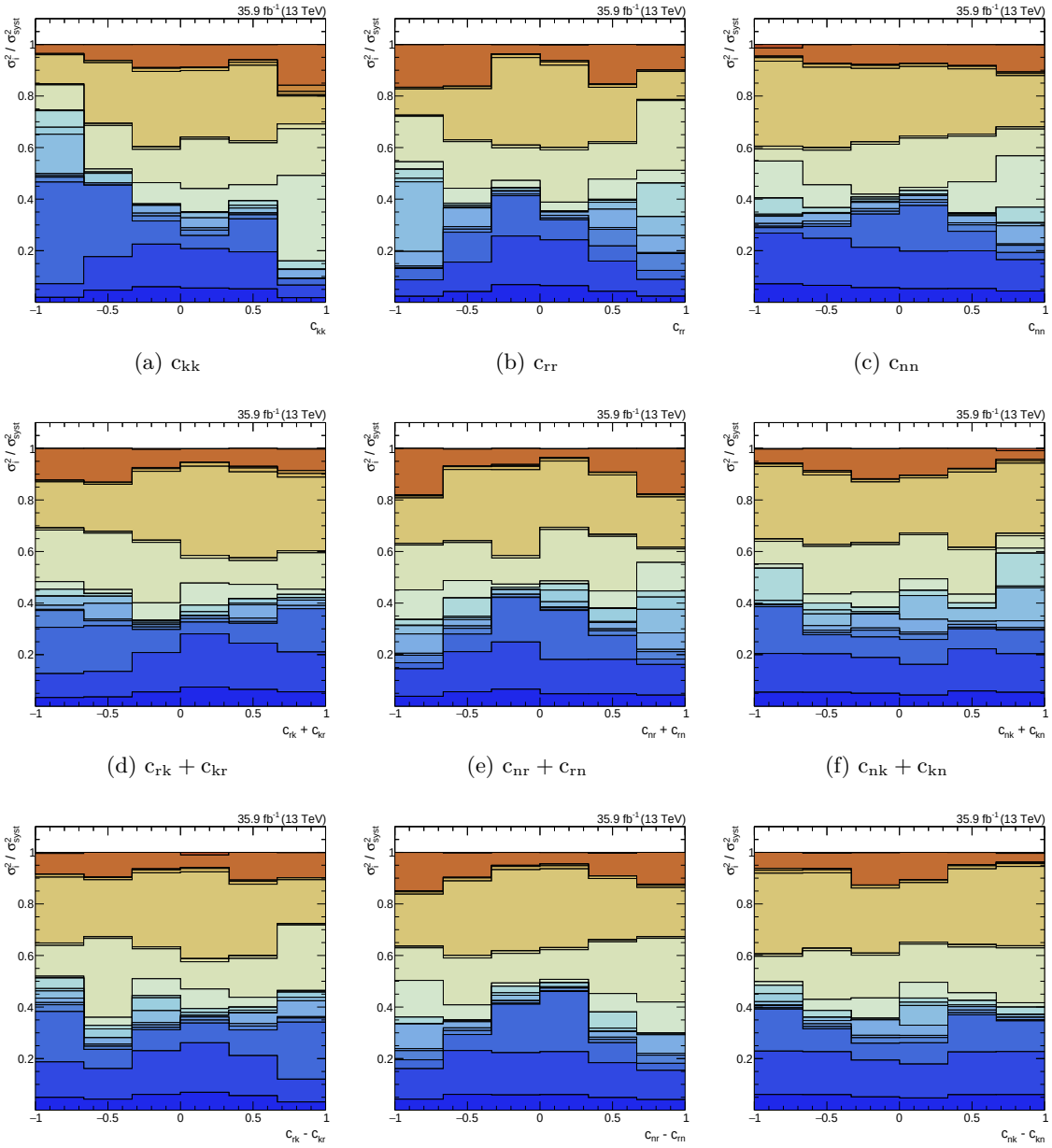

(a) c_{kk} (b) c_{rr} (c) c_{nn}

(d) $c_{rk} + c_{kr}$ (e) $c_{nr} + c_{rn}$ (f) $c_{nk} + c_{kn}$

(g) $c_{rk} - c_{kr}$ (h) $c_{nr} - c_{rn}$ (i) $c_{nk} - c_{kn}$

Figure E.2: Cumulative fractional systematic contributions to the total systematic uncertainties for unfolded c_{ii} and $c_{ij} \pm c_{ji}$ distributions in the absolute differential measurement. The legend of the plots is the same as shown in Figure E.1.

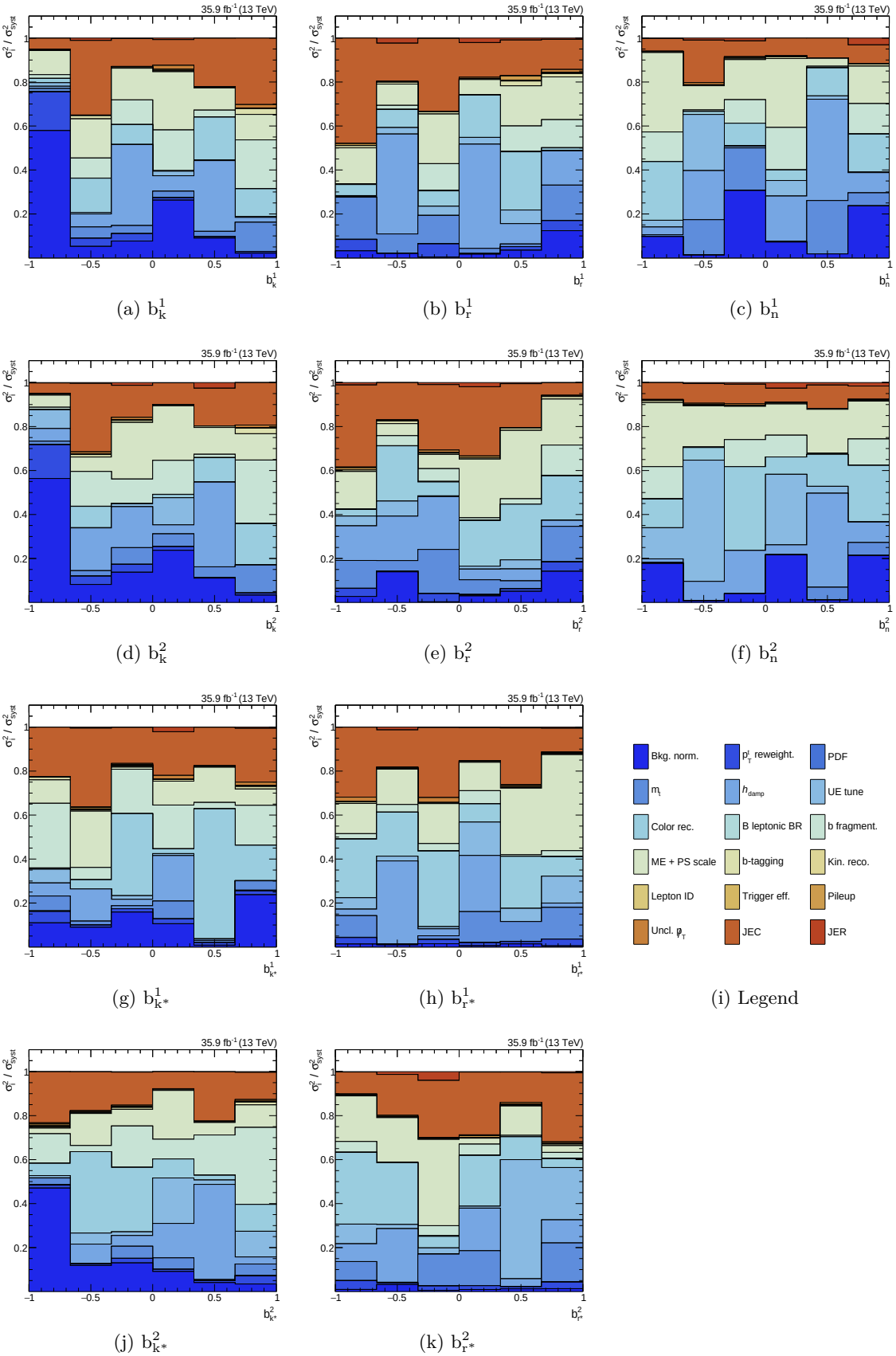

(a) b^1_k (b) b^1_r (c) b^1_n

(d) b^2_k (e) b^2_r (f) b^2_n

(g) $b^1_{k^*}$ (h) $b^1_{r^*}$ (i) Legend

(j) $b^2_{k^*}$ (k) $b^2_{r^*}$

Figure E.3: Cumulative fractional systematic contributions to the total systematic uncertainties for unfolded b^a_i distributions in the normalized differential measurement.

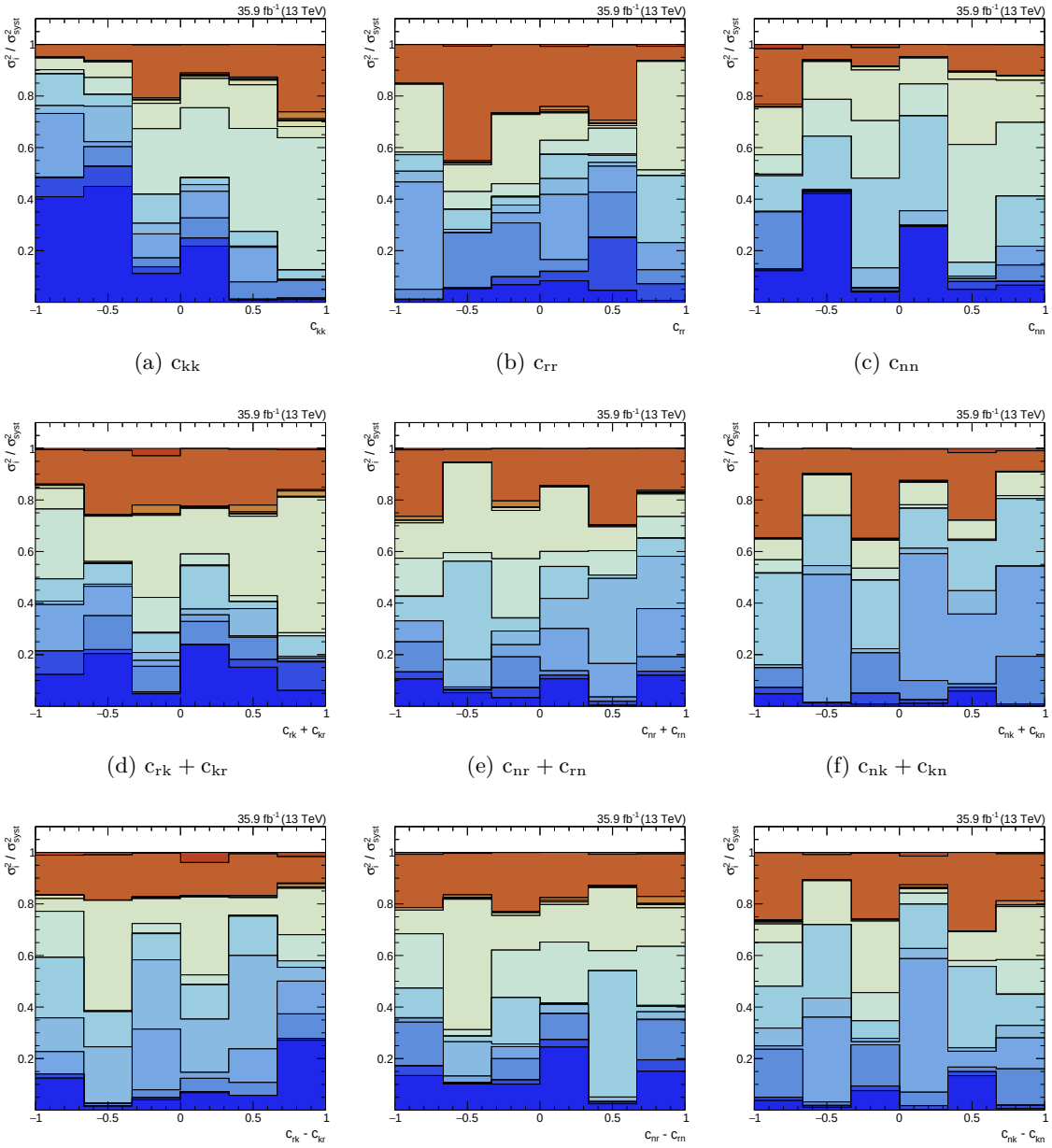

(a) c_{kk} (b) c_{rr} (c) c_{nn}

(d) $c_{rk} + c_{kr}$ (e) $c_{nr} + c_{rn}$ (f) $c_{nk} + c_{kn}$

(g) $c_{rk} - c_{kr}$ (h) $c_{nr} - c_{rn}$ (i) $c_{nk} - c_{kn}$

Figure E.4: Cumulative fractional systematic contributions to the total systematic uncertainties for unfolded c_{ii} and $c_{ij} \pm c_{ji}$ distributions in the normalized differential measurement. The legend of the plots is the same as shown in Figure E.3.

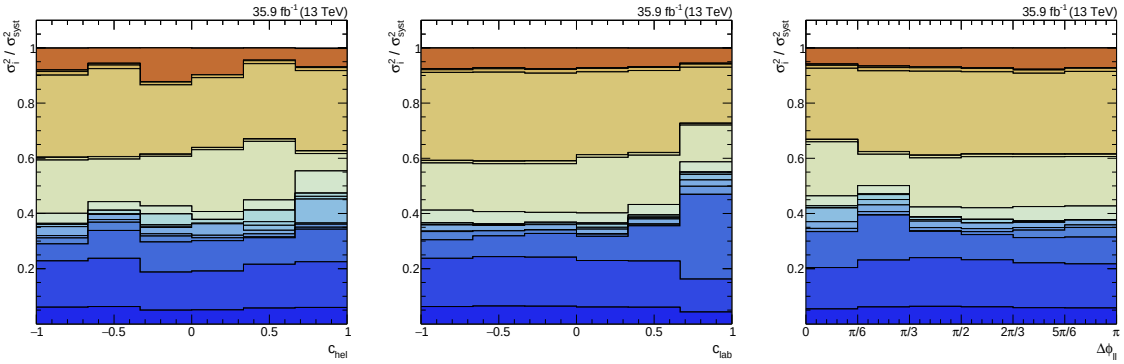

(a) c_{hel} (b) c_{lab} (c) $\Delta\phi_{\ell\ell}$

Figure E.5: Cumulative fractional systematic contributions to the total systematic uncertainties for unfolded c_{hel}, c_{lab} and $\Delta\phi_{\ell\ell}$ distributions in the absolute differential measurement. The legend of the plots is the same as shown in Figure E.1.

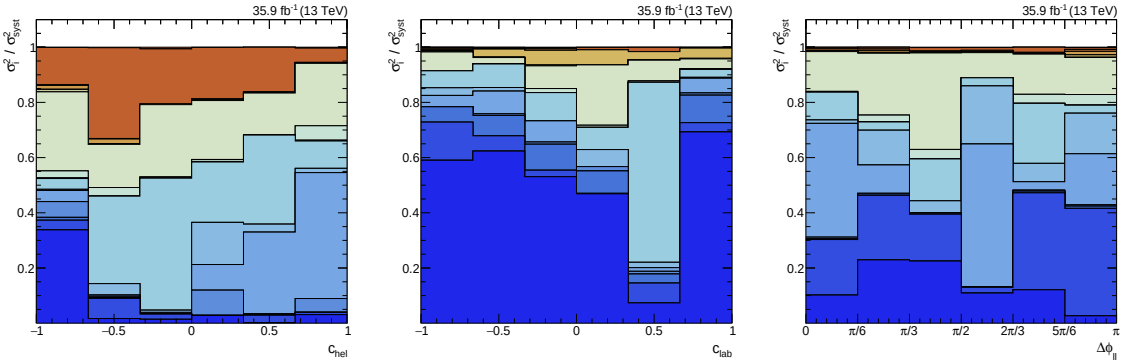

(a) c_{hel} (b) c_{lab} (c) $\Delta\phi_{\ell\ell}$

Figure E.6: Cumulative fractional systematic contributions to the total systematic uncertainties for unfolded c_{hel}, c_{lab} and $\Delta\phi_{\ell\ell}$ distributions in the normalized differential measurement. The legend of the plots is the same as shown in Figure E.3.

APPENDIX

F

CHOICE OF SPIN CORRELATION OBSERVABLES IN THE EFT FIT

Here we will be discussing how the four observables that are used in the EFT fit are chosen. For this purpose, let us introduce the so-called evolution plot, shown in Figure F.1.

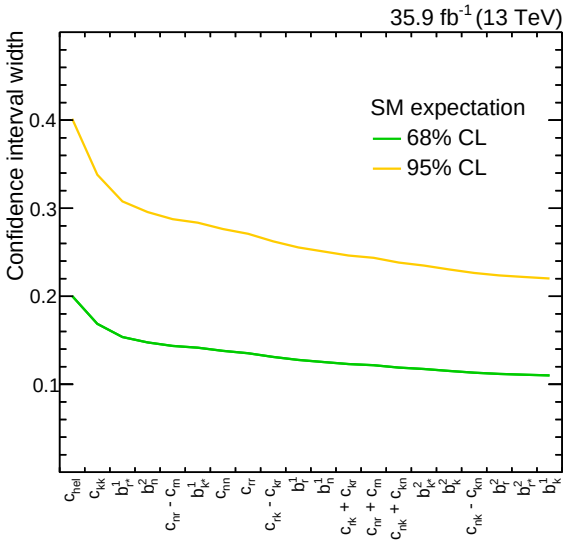

Figure F.1: Sensitivity evolution of C_{tG}/Λ^2 with all observables used in the fit.

This plot charts the evolution of sensitivity (in terms of the width of the 68% and 95% confidence intervals) as observables are added to the fit one by one, where in this case we use all observables in the fit even if they are intradependent. The first bin means that c_{hel} is the single observable that is most sensitive to C_{tG}/Λ^2, as also reported by Figure 8.32. The second bin is obtained by performing all possible 2-observable fits with one of them being c_{hel} and reporting the sensitivity of the best combination. As can be seen in Figure F.1, the best 2-observable combination is c_{hel}-c_{kk}. Here it is noted that since the combination with the

narrowest 68% and 95% confidence intervals are not necessarily the same, the 95% confidence interval is used for ranking the observable combinations. The third bin onwards are obtained in a similar way until the list of observables is exhausted. All fits in this check are performed using the SM pseudodata.

As we are dealing with a set of 20 observables, it is not trivial to track down all the possible intradependencies between them. Instead, we utilize the evolution plot for this task, exploiting the fact that all observables are measured with similar statistical precision (see Tables 8.3 and 8.4). This leads to the expectation that an observable can reduce the statistical uncertainty in a fit to a given operator only to the extent that the operator affects its distribution. Since the statistical correlations between observables are only mild (see Figure 8.22), the statistical uncertainties on the best fit value of an operator should only be reduced when distributions that are directly affected by the operator (as listed in Tables 8.7 and 8.8) are used in the fit. As it turns out, this is not the case when all 20 observables are used. Figure F.2 show the two most spectacular cases; $\hat{c}_{\mathrm{VA}}$ and $\hat{c}_{\mathrm{VV}}$.

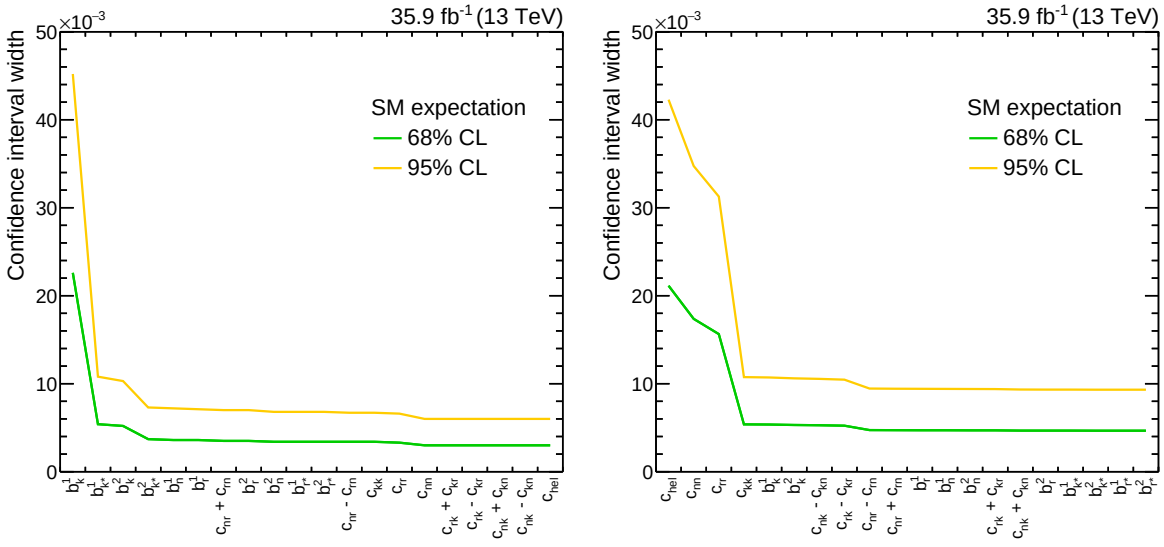

(a) $\hat{c}_{\mathrm{VA}}$ (b) $\hat{c}_{\mathrm{VV}}$

Figure F.2: Statistical evolution of $\hat{c}_{\mathrm{VA}}$ and $\hat{c}_{\mathrm{VV}}$ with all observables used in the fit.

First, let us consider $\hat{c}_{\mathrm{VA}}$; according to Table 8.7 it directly affects only $\mathrm{b}^{a}_{\mathrm{k}}$ and $\mathrm{b}^{a}_{\mathrm{r}}$. The second observable according to the evolution plot is $\mathrm{b}^{1}_{\mathrm{k}*}$, which is not within this list. Looking at the statistical correlation matrix in Figure 8.22 we see that this is due to the correlations between $\mathrm{b}^{a}_{\mathrm{k}}$ and $\mathrm{b}^{a}_{\mathrm{k}*}$, but a factor of 4 improvement in statistical precision purely from correlations is suspicious. To understand the issue better, let us consider the asymmetry between the third and fourth bins of both distributions. Since $\hat{c}_{\mathrm{VA}}$ affects $\mathrm{b}^{a}_{\mathrm{k}}$, it induces an asymmetry in its distribution i.e. increasing the third bin while reducing the fourth, or vice versa. However, since $|\mathrm{b}^{a}_{\mathrm{k}}| = |\mathrm{b}^{a}_{\mathrm{k}*}|$, $\hat{c}_{\mathrm{VA}}$ induces no asymmetry in the $\mathrm{b}^{a}_{\mathrm{k}*}$ distribution. The correlations between the two on the other hand is estimated using the bootstrapping method that can only probe linear correlations, which is insufficient to describe this effect. We therefore

conclude that the reduction in statistical uncertainty is spurious.

Next we turn our attention to $\hat{c}_{\mathrm{VV}}$. Comparing Figure F.2 (b) and Table 8.8, we see that it does indeed directly affect the first few observables. However, the reduction in uncertainty is very large only at the fourth one, indicative of a pathological behavior in the fit. The reason for this is traced to the fact that the set of $\mathrm{c_{hel}}$ and c_{ii} is intradependent since $\mathrm{c_{hel}} = -\sum \mathrm{c}_{ii}$. This is also not described by the covariance matrix, as it only provides the correlations between pairs of quantities. In order to test this hypothesis, we have performed the fits using these four observables in different orders. The sharp reduction of statistical uncertainties is always observed when the fourth observable is added, confirming the hypothesis that the reduction is caused by the intradependency between them that is not described by the covariance matrix.

The problem of tracking down all the possible intradependencies can then replaced with the problem of ensuring that no pathological reduction in statistical uncertainties are present in the fit, which can be solved iteratively by removing observables from the set one by one and monitoring the statistical sensitivity evolution. While this method is necessarily an approximation to the actual problem, the ten operators considered in this work cover distinct parts of the spin density matrix such that the approximation is a rather good one. More importantly, the primary motivation for doing so is to ensure that the sensitivity gained from using multiple observables in the fit does not result in spurious improvements; for this purpose the approximation is sufficient. The list of allowed observables for each operator are shown in Figure F.3. That the operators have somewhat different lists of obvervables is because they are chosen based on sensitivity, with the only restriction that known intradependent sets are not allowed to be complete[1], and the starred and unstarred observables are not allowed to be used together e.g. $\mathrm{b}^1_{\mathrm{k}^*}$ and $\mathrm{b}^1_{\mathrm{k}}$.

Having removed all pathological drops in statistical uncertainty, we recall that the motivation for using multiple distributions in a fit is twofold; to benefit from increased sensitivity due to the fact that a given operator may affect multiple observables and to have the additional observables help in constraining the systematic uncertainties. As such, the final selection of observables should take the latter also into account. The sensitivity evolution considering both the statistical and systematic covariance matrices are shown in Figure F.4, fixing the list of observables to be used. In a touch of conservativeness, for each fit the number of observables used is limited to four. When an operator is fitted by itself, the four observables are determined simply by capping the list, while for operators that are also used in 2D measurements, the two are fitted using the same list of observables that is made combining their respective 1D lists.

[1]For example, only three of $\mathrm{c_{hel}}$ and c_{ii} are allowed since $\mathrm{c_{hel}} = -\sum \mathrm{c}_{ii}$, and only two of b^1_i and two of b^2_i are allowed since $\sum_{i\in\{\mathrm{k/k^*,\,r/r^*,\,n}\}}(\mathrm{b}^a_i)^2 = 1$.

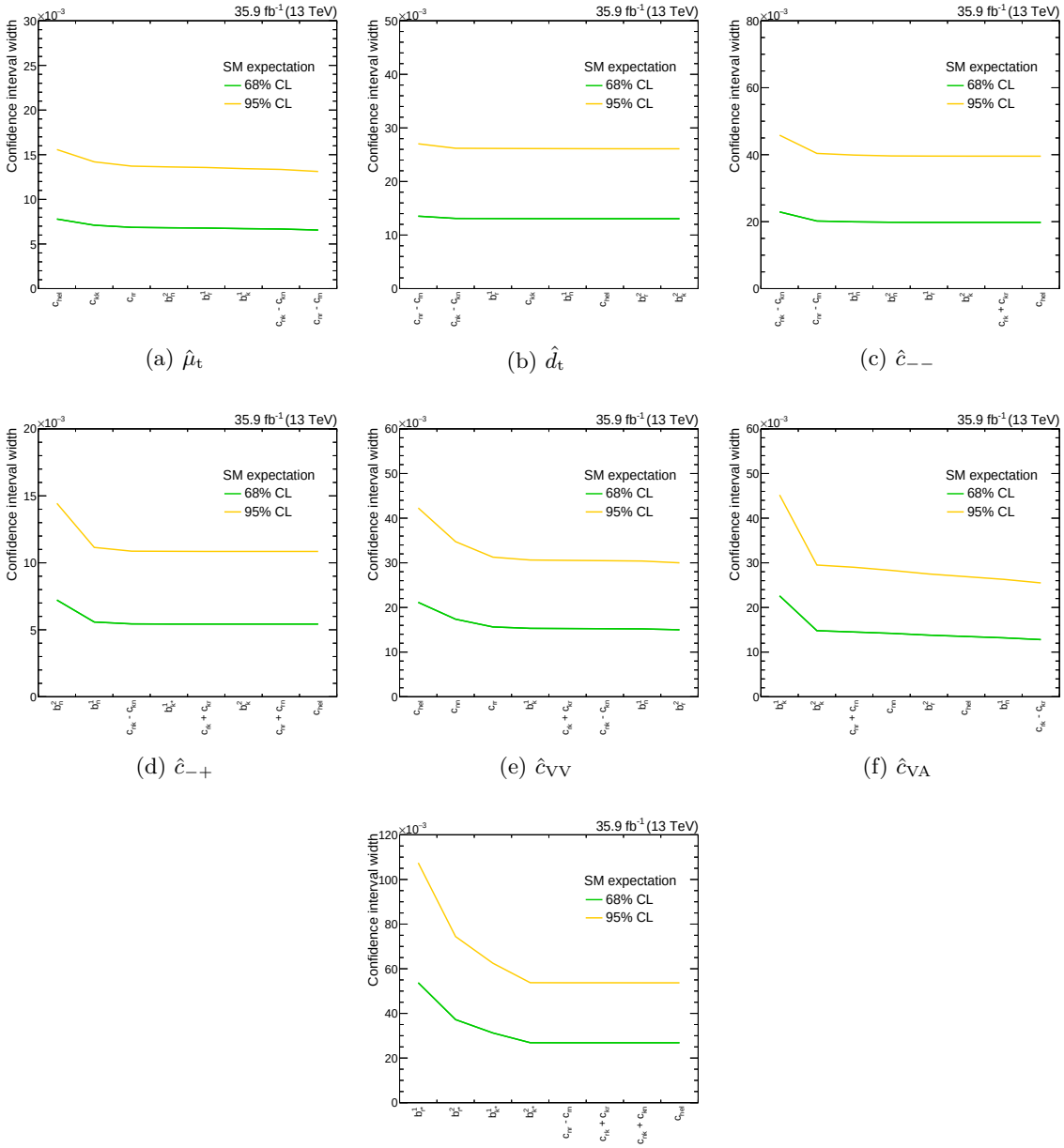

(a) $\hat{\mu}_{\mathrm{t}}$ (b) $\hat{d}_{\mathrm{t}}$ (c) $\hat{c}_{--}$

(d) $\hat{c}_{-+}$ (e) $\hat{c}_{\mathrm{VV}}$ (f) $\hat{c}_{\mathrm{VA}}$

(g) $\hat{c}_{\mathrm{AV}}$

Figure F.3: Evolution of statistical uncertainty of all considered operators after removing intradependent observables. $\hat{c}_1$, $\hat{c}_3$ and $\hat{c}_1 - \hat{c}_2 + \hat{c}_3$ are not shown as they are related by approximately constant factors to $\hat{c}_{\mathrm{VV}}$, $\hat{c}_{\mathrm{VA}}$ and $\hat{c}_{\mathrm{AV}}$.

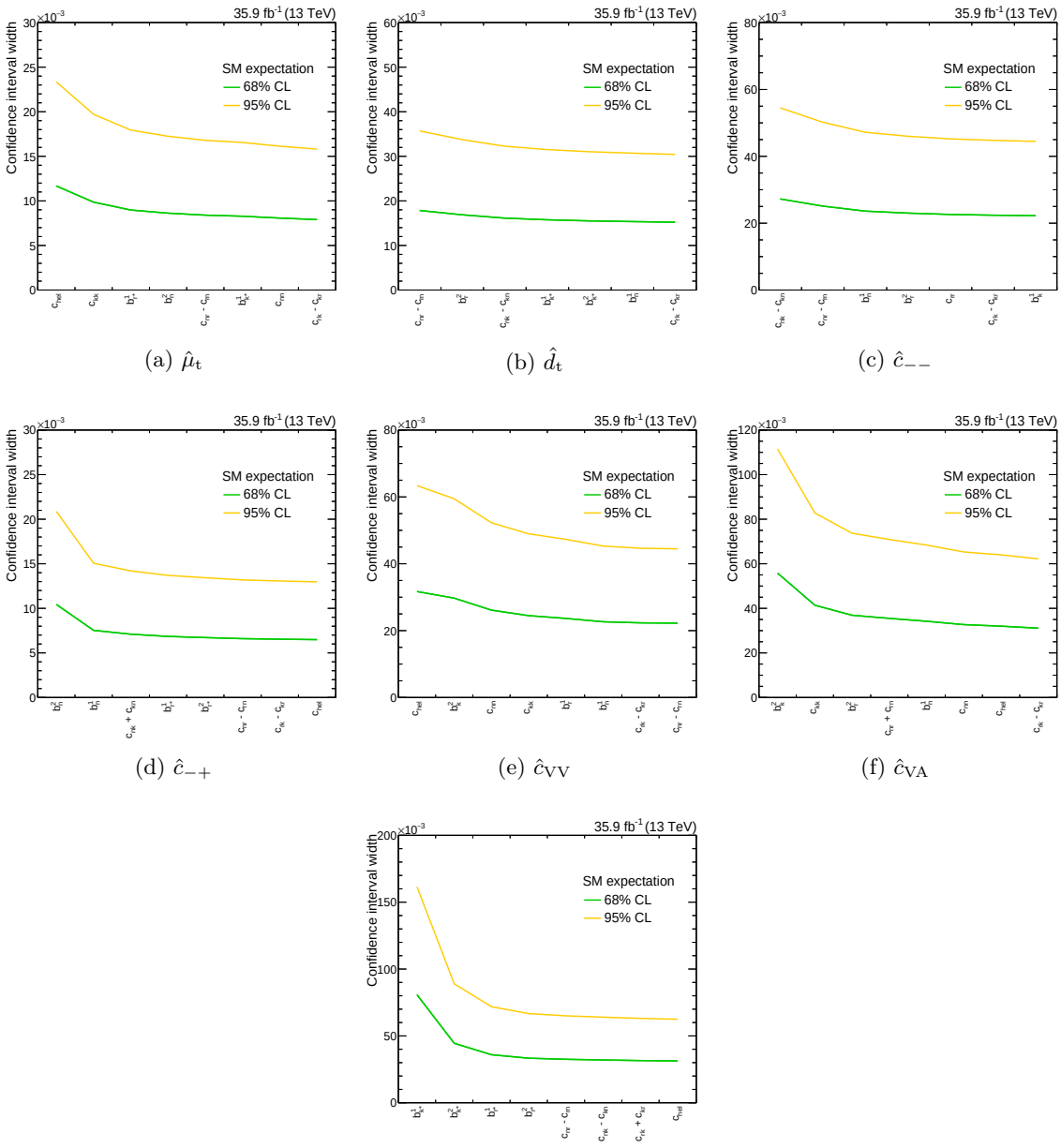

(a) $\hat{\mu}_\mathrm{t}$ (b) $\hat{d}_\mathrm{t}$ (c) $\hat{c}_{--}$

(d) $\hat{c}_{-+}$ (e) $\hat{c}_{\mathrm{VV}}$ (f) $\hat{c}_{\mathrm{VA}}$

(g) $\hat{c}_{\mathrm{AV}}$

Figure F.4: Evolution of total uncertainty of all considered operators after removing intradependent observables. $\hat{c}_1$, $\hat{c}_3$ and $\hat{c}_1 - \hat{c}_2 + \hat{c}_3$ are not shown as they are related by approximately constant factors to $\hat{c}_{\mathrm{VV}}$, $\hat{c}_{\mathrm{VA}}$ and $\hat{c}_{\mathrm{AV}}$.